

AD-A262 594



AFIT/DS/ENG/93M-01

①

20001013190

DESIGN AND PERFORMANCE EVALUATION  
OF A GAS CHROMATOGRAPH MICROMACHINED  
IN A SINGLE CRYSTAL SILICON SUBSTRATE

DISSERTATION

Rocky Russell Reston  
Captain, USAF

AFIT/DS/ENG/93M-01

DTIC  
S ELECTE D  
APR 05 1993  
E

93-06858



Approved for public release; distribution unlimited

98 4 02 017

AFIT/DS/ENG/93M-01

DESIGN AND PERFORMANCE EVALUATION  
OF A GAS CHROMATOGRAPH MICROMACHINED  
IN A SINGLE CRYSTAL SILICON SUBSTRATE

DISSERTATION

Presented to the Faculty of the School of Engineering  
of the Air Force Institute of Technology  
Air University  
In Partial Fulfillment of the  
Requirements for the Degree of  
Doctor of Philosophy

Rocky Russell Reston, B.S.E.E., M.S.E.E.  
Captain, USAF

February, 1993

DTIC QUALITY INSPECTED 4

Accession For	
NTIS	CRA&i <input checked="" type="checkbox"/>
DTIC	TAB <input type="checkbox"/>
Unannounced	<input type="checkbox"/>
Justification _____	
By _____	
Distribution / _____	
Availability Codes	
Dist	Avail and/or Special
A-1	

Approved for public release; distribution unlimited

AFIT/DS/ENG/93M-01

DESIGN AND PERFORMANCE EVALUATION  
OF A GAS CHROMATOGRAPH MICROMACHINED  
IN A SINGLE CRYSTAL SILICON SUBSTRATE

Rocky Russell Reston, B.S.E.E., M.S.E.E.

Captain, USAF

Approved:

Edward S. Kolesar 10 Feb 93

Edward S. Kolesar, Chairman

Matthew Kabrisky 10 FEB 93

Matthew Kabrisky

Yung K. Yeo 10 Feb '93

Yung K. Yeo

Mark G. Mehalic 10 Feb 93

Mark Mehalic

Robert A. Calico, Jr.

Robert A. Calico, Jr.  
Dean, School of Engineering

## *Preface*

I would like to express my sincerest appreciation to my advisor, Lt Col Edward Kolesar. His guidance kept me on the path when I was tempted to stray, and his dedication to our profession exemplifies those qualities which I would most like to emulate. I would also like to thank the members of this committee, Dr Matthew Kabrisky, Dr Yung Yeo, Maj Mark Mehalic, and Dr Milton Franke, for their advice throughout this investigation. In addition, I would like to thank Dr Dave Erwin and Dr Johnathan Kiel of the Armstrong Laboratory (AL/OEDR, Brooks AFB, TX 78235-5301) as well as Dr Japnell Braun, Dr Gary Miller, and Dr John Lavoie of EG & G Mound Applied Technologies (Miamisburg, OH 45343-0987) for their financial and material support.

I would also like to express my appreciation for the opportunities, motivation and support provided by my parents, Beverly and Russell. It was their guidance and encouragement that helped me pursue a career in science.

Finally, I am truly grateful to my wife, Denise. Without her companionship and understanding, none of this would have been possible. She kept my spirits up when I encountered difficulties, and accepted the burden of occasional solitude with undeniable grace.

Rocky Russell Reston

## Table of Contents

	Page
Preface . . . . .	iii
Table of Contents . . . . .	iv
List of Figures . . . . .	x
List of Tables . . . . .	xxviii
List of Symbols . . . . .	xxx
Abstract . . . . .	xxxviii
 I. Introduction . . . . .	 1
1.1 Objective . . . . .	2
1.2 Summary . . . . .	2
 II. Gas Chromatography . . . . .	 3
2.1 Mobile Phase . . . . .	3
2.2 Sample Injection System . . . . .	4
2.3 Columns . . . . .	6
2.3.1 Column Types . . . . .	6
2.3.2 Column Theory . . . . .	7
2.4 Micromachined Column Theory . . . . .	17
2.4.1 Column Permeability for a Two-Sided Rectangular Column . . . . .	19
2.4.2 Golay Solution for the Van Deemter Equation of a Micromachined Column . . . . .	25
2.4.3 Micromachined Column Summary . . . . .	29
2.5 Detectors . . . . .	30

	Page
2.5.1 Thermal Conductivity Detector (TCD) . . . . .	30
2.5.2 Ionization Detectors . . . . .	33
2.5.3 Quartz Crystal Microbalance Detector (QCMD) . . . . .	36
2.5.4 Hall Electrolytic Conductivity Detector (HECD) . . . . .	37
2.5.5 Chemiresistor Detector . . . . .	37
2.5.6 Detection Techniques Specific to Ammonia and Nitrogen Dioxide . . . . .	39
2.5.7 Detector Summary . . . . .	41
2.6 Summary . . . . .	41
 III. Micromachining and Related Fabrication Techniques . . . . .	 50
3.1 Micromachining . . . . .	50
3.1.1 Isotropic Etching . . . . .	52
3.1.2 Anisotropic Etching . . . . .	55
3.2 Thin Films . . . . .	63
3.3 Anodic Bonding . . . . .	65
3.3.1 MMGC Column Requirements . . . . .	65
3.3.2 Theory . . . . .	65
3.4 Summary . . . . .	66
 IV. Micromachined Gas Chromatograph and Performance Evaluation System De- sign . . . . .	 68
4.1 Micromachined Gas Chromatograph Design . . . . .	68
4.1.1 Stationary Phase . . . . .	68
4.1.2 Micromachined Sample Injection System . . . . .	76
4.1.3 Detector Considerations . . . . .	80
4.1.4 Micromachined Gas Chromatograph Design Summary . . . . .	86
4.2 Design of the Performance Evaluation System for the Microma- chined Gas Chromatograph . . . . .	86

	Page
4.2.1 Gas Generation and Delivery System . . . . .	87
4.2.2 Instrumentation System . . . . .	89
4.2.3 Performance Evaluation System Design Summary . . .	92
<b>V. Micromachined Gas Chromatograph Fabrication . . . . .</b>	<b>94</b>
5.1 Mask Design and Fabrication . . . . .	94
5.2 Wet Chemical Etching . . . . .	96
5.2.1 Potassium Hydroxide (KOH) Etch 1: V-Groove Etch . .	96
5.2.2 Potassium Hydroxide (KOH) Etch 2: Thermal Conduc- tivity Detector Cell Etch . . . . .	98
5.2.3 Isotropic Etch: Column Etch . . . . .	102
5.3 Stationary Phase Deposition . . . . .	109
5.3.1 Sublimation . . . . .	109
5.3.2 Selective Removal . . . . .	114
5.4 Final Assembly . . . . .	123
5.4.1 Gas Inlet . . . . .	123
5.4.2 Thermistor Insertion . . . . .	123
5.4.3 Anodic Bonding . . . . .	123
5.4.4 Chemiresistor Attachment . . . . .	128
5.5 Summary . . . . .	128
<b>VI. Micromachined Gas Chromatograph and Subsystems Evaluation . . . . .</b>	<b>137</b>
6.1 Thermistor Performance Evaluation . . . . .	137
6.2 Flow Rate Verification . . . . .	139
6.3 Chemiresistor Performance Evaluation . . . . .	142
6.3.1 Temperature Dependence . . . . .	142
6.3.2 Challenge Gas Concentration Response Characteristics .	145
6.4 Micromachined Gas Chromatograph Performance Evaluation . .	148
6.4.1 Retention Time . . . . .	148

	Page
6.4.2 Challenge Gas Concentration Response Characteristics .	151
6.5 Summary . . . . .	155
VII. Time-Domain Performance Model of the Micromachined Gas Chromatograph	163
7.1 Model Parameters . . . . .	163
7.2 Model Implementation . . . . .	164
7.3 Separation Factor . . . . .	166
7.4 Summary . . . . .	172
VIII. Conclusions and Recommendations . . . . .	177
Appendix A. Fabrication Processes . . . . .	179
A.1 Wafer Cleaning . . . . .	179
A.2 Oxidation . . . . .	179
A.3 Photoresist Deposition . . . . .	179
A.4 Photoresist Cure . . . . .	180
A.5 Photolithographic Mask Exposure . . . . .	180
A.6 Photoresist Development . . . . .	180
A.7 Silicon Dioxide Etch . . . . .	181
A.8 KOH Etch . . . . .	181
A.9 Isotropic Etch . . . . .	181
A.10 Rinse, Dry and Inspection . . . . .	181
Appendix B. Copper Phthalocyanine . . . . .	182
B.1 Background . . . . .	182
B.2 Qualitative CuPc Thin Film Characterization . . . . .	184
B.2.1 Infrared Spectra . . . . .	185
B.2.2 Scanning Electron Microscopy . . . . .	187
B.2.3 Transmission Electron Microscopy (TEM) and Transmis- sion Electron Diffraction (TED) . . . . .	188

	Page
B.3 Summary . . . . .	189
Appendix C. Experimental Characterization of the Adsorption Effects of NO <sub>2</sub> on the Electrical Conductivity of Copper Phthalocyanine . . . .	204
C.1 Langmuir Adsorption . . . . .	204
C.2 Chemiresistor Electrical Impedance . . . . .	205
C.3 Parameters . . . . .	207
C.4 Current Response . . . . .	207
Appendix D. Micromachined Gas Chromatograph Model Program . . . . .	210
D.1 Variable Declarations . . . . .	211
D.2 Subroutine Declarations . . . . .	212
D.3 Main Program . . . . .	218
Appendix E. Data Reduction . . . . .	219
E.1 Non-Linear Least-Squares Curve Fitting . . . . .	219
E.1.1 Main Program . . . . .	223
E.2 Chemiresistor Evaluation . . . . .	224
E.2.1 Response Function . . . . .	224
E.2.2 Computer Program Subroutine . . . . .	225
E.2.3 Data Reduction Example . . . . .	227
E.3 Micromachined Gas Chromatograph Evaluation . . . . .	228
E.3.1 Computer Program Subroutine . . . . .	228
E.3.2 MMGC Data Reduction Example . . . . .	229
E.4 Adsorption Evaluation . . . . .	230
E.4.1 Computer Program Subroutine . . . . .	231
E.4.2 Data Reduction Example . . . . .	232
Appendix F. Golay's Theory . . . . .	238

	Page
Appendix G.    Mathematica Code for Figures . . . . .	244
Appendix H.    Flowmeter Calibration Table . . . . .	248
Appendix I.    Chemiresistor Evaluation Data . . . . .	249
Appendix J.    Micromachined Gas Chromatograph Evaluation Data . . . . .	271
Appendix K.    Adsorption Evaluation Data . . . . .	305
Bibliography . . . . .	315
Vita . . . . .	325

### List of Figures

Figure	Page
1. Block Diagram of a Modern Gas Chromatograph . . . . .	4
2. Typical Liquid Sample Injection System . . . . .	5
3. Typical Gas Sample Injection System (a) Fill Position and (b) Inject Position	6
4. Fundamental Gas Chromatography Column Configurations . . . . .	7
5. Typical Resolutions of the Two Major Column Types . . . . .	8
6. Graphical Representation of the Separation of Three Components (Represented by Squares, Triangles, and Circles) at (a) $t = 0$ (injection), (b) $t > 0$ , and (c) $t \gg 0$ (Gas Flow is Represented by the Large Arrows, and Diffusion is Represented by the Small Arrows) . . . . .	9
7. Plot Used to Calculate the Number of Theoretical Plates. $V_R$ Represents the True Retention Volume, $V'_R$ Represents the Measured Retention Volume (Including the Dead Volume), $V_d$ Represents the Dead Volume of the System, and $w$ Represents the Approximate Width of the Elution Curve . . . . .	10
8. Plot of the van Deemter Equation (Solid Curve). The Horizontal Dashed Line Represents the Contribution of $A$ , the Sloped Dashed Line Represents the Contribution of $Cv_c$ , and the $(B/v_c)$ -Term Contributes the Remainder	13
9. Normalized Velocity of the Carrier Gas in a Column with Pressure Gradients of 1:1, 4:1, 7:1, and 10:1 ( $P_i:P_o$ ) . . . . .	15
10. Rectangular Column Cross Sections. (a) Two-Sided Rectangular (Sidewall Effects Neglected) and (b) Full Rectangular . . . . .	19
11. Coordinate System for Column Analysis (the $y$ - $z$ Origin is Taken to be the Lower Center of the Rectangular Cross Section). One Half of the Column's Height is $z_o$ , and $Y$ Represents the Column's Width . . . . .	20
12. Normalized Velocity Distribution Across a Two-Sided Rectangular Column	21
13. Velocity Distribution Across a Rectangular Column . . . . .	23
14. Percentage of Velocity Attained by a Two-Sided Rectangular Column versus the Aspect Ratio of a Rectangular Column . . . . .	24

Figure	Page
15. Flow Rate versus Input Pressure for a Two-Sided Rectangular Column, a Rectangular Column (Aspect Ratio 4:1), and Actual Data Points for a Micromachined Column. Column Length is 0.5 m, Gas Viscosity is 200 $\mu$ poise, Output Pressure is 1 atmosphere, Column Width is 130 $\mu$ m, and Column Height is 30 $\mu$ m . . . . .	25
16. Column Geometry Used to Develop the Modified van Deemter Equation. The Radius of the Circular Column is $r_0$ , and the Carrier Gas is Flowing in the $x$ Direction (the Column Parameters are Independent of $\theta$ ) . . . . .	26
17. Normalized Separation Factor for Round and Two-Sided Rectangular Columns ( $z_0 = r_0$ ) . . . . .	29
18. General Flame Ionization Detector (FID) versus a Selective Nitrogen-Phosphorus Detector (NPD) . . . . .	43
19. Current-Voltage Characteristics of a Typical Thermistor . . . . .	44
20. Thermistor Sensitivity Relative to Current Fluctuations . . . . .	44
21. Standard Thermal Conductivity Detector (TCD) and Schematic of the Wheatstone Bridge Configuration . . . . .	45
22. Flame Ionization Detector (FID) . . . . .	46
23. Photoionization Detector (PID) . . . . .	46
24. Electron Capture Detector (ECD), Cross-Section Detector (CSD), Argon Detector, and Helium Detector . . . . .	47
25. Nitrogen-Phosphorus Detector (NPD) . . . . .	47
26. Hall Electrolytic Conductivity Detector (HECD) . . . . .	48
27. Chemiresistor Conductivity Detector with Interelectrode Spacing, $s$ , and Finger Length, $f_l$ . . . . .	49
28. Potential Column Cross Sections. (a) (100)-Oriented Silicon Anisotropically Etched with Potassium Hydroxide (KOH), (b) (110)-Oriented Silicon Anisotropically Etched with KOH, and (c) Silicon Isotropically Etched with HF-HNO <sub>3</sub> . . . . .	52
29. Isoetch Curves for Silicon (HF:HNO <sub>3</sub> :CH <sub>3</sub> COOH System) . . . . .	55

Figure	Page
30. Diamond Crystal Structure of Silicon with Lattice Constant ' $a$ ' where Each Silicon Atom is Surrounded by Four Nearest Neighbors (Highlighted by the Internal Darkened Bars) . . . . .	56
31. Miller Indices of Important Silicon Crystal Planes with Lattice Constant ' $a$ '	57
32. Cross-Section of a Typical V-Groove Etch . . . . .	61
33. Cross-Section of a Typical Feedthrough Feature Etch . . . . .	62
34. Cross-Section of a Typical Inverted Truncated Pyramid Etch . . . . .	63
35. Typical Thin Film Evaporation Apparatus . . . . .	64
36. Anodic Bonding Mechanism . . . . .	67
37. Block Diagram of a Micromachined Gas Chromatograph . . . . .	69
38. Separation Factor (SF) versus $z_0$ for Various Input Pressures (20 psi, 30 psi, 40 psi, and 60 psi) for a Column with a Solid Stationary Phase. The Column Length is 0.9 m, Partition Coefficient is 100, Gas Viscosity is 200 $\mu$ poise, Stationary Phase Thickness is 0.2 $\mu$ m, Column Width is 300 $\mu$ m, and the Diffusion Coefficient of the Carrier Gas was Calculated Based upon the Average Pressure and a Temperature of 50°C . . . . .	74
39. Separation Factor (SF) versus $z_0$ for Various Partition Coefficients (1, 10, 100, and 1000) for a Column with a Solid Stationary Phase. The Column Length is 0.9 m, Input Pressure is 40 psi, Gas Viscosity is 200 $\mu$ poise, Stationary Phase Thickness is 0.2 $\mu$ m, Column Width is 300 $\mu$ m, Diffusion Coefficient of the Carrier Gas was Calculated Based upon the Average Pressure and a Temperature of 50°C . . . . .	75
40. Miniature Sample Injection Valve . . . . .	76
41. Exploded View of the Sample Injection Valve Used in this Investigation . .	77
42. Sample Injection Valve Connections . . . . .	78
43. Sample Injection Valve Operation . . . . .	78
44. Example of a Miniature Thermal Conductivity Detector Fabricated with a Thermistor (Top View) . . . . .	83
45. Example of a Miniature Thermal Conductivity Detector Fabricated with a Thermistor (Side View) . . . . .	84

Figure	Page
46. Improved Thermal Conductivity Detector Cell and Chemiresistor Interface Design . . . . .	85
47. Schematic of the Gas Generation System . . . . .	87
48. Schematic of the Instrumentation System . . . . .	90
49. Side View of Heater Attachment . . . . .	91
50. Photolithographic Mask Design Used for the First Potassium Hydroxide (KOH) Etch (KOH1) (V-Groove and Alignment Marks). The Outer Circle is 4 inches in Diameter . . . . .	95
51. Photolithographic Mask Design Used for the Second Potassium Hydroxide (KOH) Etch (KOH2) (TCD Cavity). The Outer Circle is 4 inches in Diameter . . . . .	96
52. Photolithographic Mask Design Used for the Isotropic Column Etch. The Outer Circle is 4 inches in Diameter . . . . .	97
53. Representative Feedthrough Structure After the First Potassium Hydroxide (KOH) Etch Process . . . . .	99
54. Representative V-Groove Structure After the First Potassium Hydroxide (KOH) Etch Process . . . . .	100
55. Representative Thermistor Cavity Structure After the Second Potassium Hydroxide (KOH) Etch Process . . . . .	101
56. Representative Silicon Column Cross-Section After the Isotropic Column Etch Process . . . . .	103
57. Expanded View of a Representative Silicon Column Cross-Section After the Isotropic Column Etch Process . . . . .	104
58. Top View of a Representative Silicon Column After the Isotropic Column Etch Process. The Diameter of the Area Shown is Approximately 4 cm . . . . .	105
59. Top View of a Section of a Representative Silicon Column After the Isotropic Column Etch Process . . . . .	106
60. Representative TCD Cell Structure After the Isotropic Column Etch Process. The Chemiresistor Interface is Provided by the Lead Channel . . . . .	107
61. Representative Gas Inlet Structure After the Isotropic Column Etch Process . . . . .	108
62. Representative Glass Column Cross-Section After the Isotropic Column Etch Process . . . . .	110

Figure	Page
63. Expanded View of a Representative Glass Column Cross-Section After the Isotropic Column Etch Process . . . . .	111
64. Top View of a Representative Glass Column After the Isotropic Column Etch Process. The Diameter of the Area Shown is Approximately 4 cm . . . . .	112
65. Top View of a Section of a Representative Glass Column After the Isotropic Column Etch Process . . . . .	113
66. Representative Profile for the 2000 Å Thick Copper Phthalocyanine Thin Film	114
67. Column After Deposition of a 2000 Å Thick CuPc Thin Film . . . . .	115
68. Column After a 2000 Å Thick CuPc Thin Film Deposition Contrasted with a Masked Area of the Etched Column (the Column Width is Approximately 300 μm) . . . . .	116
69. Column After the Final Polishing Step of the 2000 Å Thick CuPc Thin Film	117
70. Column After the Final Polishing Step of the 2000 Å Thick CuPc Thin Film Contrasted with a Masked Area of the Etched Column (the Column Width is Approximately 300 μm) . . . . .	118
71. Column After the Final Polishing Step of the 2000 Å Thick CuPc Thin Film (Silicon Wafer Surface). The Diameter of the Area Shown is Approximately 4 cm . . . . .	119
72. Section of the MMGC Column After the Final Polishing Step of the 2000 Å Thick CuPc Thin Film (Silicon Wafer Surface) . . . . .	120
73. Column After the Final Polishing Step of the 2000 Å Thick CuPc Thin Film (Glass Plate Surface). The Diameter of the Area Shown is Approximately 4 cm . . . . .	121
74. Section of the MMGC Column After the Final Polishing Step of the 2000 Å Thick CuPc Thin Film (Glass Plate Surface) . . . . .	122
75. Side View of Interconnect Tubing Attachment . . . . .	124
76. Gas Inlet After Attachment of the Interconnect Tubing (the Column Width is Approximately 300 μm) . . . . .	125
77. Typical Thermistor Bead (the Diameter of the Bead is Approximately 125 μm)	126
78. TCD Cell with Thermistor Installed (the Column Width is Approximately 300 μm) . . . . .	127

Figure	Page
79. MOSIS Fabricated Chemiresistor (Before CuPc Coating). The Interdigitated Electrode Structure is Approximately 2 mm by 2 mm . . . . .	129
80. MOSIS Fabricated Chemiresistor (Magnified View of the Interdigitated Electrode Structure) . . . . .	130
81. MOSIS Fabricated Chemiresistor (After the CuPc Thin Film Deposition—2000 Å Thick). The Interdigitated Electrode Structure is Approximately 2 mm by 2 mm . . . . .	131
82. MOSIS Fabricated Chemiresistor (Magnified Side View of the Interdigitated Electrode Structure). The CuPc Film Thickness was Increased to 3 $\mu$ m for Illustrative Purposes . . . . .	132
83. Front View of the 4-inch by 4-inch Assembled Micromachined Gas Chromatograph . . . . .	134
84. Back View of the 4-inch by 4-inch Assembled Micromachined Gas Chromatograph (Before the Chemiresistor's Placement) . . . . .	135
85. Back View of the 4-inch by 4-inch Assembled Micromachined Gas Chromatograph (After the Chemiresistor's Placement) . . . . .	136
86. Voltage versus Current Plot for the Thermistors in MMGC #1 and MMGC #2	138
87. MMGC Flowrate Verification Results Using a Nitrogen Sample . . . . .	141
88. Temperature Dependence of the Chemiresistor's Baseline and Response to a 75 ppm Concentration of Nitrogen Dioxide . . . . .	143
89. Temperature Dependence of the Chemiresistor's Baseline and Response to a 6300 ppm Concentration of Ammonia . . . . .	144
90. Concentration Dependence of the Chemiresistor's Response to Nitrogen Dioxide . . . . .	147
91. Concentration Dependence of the Chemiresistor's Response to Ammonia .	148
92. Micromachined Gas Chromatograph Evaluation Protocol. The Time Required for One Complete Evaluation Cycle is 220 minutes . . . . .	150
93. Temperature Dependence of the Nitrogen Dioxide Retention Times . . . . .	151
94. Temperature Dependence of the Ammonia Retention Times . . . . .	152
95. Experimentally Determined Partition Ratios for NO <sub>2</sub> Relative to Copper Phthalocyanine Correlated with Reciprocal Temperature . . . . .	153

Figure	Page
96. Concentration Dependence of the Nitrogen Dioxide Response for the Micromachined Gas Chromatograph . . . . .	154
97. Concentration Dependence of the Ammonia Response for the Micromachined Gas Chromatograph . . . . .	155
98. Gaussian Representation of Gas Elution (55°C, 6300 ppm NH <sub>3</sub> , and 75 ppm NO <sub>2</sub> ). Vertical Axis is the Magnitude of the Differentiated Chemiresistor Response . . . . .	156
99. Gaussian Representation of Gas Elution (66°C, 6300 ppm NH <sub>3</sub> , and 75 ppm NO <sub>2</sub> ). Vertical Axis is the Magnitude of the Differentiated Chemiresistor Response . . . . .	157
100. Gaussian Representation of Gas Elution (80°C, 6300 ppm NH <sub>3</sub> , and 75 ppm NO <sub>2</sub> ). Vertical Axis is the Magnitude of the Differentiated Chemiresistor Response . . . . .	158
101. Gaussian Representation of Gas Elution (80°C, 6300 ppm NH <sub>3</sub> , and 270 ppm NO <sub>2</sub> ). Vertical Axis is the Magnitude of the Differentiated Chemiresistor Response . . . . .	159
102. Gaussian Representation of Gas Elution (80°C, 6900 ppm NH <sub>3</sub> , and 560 ppm NO <sub>2</sub> ). Vertical Axis is the Magnitude of the Differentiated Chemiresistor Response . . . . .	160
103. Gaussian Representation of Gas Elution (80°C, 1620 ppm NH <sub>3</sub> , and 540 ppm NO <sub>2</sub> ). Vertical Axis is the Magnitude of the Differentiated Chemiresistor Response . . . . .	161
104. Gaussian Representation of Gas Elution (80°C, 480 ppm NH <sub>3</sub> , and 540 ppm NO <sub>2</sub> ). Vertical Axis is the Magnitude of the Differentiated Chemiresistor Response . . . . .	162
105. Flowchart for the Micromachined Gas Chromatograph Time-Domain Model	165
106. Column Cross Section Depicting the Movement of a Single NO <sub>2</sub> Molecule .	166
107. Typical Histogram for the Time-Domain Micromachined Gas Chromatograph Model of MMGC #1 at 55°C . . . . .	167
108. Typical Histogram for the Time-Domain Micromachined Gas Chromatograph Model of MMGC #1 at 68°C . . . . .	168

Figure	Page
109. Typical Histogram for the Time-Domain Micromachined Gas Chromatograph Model of MMGC #1 at 80°C . . . . .	169
110. Typical Histogram for the Time-Domain Micromachined Gas Chromatograph Model of MMGC #2 at 56°C . . . . .	170
111. Typical Histogram for the Time-Domain Micromachined Gas Chromatograph Model of MMGC #2 at 68°C . . . . .	171
112. Typical Histogram for the Time-Domain Micromachined Gas Chromatograph Model of MMGC #2 at 83°C . . . . .	172
113. Retention Times for the Time-Domain Gas Chromatograph Model Compared with the Experimental Data . . . . .	173
114. Separation Factor (SF) versus $z_0$ for a Column with CuPc as a Stationary Phase. The Column Length is 0.9 m, Gas Viscosity is 200 $\mu$ poise, Stationary Phase Thickness is 0.2 $\mu$ m, Column Width is 300 $\mu$ m, and the Input Pressure is 40 psi . . . . .	175
115. Micromachined Chemiresistor and Thermistor Detector Cells . . . . .	178
116. Chemical Structure of Copper Phthalocyanine (CuPc) . . . . .	183
117. Proposed Interactions Between Adsorbed Gases and Copper Phthalocyanine for (a) Nitrogen Dioxide and (b) Ammonia. The Arrows Denote the Transfer of Electrons . . . . .	185
118. Simplified Energy Band Structure of a Copper Phthalocyanine Polycrystalline p-Type Semiconductor (a) in Vacuo, (b) Saturated with NO <sub>2</sub> , and (c) Saturated with NH <sub>3</sub> . . . . .	190
119. Infrared Spectrum for Alpha-Phase Copper Phthalocyanine . . . . .	191
120. Infrared Spectrum for a Sodium Chloride IR Substrate . . . . .	192
121. Infrared Spectrum for the 6600 Å Thick Copper Phthalocyanine Thin Film Sublimed onto a Sodium Chloride Substrate . . . . .	193
122. Infrared Spectrum for the 7700 Å Thick Copper Phthalocyanine Thin Film Sublimed onto a Sodium Chloride Substrate . . . . .	194
123. Infrared Absorption Peaks from the Spectra for the 6600 Å and 7700 Å Thick, Experimentally Deposited Thin Films of Copper Phthalocyanine, Compared to Reported Peaks (Normalized with Respect to the 1120 cm <sup>-1</sup> Peak) . . .	195

Figure	Page
124. Infrared Spectrum for the 6600 Å Thick Copper Phthalocyanine Thin Film Sublimed onto a Sodium Chloride Substrate after Exposure to 770 ppm of NO <sub>2</sub> for 46 hours . . . . .	196
125. Infrared Spectrum for the 6600 Å Thick Copper Phthalocyanine Thin Film Sublimed onto a Sodium Chloride Substrate after Exposure to 770 ppm of NO <sub>2</sub> for 46 hours and Subsequent Purging at 150°C in a Nitrogen Ambient for 1.5 hours . . . . .	197
126. Infrared Absorption Peaks from the Spectra for the 6600 Å Thick Copper Phthalocyanine Thin Film for the Pre-Exposed, 770 ppm NO <sub>2</sub> Exposed, and Purged Conditions (Normalized with Respect to the 1120 cm <sup>-1</sup> Peak) . . .	198
127. Infrared Spectrum for the 7700 Å Thick Copper Phthalocyanine Thin Film Sublimed onto a Sodium Chloride Substrate after Exposure to 3700 ppm of NH <sub>3</sub> for 3 hours . . . . .	199
128. Infrared Spectrum for the 7700 Å Thick Copper Phthalocyanine Thin Film Sublimed onto a Sodium Chloride Substrate after Exposure to 3700 ppm of NH <sub>3</sub> for 3 hours and Subsequent Purging at 150°C in a Nitrogen Ambient for 1.5 hours . . . . .	200
129. Infrared Absorption Peaks from the Spectra for the 7700 Å Thick Copper Phthalocyanine Thin Film for the Pre-Exposed, 3700 ppm NH <sub>3</sub> Exposed, and Purged Conditions (Normalized with Respect to the 1120 cm <sup>-1</sup> Peak)	201
130. Transmission Electron Micrograph for a 500 Å Thick Copper Phthalocyanine Thin Film Sublimed onto a Carbon Grid . . . . .	202
131. Electron Diffraction Pattern for a 500 Å Thick Copper Phthalocyanine Thin Film Sublimed onto a Carbon Grid . . . . .	203
132. Resistive Filaments in the Chemiresistor's Electrical Impedance Model . .	206
133. Active (shaded) Area of the Interdigitated Chemiresistor Mapped into a Continuous Chemiresistor of Width, $w_c$ , and Length, $s$ . The Edge View Depicts the Volume of Gas Within One Mean Free Path, $\lambda$ , of the Active Area of the Chemiresistor . . . . .	209
134. Logical Flow of the Computer Program for the Micromachined Gas Chromatograph Model . . . . .	210
135. Flowchart for the Non-Linear Least-Squares Curve Fitting Program . . . .	220

Figure	Page
136. Gaussian Functional with $a_1 = 1$ pA, $a_2 = 4$ minutes, and $a_3 = 2$ minutes .	225
137. Erf Functional with $a_1 = 1$ pA, $a_2 = 4$ minutes, and $a_3 = 2$ minutes . . . .	226
138. Chemiresistor Evaluation Experimental Data Fit to the Functional Given by Equation 96 (75 ppm NO <sub>2</sub> at 80°C). The Baseline is 14.7 pA, and the Net Response is 1.9 pA . . . . .	227
139. Double Erf Functional with $a_1 = 1$ pA, $a_2 = 3$ minutes, $a_3 = 2$ minutes, $a_4 = 1$ pA, $a_5 = 9$ minutes, $a_6 = 2$ minutes, and $a_7 = 1$ pA . . . . .	229
140. First Trial of a Micromachined Gas Chromatograph Evaluation (75 ppm NO <sub>2</sub> , 6300 ppm NH <sub>3</sub> , at 66°C) . . . . .	230
141. Second Trial of a Micromachined Gas Chromatograph Evaluation (75 ppm NO <sub>2</sub> , 6300 ppm NH <sub>3</sub> , at 66°C) . . . . .	231
142. Third Trial of a Micromachined Gas Chromatograph Evaluation (75 ppm NO <sub>2</sub> , 6300 ppm NH <sub>3</sub> , at 66°C) . . . . .	232
143. Fourth Trial of a Micromachined Gas Chromatograph Evaluation (75 ppm NO <sub>2</sub> , 6300 ppm NH <sub>3</sub> , at 66°C) . . . . .	233
144. Fifth Trial of a Micromachined Gas Chromatograph Evaluation (75 ppm NO <sub>2</sub> , 6300 ppm NH <sub>3</sub> , at 66°C) . . . . .	234
145. Sixth Trial of a Micromachined Gas Chromatograph Evaluation (75 ppm NO <sub>2</sub> , 6300 ppm NH <sub>3</sub> , at 66°C) . . . . .	235
146. Micromachined Gas Chromatograph Evaluation Experimental Data Fitted to the Functional (75 ppm NO <sub>2</sub> , 6300 ppm NH <sub>3</sub> , and 66°C). The NH <sub>3</sub> Response is 1.5 pA, the NH <sub>3</sub> Peak Center is at 3.8 minutes, the NH <sub>3</sub> Peak Width is 1.7 minutes, the NO <sub>2</sub> Response is 2.1 pA, the NO <sub>2</sub> Peak Center is at 29.4 minutes, and the NO <sub>2</sub> Peak Width is 18.9 minutes . . . . .	236
147. Adsorption Evaluation Data Fit to a Function (100 ppb NO <sub>2</sub> at 100°C). $\alpha$ is $4.4 \times 10^{-4}$ (ppb · min) <sup>-1</sup> , $\beta$ is 1.2 (min) <sup>-1</sup> , and $a_r$ is 11 percent . . . . .	237
148. Chemiresistor Evaluation (75 ppm NO <sub>2</sub> and 50°C). The Response is 7.4 pA, and the Baseline is 5.2 pA . . . . .	251
149. Chemiresistor Evaluation (75 ppm NO <sub>2</sub> and 55°C). The Response is 5.8 pA, and the Baseline is 6.4 pA . . . . .	251

Figure	Page
150. Chemiresistor Evaluation (75 ppm NO <sub>2</sub> and 60°C). The Response is 5.1 pA, and the Baseline is 7 pA . . . . .	252
151. Chemiresistor Evaluation (75 ppm NO <sub>2</sub> and 68°C). The Response is 3.3 pA, and the Baseline is 9.4 pA . . . . .	252
152. Chemiresistor Evaluation (75 ppm NO <sub>2</sub> and 70°C). The Response is 3.1 pA, and the Baseline is 10.2 pA . . . . .	253
153. Chemiresistor Evaluation (75 ppm NO <sub>2</sub> and 80°C). The Response is 1.9 pA, and the Baseline is 14.7 pA . . . . .	253
154. Chemiresistor Evaluation (75 ppm NO <sub>2</sub> and 90°C). The Response is 1.3 pA, and the Baseline is 20.2 pA . . . . .	254
155. Chemiresistor Evaluation (255 ppm NO <sub>2</sub> and 70°C). The Response is 6.2 pA, and the Baseline is 10.1 pA . . . . .	254
156. Chemiresistor Evaluation (255 ppm NO <sub>2</sub> and 80°C). The Response is 3.9 pA, and the Baseline is 14.3 pA . . . . .	255
157. Chemiresistor Evaluation (255 ppm NO <sub>2</sub> and 90°C). The Response is 2.5 pA, and the Baseline is 20 pA . . . . .	255
158. Chemiresistor Evaluation (350 ppm NO <sub>2</sub> and 70°C). The Response is 7.2 pA, and the Baseline is 10.1 pA . . . . .	256
159. Chemiresistor Evaluation (350 ppm NO <sub>2</sub> and 80°C). The Response is 4.5 pA, and the Baseline is 14.5 pA . . . . .	256
160. Chemiresistor Evaluation (350 ppm NO <sub>2</sub> and 90°C). The Response is 3 pA, and the Baseline is 20.2 pA . . . . .	257
161. Chemiresistor Evaluation (460 ppm NO <sub>2</sub> and 70°C). The Response is 8.3 pA, and the Baseline is 10 pA . . . . .	257
162. Chemiresistor Evaluation (460 ppm NO <sub>2</sub> and 80°C). The Response is 5.4 pA, and the Baseline is 14 pA . . . . .	258
163. Chemiresistor Evaluation (460 ppm NO <sub>2</sub> and 90°C). The Response is 3.6 pA, and the Baseline is 20 pA . . . . .	258
164. Chemiresistor Evaluation (570 ppm NO <sub>2</sub> and 70°C). The Response is 9.4 pA, and the Baseline is 9.8 pA . . . . .	259

Figure	Page
165. Chemiresistor Evaluation (570 ppm NO <sub>2</sub> and 80°C). The Response is 5.9 pA, and the Baseline is 14.2 pA . . . . .	259
166. Chemiresistor Evaluation (570 ppm NO <sub>2</sub> and 90°C). The Response is 3.6 pA, and the Baseline is 20.3 pA . . . . .	260
167. Chemiresistor Evaluation (6300 ppm NH <sub>3</sub> and 55°C). The Response is 1.5 pA, and the Baseline is 6 pA . . . . .	260
168. Chemiresistor Evaluation (6300 ppm NH <sub>3</sub> and 60°C). The Response is 1.6 pA, and the Baseline is 7.2 pA . . . . .	261
169. Chemiresistor Evaluation (6300 ppm NH <sub>3</sub> and 70°C). The Response is 1.5 pA, and the Baseline is 10 pA . . . . .	261
170. Chemiresistor Evaluation (6300 ppm NH <sub>3</sub> and 75°C). The Response is 1.6 pA, and the Baseline is 12.2 pA . . . . .	262
171. Chemiresistor Evaluation (6300 ppm NH <sub>3</sub> and 80°C). The Response is 1.6 pA, and the Baseline is 14.4 pA . . . . .	262
172. Chemiresistor Evaluation (5000 ppm NH <sub>3</sub> and 70°C). The Response is 1.5 pA, and the Baseline is 10.2 pA . . . . .	263
173. Chemiresistor Evaluation (5000 ppm NH <sub>3</sub> and 80°C). The Response is 1.6 pA, and the Baseline is 14.1 pA . . . . .	263
174. Chemiresistor Evaluation (5000 ppm NH <sub>3</sub> and 90°C). The Response is 1.6 pA, and the Baseline is 20.2 pA . . . . .	264
175. Chemiresistor Evaluation (4000 ppm NH <sub>3</sub> and 70°C). The Response is 1.5 pA, and the Baseline is 10 pA . . . . .	264
176. Chemiresistor Evaluation (4000 ppm NH <sub>3</sub> and 80°C). The Response is 1.5 pA, and the Baseline is 14.2 pA . . . . .	265
177. Chemiresistor Evaluation (4000 ppm NH <sub>3</sub> and 90°C). The Response is 1.6 pA, and the Baseline is 20.2 pA . . . . .	265
178. Chemiresistor Evaluation (3000 ppm NH <sub>3</sub> and 70°C). The Response is 1.6 pA, and the Baseline is 10 pA . . . . .	266
179. Chemiresistor Evaluation (3000 ppm NH <sub>3</sub> and 80°C). The Response is 1.4 pA, and the Baseline is 14.2 pA . . . . .	266

Figure	Page
180. Chemiresistor Evaluation (3000 ppm NH <sub>3</sub> and 90°C). The Response is 1.6 pA, and the Baseline is 20 pA . . . . .	267
181. Chemiresistor Evaluation (1500 ppm NH <sub>3</sub> and 70°C). The Response is 0.8 pA, and the Baseline is 9.9 pA . . . . .	267
182. Chemiresistor Evaluation (1500 ppm NH <sub>3</sub> and 80°C). The Response is 0.8 pA, and the Baseline is 14.5 pA . . . . .	268
183. Chemiresistor Evaluation (1500 ppm NH <sub>3</sub> and 90°C). The Response is 0.7 pA, and the Baseline is 20 pA . . . . .	268
184. Chemiresistor Evaluation (500 ppm NH <sub>3</sub> and 70°C). The Response is 0.4 pA, and the Baseline is 10.2 pA . . . . .	269
185. Chemiresistor Evaluation (500 ppm NH <sub>3</sub> and 80°C). The Response is 0.3 pA, and the Baseline is 14.4 pA . . . . .	269
186. Chemiresistor Evaluation (500 ppm NH <sub>3</sub> and 90°C). The Response is 0.3 pA, and the Baseline is 20.1 pA . . . . .	270
187. Micromachined Gas Chromatograph #1 Evaluation (75 ppm NO <sub>2</sub> , 6300 ppm NH <sub>3</sub> , and 55°C). The NH <sub>3</sub> Response is 1.5 pA, the NH <sub>3</sub> Peak Center is at 4 minutes, the NH <sub>3</sub> Peak Width is 1.6 minutes, the NO <sub>2</sub> Response is 3.5 pA, the NO <sub>2</sub> Peak Center is at 44.8 minutes, and the NO <sub>2</sub> Peak Width is 21.3 minutes . . . . .	275
188. Micromachined Gas Chromatograph #1 Evaluation (75 ppm NO <sub>2</sub> , 6300 ppm NH <sub>3</sub> , and 58°C). The NH <sub>3</sub> Response is 1.5 pA, the NH <sub>3</sub> Peak Center is at 3.7 minutes, the NH <sub>3</sub> Peak Width is 1.6 minutes, the NO <sub>2</sub> Response is 2.9 pA, the NO <sub>2</sub> Peak Center is at 40.5 minutes, and the NO <sub>2</sub> Peak Width is 22.7 minutes . . . . .	276
189. Micromachined Gas Chromatograph #1 Evaluation (75 ppm NO <sub>2</sub> , 6300 ppm NH <sub>3</sub> , and 66°C). The NH <sub>3</sub> Response is 1.5 pA, the NH <sub>3</sub> Peak Center is at 3.8 minutes, the NH <sub>3</sub> Peak Width is 1.7 minutes, the NO <sub>2</sub> Response is 2.1 pA, the NO <sub>2</sub> Peak Center is at 29.4 minutes, and the NO <sub>2</sub> Peak Width is 18.9 minutes . . . . .	277

190. Micromachined Gas Chromatograph #1 Evaluation (75 ppm NO<sub>2</sub>, 6300 ppm NH<sub>3</sub>, and 73°C). The NH<sub>3</sub> Response is 1.4 pA, the NH<sub>3</sub> Peak Center is at 3.4 minutes, the NH<sub>3</sub> Peak Width is 1.5 minutes, the NO<sub>2</sub> Response is 1.7 pA, the NO<sub>2</sub> Peak Center is at 23.3 minutes, and the NO<sub>2</sub> Peak Width is 19.1 minutes . . . . . 278
191. Micromachined Gas Chromatograph #1 Evaluation (75 ppm NO<sub>2</sub>, 6300 ppm NH<sub>3</sub>, and 75°C). The NH<sub>3</sub> Response is 1.6 pA, the NH<sub>3</sub> Peak Center is at 4 minutes, the NH<sub>3</sub> Peak Width is 1.6 minutes, the NO<sub>2</sub> Response is 1.4 pA, the NO<sub>2</sub> Peak Center is at 20.4 minutes, and the NO<sub>2</sub> Peak Width is 20.5 minutes . . . . . 279
192. Micromachined Gas Chromatograph #1 Evaluation (75 ppm NO<sub>2</sub>, 6300 ppm NH<sub>3</sub>, and 80°C). The NH<sub>3</sub> Response is 1.5 pA, the NH<sub>3</sub> Peak Center is at 4 minutes, the NH<sub>3</sub> Peak Width is 1.9 minutes, the NO<sub>2</sub> Response is 1.1 pA, the NO<sub>2</sub> Peak Center is at 19.5 minutes, and the NO<sub>2</sub> Peak Width is 12.8 minutes . . . . . 280
193. Micromachined Gas Chromatograph #1 Evaluation (210 ppm NO<sub>2</sub>, 6300 ppm NH<sub>3</sub>, and 80°C). The NH<sub>3</sub> Response is 1.4 pA, the NH<sub>3</sub> Peak Center is at 3.6 minutes, the NH<sub>3</sub> Peak Width is 1.6 minutes, the NO<sub>2</sub> Response is 1.7 pA, the NO<sub>2</sub> Peak Center is at 17.4 minutes, and the NO<sub>2</sub> Peak Width is 13.4 minutes . . . . . 281
194. Micromachined Gas Chromatograph #1 Evaluation (270 ppm NO<sub>2</sub>, 6300 ppm NH<sub>3</sub>, and 80°C). The NH<sub>3</sub> Response is 1.5 pA, the NH<sub>3</sub> Peak Center is at 3.7 minutes, the NH<sub>3</sub> Peak Width is 1.7 minutes, the NO<sub>2</sub> Response is 2 pA, the NO<sub>2</sub> Peak Center is at 18.5 minutes, and the NO<sub>2</sub> Peak Width is 15.6 minutes . . . . . 282
195. Micromachined Gas Chromatograph #1 Evaluation (500 ppm NO<sub>2</sub>, 6300 ppm NH<sub>3</sub>, and 80°C). The NH<sub>3</sub> Response is 1.5 pA, the NH<sub>3</sub> Peak Center is at 3.7 minutes, the NH<sub>3</sub> Peak Width is 1.7 minutes, the NO<sub>2</sub> Response is 2.3 pA, the NO<sub>2</sub> Peak Center is at 17.9 minutes, and the NO<sub>2</sub> Peak Width is 14.5 minutes . . . . . 283

196. Micromachined Gas Chromatograph #1 Evaluation (560 ppm NO<sub>2</sub>, 6900 ppm NH<sub>3</sub>, and 80°C). The NH<sub>3</sub> Response is 1.5 pA, the NH<sub>3</sub> Peak Center is at 3.7 minutes, the NH<sub>3</sub> Peak Width is 1.7 minutes, the NO<sub>2</sub> Response is 2.7 pA, the NO<sub>2</sub> Peak Center is at 17.5 minutes, and the NO<sub>2</sub> Peak Width is 12.9 minutes . . . . . 284
197. Micromachined Gas Chromatograph #1 Evaluation (500 ppm NO<sub>2</sub>, 7300 ppm NH<sub>3</sub>, and 80°C). The NH<sub>3</sub> Response is 1.7 pA, the NH<sub>3</sub> Peak Center is at 3.8 minutes, the NH<sub>3</sub> Peak Width is 1.9 minutes, the NO<sub>2</sub> Response is 2.3 pA, the NO<sub>2</sub> Peak Center is at 17.8 minutes, and the NO<sub>2</sub> Peak Width is 14.5 minutes . . . . . 285
198. Micromachined Gas Chromatograph #1 Evaluation (500 ppm NO<sub>2</sub>, 4800 ppm NH<sub>3</sub>, and 80°C). The NH<sub>3</sub> Response is 1.6 pA, the NH<sub>3</sub> Peak Center is at 3.1 minutes, the NH<sub>3</sub> Peak Width is 1.4 minutes, the NO<sub>2</sub> Response is 2.3 pA, the NO<sub>2</sub> Peak Center is at 19.4 minutes, and the NO<sub>2</sub> Peak Width is 15.3 minutes . . . . . 286
199. Micromachined Gas Chromatograph #1 Evaluation (500 ppm NO<sub>2</sub>, 4100 ppm NH<sub>3</sub>, and 80°C). The NH<sub>3</sub> Response is 1.6 pA, the NH<sub>3</sub> Peak Center is at 3.3 minutes, the NH<sub>3</sub> Peak Width is 1.9 minutes, the NO<sub>2</sub> Response is 2.2 pA, the NO<sub>2</sub> Peak Center is at 19.1 minutes, and the NO<sub>2</sub> Peak Width is 15.5 minutes . . . . . 287
200. Micromachined Gas Chromatograph #1 Evaluation (500 ppm NO<sub>2</sub>, 3500 ppm NH<sub>3</sub>, and 80°C). The NH<sub>3</sub> Response is 1.5 pA, the NH<sub>3</sub> Peak Center is at 3.7 minutes, the NH<sub>3</sub> Peak Width is 1.9 minutes, the NO<sub>2</sub> Response is 2.4 pA, the NO<sub>2</sub> Peak Center is at 18.5 minutes, and the NO<sub>2</sub> Peak Width is 12.6 minutes . . . . . 288
201. Micromachined Gas Chromatograph #1 Evaluation (500 ppm NO<sub>2</sub>, 2700 ppm NH<sub>3</sub>, and 80°C). The NH<sub>3</sub> Response is 1.3 pA, the NH<sub>3</sub> Peak Center is at 3.9 minutes, the NH<sub>3</sub> Peak Width is 1.6 minutes, the NO<sub>2</sub> Response is 2.2 pA, the NO<sub>2</sub> Peak Center is at 19.7 minutes, and the NO<sub>2</sub> Peak Width is 14.7 minutes . . . . . 289

202. Micromachined Gas Chromatograph #1 Evaluation (500 ppm NO<sub>2</sub>, 1600 ppm NH<sub>3</sub>, and 80°C). The NH<sub>3</sub> Response is 0.8 pA, the NH<sub>3</sub> Peak Center is at 4.2 minutes, the NH<sub>3</sub> Peak Width is 1.4 minutes, the NO<sub>2</sub> Response is 2.2 pA, the NO<sub>2</sub> Peak Center is at 20.7 minutes, and the NO<sub>2</sub> Peak Width is 14.6 minutes . . . . . 290
203. Micromachined Gas Chromatograph #1 Evaluation (500 ppm NO<sub>2</sub>, 480 ppm NH<sub>3</sub>, and 80°C). The NH<sub>3</sub> Response is 0.3 pA, the NH<sub>3</sub> Peak Center is at 4.1 minutes, the NH<sub>3</sub> Peak Width is 1.4 minutes, the NO<sub>2</sub> Response is 2.2 pA, the NO<sub>2</sub> Peak Center is at 18.5 minutes, and the NO<sub>2</sub> Peak Width is 13.8 minutes . . . . . 291
204. Micromachined Gas Chromatograph #2 Evaluation (90 ppm NO<sub>2</sub>, 5760 ppm NH<sub>3</sub>, and 57°C). The NH<sub>3</sub> Response is 1.6 pA, the NH<sub>3</sub> Peak Center is at 2.3 minutes, the NH<sub>3</sub> Peak Width is 1.5 minutes, the NO<sub>2</sub> Response is 4.2 pA, the NO<sub>2</sub> Peak Center is at 29.1 minutes, and the NO<sub>2</sub> Peak Width is 17.3 minutes . . . . . 292
205. Micromachined Gas Chromatograph #2 Evaluation (90 ppm NO<sub>2</sub>, 5700 ppm NH<sub>3</sub>, and 61°C). The NH<sub>3</sub> Response is 1.6 pA, the NH<sub>3</sub> Peak Center is at 2.5 minutes, the NH<sub>3</sub> Peak Width is 1.4 minutes, the NO<sub>2</sub> Response is 3.3 pA, the NO<sub>2</sub> Peak Center is at 23.7 minutes, and the NO<sub>2</sub> Peak Width is 13.7 minutes . . . . . 293
206. Micromachined Gas Chromatograph #2 Evaluation (90 ppm NO<sub>2</sub>, 5700 ppm NH<sub>3</sub>, and 68°C). The NH<sub>3</sub> Response is 1.6 pA, the NH<sub>3</sub> Peak Center is at 2.3 minutes, the NH<sub>3</sub> Peak Width is 1.1 minutes, the NO<sub>2</sub> Response is 2.5 pA, the NO<sub>2</sub> Peak Center is at 19.9 minutes, and the NO<sub>2</sub> Peak Width is 14.4 minutes . . . . . 294
207. Micromachined Gas Chromatograph #2 Evaluation (90 ppm NO<sub>2</sub>, 5700 ppm NH<sub>3</sub>, and 75°C). The NH<sub>3</sub> Response is 1.4 pA, the NH<sub>3</sub> Peak Center is at 2.6 minutes, the NH<sub>3</sub> Peak Width is 1.4 minutes, the NO<sub>2</sub> Response is 1.9 pA, the NO<sub>2</sub> Peak Center is at 14.5 minutes, and the NO<sub>2</sub> Peak Width is 15.1 minutes . . . . . 295

208. Micromachined Gas Chromatograph #2 Evaluation (90 ppm NO<sub>2</sub>, 5700 ppm NH<sub>3</sub>, and 83°C). The NH<sub>3</sub> Response is 1.4 pA, the NH<sub>3</sub> Peak Center is at 2.6 minutes, the NH<sub>3</sub> Peak Width is 1.2 minutes, the NO<sub>2</sub> Response is 1.4 pA, the NO<sub>2</sub> Peak Center is at 10.7 minutes, and the NO<sub>2</sub> Peak Width is 10.9 minutes . . . . . 296
209. Micromachined Gas Chromatograph #2 Evaluation (140 ppm NO<sub>2</sub>, 5700 ppm NH<sub>3</sub>, and 83°C). The NH<sub>3</sub> Response is 1.8 pA, the NH<sub>3</sub> Peak Center is at 2.6 minutes, the NH<sub>3</sub> Peak Width is 1.4 minutes, the NO<sub>2</sub> Response is 2 pA, the NO<sub>2</sub> Peak Center is at 8.4 minutes, and the NO<sub>2</sub> Peak Width is 13.2 minutes . . . . . 297
210. Micromachined Gas Chromatograph #2 Evaluation (240 ppm NO<sub>2</sub>, 5700 ppm NH<sub>3</sub>, and 83°C). The NH<sub>3</sub> Response is 1.6 pA, the NH<sub>3</sub> Peak Center is at 2.9 minutes, the NH<sub>3</sub> Peak Width is 1.2 minutes, the NO<sub>2</sub> Response is 2.2 pA, the NO<sub>2</sub> Peak Center is at 8.3 minutes, and the NO<sub>2</sub> Peak Width is 15.1 minutes . . . . . 298
211. Micromachined Gas Chromatograph #2 Evaluation (350 ppm NO<sub>2</sub>, 5700 ppm NH<sub>3</sub>, and 83°C). The NH<sub>3</sub> Response is 1.5 pA, the NH<sub>3</sub> Peak Center is at 2.4 minutes, the NH<sub>3</sub> Peak Width is 1.2 minutes, the NO<sub>2</sub> Response is 2.4 pA, the NO<sub>2</sub> Peak Center is at 11.6 minutes, and the NO<sub>2</sub> Peak Width is 11.5 minutes . . . . . 299
212. Micromachined Gas Chromatograph #2 Evaluation (500 ppm NO<sub>2</sub>, 5700 ppm NH<sub>3</sub>, and 83°C). The NH<sub>3</sub> Response is 1.5 pA, the NH<sub>3</sub> Peak Center is at 2.4 minutes, the NH<sub>3</sub> Peak Width is 1.4 minutes, the NO<sub>2</sub> Response is 2.6 pA, the NO<sub>2</sub> Peak Center is at 10.3 minutes, and the NO<sub>2</sub> Peak Width is 11.4 minutes . . . . . 300
213. Micromachined Gas Chromatograph #2 Evaluation (500 ppm NO<sub>2</sub>, 4500 ppm NH<sub>3</sub>, and 83°C). The NH<sub>3</sub> Response is 1.8 pA, the NH<sub>3</sub> Peak Center is at 2.5 minutes, the NH<sub>3</sub> Peak Width is 1.7 minutes, the NO<sub>2</sub> Response is 2.7 pA, the NO<sub>2</sub> Peak Center is at 11.9 minutes, and the NO<sub>2</sub> Peak Width is 10.8 minutes . . . . . 301

Figure	Page
214. Micromachined Gas Chromatograph #2 Evaluation (500 ppm NO <sub>2</sub> , 2800 ppm NH <sub>3</sub> , and 83°C). The NH <sub>3</sub> Response is 1.5 pA, the NH <sub>3</sub> Peak Center is at 2.6 minutes, the NH <sub>3</sub> Peak Width is 1.4 minutes, the NO <sub>2</sub> Response is 2.3 pA, the NO <sub>2</sub> Peak Center is at 11.3 minutes, and the NO <sub>2</sub> Peak Width is 12.5 minutes . . . . .	302
215. Micromachined Gas Chromatograph #2 Evaluation (500 ppm NO <sub>2</sub> , 1800 ppm NH <sub>3</sub> , and 83°C). The NH <sub>3</sub> Response is 0.8 pA, the NH <sub>3</sub> Peak Center is at 2.3 minutes, the NH <sub>3</sub> Peak Width is 1.2 minutes, the NO <sub>2</sub> Response is 2.6 pA, the NO <sub>2</sub> Peak Center is at 11 minutes, and the NO <sub>2</sub> Peak Width is 10.6 minutes . . . . .	303
216. Micromachined Gas Chromatograph #2 Evaluation (500 ppm NO <sub>2</sub> , 500 ppm NH <sub>3</sub> , and 83°C). The NH <sub>3</sub> Response is 0.5 pA, the NH <sub>3</sub> Peak Center is at 2.8 minutes, the NH <sub>3</sub> Peak Width is 1.7 minutes, the NO <sub>2</sub> Response is 3.3 pA, the NO <sub>2</sub> Peak Center is at 8.4 minutes, and the NO <sub>2</sub> Peak Width is 14.7 minutes . . . . .	304
217. Adsorption Evaluation (100 ppb NO <sub>2</sub> ). $\alpha$ is $3.9 \times 10^{-4}$ (ppb · min) <sup>-1</sup> , $\beta$ is 1.0 (min) <sup>-1</sup> , and $\alpha_r$ is 11 percent . . . . .	306
218. Adsorption Evaluation (100 ppb NO <sub>2</sub> ). $\alpha$ is $4.1 \times 10^{-4}$ (ppb · min) <sup>-1</sup> , $\beta$ is 1.0 (min) <sup>-1</sup> , and $\alpha_r$ is 13 percent . . . . .	307
219. Adsorption Evaluation (100 ppb NO <sub>2</sub> ). $\alpha$ is $4.4 \times 10^{-4}$ (ppb · min) <sup>-1</sup> , $\beta$ is 1.2 (min) <sup>-1</sup> , and $\alpha_r$ is 11 percent . . . . .	308
220. Adsorption Evaluation (200 ppb NO <sub>2</sub> ). $\alpha$ is $4.1 \times 10^{-4}$ (ppb · min) <sup>-1</sup> , $\beta$ is 1.4 (min) <sup>-1</sup> , and $\alpha_r$ is 12 percent . . . . .	309
221. Adsorption Evaluation (200 ppb NO <sub>2</sub> ). $\alpha$ is $5.4 \times 10^{-4}$ (ppb · min) <sup>-1</sup> , $\beta$ is 1.2 (min) <sup>-1</sup> , and $\alpha_r$ is 14 percent . . . . .	310
222. Adsorption Evaluation (200 ppb NO <sub>2</sub> ). $\alpha$ is $3.8 \times 10^{-4}$ (ppb · min) <sup>-1</sup> , $\beta$ is 1.0 (min) <sup>-1</sup> , and $\alpha_r$ is 17 percent . . . . .	311
223. Adsorption Evaluation (400 ppb NO <sub>2</sub> ). $\alpha$ is $3.1 \times 10^{-4}$ (ppb · min) <sup>-1</sup> , $\beta$ is 1.5 (min) <sup>-1</sup> , and $\alpha_r$ is 14 percent . . . . .	312
224. Adsorption Evaluation (400 ppb NO <sub>2</sub> ). $\alpha$ is $3.1 \times 10^{-4}$ (ppb · min) <sup>-1</sup> , $\beta$ is 1.5 (min) <sup>-1</sup> , and $\alpha_r$ is 15 percent . . . . .	313
225. Adsorption Evaluation (400 ppb NO <sub>2</sub> ). $\alpha$ is $2.7 \times 10^{-4}$ (ppb · min) <sup>-1</sup> , $\beta$ is 1.4 (min) <sup>-1</sup> , and $\alpha_r$ is 14 percent . . . . .	314

### List of Tables

Table	Page
1. Chemical and Toxicological Properties of NO <sub>2</sub> and NH <sub>3</sub> . . . . .	2
2. Gas Chromatograph Detector Functions . . . . .	30
3. Micromachined Gas Chromatograph (MMGC) Detector Candidate Summary. Estimated Sensitivities are Given as Concentrations Within a 10 $\mu$ l Sample Loop. . . . .	42
4. Planar Density Properties of the Major Silicon Crystal Planes . . . . .	57
5. Approximate Etch Rate of the (100) Plane in the KOH-DIW System ( $\mu$ m/min). Concentration Reported as a Percent by Weight in Water . . . . .	58
6. Approximate Etch Rate of Silicon Dioxide in the KOH-DIW System ( $\text{\AA}$ /min). Concentration Reported as a Percent by Weight in Water . . . . .	58
7. Etch Ratio of (100)-Oriented Silicon Relative to Silicon Dioxide. Concentra- tion Reported as a Percent by Weight in Water . . . . .	59
8. Time (Hours) Required to Etch 300 $\mu$ m of (100)-Oriented Silicon. Concen- tration Reported as a Percent by Weight in Water . . . . .	59
9. Approximate Oxide Thickness ( $\mu$ m) Required to Mask an Etch of 300 $\mu$ m into (100)-Oriented Silicon. Concentration Reported as a Percent by Weight in Water . . . . .	60
10. Range of the Number of Molecules Injected for the Three Sample Loop Vol- umes Compared to the Column's Capacity . . . . .	79
11. Summary of Micromachined Gas Chromatograph Components . . . . .	86
12. Theoretical, Experimental, and Computed Model Values for the Separation Factor (SF) . . . . .	174
13. Revised Theoretical, Experimental, and Computed Model Values for the Sep- aration Factor (SF) . . . . .	174
14. Physical, Operational, and Experimental Parameters Used to Calculate the Separation Factor (SF) at 80°C . . . . .	176
15. Chemical and Physical Properties of Copper Phthalocyanine . . . . .	182

Table	Page
16. Reported and Experimental Values for Copper Phthalocyanine Crystal Plane Spacings . . . . .	188
17. Flowmeter Calibration Table (Gilmont Instruments, Inc., Model 8555-8654)	248
18. Chemiresistor Evaluation Summary with NO <sub>2</sub> as the Challenge Gas . . . .	249
19. Chemiresistor Evaluation Summary with NH <sub>3</sub> as the Challenge Gas . . . .	250
20. Summary of the NO <sub>2</sub> Parameters Collected from MMGC #1 During the Micromachined Gas Chromatograph Evaluation . . . . .	271
21. Summary of the NH <sub>3</sub> Parameters Collected from MMGC #1 During the Micromachined Gas Chromatograph Evaluation . . . . .	272
22. Summary of the NO <sub>2</sub> Parameters Collected from MMGC #2 During the Micromachined Gas Chromatograph Evaluation . . . . .	273
23. Summary of the NH <sub>3</sub> Parameters Collected from MMGC #2 During the Micromachined Gas Chromatograph Evaluation . . . . .	274
24. Summary of the Parameters Collected During the Adsorption Evaluation .	305

### *List of Symbols*

$s$	Cross-Sectional Area of Column or Crystal Lattice Constant
A	Ampere
$A$	Multipath Diffusion Constant
$\text{\AA}$	Angstroms ( $10^{-10}$ Meter)
$a_1 - a_7$	Curve Fitting Parameters
AFIT	Air Force Institute of Technology
Al	Aluminum
$A_n$	Coefficients of the Characteristic Solution
$a_r$	Adsorption Ratio
Au	Gold
$B$	Molecular Diffusion Constant
$B_o$	Molecular Diffusion Constant at the Column's Outlet
$c$	Partition Coefficient
C	Carbon
$^{\circ}\text{C}$	Degrees Centigrade
$C$	Resistance to Mass Transfer Constant
$C_g$	Resistance to Mass Transfer (in Carrier Gas) Constant
$\text{CH}_3\text{COOH}$	Acetic Acid
cm	Centimeter ( $10^{-2}$ Meter)
$C_o$	Minimum Detectable Analyte Concentration
$c_p$	Concentration in Parts-Per-Million (ppm)
Cr	Chromium
$C_s$	Resistance to Mass Transfer (in Stationary Phase) Constant
CSD	Cross-Section Detector
Cu	Copper
CuPc	Copper Phthalocyanine
$D$	Diffusion Coefficient
$D_1$	Stationary Phase Diffusion Coefficient
$d_c$	Column Diameter
$d_e$	Etch Depth for an Inverted Truncated Pyramid
$d_f$	Effective Depth for a Feedthrough Etch
$d_g$	Etch Depth for a V-Groove
$d_v$	Virtual V-Groove Depth for an Inverted Truncated Pyramid

DC	Direct Current
DIMP	Diisopropyl Methylphosphonate
DIW	Deionized Water
E	Electric Field
$e^-$	Electron
$E_a$	Heat of Adsorption
EC	Electronegative Component
$E_c$	Conduction Band
ECD	Electron Capture Detector
$E_f$	Fermi Energy Level
$E_i$	Intrinsic Fermi Energy Level
$E_{NH_3}$	Ammonia Energy Level
$E_{NO_2}$	Nitrogen Dioxide Energy Level
$E_{trap}$	Trap Energy Level
eV	Electron Volt
$E_v$	Valence Band
$f, f(x, t)$	Gas Packet Density
$\bar{f}$	Average Gas Packet Diffusion
F	Effective Surface Area Ratio
FID	Flame Ionization Detector
$f_l$	Chemiresistor Finger Length
$f_p$	Permeation Tube Flow Rate
$g$	Apparent Plate Height Correction Factor
$g(t)$	Gaussian Functional
GC	Gas Chromatograph
GPIB	General Purpose Interface Bus
$h$	Height Equivalent of a Theoretical Plate (Plate Height)
$h^+$	Hole
$h_1, h_2$	$z$ -axis Miller Index for Planes 1 and 2
$H$	Apparent Plate Height
$H_2$	Hydrogen Molecule
$H_2O$	Water
$H_2O_2$	Hydrogen Peroxide
$H_2SiF_6$	Fluosilicic Acid
$H_2SO_4$	Sulfuric Acid

HCl	Hydrochloric Acid
$h_{cr}$	Cylindrical Crystallite Height
HECD	Hall Electrolytic Conductivity Detector
HF	Hydrofluoric Acid
HNA	Hydrofluoric Acid, Nitric Acid, and Acetic Acid Etch System
HNO <sub>3</sub>	Nitric Acid
$h_{round}$	Plate Height for a Round Column
hrs	Hours
$h_{TSR}$	Plate Height for a Two-Sided Rectangular Column
$i, I$	Generalized Current
$i$	Summation Increment Variable
IC	Integrated Circuit
$i_{conc}$	Injected Concentration
i.d., ID	Inner Diameter
in	Inch
IR	Infrared
$j$	Compressibility Correction Factor
$k$	Partition Ratio
$k_1, k_2$	y-axis Miller Index for Planes 1 and 2
$^{\circ}K$	Degrees Kelvin
$k_b$	Boltzmann's Constant
KBr	Potassium Bromide
kg	Kilogram (10 <sup>3</sup> Gram)
$k_o$	Partition Ratio Constant
KOH	Potassium Hydroxide
K $\Omega$	Kilo-Ohm (10 <sup>3</sup> Ohm)
$l_1, l_2$	z-axis Miller Index for Planes 1 and 2
$L$	Column Length
$L_{con}$	Interconnect Length
m	Meter
$m$	Moles of Gas or Generalized Mass
M	Generalized Mass
mA	Milliampere (10 <sup>-3</sup> Ampere)
$m(t)$	Double Erf Functional
mbar	Millibar (10 <sup>-3</sup> Bar)

$m_h$	Mass of a Helium Molecule
MHz	Megahertz ( $10^6$ Hertz)
min	Minute
mins	Minutes
ml	Milliliter ( $10^{-3}$ Liter)
mm	Millimeter ( $10^{-3}$ Meter)
MMGC	Micromachined Gas Chromatograph
$m_n$	Mass of a Nitrogen Dioxide Molecule
MOSIS	Metal-Oxide-Semiconductor Implementation System
ms	Millisecond ( $10^{-3}$ Second)
mW	Milliwatt ( $10^{-3}$ Watt)
M $\Omega$	Mega-Ohm ( $10^6$ Ohm)
$n$	Summation Increment Variable
N	Nitrogen
$N$	Number of Theoretical Plates or Number of Resistors
$N_2$	Nitrogen Molecule
$N_2^+$	Nitrogen Ion
$N_A$	Number of Adsorbed Sites
Na	Sodium
$Na^+$	Sodium Ion
$n_c$	Number of Molecular Collisions
$n_{conc}$	Effective Nitrogen Dioxide Concentration
$n_f$	Number of Driven Chemiresistor Fingers
ng	Nanogram ( $10^{-9}$ Gram)
$n_h$	Number of Helium Molecules
$NH_3$	Ammonia
$NH_4F$	Ammonium Fluoride
nl	Nanoliter ( $10^{-9}$ Liter)
nm	Nanometer ( $10^{-9}$ Meter)
NO	Nitrous Oxide
$NO_2$	Nitrogen Dioxide
NPD	Nitrogen-Phosphorus Thermionic Detector
o.d., OD	Outer Diameter
$OH^-$	Hydroxide Ion
$p$	Generalized Power

<b><math>P</math></b>	Generalized Pressure
<b><math>p_0</math></b>	Thermistor Characteristic Power 0
<b><math>p_1</math></b>	Thermistor Characteristic Power 1
<b><math>p_2</math></b>	Thermistor Characteristic Power 2
<b><math>pA</math></b>	Picoamperes ( $10^{-12}$ Amperes)
<b>PbPc</b>	Lead Phthalocyanine
<b>PC</b>	Personal Computer
<b><math>P_i</math></b>	Input Pressure
<b>PID</b>	Photo-Ionisation Detector
<b><math>P_{int}</math></b>	Interconnect Pressure
<b><math>P_o</math></b>	Output Pressure
<b>ppb</b>	Parts-Per-Billion
<b>ppm</b>	Parts-Per-Million
<b>psi</b>	Pounds-Per-Square Inch
<b><math>q</math></b>	Generalised Column Permeability or Fundamental Unit of Charge
<b>QCMD</b>	Quartz Crystal Microbalance Detector
<b><math>q_r</math></b>	Column Permeability for a Round Column
<b><math>q_{rec}</math></b>	Column Permeability for a Rectangular Column
<b><math>q_{TSR}</math></b>	Column Permeability for a TSR Column
<b><math>r</math></b>	Radius Variable
<b><math>R</math></b>	Universal Gas Constant
<b><math>R_A</math></b>	Adsorbed Resistance
<b><math>R_c</math></b>	Chemiresistor Resistance
<b><math>r_{cr}</math></b>	Cylindrical Crystallite Radius
<b><math>R_{dc}</math></b>	Static (Equilibrium) Thermistor Resistance
<b>RF</b>	Radio Frequency
<b><math>r_o</math></b>	Radius of a Round Column
<b><math>R_o</math></b>	Thermistor Resistance at Temperature $T_o$
<b><math>R_p</math></b>	Purged Resistance
<b><math>R_T</math></b>	Sensitivity of the Thermistor Voltage to Current
<b><math>R_{TOT}</math></b>	Total Resistance of the Chemiresistor Model
<b><math>s</math></b>	Second
<b><math>s</math></b>	Interelectrode Chemiresistor Spacing or Effective Surface Area
<b><math>S</math></b>	Separation Factor (Symbol)
<b>SAWD</b>	Surface Acoustic Wave Detector

sec	Seconds
SEM	Scanning Electron Microscopy
SF	Separation Factor (Acronym)
$\sigma_{\text{He}}$	Effective Helium Collisional Radius
Si	Silicon
$\text{Si}^{2+}$	Silicon Ion
$\text{SiO}_2$	Silicon Dioxide
$\text{Si(OH)}_2$	Disilicic Acid
$\text{Si(OH)}_4$	Orthosilicic Acid
$\text{Si(OH)}_6$	Hexasilicic Acid
$S_{\text{max}}$	Maximized Separation Factor
$\sigma_{\text{N}_2}$	Effective Nitrogen Dioxide Collisional Radius
STP	Standard Temperature and Pressure
$t$	Generalized Time
$T$	Temperature, Wafer Thickness
$T_c$	Column's Temperature
TCD	Thermal Conductivity Detector
$t_{\text{col}}$	Time Spent in a Column
$t_{\text{con}}$	Time Spent in an Interconnect
TED	Transmission Electron Diffraction
TEM	Transmission Electron Microscopy
$T_f$	Thickness of a Chemiresistor's Gas Sensitive Film
$T_{\text{int}}$	Temperature of an Interconnect
$T_o$	Temperature at which $R_o$ is Measured
$t_R$	Retention Time
$t_{rp}$	Retention Time for a Column with a Pressure Gradient
TSR	Two-Sided Rectangular (Sidewall Effects Neglected)
$T_T$	Thermistor Temperature
$T_w$	Thermistor Cell Wall Temperature
$u, du$	Second Moment, Incremental Second Moment
UV	Ultraviolet
$v$	Generalized Gas Velocity
$\bar{v}$	Average Linear Velocity
$\vec{v}$	Vector Velocity of the Carrier Gas
$V$	Generalized Gas Volume

$V$	Volts
$\dot{V}$	Volume Flow Rate
$v_c$	Velocity of the Carrier Gas
$\dot{V}_c$	Column Output Volume Flow Rate
$v_{av}$	Average Molecular Velocity
$v_{char}$	Characteristic Solution for the Column's Velocity
$V_d$	System Dead Volume
$v_{gc}$	Volume of the Gas Chromatograph
$\dot{V}_{int}$	Interconnect Volume Flow Rate
$v_{int}$	Interconnect Gas Velocity
$v_{loop}$	Volume of the Sample Loop
VLSI	Very Large Scale Integration
$v_o$	Carrier Gas Velocity at the Column's Outlet
$\dot{V}_o$	Volume Flow Rate at the Column's Outlet
$v_{opt}$	Optimised Carrier Gas Velocity
$v_p$	Velocity of a Sample Component
$v_{part}$	Particular Solution to the Column Velocity
$V_R$	True Retention Volume
$V'_R$	Total Retention Volume
$v_{rec}$	Velocity within a Rectangular Column
$\bar{v}_{rec}$	Average Velocity within a Rectangular Column
$v_{TSR}$	Velocity within a TSR Column
$\bar{v}_{TSR}$	Average Velocity within a TSR Column
$w$	Elution Curve Width
W	Watt
$W$	Width of the V-Groove Photolithographic Mask
$W_{bottom}$	Width of the Bottom of an Inverted Truncated Pyramid Etch
$w_o$	Chemiresistor Effective Width
$W_{hole}$	Width of the Hole of a Feedthrough Etch
$W_{mask}$	Width of an Inverted Truncated Pyramid Photolithographic Mask
$z$	Distance From the Column's Inlet, Direction of Gas Flow
$z_1$	$z$ -Coordinate Mapped onto a Gas Packet
$y$	Direction of Column Width
$Y$	Column Width
$z$	Direction of the Column's Height

$x_0$	One Half of the Column's Height
$\alpha$	Radiation Type or Adsorption Constant
$\beta$	Thermistor Constant, Adsorption Constant or Radiation Type
$\delta$	Dissipation Constant Seen by the Thermistor
$\Delta$	Variation of a Given Variable
$\Delta I$	Change in the Electrical Current
$\zeta$	Variable of Substitution for the Retention Time Integral
$\theta$	Angle Coordinate
$\Theta$	Normalized Surface Coverage
$\kappa$	Sticking Probability
$\lambda$	Mean Free Path of a Molecule
$\mu$	Gas Viscosity
$\mu l$	Micro-Liter ( $10^{-6}$ Liter)
$\mu m$	Micron ( $10^{-6}$ Meter)
$\mu_p$	Hole Mobility
$\mu\text{poise}$	Micro-Poise ( $10^{-6}$ Poise)
$\mu_T$	Sensitivity of the Thermistor Voltage to Temperature
$\mu_\delta$	Sensitivity of the Thermistor Voltage to the Dissipation Constant
$\nu$	Adsorption Lifetime Constant
$\rho$	Resistivity
$\tau$	Arbitrary Time
$\sigma_V$	Standard Deviation of the Elution Curve
$\phi$	Angle Between Two Crystal Planes or Ionization Efficiency
$\chi^2$	Error Measure
$\Omega$	Ohm
$\nabla$	Gradient Operator
$\nabla^2$	Laplacian Operator
$\angle$	Angle

*Abstract*

This investigation resulted in the development of a miniature gas chromatograph (GC) system using silicon micromachining and integrated circuit processing techniques. The GC is composed of a miniature sample injector incorporating a 10  $\mu$ l sample loop; a 0.9 m long, rectangular-shaped (300  $\mu$ m width and 10  $\mu$ m height) capillary column coated with a 0.2  $\mu$ m thick copper phthalocyanine (CuPc) solid phase; and a dual-detector scheme based upon a CuPc-coated chemiresistor and a commercially available, 125  $\mu$ m diameter thermal conductivity detector (TCD) bead. Silicon micromachining was employed to fabricate the interface between the sample injector and the GC column, the GC column itself, and the dual-detector cavity. A novel processing technique was developed to sublime the CuPc solid-phase coating on the GC column walls micromachined in the host silicon wafer substrate and the Pyrex cover plate which were subsequently electrostatically bouded together. The miniature GC system has demonstrated the capability to directly and completely separate parts-per-million (ppm) ammonia and nitrogen dioxide concentrations when isothermally operated (55-80°C). With a helium carrier gas and nitrogen diluent, a 10  $\mu$ l sample volume containing ammonia and nitrogen dioxide injected at 40 psi could be separated in less than 30 minutes. Relative to this accomplishment, a secondary discovery was the determination of the heat of adsorption of NO<sub>2</sub> (0.38 eV) on a CuPc thin film (0.2  $\mu$ m thick). Furthermore, this research served as a proof-of-concept concerning the utilization of a miniature GC to investigate the adsorptive properties of thin films. In addition, the development of a time-domain performance model of the miniature GC will facilitate the optimization of future miniature GCs by providing a tool to estimate their performance.

# DESIGN AND PERFORMANCE EVALUATION OF A GAS CHROMATOGRAPH MICROMACHINED IN A SINGLE CRYSTAL SILICON SUBSTRATE

## *I. Introduction*

The ability of a gas chromatograph (GC) to separate the various components of an unknown sample, and then quantify the characteristics of these components (such as their concentration) makes the GC a particularly valuable instrument for the analytical chemist. A GC is typically used as the initial stage in other analytical tools (for example, a mass spectrometer) to separate the sample components and reduce the analytical "load" on the detector (1).

Gas chromatography is also an important tool for a variety of other disciplines, including the manufacture of drugs and pharmaceuticals (2), the determination of food components (3), the study of the environment (air pollution management) (4), the evaluation of fuels (5), the diagnostic and forensic analysis of biological fluids (6), and the detection of pesticides (4). Perhaps a more specific application (and the thrust of this research) is the detection of nitrogen dioxide ( $\text{NO}_2$ )—a toxic and corrosive gas that is both an industrial pollutant and is known to be emitted when certain munition detonators age, both in storage and on the battlefield (7). Additionally, it is thought that ammonia ( $\text{NH}_3$ ) is a precursor to  $\text{NO}_2$  in the stratosphere, so a GC which was capable of separating  $\text{NO}_2$  from  $\text{NH}_3$  would facilitate environmental studies and be a valuable sensor to determine the viability of munition detonators (8, 9). A summary of the chemical and toxicological properties of  $\text{NO}_2$  and  $\text{NH}_3$  are presented in Table 1.

Unfortunately, modern GCs are much too bulky and fragile to be operated in the battlefield or in remote weapons storage facilities. Consequently, this situation, along with many others, has motivated research into alternative and portable GC configurations (11, 12). Although these alternative configurations use advanced single crystal silicon wafer

Table 1. Chemical and Toxicological Properties of NO<sub>2</sub> and NH<sub>3</sub>(10).

Property	NO <sub>2</sub>	NH <sub>3</sub>
Molecular Weight	46.01	17.04
Melting Point (°C)	-9.3	-77.7
Boiling Point (°C)	21	-33.5
Permissible Exposure Limit (ppm)	5	50
Classification	Poison and Oxidizer	Poison

micromachining processes to fabricate the major components of the GC, the fundamental operation of the portable GC is similar to conventional GCs.

### 1.1 Objective

This research is concerned with the design, fabrication and performance evaluation of a micromachined gas chromatograph (MMGC) based upon a copper phthalocyanine (CuPc) stationary phase which can separate NO<sub>2</sub> and NH<sub>3</sub> in a nitrogen diluent when helium is used as the carrier gas. The miniaturized components fabricated in this investigation include the column and the detectors. The resulting MMGC was designed to facilitate the separation and detection of NO<sub>2</sub> and NH<sub>3</sub> in a compact package—something that is currently difficult to accomplish because of the physical size and other constraints imposed by conventional laboratory GCs. Additionally, data from the MMGC has provided a unique insight into the adsorption properties (i.e., the heat of adsorption) of the CuPc stationary phase used to coat the column.

### 1.2 Summary

This dissertation begins with a review and discussion of the basic operating principles of conventional gas chromatographs and the micromachining "tools" used to fabricate the MMGC. Once this framework is established, the design of the MMGC will be addressed, followed by the actual fabrication process of the MMGC, focusing on those features which make this GC design unique. Finally, experimental data obtained from the MMGC will be presented and correlated with existing theory in the form of a time-domain simulation of the gas kinetics within the MMGC.

## II. Gas Chromatography

Chromatography, as defined by the *CRC Handbook of Chromatography*, is "a separation method in which a mixture is applied as a narrow initial zone to a stationary, porous sorbent and the components are caused to undergo differential migration by the flow of the mobile phase, a liquid or gas" (13:1). The type of mobile phase subdivides chromatography into two major classifications: gas chromatography and liquid chromatography. Since  $\text{NO}_2$  and  $\text{NH}_3$  are gases at room temperature and pressure, gas chromatography is the major subdivision of interest in this research.

There are four major components in a modern gas chromatograph: the carrier gas, the sample injection system, the column, and the detector. Figure 1 depicts a typical GC configuration, including the support components (i.e., flow meters, flow controllers, and ovens). The carrier gas, also known as the *mobile phase*, is a high purity gas that transports the sample of interest through the column. The sample injection system provides a means for introducing a known quantity of the sample into the carrier gas flowing through the column. The column itself is coated with a *stationary phase* that interacts with the sample and carrier gas, in accordance with GC theory, to produce propagation delays for the various components of the sample, causing the sample to separate into its constituents. Since the components of the original sample leave the column at different times, the detector at the output of the column can sense a physical variable (such as thermal conductivity) with respect to time. The change in the output of the detector versus time, the *chromatogram*, provides the data required to quantitatively determine the composition of the original sample (the area beneath a component's peak corresponds to the concentration of that component in the sample) (14:368).

### 2.1 Mobile Phase.

Control of the mobile phase can affect the quality and resolution of a chromatogram. It is imperative to have flow conditions which are constant and reproducible. Grob, in the *Modern Practice of Gas Chromatography*, provides a list of requirements for the mobile phase to facilitate obtaining consistent and reproducible results (16:85-87):

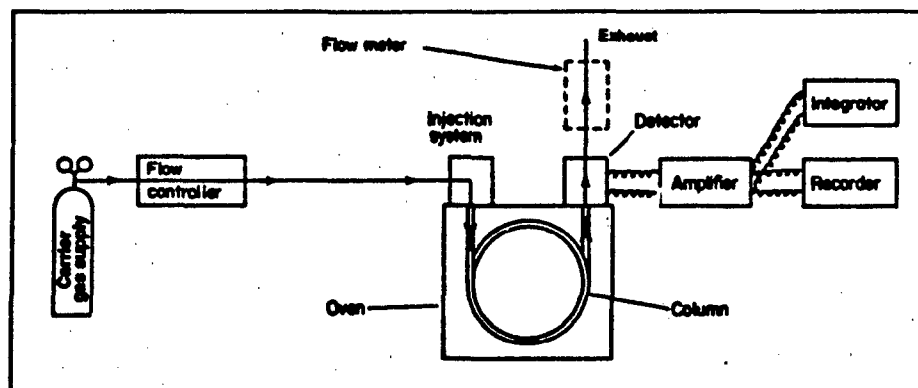


Figure 1. Block Diagram of a Modern Gas Chromatograph (15:10).

1. **Gas Cylinder or Generator:** In most cases the supply of mobile phase is from commercial cylinders. These are connected to the carrier gas system of the chromatograph by means of a reducing valve.
2. **Pressure and/or Flow Controls:** Gas valve regulators supplied by most gas suppliers are adequate to control pressure and flow...
3. **Pressure-Measuring Device:** Accurate pressure measurements are made with a manometer if needed.
4. **Flowmeter:** To monitor the flow of carrier gas, a variety of devices are available, such as differential capillary, thermal conductivity, ionization, rotameters, and calibrated soap-film tubes. Measurement of the flow may either be continuous or intermittent, and the flowmeter may be placed either in front of the column or at the carrier gas outlet. The soap-film type is most commonly used because of its economy and ease of operation.

Although maintaining a uniform gas flow is important, it is not sufficient to insure reproducible results. Perhaps the most difficult task in making a reproducible gas chromatographic analysis is the injection of the sample into the carrier gas stream (15:23).

## 2.2 Sample Injection System.

Sample injection is so vital and potentially difficult to accomplish with a significant degree of reproducibility, that Willett, in his book *Gas Chromatography*, warns: "...it [sample injection] probably gives more trouble, especially to beginners, than any other single area" (15:23). This issue is prevalent regardless of the type of injection system as long as manual operation of a syringe or valve is required. However, in some recent GCs,

provisions have been made to improve reproducibility by automating the sample injection system. Apart from the choice of a manual or automatic system, there are two fundamental methods for introducing the sample, the choice of which depends upon whether the sample is in a liquid or gaseous state.

In the first case, it is necessary to vaporize the sample before it can be separated into its components by the column. Figure 2 shows a typical sample injection system with an injection heater. The liquid sample is first drawn into a syringe, and then it is injected through a silicone rubber septum into the injection head. Since carrier gas is continually flowing from the inlet port through the injection head and into the column, any liquid sample injected through the rubber septum will be carried to the glass wool plug where it will be volatilized by the injection heater. The volatilized sample then proceeds to the column where it undergoes separation into its components.

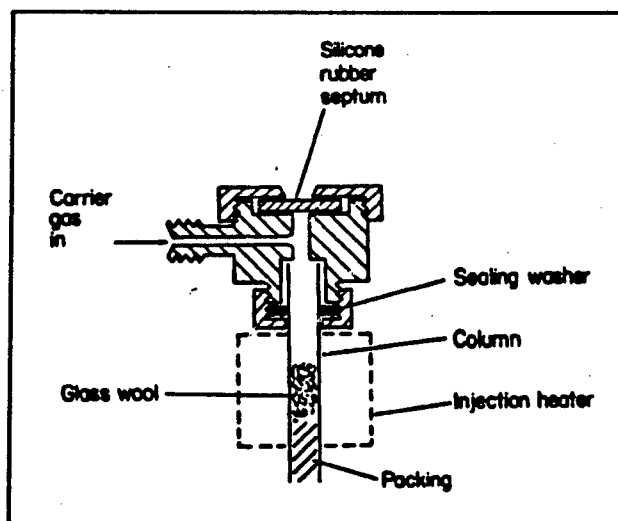


Figure 2. Typical Liquid Sample Injection System (15:20).

In the second case (gaseous samples), the gas sample of interest is transferred to a loop with a known volume. The typical sample injection system shown in Figure 3 has two valve positions. In the first position, the gas sample is forced into the sample loop (either with a vacuum pump on the waste port, or with a sample injected at the "sample in" port). When the valve is switched to the second position, the sample contained in

the loop is forced, by the pressure of the carrier gas, into the column where it undergoes separation into its components.

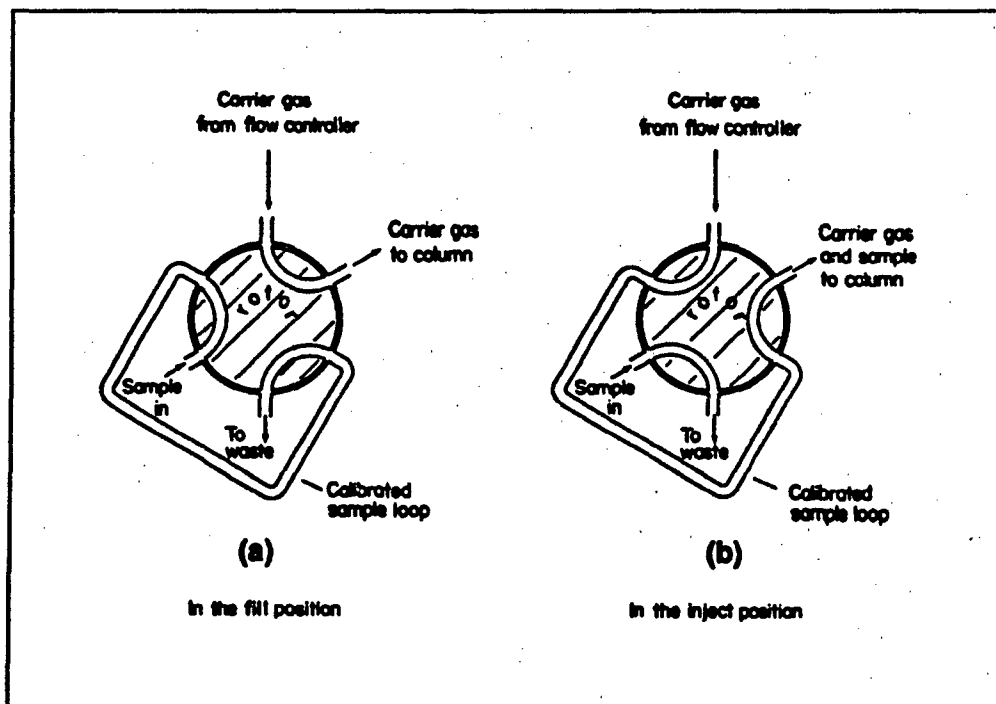


Figure 3. Typical Gas Sample Injection System (a) Fill Position and (b) Inject Position (15:23).

### 2.3 Columns.

The component which actually performs the operation unique to a GC—separation—is the column. After a sample gas has been introduced into the column, separation occurs through the interaction between the mobile phase and the stationary phase according to GC theory. The stationary phase can be deposited on the interior of the column using one of two primary techniques, resulting in the division of columns into two classes. These two types of columns are commonly referred to as *packed* and *capillary* columns (see Figure 4).

**2.3.1 Column Types.** In a packed column, the stationary phase (which is usually a nonvolatile liquid) is deposited on the surface of a coarse inert material which is *packed* into the column (alternatively, the coarse material may be a solid phase which is directly

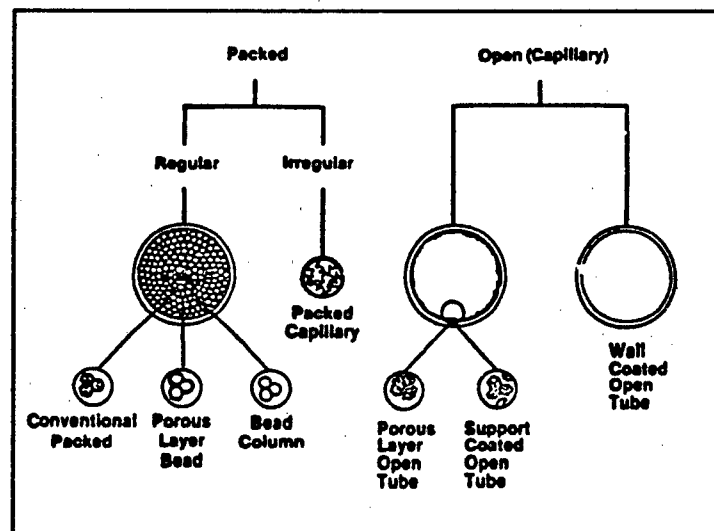


Figure 4. Fundamental Gas Chromatography Column Configurations (17).

packed into the column) (15:56). In contrast, the stationary phase in a capillary column is deposited as a thin film directly onto the walls of the column. The reduction in the number of available gas paths in a capillary column significantly enhances the component separation resolution of the column (15:60). Figure 5 compares representative chromatograms from packed and capillary columns.

Historically, packed columns were the simplest to fabricate and the first to gain widespread use. However, recent advances by several companies have made capillary columns a more attractive (and less expensive) alternative. Furthermore, due to their greater resolution, the capillary column is now the column of choice in many gas chromatography applications (17).

**2.3.2 Column Theory.** The theory which explains the operation of the column evolves from the adsorption-desorption interaction between the sample gas, the stationary phase, and the mobile phase. Since the various components of the sample are soluble to varying degrees in the stationary/mobile phase combination, the column acts to separate the components by forcing them to propagate through the column at different rates. These delays eventually translate into the components of the sample leaving the GC column at distinct times, where they can be detected. The sharpness of these *eluting* (or discharged)

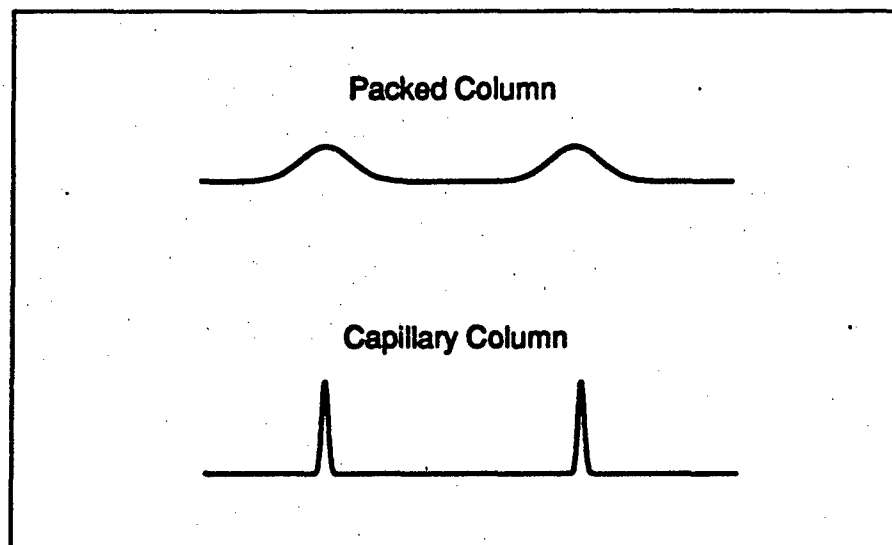


Figure 5. Typical Resolutions of the Two Major Column Types (17).

peaks, and their separation from the peaks of the other components, is referred to as the column's *resolution*. The separation process is demonstrated graphically in Figure 6.

The ability of a column to separate a sample's molecular components is based on the partition ratio,  $k$ , which is unique (and generally determined empirically) for each sample, stationary phase, mobile phase, and temperature combination. The partition ratio is defined as (18:17):

$$k = \frac{\text{weight of the sample dissolved in a unit column length of the stationary phase}}{\text{weight of the sample dissolved in a unit column length of the mobile phase}}. \quad (1)$$

This coefficient determines the portion of each particular sample component that can exist in the mobile phase. Since the components can only propagate through the column when they are in the mobile phase, the propagation velocity,  $v_p$ , is related to  $k$  by (11:3):

$$v_p = \left( \frac{1}{1+k} \right) v_c \quad (2)$$

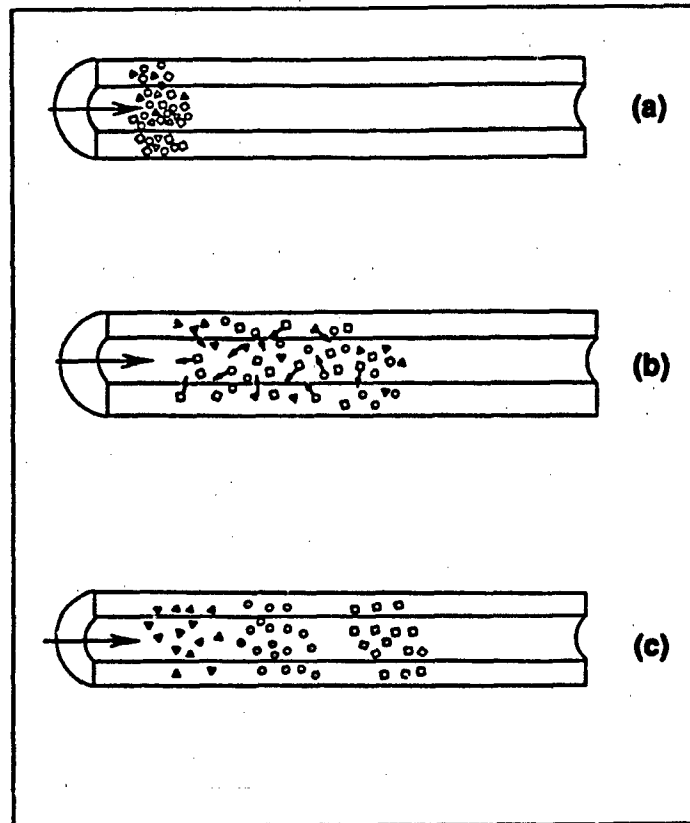


Figure 6. Graphical Representation of the Separation of Three Components (Represented by Squares, Triangles, and Circles) at (a)  $t = 0$  (injection), (b)  $t > 0$ , and (c)  $t \gg 0$  (Gas Flow is Represented by the Large Arrows, and Diffusion is Represented by the Small Arrows) (17).

where  $v_c$  is the carrier gas (mobile phase) velocity (11:3). With this relationship, the amount of time,  $t_R$ , required for the sample component to travel a column of length  $L$  is<sup>1</sup> (11:3):

$$t_R = \frac{L}{v_p} = (1 + k) \frac{L}{v_c}. \quad (3)$$

**2.3.2.1 Plate Height.** As the sample propagates through the column and interacts with the stationary and mobile phases, it begins to manifest the characteristic Gaussian distribution concentration profile shown in Figure 7 (18:11). A measure of col-

<sup>1</sup>This quantity is also often referred to as the *retention time* of the sample.

umn efficiency is the height equivalent of a theoretical plate<sup>2</sup> (or, simply, plate height),  $h$ , which is defined as the increase in the variance of the length of the Gaussian peak per unit column length (11:7). In terms of volume, this becomes (18:150):

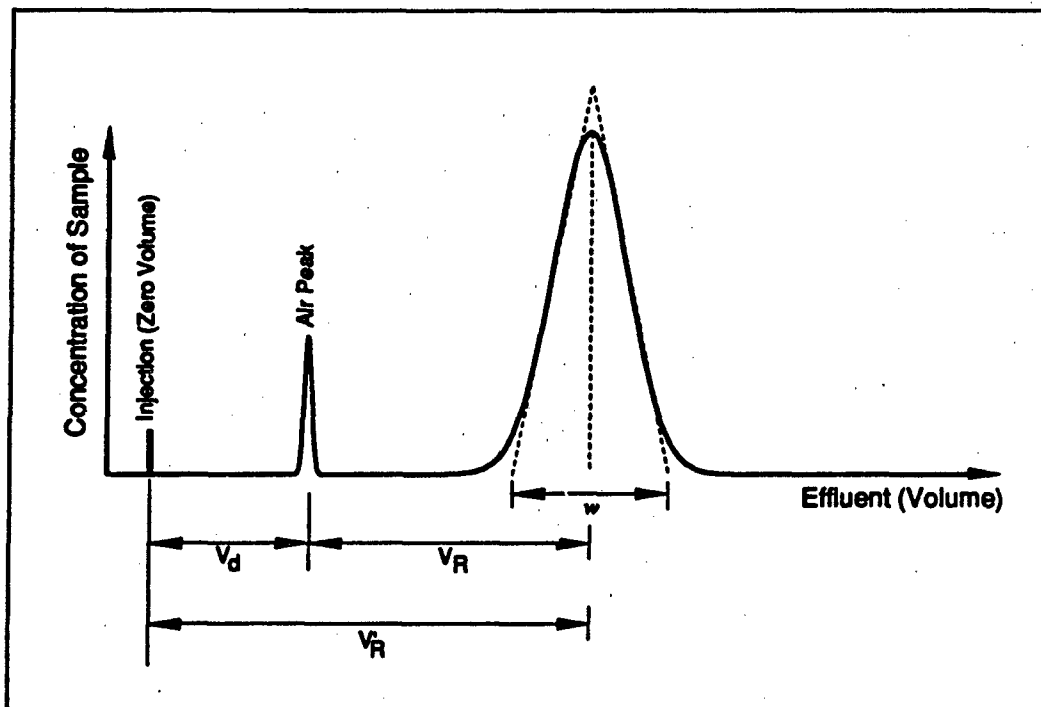


Figure 7. Plot Used to Calculate the Number of Theoretical Plates.  $V_R$  Represents the True Retention Volume,  $V_R'$  Represents the Measured Retention Volume (Including the Dead Volume),  $V_d$  Represents the Dead Volume of the System, and  $w$  Represents the Approximate Width of the Elution Curve (11:8).

$$h = \left( \frac{\sigma_v}{V_R} \right)^2 L \quad (4)$$

where  $\sigma_v$  is the standard deviation of the Gaussian peak (from Figure 7,  $w = 4\sigma_v$ ), and  $V_R'$  is the volume of the gas eluted from the column (measured relative to the time when the sample was injected and the peak appears—see Figure 7) (11:8). The number of theoretical plates,  $N$ , contained in a column of length  $L$  is calculated as follows (18:150):

<sup>2</sup>This term "...comes from distillation, where the number of theoretical plates in a fractioning column is a measure of the ability of the column to separate substances having different boiling points" (14:376).

$$N = \frac{L}{h} = \left( \frac{V'_R}{\sigma_V} \right)^2 \quad (5)$$

A large value of  $N$  implies that the column is able to efficiently separate a given component (14:379). Since  $h$  is inversely proportional to  $N$ , a smaller  $h$  implies a more efficient column<sup>3</sup>.

The standard deviation required in Equation 5 can be obtained graphically, since the width of the base of a triangle constructed from the tangents to the inflection points of the peak would be approximately four standard deviations wide (14:376). Equation 5 then becomes (14:376):

$$N = 16 \left( \frac{V'_R}{w} \right)^2 = 16 \left( \frac{V_R + V_d}{w} \right)^2 \quad (6)$$

where  $w$ ,  $V_R$ , and  $V_d$  are defined in Figure 7. Both the plate height and the number of theoretical plates provide an indication of the efficiency of a column in terms of separating a single component. These figures, however, do not address the ability of a column to separate a sample composed of multiple gas components.

**2.3.2.2 Separation Factor.** The problem of quantifying separation was discussed by Purnell in his paper, *The Correlation of Separating Power and Efficiency of Gas-Chromatographic Columns* (19:1268):

The theoretical-plate concept...has proved the most profitable approach to quantitative description of the efficiency of chromatographic columns. The theory is based on a model in which a single substance is eluted through a column by a carrier fluid; ...[however,] the theory has never been explicitly applied to the problem of the separation of mixed solutes. ...Apart from those interested in the theoretical aspects of chromatography few workers use theoretical plate numbers: analysts, for instance, are concerned more with the degree of separation attainable with a column than with its apparent efficiency.

<sup>3</sup>Alternatively, "the height of a theoretical plate  $h$  may be interpreted as the length of column that must be traversed for a mixture to be separated to the same extent as it would be separated in a single batch equilibrium between the mobile and stationary phases...a column that separates substances well will have a lower  $h$  than a less efficient column" (14:371).

Purnell then demonstrated that, independent of  $N$ , in order to achieve the same degree of separation between two components, the ratio  $V_R/w$  must remain constant (19:1270). Using this property, Purnell defined the separation factor,  $S$ , as (19:1270):

$$S = 16 \left( \frac{V_R}{w} \right)^2. \quad (7)$$

When Equations 6 and 7 are combined with the relationship between the partition ratio and the retention volume ( $k = V_R/V_d$ ), the separation factor can be defined in terms of  $N$ ,  $L$ , and  $h$  as (11:10):

$$S = N \left( \frac{k}{1+k} \right)^2 = \frac{L}{h} \left( \frac{k}{1+k} \right)^2. \quad (8)$$

Thus, the theoretical separation factor for a column can be established if the plate height is known. However, from the previous discussion, it is apparent that the only way to establish the true plate height of a column is empirically.

**Van Deemter Equation.** Fortunately, a basic "rate theory" was developed in 1956 by van Deemter which related the plate height of a given column to four fundamental physical parameters: flow rate, multipath diffusion, molecular diffusion, and resistance to mass transfer (20:88). Although the complexities involved with the van Deemter equation are treated in a number of texts, a brief description of the equation will be valuable (16, 21, 22). The abbreviated van Deemter equation is (14:392):

$$h = A + \left( \frac{B}{v_c} \right) + C v_c \quad (9)$$

where  $h$  represents the plate height,  $A$  is a term representing multipath diffusion<sup>4</sup>,  $B$  is a term representing molecular diffusion<sup>5</sup>,  $C$  is a term representing resistance to mass transfer<sup>6</sup>, and  $v_c$  represents the carrier gas (mobile phase) velocity (14:392). A graphical

<sup>4</sup>This term represents the peak broadening due to multiple gas paths that predominantly occur in a packed column.

<sup>5</sup>Molecular diffusion refers to the peak broadening due to the diffusion of the sample in the carrier gas along the direction of flow.

<sup>6</sup>Resistance to mass transfer refers to the rate of equilibration between the sample, the carrier gas, and the stationary phase. The thinner the stationary phase coating, the faster the equilibration.

representation of the van Deemter equation is shown in Figure 8. It is apparent from this figure that there is an optimal velocity which minimizes the plate height.

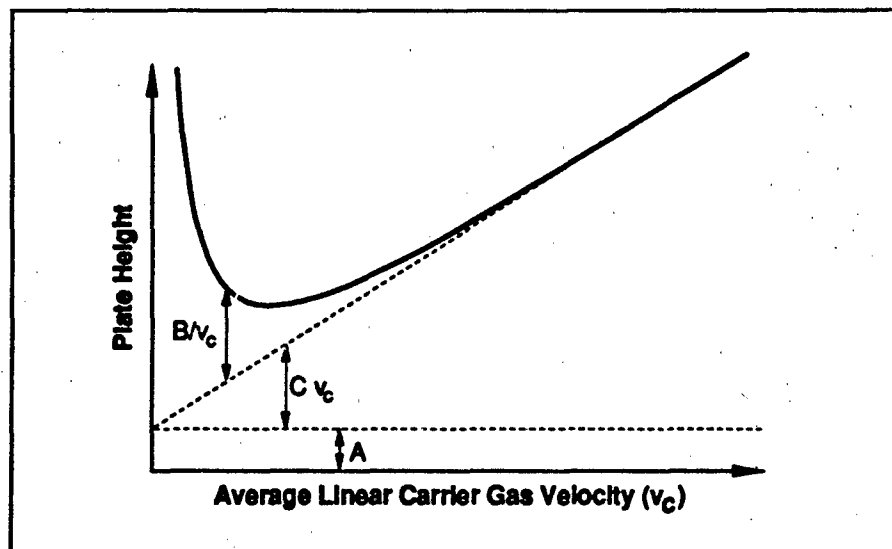


Figure 8. Plot of the van Deemter Equation (Solid Curve). The Horizontal Dashed Line Represents the Contribution of  $A$ , the Sloped Dashed Line Represents the Contribution of  $C v_c$ , and the  $(B/v_c)$ -Term Contributes the Remainder (14:393).

For a capillary column, there is only one gas path; and, due to the simplified geometry compared to a packed column, the resistance to mass transfer can be regarded as occurring separately in the mobile and stationary phases. Thus (assuming  $v_c$  is constant), Equation 9 can be written as (20:276):

$$h = \left( \frac{B}{v_c} \right) + C_g v_c + C_s v_c \quad (10)$$

where the multipath term,  $A$ , can be neglected (since there is only one gas path through a capillary column), and the  $C_g$  and  $C_s$  terms represent resistance to mass transfer in the gas and stationary phases, respectively (20:276). Since a smaller  $h$  implies a more efficient column, and Equation 10 (which relates  $h$  to  $v_c$ ) has a minimum (see Figure 8), the optimum carrier gas velocity,  $v_c$ , can be determined using calculus. Taking the first derivative of Equation 10 with respect to  $v_c$  yields (20:277):

$$\frac{dh}{dv_c} = -\frac{B}{v_c^2} + C_g + C_s. \quad (11)$$

Setting this equation equal to zero and solving for  $v_c$  yields the optimized carrier gas velocity ( $v_{opt}$ ) (20:277):

$$v_{opt} = \sqrt{\frac{B}{C_g + C_s}}. \quad (12)$$

Taking the second derivative of Equation 10 with respect to  $v_c$  and substituting the velocity found in Equation 12 produces:

$$h''(v_{opt}) = \frac{(C_g + C_s)^{3/2}}{\sqrt{B}} > 0 \quad (13)$$

which indicates that  $v_{opt}$  is a minimum (since the constants are all positive quantities). Furthermore, since Equation 8 is maximized when  $h$  is minimized, the maximum separation factor can be found. That is,  $S_{max}$  is given by (11:17):

$$S_{max} = \left(\frac{k}{1+k}\right)^2 \frac{L}{2\sqrt{B(C_g + C_s)}}. \quad (14)$$

**2.3.2.3 Pressure Gradient.** Unfortunately, the previous treatment assumes that the carrier gas velocity,  $v_c$ , is constant throughout the column. This condition is not necessarily true in the case of capillary columns with small cross sections since the carrier gas is known to behave like a compressible fluid (20:73). In order to determine the minimum plate height (or maximum separation factor) attainable for a given column, the velocity of the carrier gas (which is a function of position in the column) will first be defined in terms of the inlet and outlet pressures by the following expression<sup>7</sup>(18:26):

$$\frac{v(\frac{P}{P_o})}{v_o} = \frac{1}{\sqrt{\left(\frac{P_o}{P}\right)^2 (1 - \frac{P}{P_o}) + \left(\frac{P}{P_o}\right)}} \quad (15)$$

<sup>7</sup>This equation was derived by Littlewood by applying Boyle's law to the differential equation which describes the pressure gradient in the column:  $dP/dx = -(\mu/q)v$  where  $P$  is the gas pressure,  $\mu$  is the gas viscosity,  $q$  is the column permeability, and  $v$  is the gas velocity (18:25).

where  $v(x/L)$  is the carrier gas velocity at a distance of  $(x/L)$  into the column,  $v_o$  is the carrier gas velocity at the column outlet,  $P_i$  is the pressure at the column inlet, and  $P_o$  is the pressure at the column outlet (18:26). The change in velocity of the carrier gas as it travels through a column with a pressure gradient is shown graphically<sup>8</sup> in Figure 9.

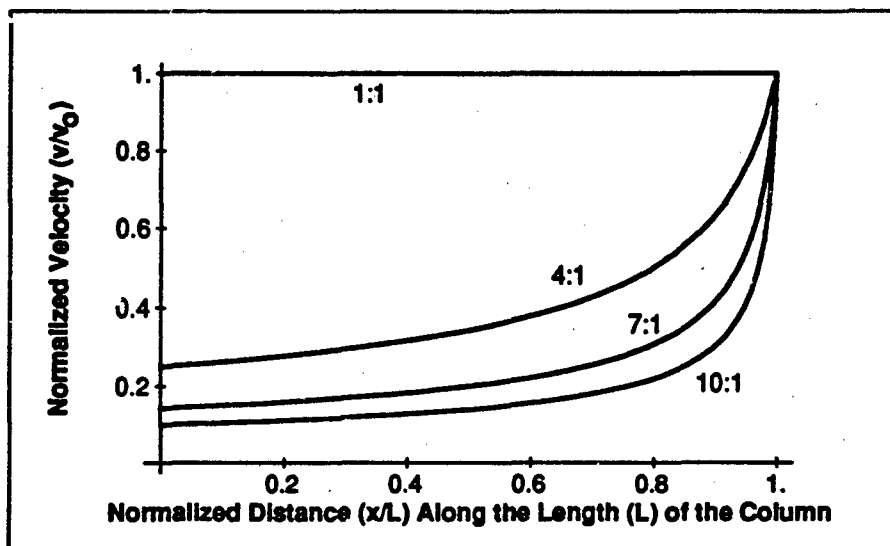


Figure 9. Normalized Velocity of the Carrier Gas in a Column with Pressure Gradients of 1:1, 4:1, 7:1, and 10:1 ( $P_i:P_o$ ) (18:27).

Because the velocity of the carrier gas in a column with a pressure gradient can no longer be considered constant, the retention time (Equation 3) must be reformulated. Although Equation 3 is not valid for the entire column length, it still remains valid for incremental lengths along the column (where the velocity can be regarded as a constant). Therefore, the retention time for a column with a pressure gradient,  $t_{rp}$ , is (since  $k$  is a constant for a given temperature, carrier gas and sample):

$$t_{rp} = (1 + k) \int_0^L \frac{dx}{v\left(\frac{x}{L}\right)} \quad (16)$$

where  $v(x/L)$  is defined by Equation 15. Making a simple change of variable ( $\zeta = x/L$ ) yields:

<sup>8</sup>The code used to generate Figure 9 is in Appendix G.

$$t_{rp} = L(1+k) \int_0^1 \frac{d\zeta}{v(\zeta)}. \quad (17)$$

Substituting Equation 15 and evaluating the integral produces:

$$t_{rp} = \frac{L(1+k)}{v_o} \left[ \frac{2 \left( \frac{P_o}{P_o} \right)^3 - 1}{3 \left( \frac{P_o}{P_o} \right)^2 - 1} \right]. \quad (18)$$

Apart from the term in the square brackets, this expression is identical to Equation 3. Consequently, the additional term (the compressibility correction factor) is referred to as  $j$ , where (20:74):

$$j = \left[ \frac{2 \left( \frac{P_o}{P_o} \right)^3 - 1}{3 \left( \frac{P_o}{P_o} \right)^2 - 1} \right]^{-1}. \quad (19)$$

This correction factor will also be incorporated into the subsequent modifications to the van Deemter equation.

**2.3.2.4 Optimization of a Column with a Pressure Gradient.** Since the van Deemter equation (Equation 10) is velocity dependent, and velocity is a function of distance along a column with a pressure gradient, it must be written as (18:220):

$$h(x) = \frac{B(x)}{v(x)} + [C_s(x) + C_o(x)]v(x). \quad (20)$$

Regrettably, the plate height is now a function of  $x$ , and it becomes very difficult to establish an optimum velocity. However, Giddings, in his paper, *Plate Height in Gas Chromatography*, introduces an "apparent" plate height,  $\mathcal{H}$ , which is independent of  $x$  (23:868):

$$\mathcal{H} = \left( \frac{B_o}{v_o} + C_s v_o \right) g + C_o v_o j \quad (21)$$

where  $B_o$  is the molecular diffusion term at the output of the column,  $j$  is defined in Equation 19, and

$$g = \frac{9 \left[ \left( \frac{P_i}{P_o} \right)^4 - 1 \right] \left[ \left( \frac{P_i}{P_o} \right)^2 - 1 \right]}{8 \left[ \left( \frac{P_i}{P_o} \right)^3 - 1 \right]^2} \quad (22)$$

Using these equations, and a method similar to that used to derive Equation 12, it is possible to determine the input pressure which minimizes the apparent plate height for a micromachined column. Since the relationship between input pressure and output velocity strongly depends on the geometry of the column, the following analysis assumes a rectangular micromachined column<sup>9</sup>.

#### 2.4 Micromachined Column Theory.

With the cross section and the stationary phase of the channel established, the theoretical analysis presented in Section 2.3.2 can be expanded by determining the effect of the column's cross section on the average velocity of the carrier gas. This, in turn, influences the constants in van Deemter's equation.

Assuming a uniform temperature throughout the column, Boyle's Law states that the product of the pressure and volume of the gas at any point in the column is a constant<sup>10</sup>. Equating the product of pressure and volume at two points in the column, and taking the derivative of the volume with respect to time on both sides of the equation, yields the following relationship (18:25):

$$P\dot{V} = P_o\dot{V}_o \quad (23)$$

where  $P$  is the pressure at a specific point in the column,  $\dot{V}$  is the volume flow rate at the point of interest,  $P_o$  is the pressure at the output of the column (normally atmospheric pressure), and  $\dot{V}_o$  is the output volume flow rate (measurable with a flow meter on the

<sup>9</sup>This choice will be justified in Section 3.1.

<sup>10</sup>Boyle's Law is  $PV = mRT$  where  $P$  represents pressure,  $V$  represents volume,  $m$  represents the number of moles,  $R$  represents the universal gas constant, and  $T$  represents temperature. If the same amount of gas is considered at any point in an isothermal column, the product  $P(x)V(x)$  (where  $P(x)$  and  $V(x)$  are, respectively, the pressure and volume at point  $x$  in the column) is a constant (24:375).

output port). Due to viscous flow<sup>11</sup>, the flow rate measured at various points in the cross section of the channel will be different; thus, it is advantageous to deal with the average linear velocity<sup>12</sup>,  $\bar{v}$ . Furthermore, since the average linear velocity of the gas flow at a point in a column is proportional to the pressure gradient at that point, the following relationship holds (18:25):

$$\frac{dP}{dx} = -q\bar{v} \quad (24)$$

where  $(dP/dx)$  represents the pressure gradient, and  $q$  is a proportionality coefficient representing the *column permeability*<sup>13</sup>. Since  $q$  is dependent on the column cross section, it must be found for each cross section of interest. Two important cross sections include: the two-sided rectangular (TSR) cross section<sup>14</sup> investigated by Golay (25) (and subsequently used by Terry (11) in the development of his miniature GC) and the rectangular cross section (see Figure 10). Before developing the expressions for the column permeabilities, it will be useful to relate the column permeability to observable variables (i.e., input pressure and output flow rate).

Substituting Equation 24 into Equation 23 (after converting to linear velocity) yields (25:42):

$$P dP = -qv_o P_o dx \quad (25)$$

where  $v_o$  is taken to be the average linear velocity of the carrier gas at the column outlet. Integrating this equation with the boundary condition that  $P = P_i$  at  $x = 0$  (the column inlet), and solving for  $v_o$  at  $x = L$  (and  $P = P_o$ ) yields (11:34):

<sup>11</sup>Viscous flow implies that the velocity of the fluid is zero at the physical boundaries of the constraining channel.

<sup>12</sup>Assuming a constant cross-sectional area,  $a$ , throughout the length of the column, the linear velocity is related to the volume flow rate by ' $\bar{v}$ ' (i.e.,  $\bar{V} = a\bar{v}$  where  $\bar{V}$  is the volume flow rate and  $\bar{v}$  is the average linear velocity) (18:25).

<sup>13</sup>The column permeability can be regarded as the fluid dynamics analog to electrical resistivity. It is a measure of how "constraining" the column is.

<sup>14</sup>The TSR cross section neglects the effects of the sidewalls of a rectangular column. As long as the width is much greater than the height of the column, this approximation is valid. Subsequent calculations will show where this approximation fails.

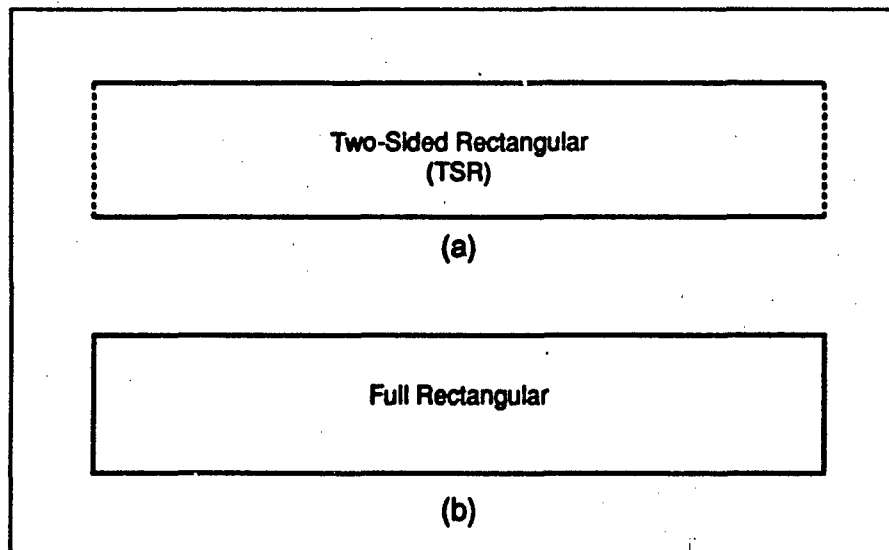


Figure 10. Rectangular Column Cross Sections. (a) Two-Sided Rectangular (Sidewall Effects Neglected) and (b) Full Rectangular.

$$v_o = \frac{(P_i^2 - P_o^2)}{2P_o q L} \quad (26)$$

This equation establishes the relationship between output flow velocity, input pressure and column permeability. In order to evaluate the fabricated columns, it will be necessary to determine the column permeabilities for the TSR column (which was used by Terry to predict his flow rates) and the rectangular column (which will be used in this research to predict flow rates).

**2.4.1 Column Permeability for a Two-Sided Rectangular Column.** The Navier-Stokes equation<sup>15</sup> for the motion of a fluid through a TSR column is (assuming the geometry shown in Figure 11, for flow in the  $x$ -direction only) (26:301):

$$\mu \frac{d^2 v_{TSR}}{dz^2} = -\frac{dP}{dx} \quad (27)$$

<sup>15</sup>This equation, named after Louis Navier and George Stokes, is the fundamental equation describing a fluid in motion (26:41).

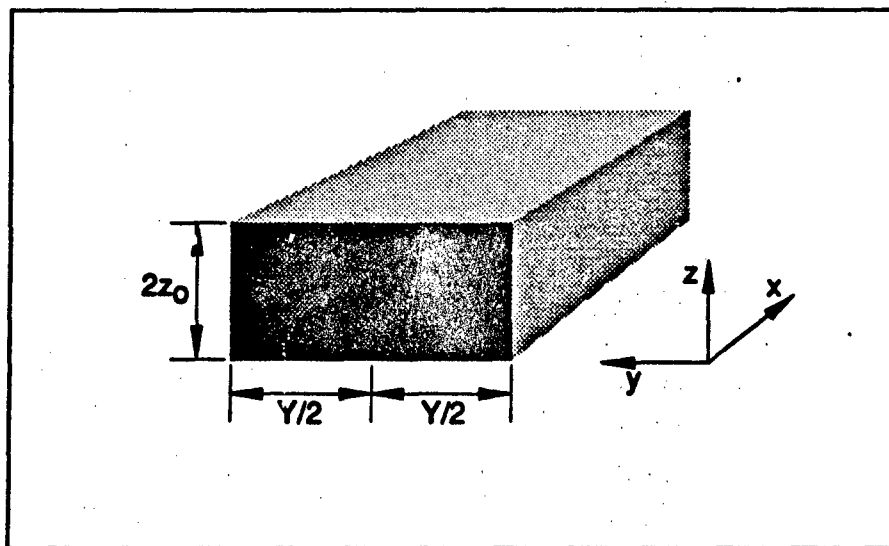


Figure 11. Coordinate System for Column Analysis (the  $y$ - $z$  Origin is Taken to be the Lower Center of the Rectangular Cross Section). One Half of the Column's Height is  $z_0$ , and  $Y$  Represents the Column's Width.

where  $\mu$  is the viscosity of the carrier gas (and can be regarded as constant for isothermal flows), and  $v_{TSR}$  is the velocity of the carrier gas. Integrating twice with respect to  $z$  and using the boundary conditions for viscous flow ( $v_{TSR} = 0$  at  $z = 0$  and  $z = 2z_0$ ) yields:

$$v_{TSR}(z) = - \left( \frac{dP}{dx} \right) \left( \frac{1}{2\mu} \right) (2z_0 z - z^2). \quad (28)$$

The resulting velocity distribution across the column has the parabolic shape shown<sup>16</sup> in Figure 12.

With this velocity distribution, the average velocity of the carrier gas in a cross-sectional slice of the column,  $\bar{v}_{TSR}$ , can be formulated by integrating over the cross section of the column and dividing by the column area<sup>17</sup>:

$$\bar{v}_{TSR} = - \left( \frac{dP}{dx} \right) \left( \frac{1}{2\mu} \right) \left( \frac{1}{z_0} \right) \int_0^{z_0} (2z_0 z - z^2) dz = - \left( \frac{dP}{dx} \right) \left( \frac{z_0^2}{3\mu} \right). \quad (29)$$

<sup>16</sup>The code used to generate Figure 12 is in Appendix G.

<sup>17</sup>Note that the velocity is independent of  $y$ , so the integration only takes place over  $z$ .

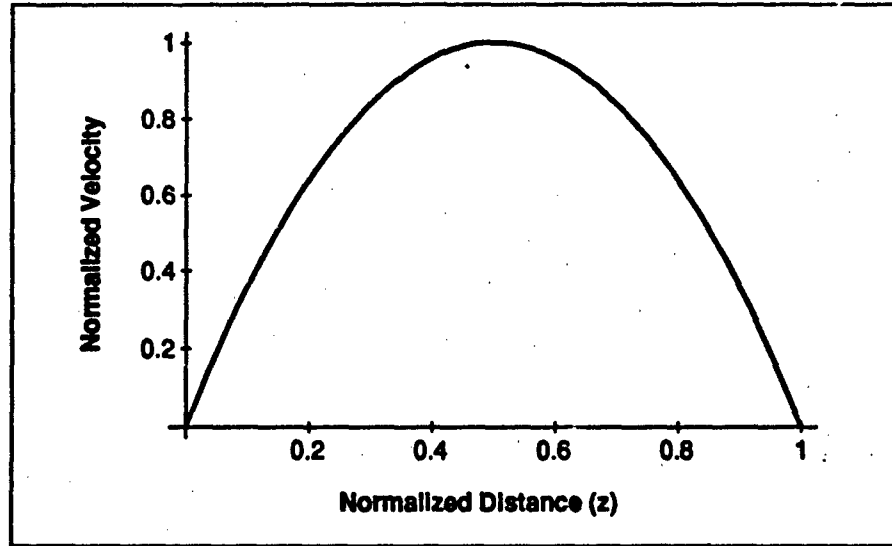


Figure 12. Normalized Velocity Distribution Across a Two-Sided Rectangular Column.

The column permeability for a TSR column,  $q_{TSR}$ , can then be found by applying Equation 24 to Equation 29 (25:43):

$$q_{TSR} = \frac{3\mu}{z_0^2}. \quad (30)$$

Since the Navier-Stokes equation for a TSR column was made essentially one-dimensional (by ignoring the effects of the side walls), it yielded an analytically simple column permeability. The Navier-Stokes equation for a rectangular column, however, is two-dimensional, and the column permeability found for the TSR column must be modified to more accurately consider the effects of the side walls.

*Column Permeability for a Rectangular Column.* The Navier-Stokes equation for a rectangular column is (26:309):

$$\mu \left( \frac{\partial^2}{\partial y^2} + \frac{\partial^2}{\partial z^2} \right) v_{rec} = -\frac{dP}{dx}. \quad (31)$$

The solution for  $v_{rec}$  can be written as the sum of a particular solution,  $v_{part}$ , which solves as:

$$\mu \left( \frac{\partial^2}{\partial y^2} + \frac{\partial^2}{\partial z^2} \right) v_{part} = -\frac{dP}{dx}, \quad (32)$$

and a complementary solution,  $v_{char}$ , which solves as:

$$\mu \left( \frac{\partial^2}{\partial y^2} + \frac{\partial^2}{\partial z^2} \right) v_{char} = 0. \quad (33)$$

The boundary conditions for viscous flow imply that  $v_{rec} = v_{part} + v_{char}$  must be zero at  $y = -Y/2$ ,  $y = Y/2$ ,  $z = 0$ , and  $z = 2z_o$  (see Figure 11). Since the solution for the Navier-Stokes equation of a TSR column (Equation 28) is independent of  $y$  and solves Equation 32 for the associated boundary conditions of  $v_{part} = 0$  at  $z = 0$  and  $z = 2z_o$ , it serves as the particular solution,  $v_{part}$ , of the rectangular column. The task then becomes the determination of the solution to Equation 33 with the following boundary conditions:  $v_{char} = 0$  at  $z = 0$  and  $z = 2z_o$ , and  $v_{part} = -v_{char}$  at  $y = -Y/2$  and  $y = Y/2$  (26:310). Using the technique of separation of variables (along with the  $z$  boundary conditions and the fact that the  $y$  boundary conditions are symmetrical) gives (26:310):

$$v_{char} = \sum_{n=1}^{\infty} \left[ A_n \cosh \left( \frac{n\pi y}{2z_o} \right) \sin \left( \frac{n\pi z}{2z_o} \right) \right] \quad (34)$$

where  $A_n$  is a set of coefficients which will be used to satisfy the  $y$  boundary conditions. Using the orthogonality property of the sine function (and the  $y$  boundary conditions), the coefficients  $A_n$  can be found (26:311):

$$A_n \cosh \left( \frac{n\pi Y}{4z_o} \right) = -\frac{1}{z_o} \int_0^{2z_o} v_{part}(z) \sin \left( \frac{n\pi z}{2z_o} \right) dz = -\left( \frac{dP}{dx} \right) \frac{8z_o^3}{(n\pi)^3} [1 - \cos(n\pi)]. \quad (35)$$

The complete solution for viscous flow through a rectangular column is given by the sum of Equations 28 and 34 (with the coefficients described by Equation 35). A three-dimensional representation of the gas velocity across the column is shown<sup>18</sup> in Figure 13. As expected, the gas flow retains its parabolic shape in the  $y$  and  $z$  directions.

<sup>18</sup>The code used to generate Figure 13 is in Appendix G.

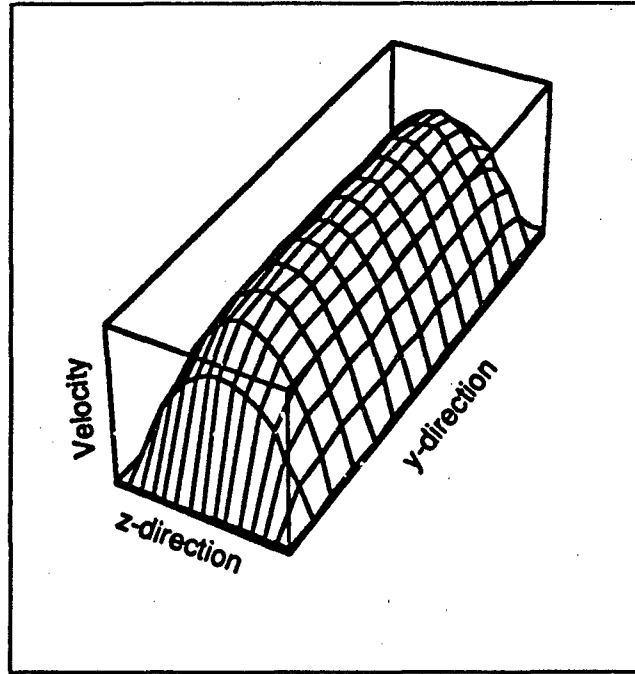


Figure 13. Velocity Distribution Across a Rectangular Column.

The average velocity across the rectangular column,  $\bar{v}_{rec}$ , can be found by integrating the sum of  $v_{part}$  and  $v_{char}$  over the area of the column and dividing by that area. This calculation yields:

$$\bar{v}_{rec} = \frac{2}{Y z_o} \int_0^{z_o} \int_0^{Y/2} (v_{rec}) dy dz = \frac{dP}{dx} \left[ \frac{z_o^2}{3\mu} - \frac{128z_o^3}{Y\mu} \sum_{n=1,3,\dots}^{\infty} (n\pi)^{-5} \tanh\left(\frac{n\pi Y}{4z_o}\right) \right] \quad (36)$$

for the average velocity, and:

$$q_{rec} = \left[ \frac{z_o^2}{3\mu} - \frac{128z_o^3}{Y\mu} \sum_{n=1,3,\dots}^{\infty} (n\pi)^{-5} \tanh\left(\frac{n\pi Y}{4z_o}\right) \right]^{-1} \quad (37)$$

for the column's permeability (following the same steps used to obtain Equation 30). The first terms in both of the above equations (Equations 36 and 37) are identical to the values found for the TSR column (Equations 29 and 30). The added summation term takes into account the effects of the column walls (and goes to zero as the width of the column,  $Y$ ,

approaches infinity). Figure 14 shows<sup>19</sup> the percentage of the TSR column velocity that is attained by a rectangular column with different aspect ratios.

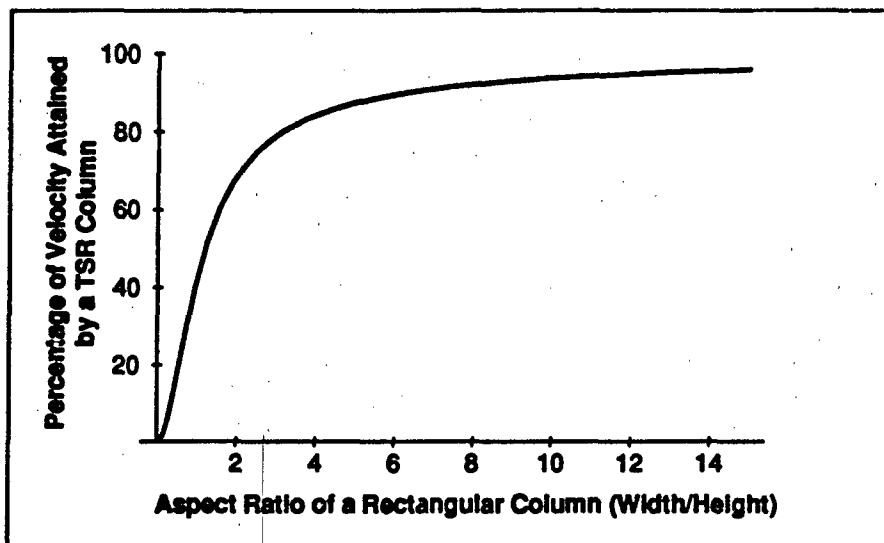


Figure 14. Percentage of Velocity Attained by a Two-Sided Rectangular Column versus the Aspect Ratio of a Rectangular Column.

From Figure 14, it is apparent that the TSR column relationship is only valid for aspect ratios greater than approximately 4:1. The aspect ratio of the micromachined column created by Terry was approximately 4:1 (width-to-height)<sup>20</sup> (11). A comparison of flow rate versus input pressure is shown<sup>21</sup> in Figure 15 for a TSR column, a rectangular column, and Terry's micromachined column. The rectangular column equation better predicts the flow/pressure relationship for the micromachined column since it takes into account the effects of the side walls. For subsequent verification of the flow rates through the columns which have been fabricated, the additional complexity of the side-wall term is negligible (the column permeability need only be calculated once for a specific geometry).

However, if the side-walls are taken into account in the development of a modified van Deemter equation, it would have to be done numerically due to the complexity of the initial equation which describes the diffusion of a gas packet through a column coated with

<sup>19</sup>The code used to generate Figure 14 is in Appendix G.

<sup>20</sup>The column fabricated for this research was approximately 30:1

<sup>21</sup>The code used to generate Figure 15 is in Appendix G.

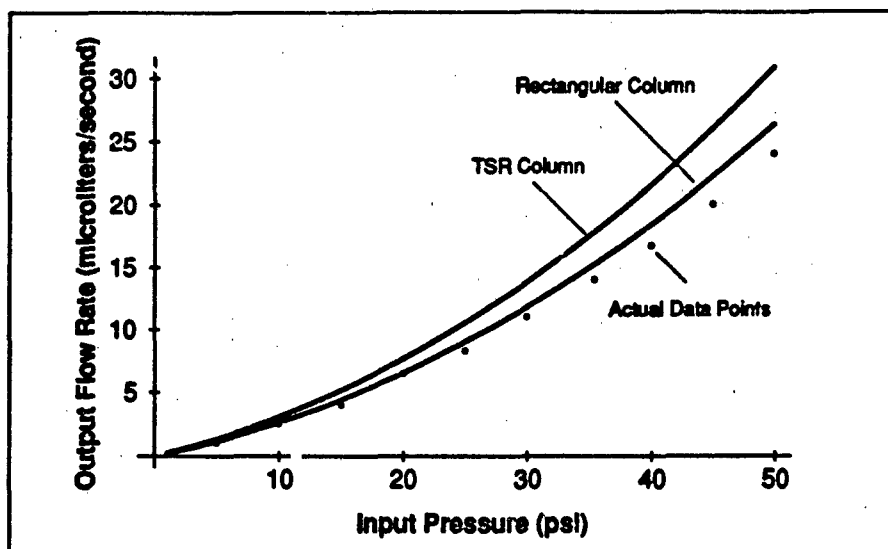


Figure 15. Flow Rate versus Input Pressure for a Two-Sided Rectangular Column, a Rectangular Column (Aspect Ratio 4:1), and Actual Data Points for a Micromachined Column. Column Length is 0.5 m, Gas Viscosity is 200  $\mu$ poise, Output Pressure is 1 atmosphere, Column Width is 130  $\mu$ m, and Column Height is 30  $\mu$ m (11:36).

a retarding stationary phase. Fortunately, this is not required since the fabricated columns used in this investigation have aspect ratios in excess of 30:1, so the TSR approximation holds (it was shown to be valid for column aspect ratios greater than 4:1). Since a form of van Deemter's equation is necessary to study the influence of the column parameters relative to each other (i.e., width, height, length, and input pressure), van Deemter's equation will be modified for a TSR column. In this manner, appropriate values can be chosen for initial column operational variables.

#### 2.4.2 Golay Solution for the Van Deemter Equation of a Micromachined Column.

Golay, in *Theory of Chromatography in Open and Coated Tubular Columns with Round and Rectangular Cross Sections*, developed two sets of equations describing the interaction between the sample, carrier gas and stationary phase for two column geometries: round columns and TSR columns (25). The two sets of equations have a parallel development,

but the boundary condition for the round cross section analysis is easier to visualize, so the round cross section (using Figure 16) will be discussed first<sup>22</sup>.

The general equation which describes the diffusion of a gas packet through a column can be expanded by invoking the chain rule of calculus to express the total derivative. This gives (25:37):

$$D\nabla^2 f = \frac{df}{dt} = \frac{\partial f}{\partial t} + \bar{v} \cdot \nabla f \quad (38)$$

where  $D$  is the diffusion coefficient of the sample in the carrier gas,  $f$  is the density of the sample<sup>23</sup> and is a function of both  $x$  and  $t$ ,  $\bar{v}$  is the velocity of the carrier gas, and  $t$  is time (25:37).

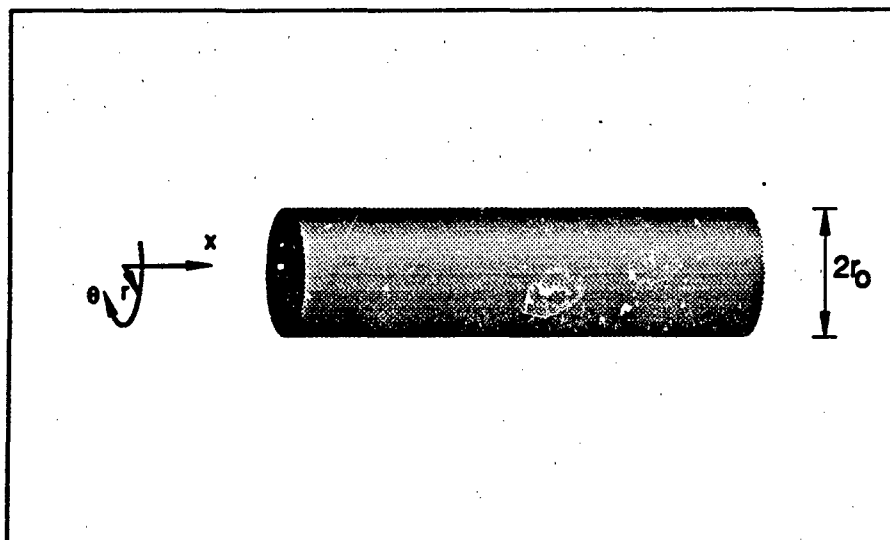


Figure 16. Column Geometry Used to Develop the Modified van Deemter Equation. The Radius of the Circular Column is  $r_0$ , and the Carrier Gas is Flowing in the  $x$  Direction (the Column Parameters are Independent of  $\theta$ ).

Converting to cylindrical coordinates and introducing the expression for viscous flow in the  $x$  direction only (i.e.,  $v = 0$  at  $r = r_0$ ) yields (25:38):

<sup>22</sup>Golay's development is presented in Appendix F.

<sup>23</sup>The density,  $f(x, t)$ , at any time,  $t$ , will be normalized to unity using the fact that  $\int_{-\infty}^{+\infty} f dx = 1$  (25:37).

$$D \left( \frac{\partial^2}{\partial r^2} + \frac{1}{r} \frac{\partial}{\partial r} + \frac{\partial^2}{\partial x^2} \right) f = \frac{\partial f}{\partial t} + 2v_0 \left( 1 - \frac{r^2}{r_0^2} \right) \frac{\partial f}{\partial x} \quad (39)$$

where  $v_0$  is the average velocity of the carrier gas through a cross-sectional slice of the column.

Assuming instantaneous equilibration in the stationary phase<sup>24</sup>, the time rate of change of the density of the sample in the *stationary phase* is proportional (through the partition ratio) to the rate of change (with respect to time) of the sample density in the carrier gas at  $r = r_0$  (i.e., if the sample density at the edge of the column is increasing with time, the concentration of the sample in the stationary phase will also increase). Likewise, the time rate of change of the density of the sample in the *carrier gas* at any point in the tube is inversely proportional (through the diffusion coefficient and a geometrical factor<sup>25</sup>) to the rate of change (with respect to the radius) of the sample density (i.e., if the density of the sample is decreasing from the center of the column, the sample will diffuse in a positive  $r$  direction, and vice versa). At the boundary of the column, these two processes must be equal. Thus, the boundary condition for a circular column is (25:38):

$$-2 \frac{D}{r_0} \left( \frac{\partial f}{\partial r} \right)_{r=r_0} = k \left( \frac{\partial f}{\partial t} \right)_{r=r_0} \quad (40)$$

where  $k$  is the partition ratio<sup>26</sup>.

Since, by definition, the height equivalent of a theoretical plate,  $h$ , is related to the variance (incremental second moment) of the sample<sup>27</sup>, Golay solved Equation 39 with the boundary condition described by Equation 40 for the incremental second moment (25:38-41). This yields:

<sup>24</sup>In other words, the sample concentration across the width of the stationary phase is uniform since the layer is very thin.

<sup>25</sup>This factor—considering a two dimensional cross section—is the perimeter (or diffusion “front”) divided by the area that is diffusing. In the case of a round column, this becomes  $2\pi r / \pi r^2 = 2/r$ .

<sup>26</sup>The partition ratio,  $k$ , is dependent on both the geometry of the column and  $c$ , the partition coefficient (which is a fundamental characteristic of the stationary phase).  $k$  is related to  $c$  by:  $k = (\text{area of stationary phase} / \text{area of column})c$ . Thus, the effective partition ratio for a round column is twice that of a TSR column (assuming the thickness of the deposited stationary phase is identical in both cases).

<sup>27</sup>The incremental second moment,  $ds$ , of the sample component described by  $f$  is defined as:  $ds = d \int_{-\infty}^{+\infty} f x^2 dx$  (25:38). The incremental second moment is also the change in variance per unit length (which is the definition of the plate height—see Section 2.3.2.1) (27:918).

$$h_{\text{round}} = 2\frac{D}{v_o} + \frac{1 + 6k + 11k^2}{24(1 + k)^2} \frac{v_o r_o^2}{D}. \quad (41)$$

Following a similar development, Golay also derived the plate height for a TSR column (25:42):

$$h_{\text{TSR}} = 2\frac{D}{v_o} + \frac{4(1 + 9k + 51k^2/2)}{105(1 + k)^2} \frac{v_o z_o^2}{D} \quad (42)$$

where  $z_o$  is half of the column height (see Figure 11). Both Equation 41 and 42 parallel van Deemter's equation for a capillary column (see Equation 10). In fact, the two terms in Golay's equation can be thought of as the coefficients in van Deemter's equation where the first term on the right represents molecular diffusion, and the second term represents resistance to mass transfer in the carrier gas. However, there is no corresponding term representing resistance to mass transfer in the stationary phase since the initial assumption was that the stationary phase layer was so thin that equilibration across this layer was instantaneous (alternately, if the stationary phase was a solid whose mode of retention was adsorption-desorption at the solid's surface, the sample would not penetrate into the bulk of the material, so resistance to mass transfer in the stationary phase could be neglected).

Using Equation 8 to determine the corresponding separation factors permits the comparison of the relative efficiencies of round and TSR columns. The normalized separation factor for the two column geometries<sup>28</sup> is shown in Figure 17. From Figure 17, it is readily apparent that the round column is always more efficient than the TSR column (when operated under identical conditions). This improved efficiency is primarily due to the increased ratio of column wall (or perimeter) to column area (which increases the relative partition ratio) and the addition of viscous flow at the curved "side walls" of the round column (which decreases the plate height for large values of  $k$ ).

Since a round column (with radius  $r_o$ ) is more efficient than a TSR column (with  $z_o = r_o$ ), a rectangular column with a finite width and a height of  $2z_o = 2r_o$  will also be more efficient than a TSR column due to the two additional sidewalls which interact with the sample. Thus, calculating column parameters for a rectangular column with an aspect

<sup>28</sup>The code used to generate Figure 17 is in Appendix G.

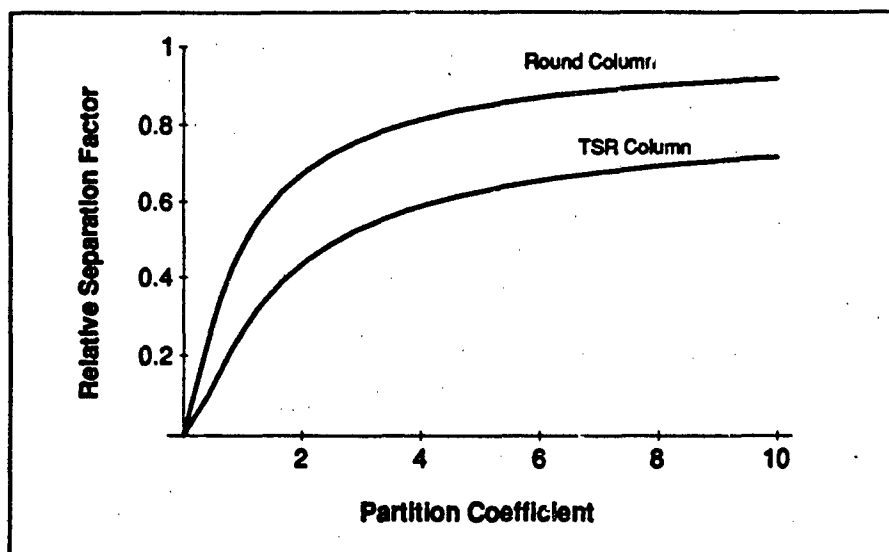


Figure 17. Normalized Separation Factor for Round and Two-Sided Rectangular Columns ( $z_o = r_o$ ).

ratio less than 4:1, based on Equation 42, would result in a worst-case design (whose actual performance would be better than the calculations indicate since the additional sidewalls would improve the column performance). Fortunately, the columns actually fabricated in this investigation have aspect ratios on the order of 30:1. Therefore, these equations will be used in Chapter 4 to justify the column design used and the associated parameter choices.

**2.4.3 Micromachined Column Summary.** With this discussion of GC column theory applied to a micromachined column, it is now apparent that the column (with a stationary phase<sup>29</sup> coating) performs the critical function in a gas chromatograph (since it determines how effectively the components will be separated). However, separating the components is not enough. A useful GC must also contain a detector with sufficient sensitivity (minimum detectable concentration) and selectivity (isolated detection of the compounds of interest).

<sup>29</sup>The selection of a suitable stationary phase, as well as a discussion of alternative stationary phases, will be presented in Section 4.1.1.

## 2.5 Detectors.

There are two basic classes of detectors: general detectors and selective detectors. A general detector is sensitive to a wide variety of compounds (or a class of compounds which is large; for example, organic compounds), whereas a selective detector responds only to a certain class of compounds (with a finite number of members) (see Figure 18). The choice of a detector generally depends on the type of measurement that is required. Table 2 lists typical GC functions with the corresponding detector requirements. These detector requirements facilitate the determination of suitable detectors, since there are a wide variety of detectors available. Throughout this discussion, any references made to sensitivity are based upon concentration levels within a 10  $\mu$ l sample loop<sup>30</sup>.

Table 2. Gas Chromatograph Detector Functions (28:217).

Function	Detector Requirement
Measure relative amounts of compounds	Stability of response factors and linearity over a specific concentration range
Measure compounds without standards	Predictability of response factors
Measure peaks in the presence of background	Specificity and freedom from quenching or enhancement of response
Sense trace levels	Minimum detectable level and sensitivity
Sense a wide variety of compounds	Universality of response (general detector)
Sense peaks unresolved from background	Specificity of response (selective detector)
Confirm a molecular property of a compound	Predictability of specific response
Identify unknown compounds	Produce spectra, interpretable or comparable with a library of known spectra

**2.5.1 Thermal Conductivity Detector (TCD).** The most common GC detector is the TCD, which operates by sensing a difference in thermal conductivity between heated filaments (or thermistors), whose resistance changes as a function of temperature, when they are suspended in two chambers (29:70). Typically, one chamber has pure carrier gas flowing through it, and the second chamber has the output gas of the GC column flowing through it (30:44). A change in the thermal conductivity of the second chamber can be detected using a common Wheatstone bridge configuration (30:44). The TCD is

<sup>30</sup>This sample loop size will be discussed in Section 4.1.2.

considered a general detector since it is "capable of detecting almost everything" (15:33). For a thermistor based TCD (which is compatible with the scale of the MMGC), the most important aspect in its sensitivity is the operating point<sup>31</sup>.

In order to determine an appropriate operating point for the TCD, it is important to have an understanding of the relationship between the thermistor and the noise produced by the power supply. Therefore, the sensitivity of a thermistor's response to fluctuations in the power supply will be developed from the basic thermistor equations.

**2.5.1.1 Thermistor Theory.** The equation describing the operation of a thermistor in the self-heated mode<sup>32</sup> at thermal equilibrium is (31:1292):

$$p = VI = \delta(T_T - T_w) \quad (43)$$

where  $p$  is the power dissipated by the thermistor,  $V$  is the thermistor voltage,  $I$  is the thermistor current,  $\delta$  is the thermistor dissipation constant<sup>33</sup>,  $T_T$  is the thermistor temperature, and  $T_w$  is the temperature of the thermistor cell wall. Also, when a constant current,  $I$ , is allowed to flow through the thermistor, the voltage drop across it at thermal equilibrium is given by (32:715):

$$V = IR_{dc} = IR_o \exp \left[ -\beta \left( \frac{1}{T_o} - \frac{1}{T_T} \right) \right] \quad (44)$$

where  $R_{dc}$  is the resistance of the thermistor at thermal equilibrium,  $R_o$  is the resistance of the thermistor when it is maintained at a temperature of  $T_o$ , and  $\beta$  is the characteristic thermistor temperature (a material parameter).

Solving Equation 43 for  $T_T$ , substituting the result in Equation 44, solving for  $V$ , and making the assumption that  $T_o = T_w$  yields<sup>34</sup> (32:716):

<sup>31</sup>Since the TCD was identified as the secondary detector for this investigation, a more rigorous treatment of its fundamental theory (relative to the other detectors discussed in this section) is provided here.

<sup>32</sup>In the self-heated mode, the thermistor is dissipating sufficient power to raise its temperature above the ambient temperature (31:1292).

<sup>33</sup>This term is defined as "the ratio, at a specified ambient temperature, of a change in power dissipation in a thermistor to the resultant body temperature change" (31:1292).

<sup>34</sup>This assumption is valid if  $R_o$  is measured at the anticipated ambient temperature of the TCD cell. For the proposed MMGC, both  $T_o$  and  $T_w$  are considered to be room temperature (25°C).

$$V = IR_o \exp \left[ \frac{-p/p_o}{1 + p/p_1} \right] \quad (45)$$

where  $p_o$  is a characteristic power of the thermistor defined by  $p_o = (\delta T_w^2)/\beta$ , and  $p_1$  is the characteristic power of the thermistor defined by  $p_1 = \delta T_w$ . Since  $p$  is dependent on  $V$ , there is no analytical solution for Equation 45. However, by numerically solving for  $V$  in terms of  $I$ , the current-voltage characteristics of a thermistor<sup>35</sup> can be plotted (see Figure 19).

**2.5.1.2 Power Supply Sensitivity.** From the current-voltage characteristics of the thermistor (Figure 19), it is apparent that there is a minimum current (approximately 0.5 mA) after which the thermistor behaves with a negative resistance. Taking the partial derivative of Equations 43 and 44 with respect to  $I$ , and solving them for  $(\partial V/\partial I)$  yields<sup>36</sup> (32:717):

$$\frac{\partial V}{\partial I} = R_T = R_{dc} \frac{[(1 + p/p_1)^2 - p/p_o]}{[(1 + p/p_1)^2 + p/p_o]} \quad (46)$$

where  $R_T$  is defined as the thermistor's sensitivity to changes in current. A plot of Equation 46 is shown in Figure 20. Thus, to minimize the effects of current fluctuations, the operating point should be chosen such that  $R_T$  is in the negative resistance region.

The plots presented in Figures 19 and 20 are based upon the published specifications of a specific thermistor. In practice, a calibration plot of current versus voltage for the finished TCD is generated (this curve has the same basic shape as Figure 19). It is then possible to numerically differentiate the I-V plot to determine the minimum power supply sensitivity and find a useful operating point.

Typical detection limits for a TCD to the gases of interest within a 10  $\mu$ l sample volume are approximately 30 ppm for  $\text{NO}_2$ , and 90 ppm for  $\text{NH}_3$  (13). Two major advantages

<sup>35</sup>For the purposes of this discussion, the thermistor is assumed to be a 125  $\mu$ m diameter Thermometrics B05 Thermobead (Thermometrics, Inc., Series B05, Edison, NJ) with the following constants:  $\beta = 3359^\circ\text{K}$ ,  $\delta = 0.045 \text{ mW/}^\circ\text{K}$ , and  $R_o = 10 \text{ K}\Omega$  (33:B-2).

<sup>36</sup>Since  $T_T$  is a function of  $V$ ,  $I$ ,  $T_w$ , and  $\delta$  (from Equation 43), and  $V$  is a function of  $T_T$  (from Equation 44), both  $T_T$  and  $V$  are functions of  $I$ ,  $T_w$ , and  $\delta$ .

of this detector are that it is nondestructive with respect to the column effluent (thus, the effluent from the TCD can be passed to another detector), and thermistor sensing elements can be made very small (on the order of the features in the MMGC). Therefore, the TCD, is an excellent general purpose detector for the MMGC. An example of a standard thermal conductivity detector is shown in Figure 21.

**2.5.2 Ionization Detectors.** Another common form of GC detector is based on the ionization of the column effluent to produce a time-varying current between two electrodes within the detector. Although the basic principle behind all ionization detectors is the same, they differ in the way that the effluent is ionized.

**2.5.2.1 Flame Ionization Detector (FID).** Figure 22 depicts a typical FID. The basic principle behind the operation of the FID involves the combustion of the column effluent by mixing it with hydrogen. Two electrodes with fixed potentials are placed near the flame, and the current between them is measured. This current varies with the amount of carbon (from organic compounds) which is combusted. Sternberg provides an explanation for the ionization effect:

[A] hydrogen-air or hydrogen-oxygen diffusion flame provides [the] high temperature and reactive intermediates to strip and crack organic sample molecules. Sample fragments react with flame intermediates in [the] zone in exothermic reactions; for given flame conditions there is a fixed probability of reaction of [the] proper fragment with sufficiently energetic intermediate[s] to produce ionic products through chemi-ionization reactions. There is, therefore, for a particular molecular species under given operating conditions[,] a certain ionization efficiency,  $\phi$ . [The] diffusion, heat capacity and thermal conductivity properties of [the] carrier gas affect [the] magnitude of  $\phi$ . Ions and electrons are completely collected by [the] application of [an] electrical field, and [a] current,  $i$ , is measured (34:183).

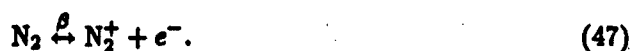
Although the FID primarily detects organic compounds, it is still considered a general detector since it is not selective with respect to the *type* of organic compound it detects (15:37). The FID is useful for making quantitative analyses since it "...is linear over several orders of magnitude, and because the peak areas of the chromatogram are a direct

measure of the size of the sample injected, without being affected by minor variations in the flow rate of the carrier gas" (35:135).

Unfortunately, the FID is not highly sensitive to the two gases of interest,  $\text{NO}_2$  and  $\text{NH}_3$  (36:266). This lack of response, coupled with the difficulty of incorporating the complex FID structure using micromachining techniques, implies that the FID should not be considered as a candidate detector for the MMGC system.

**2.5.2.2 Photoionization Detector (PID).** The photoionization detector is similar to the flame ionization detector, except that a UV irradiation source is substituted for the hydrogen gas flame (see Figure 23) (17). The UV source ionizes the column effluent gas, and the subsequent ions are detected as a time-varying current. Although it is listed under general detectors, the PID is somewhat selective since it "...is only suitable for detecting those substances which give a response on a flame ionization detector" (37:42). Again, this implies that the PID is not a viable candidate for the MMGC.

**2.5.2.3 Electron Capture Detector (ECD).** The ECD (see Figure 24) is very selective towards halogenated compounds. It uses a  $\beta$ -radiation source to ionize the column effluent and records the current flowing between two electrodes held at a fixed potential. Since the carrier gas (typically nitrogen or argon) is easily ionized, a steady-state current response can be obtained (15:43):



However, when a highly electronegative species (primarily halogenated compounds) enters the chamber, the current drops sharply since the electronegative component, represented by *EC* in the following equations, can capture free electrons (38:131):



The resultant anions are too heavy to avoid the nitrogen cations, and are captured by them, producing (15:44):



Therefore, the decrease in the current represents the quantity of the halogenated compound in the chamber, and this change can readily be measured. Since the ECD is configured for halogens, and requires a radiation source, it would not be a suitable detector for this research.

**2.5.2.4 Cross-Section Detector (CSD).** The cross-section detector has a similar construction and operating principle as does the ECD in that it is based on an  $\alpha$ - or  $\beta$ -radiation source which ionizes the column effluent (see Figure 24) (18). However, instead of relying upon the nitrogen cations to capture the halogen anions, the CSD is based upon detecting the increase in current created by the ionized column effluent. Since the probability of collision between a gas molecule and a particle is proportional to its cross-sectional area, a carrier gas with a small cross-section is recommended (typically hydrogen or helium) (13). It is considered a general detector since it responds to any gas which can be ionized by the radiation source. Typical sensitivity of the CSD to a 10  $\mu$ l sample of  $NO_2$  is on the order of 50 ppm, and to a 10  $\mu$ l sample of  $NH_3$  is on the order of 90 ppm (13). The significant disadvantages of the CSD are the complexities involved with handling the required radiation source, and the difficulty encountered with fabricating the CSD on a scale compatible with the MMGC. Thus, the CSD is considered an unsuitable detector for this investigation.

Two other detectors developed from the CSD are the *argon* and *helium* detectors. The argon detector differs from the CSD in that the carrier gas must be argon which is excited (but not ionized) to a metastable state (11.6 eV). The excited argon atoms are then capable of interacting with (and ionizing) the other gases present in the column effluent (18). Since the metastable state is not ionized, the carrier gas does not contribute to the conductivity within the ionization chamber, but the other ionized species enhance the conductivity which can be detected by the chamber electrodes (see Figure 24) (18). Additionally, the excited argon atoms increases the probability of ionization for the other gas species. This feature improves the detector's sensitivity, and for the gases of interest,

a typical minimum detectable concentration in a 10  $\mu$ l sample loop is 0.05 ppm for NO<sub>2</sub>, and 0.15 ppm for NH<sub>3</sub> (13).

The helium detector operates in the same manner as the argon detector; however, since the metastable state of helium is 19.8 eV, it is capable of ionizing more species (i.e., the permanent gases). For the gases of interest, a typical minimum detectable concentration in a 10  $\mu$ l sample loop is 0.001 ppm for NO<sub>2</sub>, and 0.003 ppm for NH<sub>3</sub> (13). Both the helium and argon detectors share the same disadvantage as the ECD and the CSD; the requirement of a radiation source.

**2.5.2.5 Nitrogen-Phosphorus Thermionic Detector (NPD).** The NPD responds "...to nitrogen- and phosphorus-containing compounds by surface ionization on heated alkali-impregnated sources" (39:285). It is very specific and ideal for detecting any compounds which contain nitrogen or phosphorus. Figure 25 shows a typical configuration of a nitrogen-phosphorus detector with a rubidium bead as the alkali source. For a 10  $\mu$ l sample, the NPD is theoretically capable of detecting NO<sub>2</sub> concentrations as low as 0.2 ppm and NH<sub>3</sub> concentrations as low as 0.6 ppm. However, since heating of the alkali source is accomplished through the combustion of the hydrogen carrier gas, this detector would not be compatible with the scale or thermal requirements of the MMGC.

**2.5.3 Quartz Crystal Microbalance Detector (QCMD).** Originally used as a thickness monitor for integrated circuit (IC) thin film deposition processes, the quartz crystal microbalance has been used in recent years as a gas detector (40). In principle, the QCMD is based upon altering the fundamental oscillation frequency of a quartz crystal oscillator by the adsorption of gas molecules onto an adsorbent coating. Based upon the coating, the QCMD can be made selective to certain classes of compounds. Assuming a coating which adsorbed both NO<sub>2</sub> and NH<sub>3</sub> (possibly CuPc, itself), theoretical sensitivities of a 10 MHz QCMD to these gases in a 10  $\mu$ l sample loop would be 50 ppm for NO<sub>2</sub>, and 140 ppm for NH<sub>3</sub> (41). Since it is compatible with the geometries required for the MMGC, the QCMD is a potential candidate for an MMGC detector.

A related detector, the surface acoustic wave detector (SAWD), operates in a similar manner to the QCMD (gas adsorption causes a shift in the fundamental oscillation frequency); however, the mechanical wave in a SAWD is confined to the top surface of the piezoelectric material (42). This feature permits the use of IC fabrication technology which gives the SAWD the ability to operate at higher frequencies, thus improving its sensitivity (41). Again, assuming a coating which adsorbed both  $\text{NO}_2$  and  $\text{NH}_3$ , theoretical sensitivities of a 100 MHz SAWD to these gases in a 10  $\mu\text{l}$  sample loop would be 1 ppm for  $\text{NO}_2$  and 2.8 ppm for  $\text{NH}_3$  (41). Because of its compatibility with IC fabrication processes, the SAWD is also a potential candidate for an MMGC detector.

**2.5.4 Hall Electrolytic Conductivity Detector (HECD).** Like the electron capture detector, the HECD is selective towards detecting halogenated compounds. It functions as follows (38:132):

Halogens in the column effluent are catalytically converted to acids and mixed with a solvent to form a heterogeneous mixture of liquid and gas phases. The liquid phase which is extracted from this mixture, passes through a bridge type differential conductivity detector. The presence of acidic species in the flowing solvent causes changes in the detector's liquid baseline reading thus giving the chromatogram. The gas and liquid phases are then recombined and returned to the solvent reservoir (38:132).

The complexity of this detector argues against its use in a micromachined environment, where simplicity is key. Additionally, since the HECD is selective towards halogens, it would not make a good choice for the MMGC detector. Figure 26 depicts the catalytic reactor and conductivity cell of a commercial Hall electrolytic conductivity detector.

**2.5.5 Chemiresistor Detector.** A typical chemiresistor consists of a pair of planar interdigitated electrodes (one "driven" by an external voltage source, and the other referenced to ground) that are covered by a chemically sensitive thin film whose electrical resistance changes in the presence of a gas (see Figure 27). For an interdigitated array, the geometry is a critical design factor since the length of the effective resistive path, along with its width, determines the overall resistance of the chemiresistor.

In order to sense changes in the resistance of the chemically-sensitive film, the length and width of the interdigitated electrode array must be chosen such that the overall resistance (and anticipated changes upon exposure to a challenge gas) is compatible with the range that can be detected by the external instrumentation. Thus, it is necessary to quantify the relationship between the interdigitated electrode structure (i.e., number of fingers, finger length, and interelectrode spacing) and the equivalent length and width of the effective resistive path.

For finger length,  $f_l$ , number of driven fingers,  $n_f$ , and assuming that the electrode spacing,  $s$  is much less than  $f_l$  (see Figure 27), the effective chemiresistor width,  $w_e$ , can be approximated<sup>37</sup> by:

$$w_e = 2n_f f_l \quad (50)$$

since each driven finger has two sides of length  $f_l$ . Knowing the resistivity,  $\rho$ , of the chemically sensitive film (both before and after exposure), then, permits calculation of the overall resistance of the chemiresistor,  $R_c$ , using the following equation (44):

$$R_c = \frac{\rho s}{w_e T_f} \quad (51)$$

where  $T_f$  is the thickness of the film, and  $s$  is the interelectrode spacing (or the effective length of the chemiresistor).

Using standard IC processes, chemiresistors are relatively easy to construct. However, the mechanism behind their operation, although simple in general principle, is highly dependent on the chemically-sensitive film. An area of ongoing research is the copper phthalocyanine based chemiresistor, since copper phthalocyanine has shown remarkable sensitivity to nitrogen dioxide (on the order of parts-per-billion) (7, 43, 45). Also, the chemiresistor can be manufactured using IC fabrication techniques, so it is compatible with the small geometries associated with the MMGC. Experimentally determined detection

<sup>37</sup>A more accurate expression which incorporates the electrode-end contribution is:  $w_e = (n_f - 1)(4s + 2f_l) + 2f_l + s$ , which reduces to Equation 50 as the ratio  $s/f_l$  approaches zero.

limits of a 10  $\mu$ l sample for the gases of interest are 25 ppm for NO<sub>2</sub> and 250 ppm for NH<sub>3</sub>. Thus, the chemiresistor is a potential candidate for an MMGC detector<sup>38</sup>.

**2.5.5.1 Optical Detectors.** There are also a wide variety of sensitive, optical detectors based upon the absorption or transmission of light. However, due to the scope of this investigation, these detectors were not considered because of their requirements for specialized instrumentation.

**2.5.6 Detection Techniques Specific to Ammonia and Nitrogen Dioxide.** After reviewing the common GC related detectors, it is appropriate to discuss alternative detection schemes designed specifically for NO<sub>2</sub> and NH<sub>3</sub>, since the ultimate goal of this research is to separate and detect these two gases. Some of these detection techniques can be coupled with a GC to help remove the effects of interfering compounds; however, many of these techniques are stand-alone chemical processes that, while they provide accurate measures, require a pre-concentrated sample, a significant amount of time, and complex chemical reagents.

**2.5.6.1 Ammonia.** One of the standard techniques for determining the ammonia concentration in air is the indophenol method (46). Using this method, ammonia is collected by bubbling an air sample through a solution of sulfuric acid to form ammonium sulfate. The ammonium sulfate is then converted to indophenol (a blue dye), which is analyzed colorimetrically (46). This method is considered reliable, "but it is rather tedious and time-consuming for routine analysis" (47). Also, the detection limit for a 10  $\mu$ l sample is high (approximately  $1.5 \times 10^5$  ppm), and this method is not readily adaptable to the MMGC (46).

Another method of NH<sub>3</sub> detection involves the continuous monitoring of the challenge gas using a membrane-electrode system where a buffer solution is continually passed through a microporous tube, which absorbs the ammonia that is present. The solution is

---

<sup>38</sup>Since the chemiresistor was identified as the primary detector for this investigation, the actual design of the chemiresistor is presented in Section 4.1.3.1. Also, a more detailed discussion of the properties of copper phthalocyanine, and its use in a chemiresistor gas detector is presented in Appendix B, and additional specifics on a CuPc based chemiresistor are presented in Section C.

then examined with an ion-selective electrode "tuned" to ammonia (8). Sensitivity to  $\text{NH}_3$  in a 10  $\mu\text{l}$  sample is approximately 1200 ppm (8). Although this method can continuously monitor ammonia levels, and could possibly be modified to function as a GC detector, it is not compatible with the scale imposed by the MMGC. Additionally, it suffers from exclusive selectivity, and it is not responsive to  $\text{NO}_2$ .

There are also a wide variety of methods that involve the use of denuder<sup>39</sup> tubes or filter packs to concentrate  $\text{NH}_3$  for subsequent detection (47, 48). Since these methods of analysis are intended for long-term sampling of a challenge gas, they are not compatible with the necessarily small sample sizes used in the MMGC (a typical detection limit of  $\text{NH}_3$  in a 10  $\mu\text{l}$  sample is approximately  $1.5 \times 10^5$  ppm) (47). These techniques are also applicable to the detection of  $\text{NO}_2$ , but they suffer from some or all of the aforementioned disadvantages (i.e., exclusive selectivity and incompatibility with the MMGC).

**2.5.6.2 Nitrogen Dioxide.** A frequently used technique for detecting atmospheric  $\text{NO}_2$  is the Saltzman method which is similar to the  $\text{NH}_3$  indophenol technique. That is, the  $\text{NO}_2$  is absorbed by a dye forming reagent, and the product is then analyzed colorimetrically (49, 50, 51). This technique has the same limitations with respect to this research as the colorimetric technique used to detect  $\text{NH}_3$ . The detection limit for this technique using a 10  $\mu\text{l}$  sample is approximately a 2000 ppm concentration of  $\text{NO}_2$  (50).

Nitrogen dioxide can also be continuously monitored using a chemiluminescent reaction with ozone (after it is converted to NO) (52, 53). This could be incorporated into a GC using a commercial converter (52). However, to determine the actual  $\text{NO}_2$  concentration, a cyclic mode of operation<sup>40</sup> is required which nearly doubles the analysis time. The  $\text{NO}_2$  detection limit is approximately 2500 ppm in a 10  $\mu\text{l}$  sample. Additionally, the size of the apparatus required is not directly compatible with the MMGC.

<sup>39</sup>A denuder tube is typically a glass tube with a sorbent wall coating (47).

<sup>40</sup>This would require two GC runs. On the first run, the  $\text{NO}_2$  would be converted to NO and the sum of the natural NO and the converted NO would be detected. On the second run, the converter would be removed from the line, and the natural NO would be detected. Subtracting the results of the two runs would yield the  $\text{NO}_2$  concentration (54).

A modified chemiluminescent technique that overcomes some of the problems associated with the standard technique discussed above has been described by Burkhardt (55). A luminol solution replaces the ozone reaction, eliminating the need for NO<sub>2</sub> conversion to NO for detection while enhancing the detectable signal (55). The NO<sub>2</sub> detection limit attributed to the improved signal is reduced to approximately 0.3 ppm in a 10 µl sample. However, interference with NO was reported (implying that the NO<sub>2</sub> detection might not be accurate if NO is present) and aging of the luminol reagent caused baseline shifts (48).

**2.5.7 Detector Summary.** Table 3 summarizes the selectivity, theoretical minimum detectable concentrations, and MMGC compatibility for the various detection methods described in this section. Of the detectors and detection methods discussed above, only four were considered compatible with the small scale of the MMGC: the SAWD, the chemiresistor, the TCD, and the QCMD. Of these four detectors, the two which would require the most straightforward instrumentation were the TCD and chemiresistor. Both the SAWD and the QCMD would require external RF sources to operate (with the associated requirements for electrical connections and shielding). Additionally, since the TCD and chemiresistor were both non-destructive with regards to the column effluent, they could be used in a dual-detector (tandem) configuration. This implementation would have the added benefit of the TCD and chemiresistor complementing each other (the TCD is a universal detector, while the chemiresistor is a selective detector). Further discussion of these two detectors and their specific implementation in the MMGC will take place in Chapter 4.

## **2.6 Summary.**

This section discussed and summarized the basic operation of a gas chromatography system from the perspective of introducing the mobile phase, a consideration of the injection of the test sample, the separation phenomena performed by the column, and finally, the detection of the column effluent (reviewing the current technology concerning NO<sub>2</sub> and NH<sub>3</sub> detection). With the operation of a standard, "macro" GC established, the problems associated with designing a "micro" GC will be discussed in the Chapter 4, after a review of some of the tools and techniques available to the micromachinist in the next chapter.

**Table 3. Micromachined Gas Chromatograph (MMGC) Detector Candidate Summary.**  
 Estimated Sensitivities are Given as Concentrations Within a 10  $\mu$ l Sample Loop (13).

Detector	Selectivity	NO <sub>2</sub> Sensitivity (ppm)	NH <sub>3</sub> Sensitivity (ppm)	MMGC Compatibility
Helium	Universal	0.001	0.003	No
Argon	Universal	0.05	0.15	No
NPD	N/P	0.2	0.6	No
SAWD (100 MHz)	NO <sub>2</sub> /NH <sub>3</sub>	1	2.8	Yes
Chemiresistor	NO <sub>2</sub> /NH <sub>3</sub>	25	250	Yes
TCD	Universal	30	90	Yes
QCMD (10 MHz)	Universal	50	140	Yes
CSD	Universal	50	140	No
Indophenol	NH <sub>3</sub>	—	$1.5 \times 10^5$	No
Membrane-Electrode	NH <sub>3</sub>	—	1200	No
Denuder Tube	NH <sub>3</sub> or NO <sub>2</sub>	$1.5 \times 10^5$	$1.5 \times 10^5$	No
Saltzman Method	NO <sub>2</sub>	2000	—	No
Chemiluminescence	NO <sub>2</sub>	2500	—	No
Luminol	NO <sub>2</sub>	0.3	—	No
PID	Organics	—	—	No
FID	Organics	—	—	No
ECD	Halogens	—	—	No
HECD	Halogens	—	—	No

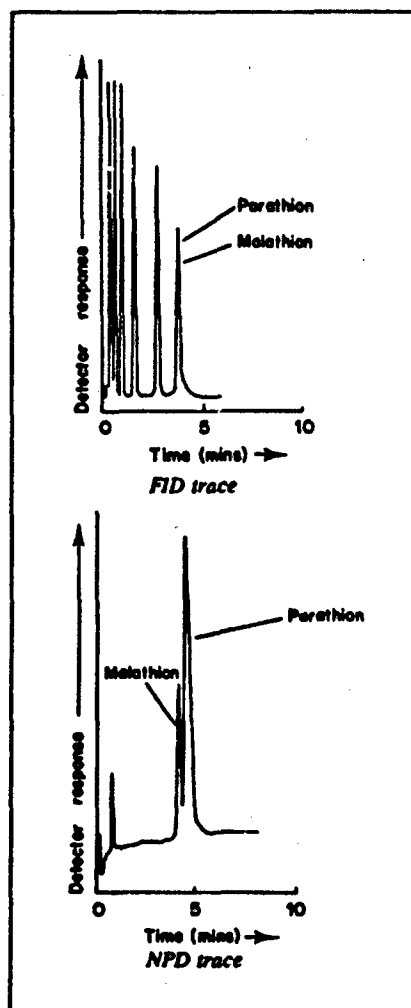


Figure 18. General Flame Ionization Detector (FID) versus a Selective Nitrogen-Phosphorus Detector (NPD) (15:40).

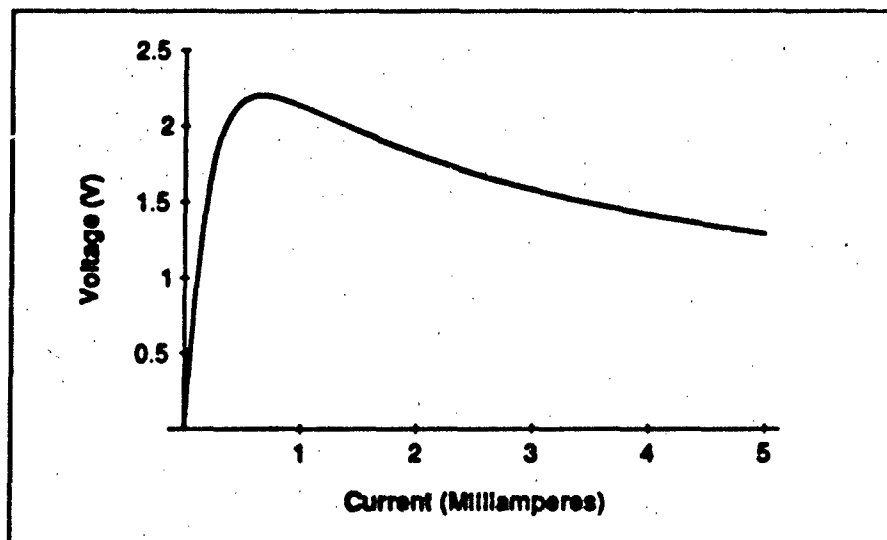


Figure 19. Current-Voltage Characteristics of a Typical Thermistor.

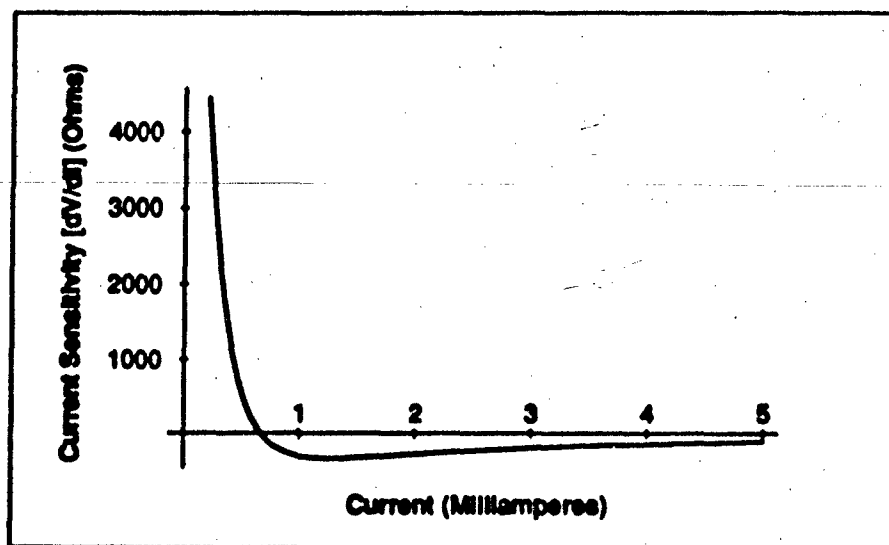


Figure 20. Thermistor Sensitivity Relative to Current Fluctuations.

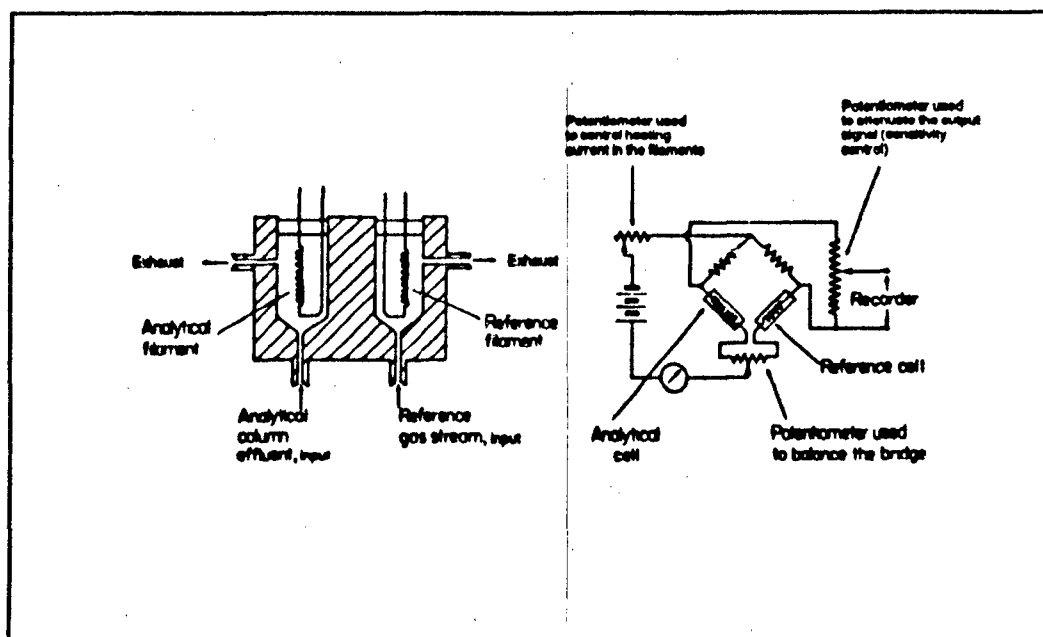


Figure 21. Standard Thermal Conductivity Detector (TCD) and Schematic of the Wheatstone Bridge Configuration (15:28).

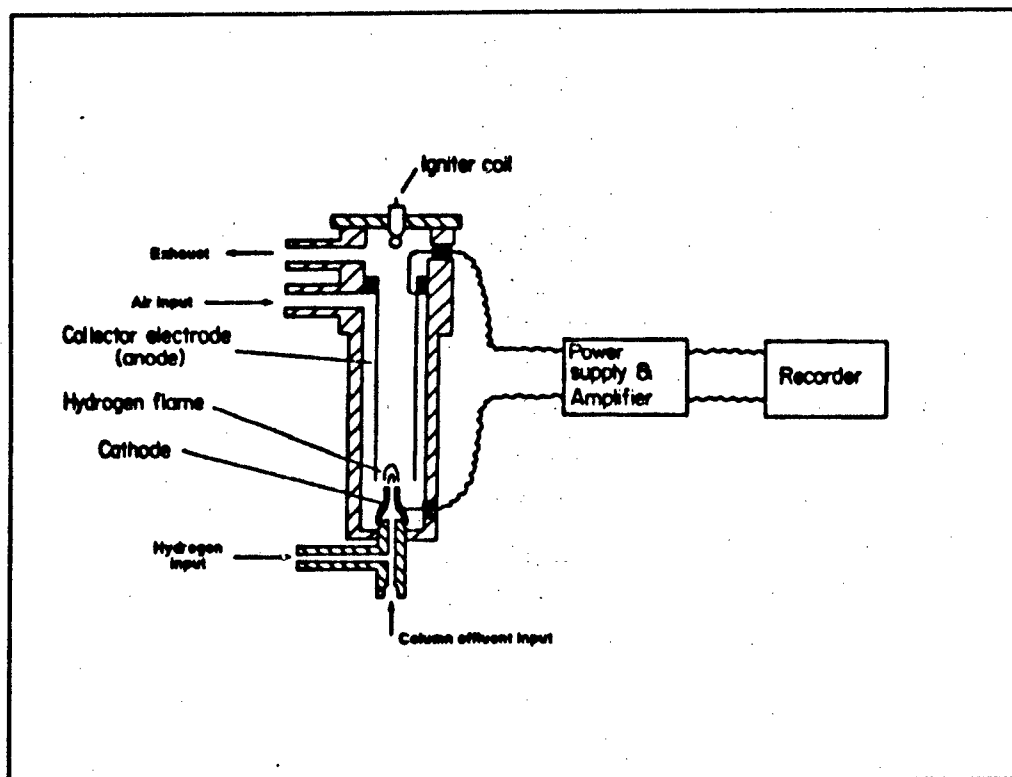


Figure 22. Flame Ionization Detector (FID) (15:35).

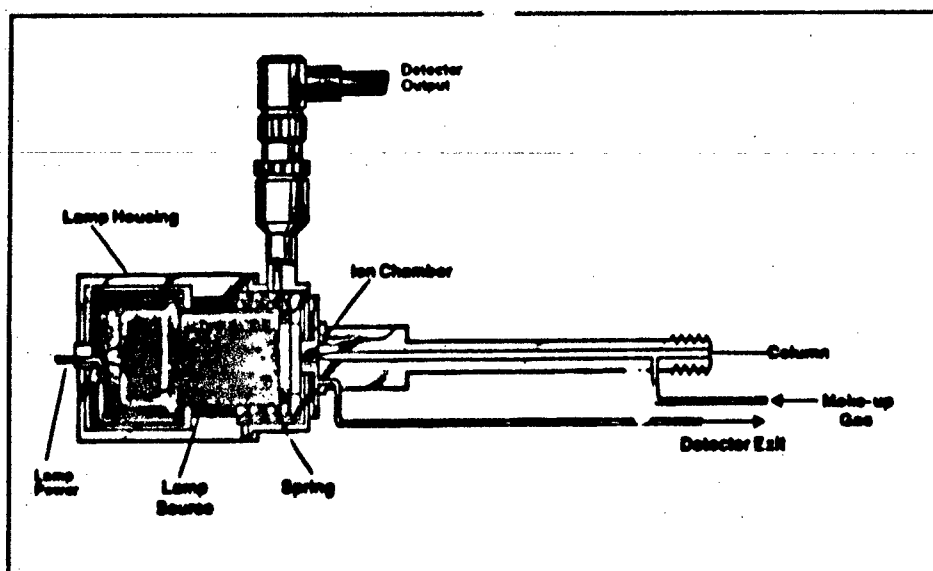


Figure 23. Photoionization Detector (PID) (38:134).

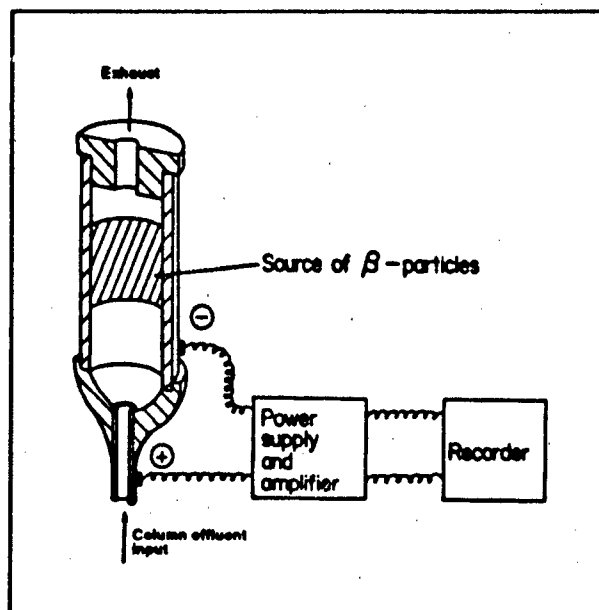


Figure 24. Electron Capture Detector (ECD), Cross-Section Detector (CSD), Argon Detector, and Helium Detector (15:43).

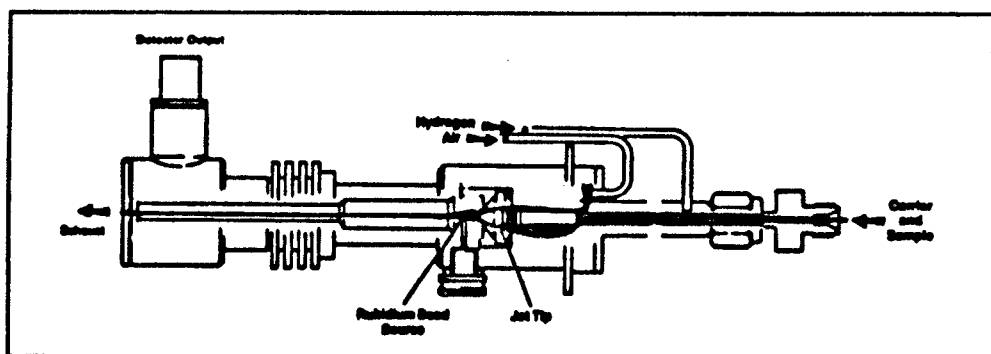


Figure 25. Nitrogen-Phosphorus Detector (NPD) (38:128).

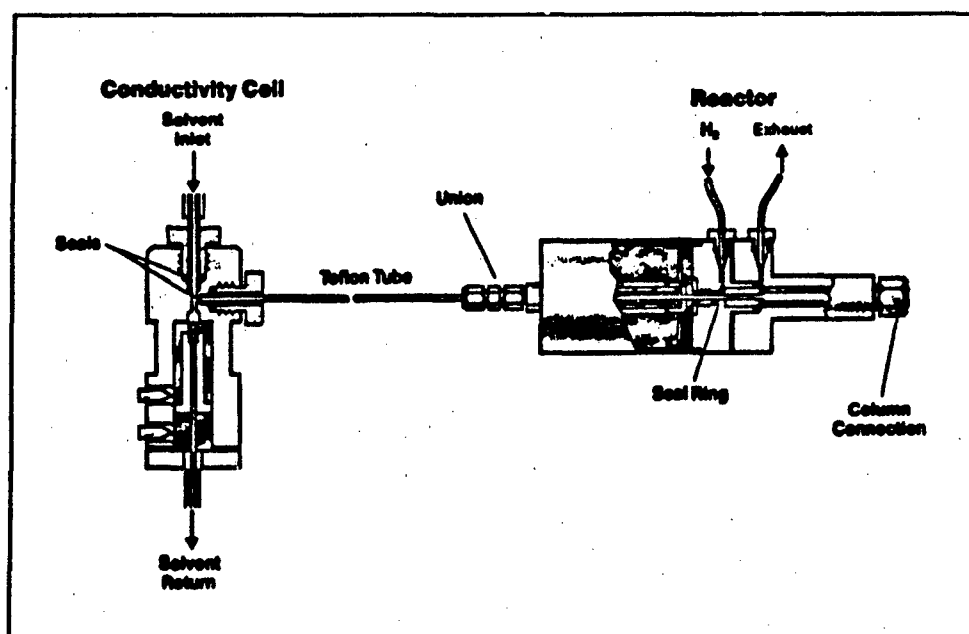


Figure 26. Hall Electrolytic Conductivity Detector (HECD) (38:133).

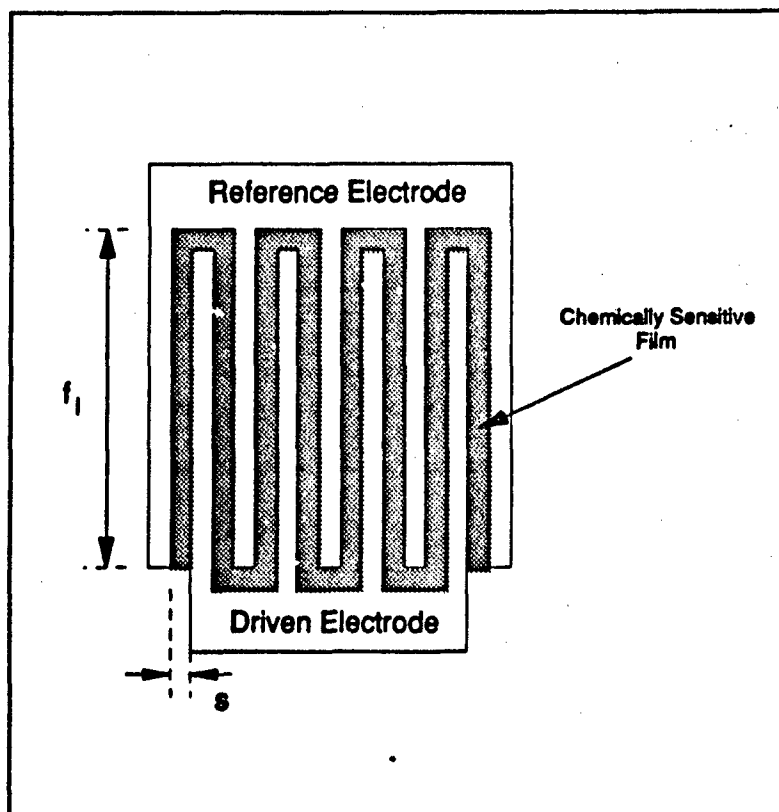


Figure 27. Chemiresistor Conductivity Detector with Interelectrode Spacing,  $s$ , and Finger Length,  $f_l$  (43:346).

### *III. Micromachining and Related Fabrication Techniques*

For the micromachined gas chromatograph, the primary tools used in its fabrication are wet chemical etching (both isotropic and anisotropic), thin film deposition (as a means to uniformly coat surfaces), and anodic bonding (as a means for joining separate components). In the following sections, each of these tools are discussed relative to their potential to facilitate the fabrication of the MMGC.

#### *3.1 Micromachining.*

Micromachining is, as its name implies, the fabrication of very small three-dimensional physical structures. W. H. Ko defines it more precisely as "a combination of precise etching, insulator-to-silicon or silicon-to-silicon bonding techniques, connection between layers, and standard integrated circuit methods to fabricate precise three-dimensional silicon-based microstructures of great diversity..." (56). A diversity of applications has been realized as demonstrated by the variety of papers published in recent years. Some of the applications for micromachining include: pumps (57-59), valves (59-61), blood gas analyzers (62), gears (63-65), tongs (64), turbines (63, 64, 66), flow sensors (67-71), pressure sensors (61, 67, 70-73), actuators (65, 74, 75), springs (65), radiation sensors (76), membrane oscillators (66, 70), pipes (77), and bridges (78, 79).

Related to these applications is the investigation of how micromechanical systems operate. Substantial interest has been shown in the process for miniaturizing mechanical systems, and how these systems behave compared to their macroscopic counterparts (80-85). Fortunately, those aspects of micro-fluid dynamics that would have an impact on the MMGC have been addressed by capillary chromatographers and were presented in the previous chapter. The general micromachining techniques used, however, are important in understanding the MMGC design constraints.

Although micromachining in its most general sense includes a variety of methods, for the purpose of this research, micromachining refers exclusively to modifications performed to the substrate's surface by etching. There are three major families of etching pro-

cesses used to accomplish micromachining. These include: wet chemical etching<sup>1</sup>, plasma processing<sup>2</sup>, and sacrificial layer processing<sup>3</sup> (88). Of these three techniques, the simplest to implement is wet chemical etching. So, in the interest of developing a straightforward fabrication approach, the simplest technique that could accomplish the objective was selected. As will be demonstrated, wet chemical etching was the fundamental tool used to fabricate the MMGC.

Wet chemical etching is one of the most common forms of modifying the silicon surface in IC manufacturing. It is used in this sense to polish wafers so that their surface is clean, flat, and free of damage (89:451). Since wet chemical etching of silicon is well understood, and it has had a demonstrated reproducibility in the AFIT laboratories, it was chosen as the etching technique for this research. In general, wet chemical etching involves three major steps, and they are summarized by Sze in *Semiconductor Devices: Physics and Technology* as:

- (1) The reactants are transported (e.g., by diffusion) to the reacting surface, (2) chemical reactions occur at the surface, and (3) the products from the surface are transported away (e.g., by diffusion)... In IC processing, most wet chemical etchings proceed by dissolution of a material in a solvent or by conversion of a material into a soluble compound which subsequently dissolves in the etching medium. (89:451)

Wet chemical etching, as a process, can be subdivided into two types: isotropic and anisotropic. In an *isotropic* etch, there are no significant etch rate differences relative to crystallographic directions. In other words, an isotropic etch proceeds at the same rate

---

<sup>1</sup>The "simple dissolution of a material in a solvent as well as the conversion of the material into a soluble compound which can be dissolved by the etching medium" (86:476).

<sup>2</sup>"A radio-frequency source is used to ionize some fraction of the gas molecules, creating a plasma. The plasma contains positive ions, negative ions, electrons, and neutral gas atoms, such that a condition of near charge neutrality exists. It may also contain free radicals—atoms or molecules that are extremely reactive. Depending on the surface layer to be etched and the desired outcome of the etching process, the exposed silicon surface may be chemically etched by the free radicals (plasma etching), or it may be physically etched by positive ion bombardment (sputter etching). There is also a third alternative; vacuum pressure, RF energy, and wafer placement may be arranged so that both chemical etching and ion bombardment take place. This third alternative is called reactive ion etching" (87:260).

<sup>3</sup>"Processes in which the mechanical object to be manufactured is not 'machined' in the substrate, but in the thin layers that have been deposited on it.... Nearly all these processes use the 'sacrificial' layer technique, which consists of liberating mechanical structures that have been deposited or doped by under-etching another underlying thin layer" (88:134).

throughout the material, yielding the profile shown in Figure 28(c). This is the same type of etched profile that is commonly obtained with a polycrystalline or amorphous material (i.e., a Pyrex borosilicate glass plate). An *anisotropic* etchant, however, possesses an etch rate that is orientation dependent, which yields profiles which are significantly different, depending upon the crystallographic orientation of the material (see Figure 28(a, b)). Both of these types of etchants have an important role in the fabrication of the MMGC, but the isotropic etchant will be presented first since it forms the basis of the column cross section.

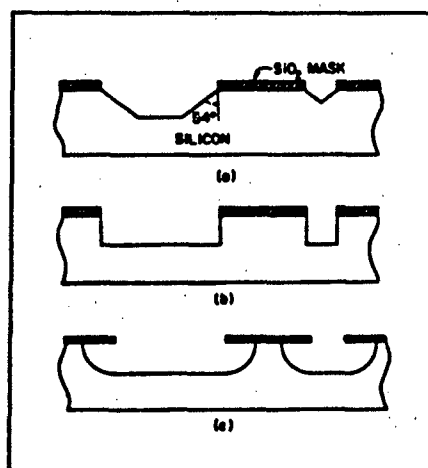


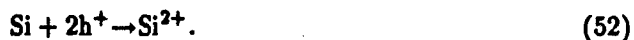
Figure 28. Potential Column Cross Sections. (a) (100)-Oriented Silicon Anisotropically Etched with Potassium Hydroxide (KOH), (b) (110)-Oriented Silicon Anisotropically Etched with KOH, and (c) Silicon Isotropically Etched with  $\text{HF-HNO}_3$  (12:1881).

**3.1.1 Isotropic Etching.** Since the cross section of the MMGC column's channel is determined by the etching technique used to process the silicon wafer, an isotropic etchant was chosen because the resulting etch profiles are similar between silicon and glass—a rectangle with rounded corners (see Figure 28c). Although anisotropic etchants are available, there are several problems associated with fabricating the channels with a perfect rectangular cross section. First, the wet chemical anisotropic etching techniques are orientation dependent (and would only work with single crystal silicon); therefore, it would be impossible to etch a spiral shaped GC column. Second, if a GC spiral shaped column with a rectangular cross section were etched, the  $90^\circ$  angle between the side-walls and bottom of the cavity would complicate the homogeneous distribution of the stationary

phase. This feature could result in a degradation of the resolution of the column (depending on the state—solid or liquid—of the stationary phase) (90). Accordingly, the primary etching technique adopted was a wet chemical isotropic etchant, yielding a column cross section similar to that shown in Figure 28c.

The most common isotropic silicon etchant, the HNA system<sup>4</sup>, which is composed of a mixture of nitric acid (HNO<sub>3</sub>), hydrofluoric acid (HF) and acetic acid (CH<sub>3</sub>COOH), was characterized as early as 1960 (91). Although water can be used as the diluent in place of the acetic acid, acetic acid is used to extend the useful life of the etchant (86:480). The chemical reactions involved with etching the silicon with this system can be summarized in two major steps: oxidation of the silicon surface followed by removal of the silicon dioxide (89).

**3.1.1.1 Etchant Reactions.** In the oxidation portion of the reaction, two holes (denoted by h<sup>+</sup>) are required<sup>5</sup> and react as follows (89):



The water in the system dissociates, yielding (89):



The OH<sup>-</sup> ion from Equation 53 and the Si<sup>2+</sup> ion from Equation 52 combine to form an intermediate product (89):



Hydrogen gas is then liberated through the following reaction as silicon dioxide (SiO<sub>2</sub>) is formed (89):



<sup>4</sup>HNA represents Hydrofluoric acid, Nitric acid, and Acetic acid.

<sup>5</sup>These holes are created by the autocatalytic reactions:  $\text{HNO}_3 + \text{HNO}_2 \rightarrow 2\text{NO}_2^- + 2\text{h}^+ + \text{H}_2\text{O}$  and  $2\text{NO}_2^- + 2\text{H}^+ \rightarrow 2\text{HNO}_2$  (89).

In the second phase of the chemical reaction, the hydrofluoric acid (HF) manifests its utility. Specifically, it dissolves the silicon dioxide by the following chemical reaction (89):



Since  $\text{H}_2\text{SiF}_6$  is soluble in water, fresh silicon is exposed, and the etch continues (89). Although the chemical reactions are straightforward, the etch rate is highly dependent on temperature and the ratios of the constituents. Fortunately, the etch rates of this system have been well characterized (91, 92, 93, 94).

**3.1.1.2 Etch Rate.** Figure 29 depicts an isoetch plot for the HNA system at room temperature ( $25^\circ\text{C}$ ) (89, 91). As will be discussed in the next chapter, the MMGC columns were etched to a depth on the order of  $10\text{ }\mu\text{m}$ ; thus, a low etch rate was desired to maintain precise control and reproducibility. Additionally, to insure an isotropic etch, a low HF solution concentration was required<sup>6</sup>. Therefore, an etchant solution composed of  $\text{HF}:\text{HNO}_3:\text{CH}_3\text{COOH}$  (2:15:5) was used for the MMGC column's etch, which, theoretically, yields an etch rate of approximately  $5.75\text{ }\mu\text{m}/\text{min}$ .

Since  $\text{SiO}_2$  is used as an etch mask, it is also important to know the  $\text{SiO}_2$  etch rate. This information will then determine the silicon dioxide thickness that will be required for a specific etch process. Experimentally, an  $\text{SiO}_2$  etch rate of approximately  $250\text{ }\text{\AA}/\text{min}$  was determined using the (2:15:5) system described above at room temperature. This selection yields a differential etch rate of approximately 230:1 for the  $\text{Si}:\text{SiO}_2$  system with the  $\text{HF}:\text{HNO}_3:\text{CH}_3\text{COOH}$  (2:15:5) isotropic wet chemical etch system.

The second type of wet chemical etch, the anisotropic etch, was crucial for the full realization of the MMGC. As will be discussed in the next chapter, the design of the detector cavity required a deep etch process (on the order of  $100\text{ }\mu\text{m}$ ). Additionally, alignment between features on the front and back sides of the silicon wafer had to be maintained. This requirement was accomplished by etching alignment marks through the

<sup>6</sup>The low HF solution concentration region in Figure 29 "is controlled by the ability of HF to remove the  $\text{SiO}_2$  as it is formed; etchant solutions in this region are isotropic, that is, not sensitive to crystallographic orientation..." (89:453).

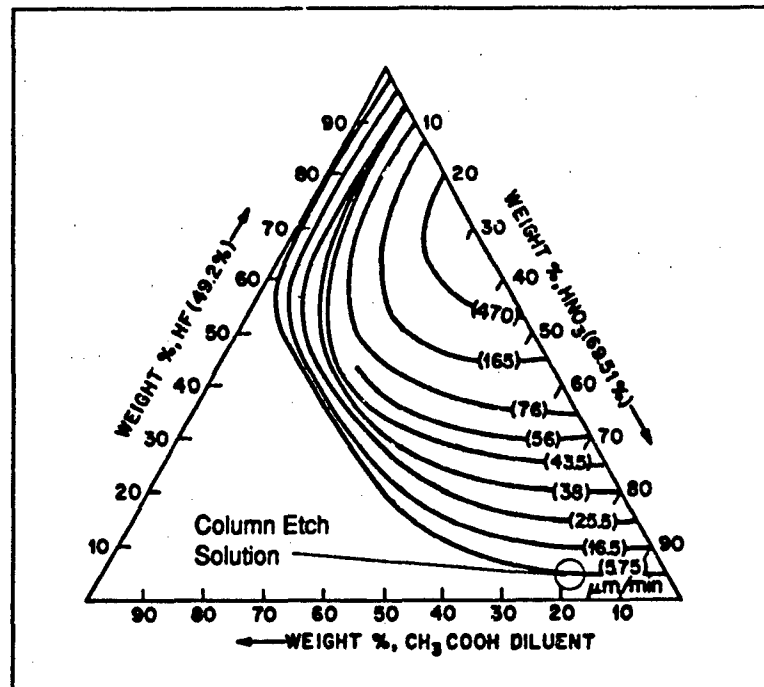


Figure 29. Isoetch Curves for Silicon (HF:HNO<sub>3</sub>:CH<sub>3</sub>COOH System) (89:453).

silicon wafer (on the order of 300  $\mu\text{m}$  thick). An anisotropic etch process using (100)-oriented<sup>7</sup> silicon wafers was used for this purpose.

**3.1.2 Anisotropic Etching.** Since the wet chemical anisotropic etching mechanism is based upon a differential etch rate between crystallographic planes within a single crystal silicon wafer, it is important to review the silicon crystal structure. Figure 30 shows a unit cell of the diamond crystal structure for crystalline silicon.

With the aid of this three-dimensional crystal structure, a number of important planes can be identified. Three of the planes which are critical to wet-chemical micromachining are shown in Figure 31 along with their corresponding Miller indices<sup>8</sup>.

<sup>7</sup>Chosen because the (100)-oriented plane is the only major plane in which the dense (111) planes intercept the surface at 90° with respect to each other, thus promoting the fabrication of rectangular shaped micromachined structures (see Figure 31) (95, 96).

<sup>8</sup>The Miller indices for a given crystal plane can be found using the following steps: "(1) Find the intercepts of the plane [of interest] on the three Cartesian coordinates in terms of the lattice constant. (2) Take the reciprocals of these numbers and reduce them to the smallest [set of] three integers having the same ratio. (3) Enclose the result in parentheses (hkl) as the Miller indices for a single plane" (89:6).

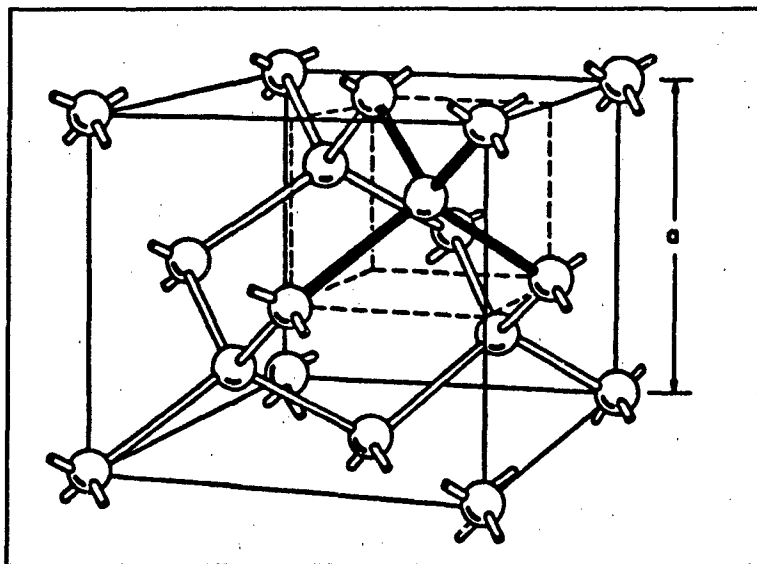


Figure 30. Diamond Crystal Structure of Silicon with Lattice Constant ' $a$ ' where Each Silicon Atom is Surrounded by Four Nearest Neighbors (Highlighted by the Internal Darkened Bars) (89:5).

W. H. Ko reports that one of the primary mechanisms responsible for the different planar etch rates observed in anisotropic etching processes is the atomic planar density (56:144). A second mechanism likely involves the number of available surface bonds; those planes which have a higher surface bond density would etch more quickly (97:49). Table 4 lists the atomic and chemical bond densities for the three important silicon crystal planes. These densities support the argument that the different etch rates for the three most common anisotropic silicon etching systems (potassium hydroxide-deionized water<sup>9</sup>, ethylenediamine-pyrocatechol-deionized water<sup>10</sup>, and hydrazine-deionized water<sup>11</sup>) are a strong function of the magnitudes of the atomic and chemical bond densities.

Of these three etching systems, the potassium hydroxide-deionized water (KOH-DIW) system was identified for several reasons. First, it has been used successfully in

<sup>9</sup>At 85°C and a 1:1 etchant component ratio, the etch rate of the (100) plane is 1.43  $\mu\text{m}/\text{min}$ , and the differential etch rate is approximately 200:1 between the (100) and (111) planes (98).

<sup>10</sup>At 115°C and a 6.25:1:2 etchant component ratio, the etch rate of the (100) plane is 1.25  $\mu\text{m}/\text{min}$ , and the differential etch rate is approximately 35:1 between the (100) and (111) planes (98).

<sup>11</sup>At 118°C and a 1:1 etchant component ratio, the etch rate of the (100) plane is 3  $\mu\text{m}/\text{min}$ , and the differential etch rate is approximately 16:1 between the (100) and (111) planes (98).

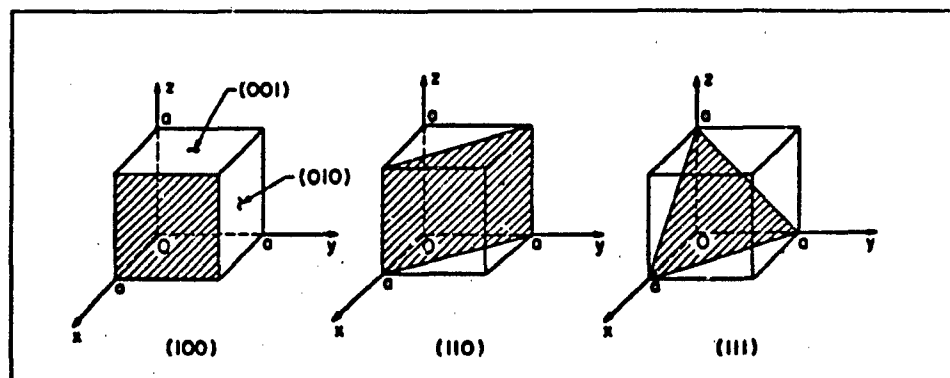


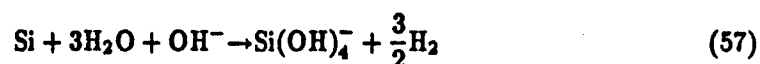
Figure 31. Miller Indices of Important Silicon Crystal Planes with Lattice Constant 'a' (89:7).

Table 4. Planar Density Properties of the Major Silicon Crystal Planes (97:48).

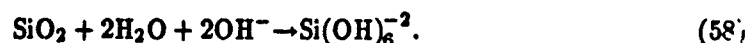
Property	Miller Orientation		
	(100)	(110)	(111)
Atomic Density ( $10^{14}/\text{cm}^2$ )	6.78	9.59	15.66
Available Bond Density ( $10^{14}/\text{cm}^2$ )	6.78	9.59	11.76

the AFIT laboratories for several years. Secondly, the KOH-DIW system has a superior differential etch rate compared to the other two systems. Also, it is less toxic compared to the other two systems, making it safer to utilize and dispose. Finally, its performance is well characterized for various temperatures and concentrations (98, 99, 100).

**3.1.2.1 Etchant Reaction.** Although the KOH-DIW system has been well characterized, the exact mechanism of the reaction is not precisely known (99, 101). Kendall, however, suggests the following reaction (99):



where  $\text{Si}(\text{OH})_4$  is orthosilicic acid (which is water soluble) (101). A similar process is believed to be responsible for the dissolution of silicon dioxide (99:111):



The approximate etch rates for a variety of concentrations and temperatures are shown in Table 5. From this table, it is apparent that the 20-30% concentration range maximizes the etch rate for the temperatures evaluated. However, before an operating point is identified, a careful examination of the silicon dioxide etch rates must be accomplished. The reason the  $\text{SiO}_2$  etch rate is so important relative to the anisotropic silicon etch process is because the silicon etch process will be on the order of several hundreds of microns deep, whereas the isotropic silicon etch process previously discussed (see Section 3.1.1) needed to be only a few microns deep. Table 6 summarizes the silicon dioxide etch rates for the same conditions reported in Table 5. The corresponding etch ratios are shown in Table 7.

Table 5. Approximate Etch Rate of the (100) Plane in the KOH-DIW System ( $\mu\text{m}/\text{min}$ ). Concentration Reported as a Percent by Weight in Water (99:109).

Concentration	Temperature ( $^{\circ}\text{C}$ )			
	30	50	70	85
5	0.01	0.06	0.2	0.3
20	0.06	0.2	0.6	1
30	0.04	0.2	0.6	1.2
40	0.02	0.1	0.4	1
55	0.01	0.04	0.2	0.4

Table 6. Approximate Etch Rate of Silicon Dioxide in the KOH-DIW System ( $\text{\AA}/\text{min}$ ). Concentration Reported as a Percent by Weight in Water (99:112).

Concentration	Temperature ( $^{\circ}\text{C}$ )			
	30	50	70	85
5	0.2	1	5	20
20	0.4	3	15	40
30	0.5	4	20	60
40	0.3	3	20	60
55	0.2	2	20	60

Although the majority of the etch ratios in Table 7 are greater than the 230:1 ratio associated with the isotropic etch process, the total silicon dioxide thickness required to

Table 7. Etch Ratio of (100)-Oriented Silicon Relative to Silicon Dioxide. Concentration Reported as a Percent by Weight in Water.

Concentration	Temperature (°C)			
	30	50	70	85
5	500	600	400	150
20	1500	670	600	250
30	800	500	300	200
40	670	330	200	170
55	500	200	100	70

accomplish a deep silicon etch could still exceed the maximum reasonable thickness of thermally grown silicon dioxide<sup>12</sup>. Since the silicon wafers used in this research were on the order of 300  $\mu\text{m}$  thick, the worst-case oxide thickness would be sufficient to accomplish a 300  $\mu\text{m}$  silicon etch process. The time required to etch through a silicon wafer is reported in Table 8 for various conditions.

Table 8. Time (Hours) Required to Etch 300  $\mu\text{m}$  of (100)-Oriented Silicon. Concentration Reported as a Percent by Weight in Water.

Concentration	Temperature (°C)			
	30	50	70	85
5	510	80	8	17
20	80	25	8	5
30	130	25	8	4
40	250	50	13	5
55	510	130	25	13

Knowing the length of time that the silicon dioxide must survive, it is a straightforward calculation (using the values in Table 6) to determine the silicon dioxide's required thickness. These results are tabulated in Table 9.

<sup>12</sup>Due to laboratory restrictions, the only type of quality silicon dioxide which can be used as an etch mask must be grown in an oxidation furnace. The practical limit on thickness for this technique (using 95°C steam and a furnace temperature of 1050°C) is approximately 4  $\mu\text{m}$ , which requires nearly 40 hours of oxidation time (86:386).

Table 9. Approximate Oxide Thickness ( $\mu\text{m}$ ) Required to Mask an Etch of  $300\ \mu\text{m}$  into (100)-Oriented Silicon. Concentration Reported as a Percent by Weight in Water.

Concentration	Temperature ( $^{\circ}\text{C}$ )			
	30	50	70	85
5	0.6	0.5	0.8	2
20	0.2	0.5	0.7	1.2
30	0.4	0.6	1	1.5
40	0.5	0.9	1.5	1.8
55	0.6	1.5	3	4.5

To accommodate a margin of safety and permit processing in a reasonable amount of time (on the order of one day for oxidation and etching), a compromise operating point of 20% KOH at  $50^{\circ}\text{C}$  was identified. With the operating point known, it is now appropriate to discuss the three primary structures that will be fabricated with this etchant system.

All three structures share a common feature since they result from the (111) plane intersecting the (100) surface. For silicon, the angle,  $\phi$ , between two planes,  $(h_1k_1l_1)$  and  $(h_2k_2l_2)$ , is given by the following equation (97:31):

$$\phi = \arccos \left( \frac{h_1h_2 + k_1k_2 + l_1l_2}{\sqrt{h_1^2 + k_1^2 + l_1^2} \sqrt{h_2^2 + k_2^2 + l_2^2}} \right). \quad (59)$$

From Equation 59, the angle between the (100) plane and the (111) plane has been calculated to be approximately  $54.74^{\circ}$ . This angle forms the basis for the design of the three structures used in the MMGC: the V-groove<sup>13</sup>, the feedthrough feature<sup>14</sup>, and the inverted truncated pyramid<sup>15</sup>.

**3.1.2.2 V-Groove.** The V-groove shown in Figure 32 is typical of a V-groove etched on (100)-oriented silicon with the KOH-DIW system. This structure occurs because at the point where the (111) planes intersect, the etch rate decreases to approximately 5%

<sup>13</sup>The V-groove is used as a channel for the TCD electrical leads.

<sup>14</sup>The feedthrough features permit the introduction of gas into the MMGC column and facilitate alignment between features on the front and back sides of the silicon wafer.

<sup>15</sup>The inverted truncated pyramid serves as the thermistor cavity for the TCD.

of the value associated with the (100) plane (102). The depth of the groove,  $d_g$ , can be calculated from the width of the silicon dioxide mask,  $W$ , (or, conversely, the silicon dioxide mask's width can be calculated that will yield a specific etch depth) using the following relationship (97:49):

$$d_g = (W/2) \tan 54.74^\circ. \quad (60)$$

As an example, a V-groove 100  $\mu\text{m}$  deep requires a silicon dioxide mask that is approximately 140  $\mu\text{m}$  wide.

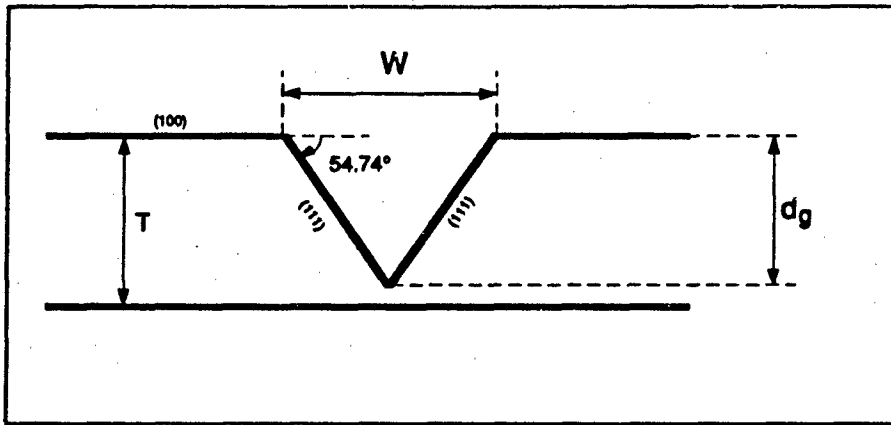


Figure 32. Cross-Section of a Typical V-Groove Etch.

**3.1.2.3 Feedthrough Feature.** The feedthrough feature is similar to a very deep V-groove since the walls are sloped  $54.74^\circ$  relative to the horizontal upper surface. However, the major difference is that the feedthrough feature's etch depth is actually greater than the wafer's thickness. In order to determine the width of the hole that is etched through the wafer, it is necessary to examine the geometry involved. Figure 33 shows the geometry of a typical feedthrough feature's etch.

Since triangle 123 in Figure 33 is a right triangle with  $\angle 312 = 54.74^\circ$ , the following relationship holds:

$$\tan 54.74^\circ = \frac{d_f - T}{W_{\text{hole}}/2}. \quad (61)$$

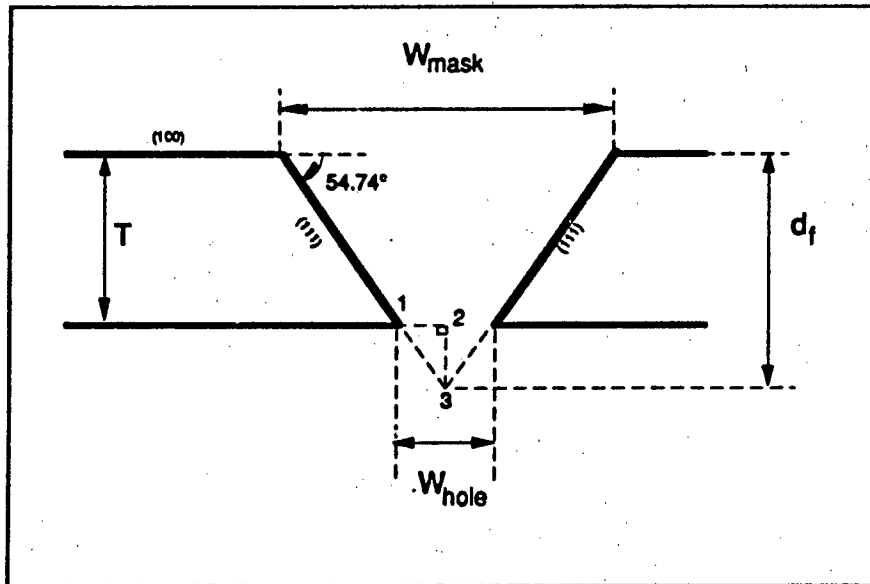


Figure 33. Cross-Section of a Typical Feedthrough Feature Etch.

Since  $d_f$  is defined by Equation 60, substituting and solving for  $W_{mask}$  yields:

$$W_{mask} = W_{hole} + \frac{2T}{\tan 54.74^\circ}. \quad (62)$$

As an example, if a  $100 \mu\text{m}$  wide hole was required in a  $300 \mu\text{m}$  thick wafer, the silicon dioxide mask aperture ( $W_{mask}$ ) would need to be approximately  $524 \mu\text{m}$  wide.

**3.1.2.4 Inverted Truncated Pyramid.** The third anisotropically etched structure required for the MMGC design is a V-groove which is terminated before the (111) planes intersect, leaving a flat bottom. This situation is depicted in Figure 34. Since the depth of this isothermal etch is controlled by etching time, the self-stopping properties of the (111) plane intersection cannot be used. Therefore, it is important to monitor the etch time as reported in Table 5.

Given a desired etch depth,  $d_e$ , it is possible to calculate the required mask width,  $W_{mask}$ , for a certain bottom width,  $W_{bottom}$ , using Equation 62 and substituting  $d_e$  for  $T$  (compare Figures 33 and 34). As an example, a  $200 \mu\text{m}$  deep etch ( $d_e$ ) with a bottom width of  $300 \mu\text{m}$  ( $W_{bottom}$ ) requires a mask width ( $W_{mask}$ ) of approximately  $583 \mu\text{m}$ .

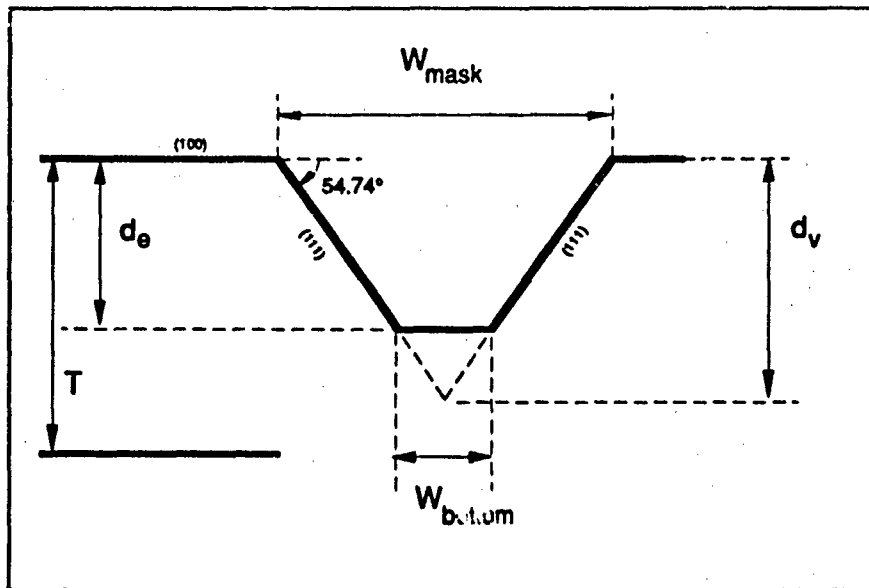


Figure 34. Cross-Section of a Typical Inverted Truncated Pyramid Etch.

These three anisotropic etch structures, in conjunction with the isotropic column etch process form the basis of the micromachining aspect of the MMGC fabrication. In order to construct a functional MMGC, though, it is necessary to coat the inside walls of the column with a stationary phase. This process can be accomplished by employing conventional IC thin film deposition techniques.

### 3.2 Thin Films.

As mentioned in Section 1.1 and later alluded to in Section 2.5.5, copper phthalocyanine (CuPc) is the stationary phase choice for the MMGC<sup>16</sup>. A uniform coating of the phase within the column can be achieved using a deposition method "borrowed" from conventional IC fabrication technology.

Of the major IC thin film deposition methods (chemical vapor deposition, molecular beam epitaxy, sputtering, and vacuum evaporation<sup>17</sup>—both thermal and electron-beam), vacuum thermal evaporation (sublimation) was chosen to deposit the stationary phase for

<sup>16</sup>The reasoning behind this choice will be discussed in detail in Section 4.1.1.

<sup>17</sup>Since CuPc sublimates (converts from the solid state to the gas state without passing through the liquid state), the standard evaporation techniques discussed here refer to sublimation with respect to CuPc.

the MMGC (89, 103). This choice was based on three considerations. First, vacuum thermal evaporation is one of the simplest (and oldest) deposition methods (103). Second, the AFIT microelectronics laboratory possesses a vacuum thermal evaporation system<sup>18</sup>. Third (and most important), vacuum evaporation has proven itself to be a reliable technique for depositing thin CuPc films (7, 43, 45).

A typical vacuum thermal evaporation system is shown in Figure 35. The operation of this system is concisely described by W. H. Ko in "Semiconductor Integrated Circuit Technology and Micromachining" (56:132):

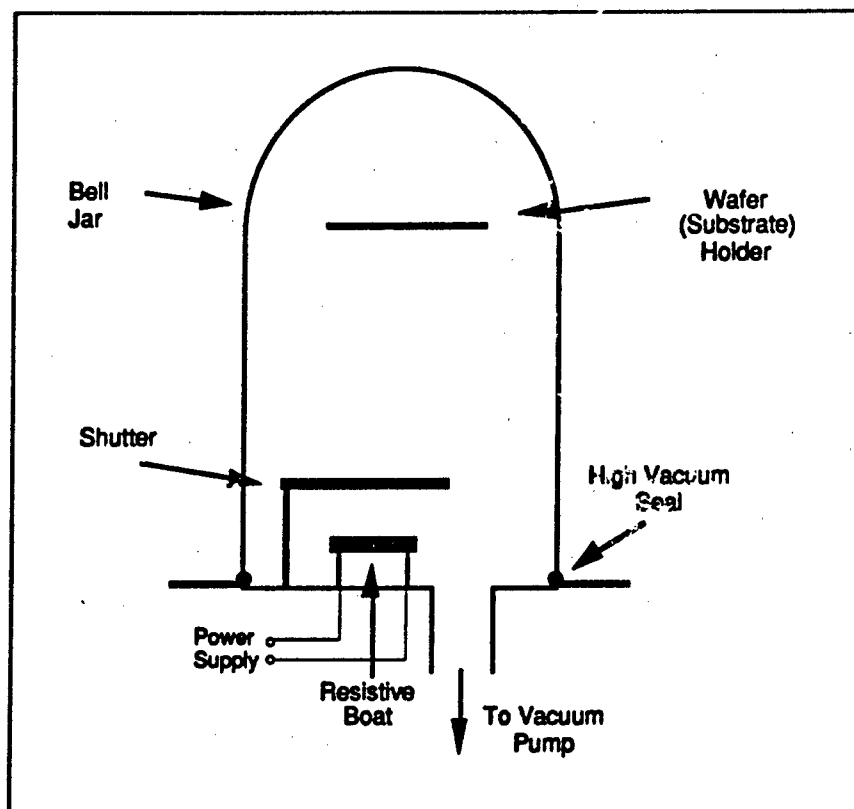


Figure 35. Typical Thin Film Evaporation Apparatus.

The substrate (e.g., silicon) and source material (e.g., Al, Au, Cr, etc.) to be evaporated are mounted in the bell jar. The system is pumped down to the appropriate pressure and the source material is heated until it vaporizes.

<sup>18</sup>Model DV-602, Denton Vacuum, Inc., Cherry Hill, NJ.

When the source material's vapor pressure exceeds that in the bell jar, the material vaporizes rapidly. Under a high vacuum, the mean free path of the vaporized atoms or molecules is greater than the distance between the source and the substrate. The vaporized atoms, radiated in all directions, condense on all lower temperature surfaces with which they collide, including the substrate and the bell jar, forming a uniform thin film.

Using this technique, it is possible to realize a uniform coating of CuPc within the MMGC's column. However, since the MMGC's column is composed of two parts (the silicon wafer and the borosilicate glass cover plate), a functional column will only result if the two halves can be brought into intimate contact. This requirement can be accomplished through anodic bonding.

### 3.3 Anodic Bonding.

**3.3.1 MMGC Column Requirements.** As discussed earlier, since the MMGC column halves will be etched with an isotropic etchant, a pair of open troughs in each substrate will be realized. In order to function as a column, these troughs must be brought into contact, aligned, and sealed. Since the MMGC column will only be on the order of a few microns deep (approximately 10  $\mu\text{m}$ —see Section 4.1.1.2), it is imperative that this seal be accomplished without introducing any foreign material into the column (i.e., an epoxy or other adhesive). A technique which has been used extensively in conjunction with micromachining to join and seal silicon structures at relatively low temperatures (180° to 500°C) is anodic bonding (104). Using a modified version of this technique (a slightly lower temperature<sup>19</sup>), channels which are etched in silicon can be rendered air tight.

**3.3.2 Theory.** The anodic (or electrostatic) bonding process is depicted in Figure 36. It was initially described by G. Wallis and D. Pomerantz in (104, 105), and later expanded upon in a number of other articles (106, 107, 108, 109). W. H. Ko in *Micromachining and Micropackaging of Transducers* describes the process as follows (107:45-47):

---

<sup>19</sup>Thermal constraints imposed by the stationary phase prevented using temperatures greater than 150°C (see Section 4.1.1).

The electrostatic bonding process can be accomplished on a hot plate in atmosphere or vacuum at temperatures between 180° and 500°C (well below the softening point of the Pyrex<sup>20</sup> glass). Electrostatic attraction between the glass and silicon pieces serves to pull the two into intimate contact, thus eliminating the need for applying mechanical pressure to the wafers.

...The electrostatic attraction between the glass and silicon wafer is developed as follows. At elevated temperatures...the positive sodium ions in the glass become quite mobile and they are attracted to the negative electrode on the glass surface where they are neutralized. The more permanently bound negative ions in the glass are left, forming a space charge layer in the glass adjacent to the silicon surface...After the Na<sup>+</sup> ions have drifted toward the cathode, most of the potential drop in the glass occurs at the surface next to the silicon. The two wafers then act as a parallel plate capacitor with most of the potential being dropped across the several micron wide air gap between them. The resulting E-field between the surfaces serves to pull them into contact with a force of approximately 350 psi for  $E = 3 \times 10^{-6}$  V/cm.

Once the wafers are in contact, almost all of the applied potential is dropped across the space charge layer in the glass. The extremely high fields which develop in that region transport oxygen out of the glass to bond with the silicon surface. The seal appears to be chemical in nature, possibly a very thin layer of grown SiO<sub>2</sub>.

Due to the thermal constraints imposed by the stationary phase, a number of initial evaluations were performed at a lower temperature of 150°C using 1.6 mm thick, 4 inch by 4 inch plates of Tempax Boro-Glass<sup>21</sup> (borosilicate glass) and (100)-oriented, 3 inch diameter silicon wafers<sup>22</sup>. These evaluations demonstrated that reliable bonds could be obtained at the lower temperature; however, the bond required approximately 20 hours at 1800 V (as opposed to approximately 15 minutes at 1000 V for 450°C) (107:48). This value was considered a reasonable amount of time considering the effort required to accomplish the other MMGC fabrication steps.

### 3.4 Summary.

This chapter discussed the theory concerning the basic tools and techniques used to manufacture the MMGC in the same sequence as it was actually fabricated. Wet chemical

<sup>20</sup>Pyrex and its related borosilicate glass products are soda-lime glass with boron added to improve the optical and mechanical properties of the glass (110).

<sup>21</sup>Similar to Pyrex 7740, but manufactured by Schott America, Yonkers, NY.

<sup>22</sup>N-type, 0.005-0.020  $\Omega$ -cm, Czochralski wafers manufactured by Polycore Electronics, Newberry Park, CA.

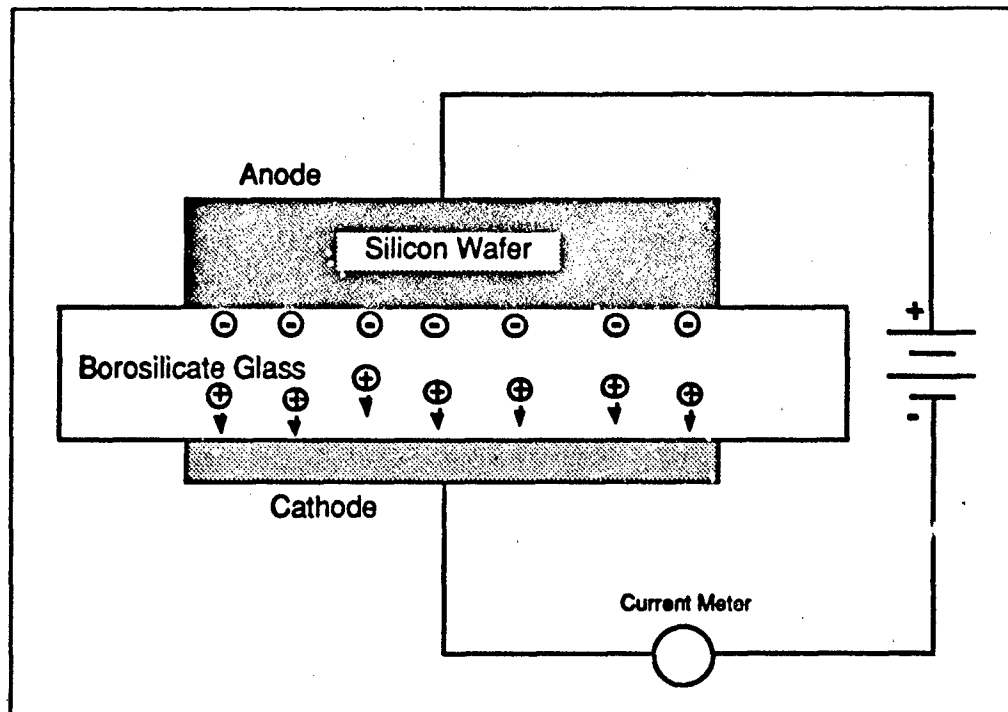


Figure 36. Anodic Bonding Mechanism.

etching is first used to micromachine the silicon and glass surfaces to create the column and detector cavities. Then, a thin film deposition process is used to realize the stationary phase. Finally, anodic bonding is used to assemble the two halves of the MMGC. The next chapter will discuss in greater detail the specifics of the MMGC design.

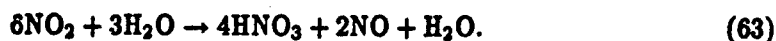
#### IV. Micromachined Gas Chromatograph and Performance Evaluation System Design

This chapter describes the rationale for the design of the MMGC and the associated performance evaluation system. The MMGC design will be discussed first since it directly influences the requirements for the performance evaluation system. Furthermore, since part of MMGC design rationale involved improvements to an existing MMGC design<sup>1</sup>, specific details of Terry's earlier design are summarized in each of the pertinent sections.

##### 4.1 Micromachined Gas Chromatograph Design.

The MMGC designed for this research is based on Terry's initial configuration (11). Like its larger counterpart, the MMGC has four major components: the mobile phase, the sample injection system, the column, and the detector (see Figure 37). At the heart of the system, of course, is the column; and central to its operation is the stationary phase. Since this area is the one which gave Terry the most difficulty, it will be discussed first. Once the choice of stationary phase (CuPc) is justified, it will then be appropriate to discuss the selection of the various parameters associated with the micromachined column geometry.

**4.1.1 Stationary Phase.** Although  $\text{NH}_3$  can be routinely separated and detected in a standard GC,  $\text{NO}_2$  is a difficult compound to analyze with standard stationary phases due to its highly reactive nature<sup>2</sup> (18:427). In fact, the standard GC technique used to analyze  $\text{NO}_2$  is to induce it to react completely with water vapor and examine the by-products (30). This reaction is given by (18:427):



<sup>1</sup>This prior miniaturized gas chromatograph was capable of separating 33,000 ppm isobutane, 142,000 ppm acetone and 37,000 ppm ethanol, and it was designed and fabricated at Stanford University by S.C. Terry (11).

<sup>2</sup>The only GC stationary phase which is used to separate  $\text{NO}_2$  from  $\text{NH}_3$  is in the form of a polymer bead (Poropak Q, packed into a column) and suffers from all of the attendant disadvantages of a packed column (111).

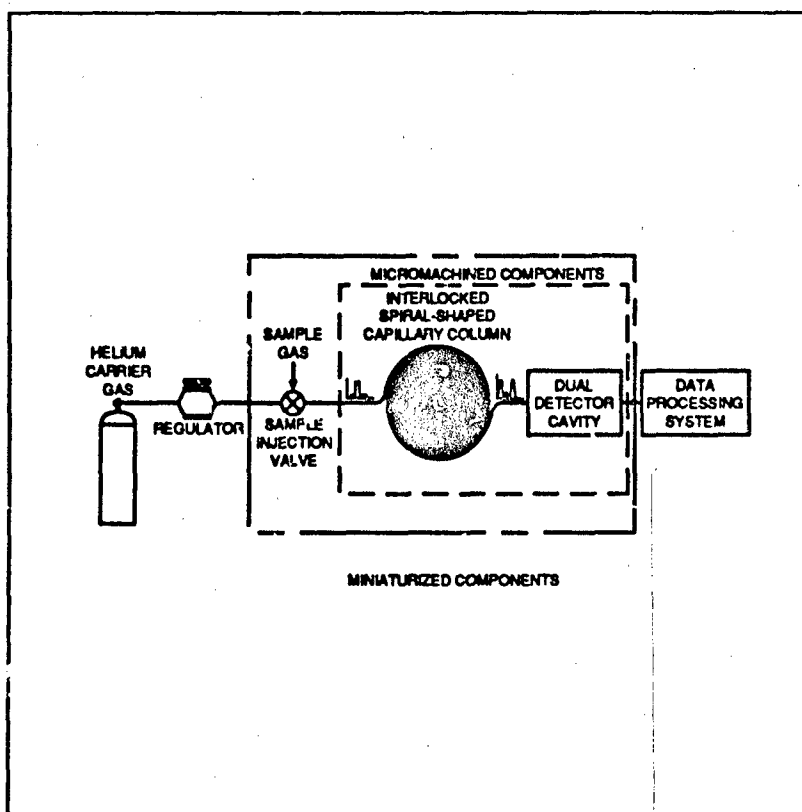


Figure 37. Block Diagram of a Micromachined Gas Chromatograph.

The nitric oxide product can readily be separated from the other components in a molecular sieve and, when detected, it will have a concentration level that is one-third less than the initial nitrogen dioxide concentration (18).

A compound which has the potential to simplify the separation of nitrogen dioxide and has shown promise as a stationary phase for other gases (in particular, ammonia) is copper phthalocyanine (CuPc) (45, 112). E. M. Vary has shown that CuPc was effective as a stationary phase for separating a variety of compounds when used as a powder suspended in silicone oil in a packed chromatographic column (112). Although she did not specifically evaluate her column with  $\text{NO}_2$  or  $\text{NH}_3$ , her work did show that CuPc had the potential to

act as a phase for separating a variety of compounds<sup>3</sup> (112). Additionally, other studies have shown that thin films of CuPc reversibly adsorb NO<sub>2</sub> and NH<sub>3</sub> (7, 45, 113).

**4.1.1.1 CuPc as a Solid Stationary Phase.** Since the adsorption of NO<sub>2</sub> and NH<sub>3</sub> on CuPc can be reversible, a thin film of CuPc has the potential to serve as a solid stationary phase within a micromachined chromatographic column. Two particular advantages of using a solid adsorbent as a phase include (18:140):

1. *Speed of Equilibration.* Physical adsorption is generally quicker than the process of solution. Thus, there is more rapid equilibration between gas and solid phase than between gas and liquid phase. ...this can lead to greater column performance, and greater separative ability. This advantage is most relevant in those columns which are specifically designed for high performance, e.g., open tube "capillary" columns, and such columns embodying adsorbents can be both fast and efficient.
2. *Involatility.* Unlike many solvents, adsorbents do not have a vapor pressure at high temperatures and thus do not "bleed."

A third advantage is the ability to predict the partition ratio based upon the heat of adsorption for a gas on a given solid. The relationship between the logarithm of the partition ratio and the heat of adsorption is linear with respect to reciprocal temperature, and it can be described by the following equation (114):

$$k = k_0 \exp(-E_a/k_b T) \quad (64)$$

where  $k$  is the partition ratio,  $k_0$  is a constant,  $E_a$  is the adsorption heat of the particular gas on the solid,  $k_b$  is Boltzmann's constant, and  $T$  is the absolute temperature (114). Thus, given the heat of adsorption of a particular gas on a solid, and one trial (to determine the constant,  $k_0$ ), it would be theoretically possible to determine the partition coefficient for that gas on the solid for any temperature.

These advantages are often compromised by the major disadvantage of using a solid adsorbent—its extreme selectivity. The majority of analytical columns (although somewhat selective) are not as selective as a column fabricated with an adsorbent stationary

<sup>3</sup>Those compounds which interacted the most strongly with CuPc in Vary's study included: water, ethanol, methanol, hydrazine, phenylhydrazine, pyridine, benzylamine (112).

phase. Thus, solid adsorbent phases are generally not as popular as their liquid counterparts. For the purposes of this research, however, the inherent selectivity of a solid adsorbent is considered an advantage, particularly since the selectivity is directed towards the gases of interest—nitrogen dioxide and ammonia. Using CuPc as a phase is not without its problems, though. One of the primary ways of obtaining pure CuPc is through its sublimation onto a substrate as a thin film. This method of coating traditional capillary GC columns would be extremely difficult (if not impossible). Also, since the micromachined columns have a very small cross-section, it would be difficult to introduce a uniform stationary phase using traditional techniques (liquid phases) after the column is fabricated.

In fact, Terry describes the post-fabrication stationary phase deposition process for his GC as follows (11:31):

[The stationary phase] liquid tends to collect in fillets running along the junctions between the cover plate and the substrate wafer, and in droplets on the groove bottom. Liquid for these pools is drawn from the flat surfaces of the capillary [column], leaving the cover plate and groove bottom essentially devoid of lining liquid...Such a lining distribution has disastrous effects on the performance of the column, increasing its plate height and peak distortion while decreasing its separating power.

These problems motivated Terry to use commercially available external columns when he patented his design as a "miniature gas chromatograph apparatus" (115).

A potential advantage of micromachined columns that Terry failed to exploit in his stationary phase deposition process is the accessibility of the inner surfaces of the column prior to anodic bonding. Therefore, to promote a homogeneous deposition of the stationary phase and eliminate the formation of thicker regions of the phase at the borosilicate glass-silicon junction<sup>4</sup>, the proposed deposition process occurs prior to the anodic bonding of the borosilicate glass plate—both on the etched silicon wafer and the etched glass plate. Thus, the CuPc is distributed uniformly throughout the column using thin film deposition

---

<sup>4</sup>This will occur if the stationary phase is dissolved in a volatile medium which is then injected into the column and allowed to evaporate (a standard method of depositing stationary phase in a capillary column) (90).

techniques which have been reported to produce films which are sensitive to both nitrogen dioxide and ammonia (7, 45, 116, 117).

This deposition technique introduces another potential problem, though. The anodic bonding process requires a clean silicon surface at the silicon-borosilicate glass interface. Therefore, the CuPc that is not on the column walls must be removed so as to leave only the CuPc deposited in the channel of the column. An aluminum oxide polishing film<sup>5</sup> has been experimentally used and verified to accomplish this task.

#### 4.1.1.2 Selection of Column Parameters.

*Column Path.* Before considering the exact dimensions of the column's cross-section, it is necessary to discuss the spiral shape used to establish the column's path. The general shape of two interlocking spirals was used by Terry, and this configuration incorporated the major advantage of locating the gas inlet and outlet far away from the complex spiral structure (11). There was no reason to deviate from the proven concept of this design (see Figure 52 in Section 5.1 for the design used in this investigation); however, choices for the column's width and inter-column spacing were determined to improve fabrication yields<sup>6</sup>. Initial experiments with the low temperature anodic bonding process on flat, 3-inch diameter silicon wafers demonstrated that a central region approximately 2 inches in diameter bonded extremely well. The outer edge of the wafer initially appeared to bond to the glass plate, but it frequently "de-bonded" within the first hour after the assembly was cooled to room temperature. This behavior was attributed to the presence of the slightly beveled edge on the silicon wafer which tended to weaken the bond (due to the lower-than-recommended temperature constraints imposed by the stationary phase<sup>7</sup>), making it more susceptible to damage by the residual strain imposed on the structure after cooling.

---

<sup>5</sup>PSI Lapping Film, Part Number 16.3-6, PSI Testing Systems, Inc., Houston TX.

<sup>6</sup>Terry's column was approximately 130 microns wide, but no information on inter-column spacing was provided (11).

<sup>7</sup>The recommended temperature for bonding is in the 180°C to 500°C range (107). CuPc begins subliming at temperatures as low as approximately 150°C under vacuum (43). Therefore, the 150°C temperature was identified to be the maximum anodic bonding temperature.

Therefore, the MMGC column was restricted to reside within the central 1.5-inch diameter region of the silicon wafer (to provide a conservative margin of error). Additionally, the remainder of the silicon wafer was etched with strain relief features (see Figure 52 in Section 5.1) to minimize the "de-bonding" effect. A 300 micron column width was identified as a compromise between column length (the wider the column, the shorter the column length that can fit in a 1.5-inch diameter circle), and achieving conditions suitable for the TSR approximation (column width to height aspect ratios greater than 4:1<sup>8</sup>). As will be shown in the next section, the aspect ratio for the fabricated column was approximately 30:1, which permits the TSR approximation to be invoked.

Finally, for a column width of 300 microns, an inter-column spacing needed to be specified that balanced the two competing criteria: fabrication yield<sup>9</sup> and column length<sup>10</sup>. Since the dust voids for the initial bonding experiments were typically on the order of 0.5 mm, an inter-column spacing of 1 mm was chosen as a compromise dimension to realize acceptable fabrication yield and column length. The column's length, based on these parameters<sup>11</sup>, was determined to be approximately 0.9 m.

When the general shape of the column's cross-section was established and correlated with the constraints imposed by the column's path, the analytical equations developed in Section 2.4 were used to calculate the remaining column geometrical and operational parameters.

*Column Cross-Section.* Since the stationary phase identified for use in this research is CuPc, which is a stable solid at the temperatures of interest (between 25°C and 150°C), the equations presented in Chapter 2 (Section 2.4) are valid (43). That is, the resistance to mass transfer in the stationary phase can be neglected. By applying the  $v_o$  coefficients in Equation 42 to the pressure corrected form of the van Deemter equation

---

<sup>8</sup>See Section 2.4.1.

<sup>9</sup>If the inter-column spacing was too small, dust particles, which invariably contaminate the bonding surfaces, would create voids between adjacent columns, thus "shorting" them and compromising the separating power of the MMGC column.

<sup>10</sup>The longer the column, the more effective its separating power.

<sup>11</sup>A total column area occupying a circle with a diameter of approximately 1.5 inches, an inter-column spacing of 1 mm, and a column width of 300 microns.

(Equation 21) and calculating the separation factor (using "order of magnitude" values for the remaining unknowns<sup>12</sup>), plots of the separation factor (SF) versus  $z_0$  can be generated.

In order to determine a column height that maximized the separation factor for a practical operating pressure (20–60 psi), the SF versus  $z_0$  was plotted for various input pressures. A maximum pressure of 60 psi was identified as an upper limit for the MMGC interconnections (since Terry's connections could only withstand 60 psi) (11:18). The result of this analysis (using the equations for a TSR column) is shown in Figure 38.

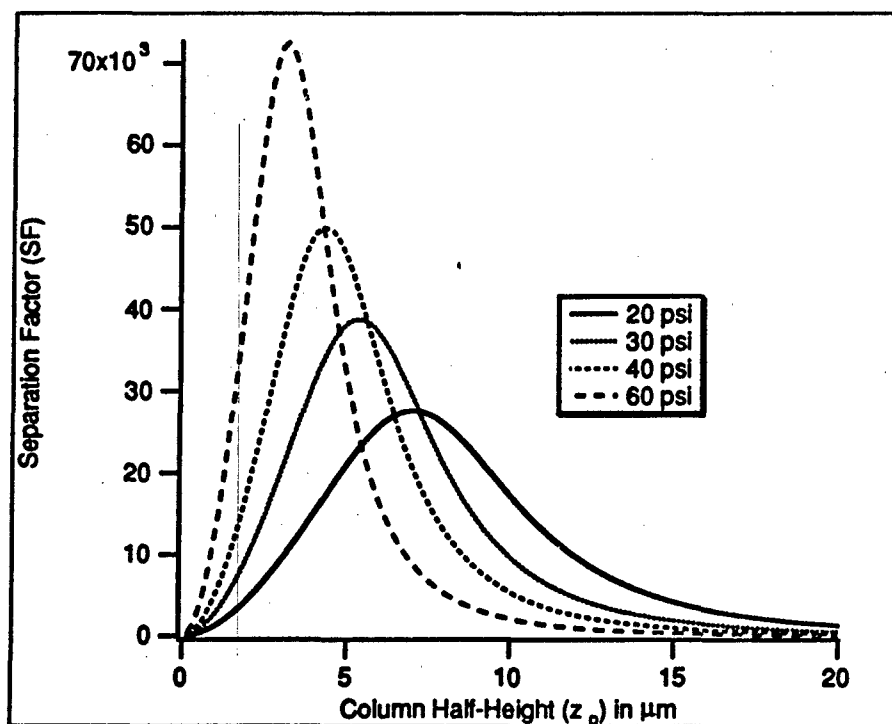


Figure 38. Separation Factor (SF) versus  $z_0$  for Various Input Pressures (20 psi, 30 psi, 40 psi, and 60 psi) for a Column with a Solid Stationary Phase. The Column Length is 0.9 m, Partition Coefficient is 100, Gas Viscosity is 200  $\mu$ poise, Stationary Phase Thickness is 0.2  $\mu$ m, Column Width is 300  $\mu$ m, and the Diffusion Coefficient of the Carrier Gas was Calculated Based upon the Average Pressure and a Temperature of 50°C.

<sup>12</sup>The viscosity of the carrier gas was taken to be that of helium—the best carrier gas to use with a TCD—at room temperature ( $\approx 200$   $\mu$ poise). The diffusivity of the carrier gas was calculated based upon an average pressure and a temperature of 50°C, the thickness of the stationary phase was taken to be 2000 Å (see Section 4.1.3.1), and the column length was identified (as was described in the previous section) to be 0.9 m (118).

The 30–40 psi input pressure range was identified as a compromise to maximizing the SF while minimizing the risk of inducing interconnect failure (due to excessive pressure). This decision yields a corresponding value for  $z_0$  of approximately 5  $\mu\text{m}$ . The only variable which did not have an “order of magnitude” estimate in the calculation for the plot in Figure 38 was the partition coefficient (since there are no published values for CuPc deposited as a thin film). In order to establish the independence of  $z_0$  with respect to  $c$ , four orders of magnitude of  $c$  were evaluated to prepare Figure 39. From Figure 39, it is apparent that the 5  $\mu\text{m}$  value of  $z_0$  will be a favorable choice for any (reasonable<sup>13</sup>) value of  $c$ .

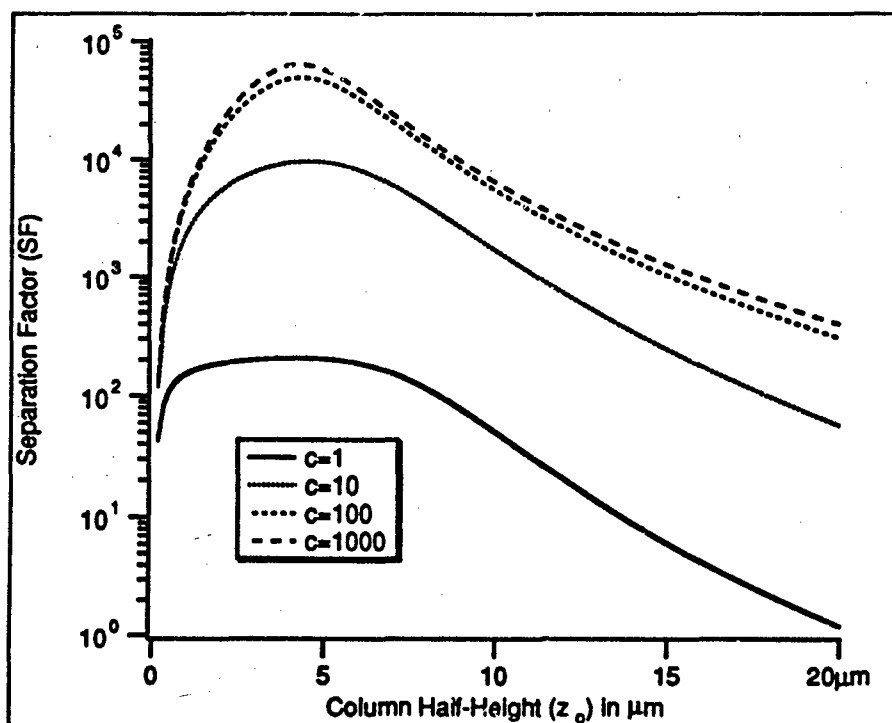


Figure 39. Separation Factor (SF) versus  $z_0$  for Various Partition Coefficients (1, 10, 100, and 1000) for a Column with a Solid Stationary Phase. The Column Length is 0.9 m, Input Pressure is 40 psi, Gas Viscosity is 200  $\mu\text{poise}$ , Stationary Phase Thickness is 0.2  $\mu\text{m}$ , Column Width is 300  $\mu\text{m}$ , Diffusion Coefficient of the Carrier Gas was Calculated Based upon the Average Pressure and a Temperature of 50°C.

<sup>13</sup>Typical partition coefficients span the range of 100 to 1000 (18).

With the column parameters identified in the above discussion ( $z_o = 5 \mu\text{m}$ ,  $P_i = 40 \text{ psi}$ ,  $Y = 300 \mu\text{m}$  and  $L = 0.9 \text{ m}$ ), the column geometry is fixed, so the sample injection design issues can now be discussed.

#### 4.1.2 Micromachined Sample Injection System

**4.1.2.1 Gaseous Sample Injection.** The MMGC will be used to sample only gaseous atmospheres, so no capability for vaporizing liquid samples was included in the design. Terry's method of injecting gaseous samples involved a diaphragm valve (see Figure 40). This valve design manifested problems with dead space and reproducible actuation cycles. In order to facilitate a more precise injection of the gaseous samples into the MMGC, it was decided to use a miniaturized, commercially-available sample injector (this technology has significantly progressed since Terry's research, and several commercial injectors capable of injecting repeatable volumes of less than  $2 \mu\text{l}$  are now available). These injector designs are based upon the gas sample loop technology discussed in Chapter 2 (see Figure 3).

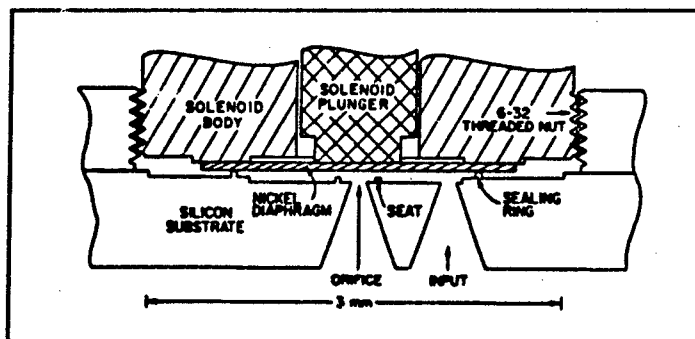


Figure 40. Miniature Sample Injection Valve (12:1882).

The commercial gas sample valve<sup>14</sup> shown in Figure 41 was mated to the MMGC using 5 mil ID stainless steel tubing as shown in Figure 42. The sample valve was operated by continuously injecting the challenge gas into the sample loop while the carrier gas was injected into the column through the valve (Position A in Figure 43). When an analysis was desired, the valve was rotated  $60^\circ$  clockwise with an internal electric actuator. With

<sup>14</sup>Valco Instruments Co. Inc., Part Number E6N6W, Houston, TX (119).

the valve in this new position (Position B in Figure 43), the gas sample trapped in the sample loop of the valve was connected in-line with the carrier gas traveling to the column. Thus, the carrier gas swept the sample gas into the column, where it was separated. Since the volume of the sample loop was a given, and any gas trapped in the loop was sent to the column, there was virtually no dead-space. Also, the problems associated with the precise cycle timing of Terry's valve were eliminated, since the sample gas can be injected into the column only when it was in-line with the carrier gas.

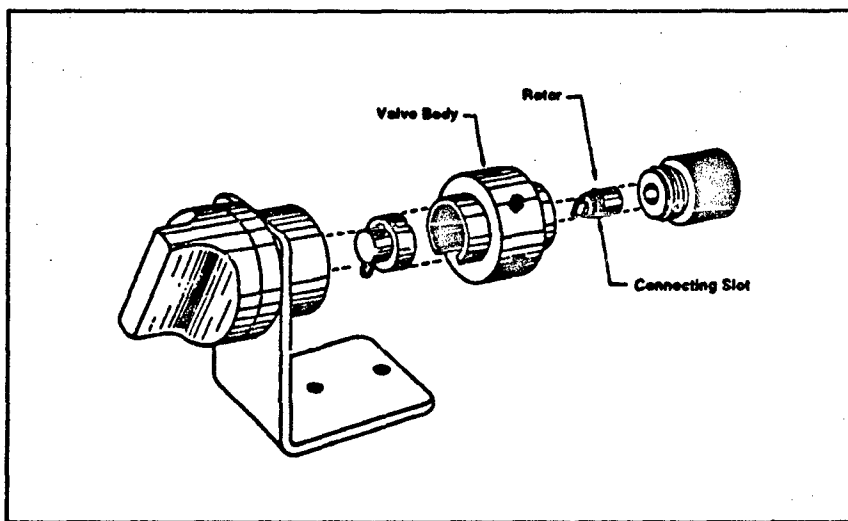


Figure 41. Exploded View of the Sample Injection Valve Used in this Investigation (119).

**4.1.2.2 Sample Loop Size.** The optimal sample loop volume is a function of several critical variables. Three variables of particular concern include the detector's sensitivity, the column's capacity, and the gas concentration range. As a general rule, the smallest sample volume containing the minimum gas concentration that satisfies the detector sensitivity requirements is used (18). Any volume, when combined with the maximum gas concentration, that exceeds the column's capacity will tend to produce asymmetrical peaks. Using these basic principles and several approximate calculations for column capacity, the sample loop volume range can be established that satisfies these requirements.

In order to determine the optimum sample loop volume to use, it is necessary to know the approximate capacity of the micromachined column. Since the column dimensions are

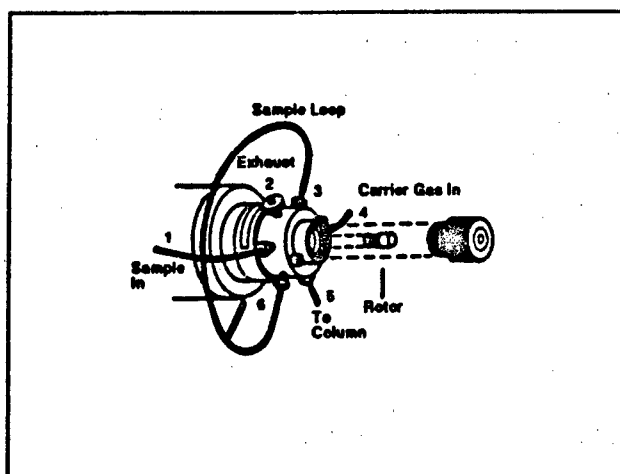


Figure 42. Sample Injection Valve Connections (119).

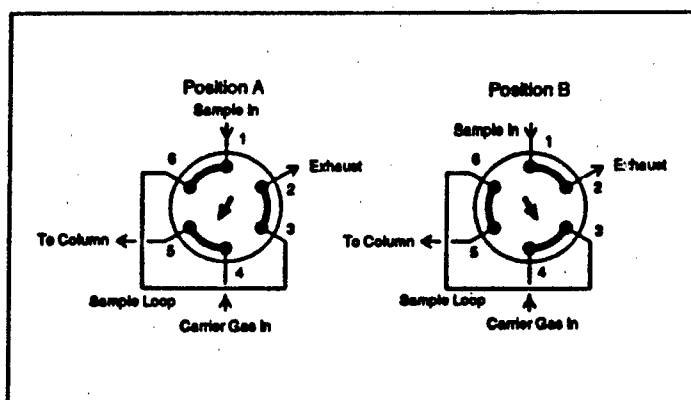


Figure 43. Sample Injection Valve Operation (119).

known, and the spacing between adjacent CuPc molecules is known<sup>15</sup>, all that remains is an approximation of the surface area of the CuPc film that is available to interact with (and adsorb) the challenge gas. Therefore, to account for the effective surface area of the CuPc film, it is assumed that the film is composed of a conglomeration of cylinders with an approximate radius of 300 Å (see Appendix B and Equation 74). Using these values, the ratio of the effective surface area of the CuPc film (due to its "roughness") to the area occupied by the film is approximately 14:1. If this ratio is then applied to the surface area

<sup>15</sup> Approximately 25 Å(43).

of the column, the approximate number of available adsorption sites (assuming one site per CuPc surface molecule) is on the order of  $10^{15}$ .

The three commercially available sample loop volumes which are compatible with the sample injection valve are 2, 10, and 20 microliters. For the smallest loop, it was experimentally determined that the gas flow was restricted to a maximum of approximately 75 ml/min (for the larger loops, the maximum flow was approximately 145 ml/min). For all three loops, the minimum reliable flowrate was approximately 1.44 ml/min. These flowrates are important because they determine the concentration of  $\text{NO}_2$  and  $\text{NH}_3$  molecules injected<sup>16</sup> (this issue will be thoroughly discussed in Section 4.2.1).

For  $\text{NO}_2$ , the maximum concentration (based upon the lowest flowrate<sup>17</sup>) that could be generated was approximately 1700 ppm. The minimum concentration was 17 ppm (32 ppm for the smaller loop). These concentration limits, when combined with the volume of the loop, determine the number of  $\text{NO}_2$  molecules that are injected. Knowing the number of molecules injected for each of the available sample loops (and how these numbers compare with the approximate column capacity) determines the potential effectiveness of a given sample loop. These ranges (as a percent of column capacity) are presented in Table 10.

Table 10. Range of the Number of Molecules Injected for the Three Sample Loop Volumes Compared to the Column's Capacity.

Sample Loop Volume	Minimum	Maximum
2 $\mu\text{l}$	0.1%	7%
10 $\mu\text{l}$	0.3%	34%
20 $\mu\text{l}$	0.7%	70%

From Table 10, it is apparent that the largest loop volume is close to saturating the column when it is filled with the highest  $\text{NO}_2$  concentration; thus, the effective performance evaluation range would be reduced. The smallest loop volume appears to be the best of

<sup>16</sup>Since the chemiresistor detector was more sensitive to  $\text{NO}_2$ , the sample loop volume was chosen based upon the anticipated  $\text{NO}_2$  concentration values.

<sup>17</sup>See Section 4.2.1.

the three choices in terms of injecting a sample with less than saturation levels of  $\text{NO}_2$ . Unfortunately, it was experimentally determined that the smaller loop did not provide a sufficient volume of the challenge gas (in terms of the sheer number of molecules) to generate reproducible signals with the chemiresistor detector. Therefore, as a compromise, the 10  $\mu\text{l}$  sample loop was chosen for the design of the MMGC.

This sample injection system, together with the micromachined column, form two of the three major component areas of the micromachined gas chromatograph. The final MMGC component design requirement—the detectors—will now be discussed.

**4.1.3 Detector Considerations.** In order to facilitate detection of nitrogen dioxide and ammonia, a chemiresistor “tuned” to these gases (i.e., a CuPc chemically-sensitive thin film) is ideal. However, the chemiresistor detector, by its very nature, is insensitive to the nitrogen diluent, and thus, crucial retention time<sup>18</sup> information will be lost. Therefore, a means of detecting the unretained diluent (nitrogen) must also be incorporated into the detector’s design. For these reasons, a dual detector system was incorporated into the MMGC: a sensitive chemiresistor as the primary detector (for  $\text{NO}_2$  and  $\text{NH}_3$ ), and a general TCD as a secondary detector (to capture the leading nitrogen peak).

Although the chemiresistor and TCD are both suitable detectors for the micromachined gas chromatograph, the goals of this research were to design, develop, fabricate, and evaluate the performance of a complete MMGC using a phase that manifests strong adsorption characteristics toward  $\text{NO}_2$  and  $\text{NH}_3$ —and not necessarily the improvement of these detectors<sup>19</sup>. A summary of the development and operation of the CuPc chemiresistor will be presented here with specific attention devoted to those design issues that were modified for this research (additional details concerning the physical and electrical properties of CuPc and its use as a chemiresistor gas-sensitive thin film are provided in Appendices B and C).

---

<sup>18</sup>The difference in exhaust time between unretained gases and the gases of interest.

<sup>19</sup>In any event, improved TCDs are already under investigation and development by commercial companies (120:8). Additionally, research performed at AFIT has characterized the chemiresistors which were used in the MMGC (116, 117).

**4.1.3.1 Chemiresistor.** The chemiresistor used in this research is based upon a design which has been used successfully at AFIT for a number of years (116, 117, 121). Modifications were made to the existing design so that its sensitivity would be enhanced.

The previous design for the interdigitated electrode structure was comprised of 30, 1140 micron long fingers for the ground electrode, and 29, 1140 micron long fingers for the driven electrode, (see Figure 27). The spacing between the electrodes (and the electrode width itself) was 10 microns. Using Equation 50, this yields a serpentine length of approximately 66 mm. Initial experiments with this design, and a 2000 Å thick CuPc film<sup>20</sup> yielded an overall resistance<sup>21</sup> of approximately  $3 \times 10^{10} \Omega$ . From Equations 50 and 51, the CuPc resistivity was approximately  $40 \times 10^6 \Omega\cdot\text{m}$ . Reported values for CuPc resistivity span the range of  $1 \times 10^5 \Omega\cdot\text{m}$  for compressed CuPc powder in nitrogen to  $6.2 \times 10^{11} \Omega\cdot\text{m}$  for single crystal CuPc in vacuo (45, 122).

In order to improve the signal level (current) by decreasing the overall resistance of the chemiresistor, the new chemiresistor design incorporated a longer serpentine path<sup>22</sup>, and a ground-plane beneath the electrodes for shielding. However, due to potential yield problems (shorts across the electrodes created during fabrication), the interelectrode spacing was kept the same (10 microns). Even with this spacing, the fabrication yield was only approximately 35 percent. Additionally, due to time constraints<sup>23</sup>, the usable circuit area was limited to 2000 microns by 2000 microns. The chemiresistor geometry which fit these constraints had a finger length of 1980 microns with 50 fingers on the driven electrode. Using Equation 50, the active length for this geometry is approximately 0.2 m, with an anticipated resistance (based upon the reported thin-film resistivity value) of approximately  $10 \times 10^{10} \Omega$  after CuPc deposition, which is within the measurement range of the instrumentation<sup>24</sup>.

<sup>20</sup>This thickness was chosen as a compromise between reducing the overall resistance (thicker films) and improving the reversibility (thinner films) (43). The initial resistance of the uncoated chemiresistor was too small to measure with the available equipment. For more detail on this selection, see Appendix B.

<sup>21</sup>Measurements were made at room temperature in dry air.

<sup>22</sup>From Equation 51, the serpentine length of the chemiresistor is inversely proportional to the resistance.

<sup>23</sup>The chemiresistors were fabricated by the Metal-Oxide-Semiconductor Implementation Service (MO-SIS), Marina del Rey, CA. The shortest turn-around time was associated with their *Tiny Chip* sized die. The usable area on this die (reserving space for bonding pads) was approximately 2000 microns by 2000 microns.

<sup>24</sup>Actual resistances (measured in helium) were on the order of  $10^{12} \Omega$ , yielding a resistivity of  $4 \times 10^9 \Omega$  which is closer to the single crystal CuPc in vacuo measurement.

**4.1.3.2 Thermistor.** In Section 2.5, a standard thermal conductivity detector was discussed (along with several other detector types). There are three major reasons why the TCD is an ideal candidate as a secondary MMGC detector. First, the TCD is a very simple device requiring the exposure of only a single sensing element to the column effluent. Secondly, since the sensing element is typically a thermistor, and thermistors are commercially available with very small geometries (a bead with a diameter of 125  $\mu\text{m}$ —Thermometrics, Inc., Series B05, Edison, NJ), a thermistor based TCD is compatible with the micron-sized dimensions of the MMGC (33:B-2). Finally, a TCD does not alter the molecular structure of the gas, so the effluent can also be passed to the more sensitive and selective primary detector—the chemiresistor. Thus, the primary functions of the TCD include the detection of inert gas pulses to insure that the MMGC is leak-free, and the detection of the nitrogen diluent as a timing mark for the chemiresistor's response.

**TCD Cell and Chemiresistor Interface Design.** The most complicated portion of the MMGC (as far as micromachining is concerned) is the TCD cell. In addition to housing the thermistor bead, it functions as the interface between the column and the chemiresistor detector. The column is simply a shallow isotropic etch, but the TCD cell is micromachined to a controlled depth (to accommodate the thermistor) with a means for introducing the thermistor leads. Terry's TCD cell design essentially consisted of a deep well etched into the silicon wafer that housed the thermistor bead, and two holes etched through the wafer for the thermistor leads (see Figures 44 and 45).

For this MMGC design, a unique TCD cell design was realized. Instead of etching holes and channels for the leads (which increase TCD cell volume), the wafer was etched twice with the anisotropic KOH etchant (see Section 3.1.2). The first etch process produced a self-aligning V-groove on the back of the wafer. Simultaneously, feedthroughs were used to realize a connection to the external sample injector, and alignment marks were etched through the wafer during this etch process. The second KOH etch produced a deep inverted truncated pyramid on the front surface of the wafer, intersecting the first KOH etch V-groove (see Figure 46). This design accommodates lead channels without introducing the additional deadspace found in Terry's design (11).

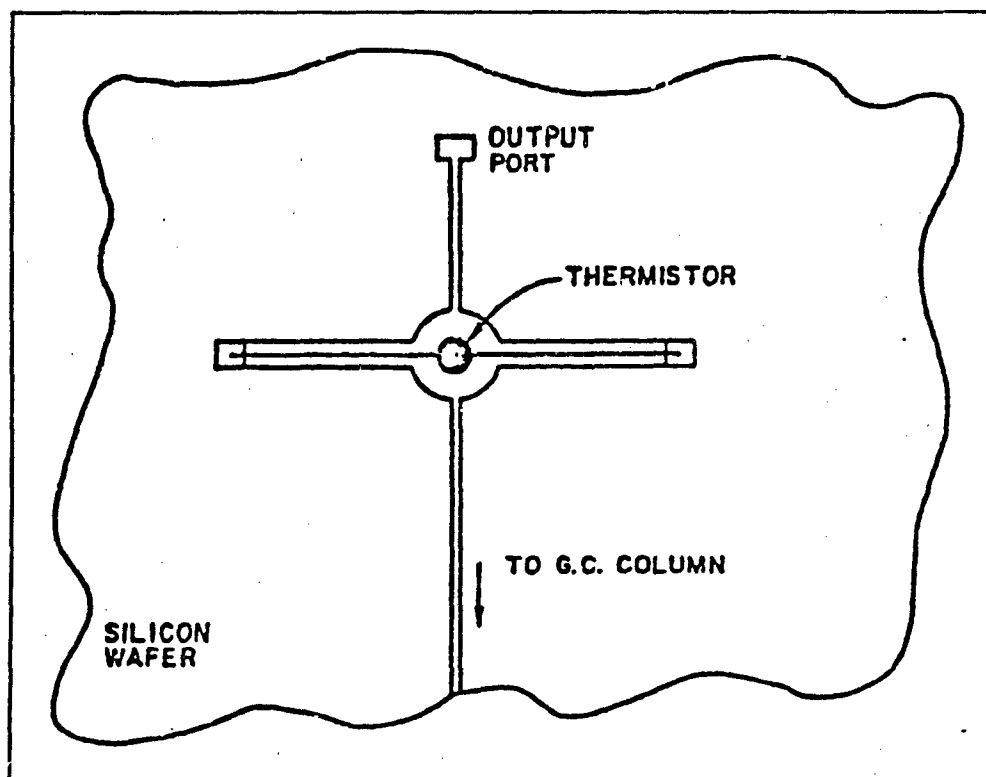


Figure 44. Example of a Miniature Thermal Conductivity Detector Fabricated with a Thermistor (Top View) (11:70).

*First KOH Etch.* Since the silicon wafers spanned the range of being 365 to 385 microns thick, from Equation 62, the mask for the feedthrough holes had to be a minimum of 545 microns (for a hole with zero width in the thickest wafer). However, since the interconnect tubing<sup>25</sup> had an ID of 254 microns and an OD of 794 microns, the maximum hole width was established to be the OD of the interconnect tubing. Additionally, in order to match the column cross-sectional area<sup>26</sup> (so that the flowrate reduction occurred outside of the column), the hole width was chosen to be approximately 55 microns. Using Equation 62, this dimension yielded a mask width of approximately 600 microns (for the thickest wafer). Since this dimension was narrower than the OD of

<sup>25</sup>Part number T20N10D, Valco Instruments Co. Inc., Houston, TX.

<sup>26</sup>This was calculated to be approximately 3000  $\mu\text{m}^2$ .

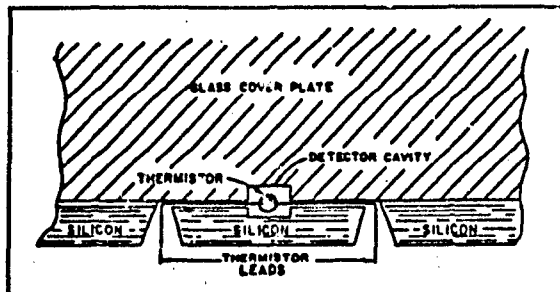


Figure 45. Example of a Miniature Thermal Conductivity Detector Fabricated with a Thermistor (Side View) (11:70).

the interconnect tubing, the interconnect tubing was manually tapered so that it would fit into the etched feedthrough.

For the V-groove portion of the first KOH etch process, the size of the thermistor lead wires were considered. Since the thermistor lead wire was approximately 20 microns in diameter, the V-groove had to intersect the TCD cavity structure with a 40 micron overlap (to facilitate routing the leads through the opening), but had to remain less than the diameter of the thermistor bead (approximately 125 microns). Also, the TCD cavity for the second KOH etch process was to be approximately 200 microns deep to accommodate the thermistor bead. Assuming a nominal silicon wafer thickness of 380 microns, and a TCD cavity etch depth of 200 microns,  $T$  in Equation 62 becomes 180 microns, and  $W_{hole}$  is 40 microns. Finally, the required mask width for this etch process is approximately 300 microns.

*Second KOH Etch.* The mask for the second KOH etch (on the front of the wafer) incorporated mirror image alignment marks consistent with the first mask<sup>27</sup>, and a square feature that was approximately 500 microns on a side for the TCD cavity. Since the thermistor beads were approximately 125 microns in diameter, a bottom cavity width of 200 microns, and an etch depth of 200 microns, was considered sufficient to

<sup>27</sup>These alignment marks were not intended to be etched during the second KOH etch. They were only used to align the second mask with the first etch which was on the back of the wafer. Therefore, these marks were smaller than those used to actually etch during the first KOH etch (approximately 50 microns).

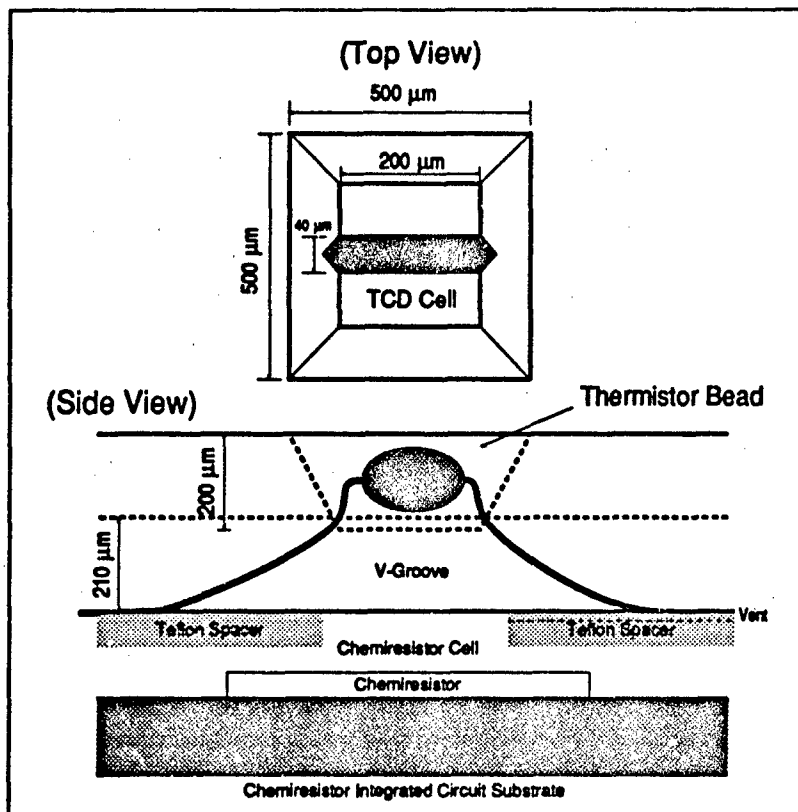


Figure 46. Improved Thermal Conductivity Detector Cell and Chemiresistor Interface Design.

provide a practical fit tolerance. Using these dimensions in conjunction with Equation 62 (as discussed in Section 3.1.2.4) yielded a mask width of approximately 500 microns.

The approximate volume of this TCD cell is 20 nl (compared with Terry's volumes that spanned 40 to 200 nl) (11:98). Additionally, thermistor insertion is simplified, because prior to anodic bonding, the thermistor is positioned in the cavity and the leads are inserted through the slot made by the V-groove on the opposite side of the silicon wafer. This results in a simpler process compared with Terry's TCD cell design, where the leads had to be placed within narrow troughs so that they would not interfere with the anodic bonding process, and it implements the required capability of interfacing with the primary detector (the chemiresistor).

**4.1.4 Micromachined Gas Chromatograph Design Summary.** This section discussed the specific MMGC design issues based upon the theory and background presented in Chapters 2 and 3. Beginning with a justification for the choice of CuPc as the stationary phase, and how it influenced the column design, the geometrical and operational parameters of the column were established. Next, the column parameters and stationary phase choice were used to determine practical sample loop volumes for the sample injection system. Finally, the issues associated with designing the detectors were discussed, along with the specific micromachining requirements to implement the TCD cavity. Table 11 summarizes the MMGC design choices. The next aspect of the micromachined gas chromatograph design involved devising an appropriate challenge gas generation and delivery system, as well as an instrumentation network capable of recording the signals produced by the MMGC.

Table 11. Summary of Micromachined Gas Chromatograph Components.

Component	Description
Stationary Phase	Copper Phthalocyanine
Column	10 $\mu\text{m}$ $\times$ 300 $\mu\text{m}$ $\times$ 0.9 m
Mobile Phase	40 psi Helium
Sample Injection System	Gas Sample Valve with 10 $\mu\text{l}$ Sample Loop
Detectors	Chemiresistor and Thermal Conductivity

#### **4.2 Design of the Performance Evaluation System for the Micromachined Gas Chromatograph.**

The MMGC performance evaluation system was composed of two fundamental sub-systems: the gas generation and delivery system, and the electrical instrumentation system. In order to generate reproducible concentrations of the challenge gases and introduce them into the MMGC for evaluation, a gas generation and delivery system was devised which incorporated flowmeters at appropriate locations to insure that the correct gas mixture was generated. Additionally, the chemiresistor and thermistor detectors were connected to an instrumentation system which provided the required amplification and data recording functions. Each of these systems will be discussed individually.

**4.2.1 Gas Generation and Delivery System.** A schematic of the gas generation and delivery system is shown in Figure 47. Within this system, there are three major areas of interest: the carrier gas, the challenge gases, and the MMGC interface (through the sample injection valve).

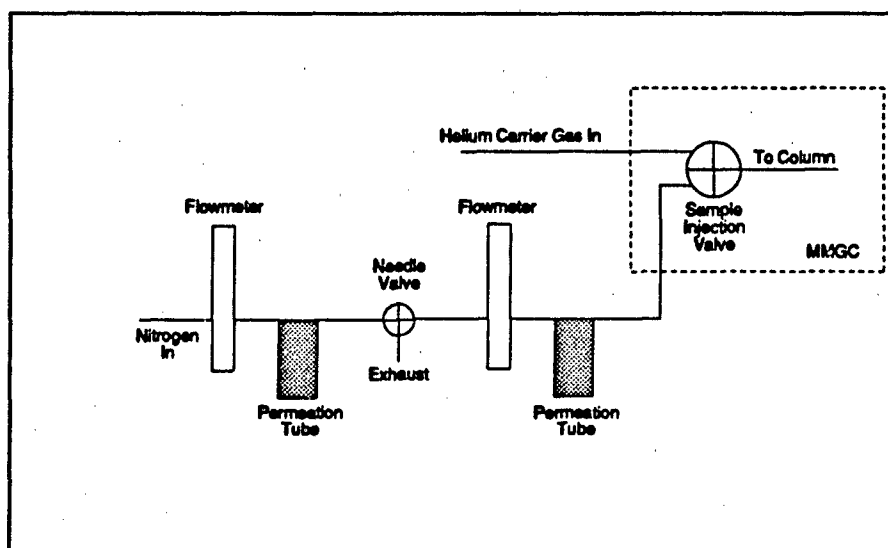


Figure 47. Schematic of the Gas Generation System.

**4.2.1.1 Carrier Gas.** The choice of the carrier gas was primarily motivated by the thermal conductivity detector. In order to sense the nitrogen diluent (to provide timing information when injection occurs), the carrier gas was required to have a significantly different thermal conductivity relative to nitrogen. Nitrogen has a thermal conductivity at room temperature of  $26 \times 10^{-3} \text{ W/(m}^\circ\text{K)}$  (123). The gas which has the highest thermal conductivity is hydrogen,  $187 \times 10^{-3} \text{ W/(m}^\circ\text{K)}$  (123). However, due to safety considerations, the second most thermally conductive gas was chosen; helium has a thermal conductivity of  $151 \times 10^{-3} \text{ W/(m}^\circ\text{K)}$  (123). This choice resulted in a thermal conductivity ratio of approximately 6:1 (helium:nitrogen). As will be shown in Chapter 6, this choice was sufficient to detect the nitrogen diluent<sup>28</sup>.

<sup>28</sup>The TCD was only designed to respond to the nitrogen diluent, so the thermal conductivities of the two challenge gases ( $\text{NO}_2$  and  $\text{NH}_3$ ) were not critical for determining the carrier gas to use (other than insuring that the carrier gas was inert relative to the challenge gases). However, for comparison, the two challenge gases had similar thermal conductivities—approximately  $25 \times 10^{-3} \text{ W/(m}^\circ\text{K)}$  (123).

4.2.1.2 *Challenge Gases.* Since there were two challenge gases of interest, two permeation tubes<sup>29</sup> were required. Each of these permeation tubes required independent control of the diluent flow (so that various concentration ratios could be obtained). To accomplish this objective, the permeation tube requiring the highest flowrate was located first in the diluent stream (see Figure 47). Any excess flow was then vented to the exhaust (controlled by a needle valve<sup>30</sup>) before the reduced flow was passed to the second permeation tube. The first flowmeter<sup>31</sup> was used to actually control the input flow to the first permeation tube. However, the second flowmeter<sup>32</sup> was used solely as a meter (the flow to the second permeation tube was controlled by the needle valve).

Since the tube's permeation rate strongly depends upon its operating temperature, provisions were made within the gas generation system to accommodate a thermocouple attached to one of the permeation tube's surface (since both tubes were at ambient temperature and in close proximity to each other, only one tube's temperature was measured). The thermocouple's signal was then routed to the thermocouple scanner (which will be addressed in the instrumentation system section) where it was recorded.

Using this system, a wide variety of NO<sub>2</sub> and NH<sub>3</sub> concentration combinations can be obtained. For example, if the lowest flowrate setting is used (1.4 ml/min), the NO<sub>2</sub> permeation tube would generate a 1700 ppm concentration, and the NH<sub>3</sub> tube would generate a 21,000 ppm concentration. Thus, concentration ranges from 0 ppm (with the tube disconnected) to these maximums could be generated with this system. Once generated, the mixture flows through the sample injection loop (which serves as the interface to the MMGC).

---

<sup>29</sup>Tubes that are calibrated to permeate at a specified rate at a given temperature. If the flowrate of carrier gas across the tube is known, the concentration can be calculated. Both the ammonia (model number 23-7014) and nitrogen dioxide (model number 23-7052) permeation tubes were obtained from GC Industries, Inc., Fremont, CA. For the NO<sub>2</sub> permeation tube, the concentration in ppm,  $c_p$ , is related to the flowrate in ml/min,  $f_p$ , by the following GC Industries supplied formula:  $c_p = 2394/f_p$ . Similarly, for the NH<sub>3</sub> permeation tube,  $c_p = 29400/f_p$ .

<sup>30</sup>Model W-1287-4, Whitey Co., Highland Heights, OH.

<sup>31</sup>Model Number 8555-8654, Gilmont Instruments, Inc., Great Neck, NY. The calibration chart relating flowmeter reading and flowrate is presented in Appendix H.

<sup>32</sup>Model Number 8555-8654, Gilmont Instruments, Inc., Great Neck, NY. The calibration chart relating flowmeter reading and flowrate is presented in Appendix H.

**4.2.1.3 MMGC Interface.** The gas generation and delivery system was connected to the MMGC through the sample injection system, which was based upon the six-port valve that is shown in Figure 43. Normally (prior to injection), the sample injector is configured as shown in Figure 43 (Position A). In this configuration, pure helium carrier gas is flowing through the MMGC, and purging it, while the challenge gases are flowing through the sample loop. When an injection is desired, a control signal<sup>33</sup> triggers the sample injection valve to toggle to its second position, as shown in Figure 43 (Position B). In this position, the challenge gases "stored" in the sample loop are introduced with the helium carrier gas flow into the MMGC. The 5-V control signal which causes this injection is generated by the instrumentation system.

**4.2.2 Instrumentation System.** The critical elements of the instrumentation system were the general purpose instrumentation bus (GPIB) controller and a dedicated personal computer (PC). The GPIB controller was able to coordinate the operation of the three major pieces of instrumentation: the thermocouple scanner, the heater power supply, and the semiconductor parameter analyzer. Additionally, the controller was able to query each instrument for pertinent data so that it could be recorded in a data file.

**4.2.2.1 Instrumentation Bus Controller.** The GPIB controller<sup>34</sup> programming was accomplished with a compiled Pascal<sup>35</sup> program that incorporated the test protocol for a particular evaluation (these test protocols are described in Chapter 6). Since the GPIB interface is a standard among laboratory instruments, it was a relatively straightforward task to connect each of the instruments to the bus.

**4.2.2.2 Thermocouple Scanner.** The thermocouple scanner<sup>36</sup> could interrogate a maximum of 16 thermocouple inputs. For this research, only three of these inputs were used. In order to monitor the temperature of the MMGC, a thermocouple was mounted on the glass side of the MMGC (between the heater strip and the MMGC). The

<sup>33</sup>A 5-V signal connected to the sample injector valve's "inject" control line as described by the manufacturer.

<sup>34</sup>Model HP82335A, HP-IB Interface and Command Library, Hewlett-Packard, Palo Alto, CA.

<sup>35</sup>Turbo Pascal, Borland International, Inc., Scotts Valley, CA.

<sup>36</sup>Model 630, Stanford Research Systems, Sunnyvale, CA.

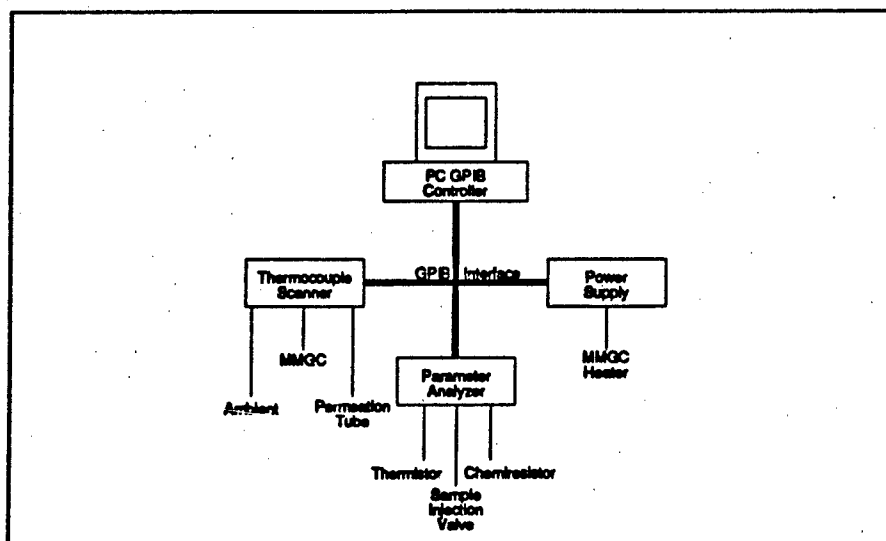


Figure 48. Schematic of the Instrumentation System.

second thermocouple was mounted on the surface of one of the permeation tubes. The final thermocouple was used to measure the ambient laboratory temperature to monitor its fluctuations (the permeation tube's thermocouple had too much thermal mass to be sensitive to minor variations).

**4.2.2.3 Power Supplies.** The heater strips used to elevate the temperature of the MMGC were two flexible heating elements<sup>37</sup> connected in parallel and attached to the front side of the MMGC (see Figure 49). This arrangement created a net resistance of approximately 84  $\Omega$ . Experimentation revealed that approximately 0.3 A were required to raise the temperature of the MMGC to approximately 90°C (the highest test temperature). This behavior indicated that the power supply had to provide approximately 25 V at 0.3 A to drive the heater. In the interests of automating the lengthy test cycles, a GPIB controlled power supply was desired.

Unfortunately, the only available GPIB compatible power supply<sup>38</sup> could only provide a maximum of 20 V at 5 A. Therefore, a second power supply<sup>39</sup> (which did not have GPIB

<sup>37</sup> Model 5160, Minco Products, Inc., Minneapolis, MN.

<sup>38</sup> Model HP 6632A, Hewlett Packard, Palo Alto, CA.

<sup>39</sup> Model HP 6236B, Hewlett Packard, Palo Alto, CA.

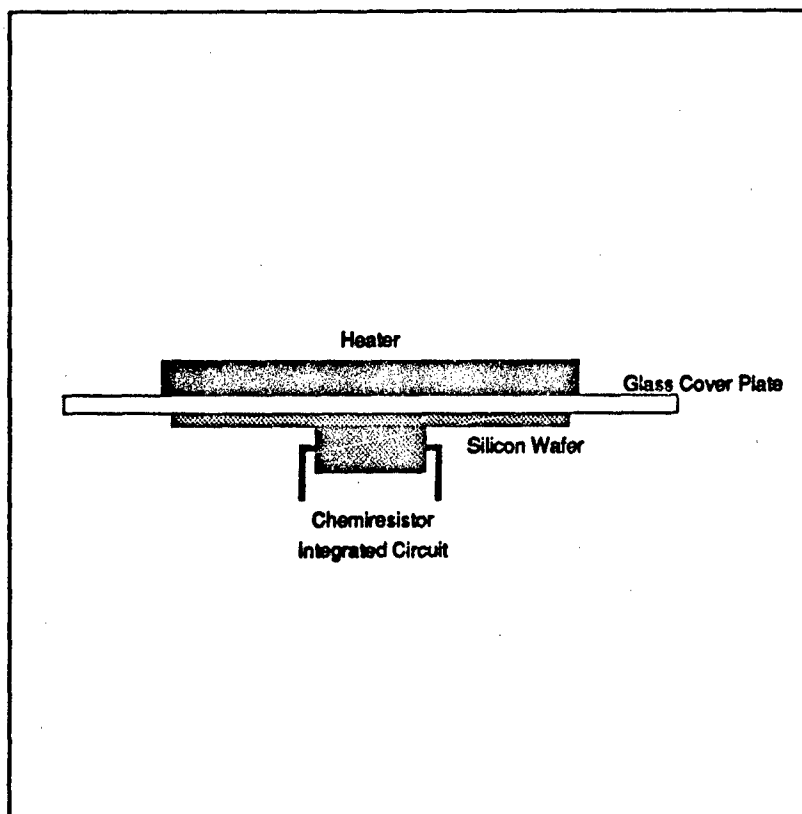


Figure 49. Side View of Heater Attachment.

capability) was placed in series with the GPIB power supply with a fixed setting of 5-V. This provided a baseline current of approximately 60 mA (with an equivalent baseline temperature of approximately 30°C), and a maximum current of approximately 0.3 A—under GPIB control.

**4.2.2.4 Semiconductor Parameter Analyzer.** A parameter analyzer<sup>40</sup> was utilized to record the output signals of both the chemiresistor and the thermistor. Additionally, it served to provide the 5 V control signal to operate the sample injection valve through one of its voltage outputs.

<sup>40</sup>Model HP 4145B, Hewlett Packard, Palo Alto, CA.

The instrumentation requirements for the chemiresistor involved current measurements in the picoampere range<sup>41</sup> while the thermistor required voltage measurements in the 2-V range. The semiconductor parameter analyzer (Model HP 4145B) was well suited to satisfy both of these objectives, and it permitted measurement intervals as short as 10 ms or as long as 10 s. However, only 1024 data points could be stored for a single measurement cycle. Since there were two channels (chemiresistor and thermistor), this limitation meant that the maximum duration of any measurement cycle was 85 min. This was not considered a problem since a practical goal of this research was to be able to operate the MMGC with an analysis time of less than one hour.

The third function of the semiconductor parameter analyzer was to provide a control signal to the sample injection valve. Since part of the capability of the semiconductor parameter analyzer includes the ability to generate arbitrary DC signals on any (or all) of six possible output channels, one of these channels was used to provide the 5-V signal to the sample injector's "inject" control line. During normal operation (purging—no injection), the control signal is low (0 V). When an injection is desired, the parameter analyzer is triggered (through the GPIB) to produce a control signal that is high (5 V), and the circuitry within the sample injection valve responds by rotating to the inject position. When a measurement cycle is complete, the control signal is reduced to the low (0 V) value, and the sample injection valve responds by rotating back to the load position. Thus, an entire MMGC analysis could be accomplished automatically, with the central GPIB controller dictating the sequence.

*4.2.3 Performance Evaluation System Design Summary.* This section summarized the two fundamental components of the experimental MMGC performance evaluation system. In order to produce a variety of challenge gas mixtures, a gas generation and delivery system was designed which would generate concentration ranges spanning several orders of magnitude for each of the two gases. The MMGC performance evaluation system also included an electronic instrumentation network. Central to this network was the GPIB

<sup>41</sup>Since noise figures were extremely sensitive to the physical instrumentation configuration (triboelectric effects), experiments were conducted to determine typical noise values for the test configuration. These experiments revealed an average noise figure of approximately 0.25 pA (see Appendix E).

controller which directed the power settings for the MMGC heater, recorded data from the thermocouple scanner, and prompted the semiconductor parameter analyzer to accomplish the performance evaluation protocols (as described in Chapter 6). With the design information presented in this chapter, the fabrication of the MMGC can now be discussed. These fabrication steps, and their results, are presented in the next chapter.

## *V. Micromachined Gas Chromatograph Fabrication*

Fabrication of the MMGC was accomplished through several phases. In the first phase, a photolithographic mask set was devised which incorporated the features discussed in the previous chapter. In the second phase, the actual micromachining steps were performed to physically realize the features imaged in the photolithographic mask set. The third phase consisted of the steps required to deposit and selectively remove the MMGC column's stationary phase. The fourth phase involved attaching the interconnect tubing and thermistor followed by the anodic bonding process. The last phase involved positioning and securing the chemiresistor to the output of the TCD cell. These phases will be expanded upon in the following sections in the order in which they were performed.

### *5.1 Mask Design and Fabrication*

Using the column dimensions established in the previous chapter, a photolithographic mask set was prepared. It consisted of three photolithographic masks, each corresponding to a specific chemical process etch. All three photolithographic masks were realized by implementing similar techniques for their layout and fabrication.

In order to generate the photolithographic mask layouts, an artwork generating program<sup>1</sup> was used to place the required photolithographic mask features (i.e., rectangles and spirals) in precise relative locations, insuring that the various layers (corresponding to the different chemical etch processes) were properly aligned (see Figures 50-52). Each layer was then printed on a laser printer (at 5 times magnification) and transferred to a transparency<sup>2</sup> which was subsequently photographed with a reduction camera<sup>3</sup> to generate the actual photolithographic masks.

The first photolithographic mask layer (used for the first KOH etch on the back of the wafer) required a narrow rectangle for the TCD V-groove as well as the feedthrough holes

<sup>1</sup>Adobe Illustrator 3.0, Adobe Systems Incorporated, Mountain View, CA.

<sup>2</sup>IR 1120 Infrared Transparency Film, 3M Company, Austin, TX.

<sup>3</sup>Dekacon III, HLC Engineering, Co., Oreland, PA. The camera settings for the 12 inch lens included an f-stop value of 11 and an exposure duration of 120 sec. The front of the camera was set to approximately 23.8, and the rear of the camera was set to approximately 46.8.

for the gas inlet and alignment marks. The second image layer (used for the second KOH etch on the front surface of the wafer) consisted of the TCD cavity feature and smaller versions of the alignment marks that are used in the first mask<sup>4</sup>. The third layer (used to etch the column and strain relief rings) was created as two, mirror image versions (one for the silicon wafer, and one for the borosilicate glass plate). The resultant photolithographic masks were then used in the wet chemical etching phase.

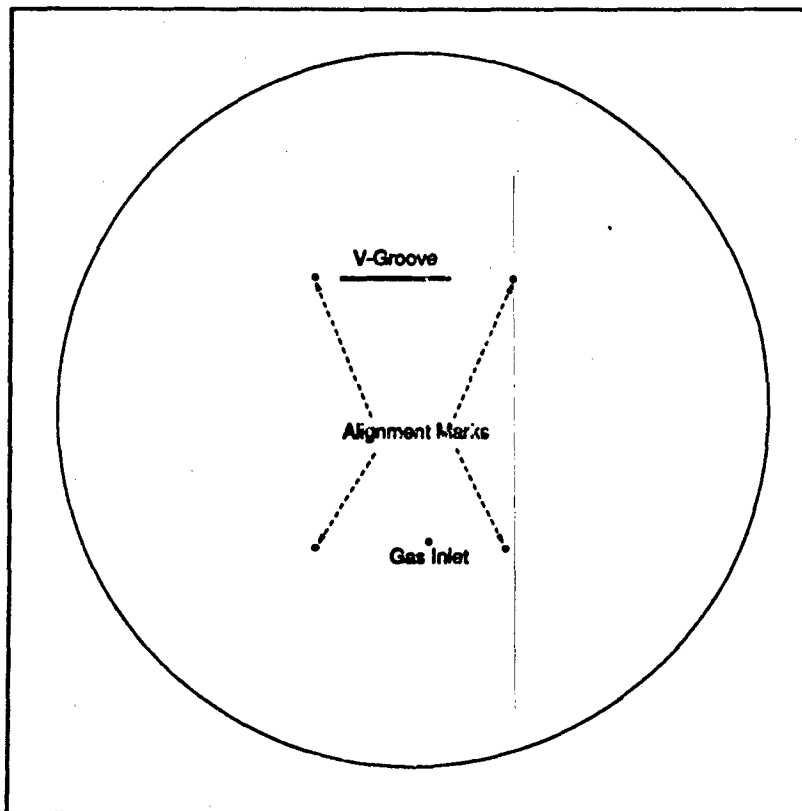


Figure 50. Photolithographic Mask Design Used for the First Potassium Hydroxide (KOH) Etch (KOH1) (V-Groove and Alignment Marks). The Outer Circle is 4 inches in Diameter.

<sup>4</sup>These alignment marks were the mirror image of those used on the back side of the wafer.

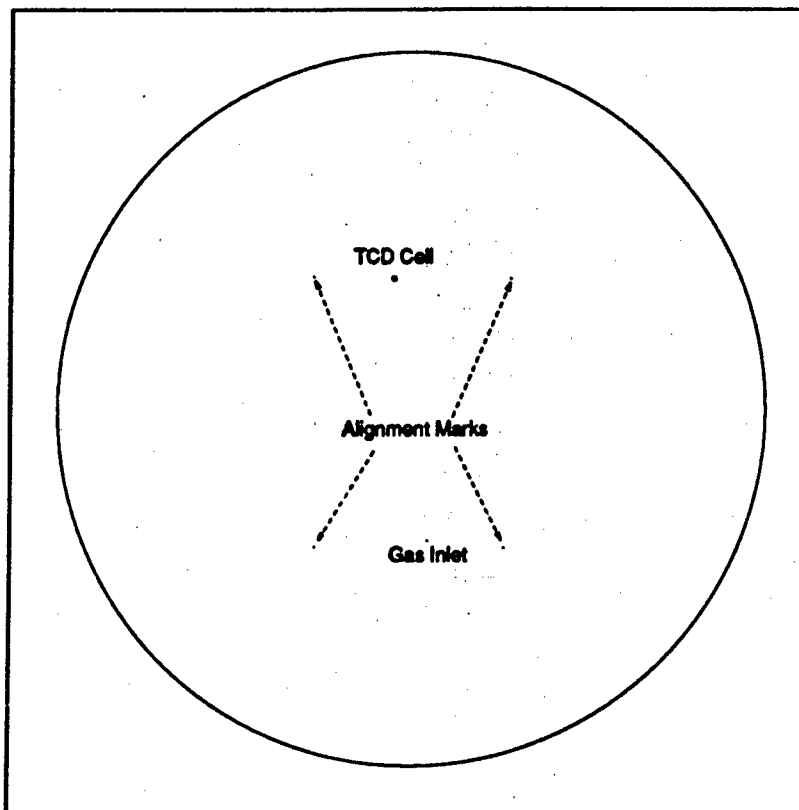


Figure 51. Photolithographic Mask Design Used for the Second Potassium Hydroxide (KOH) Etch (KOH2) (TCD Cavity). The Outer Circle is 4 inches in Diameter.

## 5.2 Wet Chemical Etching.

**5.2.1 Potassium Hydroxide (KOH) Etch 1: V-Groove Etch.** The purpose of this etch was two-fold: first, to create a V-groove on the back of the wafer which would be used to accommodate the thermistor leads while serving as an interface to the chemiresistor cell, and second, to create alignment marks and gas ports for the subsequent photolithographic masks. Both of these objectives were accomplished using an anisotropic KOH etch<sup>5</sup>. The results of this etch process are shown in Figures 53 and 54. The critical processing steps required to accomplish this wet chemical etch are listed below<sup>6</sup>:

<sup>5</sup>KOH was used since the alignment marks had to be etched through the entire wafer, and the V-groove had to stop at a specified depth within the wafer. As discussed in Section 3.1.2, the self-stopping etch properties of KOH made this possible.

<sup>6</sup>The details of each of the processing steps are presented in Appendix A.

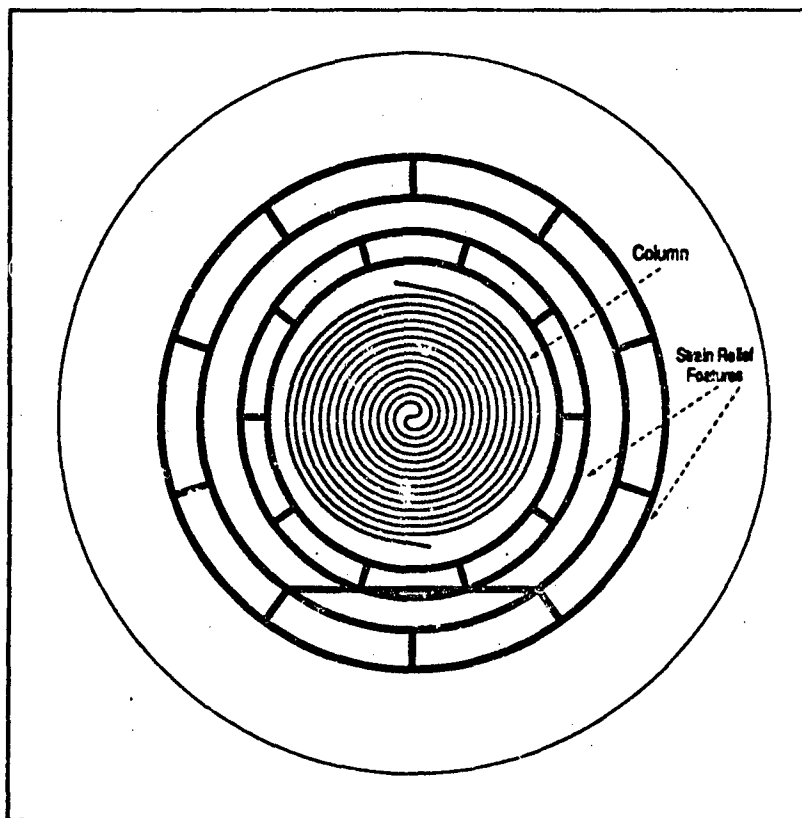


**Figure 52.** Photolithographic Mask Design Used for the Isotropic Column Etch. The Outer Circle is 4 inches in Diameter.

1. *Wafer Cleaning*
2. *Oxidation*
3. *Front Side Photoresist<sup>7</sup> Deposition (Protection)*
4. *Photoresist Cure*
5. *Back Side Photoresist Deposition (Image Capture)*
6. *KOH<sup>1</sup> Photolithographic Mask Exposure (Back Side Photoresist)*
7. *Photoresist Development*
8. *Oxide Etch*

<sup>7</sup>For all of the photolithographic processing steps, Waycoat HR100 negative photoresist (Olin Hunt Specialty Products Inc., West Paterson, NJ) was used (124).

9. *Wafer Cleaning*

10. *KOH Etch*

11. *Rinse, Dry and Inspect.*

**5.2.2 Potassium Hydroxide (KOH) Etch 2: Thermal Conductivity Detector Cell Etch.** This wet chemical etch process was required to fabricate the TCD cavity and, by intersecting the V-groove fabricated in the KOH etch 1 process, to provide a means for introducing the column effluent into the chemiresistor cell. As in the previous etch process, KOH was used to facilitate the deep etch required to accommodate the thermistor bead. The result of this wet chemical etch process is shown in Figure 55, and the processing steps are listed below<sup>8</sup>:

1. *Wafer Cleaning*
2. *Oxidation*
3. *Front Side Photoresist Deposition (Image Capture)*
4. *KOH2 Photolithographic Mask Exposure*
5. *Photoresist Development*
6. *Back Side Photoresist Deposition (Protection)*
7. *Photoresist Cure*
8. *Oxide Etch*
9. *Wafer Cleaning*
10. *KOH Etch*
11. *Rinse, Dry and Inspect.*

---

<sup>8</sup>The details of each of the processing steps are presented in Appendix A.

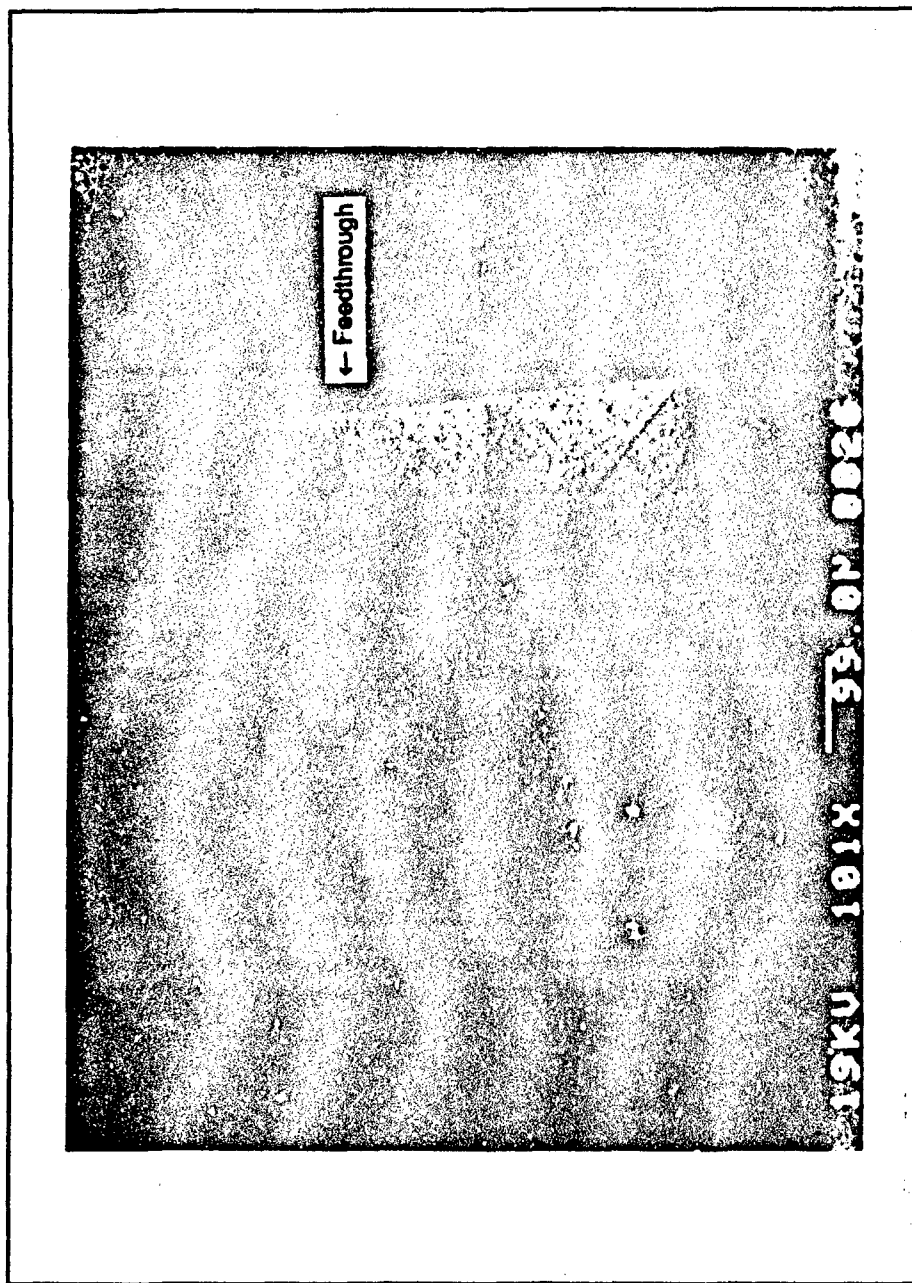


Figure 53. Representative Feedthrough Structure After the First Potassium Hydroxide (KOH) Etch Process.

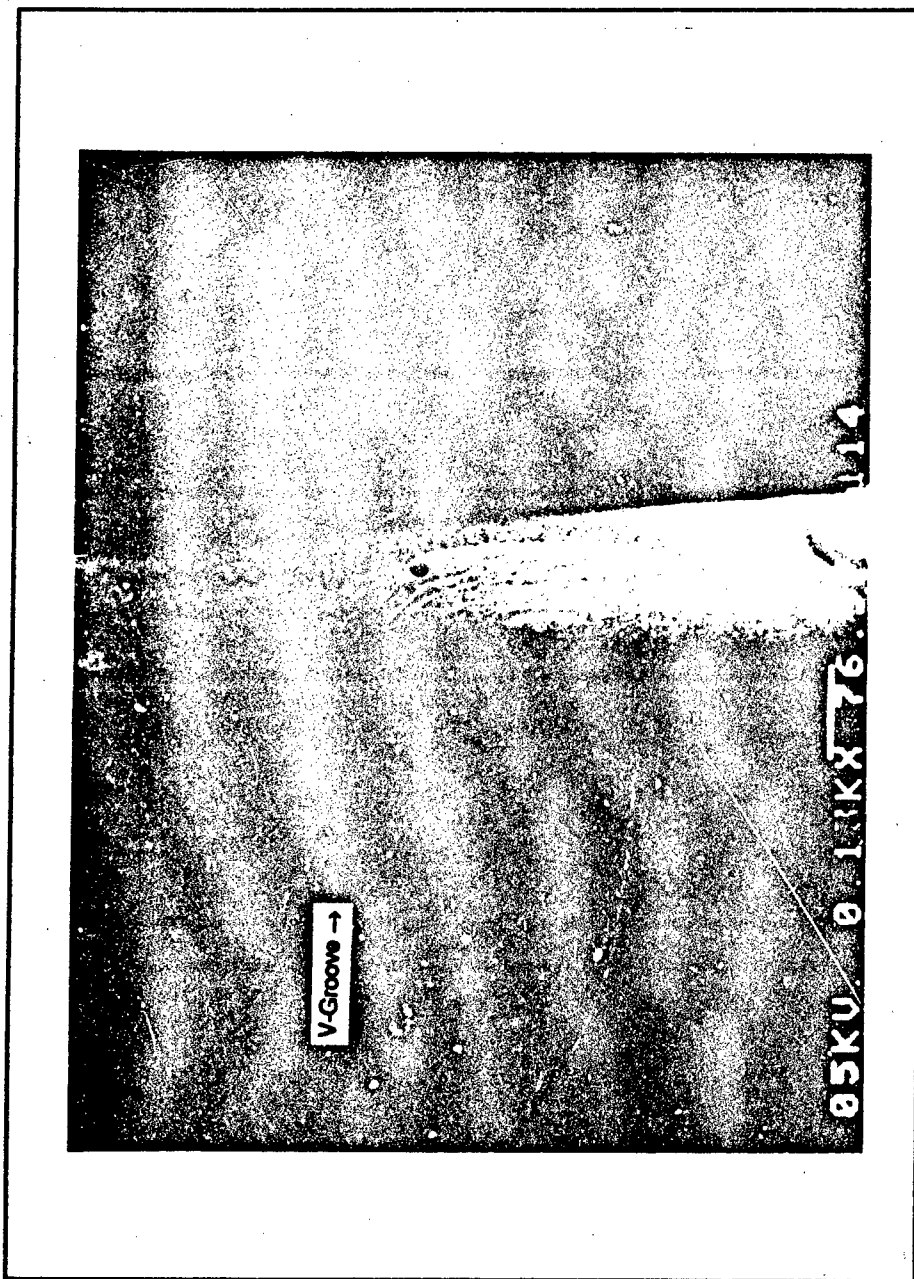


Figure 54. Representative V-Groove Structure After the First Potassium Hydroxide (KOH) Etch Process.

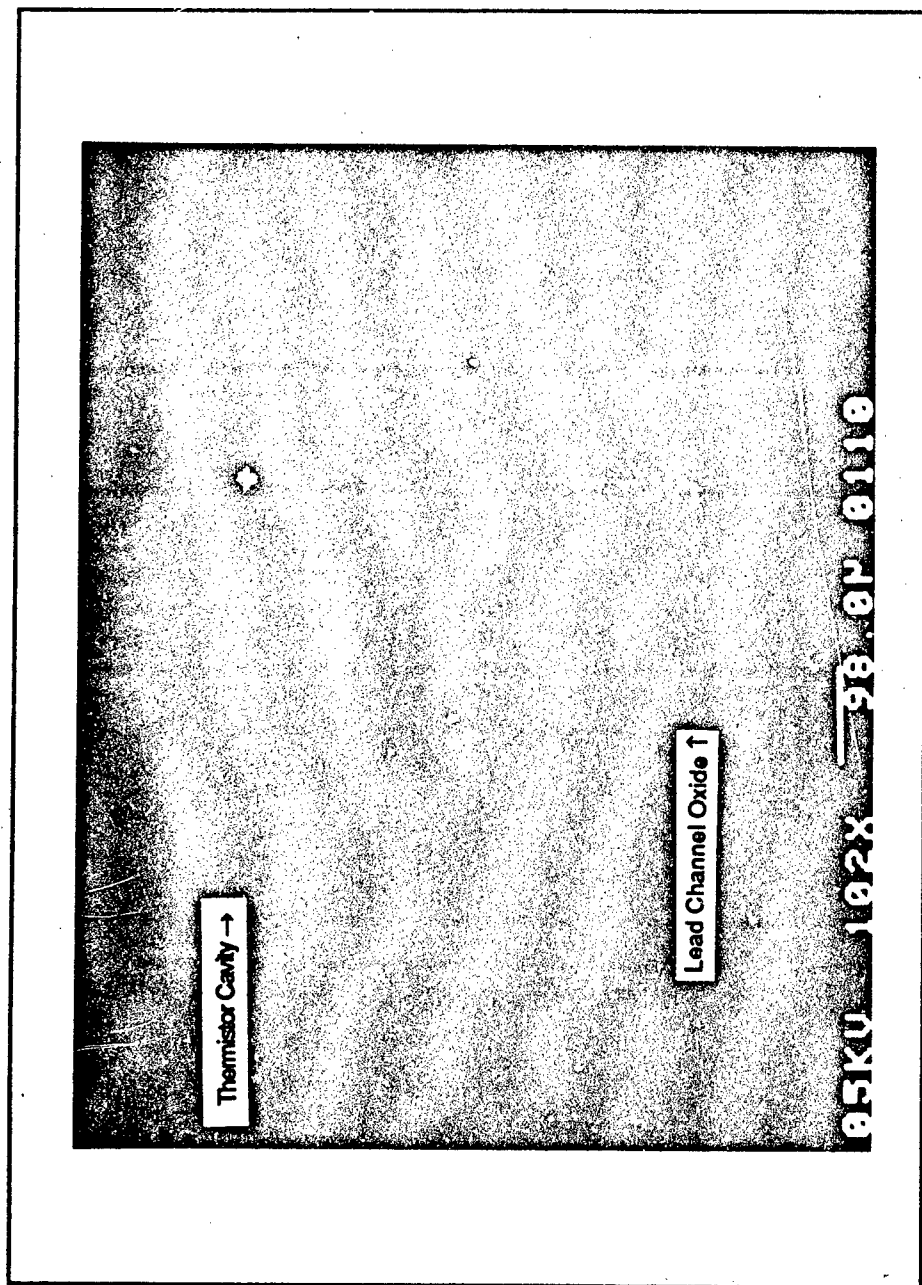


Figure 55. Representative Thermistor Cavity Structure After the Second Potassium Hydroxide (KOH) Etch Process.

**5.2.3 Isotropic Etch: Column Etch.** This wet chemical etch process created the micromachined column using the etchant described in Section 3.1.1. Since the MMGC column etch took place on two different substrates (the silicon wafer and the glass cover plate), two different etch processes were followed.

**5.2.3.1 Silicon Wafer Etch.** The results of the silicon wafer etch process are shown in Figures 56 through 61, and the processing steps are listed below<sup>9</sup>:

1. *Wafer Cleaning*
2. *Oxidation*
3. *Front Side Photoresist Deposition (Image Capture)*
4. *Isotropic Mask Exposure*
5. *Photoresist Development*
6. *Back Side Photoresist Deposition (Protection)*
7. *Photoresist Cure*
8. *Oxide Etch*
9. *Wafer Cleaning*
10. *Isotropic Etch*
11. *Rinse, Dry and Inspect.*

**5.2.3.2 Glass Cover Plate Etch.** The results of the glass cover plate etch process are shown in Figures 62 through 65, and the processing steps are listed below<sup>10</sup>:

1. *Wafer Cleaning*
2. *Front Side Photoresist Deposition (Image Capture)*
3. *Isotropic Mask Exposure*

---

<sup>9</sup>The details of each of the processing steps are presented in Appendix A.

<sup>10</sup>The details of each of the processing steps are presented in Appendix A.

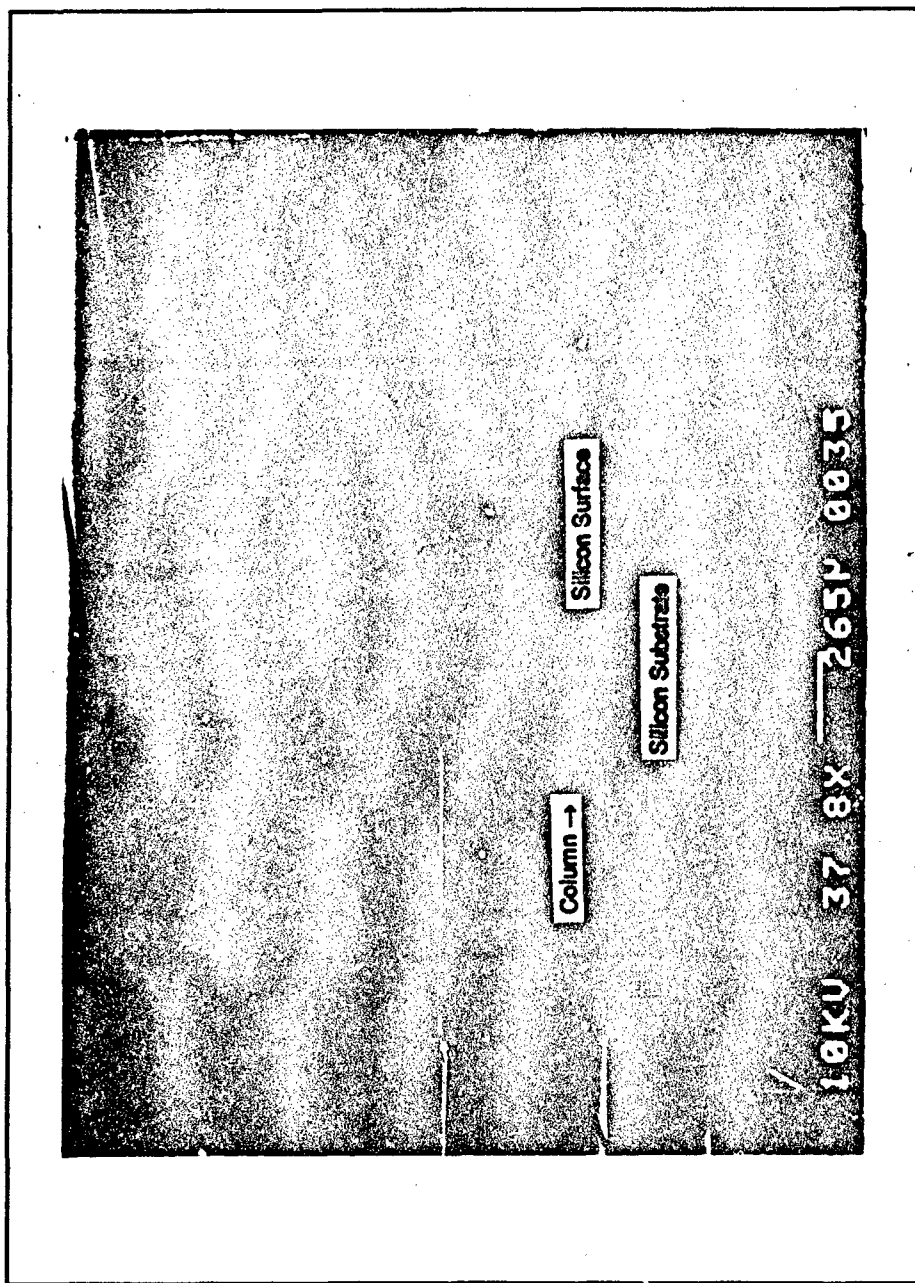


Figure 56. Representative Silicon Column Cross-Section After the Isotropic Column Etch Process.

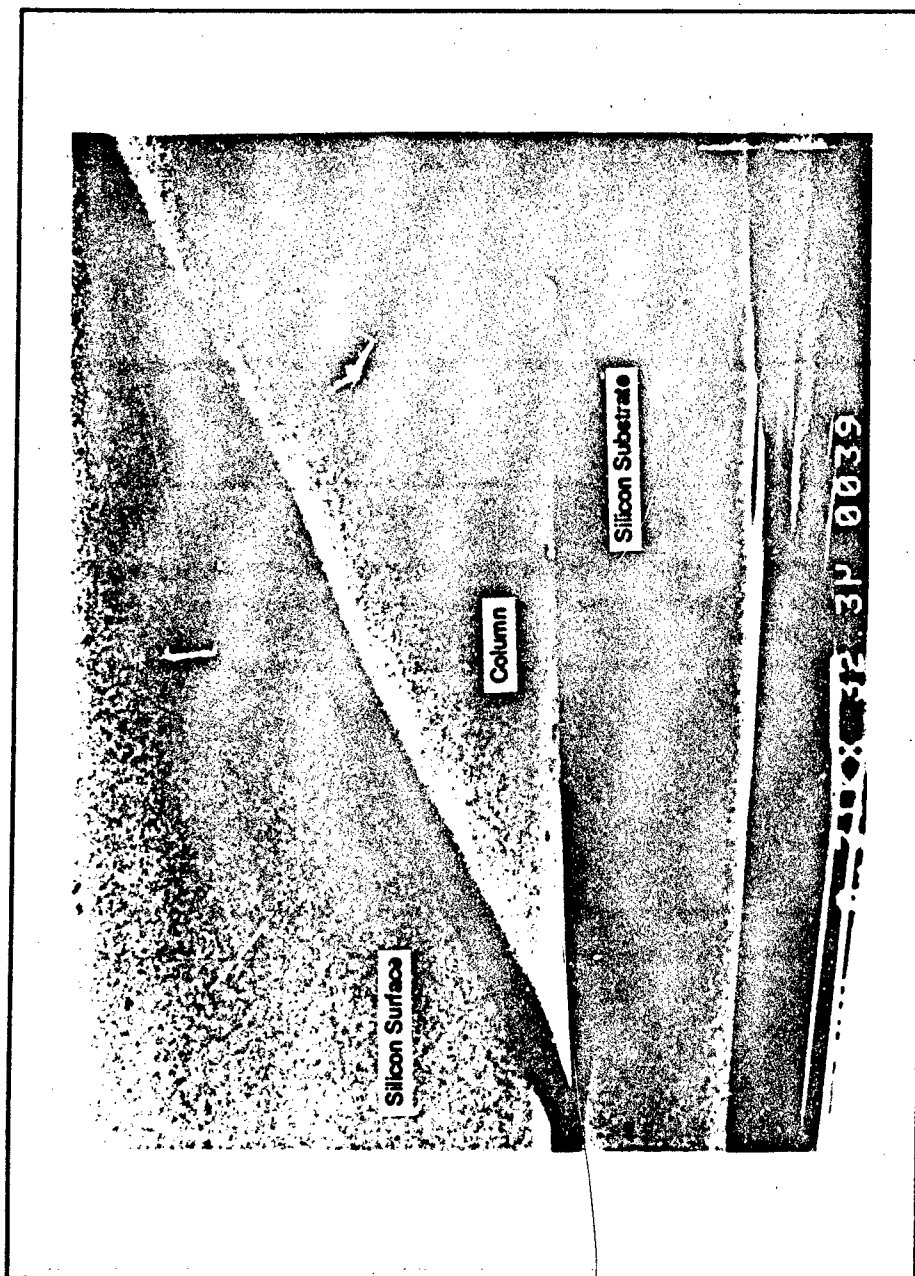


Figure 57. Expanded View of a Representative Silicon Column Cross-Section After the Isotropic Column Etch Process.

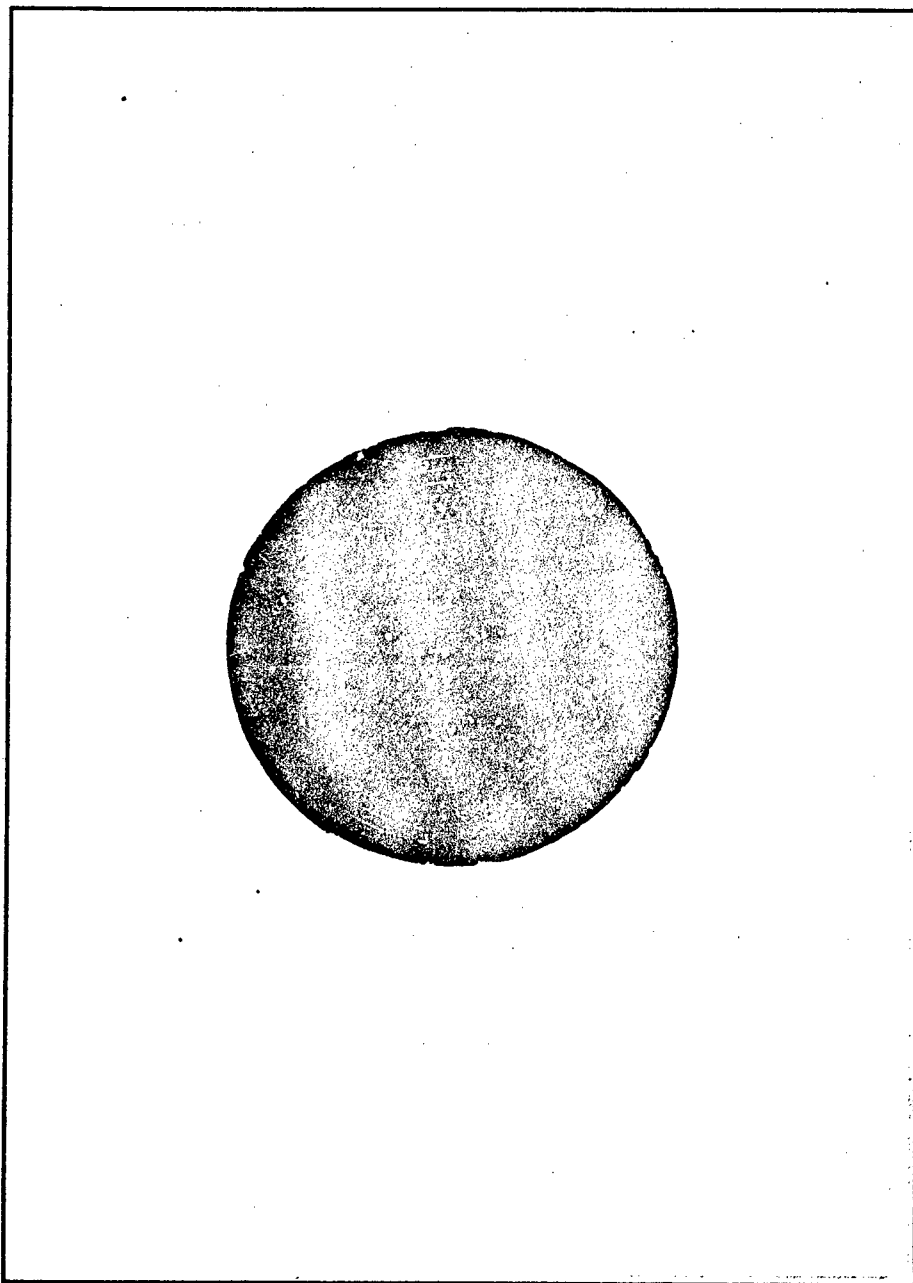


Figure 58. Top View of a Representative Silicon Column After the Isotropic Column Etch Process. The Diameter of the Area Shown is Approximately 4 cm.

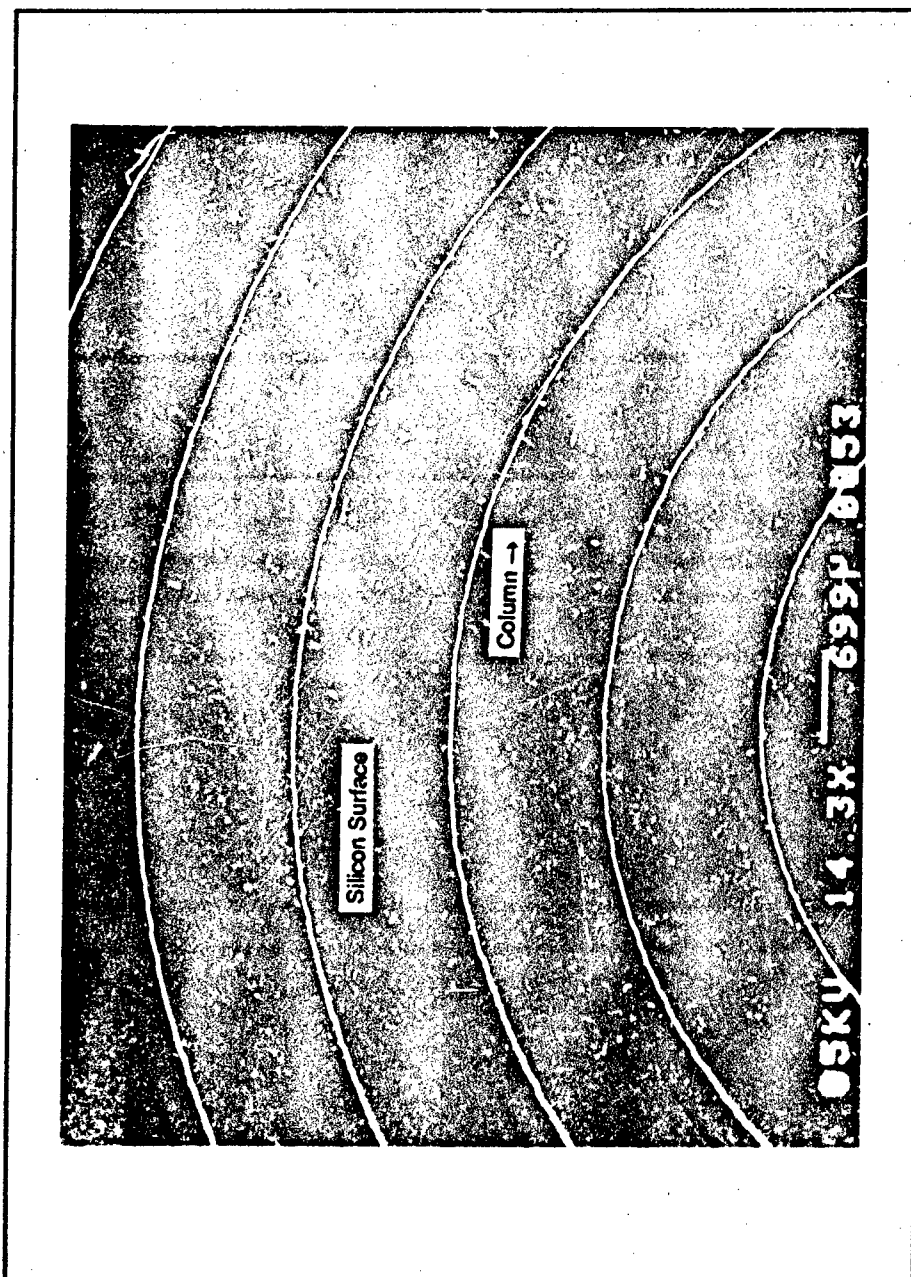


Figure 59. Top View of a Section of a Representative Silicon Column After the Isotropic Column Etch Process.

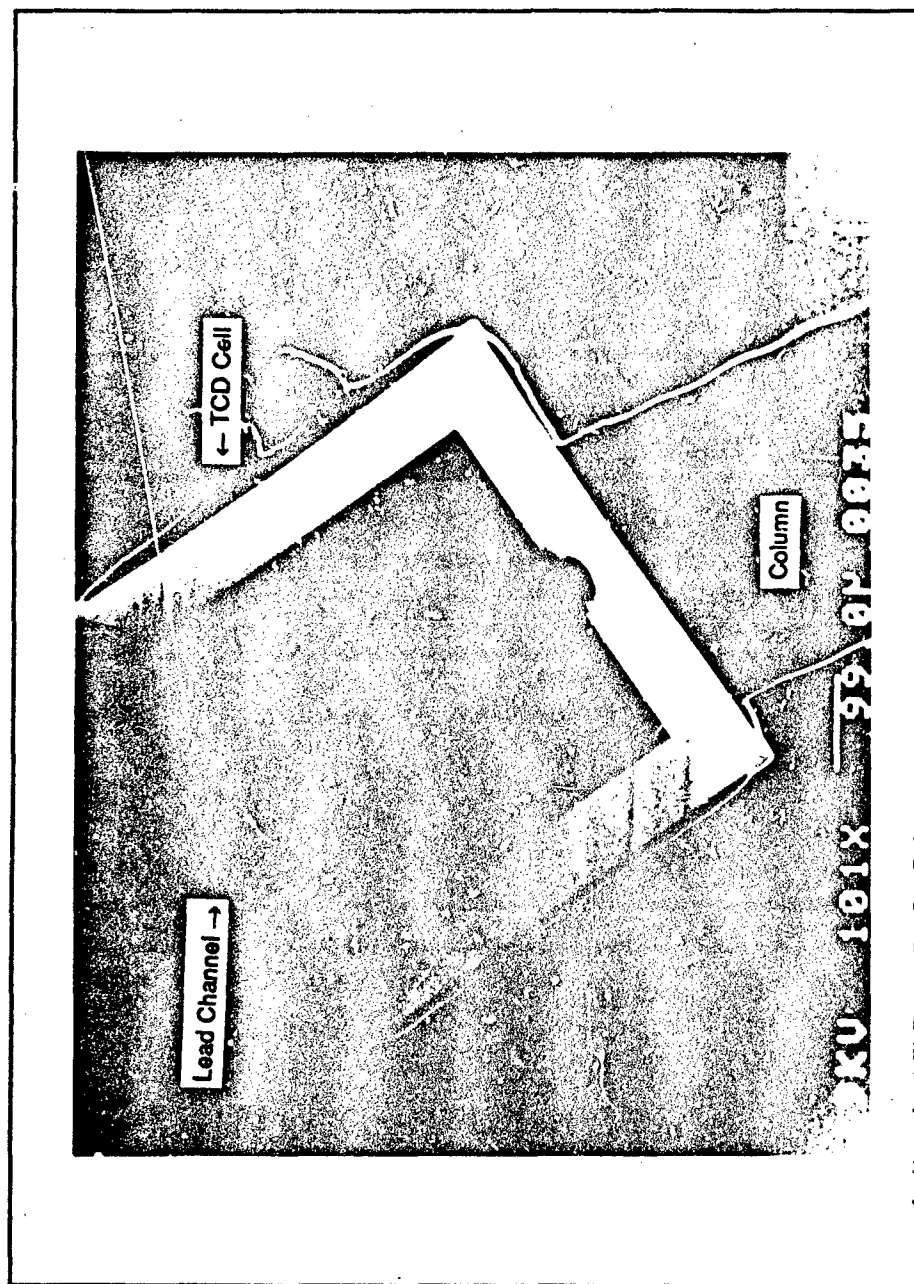


Figure 60. Representative TCD Cell Structure After the Isotropic Column Etch Process. The Chemiresistor Interface is Provided by the Lead Channel.

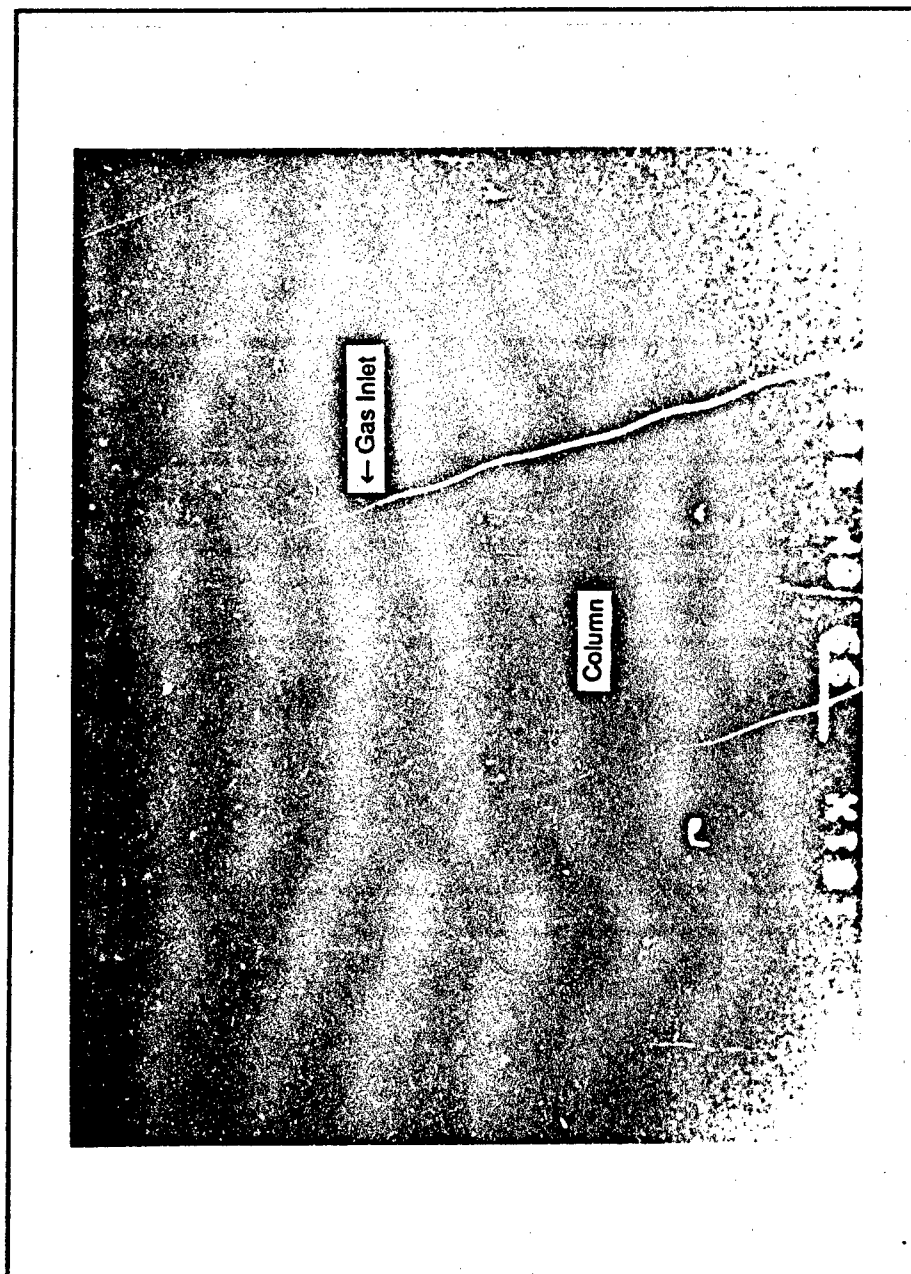


Figure 61. Representative Gas Inlet Structure After the Isotropic Column Etch Process.

#### 4. Photoresist Development

#### 5. Photoresist Cure

#### 6. Oxide Etch<sup>11</sup>

#### 7. Wafer Cleaning

#### 8. Rinse, Dry and Inspect.

With the completion of this wet chemical etch process, the micromachining phase of the MMGC fabrication was also completed. The next phase of the MMGC fabrication process involved coating the column walls with the CuPc stationary phase.

### 5.3 Stationary Phase Deposition.

In Chapters 2 and 4, the importance of a smooth, uniform, stationary phase within the column was discussed. In order to accomplish this goal for the MMGC, CuPc was sublimed onto the surface of both the etched silicon wafer and the etched glass plate. Since the sublimation process produces uniform<sup>12</sup> thin films, that part of the deposition goal can be readily accomplished. Unfortunately, the deposition process coats the entire wafer (or glass plate), not just the interior of the column. Therefore, a means of selectively removing the excess CuPc is crucial for accomplishing the ultimate goal of fabricating the MMGC. The CuPc deposition process required two critical steps: first, CuPc sublimation, and second, the selective removal of CuPc from the inter-column surface.

**5.3.1 Sublimation.** The bulk CuPc<sup>13</sup> powder was placed in a resistively-heated boat in a thermal evaporation chamber<sup>14</sup> (see Section 3.2). The chamber was evacuated with a helium cryogenic pump to a pressure of  $10^{-6}$  Torr, and the current through the resistively-heated boat was adjusted to produce a sublimation rate of approximately 3 Å/sec (determined with a calibrated piezoelectric quartz crystal film thickness monitor<sup>15</sup>). Since the

<sup>11</sup>The oxide etch is actually the isotropic etch for the glass plate.

<sup>12</sup>Uniform in the sense that the CuPc covers the MMGC column with a uniform thin film—see Figure 67.

<sup>13</sup>Fluke Chemical Corp., Rozkonkoma, NY.

<sup>14</sup>Model DV-602, Denton Vacuum, Inc., Cherry Hill, NJ.

<sup>15</sup>Model TM-100R, Maxtek, Torrance, CA.

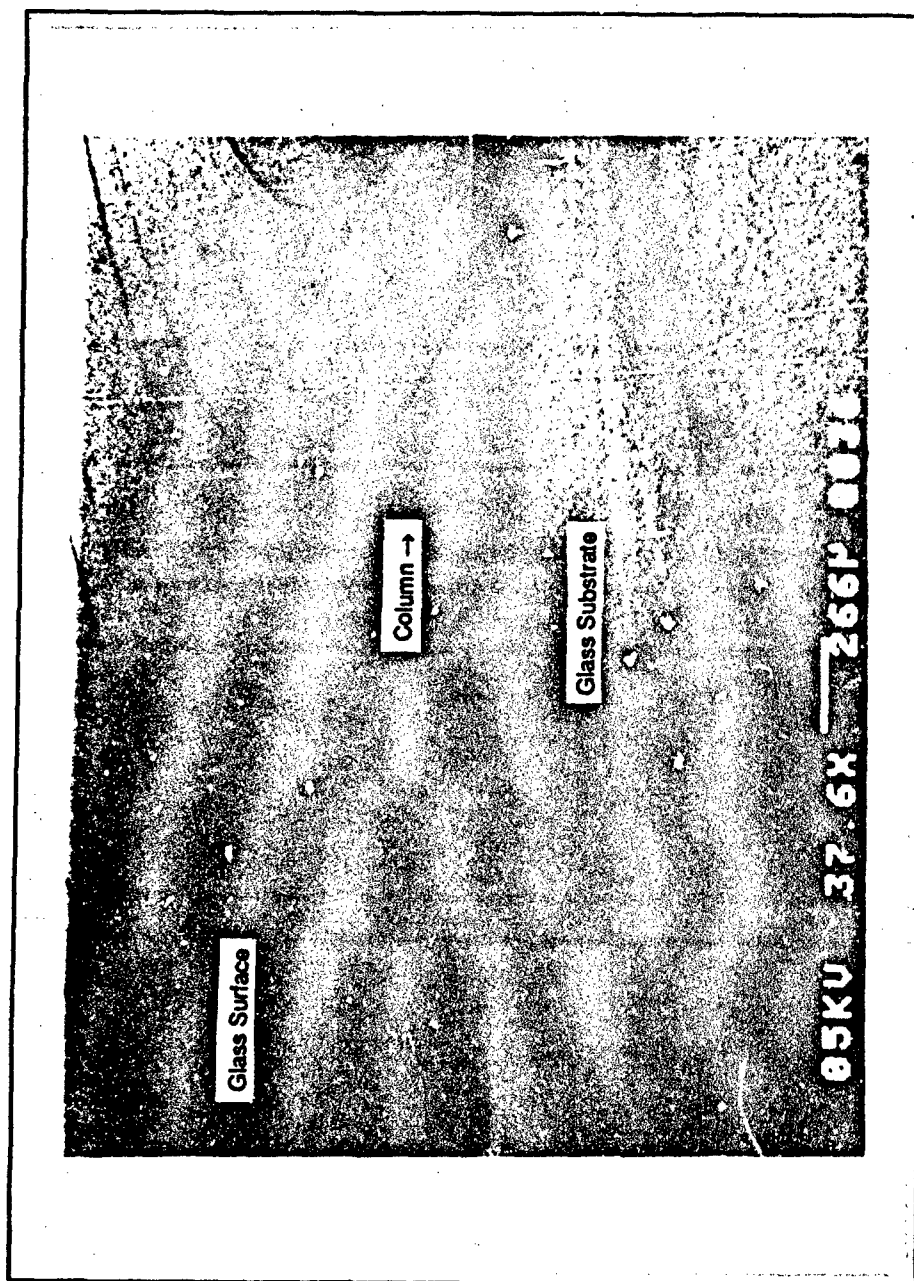


Figure 62. Representative Glass Column Cross-Section After the Isotropic Column Etch Process.

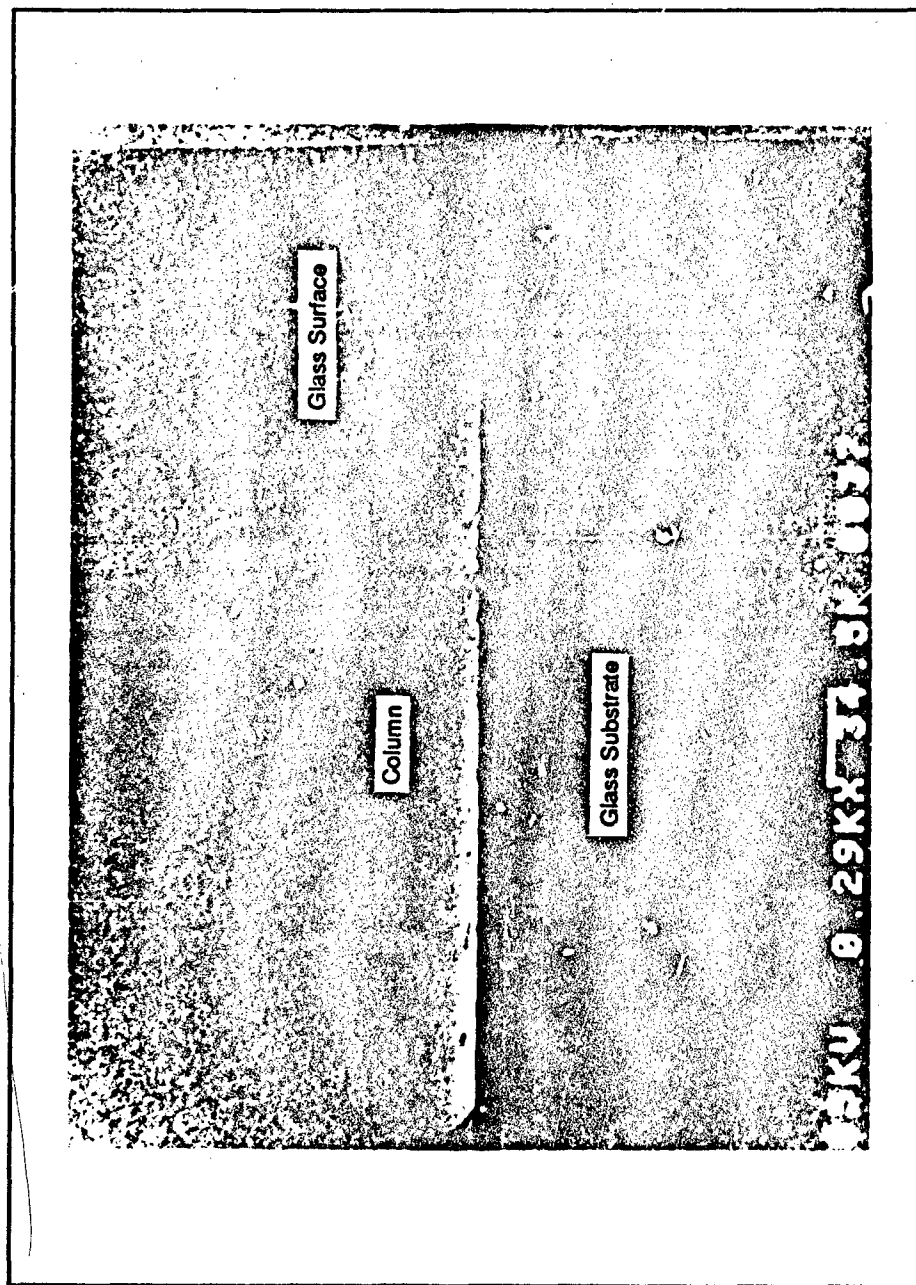


Figure 63. Expanded View of a Representative Glass Column Cross-Section After the Isotropic Column Etch Process.

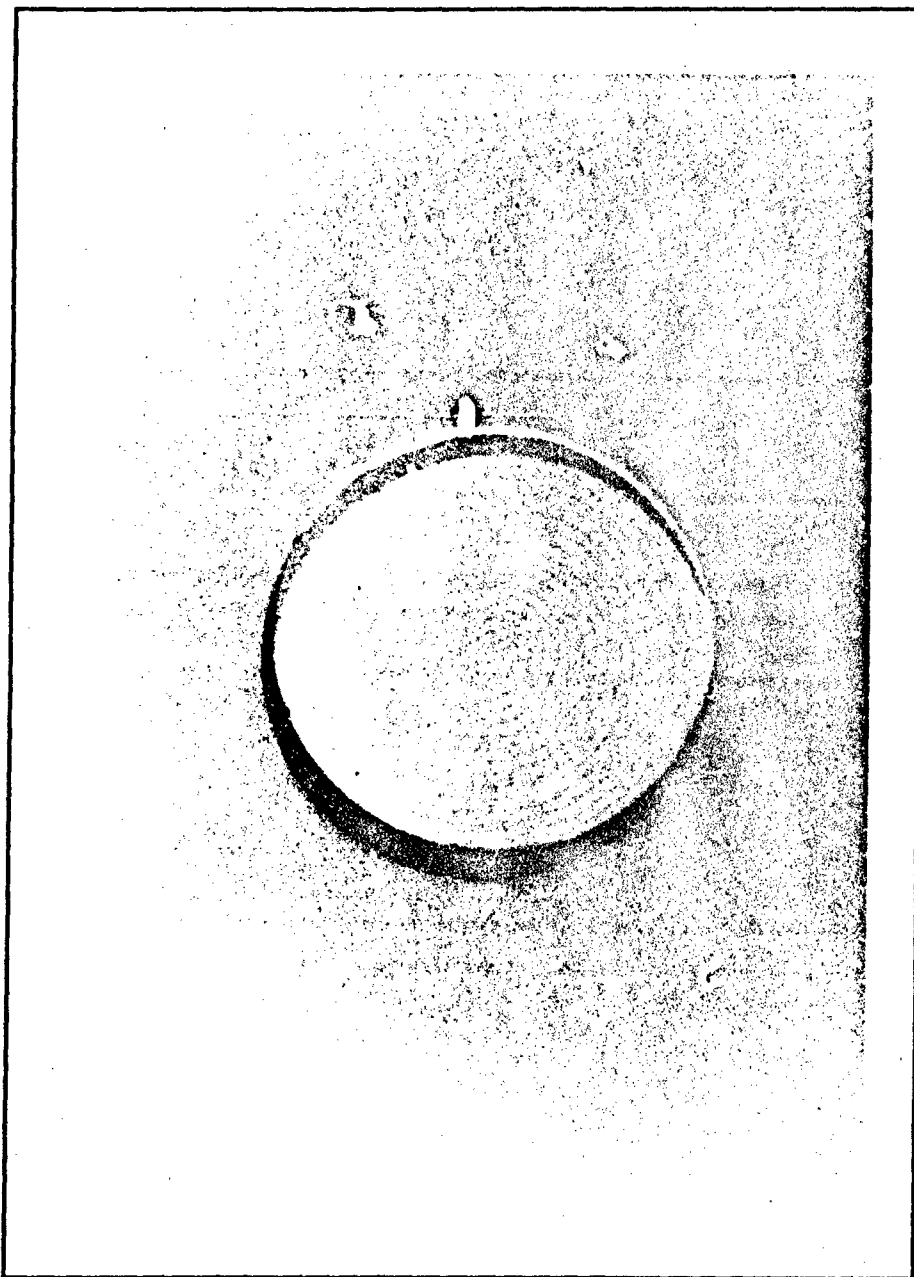


Figure 64. Top View of a Representative Glass Column After the Isotropic Column Etch Process. The Diameter of the Area Shown is Approximately 4 cm.

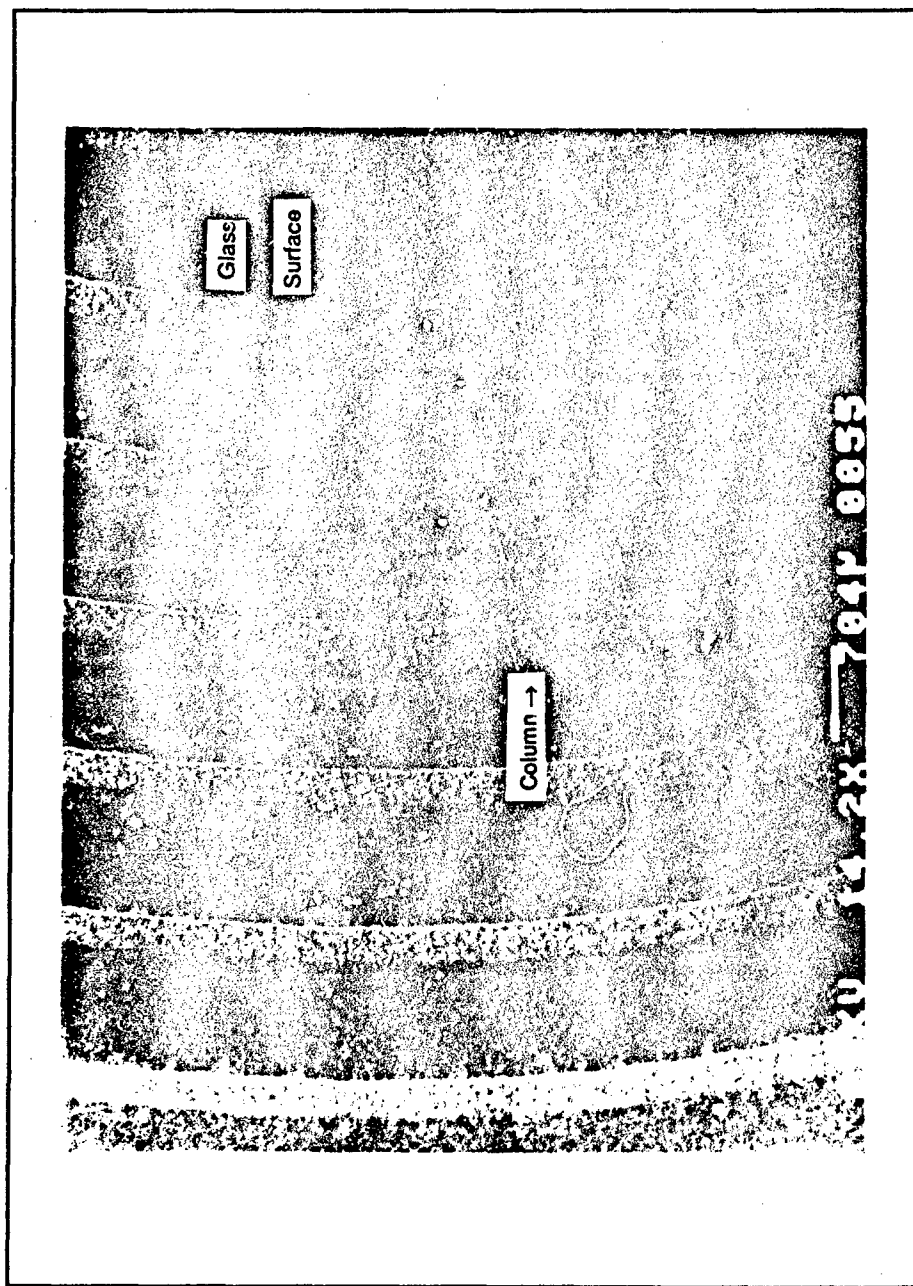


Figure 65. Top View of a Section of a Representative Glass Column After the Isotropic Column Etch Process.

CuPc target film thickness was 2000 Å, the deposition times were on the order of 10 min. The actual film thickness was verified with a profilometer<sup>16</sup> (see Figure 66). Figures 67 and 68 show the results of the CuPc deposition process.

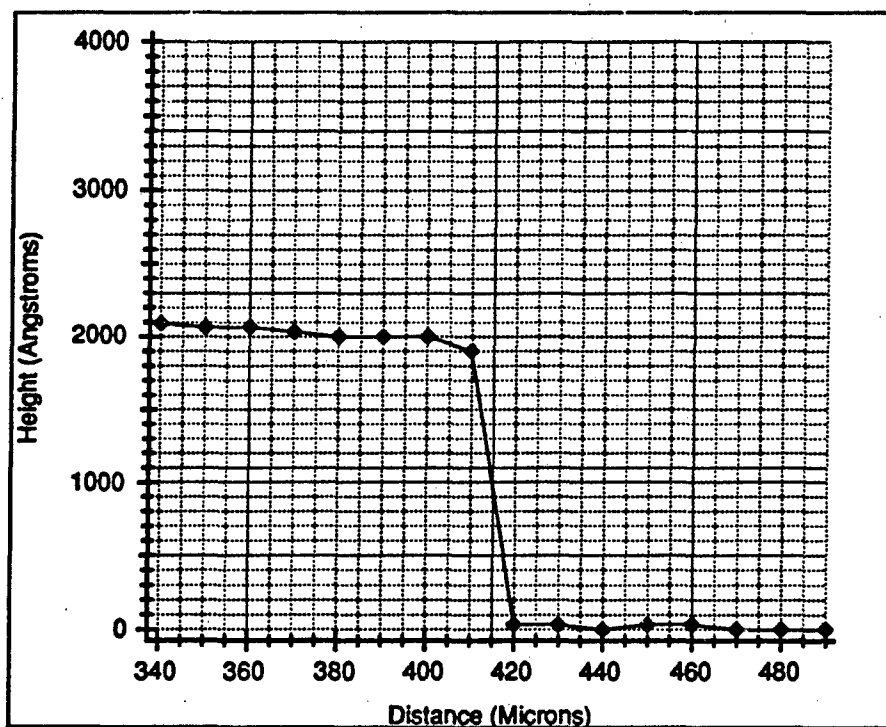


Figure 66. Representative Profile for the 2000 Å Thick Copper Phthalocyanine Thin Film.

**5.3.2 Selective Removal.** To selectively remove the CuPc film from the substrate's surface, while leaving the CuPc within the column, involved polishing the substrate with a 0.3 micron diameter aluminum oxide coated lapping film<sup>17</sup>. The lapping film was secured to a marble plate and lubricated with DIW. The substrate was then carefully moved across the surface of the lapping film in a figure-eight motion until the CuPc was removed. Figures 69 through 74 show the results of the selective removal process. Once the CuPc was removed from the surface of both the silicon wafer and glass plate (verified by examination under a microscope), the two column components were stored for their final assembly.

<sup>16</sup>Dektak IIA, Sloan Technology Corporation, Santa Barbara, CA.

<sup>17</sup>Part Number 16.3-6, PSI Testing Systems, Inc., Houston, TX.

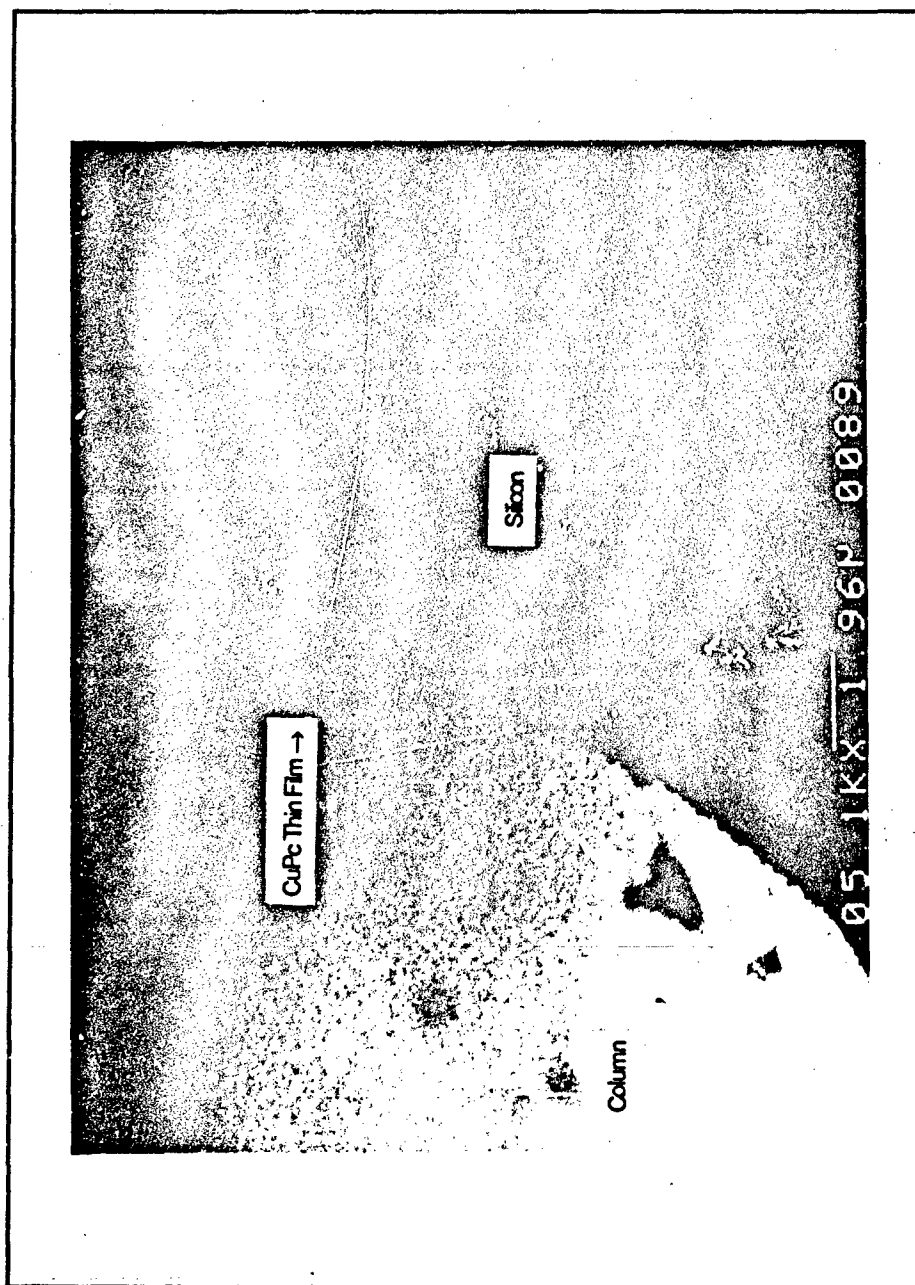


Figure 67. Column After Deposition of a 2000 Å Thick CuPc Thin Film.

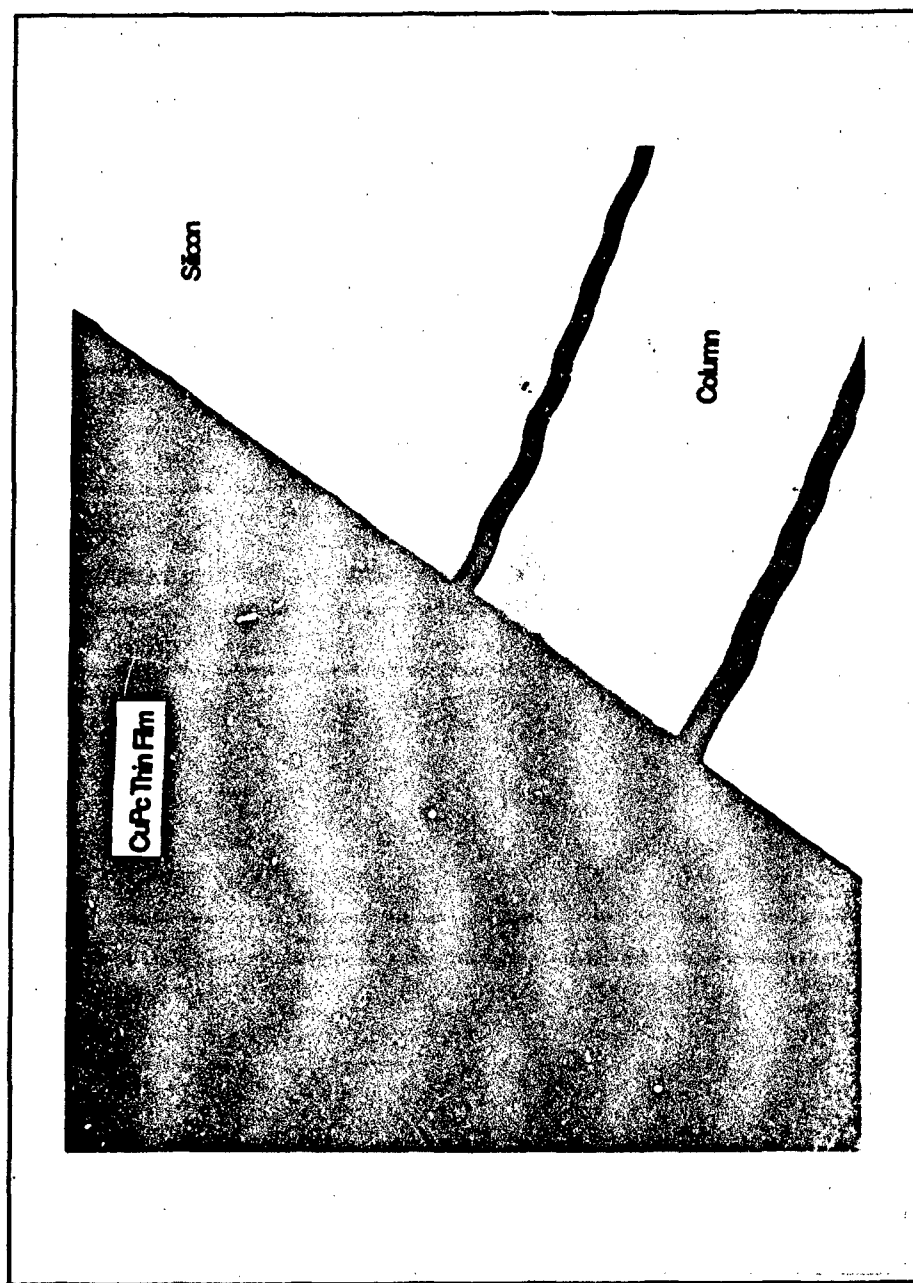


Figure 68. Column After a 2000 Å Thick CuPc Thin Film Deposition Contrasted with a Masked Area of the Etched Column (the Column Width is Approximately 300  $\mu\text{m}$ ).

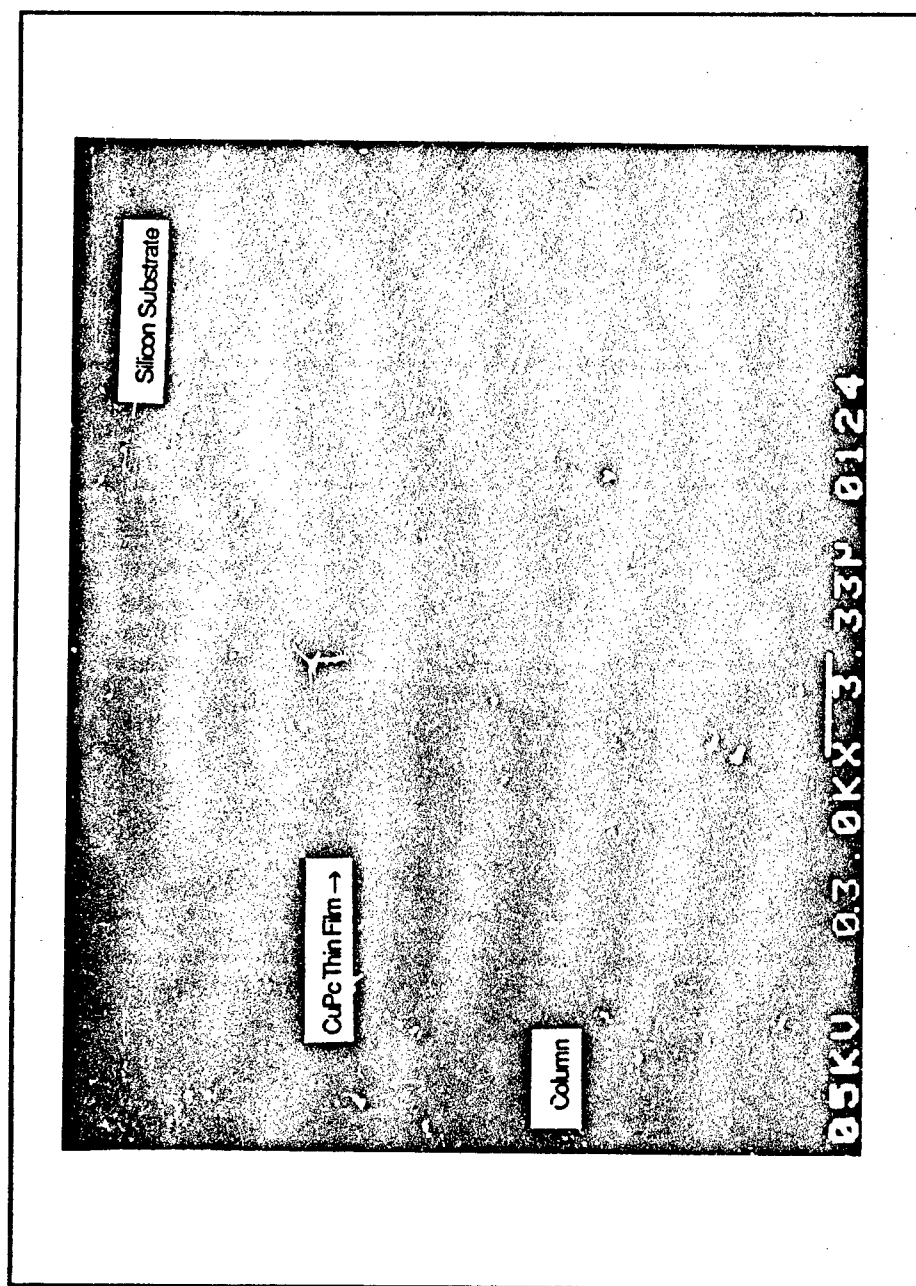


Figure 69. Column After the Final Polishing Step of the 2000 Å Thick CuPc Thin Film.

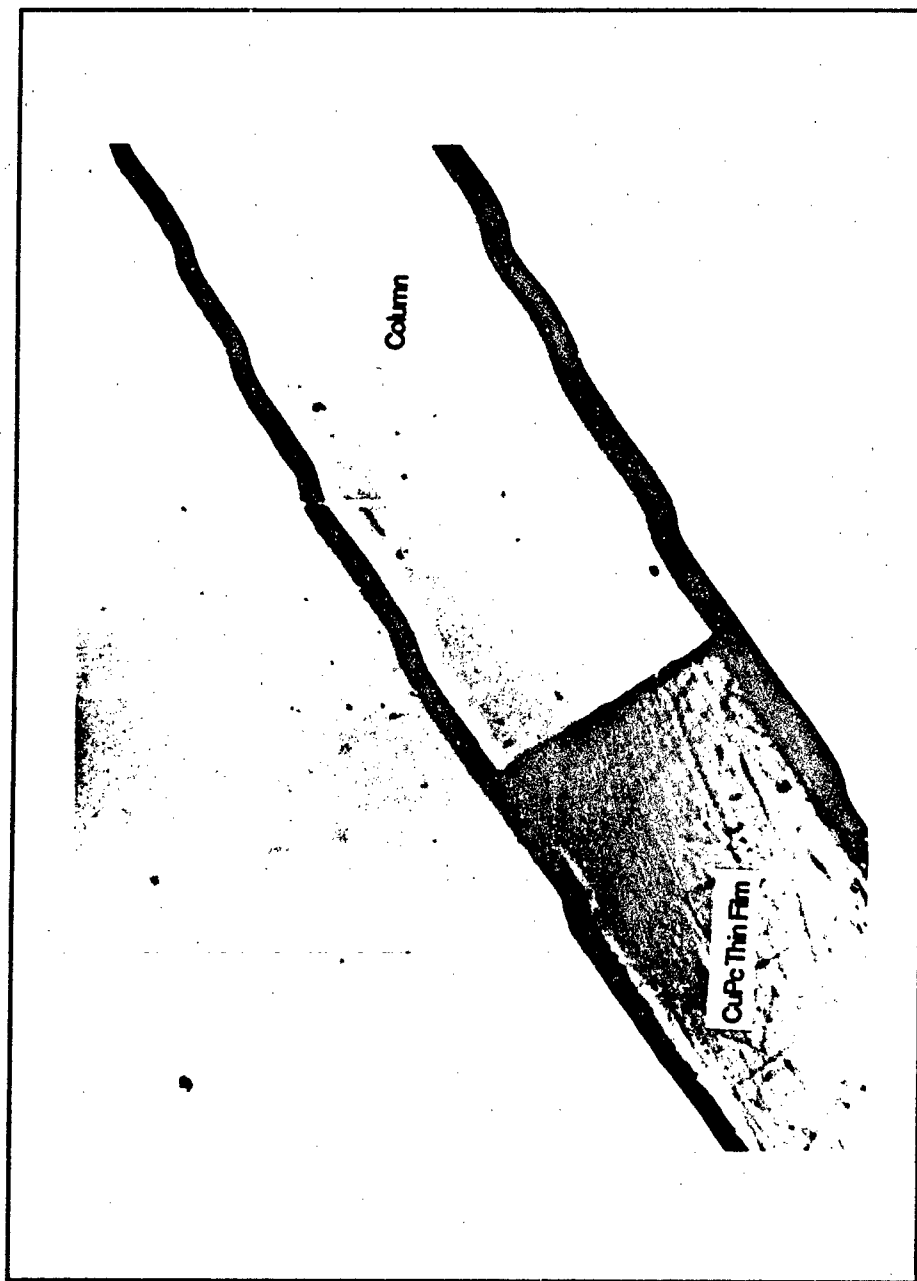


Figure 70. Column After the Final Polishing Step of the 2000 Å Thick CuPc Thin Film Contrasted with a Masked Area of the Etched Column (the Column Width is Approximately 300  $\mu\text{m}$ ).

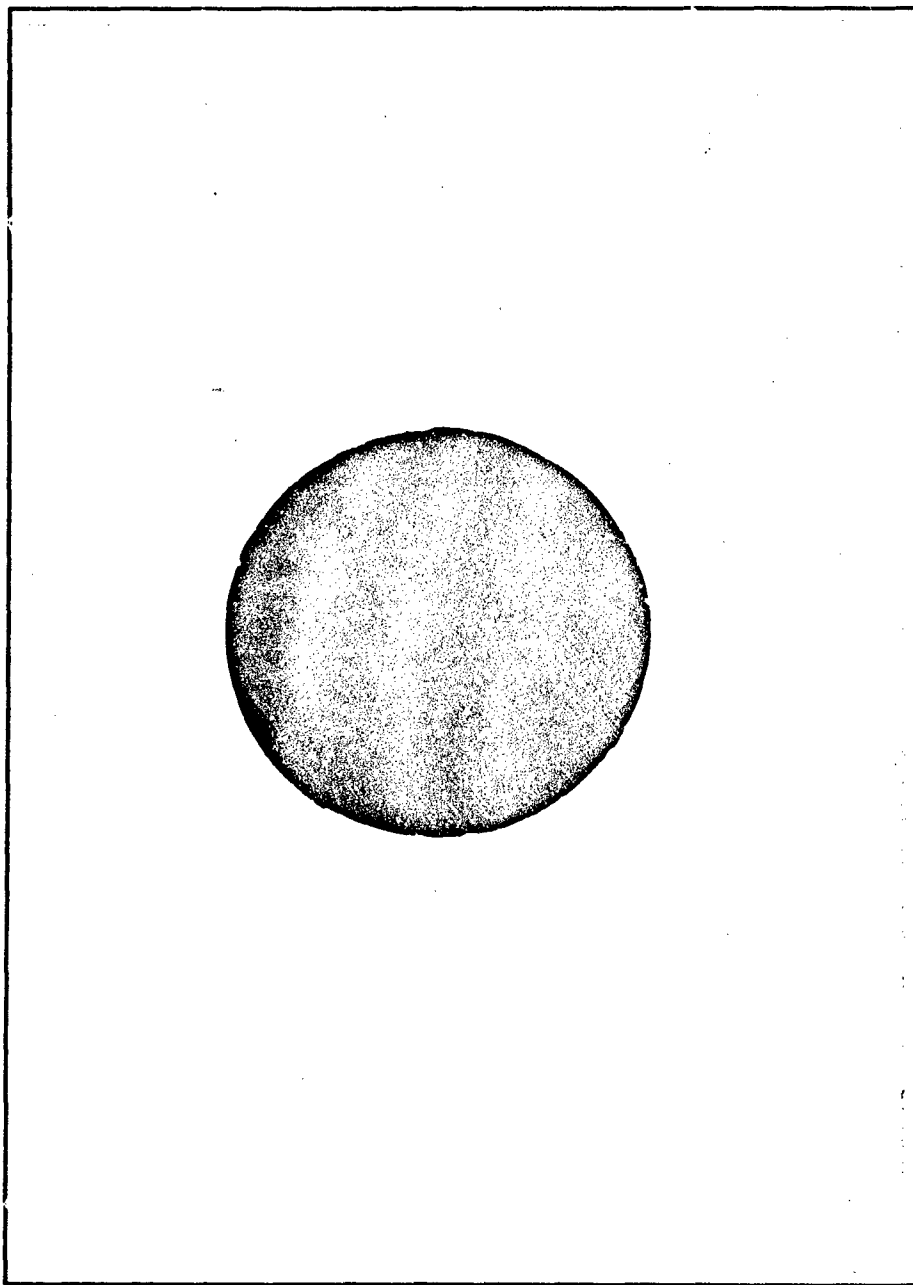


Figure 71. Column After the Final Polishing Step of the 2000 Å Thick CuPc Thin Film (Silicon Wafer Surface). The Diameter of the Area Shown is Approximately 4 cm.

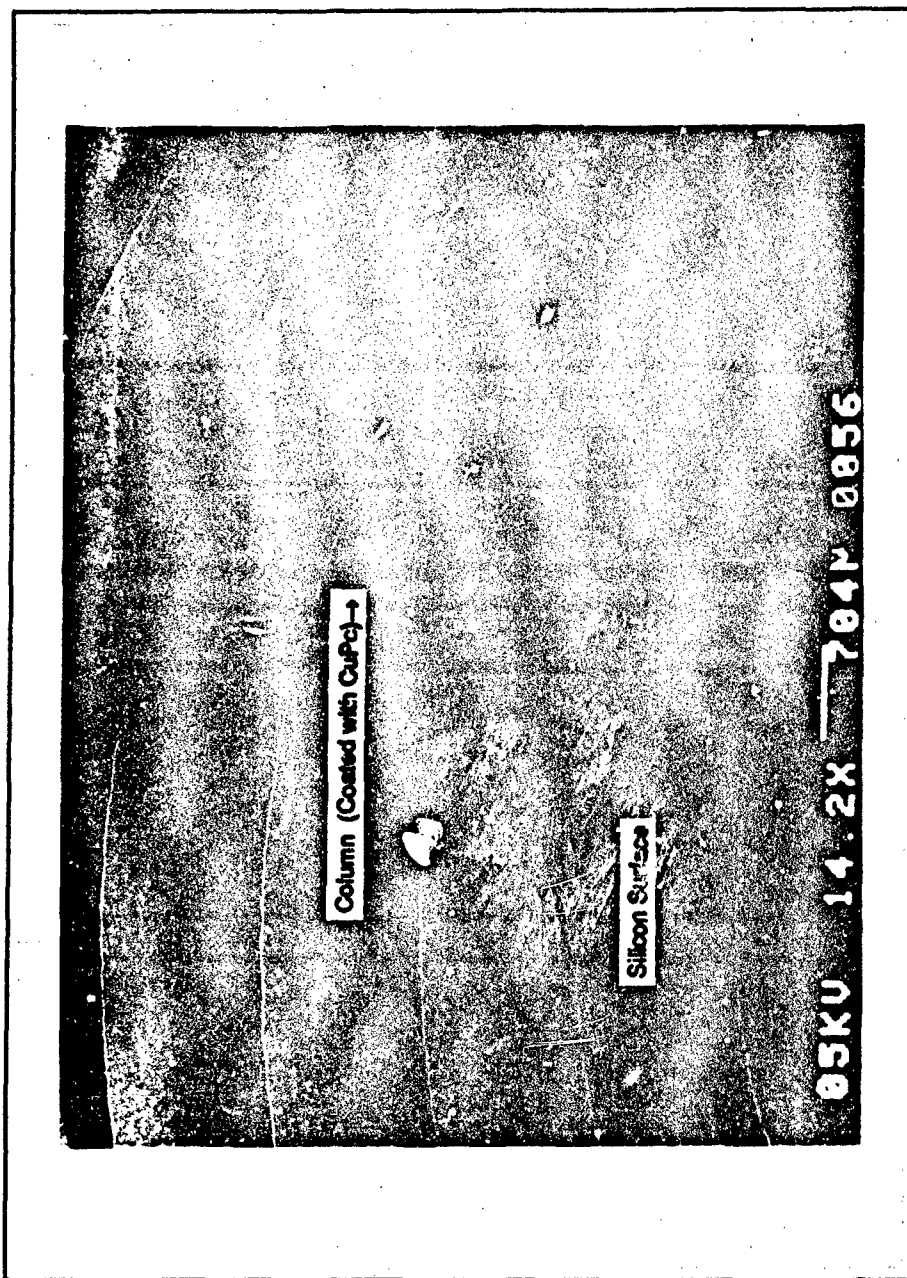


Figure 72. Section of the MMGC Column After the Final Polishing Step of the 2000 Å Thick CuPc Thin Film (Silicon Wafer Surface).

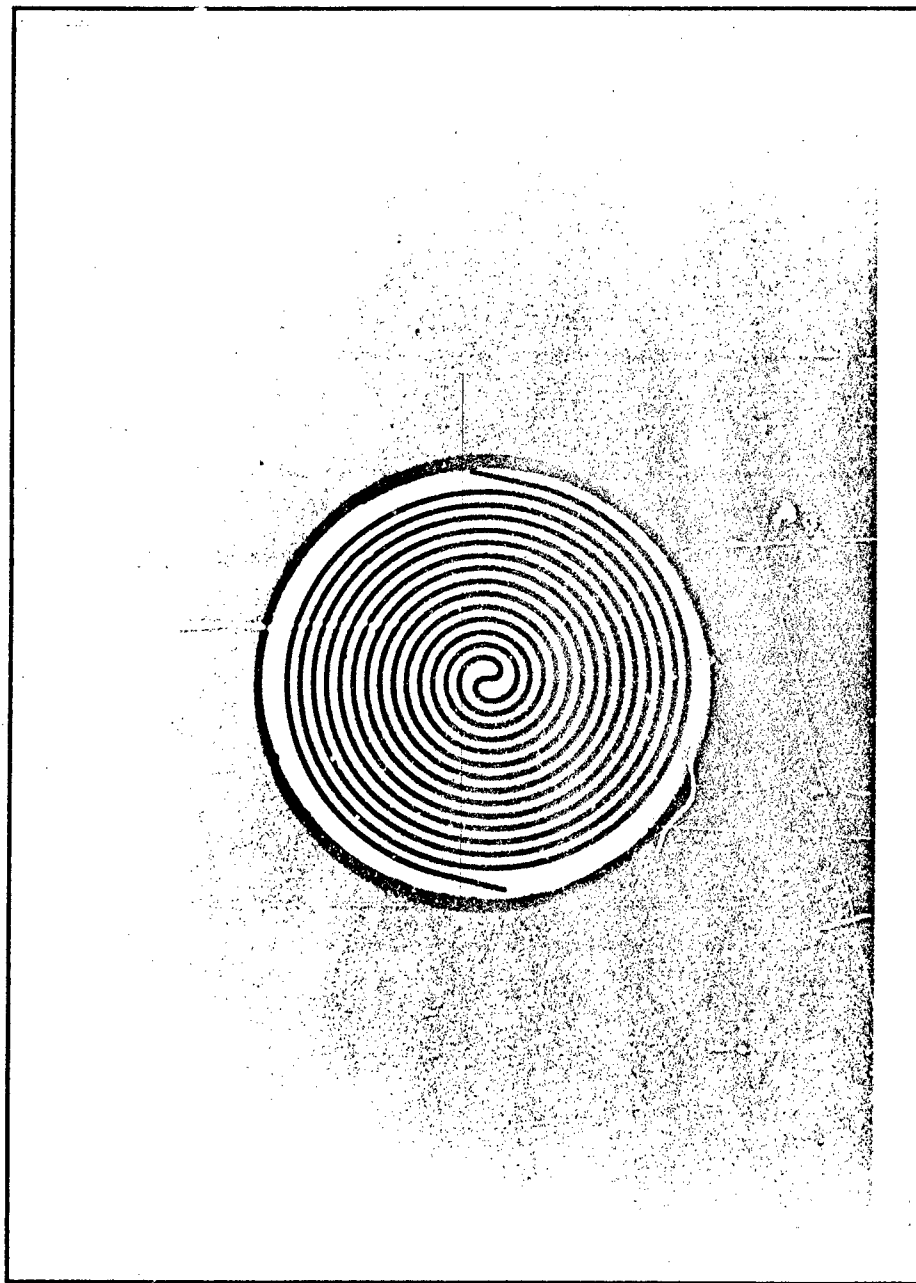


Figure 73. Column After the Final Polishing Step of the 2000 Å Thick CuPc Thin Film (Glass Wafer Surface). The Diameter of the Area Shown is Approximately 4 cm.

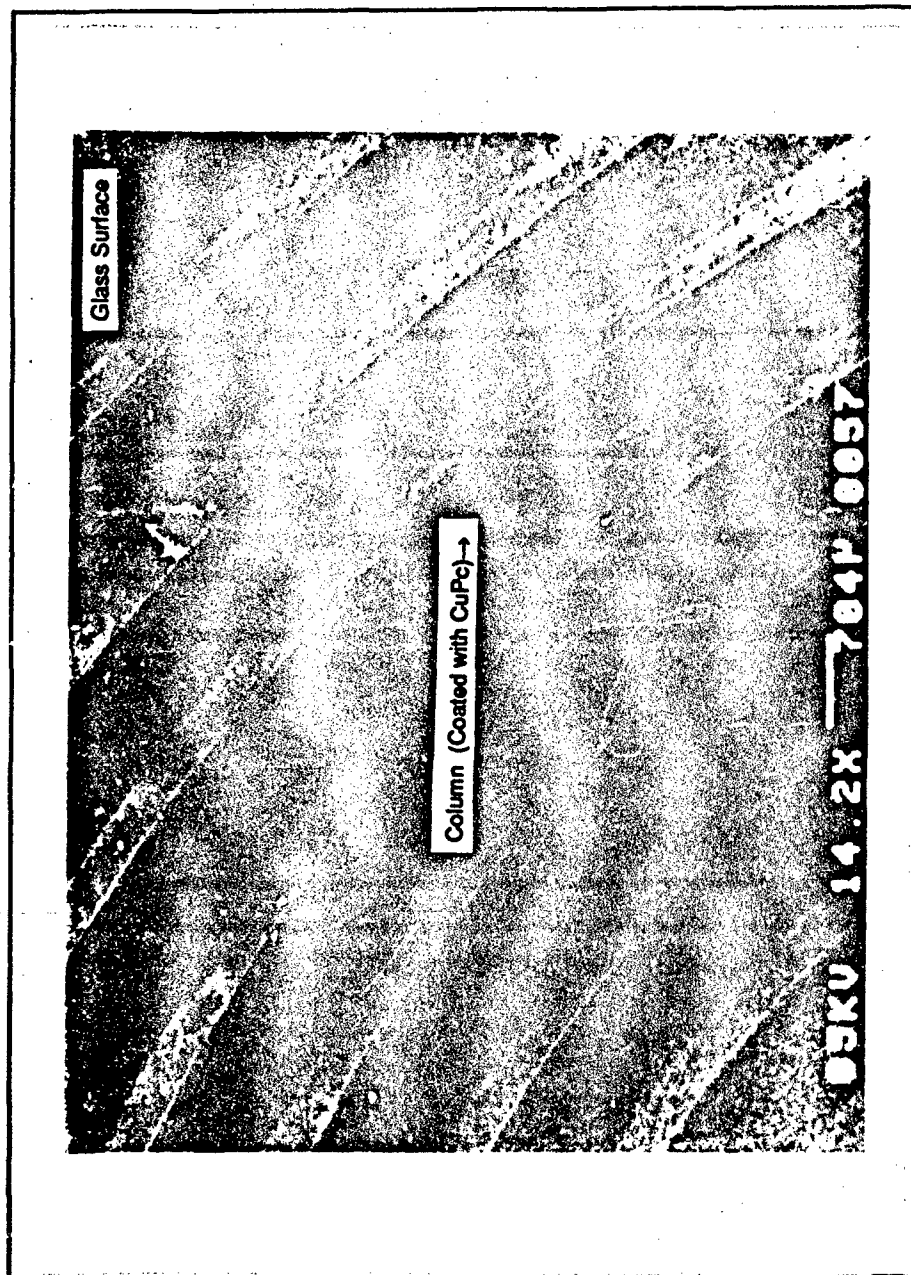


Figure 74. Section of the MMGC Column After the Final Polishing Step of the 2000 Å Thick CuPc Thin Film (Glass Plate Surface).

#### 5.4 Final Assembly.

The final MMGC assembly involved mounting both the internal (e.g., thermistor) and external (e.g., interconnect tubing) hardware, anodically bonding the silicon wafer to the glass plate, and attaching the chemiresistor to the output port of the TCD cell. The sequence in which these steps were accomplished was important with respect to being able to rapidly correct process induced defects. The first step involved attaching the interconnecting gas inlet tube to the gas feedthrough structure etched in the silicon wafer (see Figure 53).

**5.4.1 Gas Inlet.** The reason this step was accomplished first can be attributed to the epoxy<sup>18</sup> used to bond the tube to the silicon wafer (see Figure 75). If the epoxy flows too much during cure, it may obstruct the opening in the interconnect tube. As long as access is maintained to the front surface of the silicon wafer, a small metal alignment probe can be used to clear the tube. However, if the tube were to be attached after the anodic bonding process, the epoxy obstruction problem would be irreversible. Figure 76 shows the results of a successful interconnect tube attachment<sup>19</sup>.

**5.4.2 Thermistor Insertion.** Once the gas inlet epoxy cured (and was visually inspected to insure that there was no obstruction of the interconnect tube's ID), the thermistor (see Figure 77) was carefully inserted into the TCD cavity. Each lead was threaded separately through their respective lead slot (V-groove—see Figures 46 and 60) using a pair of wire-bonding tweezers. The leads were then gently pulled until the thermistor came to rest in the cavity. To complete this assembly process, the leads were secured with silver conductive epoxy to the surface of the glass plate. Figure 78 shows the results of a successful thermistor installation.

**5.4.3 Anodic Bonding.** Once the interconnect tubing was successfully attached and the thermistor was inserted, the glass plate was positioned over the silicon wafer (with the glass plate's CuPc-coated column facing towards the corresponding CuPc-coated column

<sup>18</sup>Epoxy 907, Miller Stephenson Chemical Co., Inc., Danbury, CT.

<sup>19</sup>This photograph was taken after the final MMGC assembly was complete; therefore, the glass portion of the column is shown.

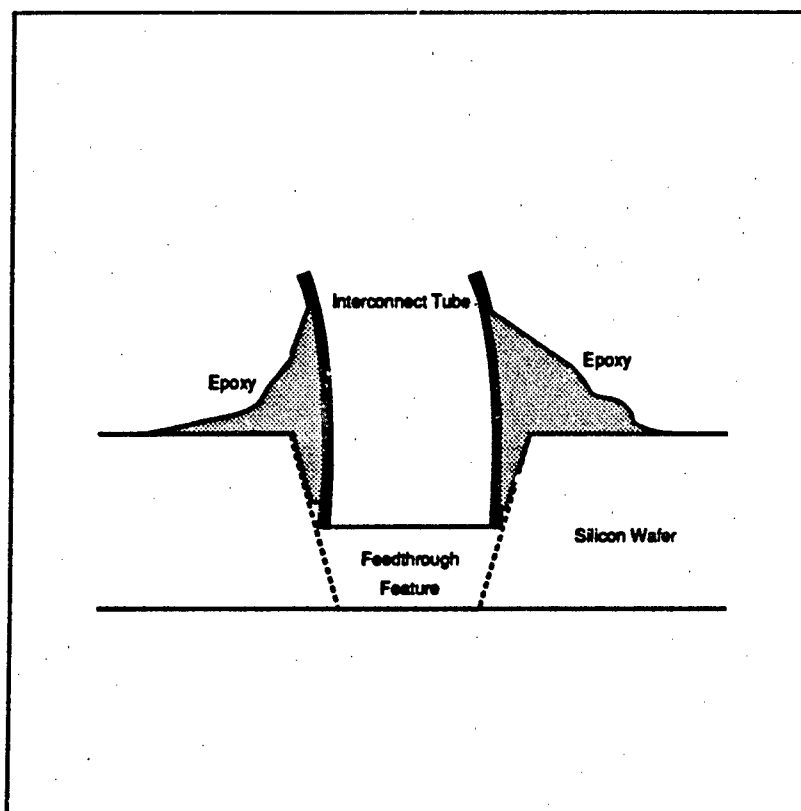


Figure 75. Side View of Interconnect Tubing Attachment.

in the silicon wafer). With the aid of a low-power binocular microscope, the column features in the glass plate and silicon wafer were carefully aligned, and the two halves of the MMGC column were secured with adhesive tape. Next, the cathode was attached to the opposite side of the glass plate with adhesive tape (see Figure 36). Finally, the assembly was transferred to a furnace<sup>20</sup> and heated to 150°C (the adhesive tape was capable of maintaining a bond at this temperature). Once heated (approximately 30 min after insertion into the furnace), an 1800 V, DC bias was applied<sup>21</sup> (as depicted in Figure 36) between the silicon wafer and the cathode, and this configuration was processed for 24 hours. The next day, the DC bias was removed from the MMGC assembly, and the furnace was permitted to cool for approximately 1 hour before it was opened. The cathode was then removed,

<sup>20</sup>Type 30400 Thermolyne Furnace, Barnstead/Thermolyne, Subsidiary of Sybron Corporation, Dubuque, IA.

<sup>21</sup>Using the high-voltage power supply in a Model 577 Curve Tracer, Tektronix, Inc., Beaverton, OR.

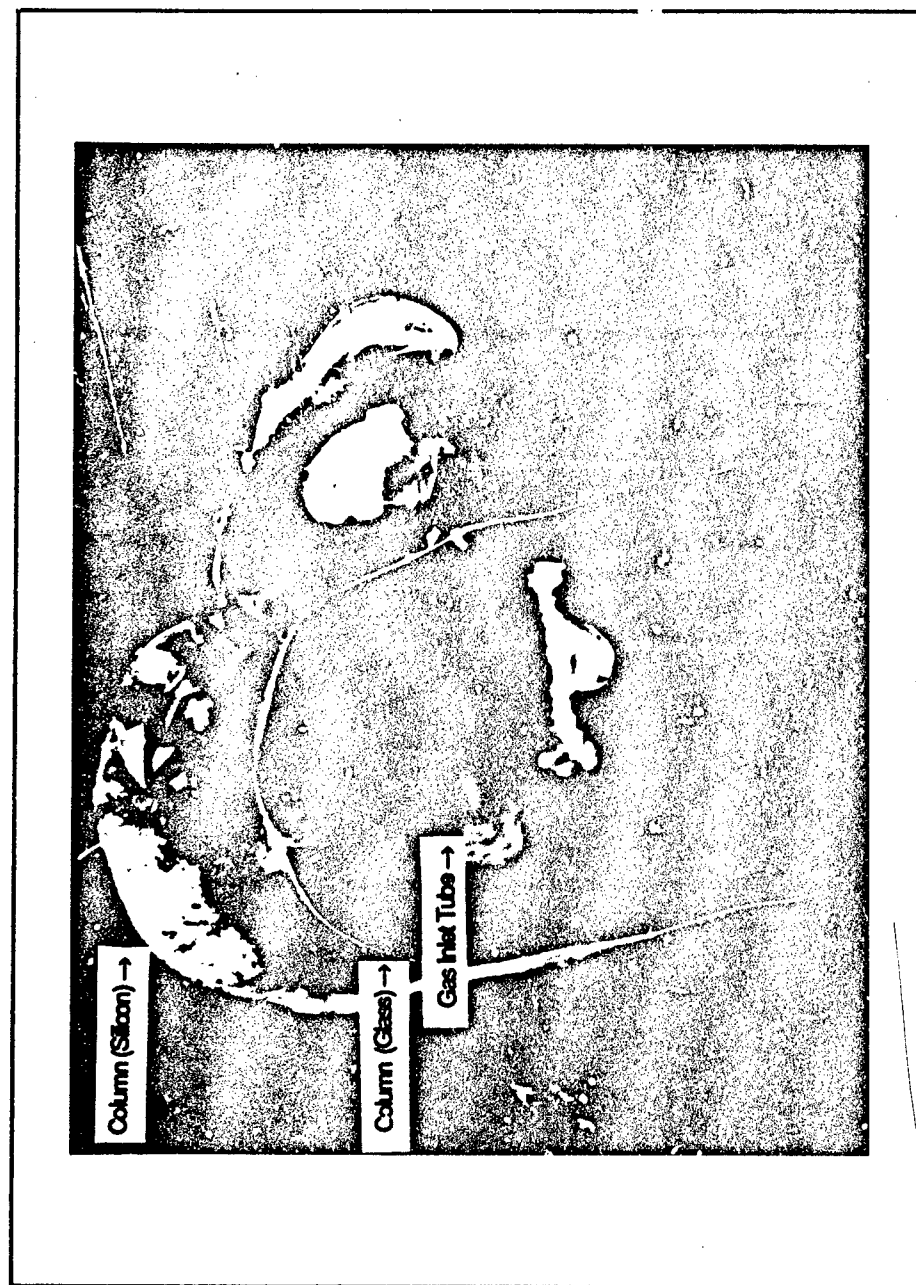


Figure 76. Gas Inlet Aftc. Attachment of the Interconnect Tubing (the Column Width is Approximately 300  $\mu\text{m}$ ).

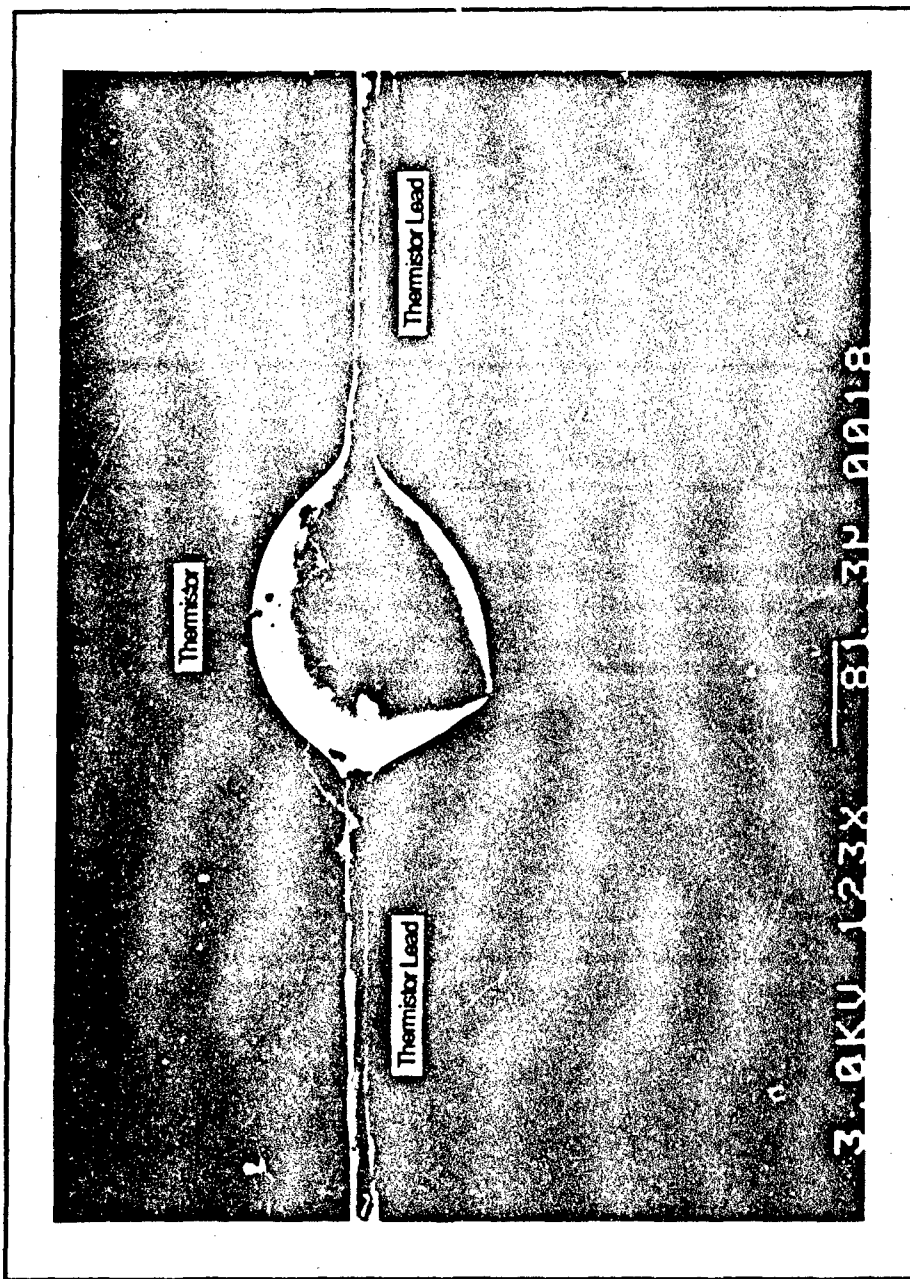


Figure 77. Typical Thermistor Bead (the Diameter of the Bead is Approximately 125  $\mu\text{m}$ ).

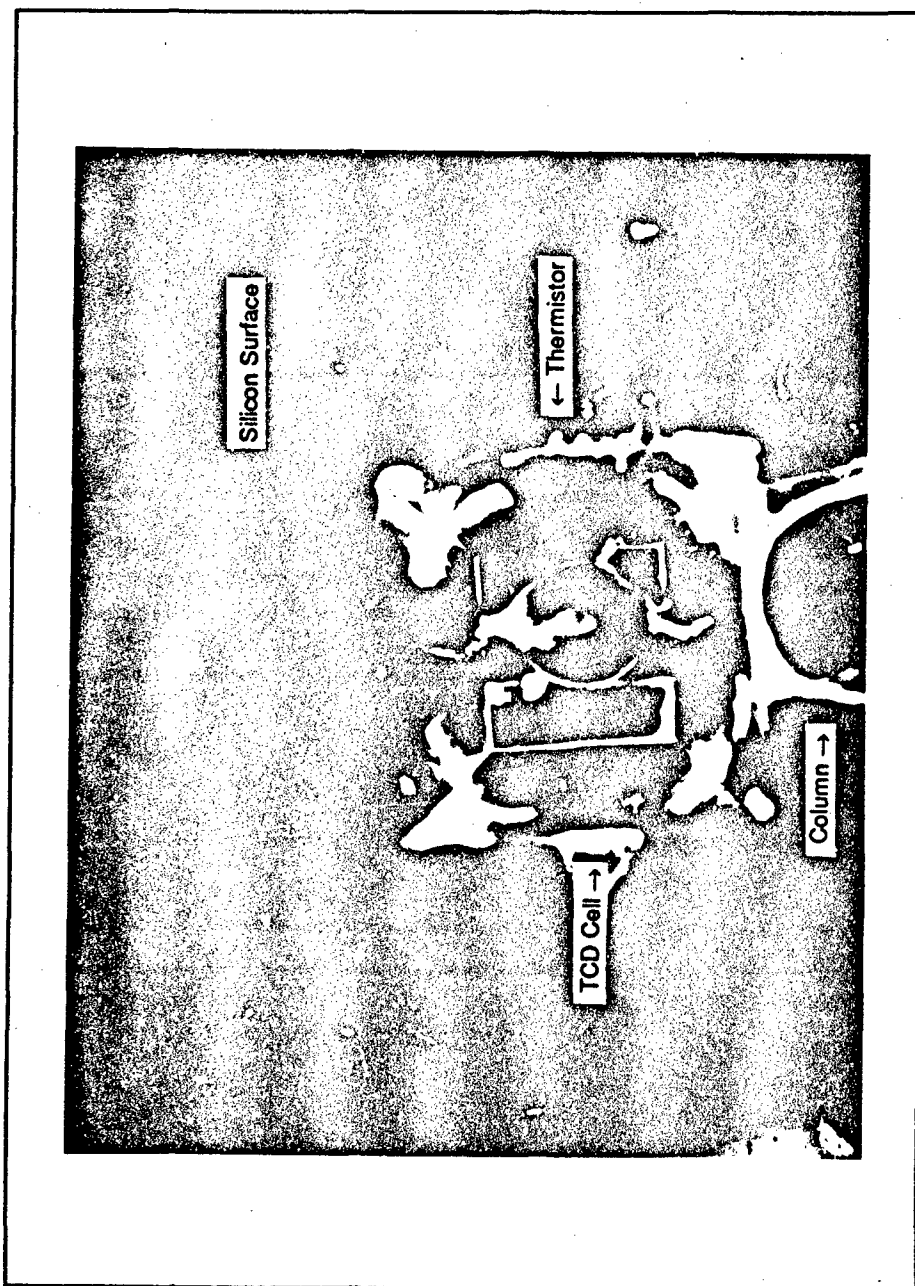


Figure 78. TCD Cell with Thermistor Installed (the Column Width is Approximately 300  $\mu\text{m}$ ).

and the bond was examined. If the anodic bond was successful (no voids between adjacent columns), the MMGC assembly was assessed to be ready for implementing the last fabrication step.

**5.4.4 Chemiresistor Attachment.** The last step in the assembly of the MMGC involved attaching the chemiresistor (see Figure 46). The chemiresistors (shown in Figures 79 and 80) were fabricated and packaged by MOSIS (as discussed in Section 4.1.3.1). However, MOSIS does not offer the service of depositing CuPc films, so the same procedure used to deposit the CuPc thin film on the MMGC column walls was used to coat the interdigitated electrode portion of the chemiresistor (see Section 5.3.1). The same film thickness was chosen for the chemiresistor as a compromise to attain reasonable reversibility and sensitivity. Figure 79 shows a chemiresistor before the coating process, and Figures 81 and 82 show a chemiresistor after the CuPc thin film deposition.

Once the chemiresistors were prepared, they were attached to the back of the MMGC directly over the lead channel of the TCD cell (see Figure 60). In order to protect the thermistor leads, a teflon spacer was machined from a 4 cm square of stock material that was 125 microns thick<sup>22</sup>. A square window approximately 0.5 cm on a side was removed from the center of the teflon sheet, and the spacer was then positioned between the chemiresistor and the MMGC (see Figure 46). The assembly was then secured with a mechanical clamp.

## 5.5 Summary.

This chapter presented the sequence of steps followed during the fabrication of the MMGC design discussed in Chapter 4, beginning with the photolithographic mask fabrication required for the wet chemical etching process. Next, the actual etching procedures were described, and they were followed by a discussion of the stationary phase deposition and patterning technique. In the final assembly section, the internal and external hardware configuration was described along with the anodic bonding process. The final result of this fabrication process is depicted in Figures 83 through 85. The performance of the MMGC

---

<sup>22</sup>Part Number D-VT-5, Small Parts Inc., Miami, FL.

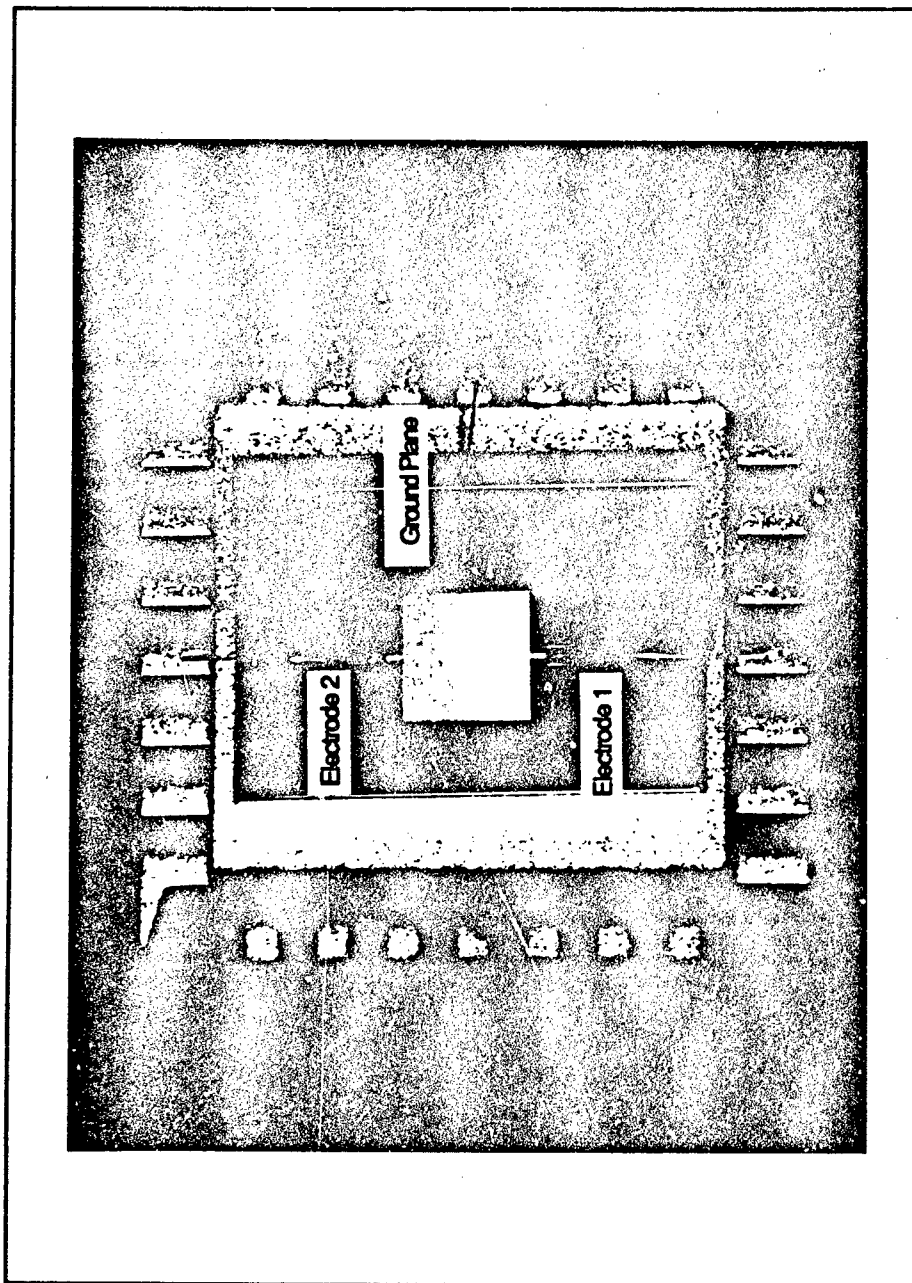


Figure 79. MOSIS Fabricated Chemiresistor (Before CuPc Coating). The Electrode Structure is Approximately 2 mm by 2 mm.

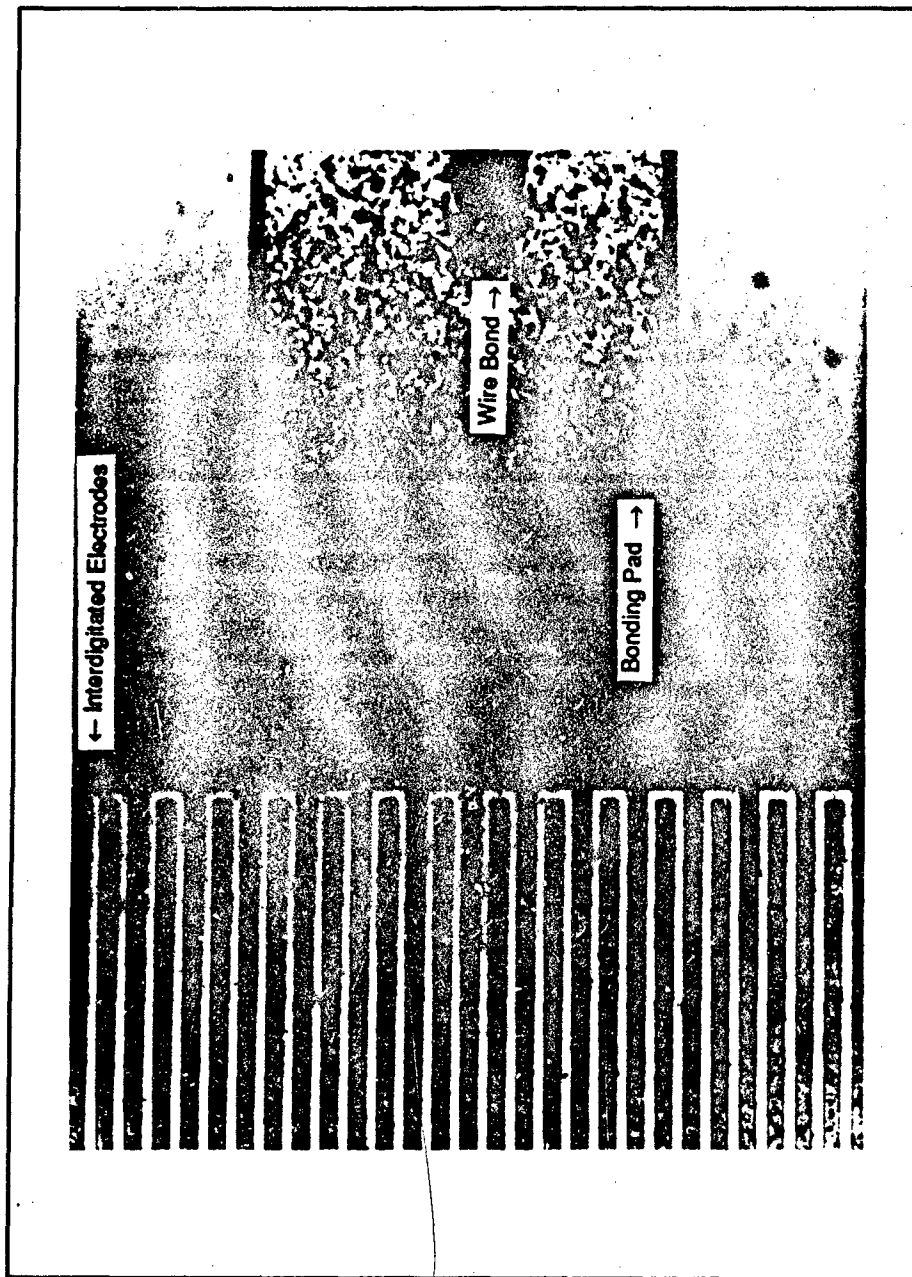


Figure 80. MOSIS Fabricated Chemiresistor (Magnified View of the Interdigitated Electrode Structure).

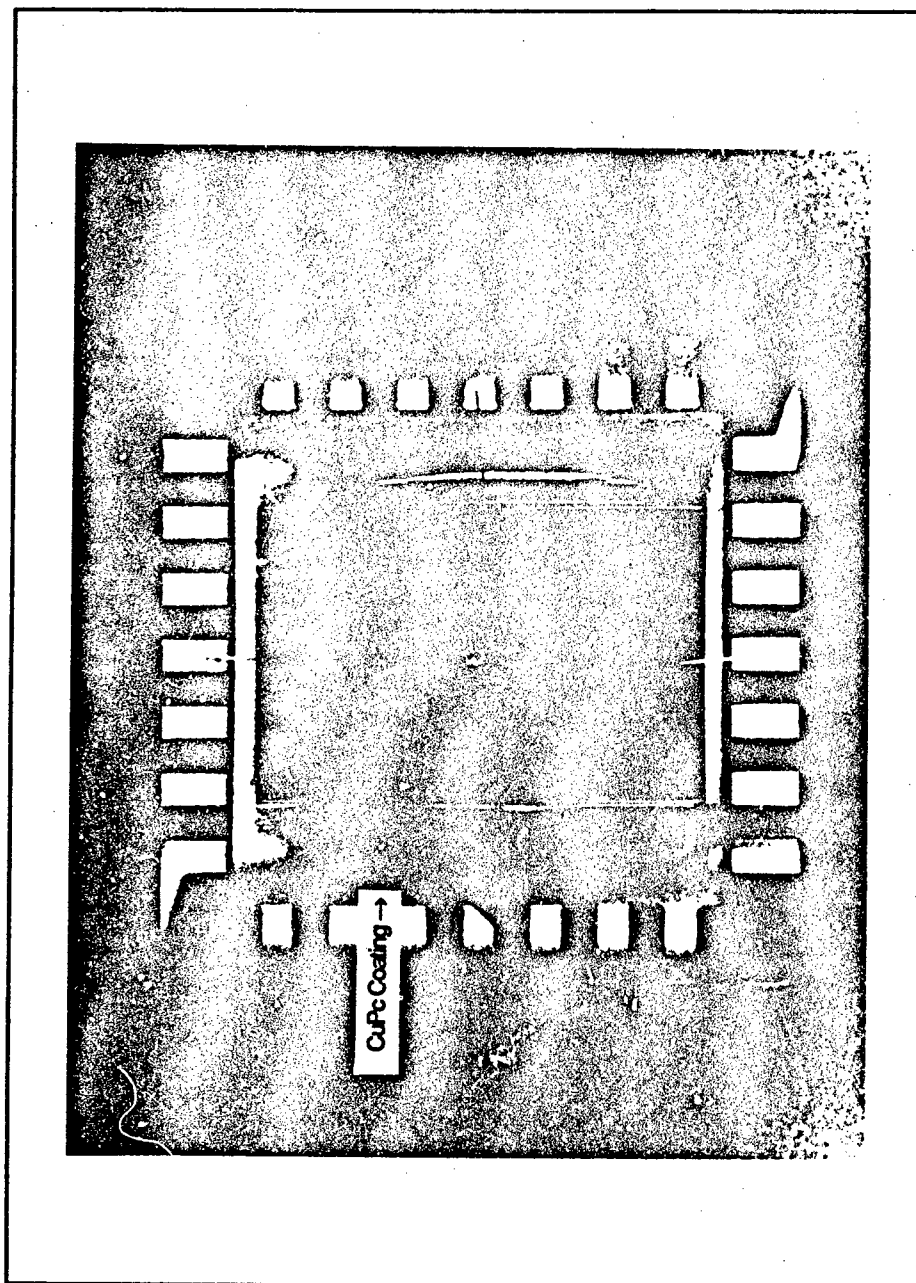


Figure 81. MOSIS Fabricated Chemiresistor (After the CuPc Thin Film Deposition). The Interdigitated Electrode Structure is Approximately 2 mm by 2 mm.

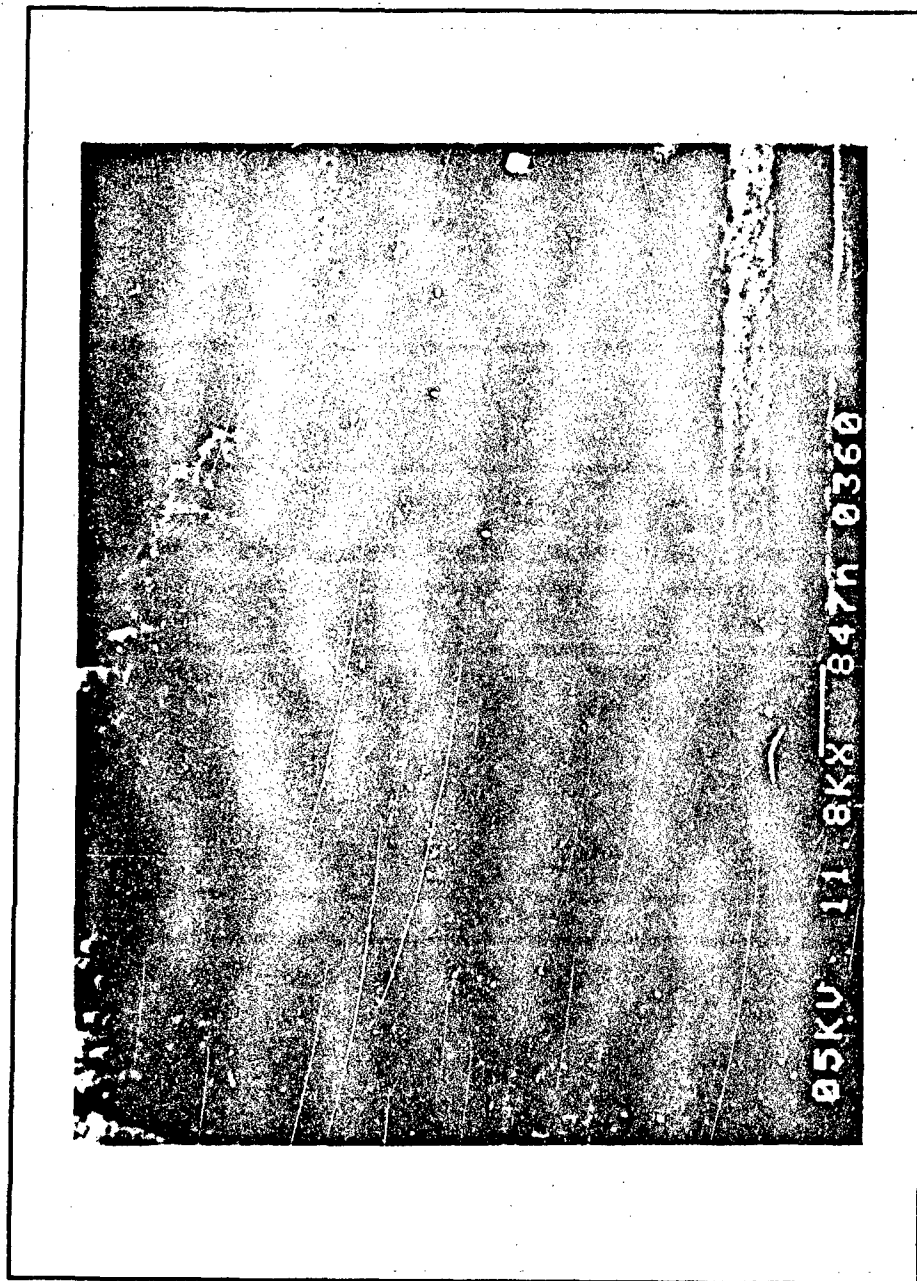


Figure 82. MOSIS Fabricated Chemiresistor (Magnified Side View of the Interdigitated Electrode Structure). The CuPc Film Thickness was Increased to 3  $\mu\text{m}$  for Illustrative Purposes.

was then evaluated using the experimental performance evaluation system discussed in Section 4.2.

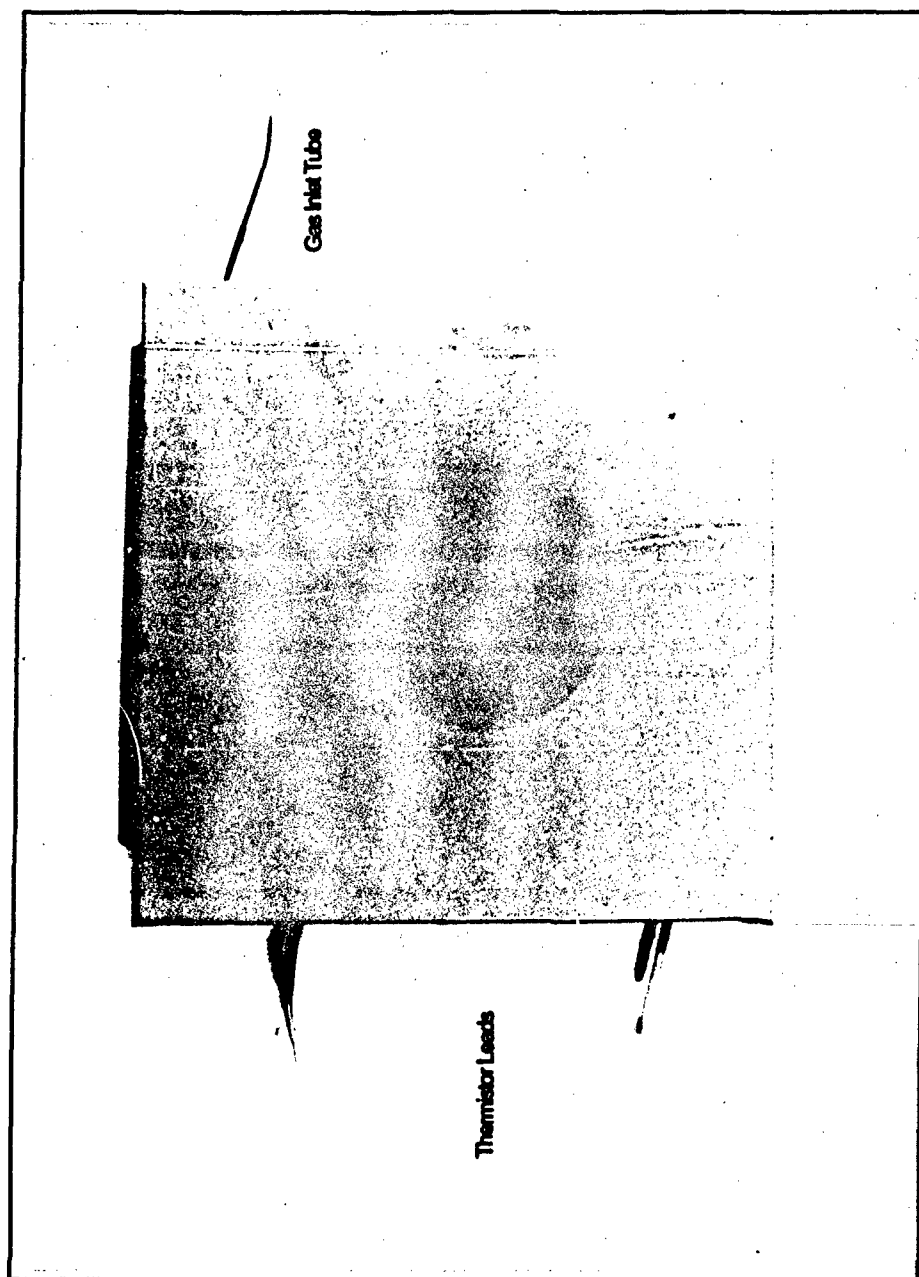


Figure 83. Front View of the 4 inch by 4 inch, Assembled Micromachined Gas Chromatograph.

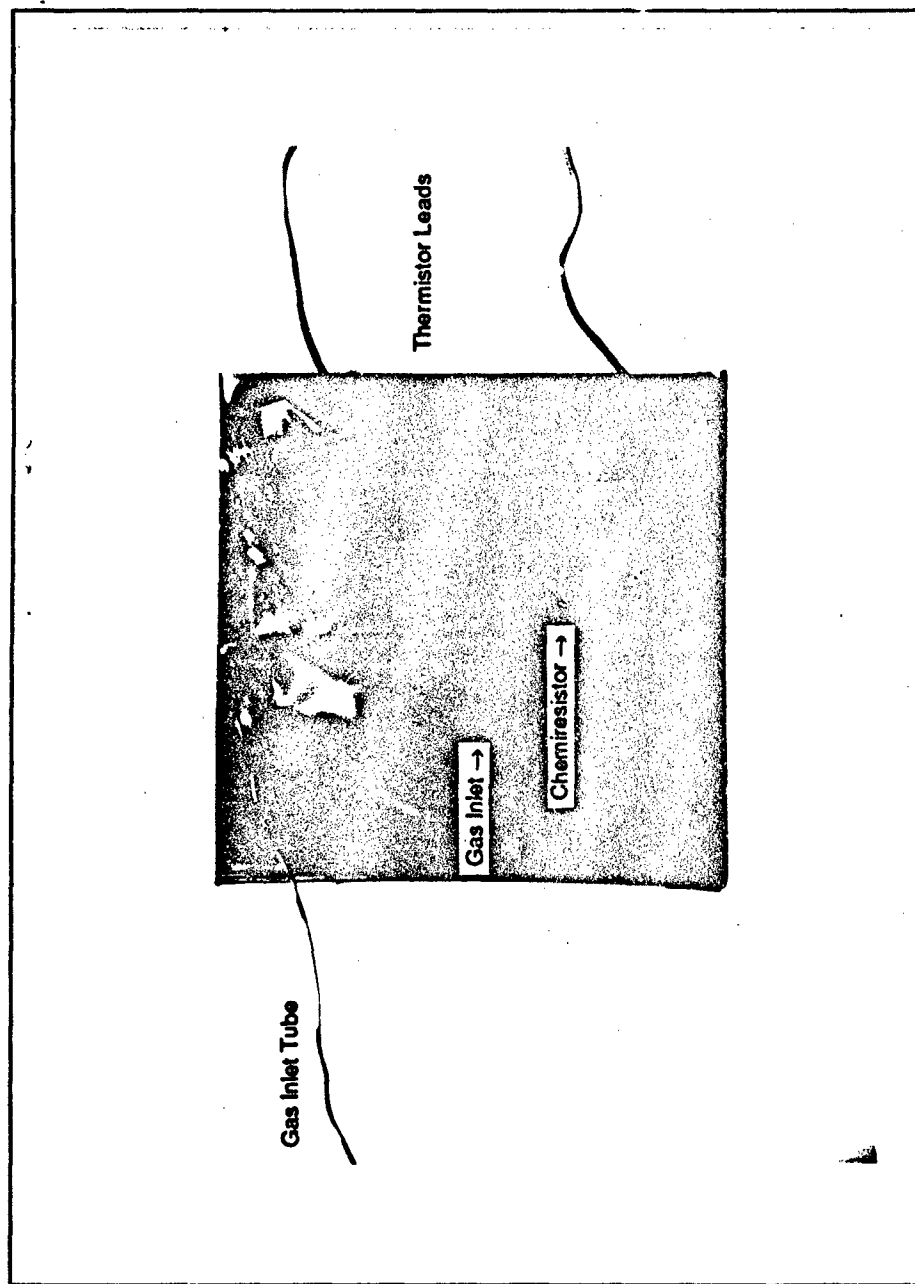


Figure 85. Back View of the 4 inch by 4 inch, Assembled Micromachined Gas Chromatograph (After the Chemiresistor's Placement).

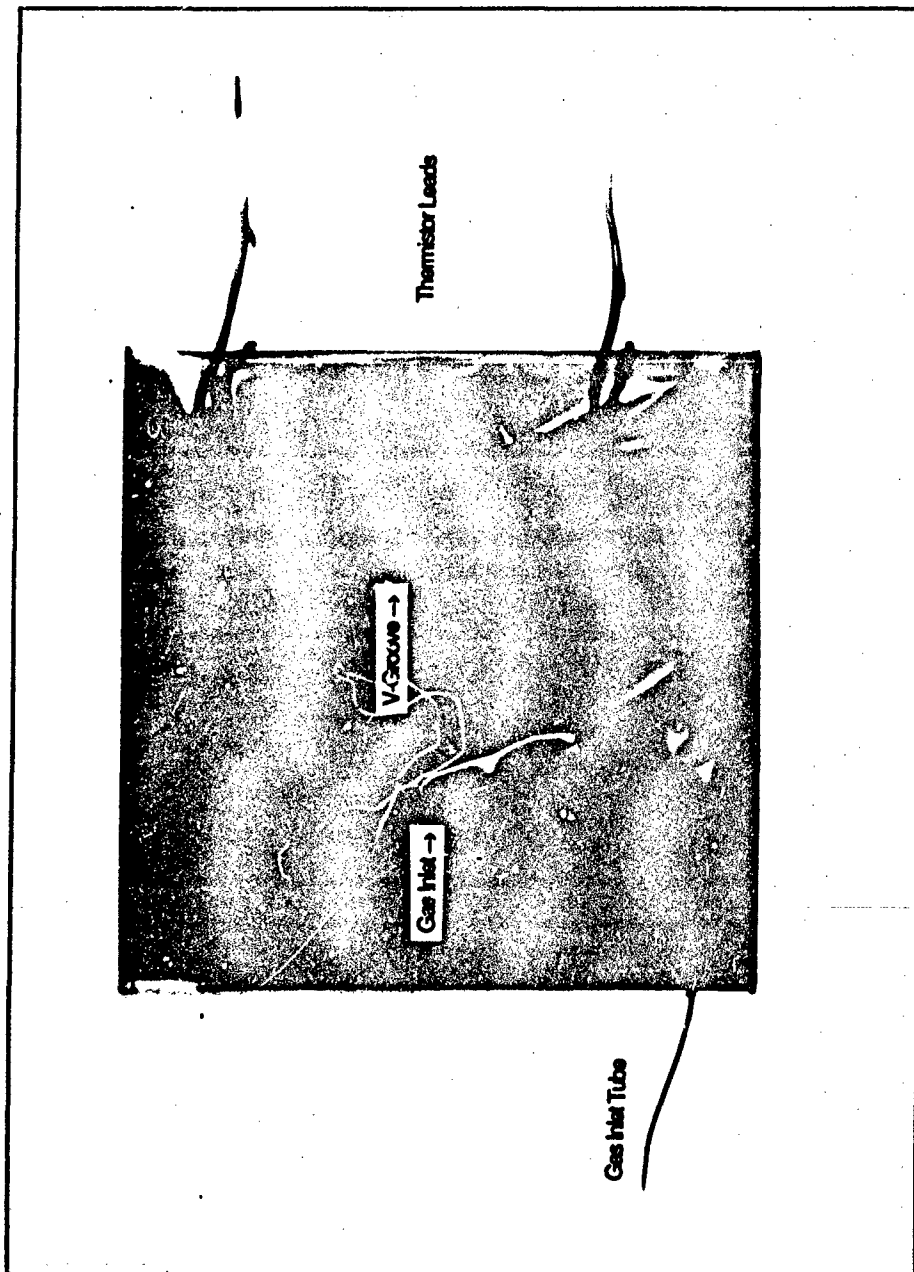


Figure 84. Back View of the 4 inch by 4 inch, Assembled Micromachined Gas Chromatograph (Before the Chemiresistor's Placement).

## *VI. Micromachined Gas Chromatograph and Subsystems Evaluation*

This chapter presents and discusses the results of the various evaluations performed on the two MMGCs that were fabricated. Evaluation of each MMGC and its associated subsystems was accomplished in four phases: thermistor evaluation, flowrate verification, chemiresistor evaluation, and the complete MMGC system evaluation. Since several of the evaluation phases required fully-functional subsystems, this limitation established the order in which the evaluations were accomplished (for example, to measure flowrates, the thermistor detector had to be fully-functional).

The thermistor evaluation was accomplished with the objective of identifying an operating current for the thermistor (in addition to insuring that its lead integrity was maintained after fabrication). Once the thermistor operating current was identified, the flowrate evaluations were performed which tested the integrity of the MMGC gas paths, the sample injection system, and contributed information regarding the thermistor's sensitivity.

Next, the chemiresistor's sensitivity was evaluated under the operating conditions (both temperature and challenge gas concentration) anticipated for the complete MMGC system. Once the primary detector had been characterized, the complete MMGC system evaluation phase was accomplished to discern if the MMGC could separate  $\text{NO}_2$  and  $\text{NH}_3$  relative to the nitrogen diluent.

### *6.1 Thermistor Performance Evaluation.*

Since the thermistor packaging was one of the most delicate operations accomplished during the fabrication phase (the lead wires were only 20 microns in diameter, and they were very fragile), it was necessary to insure that the thermistor leads were mechanically and electrically robust. To this end, the electrical conductivity between the epoxied thermistor leads was checked with a conventional laboratory ohm-meter and compared with the vendor reported nominal value of  $10 \text{ K}\Omega$  at room temperature. If the measured value was within  $\pm 10$  percent of the nominal value, the thermistor packaging process was considered to be successful, and the current-voltage (I-V) relationship of the thermistor was then characterized as a prelude for identifying an operating point. MMGC #1 had a thermistor

resistance of 10.14 K $\Omega$ , and MMGC #2 had a resistance of 10.29 K $\Omega$ , so both thermistor packaging processes were assessed to be successful.

Since the thermistor was to be operated in a predominantly helium atmosphere at temperatures between 25°C and an upper limit<sup>1</sup> of 110°C, the I-V curve was obtained using an HP4145 semiconductor parameter analyzer while 40 psi of helium flowed through each MMGC at a temperature<sup>2</sup> of 68°C. The results of this test for both MMGCs is shown in Figure 86.

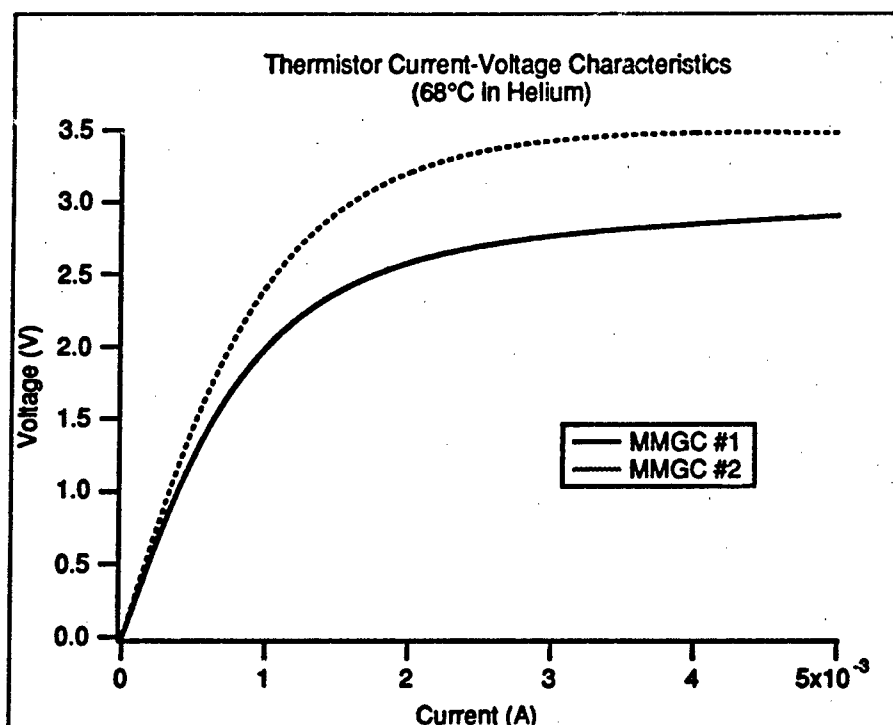


Figure 86. Voltage versus Current Plot for the Thermistors in MMGC #1 and MMGC #2.

From the information shown in Figure 86, it is apparent that the desired negative resistance region exceeds the maximum current level tested (5 mA). Due to the power handling limitations of the thermistor (a maximum of 12 mW at steady-state), continuous operation at currents greater than 3.5 mA would cause permanent damage (or destruction)

<sup>1</sup>Since the anodic bonding process was implemented at approximately 150°C, a 25 percent safety margin was chosen as a reasonable value for establishing the MMGC's maximum evaluation temperature.

<sup>2</sup>The average temperature between 25 and 110 °C.

to the thermistor. Therefore, 3 mA was identified as the operating point, since it represents the highest current level which maintains a safety margin of approximately 25 percent.

## 6.2 Flow Rate Verification.

Once the operating point was identified for the thermistor, it was possible to test each MMGC for gas leakage paths between adjacent portions of the spiral column and to insure that the sample injection system performed as expected. In order to accomplish this objective, the gas inlet port of the MMGC was connected to the sample injection valve as shown in Figure 42. The helium carrier gas was connected as shown, but the challenge gas permeation tubes ( $\text{NO}_2$  and  $\text{NH}_3$ ) were removed, which meant that the sample loop was filled with the nitrogen diluent gas only<sup>3</sup>.

In order to predict the time required for the nitrogen sample to propagate the length of the interconnect tubing and the MMGC's column, it was first necessary to calculate the pressure drop within the interconnect tubing to determine the amount of time the nitrogen sample spent within it. Since at steady state, with no leaks, the number of gas molecules per unit time (the gas "current") flowing through the interconnect tubing must be equal to that in the MMGC column, it is possible to iteratively solve for the pressure at the interconnect tubing's interface using Boyle's law (see Section 2.4) to establish the following relationship:

$$\frac{P_{int}\dot{V}_{int}}{T_{int}} = \frac{P_o\dot{V}_c}{T_c} \quad (65)$$

where  $P_{int}$  is the pressure at the interconnect tubing's interface,  $\dot{V}_{int}$  is the volume flow rate at the interface,  $T_{int}$  is the gas temperature at the interface,  $P_o$  is the pressure at the output of the column (normally atmospheric pressure),  $\dot{V}_c$  is the column's output volume flowrate, and  $T_c$  is the column's temperature. The average linear velocity of the gas at the output of either the interconnect or the column is given by Equation 26, where the permeability for the column is given by Equation 30, and the permeability for a round column (that is, for the interconnect tubing) is given by,  $q_r = \frac{8\mu}{r_o^2}$  (25). Additionally, since

<sup>3</sup>The thermal conductivity difference between nitrogen and helium was sufficient to detect with the thermistor-based TCD (see Section 2.5.1).

the average linear velocity is related to the volume flowrate by the cross-sectional area (see Section 2.4), Equation 65 becomes:

$$\frac{P_{int} v_{int} \pi r_o^2}{T_{int}} = \frac{P_o v_c 2z_o w}{T_c} \quad (66)$$

where  $v_{int}$  is the average linear gas velocity at the interconnect tubing's interface,  $r_o$  is the radius of the interconnect tube,  $v_c$  is the average linear gas velocity at the output of the column,  $2z_o$  is the thickness (height) of the column, and  $w$  is the width of the column. Since  $v_{int}$  depends upon the input pressure,  $P_i$ , and  $P_{int}$  through Equation 26, and  $v_c$  depends upon the input pressure to the column (which is  $P_{int}$ ) and  $P_o$ , the only unknown is  $P_{int}$ . Therefore, for MMGC #1 (given a column thickness of 9.5 microns, column length of 0.9 m, column width of 330 microns, interconnect radius of 0.005 in, interconnect tubing length of 40 cm, input pressure of 40 psi above atmospheric, and an output pressure of 1 atmosphere), the interconnect pressure can be iteratively solved to be approximately 39.998 psi above atmospheric. This result indicates that the majority of the pressure drop occurs within the column, which is not surprising since the area ratio of the interconnect tubing to that of the column is approximately 17:1. For MMGC #2, the column thickness was 11.3 microns, and the other variables were the same as for MMGC #1. This situation yields an interconnect pressure of approximately 39.997 psi above atmospheric.

Since the pressure drop within the interconnect tubing is very small, the time it takes for the nitrogen sample to propagate through the sample loop and the interconnect,  $t_{con}$ , is given by:

$$t_{con} = \frac{v_{loop} + L_{con} \pi r_o^2}{v_{int} \pi r_o^2} \quad (67)$$

where  $v_{loop}$  is the effective volume of the sample loop<sup>4</sup>, and  $L_{con}$  is the length of the interconnect tubing. The numerator of Equation 67 represents the volume that corresponds to the midpoint that the nitrogen's peak travels, while the denominator is the volume

<sup>4</sup>Since the sample loop is filled at atmospheric pressure, and the point of interest is the nitrogen peak, which starts at the midpoint of the sample loop, the effective volume of a 10  $\mu$ l sample loop is given by:  $v_{loop} = (1/2)(P_o/P_i)(10\mu\text{l})$ . The factor of 1/2 accounts for the midpoint, and the  $P_o/P_i$  ratio accounts for the decreased volume when the sample loop is exposed to the higher pressure carrier gas.

flowrate of the gas through the interconnect. For MMGC #1,  $t_{con}$  is calculated to be approximately 67 sec, and for MMGC #2,  $t_{con}$  is approximately 39 sec.

Once the nitrogen sample reaches the column, the time required for it to traverse the column,  $t_{col}$ , is given by Equation 18, where the partition ratio is taken to be 0 (since nitrogen is not appreciably retained by the column's CuPc stationary phase). For MMGC #1,  $t_{col}$  is approximately 9 sec, and for MMGC #2,  $t_{col}$  is approximately 7 sec. These results yield an overall nitrogen sample propagation time of approximately 76 sec for MMGC #1 and 46 sec for MMGC #2. Figure 87 shows the thermistor response for nitrogen injections into both gas chromatographs, along with the predicted peak locations.

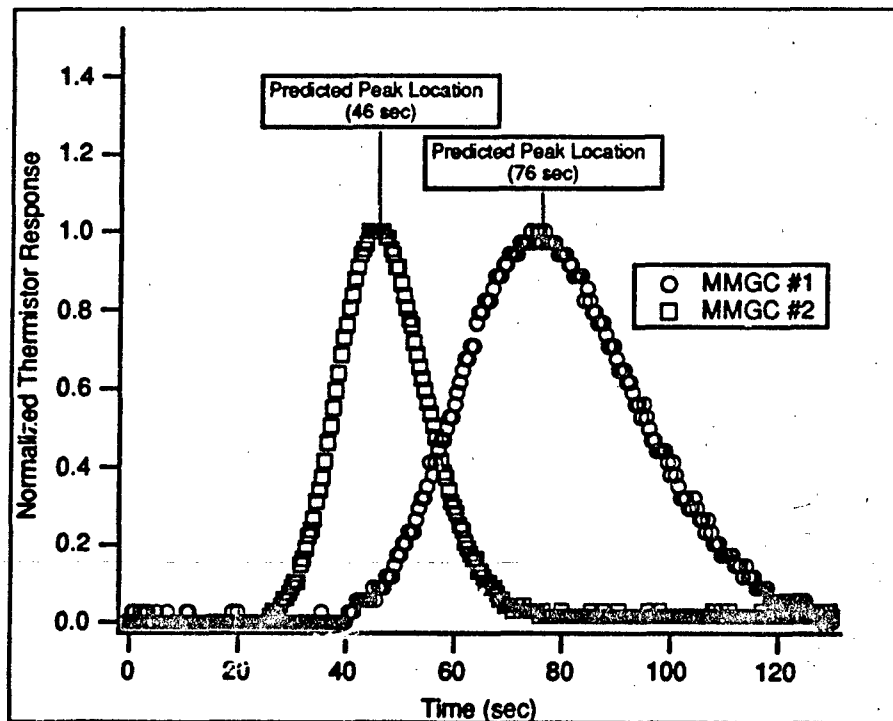


Figure 87. MMGC Flowrate Verification Results Using a Nitrogen Sample.

Because of the favorable correspondence between the predicted and actual nitrogen sample peak locations<sup>5</sup>, and the avoidance of multiple peaks (which would indicate leakage paths between adjacent columns), both MMGCs were regarded as functional with respect

<sup>5</sup>Repeated evaluations yielded data nearly identical to that shown in Figure 87. Therefore, any variations were less than the resolution of the instrumentation (approximately 0.5 seconds).

to the sample injection system, the interconnecting tubing, and the integrity of the column. The next phase of the evaluation process targeted the remaining, untested component—the chemiresistor.

### 6.3 Chemiresistor Performance Evaluation.

Since the response of the chemiresistor depended upon the challenge gas concentration and the operating temperature (see Appendix B), it was important to independently characterize both dependencies. To this end, a series of experiments were devised which fixed the challenge gas concentration while the operating temperature was varied. This situation facilitated establishing the temperature dependence of the chemiresistor's response, thereby establishing the practical operating temperature range for the subsequent MMGC evaluations. Next, a second series of experiments were performed where the temperature was now held constant, and the challenge gas concentrations were varied. This investigation was important to establish the response of the chemiresistor to the MMGC effluent so that the minimum detectable challenge gas concentrations could be determined.

**6.3.1 Temperature Dependence.** Temperatures spanning 55°C to 80°C were identified to characterize the chemiresistor. This choice was based upon the initial MMGC experiments which revealed retention times in excess of 45 min for temperatures less<sup>6</sup> than 55°C. In addition, the 80°C temperature was identified as an upper bound since reproducibility was enhanced when the system was purged at an elevated temperature (effective for desorbing strongly bound challenge gases from the CuPc column's coating). Since a maximum temperature of 110°C was established in Section 6.1, the maximum evaluation temperature was chosen to be 30°C less than the 110°C maximum<sup>7</sup>.

**6.3.1.1 Test Protocol.** There were two major response parameters in this evaluation: the chemiresistor's baseline, and its challenge gas response. Prior to injection of

---

<sup>6</sup>Since the instrumentation system was only capable of recording events with a maximum duration of 85 min, 45 min retention times were regarded as a maximum time limit (approximately half of the allowable recording time).

<sup>7</sup>Although the test protocol for both the chemiresistor and MMGC evaluations required only a 10°C purge temperature increase, the 30°C difference provided both a safety margin and the capability for accelerated purges (if desired).

the challenge gas, the chemiresistor was purged at a 10°C elevated temperature (relative to the operating temperature, 55°C to 80°C) with helium for approximately 85 min. The temperature was then reduced to the operating temperature and allowed to stabilize for a minimum of 40 min. The parameter analyzer was then activated to record the chemiresistor's signal, and approximately 15 minutes later, a sample injection was accomplished. The initial 15 minute response cycle provided baseline information, while the remainder of the trial contributed information concerning the challenge gas response<sup>8</sup>. This protocol was implemented for five distinct temperatures per challenge gas. The chemiresistor response was processed, and the error was estimated according to the procedures discussed in Appendix E. The results<sup>9</sup> are summarized in Figures 88 and 89.

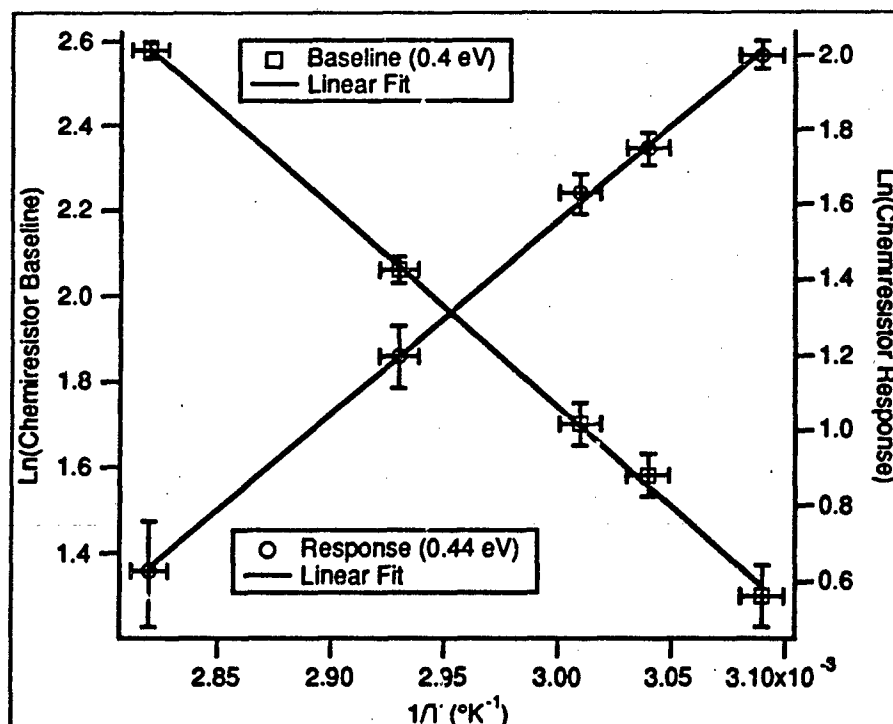


Figure 88. Temperature Dependence of the Chemiresistor's Baseline and Response to a 75 ppm Concentration of Nitrogen Dioxide.

<sup>8</sup>The challenge gas concentration was identified to generate a response at least 3 times greater than the noise level of the chemiresistor (approximately 0.5 pA peak-to-peak). For  $\text{NO}_2$ , this concentration was approximately 75 ppm, and for  $\text{NH}_3$ , it was approximately 6300 ppm.

<sup>9</sup>The actual data collected is presented in Appendix I.

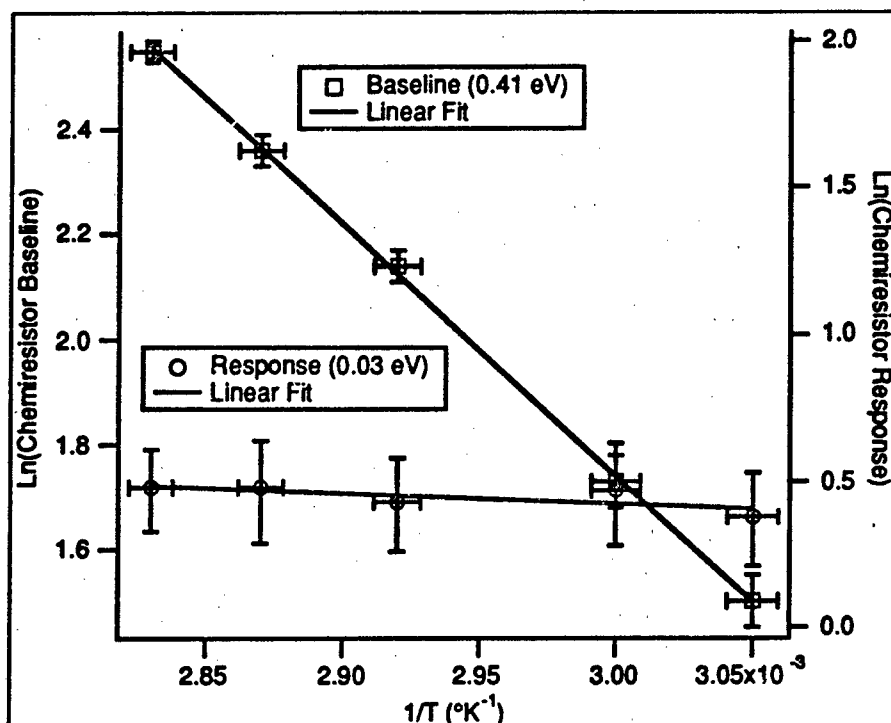


Figure 89. Temperature Dependence of the Chemiresistor's Baseline and Response to a 6300 ppm Concentration of Ammonia.

From the chemiresistor's challenge gas data, it is apparent there is a strong temperature dependence for the baseline level and the  $\text{NO}_2$  response. The  $\text{NH}_3$  response appears to be independent of temperature; unfortunately, the error associated with these measurements (see Appendix E) indicates that the ammonia response temperature dependence is inconclusive. The reason for the increased error attributed to the  $\text{NH}_3$  results compared to those for  $\text{NO}_2$ , emerge from the fact that  $\text{NH}_3$  is an electron-donor, whereas  $\text{NO}_2$  is an electron-acceptor (45). Since CuPc is a p-type semiconductor,  $\text{NO}_2$  adsorption leads to an increase in electrical conductivity, while  $\text{NH}_3$  adsorption leads to a reduction in electrical conductivity (see Appendix B).

As a hypothetical example, if the chemiresistor were operated with a baseline current of 10 pA, and a noise level of 0.5 pA. A signal 15 times greater than the noise level would require an increase in the baseline conductivity by a factor of 1.75 for  $\text{NO}_2$ , and a decrease in the baseline conductivity by a factor of 4 for  $\text{NH}_3$ . A signal 19 times greater than the

noise level would require a 1.95 factor increase in conductivity for  $\text{NO}_2$ , and a decrease by a factor of 20 for  $\text{NH}_3$ . The ultimate limit for  $\text{NH}_3$  in this situation would be a signal 20 times greater than the noise level (which would reduce the current to essentially 0 A). Therefore, because the baseline currents are small (generally between 3 pA and 15 pA), the  $\text{NH}_3$  resolution is much lower than the  $\text{NO}_2$  resolution, and the relative noise level is greater for  $\text{NH}_3$  than for  $\text{NO}_2$ .

Although this evaluation did not reveal a temperature dependence for  $\text{NH}_3$ , it did confirm that the baseline response does increase with increasing temperature (corresponding to the greater contribution of thermally generated carriers). The literature reports that there is a trap level located at 0.37 eV above the valence band edge (122). From Figures 88 and 89, the experimental activation energies were on the order of 0.4 eV, which correlates well with this trap level (see Appendix B).

**6.3.2 Challenge Gas Concentration Response Characteristics.** In this evaluation, the  $\text{NO}_2$  and  $\text{NH}_3$  concentrations were varied for three different temperatures: 70, 80, and 90°C. The 80°C temperature limit was identified consistent with the desire to operate the MMGC at the highest possible temperature where the challenge gas detection process was still reliable (the higher the operating temperature, the faster a chromatogram could be obtained). From the previous test, the 80°C temperature limit still had a reasonably strong signal (approximately 4 times the 0.5 pA noise level for  $\text{NO}_2$ , and 3 times the noise level for  $\text{NH}_3$ —see Appendix E). The other two temperatures were selected to bracket the 80°C temperature.

**6.3.2.1 Test Protocol.** The test protocol was very similar to that used in the prior temperature evaluation process (Section 6.3.1). However, instead of adjusting the temperature between runs, the challenge gas concentration was varied by adjusting the nitrogen diluent flowrate and allowing the flow to stabilize during the heated purge stage. Prior to injecting the challenge gas, the chemiresistor was purged at a 10°C elevated temperature (relative to the operating temperature range of 70°C to 90°C) with helium for approximately 85 min. The temperature was then reduced to the desired operating value and allowed to stabilize for a minimum of 40 min. The parameter analyzer was then activated

to record the chemiresistor's response, and approximately 15 minutes later, a challenge gas injection was performed. For  $\text{NO}_2$ , the concentration was varied from 75 ppm (established in the previous test—Section 6.3.1) to 570 ppm (corresponding to the minimum reproducible flowrate of approximately 4.2 ml/min). Similarly, the  $\text{NH}_3$  concentration was varied between 500 ppm and 5000 ppm. This reduced  $\text{NH}_3$  concentration range was utilized since the 6300 ppm concentration used in the temperature dependence evaluation experiment was on the order of the column's saturation concentration (estimated to be approximately 5000 ppm). Therefore, the concentration regime below this 5000 ppm limit was explored to determine if detectable concentrations below saturation were possible. The 500 ppm  $\text{NH}_3$  concentration lower limit corresponded to the highest flowrate with a nitrogen diluent gas pressure of 10 psi (higher pressures resulted in substantial flowrate variations with respect to time).

This protocol was implemented at each operating temperature value for five concentrations of each challenge gas type ( $\text{NH}_3$  and  $\text{NO}_2$ ). The chemiresistor signal was then processed according to the procedure described in Appendix E (where the response is defined as the magnitude of the amplitude of the fitting functional<sup>10</sup>). The results<sup>11</sup> are summarized in Figures 90 and 91.

For  $\text{NO}_2$ , there is an approximate linear relationship between the injected concentration and the chemiresistor's response for all three temperatures. As expected, when the temperature is increased, the response decreases. Because of this decreased response at higher temperatures, the signal tends to overlap at the higher concentrations for the 90°C test. For this reason, the MMGC evaluations were conducted below 90°C.

The  $\text{NH}_3$  test confirmed the relative concentration independence of the chemiresistor to concentrations greater than 3000 ppm. This independence is attributed to the way that  $\text{NH}_3$  affects the chemiresistor's electrical conductivity (see Appendix B). Since the electrical conductivity decreases,  $\text{NH}_3$  concentrations greater than a specific critical level will not respond differently. This critical level appears to be approximately 3000 ppm (for

---

<sup>10</sup> $\text{NH}_3$  causes a decrease in the chemiresistor's current, while  $\text{NO}_2$  causes an increase in the same current. Defining the response as the magnitude of this change permits the direct comparison between  $\text{NH}_3$  and  $\text{NO}_2$  results.

<sup>11</sup>The actual data collected is presented in Appendix I.

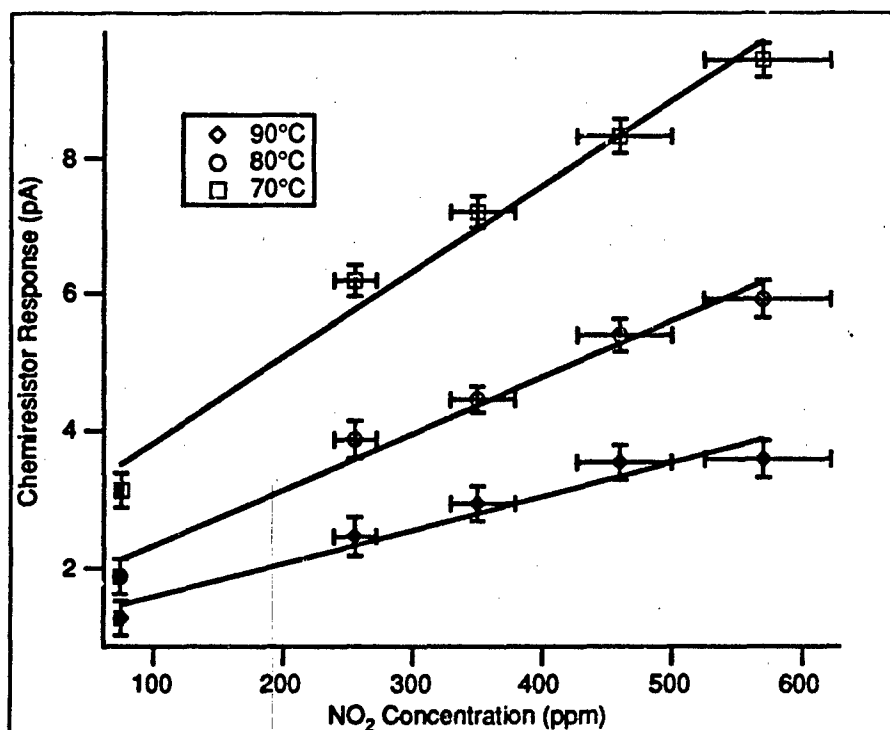


Figure 90. Concentration Dependence of the Chemiresistor's Response to Nitrogen Dioxide.

temperatures spanning 70°C to 90°C). Below this level, there is a concentration dependence, but the signal level is so small (on the order of the noise level—approximately 0.5 pA peak-to-peak), that operation in this concentration regime would produce spurious and inconclusive results. For this reason, the MMGC evaluation concerning retention time (see the following section) was performed using large concentrations (approximately 6300 ppm) of NH<sub>3</sub>.

Although the results concerning the detection of small NH<sub>3</sub> challenge gas concentrations were disappointing, the chemiresistor was still regarded as being sufficiently sensitive to perform "binary" (yes or no) detection at the greater-than 3000 ppm NH<sub>3</sub> challenge gas level. With regard to NO<sub>2</sub>, the chemiresistor was definitely sensitive to concentrations in the 75 ppm to 570 ppm range, exhibiting a nearly linear response to these concentrations at temperatures less than 80°C. Overall, the chemiresistor evaluation was considered suc-

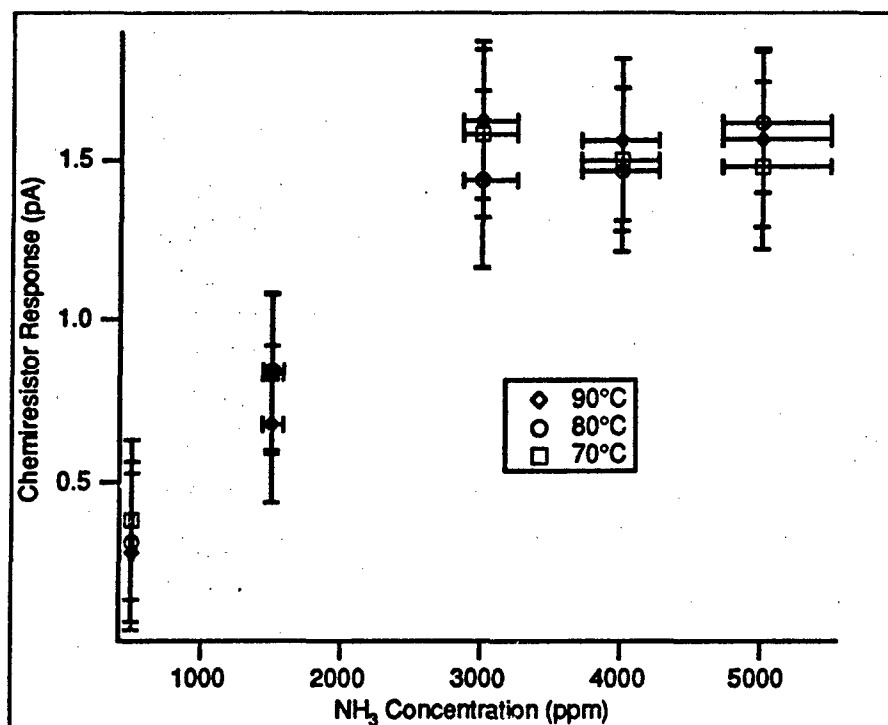


Figure 91. Concentration Dependence of the Chemiresistor's Response to Ammonia.

cessful, and the performance information gained was used as the basis for establishing the temperature and concentration operational parameters used in the MMGC evaluation.

#### 6.4 Micromachined Gas Chromatograph Performance Evaluation.

In its capacity as a quantitative tool for gas analysis, the gas chromatograph depends on two fundamental parameters: the retention time of a given gas (to separate it from competing gases) and the corresponding amplitude of the response peak (to determine gas concentration). In order to qualify the MMGCs fabricated during this investigation, two independent evaluations were performed on each MMGC. The first evaluation addressed the retention time issue, while the second evaluation addressed the gas concentration sensitivity characteristic.

**6.4.1 Retention Time.** From Section 2.3.2, the relationship between the heat of adsorption for a solid stationary phase and the retention time was presented as Equation 64.

This relationship is linear if the logarithm of the retention time is compared with reciprocal temperature. In order to identify the heat of adsorption for CuPc for the two challenge gases, a binary mixture of these gases was injected at several temperatures. The choice of the challenge gas concentrations was determined by the previous chemiresistor evaluations: approximately 6000 ppm  $\text{NH}_3$  and 75 ppm  $\text{NO}_2$ .

**6.4.1.1 Test Protocol.** Prior to injection of the challenge gas, the chemiresistor was purged at a  $10^\circ\text{C}$  elevated temperature (relative to the operating temperature) with helium for approximately 85 min. The temperature was then reduced to the test value and allowed to stabilize for 85 min. The parameter analyzer was then activated to record the chemiresistor's response, and simultaneously, the sample injection valve was triggered. The chemiresistor's response for the next 50 minutes was recorded. This protocol (depicted graphically in Figure 92) was implemented six times for each of the five operational temperatures evaluated for the two MMGCs. The results<sup>12</sup> are summarized<sup>13</sup> in Figures 93 and 94.

From the  $\text{NO}_2$  data, it is apparent that there is a strong linear correlation between the logarithm of the retention time and reciprocal temperature. The slope of the least-squares line drawn through the data for both MMGCs corresponds to an average heat of adsorption that is approximately 0.38 eV, and this value is comparable with the adsorption heats associated with weak chemisorption or strong physisorption processes (125). Since the adsorption heat is known, it is now possible to calculate the partition ratio for  $\text{NO}_2$  and CuPc in the MMGC.

**6.4.1.2  $\text{NO}_2$  Partition Ratio.** Using Equation 18, the  $\text{NO}_2$  partition ratio for each of the MMGCs relative to the evaluation temperature range can be calculated. Furthermore, a general expression for the partition ratio can be developed since the partition ratio for solid adsorbents exhibit the following relationship with respect to temperature (114):

---

<sup>12</sup>The actual data collected is presented in Appendix J.

<sup>13</sup>The parameter plotted is the log of the retention time as determined by the data reduction algorithm described in Appendix E.

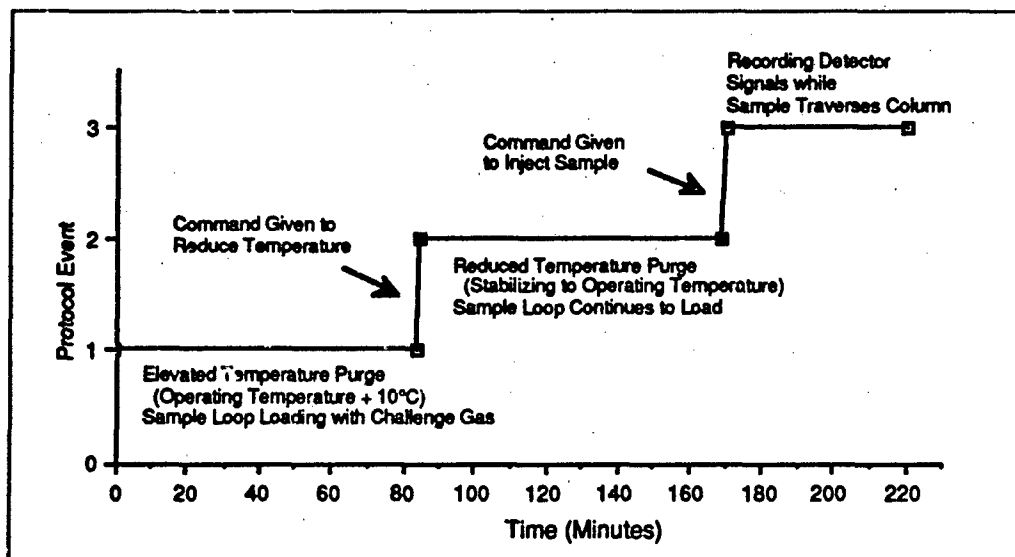


Figure 92. Micromachined Gas Chromatograph Evaluation Protocol. The Time Required for One Complete Evaluation Cycle is 220 minutes.

$$k = k_0 \exp(-E_a/k_b T) \quad (68)$$

where  $k_0$  is a constant,  $E_a$  is the adsorption energy,  $k_b$  is Boltzmann's constant, and  $T$  is the absolute temperature. The logarithm of the calculated partition ratios was also plotted versus reciprocal temperature as shown in Figure 95 (114).

The slope of the line in Figure 95 corresponds to a partition ratio of the form given by Equation 68, where  $k_0$  is approximately  $4 \times 10^{-4}$  and  $E_a$  is approximately 0.38 eV (the same value of  $E_a$  was calculated for the  $\text{NO}_2$  retention time data).

Unfortunately, a partition ratio for  $\text{NH}_3$  could not be calculated since the  $\text{NH}_3$  data manifests an independence of retention time with respect to temperature. This behavior is due to the fact that the injected  $\text{NH}_3$  concentrations, in order to be detectable, exceeded the column's capacity. Since there were more ammonia molecules compared to available adsorption sites, most of the ammonia flowed through the column and was not retained. The  $\text{NH}_3$  that was retained was of too small a concentration to be precisely measured by

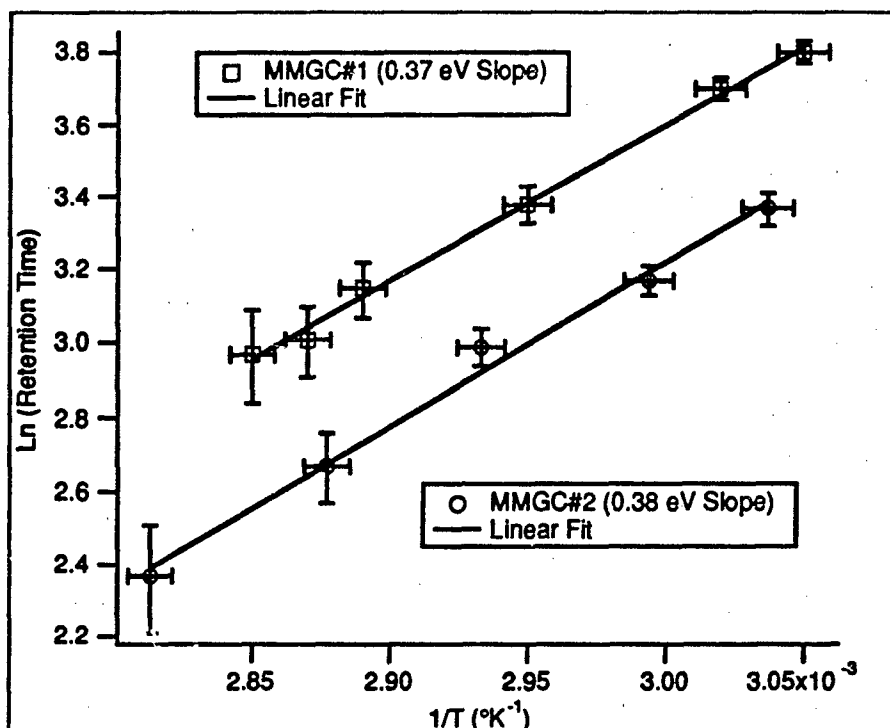


Figure 93. Temperature Dependence of the Nitrogen Dioxide Retention Times.

the detector. Further confirmation of this observation will be discussed in the next section where the  $\text{NH}_3$  challenge gas concentration was systematically varied.

Of the temperatures tested, the highest ( $80^\circ\text{C}$ ) was considered to be most favorable in terms of establishing the minimum retention time (approximately 20 min). Higher temperatures would be expected to further reduce the retention time, but would also compromise the sensitivity of the chemiresistor detector. On the other hand, lower temperatures would improve the detector's sensitivity, but this feature would be gained at the expense of increasing the retention time. Therefore, the  $80^\circ\text{C}$  temperature was used to conduct the next set of tests.

**6.4.2 Challenge Gas Concentration Response Characteristics.** In order to verify quantitative operation of the MMGC, it was necessary to evaluate its response to different concentrations of the challenge gases. The same concentration ranges were used as discussed in the chemiresistor detector's challenge gas concentration evaluation; however,

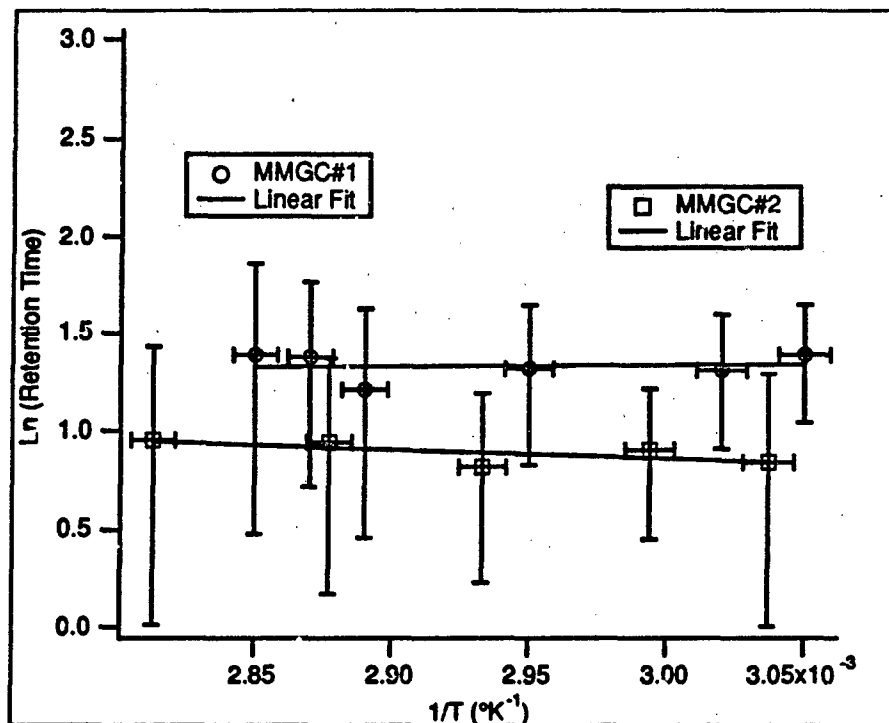


Figure 94. Temperature Dependence of the Ammonia Retention Times.

binary gas mixtures were used to demonstrate the capability of the MMGC to separate the components prior to detection. The  $\text{NO}_2$  tests were performed with approximately 6300 ppm  $\text{NH}_3$ , and the  $\text{NH}_3$  tests were performed with approximately 500 ppm  $\text{NO}_2$ .

**6.4.2.1 Test Protocol.** Prior to injecting the challenge gas mixture the chemisorbent was purged at a  $10^\circ\text{C}$  elevated temperature (relative to the operational temperature) with helium for approximately 85 min to ensure a completely purged state and baseline response. The temperature was then reduced to the test value and allowed to stabilize for 85 min. The parameter analyzer was then activated to record the chemisorbent's response, and simultaneously, the sample injection valve was activated. The next 50 min of data was recorded. This protocol was implemented six times for each of the five challenge gas mixture concentrations for the two MMGCs. The challenge gas mixture concentrations were adjusted prior to each trial in the set of six identical measurements (approximately

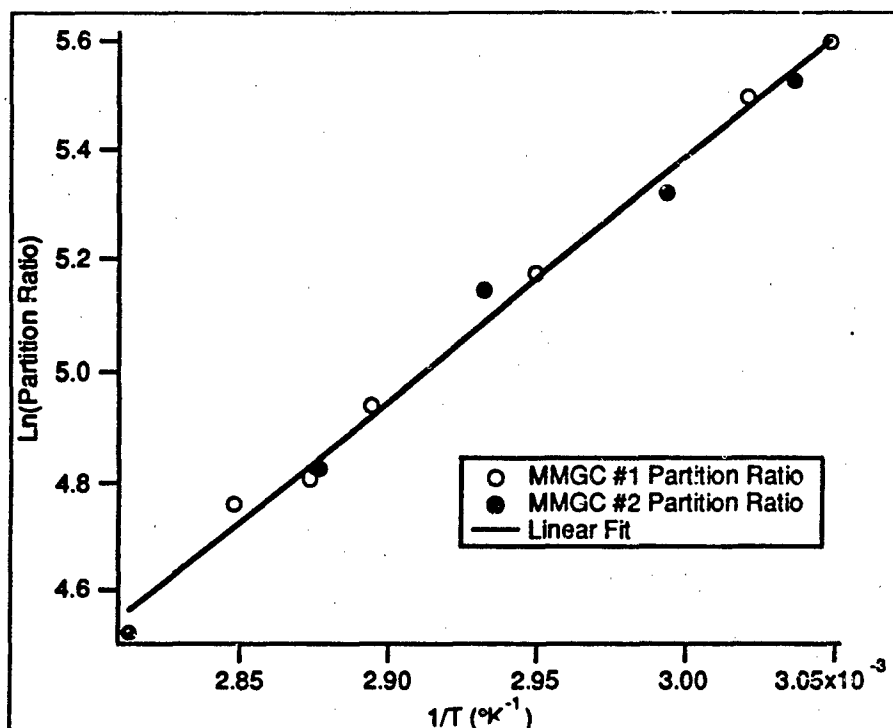


Figure 95. Experimentally Determined Partition Ratios for NO<sub>2</sub> Relative to Copper Phthalocyanine Correlated with Reciprocal Temperature.

every 24 hrs). The chemresistor's response was processed according to the procedures described in Appendix E, and the results<sup>14</sup> are summarized in Figures 96 and 97.

Comparing Figures 96 and 97 with Figures 90 and 91, it is apparent that the ammonia concentration response is very similar to that of the isolated chemiresistor's evaluation. This behavior is due to the saturation of the column with NH<sub>3</sub>, such that it behaves similar to a simple section of interconnect tubing. Unfortunately, at the concentrations where saturation is not a problem (less than 500 ppm), the detector's sensitivity towards ammonia is almost negligible.

The NO<sub>2</sub> data is much more promising. Although the magnitude of the response is somewhat attenuated when compared with the isolated chemiresistor tests, the data shows a linear trend with respect to gas concentration, thus confirming the capability of the MMGC to function as an analytical tool (with respect to NO<sub>2</sub>). Additionally, since

<sup>14</sup>The actual data collected is presented in Appendix J.

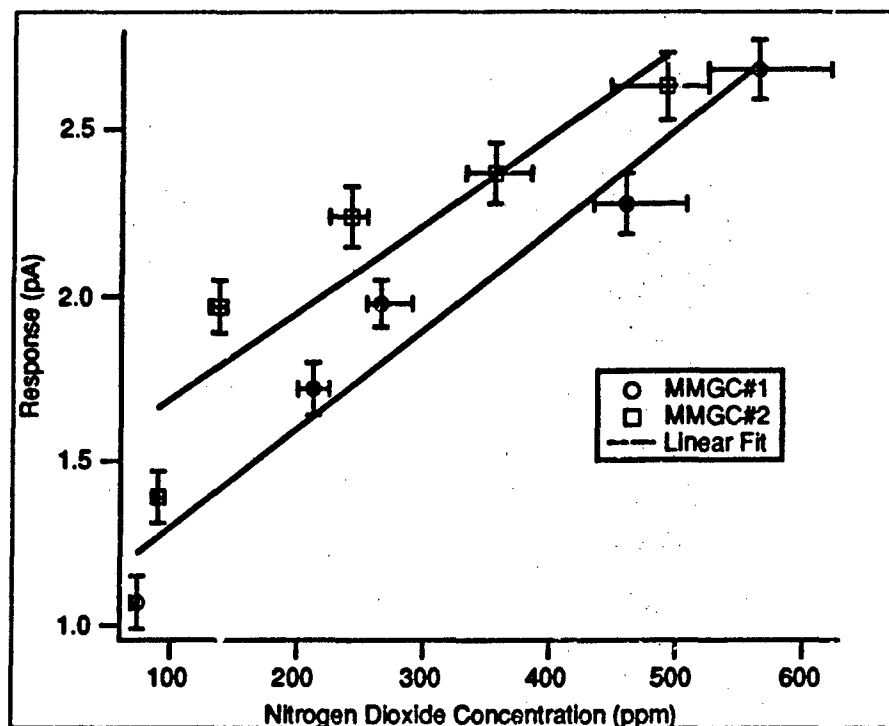


Figure 96. Concentration Dependence of the Nitrogen Dioxide Response for the Micro-machined Gas Chromatograph.

the same linear trend was evident in the isolated chemiresistor tests, this evaluation also demonstrated the capability of the MMGC to separate two potentially interfering gases prior to detection.

A synopsis of the collected data is shown in Figures 98 through 104. The actual data was collected and processed as described in Appendix E. The resulting parameters were then converted to equivalent gaussian peaks and scaled to facilitate interpretation.

In the initial series of tests, the  $\text{NH}_3$  and  $\text{NO}_2$  challenge gas concentrations were held constant while the temperature was increased from  $55^\circ\text{C}$  to  $80^\circ\text{C}$  (Figures 98 to 100). Next, the temperature and  $\text{NH}_3$  concentration were held constant while the  $\text{NO}_2$  concentration was varied from 75 ppm to 560 ppm (Figures 100 to 102). Finally, the temperature and  $\text{NO}_2$  concentration were held constant while the  $\text{NH}_3$  concentration was systematically varied from 6900 ppm to 480 ppm (Figures 102 to 104).

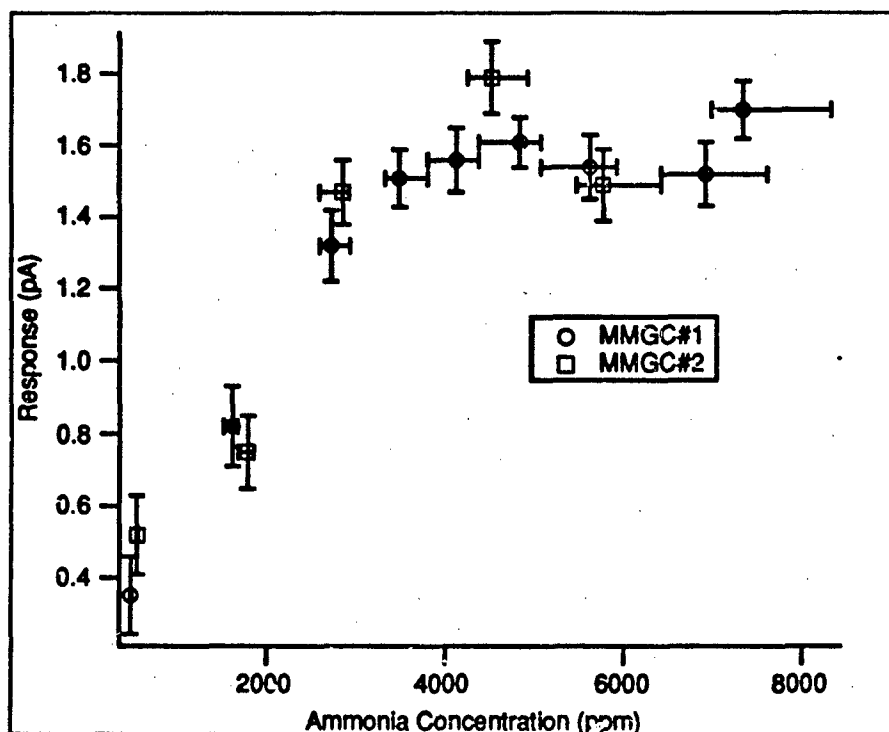


Figure 97. Concentration Dependence of the Ammonia Response for the Micromachined Gas Chromatograph.

### 6.5 Summary

In this chapter, the results of the MMGC evaluation were presented and discussed. The initial thermistor evaluation verified the operation and viability of the thermistor and provided valuable information concerning the identification of an operating point for the TCD. Once the TCD operating point was established, the flowrate evaluations yielded two critical pieces of information. First, the correlation between the experimental results and the theoretical calculations verified that there were no gas leakage paths in the anodic bond between adjacent portions of the MMGC columns. Second, operation of the commercial sample valve was confirmed via the injection of pure nitrogen into the helium carrier gas. After establishing the injection valve's operation, the chemiresistor was evaluated under a variety of thermal and challenge gas concentration conditions. These evaluations confirmed the expected thermal generation of carriers in a semiconductor by the increase in the baseline response with respect to increasing temperature. Furthermore, a range of

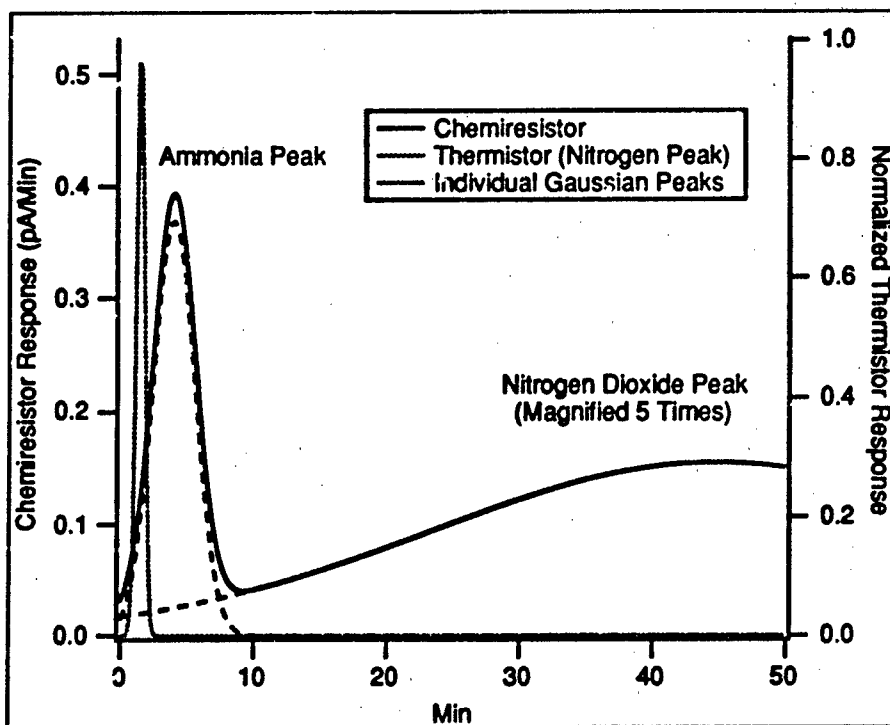


Figure 98. Gaussian Representation of Gas Elution (55°C, 6300 ppm  $\text{NH}_3$ , and 75 ppm  $\text{NO}_2$ ). Vertical Axis is the Magnitude of the Differentiated Chemiresistor Response.

detectable concentrations for  $\text{NH}_3$  and  $\text{NO}_2$  was established for use in the final series of evaluations.

The final set of evaluations was performed on the complete MMGC system to demonstrate its capability for separating and detecting various concentrations of  $\text{NO}_2$  and  $\text{NH}_3$  under a variety of thermal conditions. This capability was confirmed, and the information manifested by the relationship between the  $\text{NO}_2$  retention time and temperature was regarded as particularly valuable with respect to establishing the heat of adsorption of  $\text{NO}_2$  on CuPc. Unfortunately, due to the chemiresistor detector's limitations, the minimum  $\text{NH}_3$  concentration that could reliably be detected exceeded the column's saturation limit. Therefore, the heat of adsorption could only be calculated for  $\text{NO}_2$ .

As will be seen in the next chapter, the  $\text{NO}_2$  heat of adsorption can be used (along with some additional information) to characterize the overall interaction between  $\text{NO}_2$

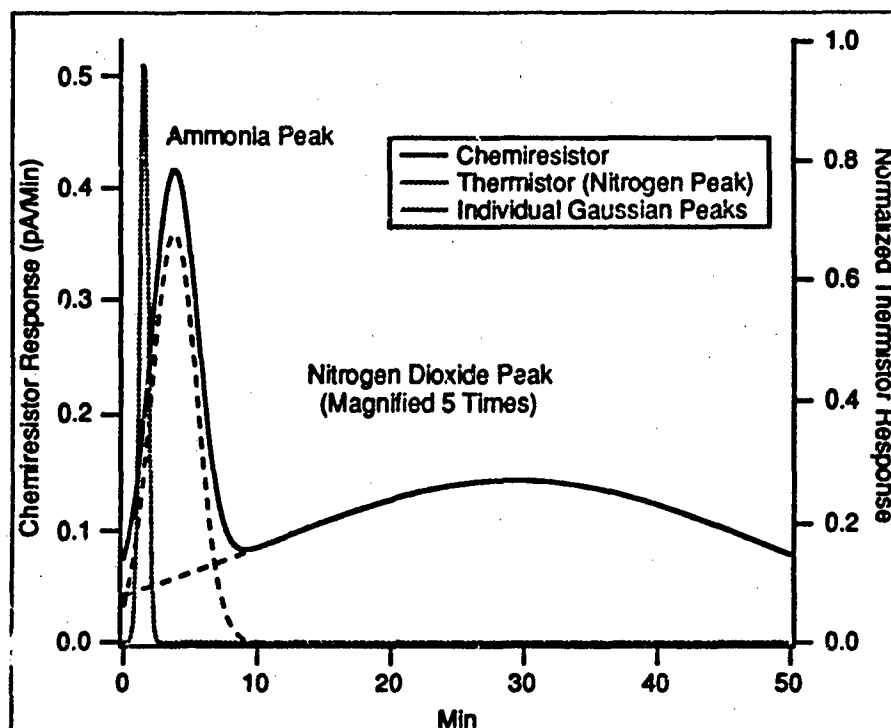


Figure 99. Gaussian Representation of Gas Elution (66°C, 6300 ppm NH<sub>3</sub>, and 75 ppm NO<sub>2</sub>). Vertical Axis is the Magnitude of the Differentiated Chemiresistor Response.

molecules and the CuPc coated MMGC column walls. This interaction will then be used in a model of the MMGC's operation to further confirm the experimental data and correlate it with the theory discussed in Chapter 2.

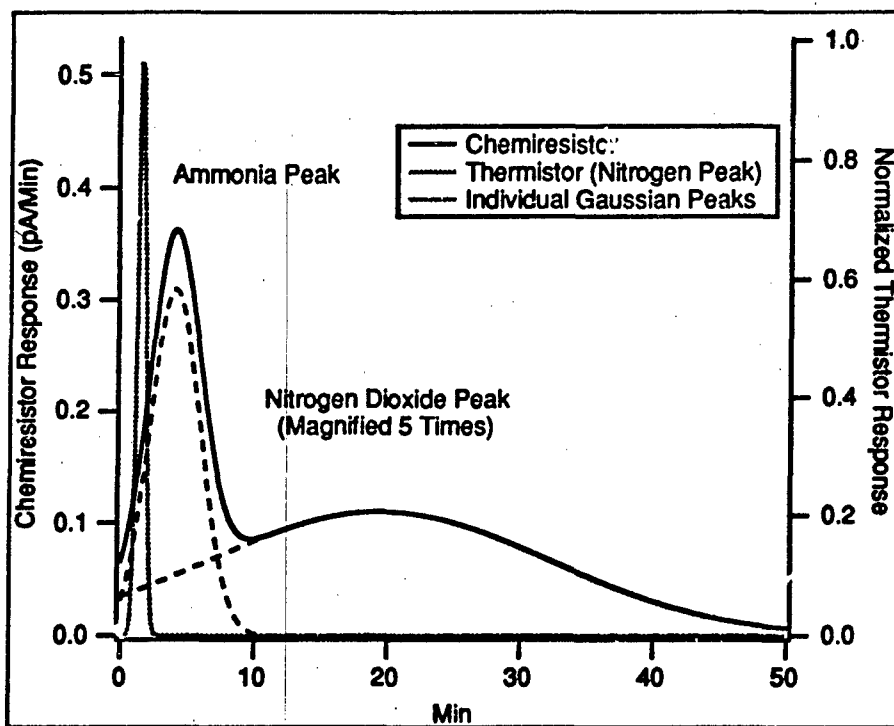


Figure 100. Gaussian Representation of Gas Elution (80°C, 6300 ppm NH<sub>3</sub>, and 75 ppm NO<sub>2</sub>). Vertical Axis is the Magnitude of the Differentiated Chemiresistor Response.

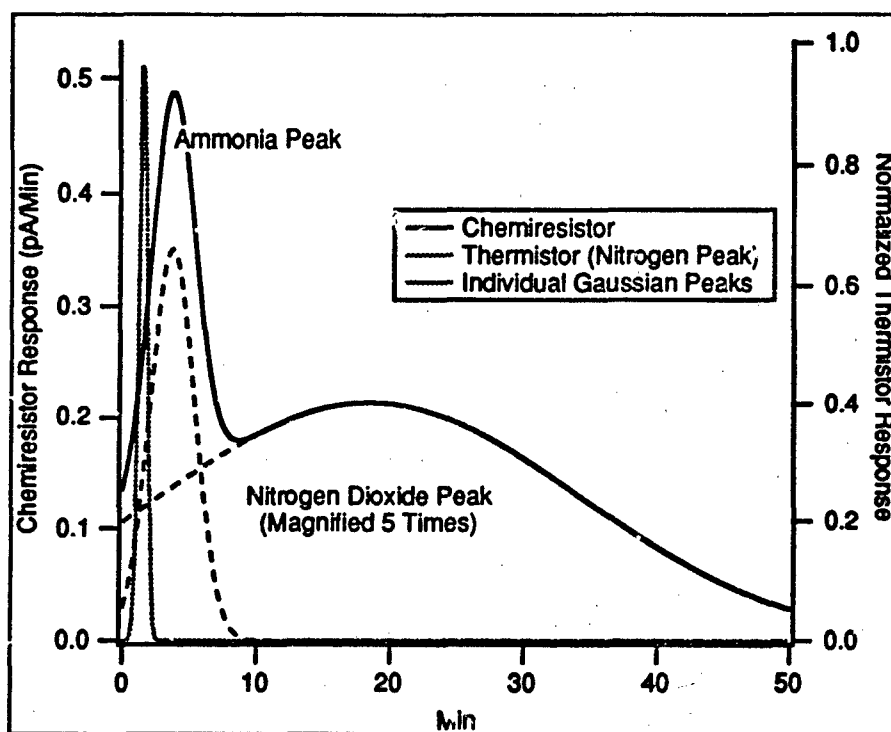


Figure 101. Gaussian Representation of Gas Elution (80°C, 6300 ppm NH<sub>3</sub>, and 270 ppm NO<sub>2</sub>). Vertical Axis is the Magnitude of the Differentiated Chemiresistor Response.

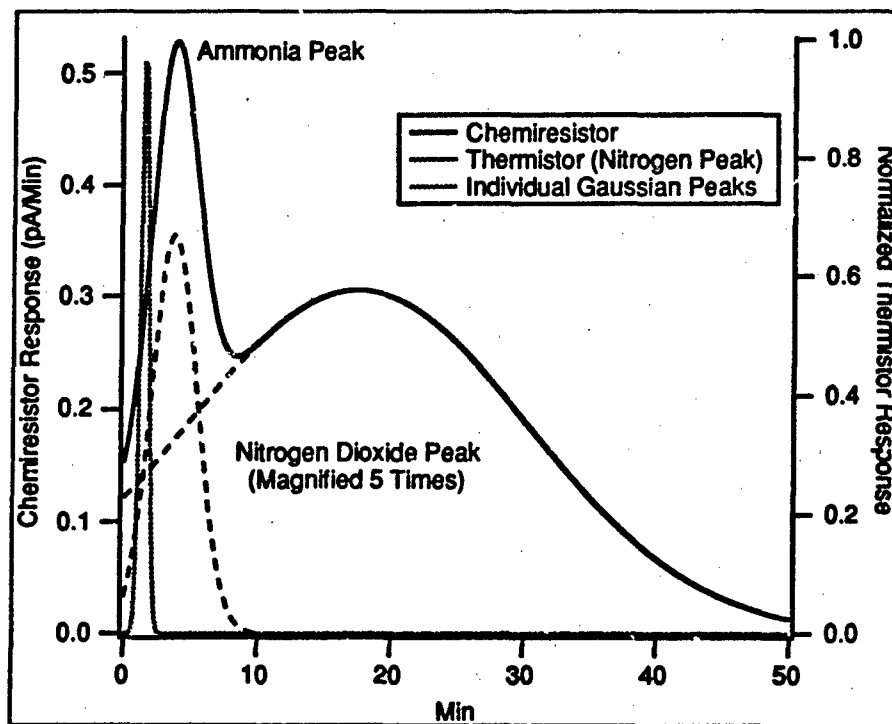


Figure 102. Gaussian Representation of Gas Elution (80°C, 6900 ppm NH<sub>3</sub>, and 560 ppm NO<sub>2</sub>). Vertical Axis is the Magnitude of the Differentiated Chemiresistor Response.

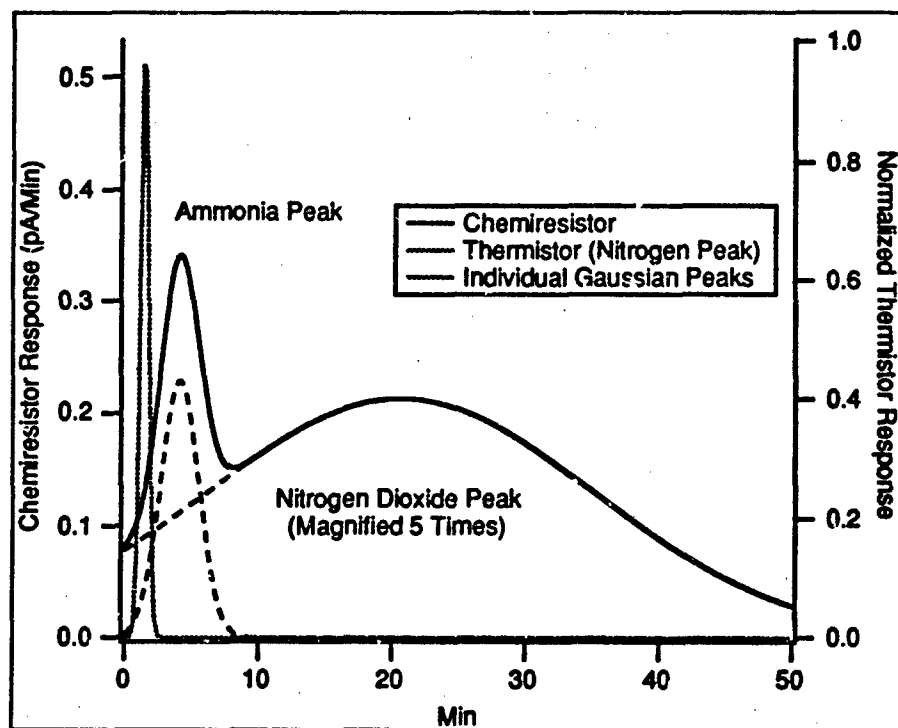


Figure 103. Gaussian Representation of Gas Elution (80°C, 1620 ppm NH<sub>3</sub>, and 540 ppm NO<sub>2</sub>). Vertical Axis is the Magnitude of the Differentiated Chemiresistor Response.

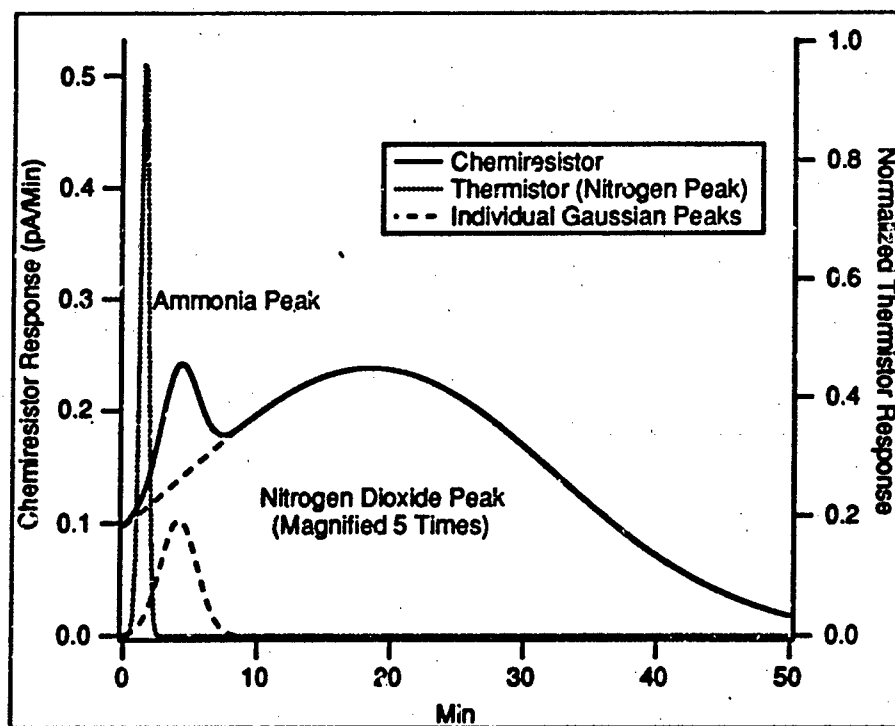


Figure 104. Gaussian Representation of Gas Elution (80°C, 480 ppm NH<sub>3</sub>, and 540 ppm NO<sub>2</sub>). Vertical Axis is the Magnitude of the Differentiated Chemiresistor Response.

## VII. Time-Domain Performance Model of the Micromachined Gas Chromatograph

Due to the complexity of the MMGC system (the large pressure gradient, the pseudo-rectangular walls, and the nearly uniform solid adsorbent), it is necessary to invoke fundamental gas kinetics in conjunction with the experimentally obtained adsorption data to be able to compare the performance evaluation results with existing GC theory. Since the only challenge gas which yielded meaningful adsorption data was NO<sub>2</sub>, the model presented in this chapter will focus solely on NO<sub>2</sub> in a helium diluent that interacts with a CuPc stationary phase which coats the MMGC walls. First, the diffusion coefficient for NO<sub>2</sub> in helium will be calculated. Second, the experimental data will be used to establish approximate values for the probability of adsorption and adsorption lifetime. Third, these values will be used in an iterative, time-domain performance model of the MMGC to simulate a series of NO<sub>2</sub> molecules interacting with the column.

### 7.1 Model Parameters.

The average molecular velocity,  $v_{av}$ , of an ideal gas with mass  $m$  is given by (125):

$$v_{av} = \sqrt{\frac{8RT}{\pi m}} \quad (69)$$

where  $R$  is the gas constant, and  $T$  is the temperature of the gas. For NO<sub>2</sub> ( $m \approx 0.047$  kg/mole) at 80°C,  $v_{av}$  is approximately 400 m/sec.

Since the number of helium molecules in a typical MMGC challenge gas mixture is much greater than the number of NO<sub>2</sub> molecules (especially for concentrations less than 500 ppm), an approximation for the diffusion coefficient can be established based upon the mean free path of a single NO<sub>2</sub> molecule in helium. Under this dilute approximation, the number of collisions,  $n_c$ , experienced by a single NO<sub>2</sub> molecule in helium is given by (126):

$$n_c = 2\sqrt{2}n_h \left( \frac{s_h + s_n}{2} \right)^2 \sqrt{\frac{\pi RT}{\left( \frac{m_h m_n}{m_h + m_n} \right)}} \quad (70)$$

where  $n_h$  ( $\approx 5.5 \times 10^{25} \text{ m}^{-3}$ ) is the density of helium molecules<sup>1</sup>,  $s_h$  ( $\approx 2 \text{ \AA}$ ) and  $s_n$  ( $\approx 9 \text{ \AA}$ ) are the effective diameters for helium and  $\text{NO}_2$ , respectively, and  $m_h$  ( $\approx 0.004 \text{ kg/mole}$ ) and  $m_n$  ( $\approx 0.047 \text{ kg/mole}$ ) are the masses of single helium and  $\text{NO}_2$  molecules. For the average pressure of within the MMGC column (calculated to be 23.8 psi above atmospheric pressure), the corresponding collision frequency is approximately  $7.6 \times 10^{10}$  collisions/sec.

Based upon the average velocity and collision frequency, the mean free path,  $\lambda$ , can be calculated using the following simple expression (126):

$$\lambda = \frac{v_{av}}{n_c}. \quad (71)$$

In this case, the mean free path for a single  $\text{NO}_2$  molecule in helium is approximately  $5.2 \times 10^{-9} \text{ m}$ , which corresponds to an effective diffusion coefficient,  $D$ , of approximately  $1.04 \times 10^{-6} \text{ m}^2/\text{sec}$  through the following relationship (126):

$$D = \frac{v_{av}\lambda}{2}. \quad (72)$$

In addition to the gas kinetics, the adsorptive interaction between  $\text{NO}_2$  and CuPc is a major factor affecting the propagation of  $\text{NO}_2$  molecules through the column. Unfortunately, the existing experimental data concerning the adsorptive properties of CuPc thin films is inconclusive, so separate experiments were conducted using the chemiresistors (which were coated with CuPc at the same time that the MMGCs were fabricated) to approximate the parameters of interest. A summary of these experiments, along with a chemiresistor adsorption model, is presented in Appendix C. These evaluations yielded the following parameters: a lifetime constant,  $\nu$ , of  $2900 \text{ sec}^{-1}$ , and an adsorption probability,  $\kappa$ , of  $2.9 \times 10^{-5}$ .

## 7.2 Model Implementation.

The time-domain model of the MMGC simulates the propagation of one  $\text{NO}_2$  molecule as it travels through the MMGC. The computer code required to implement the MMGC

<sup>1</sup>At pressure  $P$  and temperature  $T$ , the number of ideal gas molecules per unit volume is  $P/(k_b T)$ , where  $k_b$  is Boltzmann's constant (126).

model is presented in Appendix D. A summary of the model is shown in the flowchart depicted in Figure 105.

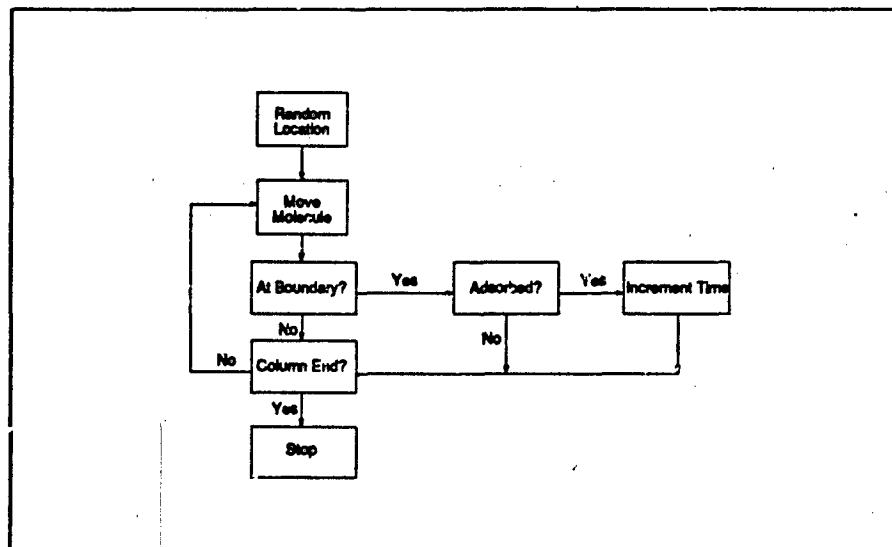


Figure 105. Flowchart for the Micromachined Gas Chromatograph Time-Domain Model.

The first step for each molecule involves selecting a random starting position within the MMGC column's cross-section (so that the results are not biased by the origin of the  $\text{NO}_2$  molecule). Once this requirement is accomplished, the model will iteratively move the molecule through the MMGC column based upon the flowrate at the given location (see Equation 15) and the diffusion coefficient<sup>2</sup> (see Figure 106). Once the molecule has been moved, a check is made to see if it is at one of the column walls.

If the  $\text{NO}_2$  molecule is on one of the MMGC column walls, another check is made to see if it is adsorbed (based upon the probability of adsorption). If the molecule is adsorbed, the time variable is incremented by the mean adsorption lifetime. Otherwise, a final check is made to see if the  $\text{NO}_2$  molecule has propagated to the end of the column. If the  $\text{NO}_2$  molecule has, the model terminates the analysis for that molecule, providing

<sup>2</sup>Effectively, the molecule is moved to a random location on the surface of a sphere with a radius equivalent to the diffusion length of the molecule, and a center displaced from the previous location by a distance related to the flowrate through the column.

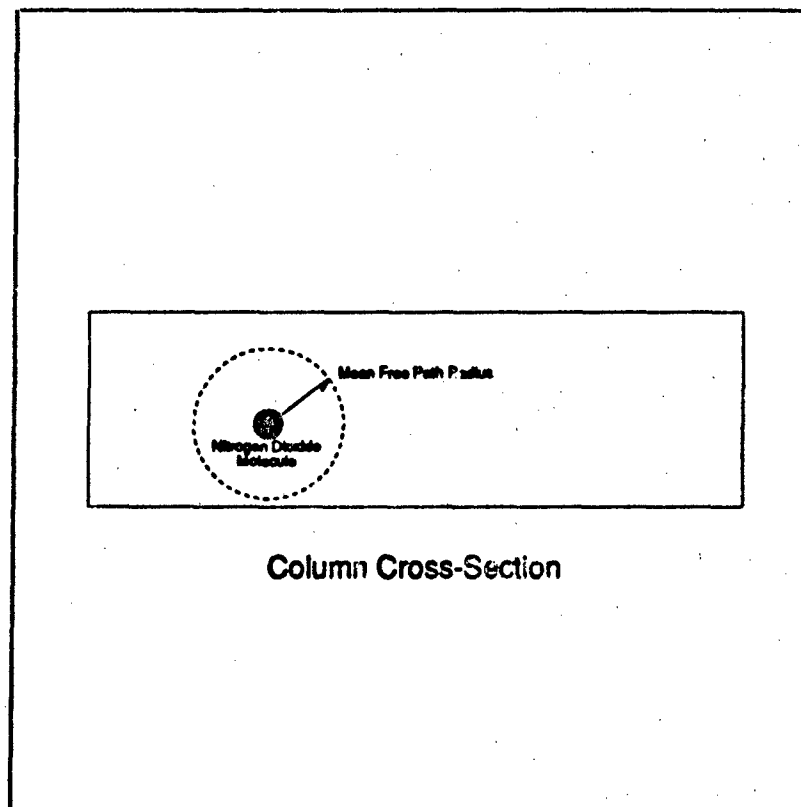


Figure 106. Column Cross Section Depicting the Movement of a Single  $\text{NO}_2$  Molecule.

the time variable as an indicator of the retention time for that particular molecule. If the molecule is still in the column, the overall process is repeated.

Figures 107 through 112 depict typical results from this model (for 5000 simulated molecules). As the temperature is varied, and parameter changes are made to model the two different MMGC geometries, the retention times correlate reasonably well with the experimental retention times. These behavioral characteristics are compared in Figure 113.

### 7.3 Separation Factor.

Finally, using the separation factor discussed in Section 2.3.2.2, the accuracy of the assumptions made in the design phase can be evaluated with respect to the actual experimental data and the model results. Additionally, a modification to Golay's theory

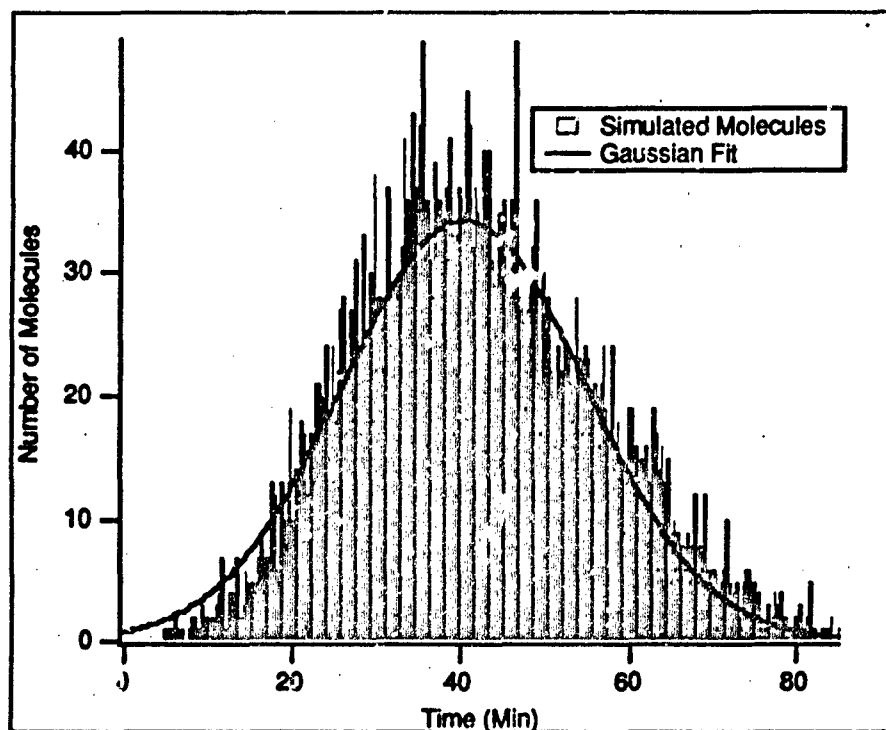


Figure 107. Typical Histogram for the Time-Domain Micromachined Gas Chromatograph Model of MMGC #1 at 55°C.

will be proposed that, in part, rectifies the disparity between the theoretical calculations and the experimental data.

From Equation 7, the  $\text{NO}_2$  retention time data, and the partition ratio (see Section 6.4.1.2), the actual separation factors for the two MMGCs for different operating temperatures can be calculated and compared with the predicted separation factors (using the method described in Section 4.1.1.2), and the separation factors calculated from the model's data. The results of these calculations are summarized in Table 12.

From Table 12, it is apparent that there is a significant discrepancy between the predicted and actual separation factors (a difference of more than four orders of magnitude), whereas the experimental and model separation factors are within an order of magnitude of each other. This relationship implies that there is a fundamental problem with the assumptions which were made in using Golay's theory. In Section 2.4.2, the statement was made that "...if the stationary phase was a solid whose mode of retention was adsorption-

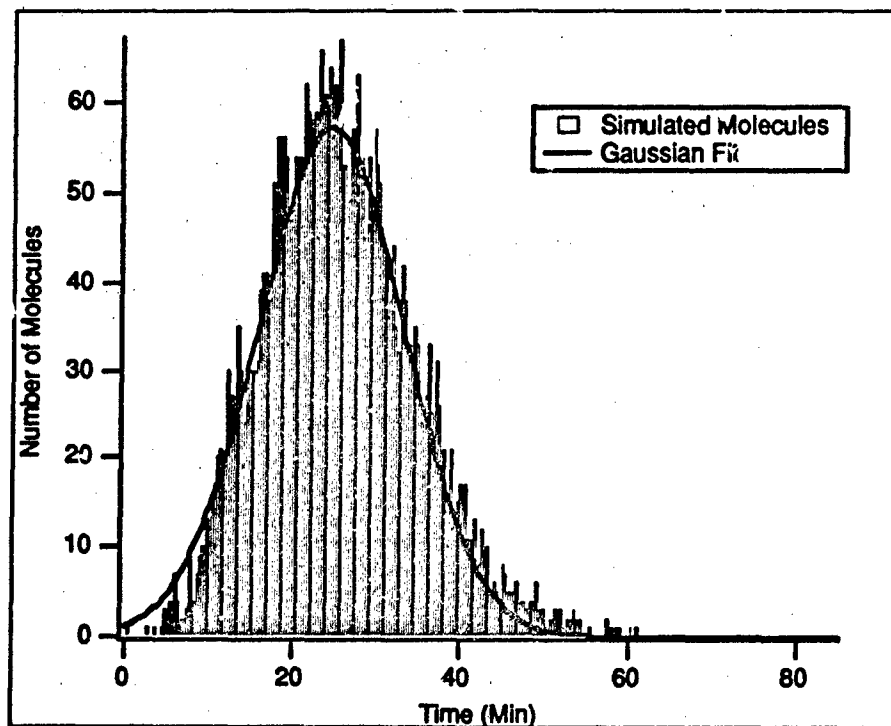


Figure 108. Typical Histogram for the Time-Domain Micromachined Gas Chromatograph Model of MMGC #1 at 68°C.

desorption at the solid surface, the sample would not penetrate into the bulk of the material, so resistance to mass transfer in the stationary phase could be neglected." This situation, however, does not appear to be precisely the case.

Since CuPc is such a strong adsorbent of  $\text{NO}_2$  (in the region between physi- and chemisorption), there is an equivalent retention time which mimics the diffusion of a gas sample into a liquid phase. Fortunately, Golay addressed the effect of slow diffusivity into the stationary phase by abandoning the assumption that diffusion within the stationary phase is instantaneous, yielding a third term to Equation 42, which becomes (25):

$$h_{\text{TSR}} = 2 \frac{D}{v_o} + \frac{4(1 + 9k + 51k^2/2)}{105(1 + k)^2} \frac{v_o z_o^2}{D} + \frac{2k^3}{3(1 + k)^2} \frac{v_o z_o^2}{F^2 c^2 D_1} \quad (73)$$

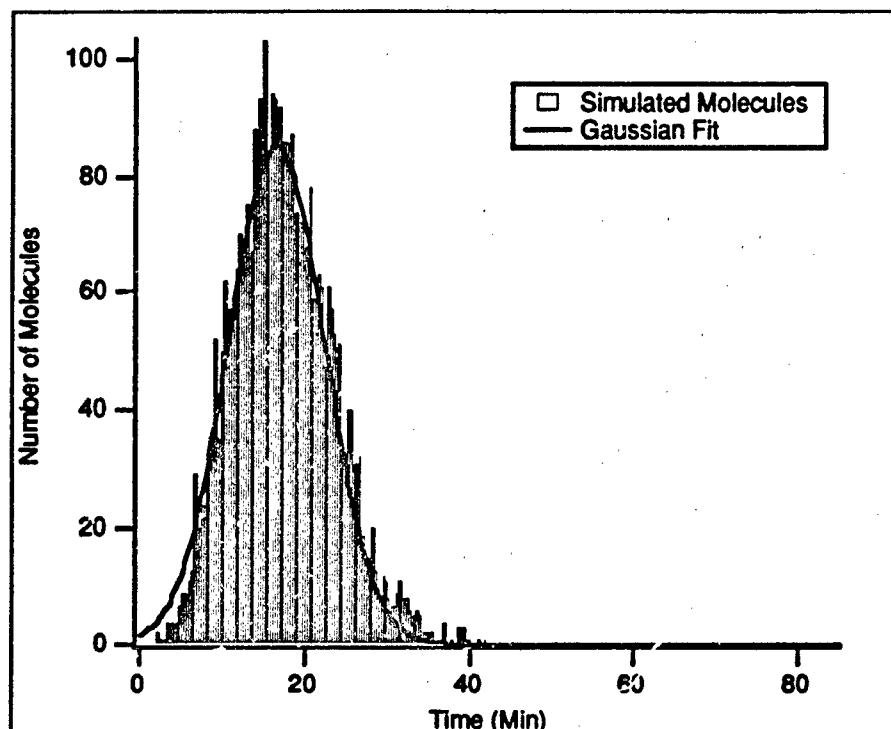


Figure 109. Typical Histogram for the Time-Domain Micromachined Gas Chromatograph Model of MMGC #1 at 80°C.

where  $F$  is the ratio of the effective surface area of the stationary phase relative to the actual area, and  $D_1$  is the diffusivity of the stationary phase<sup>3</sup>. To utilize this result, it is necessary to establish estimates for the two additional variables ( $F$  and  $D_1$ ) in order to determine the effect of the additional Golay term on the value of the separation factor (SF). Fortunately, because of the information gained during the experimental evaluation phase, these estimates can be calculated.

From the transmission electron microscopy studies (see Appendix B),  $F$  can be estimated from the average size of the CuPc polycrystals and the thickness of the CuPc film by assuming that it is composed of a conglomeration of cylindrical-shaped crystallites. If each cylinder has a characteristic radius,  $r_{cr}$ , and a characteristic height,  $h_{cr}$ , the total surface area of the cylinder is  $2\pi r_{cr} h_{cr} + \pi r_{cr}^2$ , and the column area occupied by the crystallite is simply  $\pi r_{cr}^2$ . Hence,  $F$  can be approximated by taking the ratio of these two expressions:

<sup>3</sup>See Section 2.4.2 for a discussion of  $D$ ,  $v_o$ ,  $k$ , and  $x_o$ .

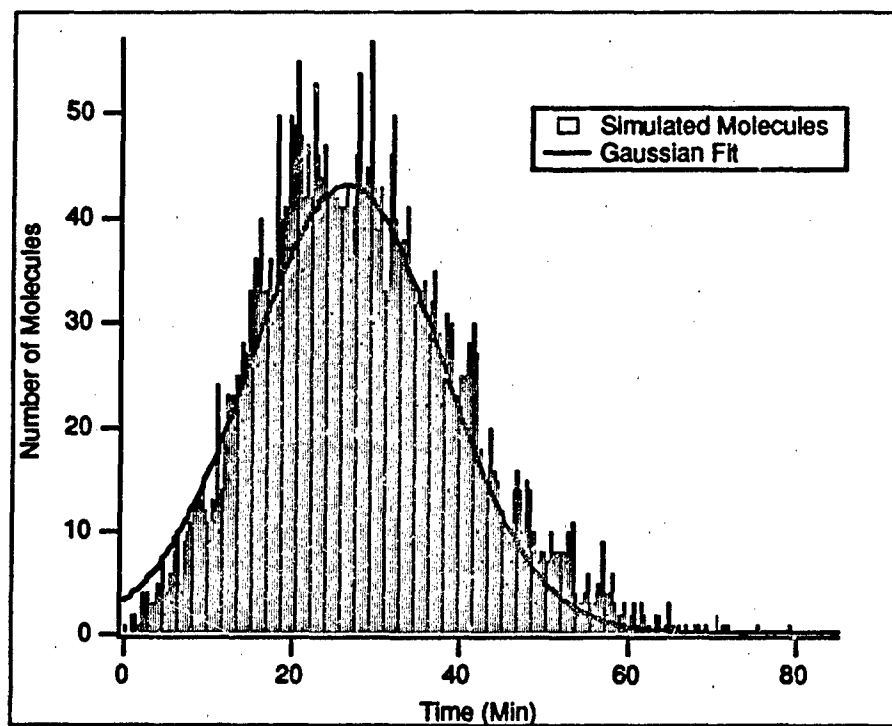


Figure 110. Typical Histogram for the Time-Domain Micromachined Gas Chromatograph Model of MMGC #2 at 56°C.

$$F = \frac{2\pi r_{cr} h_{cr} + \pi r_{cr}^2}{\pi r_{cr}^2} \quad (74)$$

where  $r_{cr}$  is the average crystallite radius (approximately 300 Å from Figure 130 in Appendix B) and  $h_{cr}$  is the average crystallite height (approximately 2000 Å from the thickness of the CuPc thin film). Using these values, an estimate for  $F$  is calculated to be 14.

The other variable,  $D_1$ , can be estimated assuming that a given adsorbed  $\text{NO}_2$  molecule moves a distance of two<sup>4</sup> mean-free-paths per average adsorbed lifetime (see Equation 71). Using Equation 72, and assuming that  $v_{av} = 2\lambda\beta$ , where  $1/\beta$  is the average adsorbed lifetime (see Appendix C, Equation 87),  $D_1$  is approximately  $2 \times 10^{-19} \text{ m}^2/\text{sec}$  at 55°C.

<sup>4</sup>One mean-free-path length involved when striking the surface, and another when it leaves.

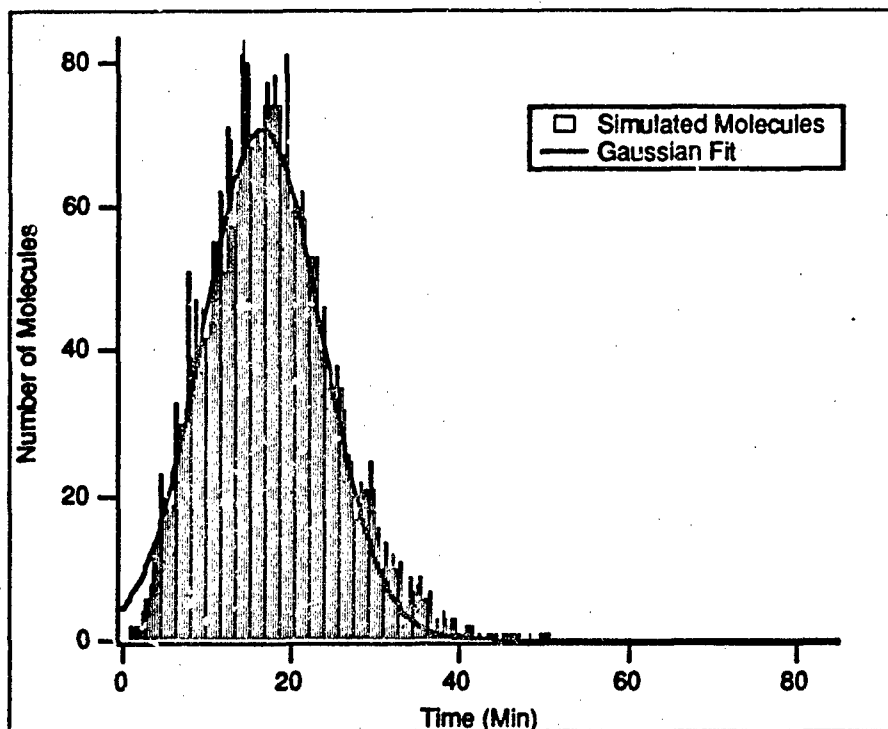


Figure 111. Typical Histogram for the Time-Domain Micromachined Gas Chromatograph Model of MMGC #2 at 68°C.

Using these numerical estimates for  $F$  and  $D_1$ , and recomputing the separation factor (SF) for the conditions specified in Table 12, yields the revised results posted in Table 13.

From Table 13, it is clear that the modified version of Golay's original equation contributes results which are much closer to the experimental and model values, and it further demonstrates that the theory proposed by Golay can be used to predict the performance of a micromachined GC. Unfortunately, the information required to use the modified Golay equation (i.e., the adsorption lifetime and partition ratio) was unavailable until after the MMGC experimental evaluations were performed. However, if approximate values for these variables are available, the model can be used to estimate the performance of an MMGC column, while the modified Golay equation can be used to optimize future MMGC work with respect to using solid adsorbents similar to CuPc.

As an example, using the information from this investigation together with the modified Golay equation yields the plot shown in Figure 114. From Figure 114 it is apparent that

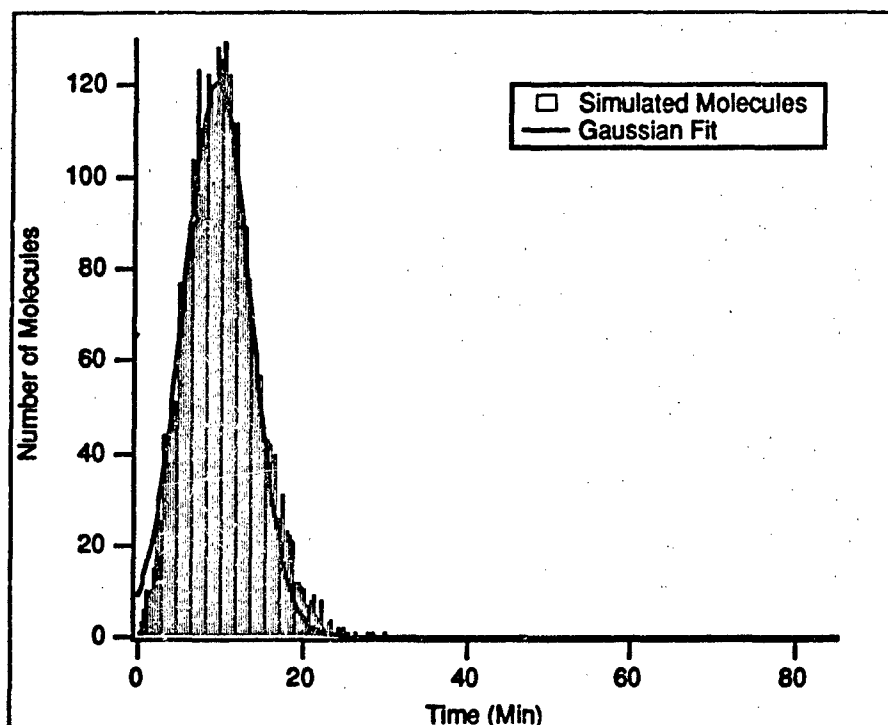


Figure 112. Typical Histogram for the Time-Domain Micromachined Gas Chromatograph Model of MMGC #2 at 83°C.

the optimum column height to use for the conditions of this investigation is approximately 0.6 microns.

#### 7.4 Summary.

The model presented in this chapter is based upon the parameters obtained theoretically and experimentally. As a single molecule propagates through the column, it has the opportunity to interact with the stationary phase, which acts to retard its movement. If a sufficient number of molecules are analyzed in the model, a picture of the retention time behavior emerges, and its behavior can be compared with the actual experimental data. For the cases modeled here, the retention times predicted by the model closely correspond to the actual retention times. Additionally, the separation factor is an indicator of the relationship between the theoretical predictions, the experimental results, and the modeled data. The model also served to illustrate that the assumptions made concerning

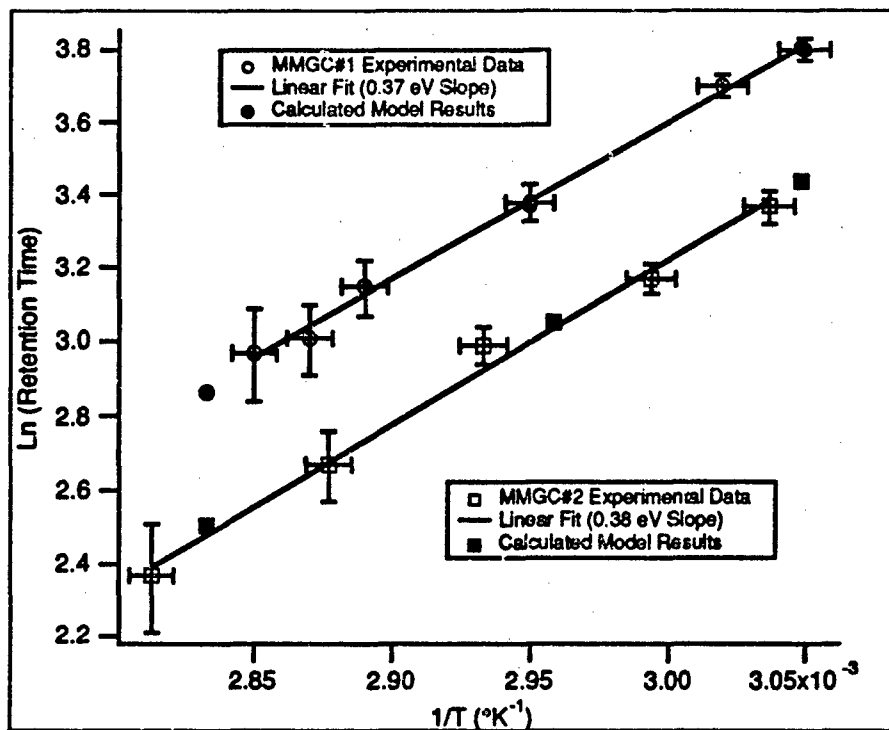


Figure 113. Retention Times for the Time-Domain Gas Chromatograph Model Compared with the Experimental Data.

the use of a solid phase were not entirely correct, but this problem can be rectified using the following information contributed by this research:

1. Diffusivity: Using the heat of adsorption, an estimate can be made for the diffusivity of the solid stationary phase.
2. Effective Surface Area: With the size of the CuPc polycrystallites obtained through the transmission electron microscopy studies, an estimate of the effective surface area can be made.
3. Modified Golay Equation: Combining the diffusivity and effective surface area with the modified Golay equation provides a more accurate picture of the MMGC column's performance.

Table 12. Theoretical, Experimental, and Computed Model Values for the Separation Factor (SF).

Temperature ( °C)	Theoretical SF	Experimental SF	Model SF
MMGC #1: 55	63900	4.4	9.0
MMGC #1: 78	62100	2.3	9.3
MMGC #2: 56	52000	2.8	6.4
MMGC #2: 83	54000	0.9	6.2

Table 13. Revised Theoretical, Experimental, and Computed Model Values for the Separation Factor (SF).

Temperature ( °C)	Theoretical SF	Experimental SF	Model SF
MMGC #1: 55	1.3	4.4	9.0
MMGC #1: 78	3.7	2.3	9.3
MMGC #2: 56	1.0	2.8	6.4
MMGC #2: 83	3.1	0.9	6.2

Using the results of this investigation, the fundamental separation factor (SF) equation used in designing the micromachined gas chromatograph can be summarized as (see Equation 8):

$$SF = \frac{L}{h_{TSR}g} \left( \frac{k}{1+k} \right)^2 \quad (75)$$

where  $h_{TSR}$  (the plate height) is defined by (see Equation 73):

$$h_{TSR} = 2\frac{D}{v_o} + \frac{4(1+9k+51k^2/2)}{105(1+k)^2} \frac{v_o z_o^2}{D} + \frac{2k^3}{3(1+k)^2} \frac{v_o z_o^2}{F^2 c^2 D_1} \quad (76)$$

$F$  (the effective surface ratio) is defined by (see Equation 74):

$$F = \frac{2\pi r_{cr} h_{cr} + \pi r_{cr}^2}{\pi r_{cr}^2} \quad (77)$$

$k$  (the partition ratio) is defined by (see Equation 68):

$$k = k_o \exp(-E_a/k_b T) \quad (78)$$

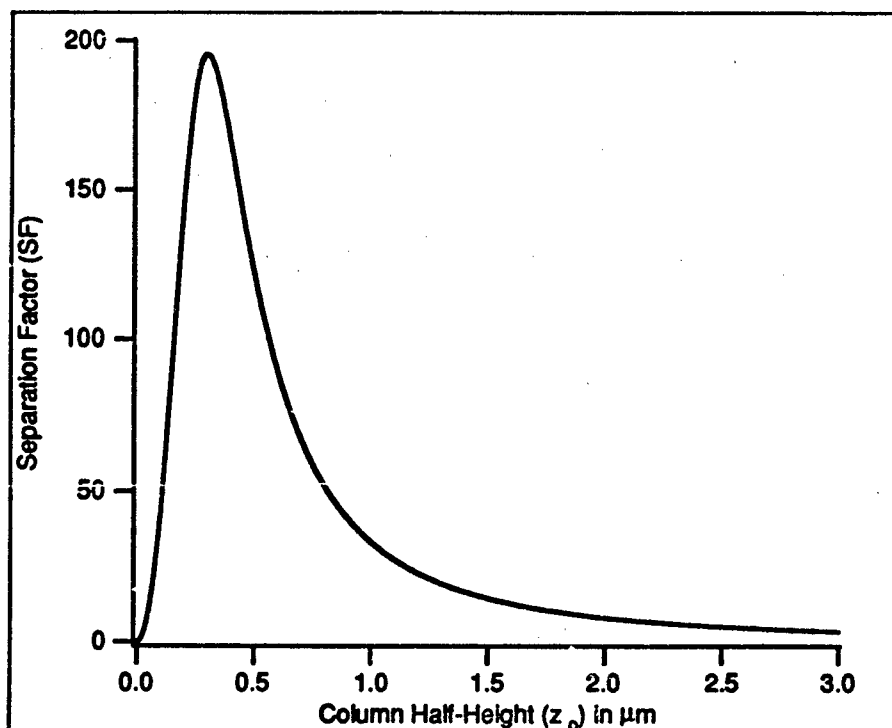


Figure 114. Separation Factor (SF) versus  $z_o$  for a Column with CuPc as a Stationary Phase. The Column Length is 0.9 m, Gas Viscosity is 200  $\mu$ poise, Stationary Phase Thickness is 0.2  $\mu$ m, Column Width is 300  $\mu$ m, and the Input Pressure is 40 psi.

$D$  (the diffusion coefficient) is defined by (see Equation 72):

$$D = \frac{v_{av}\lambda}{2} \quad (79)$$

$D_1$  (the stationary phase diffusion coefficient) is defined by (see Section 7.3):

$$D_1 = \beta\lambda^2 \quad (80)$$

$v_o$  (the carrier gas output velocity) is defined by (see Equation 26):

$$v_o = \frac{(P_i^2 - P_o^2)}{2P_o q L} \quad (81)$$

and  $g$  (the plate height correction factor) is defined by (see Equation 22):

$$g = \frac{9 \left[ \left( \frac{P_i}{P_o} \right)^4 - 1 \right] \left[ \left( \frac{P_i}{P_o} \right)^2 - 1 \right]}{8 \left[ \left( \frac{P_i}{P_o} \right)^3 - 1 \right]^2} \quad (82)$$

The values used in calculating the separation factor for 80°C are shown in Table 14, and have been divided into three major categories: physical, operational, and experimental. The physical properties are tabulated in standard references (or based on tabulated values), the operational properties were chosen in the design phase, and the experimental properties were determined in this investigation.

Table 14. Physical, Operational, and Experimental Parameters Used to Calculate the Separation Factor (SF) at 80°C.

Physical Parameters		
Parameter	Symbol	Value
Boltzmann's Constant	$k_b$	$1.38 \times 10^{-23}$ joules/kelvin
Helium Viscosity	$\mu$	200 $\mu$ poise
Diffusion Coefficient	$D$	$10^{-6}$ m <sup>2</sup> /sec
Mean Free Path	$\lambda$	$5 \times 10^{-9}$ m
Average Molecular Velocity	$v_{av}$	400 m/sec
Operational Parameters		
Parameter	Symbol	Value
Input Pressure	$P_i$	40 psi
Output Pressure	$P_o$	1 atmosphere
Column Length	$L$	0.9 m
Column Width	$Y$	300 $\mu$ m
Column Height	$2z_o$	10 $\mu$ m
Temperature	$T$	80°C
Column Permeability	$q$	$2.6 \times 10^7$ poise/m <sup>2</sup>
Correction Factor	$g$	1.08
Experimental Parameters		
Parameter	Symbol	Value
Heat of Adsorption	$E_a$	0.38 eV
Partition Ratio Constant	$k_o$	$4 \times 10^{-4}$
Adsorption Lifetime	$1/\beta$	.93 sec
CuPc Diffusion Coefficient	$D_1$	$6 \times 10^{-19}$ m <sup>2</sup> /sec
Partition Coefficient	$c$	2400
Effective Surface Area Ratio	$F$	14
Crystallite Radius	$r_{cr}$	200 Å
Crystallite Height	$h_{cr}$	2000 Å

### *VIII. Conclusions and Recommendations*

This research has demonstrated the use of single-crystal silicon micromachining to implement a gas chromatograph based upon a CuPc solid stationary phase which is capable of separating and detecting  $\text{NO}_2$  and  $\text{NH}_3$ . Additionally, valuable information concerning the adsorptive properties of CuPc has been revealed through the MMGC evaluation phase. The significant accomplishments ascertained from this research can be discussed with respect to two areas: chemical sensing and micromachining.

In the chemical sensing area, the primary accomplishment was that which was initially stated as the objective of this investigation: the separation and direct detection of  $\text{NO}_2$  and  $\text{NH}_3$ . The MMGC design evaluated in this effort was capable of directly separating  $\text{NO}_2$  and  $\text{NH}_3$  at parts-per-million concentration levels in less than 30 minutes when operated at  $80^\circ\text{C}$ . Relative to this accomplishment, a secondary discovery was the determination of the heat of adsorption of  $\text{NO}_2$  (0.38 eV) on a CuPc thin film (2000 Å thick). Furthermore, this research served as a proof-of-concept concerning the utilization of an MMGC to investigate the adsorptive properties of thin films. In addition, the development of the time-domain performance model of the MMGC will facilitate the development of future MMGCs by providing a tool which can estimate MMGC performance.

In the micromachining area, a novel TCD cell design was implemented. The key features of this design relative to the previously reported TCD cell configurations (11) include: a significantly reduced volume (20 nl—a 50% improvement over previous designs), ease of thermistor insertion, and the ability to pass the column effluent to a second detector (i.e., the chemiresistor). Also, a new technique was developed, enabling for the first time the deposition of a nearly-homogeneous solid-phase thin film (2000 Å thick) within a micromachined GC column. Finally, although not extensively investigated, the ability to perform relatively low temperature (less than  $300^\circ\text{C}$ ) anodic bonding (1800 V for 24 hours) was demonstrated. This process is important because it is compatible with thermally-sensitive thin films and other bulk materials.

With respect to recommendations for further work, improvements can be made in the column design and detector configuration of the MMGC. The MMGC column length can be

doubled by decreasing the inter-column spacing from 1 mm to 0.35 mm without sacrificing yield (by fabricating the MMGC in a clean-room environment), resulting in a doubling of the separation factor (see Equation 8). Also, as shown in Figure 115, incorporating a chemiresistor IC directly within a detector cell (using wafer-scale integration techniques) similar to the one machined for the TCD would improve the sensitivity of the chemiresistor (possibly improving chemiresistor sensitivities to detect less than 500 ppm concentrations of  $\text{NH}_3$ ). An integral heater (with controller) could also be fabricated using standard IC fabrication techniques, further reducing the requirement for external equipment. Finally, investigations concerning the adsorptive properties of other thin films (in particular, other metal-doped phthalocyanines), using the MMGC as a tool, would be of significant value to those developing chemical sensors based upon these chemically-sensitive semiconductor materials.

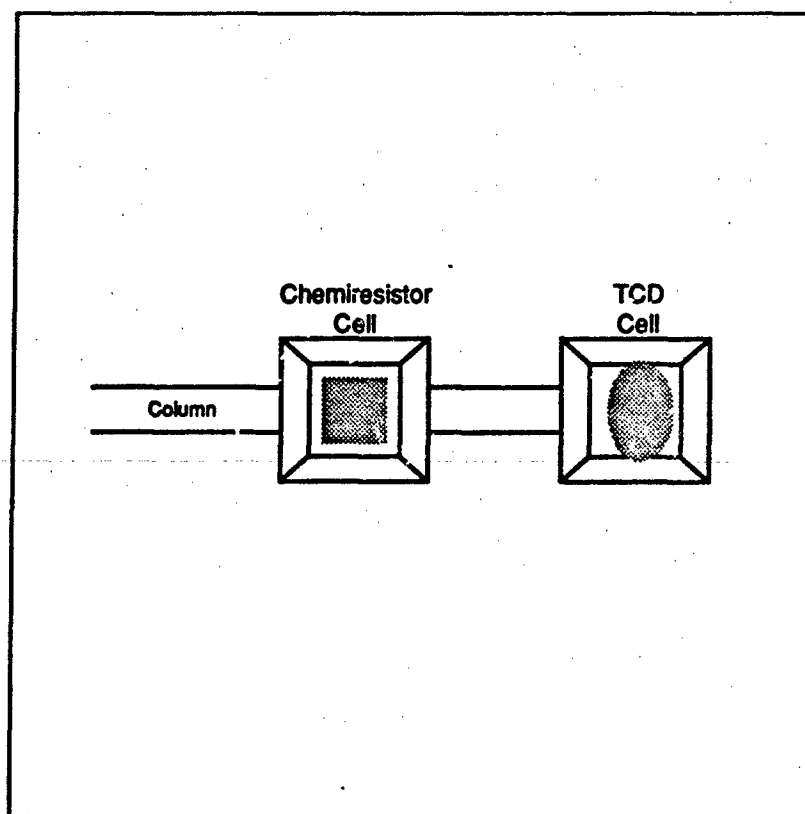


Figure 115. Micromachined Chemiresistor and Thermistor Detector Cells.

## Appendix A. *Fabrication Processes*

This appendix describes the processes used to fabricate the micromachined gas chromatograph (when the term "substrate" is used, it refers to either the silicon wafer or the borosilicate glass plate).

### A.1 *Wafer Cleaning.*

To insure that each process was initiated with substrates that were free of any organic contamination (i.e., fingerprints or residual photoresist), the substrates were cleaned in a standard solution of  $\text{H}_2\text{SO}_4:\text{H}_2\text{O}_2$  (3:2) for a period of 30 minutes. The substrates were then rinsed in deionized water (DIW) with a nitrogen bubbler until the rinse DIW attained a resistance of greater than 10 M $\Omega$ . They were then carefully blown dry with pressurized nitrogen.

### A.2 *Oxidation.*

Since certain processes required a silicon dioxide mask to protect areas of the silicon wafer from the effects of an etchant, a standard oxidation profile was used for all oxidations. This process involved placing the silicon wafers into a 1050°C furnace for 24 hours with a 5 ml/min flow of oxygen bubbled through a flask containing DIW maintained at 95°C. This process yielded a silicon dioxide layer which was approximately 2.5  $\mu\text{m}$  thick (more than sufficient for the required etches which consumed approximately 0.5  $\mu\text{m}$  of the silicon dioxide).

### A.3 *Photoresist Deposition.*

Prior to photoresist deposition, the substrate was baked in a 200°C oven for one hour to improve photoresist adhesion by evaporating any surface moisture. After cooling the substrate for 15 minutes, the substrate was centered over a piece of lens tissue which covered the wafer's spinner chuck (the lens tissue served to protect the "down" side of the substrate since both sides of the substrate were processed). Once a vacuum was applied to

the wafer's spinner chuck, approximately 3 ml of photoresist<sup>1</sup> was deposited in the center of the substrate with a dropper. The substrate was then spun at 3,000 revolutions per minute (rpm) for 15 seconds, thinning the photoresist to approximately 1.3 microns (124). After softbaking at 85°C for approximately 20 minutes (to remove solvents and improve the adhesion of the photoresist), the substrate was ready for the next process.

#### *A.4 Photoresist Cure.*

Since certain major processes required a protective coating on the entire surface of one side of a substrate<sup>2</sup>, a process was developed to expose and hardbake (cure) a photoresist layer deposited on one side of a substrate. The exposure source was the internal ultraviolet (UV) source of a mask aligner<sup>3</sup> without a mask. The substrate was positioned on the wafer holder of the mask aligner and exposed for 20 seconds. This exposure was followed by a 20 minute hardbake at 140°C.

#### *A.5 Photolithographic Mask Exposure.*

The photolithographic mask exposure required the use of the mask aligner<sup>4</sup> to align the existing features on the substrate with the mask. Once aligned, the substrate was exposed with the internal UV source for 20 seconds.

#### *A.6 Photoresist Development.*

The exposed photoresist was developed by spinning the substrate on a wafer spinner at 500 rpm and spraying its surface with xylene for 30 seconds. After development, the substrate (which was still spinning), was sprayed with n-butyl acetate for 30 seconds to stop its development. Next, the wafer spinner's speed was ramped up to approximately 3000 rpm to remove the n-butyl acetate. Finally, the developed substrate was hardbaked for 20 minutes at 140°C.

<sup>1</sup>Waycoat HR100 negative photoresist, Olin Hunt Specialty Products Inc., West Paterson, NJ.

<sup>2</sup>For example, during the first KOH etch, the front side of the silicon wafer was protected since only the back side was etched.

<sup>3</sup>Model MJB 3, UV300 Mask Aligner, Karl Suss, Waterbury Center, VT.

<sup>4</sup>Model MJB 3, UV300 Mask Aligner, Karl Suss, Waterbury Center, VT.

#### *A.7 Silicon Dioxide Etch.*

The silicon dioxide etching process utilized a buffered hydrofluoric acid solution consisting of  $\text{NH}_4\text{F}:\text{HF}$  (4:1) at room temperature. The experimentally determined etch rate was approximately  $0.25 \text{ \AA}/\text{min}$ , necessitating an etch time of approximately 10 minutes to remove the thermally grown silicon dioxide. After etching, the substrate was rinsed in DIW for 30 minutes.

#### *A.8 KOH Etch.*

For the first KOH etch, the entire wafer thickness (a maximum of 385 microns) was etched. A 20% by weight solution (KOH in DIW) at  $50^\circ\text{C}$  yielded an etch rate of approximately  $0.2 \text{ }\mu\text{m}/\text{min}$  (see Section 3.1.2). Etching for 32 hours would etch through the thickest wafer and consume only 0.58 microns of silicon dioxide (at an etch rate of  $3 \text{ \AA}/\text{min}$ —see Section 3.1.2). The second KOH etch was only 200 microns deep. With a fresh 20% by weight solution (KOH in DIW) at  $50^\circ\text{C}$  resulted in an etching time that was approximately 16.7 hours (consuming only 0.3 microns of silicon dioxide). After each KOH etch, the silicon wafer was rinsed in DIW for 30 minutes.

#### *A.9 Isotropic Etch.*

The isotropic etchant solution was composed of  $\text{HF}:\text{HNO}_3:\text{CH}_3\text{COOH}$  (2:15:5), which yielded an etch rate of approximately  $5.75 \text{ }\mu\text{m}/\text{min}$  (see Section 3.1.1). The etch process was conducted for 95 seconds, and it produced an etch depth of approximately 9 microns. After the isotropic etch process, the silicon wafer was rinsed in DIW for 30 minutes.

#### *A.10 Rinse, Dry and Inspection.*

The final step in all of the major processes involved rinsing the substrate in DIW with a nitrogen bubbler until the rinse water attained a resistance of  $10 \text{ M}\Omega$ . The substrates were then dried with a nitrogen blower and inspected under a binocular microscope.

## Appendix B. Copper Phthalocyanine (CuPc)<sup>1</sup>

### B.1 Background

Phthalocyanine and the various metal derivatives (i.e., copper phthalocyanine) possess favorable properties which has motivated their use in a variety of applications, including catalysts, colorants, lasers, lubricants, blood substitutes, and color photography (122). The phthalocyanines are based on the structure shown in Figure 116, where the substitution of different metals (e.g., copper, lead, cobalt, zinc, etc.) in the central portion of the structure influences the physio-chemical properties of the phthalocyanines. Table 15 summarizes some of the important chemical and physical properties of copper phthalocyanine.

Table 15. Chemical and Physical Properties of Copper Phthalocyanine (43).

Property	Value
Molecular Weight	576.1
Melting Point (°C)	Sublimes
Sublimation Point (°C)	300 (10 <sup>-7</sup> Torr Vacuum) to 500 (1 Atmosphere)
Density (grams/ml)	1.62

The large number of applications and the versatility inherent in the ability to substitute various metal ions in the phthalocyanine molecule has motivated extensive research into their chemical, physical, and electrical properties. Several extensive reviews and books dedicated to collecting and summarizing the large body of literature generated concerning the phthalocyanines have been published (45, 127-134). The extent of this literature has undoubtedly contributed to the adoption of the phthalocyanine materials as model compounds in the study of molecular crystals and organic semiconductors. Reviews of these materials usually include some discussion of phthalocyanines (135-140). One application for the phthalocyanine compounds which has received increasing interest is their use as the chemically-sensitive component in gas microsensors. This interest primarily stems from the high sensitivity of their electrical properties upon gas adsorption, which has been reviewed

<sup>1</sup>This Appendix was written in conjunction with John M. Wiseman, a principle investigator at AFIT concerning phthalocyanines on chemiresistors directly coupled to field effect transistors.

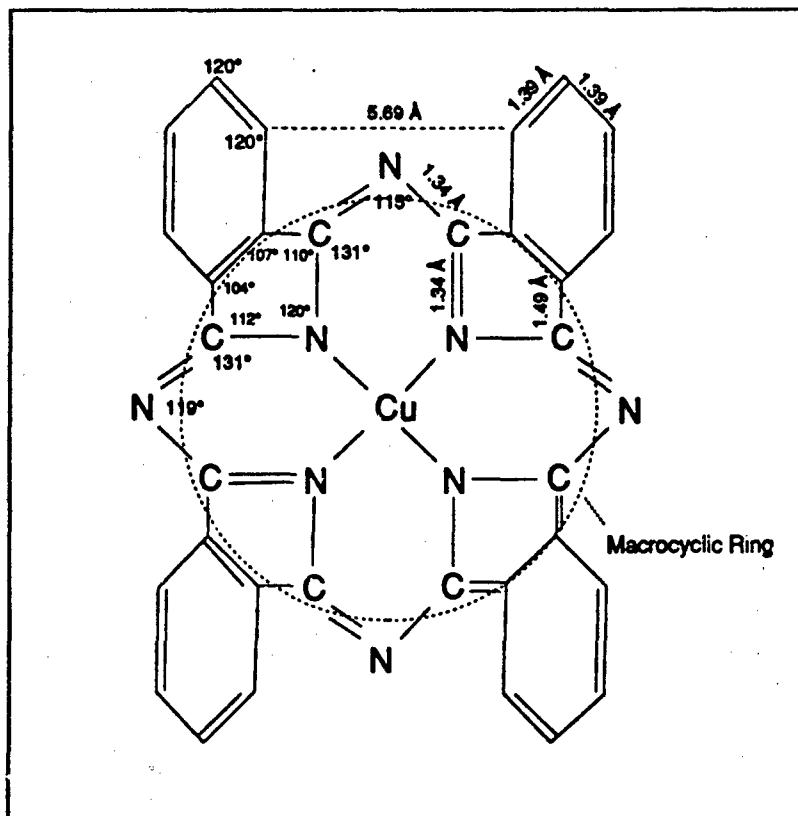


Figure 116. Chemical Structure of Copper Phthalocyanine (CuPc) (45).

in a recent article by Wright (45). In his review, Wright provides a thorough discussion of gas adsorption and its effects on the electrical properties of the phthalocyanines (45).

The electrical properties are strongly influenced by the structure of CuPc, which is characterized by the macrocyclic ring and the presence of the central copper ion (see Figure 116). The macrocyclic ring generates an extensive delocalized  $\pi$ -electron<sup>2</sup> system within the molecule that represents a highly polarizable electron cloud which, in conjunction with the presence of the hetero-atoms (nitrogen), and the central copper ion, is responsible for the electrical and adsorption properties of CuPc. This is due to the fact

<sup>2</sup>A  $\pi$ -bond is "considered not so much as providing the primary bonding holding a molecule together as supplementing an already present sigma bond" (126). Since the sigma bond occupies the space directly between the bonded atoms, the  $\pi$ -bond occurs over (and under) the plane of the CuPc molecule, thus the electrons which take part in the  $\pi$ -bond are not as tightly bound as the sigma bond electrons (see Figure 117).

that the polarizable electron cloud results in stronger van der Waals interactions with adsorbate molecules. Furthermore, the low ionization energy of these electrons makes CuPc a good electron donor (which favors charge transfer interactions with electron acceptor gases) (45). A simplified energy band structure of CuPc (shown in Figure 118a), with an overall bandgap of 0.89 eV, reveals a trap level located at approximately 0.37 eV above the top edge of the valence band (122). Activation energy measurements made on the phthalocyanines show a sharp change in the activation energy from the lower (0.37 eV) value to the intrinsic (0.89 eV) value for temperatures greater than 110°C (122, 141). This behavior is consistent with experimental observations made during this investigation, where measured activation energies were approximately 0.4 eV for temperatures less than 90°C.

When an electron acceptor gas (i.e., NO<sub>2</sub>) is adsorbed onto the surface of a CuPc crystallite (see Figure 117a), the Fermi energy level is shifted toward the valence band, as is shown in Figure 118b (the activation energy of CuPc saturated with NO<sub>2</sub> is approximately 0.1 eV), thus effectively providing more majority carriers (holes for a p-type semiconductor) to participate in electronic conduction processes (45). The opposite effect occurs when an electron donor gas (i.e., NH<sub>3</sub>) is adsorbed onto the surface (see Figures 117b and 118c). Since the bandgap for CuPc saturated with NH<sub>3</sub> is approximately 1.01 eV, electron donor gas adsorption serves to effectively reduce the number of majority carriers which can participate in electronic conduction processes (45). Based upon these responses, along with supporting Hall measurements, CuPc has been classified as a p-type semiconductor (43, 45, 122).

## *B.2 Qualitative CuPc Thin Film Characterization*

Because of its use as a chemically-sensitive membrane for strong electron acceptor gases, CuPc thin films have been successfully deposited and studied in the AFIT laboratories for a number of years, using the technique described in Section 5.3.1. From these studies, a 2000 Å CuPc film thickness was identified to balance the opposing requirements for sensitivity (thicker films) and reversibility (thinner films) of the chemiresistor (117, 121). Also, three techniques (infrared spectroscopy, scanning electron microscopy, and transmission electron microscopy) were used to examine the CuPc films used in this

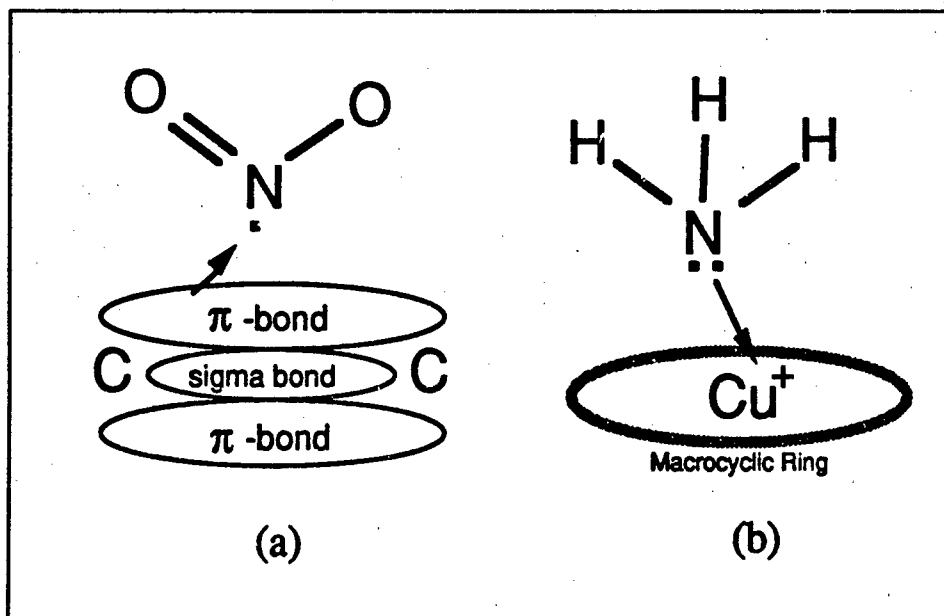


Figure 117. Proposed Interactions Between Adsorbed Gases and Copper Phthalocyanine for (a) Nitrogen Dioxide and (b) Ammonia. The Arrows Denote the Transfer of Electrons.

investigation in order to qualitatively establish that they were comparable to the CuPc thin films used in other investigations.

**B.2.1 Infrared Spectra.** The structure and morphology of the phthalocyanines and their gas adsorption properties have been studied by infrared spectroscopy (45, 122). The published spectrum for alpha-phase CuPc<sup>3</sup> is shown in Figure 119 (142).

The experimental CuPc samples prepared for the infrared spectroscopy study were deposited in the standard manner (see Section 5.3.1) onto sodium chloride substrates (IR "windows"). The thickness was increased to approximately 7000 Å (3500 Å per side) to improve the resolution of the infrared spectra. The spectrum in Figure 119 was generated from a CuPc thin film deposited on a potassium bromide substrate—which has a broader infrared transmission bandwidth (from less than 200 cm<sup>-1</sup> to greater than 4000 cm<sup>-1</sup>) compared to sodium chloride (from approximately 800 cm<sup>-1</sup> to greater than 4000 cm<sup>-1</sup>). The

<sup>3</sup>The alpha-phase form of CuPc was used in this investigation since it is the morphology which grows under the low temperature deposition process used in this investigation.

infrared transmission<sup>4</sup> for the blank sodium chloride substrate used in this investigation is shown in Figure 120, and it displays this reduced bandwidth.

Considering the low-order cutoff wave number ( $800\text{ cm}^{-1}$ ) for the sodium chloride substrates, the infrared spectra for two experimentally deposited CuPc thin films ( $6600\text{ \AA}$  and  $7700\text{ \AA}$  thick) have a comparable structure to the published spectrum in the  $800$  to  $4000\text{ cm}^{-1}$  range (comparing Figures 121 and 122 with Figure 119). A normalized peak comparison for several of the critical features also displays the similarity between the experimentally deposited CuPc thin films and the published spectrum (see Figure 123).

Additionally, to verify  $\text{NO}_2$  adsorption, the sample was subjected at room temperature to an ambient containing a  $770\text{ ppm}$   $\text{NO}_2$  challenge gas concentration for approximately 46 hours. This concentration and exposure time was based upon the estimated  $4 \times 10^{15}$  molecule capacity of the two infrared samples<sup>5</sup> (see Section 4.1.2.2). In order to insure saturation, the sample was exposed to a number of challenge gas molecules approximately 5 orders of magnitude greater than the sample capacity (number of challenge gas molecules that can be adsorbed). Using this  $\text{NO}_2$  concentration limit in the flowrate relationship in Section 4.2.1, a  $770\text{ ppm}$   $\text{NO}_2$  concentration exposure for 46 hours yielded approximately  $10^{20}$  molecules of  $\text{NO}_2$  at STP. The resulting infrared spectrum for this exposure is shown in Figure 124. It is apparent that a significant reduction in infrared transmission occurs over the entire band when this spectrum is compared with that in Figure 121. Additionally, at least four new peaks are evident (located at  $830$ ,  $1040$ ,  $1780$ , and  $2000\text{ cm}^{-1}$ ).

Subsequent purging of the sample at  $150^\circ\text{C}$  for 1.5 hours in nitrogen resulted in a spectrum which contained most of the pre-exposed features, with the exception of the  $1360\text{ cm}^{-1}$  peak (see Figure 125). This behavior indicates that  $\text{NO}_2$  is only partially (although significantly) desorbed from a CuPc sample under these test conditions (which, admittedly, were extreme). Entrapment of  $\text{NO}_2$  in the bulk of the CuPc thin film is hypothesized as a significant factor for the irreversible adsorption behavior (45). Since the challenge gas concentrations and exposure times for the MMGC and the chemiresistor were

<sup>4</sup>Using a Model 683 Infrared Spectrophotometer, Perkin-Elmer, Garden Grove, CA.

<sup>5</sup>Approximately  $3500\text{ \AA}$  deposited upon each side of the one-inch diameter sodium chloride substrates.

much less than those which the infrared sample was subjected to, essentially complete reversibility was anticipated with an elevated temperature purge. A normalized IR spectrum peak comparison between the pre-exposed, NO<sub>2</sub> exposed, and elevated temperature purged spectra is shown in Figure 126.

A similar procedure on a fresh, 7700 Å thick, CuPc sample was investigated to determine if NH<sub>3</sub> adsorption was detectable using infrared spectroscopy. Unfortunately, the results were not as dramatic as those for NO<sub>2</sub>. Figure 122 shows the infrared spectrum for the pre-exposed 7700 Å thick CuPc sample used in this experiment, and Figure 127 shows the spectrum after this sample was exposed to a 3700 ppm NH<sub>3</sub> challenge gas concentration for approximately 3 hours (which resulted in approximately the same number of challenge gas molecules as in the NO<sub>2</sub> test— $10^{20}$  molecules).

From Figures 122 and 127, it appears that there was no significant change in the infrared spectrum. Subsequent purging at 150°C for 1.5 hours (see Figure 128) yielded essentially the same spectrum as that which appears in Figures 122 and 127, indicating that either the adsorbed NH<sub>3</sub> was rapidly desorbed as the sample was transported from the challenge gas exposure chamber to the infrared spectrometer (located in a separate building), or that NH<sub>3</sub> adsorption does not cause dramatic changes in the infrared spectrum of CuPc. The normalized IR spectrum peak comparison shown in Figure 129 confirms the absence of a significant change.

Although the NH<sub>3</sub> spectra were not conclusive for verifying the adsorption of NH<sub>3</sub> on CuPc, the infrared spectra as a whole did demonstrate and verify several important aspects of this research. First, the experimentally deposited CuPc thin films have comparable infrared characteristics to the standard reference CuPc films (on a potassium bromide substrate) (142). Second, NO<sub>2</sub> adsorption on CuPc does take place. Third, elevated temperature purges facilitate the desorption of NO<sub>2</sub> from CuPc.

*B.2.2 Scanning Electron Microscopy.* Scanning Electron Microscopy (SEM) was used to verify the morphology of the deposited CuPc films during the fabrication phase (see Section 5.3.1). From the micrographs presented in Section 5.3.1, it is apparent that the CuPc crystallites form a columnar structure that is relatively uniform over the scale of

the micromachined column. To further verify the quality of the experimentally deposited CuPc films, one final set of analytical tools was used: transmission electron microscopy and transmission electron diffraction.

**B.2.3 Transmission Electron Microscopy (TEM) and Transmission Electron Diffraction (TED).** To lend further support to characterize the CuPc thin films used in this investigation, and to provide information concerning crystallite size, transmission electron microscopy<sup>6</sup> (TEM) was conducted on CuPc thin films evaporated onto a carbon grid using the technique described in Section 5.3.1. Figure 130 shows the polycrystalline nature of the sublimed CuPc thin films. From this micrograph, it is apparent that the film is composed of a conglomeration of crystallites which have a 300 Å approximate average radius.

A transmission electron diffraction (TED) micrograph was also taken and compared with reported values. The results are shown in Figure 131 and Table 16. Based on the favorable correspondence between the reported and actual spacings of the diffraction rings, along with the infrared spectroscopy data, it was concluded that polycrystalline high purity CuPc thin films could be deposited using the technique described in Section 5.3.1.

Table 16. Calculated and Experimental Values for Copper Phthalocyanine Crystal Plane Spacings.

Miller Index	Reported Spacing (143) (Å)	Experimental Spacing (Å)	Error (%)
(200)	12.96	12.96	0
(002)	11.96	11.94	0.2
(202)	8.76	8.96	-2.3
(400)	6.48	6.55	-1.1
(004)	5.98	5.97	0.2
(402)	5.68	5.59	1.6
(600)	4.32	4.35	-0.7

<sup>6</sup>Using a Model 2000FX Transmission Electron Microscope, Jeol USA Incorporated, Peabody, MA.

### ***B.3 Summary.***

This appendix presented an abbreviated tutorial concerning CuPc, including a description of the effects of its structure on gas adsorption. Additionally, two separate studies were conducted to verify the purity and composition of the CuPc films. The infrared study confirmed the chemical composition of the CuPc films, and the fact that NO<sub>2</sub> could be reversibly adsorbed. The TEM and TED studies provided additional, independent support concerning the composition of the film and the size of the CuPc crystallites.

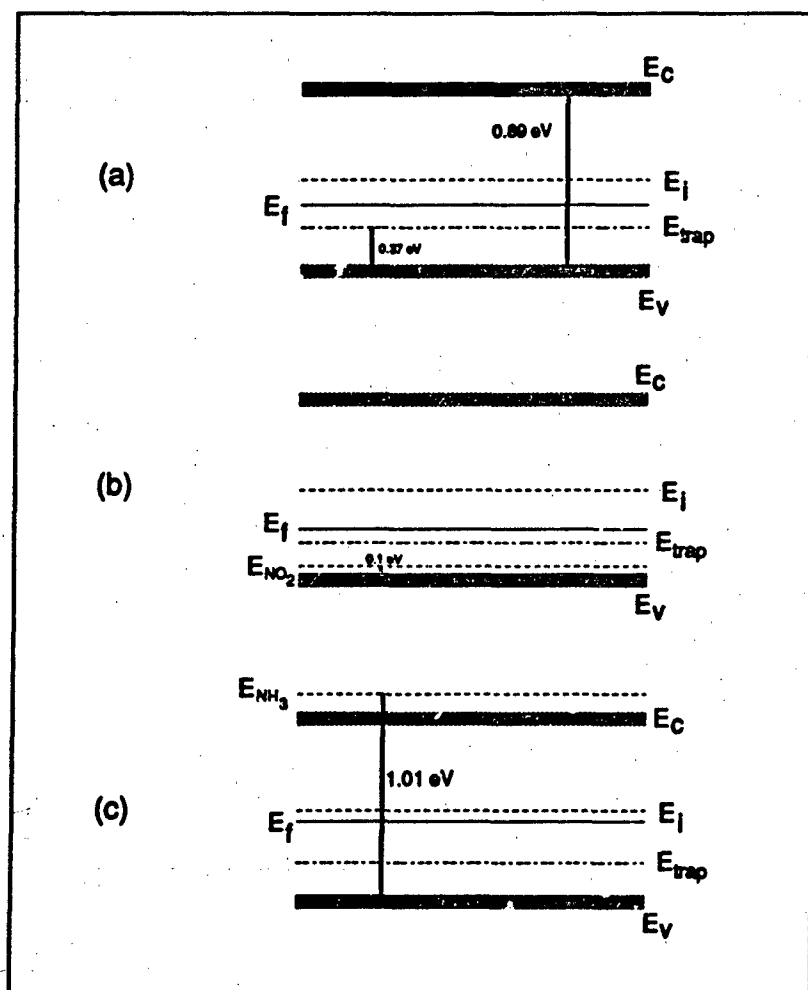


Figure 118. Simplified Energy Band Structure of a Copper Pthalocyanine Polycrystalline p-Type Semiconductor (a) in Vacuo, (b) Saturated with  $NO_2$ , and (c) Saturated with  $NH_3$  (43, 45, 122).

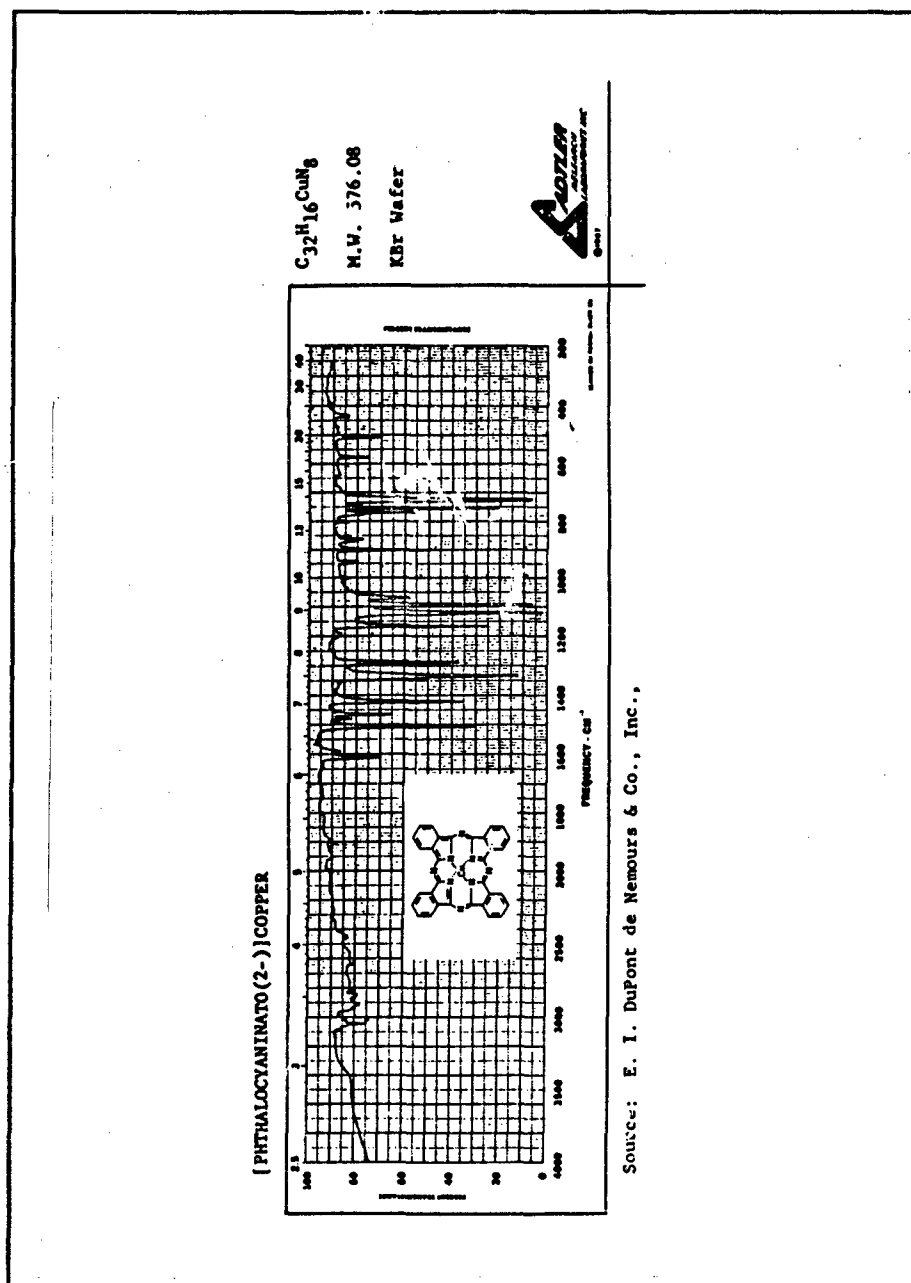


Figure 119. Infrared Spectrum for Alpha-Phase Copper Phthalocyanine (142).



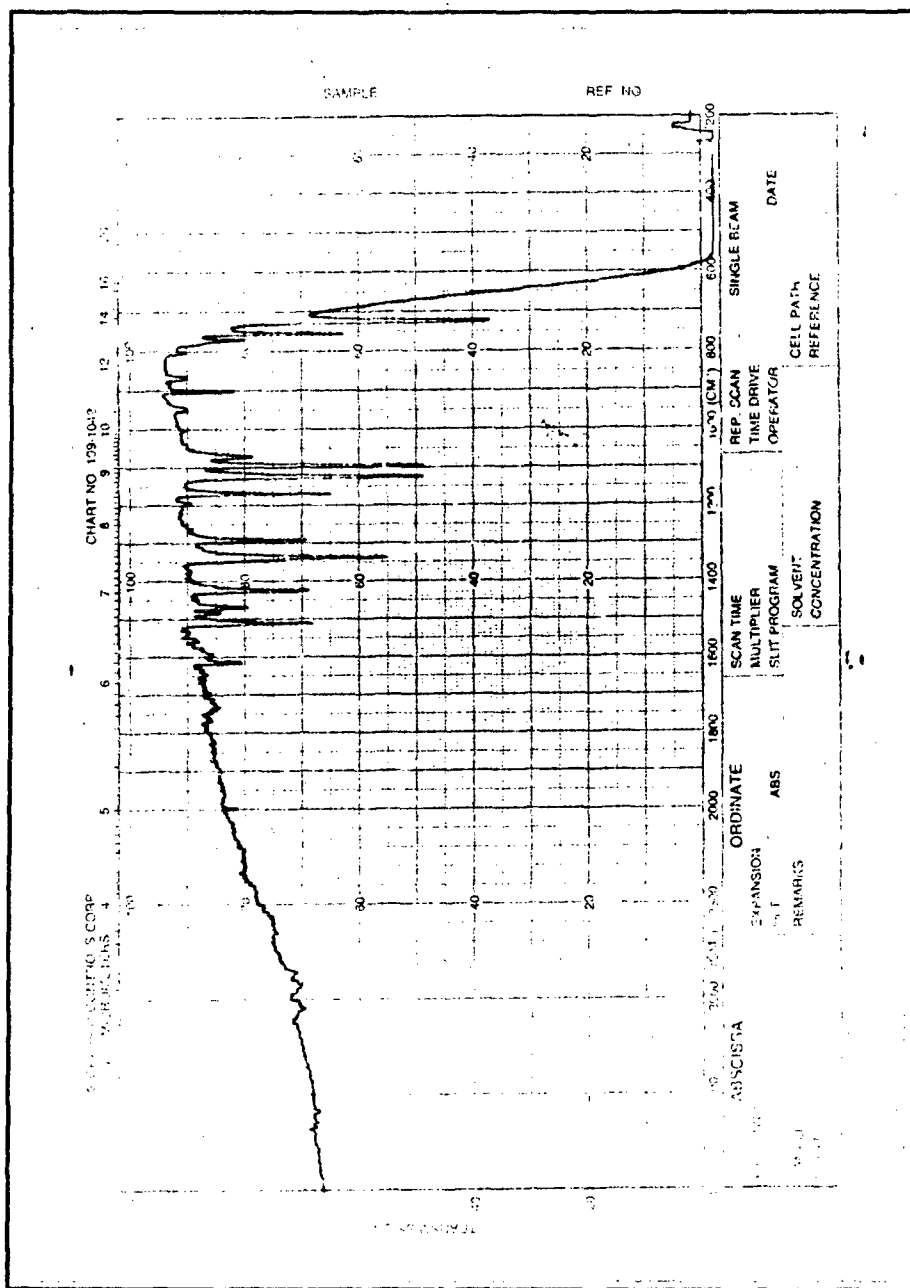


Figure 121. Infrared Spectrum for the 6600 Å Thick Copper Phthalocyanine Thin Film Sublimed onto a Sodium Chloride Substrate.

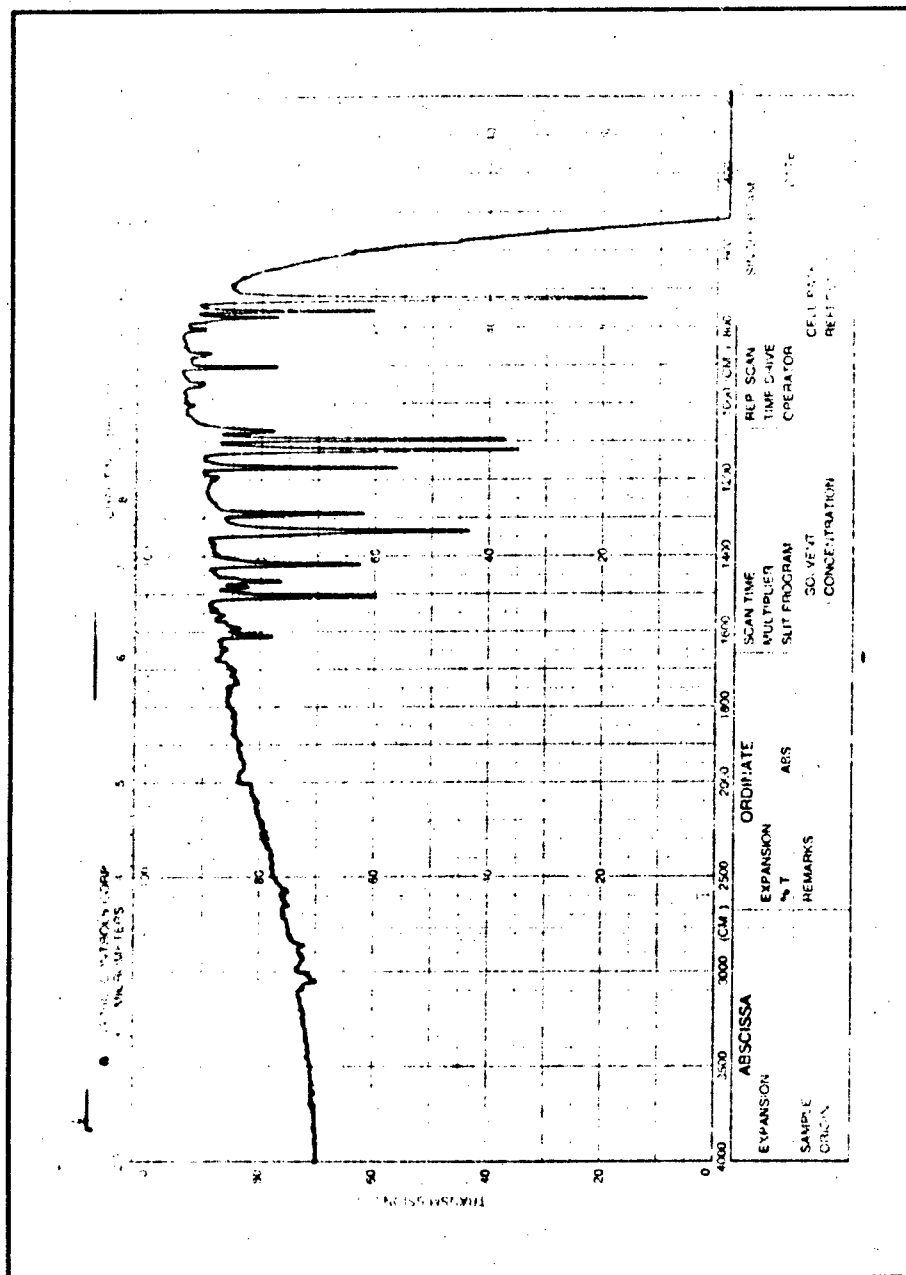


Figure 122. Infrared Spectrum for the 7700 Å Thick Copper Phthalocyanine Thin Film Sublimed onto a Sodium Chloride Substrate.

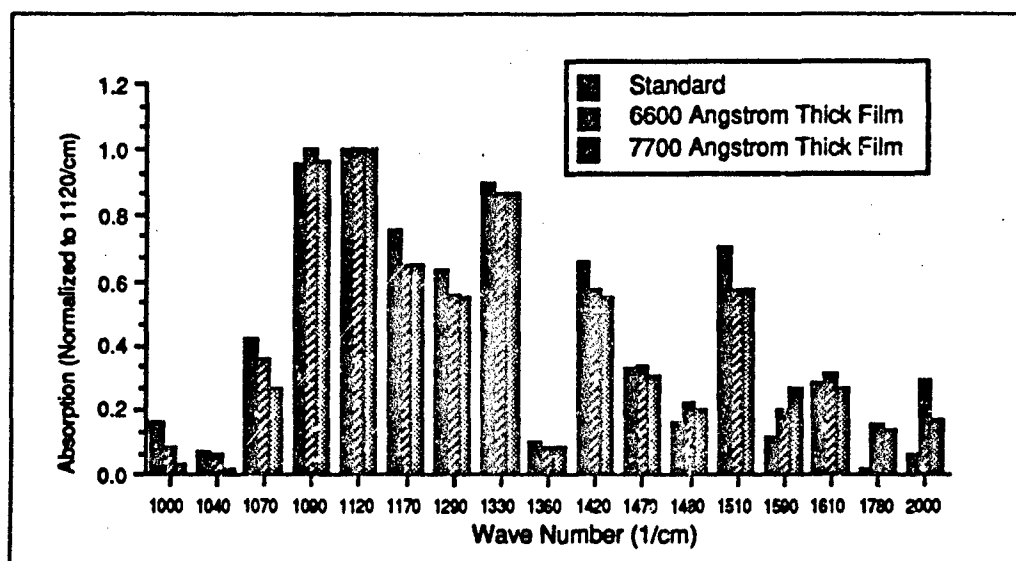


Figure 123. Infrared Absorption Peaks from the Spectra for the 6600 Å and 7700 Å Thick, Experimentally Deposited Thin Films of Copper Phthalocyanine Compared to Reported Peaks (Normalized with Respect to the 1120  $\text{cm}^{-1}$  Peak) (142).

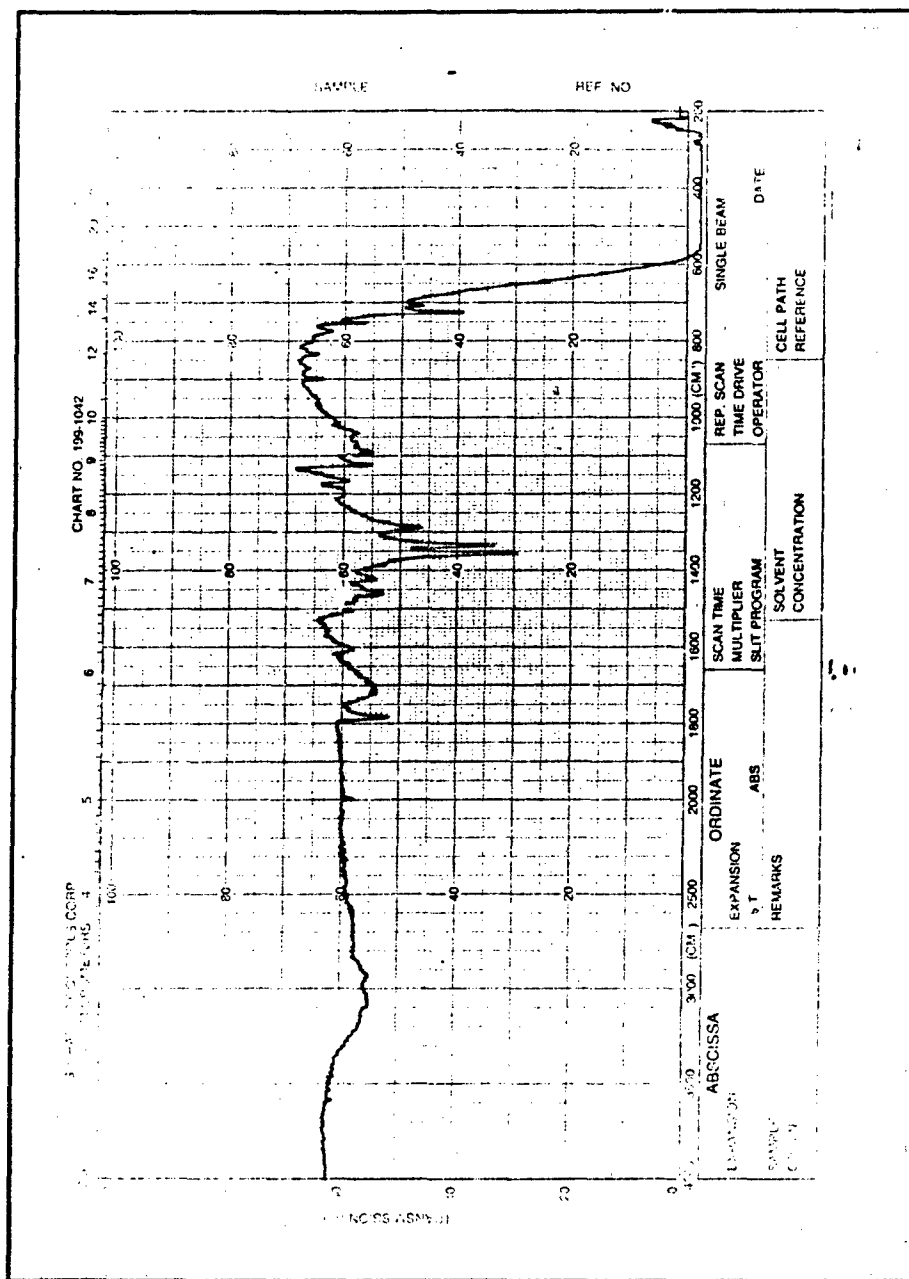


Figure 124. Infrared Spectrum for the 6600 Å Thick Copper Phthalocyanine Thin Film Sublimed onto a Sodium Chloride Substrate after Exposure to 770 ppm NO<sub>2</sub> for 46 hours.

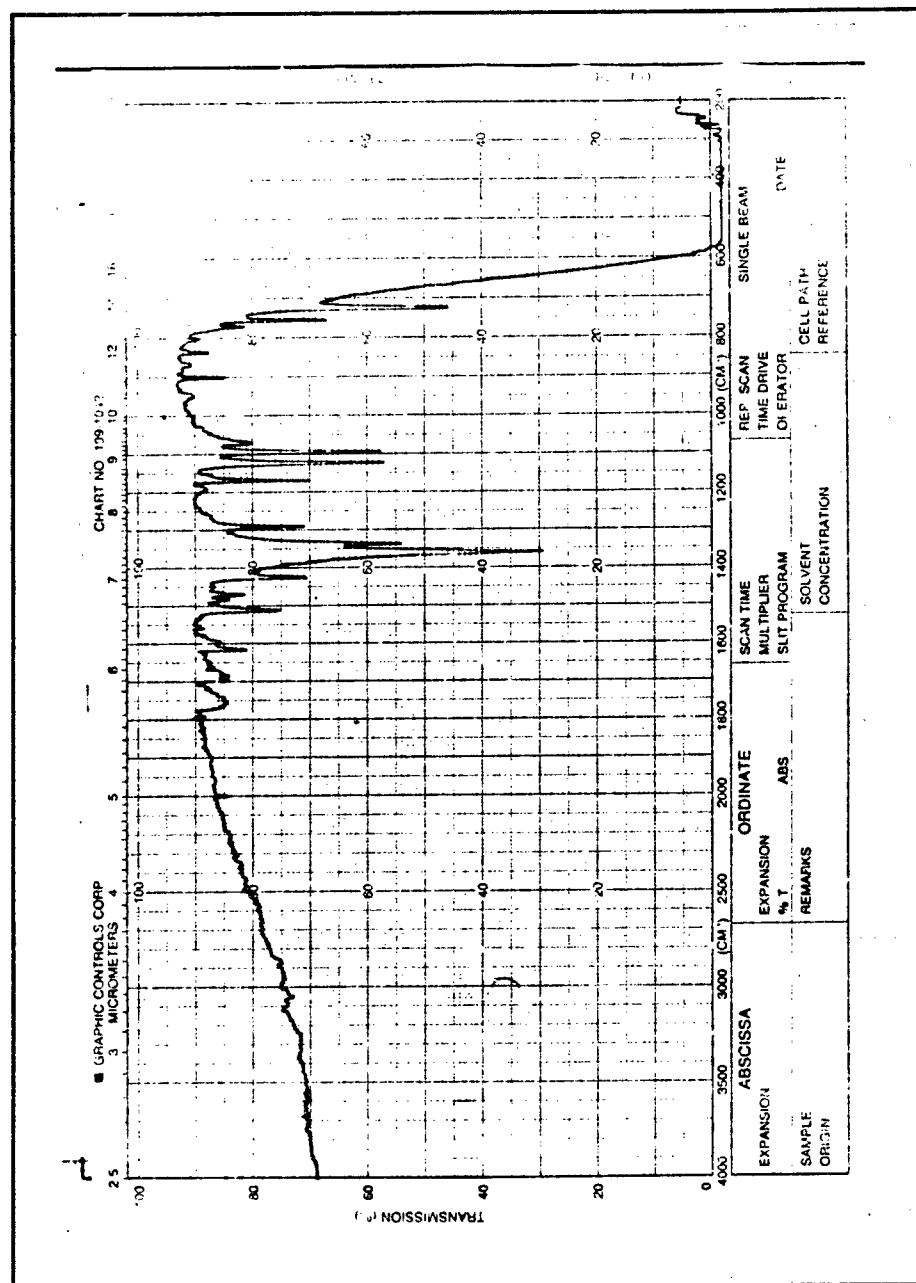


Figure 125. Infrared Spectrum for the 6600 Å Thick Copper Phthalocyanine Thin Film Sublimed onto a Sodium Chloride Substrate after Exposure to 770 ppm  $\text{NO}_2$  for 46 hours and Subsequent Purging at  $150^\circ\text{C}$  in a Nitrogen Ambient for 1.5 hours.

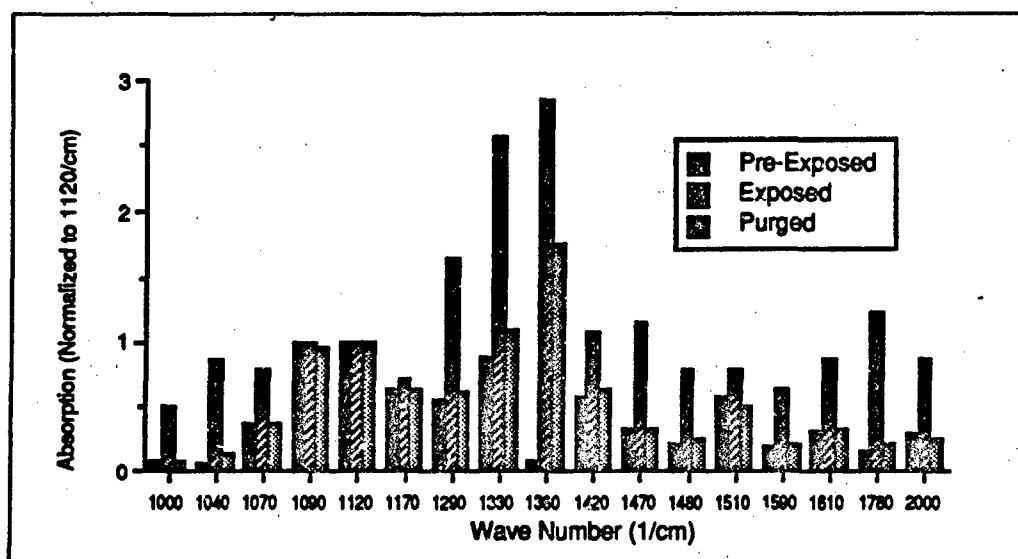


Figure 126. Infrared Absorption Peaks from the Spectra for the 6600 Å Thick Copper Phthalocyanine Thin Film for the Pre-Exposed, 770 ppm NO<sub>2</sub> Exposed, and Purged Conditions (Normalized with Respect to the 1120 cm<sup>-1</sup> Peak).

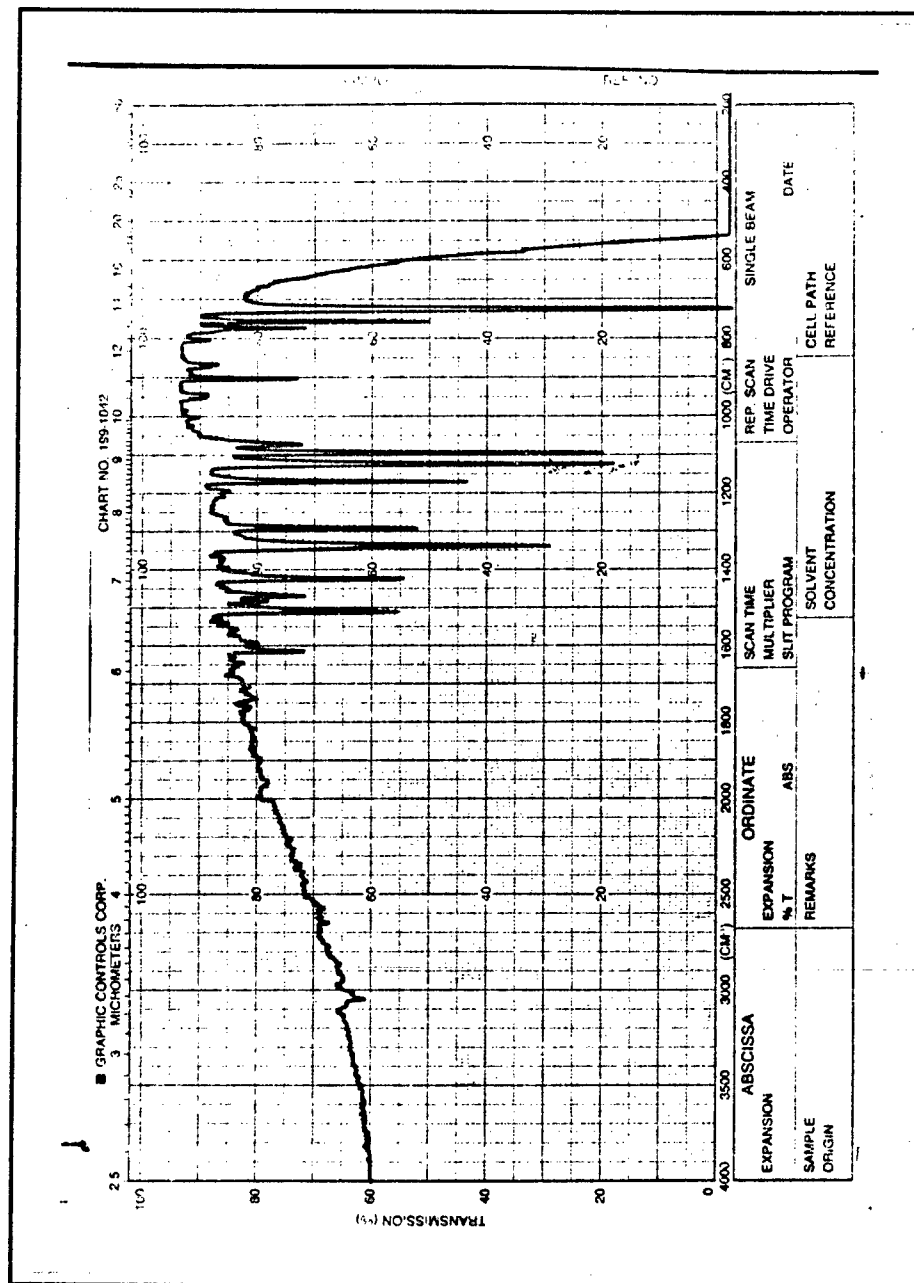


Figure 127. Infrared Spectrum for the 7700 Å Thick Copper Phthalocyanine Thin Film Sublimed onto a Sodium Chloride Substrate after Exposure to 3700 ppm  $\text{NH}_3$  for 3 hours.

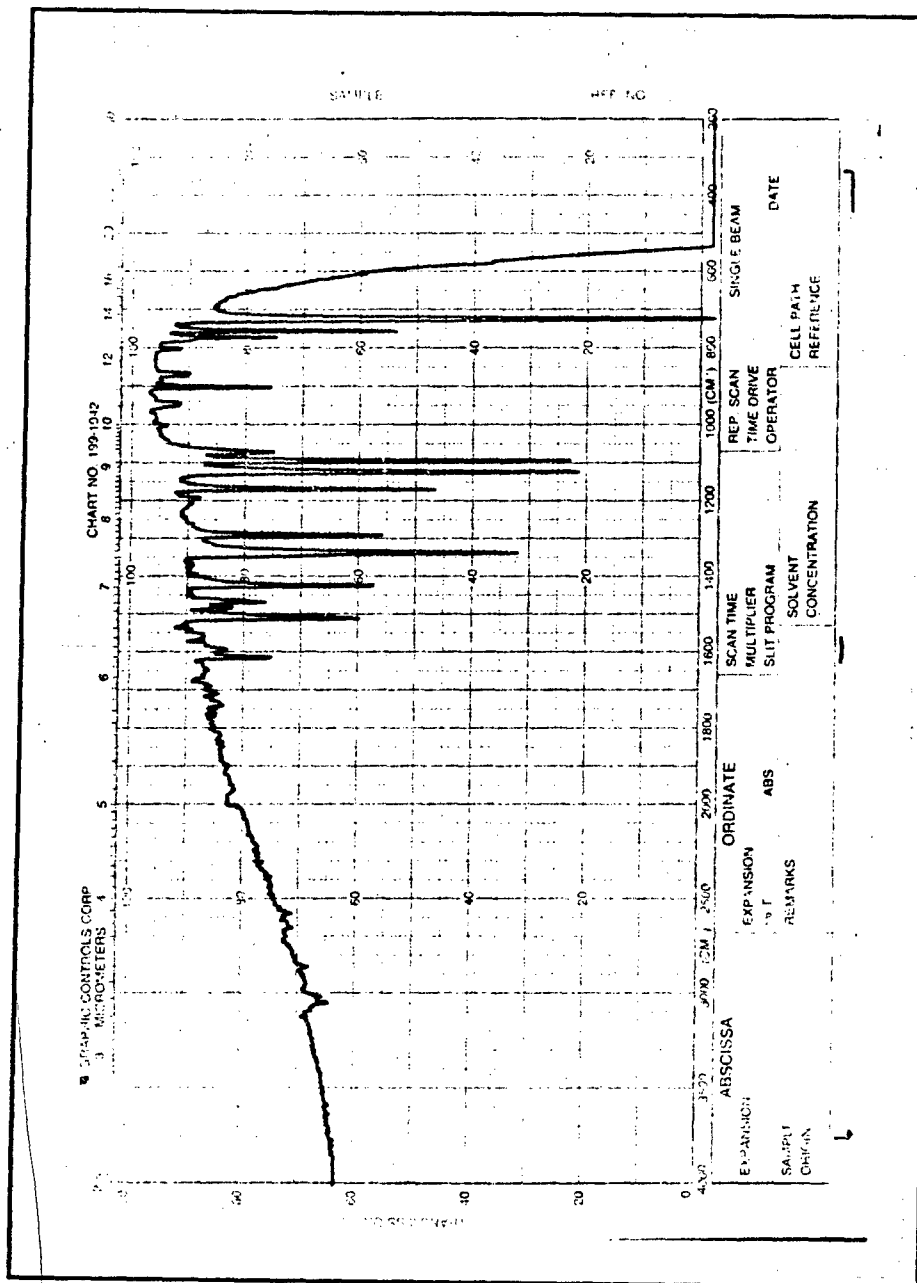


Figure 128. Infrared Spectrum for the 7700 Å Thick Copper Phthalocyanine Thin Film Sublimed onto a Sodium Chloride Substrate after Exposure to 3700 ppm  $\text{NH}_3$  for 3 hours and Subsequent Purging at  $150^\circ\text{C}$  in a Nitrogen Ambient for 1.5 hours.

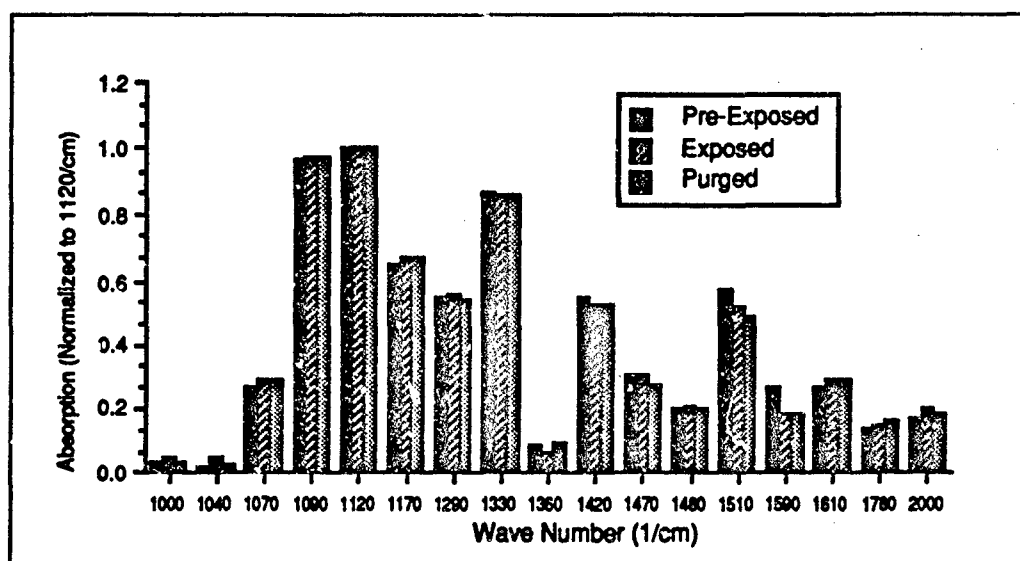
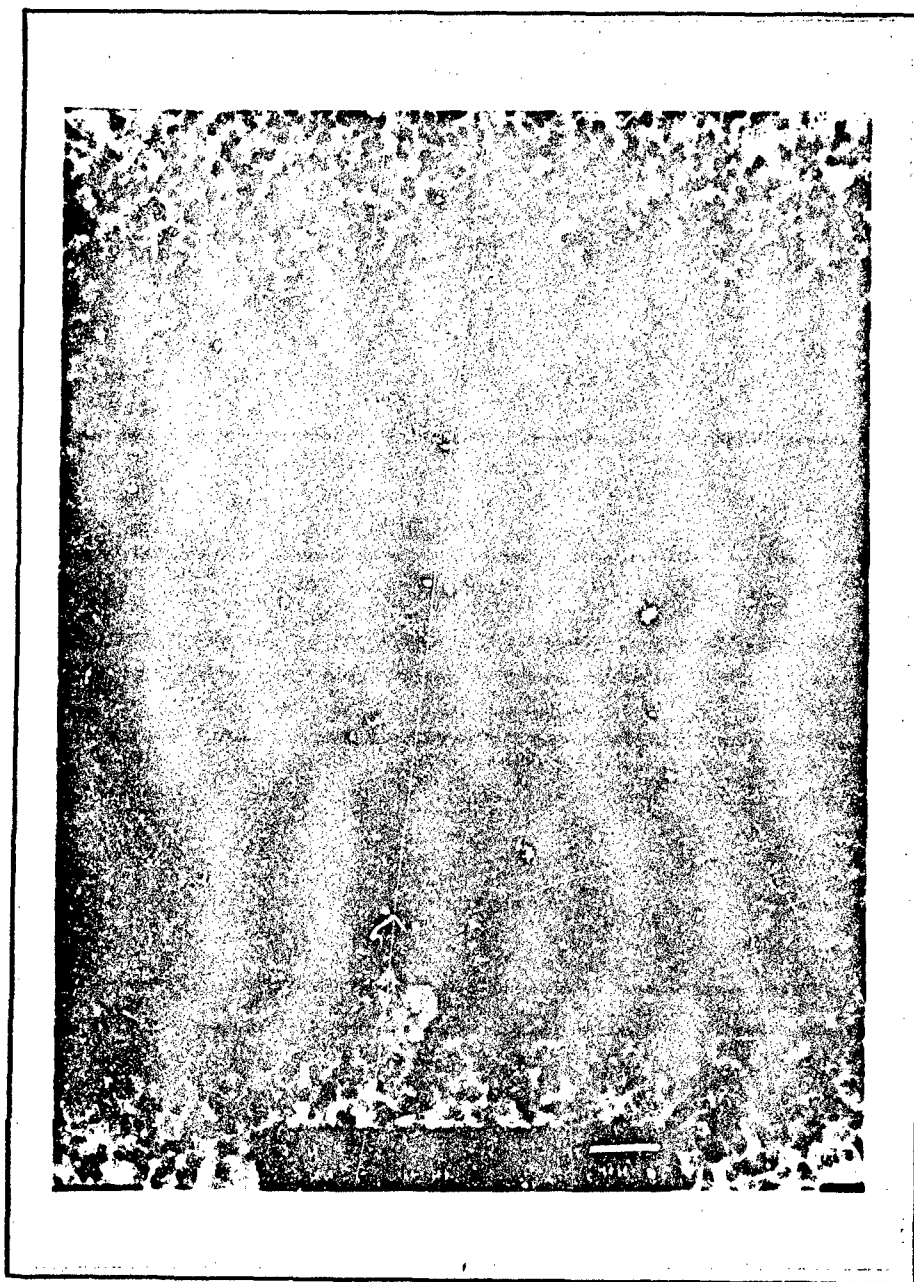
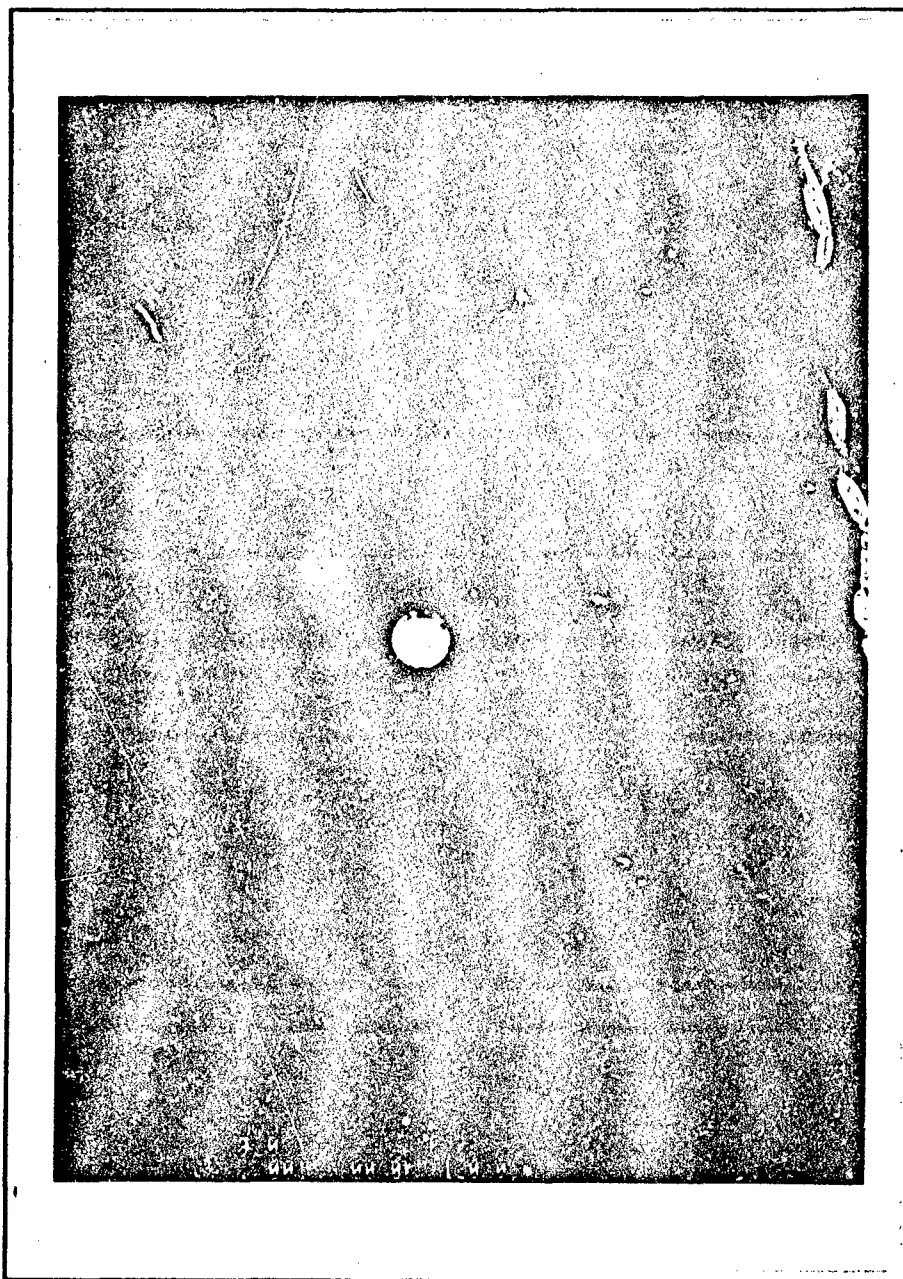


Figure 129. Infrared Absorption Peaks from the Spectra for the 7700 Å Thick Copper Phthalocyanine Thin Film for the Pre-Exposed, 3700 ppm NH<sub>3</sub> Exposed, and Purged Conditions (Normalized with Respect to the 1120 cm<sup>-1</sup> Peak).



**Figure 130.** Transmission Electron Micrograph for a 500 Å Thick Copper Phthalocyanine Thin Film Sublimed onto a Carbon Grid.



**Figure 131.** Electron Diffraction Pattern for a 500 Å Thick Copper Phthalocyanine Thin Film Sublimed onto a Carbon Grid.

### Appendix C. *Experimental Characterization of the Adsorption Effects of NO<sub>2</sub> on the Electrical Conductivity of Copper Phthalocyanine*

In order to model the interaction between NO<sub>2</sub> and the solid phase CuPc thin film used in the MMGC<sup>1</sup>, it was necessary to develop a more fundamental model for the electronic effects of NO<sub>2</sub> adsorption on the chemiresistor. To accomplish this objective, experimental values for the adsorption lifetime and probability of adsorption were determined by fitting the chemiresistor's response data to a resistance model of the chemiresistor.

#### C.1 *Langmuir Adsorption.*

The basis for the chemiresistor model is the Langmuir adsorption theory. Basically, Langmuir assumed that adsorption onto a solid surface occurred at a rate proportional to the uncovered surface, and stopped once monolayer coverage was attained. This phenomena can be represented by the following differential equation (144):

$$\frac{d\Theta}{dt} = \alpha P(1 - \Theta) - \beta\Theta \quad (83)$$

where  $\Theta$  is the normalized surface coverage,  $P$  is the gas pressure,  $\alpha$  represents the number of gas molecules arriving at the solid surface per unit pressure, and  $\beta$  represents the number of adsorbed gas molecules leaving the solid surface. The quantity,  $\alpha P(1 - \Theta)$ , represents the rate at which gas molecules are adsorbed, while the quantity,  $\beta\Theta$ , represents the rate at which the adsorbed gas molecules are desorbed. For NO<sub>2</sub> adsorption on CuPc, Langmuir's theory will be modified to take into account the assumption that only a portion of the adsorbed NO<sub>2</sub> molecules are bound strongly enough to affect the electrical conductivity of the CuPc film. This adsorption ratio,  $a_r$ , is multiplied by the surface coverage in Equation 83, yielding:

$$\frac{d\Theta}{dt} = \alpha P(1 - a_r\Theta) - \beta a_r\Theta \quad (84)$$

<sup>1</sup>Since the chemiresistor was sensitive to NH<sub>3</sub> concentrations greater than the estimated capacity of the column, valid adsorption data was obtained only for NO<sub>2</sub>. Thus, the model was developed solely for NO<sub>2</sub>.

Solving Equation 84 for  $\Theta$  (by simply integrating the reciprocal of the right-hand side and applying the boundary condition that  $\Theta = 0$  at  $t = 0$ ), yields:

$$\Theta = \frac{\alpha P}{a_r(\alpha P + \beta)} \{1 - \exp[-a_r(\alpha P + \beta)t]\} \quad (85)$$

where  $\alpha$  and  $\beta$  are further defined by (144):

$$\alpha = \frac{\kappa s}{\sqrt{2\pi M k_b T}} \quad (86)$$

and

$$\beta = \nu \exp(-E_a/k_b T). \quad (87)$$

In Equations 86 and 87,  $\kappa$  is the sticking probability for a given molecule striking the solid surface,  $s$  is the effective surface area of the gas molecule,  $k_b$  is Boltzmann's constant,  $T$  is the absolute temperature,  $M$  is the mass of the gas molecule,  $1/\nu$  is the adsorption lifetime constant, and  $E_a$  is the adsorption energy (obtained from the MMGC data). These values (in particular,  $\kappa$  and  $\nu$ ) are essential for modeling the adsorption processes in the MMGC.

## C.2 Chemiresistor Electrical Impedance.

Unfortunately, the preceding model could be used directly only if there were some way of determining the surface coverage. Since the only information available is the chemiresistor's electrical impedance as a function of time, the Langmuir model must be modified to account for the electrical resistance change upon gas adsorption. This objective can be accomplished by assuming that the two-terminal, macroscopic resistance between the driven and reference electrodes of the chemiresistor is comprised of multiple, *independent* elementary paths (see Figure 132). Each of these elementary paths being further composed of identical one-dimensional distributed resistors, where each distributed resistor can exist in only one of two states (corresponding to either the purged or  $\text{NO}_2$  adsorbed states). If the total number of "resistors" along any elementary path is  $N$ , the overall

resistance of the chemiresistor (by normalizing the parallel contribution by treating each filament as identical),  $R_{tot}$ , is given by:

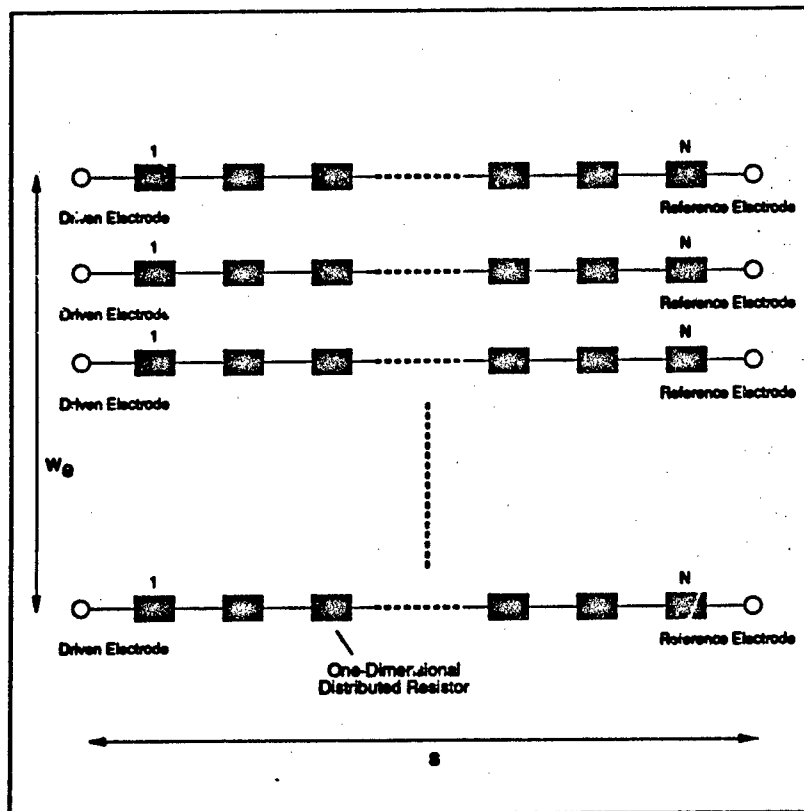


Figure 132. Resistive Filaments in the Chemiresistor's Electrical Impedance Model.

$$R_{tot} = \sum_{i=1}^{N_A} R_A + \sum_{i=1}^{N-N_A} R_P \quad (88)$$

where  $N_A$  is the number of "resistors" with  $\text{NO}_2$  adsorbed,  $R_A$  is the resistance of a "resistor" with  $\text{NO}_2$  adsorbed, and  $R_P$  is the resistance of a "resistor" which has no gas species adsorbed (the purged state). Since  $R_A$  and  $R_P$  are assumed to be constant values (identical distributed resistor elements), Equation 88 can be reduced to:

$$R_{tot} = N_A R_A + (N - N_A) R_P = N_A (R_A - R_P) + N R_P. \quad (89)$$

If Equation 89 is normalized with respect to  $N$ , it becomes:

$$R_{norm} = \Theta(R_A - R_P) + R_P \quad (90)$$

where  $\Theta = N_s/N$  (which is a metric for the normalized surface coverage) is given by Equation 85. Combining Equations 85 and 90 yields:

$$R_{norm} = R_P + \frac{(R_A - R_P)\alpha P}{a_r(\alpha P + \beta)} \{1 - \exp[-a_r(\alpha P + \beta)t]\} \quad (91)$$

which is a non-linear equation with six parameters ( $R_P$ ,  $R_A$ ,  $\alpha$ ,  $P$ ,  $a_r$ , and  $\beta$ ) that correlates time with the chemiresistor's electrical impedance.

A series of experiments, similar to the chemiresistor evaluation reported in Section 6.3, was performed to obtain data which could be analyzed with Equation 91. The only major difference in the test protocol involved the removal of the sample injection system. Since the chemiresistor had to be exposed to a continuous concentration of the  $\text{NO}_2$  challenge gas, the sample injection system was replaced with a simple manual valve. Three concentrations (100 ppb, 200 ppb, and 400 ppb) were tested for three exposure trials (each approximately 20 min in duration). Utilization of the reduced concentrations were necessary because the challenge gas was no longer a pulse generated by the sample injector.

### C.3 Parameters.

Non-linear least-squares curve fits using Equation 91 (the program is included in Appendix E) yielded an  $\alpha$  of  $3.84 \times 10^{-4} (\text{ppb} \cdot \text{min})^{-1}$ , a  $\beta$  of  $1.25 (\text{min})^{-1}$ , and an  $a_r$  of approximately 10 percent. Using Equations 86 and 87,  $\kappa$  is  $2.9 \times 10^{-5}$  and  $\nu$  is  $2900 \text{ sec}^{-1}$ . This information was then used in Section 7.1 to implement the MMGC model.

### C.4 Current Response.

As a side note, the 10 percent  $a_r$  was used to determine if the number of majority carriers (holes for a p-type semiconductor) generated by the  $\text{NO}_2$  challenge gas exposure was on the order of the change in the current of the chemiresistor observed during the MMGC evaluations. If the magnitude of the current change,  $\Delta I$ , is assumed to be caused

entirely by the additional carriers created by NO<sub>2</sub> "doping" (see Figure 118), the following expression can be used to predict the value of  $\Delta I$  (89):

$$\Delta I = q n_{conc} \mu_p \frac{V}{s} w_e T_f \quad (92)$$

where  $q$  is the fundamental unit of charge for an electron,  $n_{conc}$  is the effective NO<sub>2</sub> concentration (electron acceptors that enhance the effective concentration of mobile holes),  $\mu_p$  is the hole mobility in CuPc,  $V$  is the voltage applied to the chemiresistor,  $s$  is the interelectrode spacing,  $w_e$  is the effective width of the chemiresistor (see Equation 50), and  $T_f$  is the CuPc film's thickness. With the exception of  $n_{conc}$ , all of these variables either have published values, or have values which are easily determined from the chemiresistor design.

In order to establish a reasonable value for  $n_{conc}$ , it is necessary to make several assumptions. First, the total number of NO<sub>2</sub> molecules which could contribute to  $n_{conc}$  is a fraction of the number of helium molecules,  $n_h$ , which are within one mean free path ( $\lambda$ ) of the active area ( $w_e s$ ) of the chemiresistor's CuPc-coated surface<sup>2</sup> (see Figure 133). The value of this fraction is given by:  $n_h \lambda w_e s$ . Second, this fraction is based upon the effective probability of adsorption,  $a_r \kappa$ , and the reduced<sup>3</sup> NO<sub>2</sub> injected concentration,  $i_{conc} v_{loop} / v_{gc}$ . Thus, the value of  $n_{conc}$  can be estimated from the following relationship:

$$n_{conc} w_e s T_f = a_r \kappa \frac{v_{loop} i_{conc}}{v_{gc}} n_h \lambda w_e s \quad (93)$$

which reduces to:

$$n_{conc} = \frac{a_r \kappa \frac{v_{loop} i_{conc}}{v_{gc}} n_h \lambda}{T_f} \quad (94)$$

where  $\kappa$ , the sticking probability, and  $a_r$ , the adsorption ratio are given in Section C.3,  $v_{gc}$  is the total volume of the MMGC (both the column and the chemiresistor's cavity—approximately 70  $\mu$ l)  $v_{loop}$  is the volume of the sample loop (10  $\mu$ l),  $n_h$  is defined by

<sup>2</sup>The active area is simply the product of the effective width of the chemiresistor and the length of the chemiresistor (the interelectrode spacing).

<sup>3</sup>The injected concentration,  $i_{conc}$ , is reduced by the ratio of the sample loop volume,  $v_{loop}$ , to the increased volume associated with the MMGC column and the chemiresistor cavity,  $v_{gc}$ .

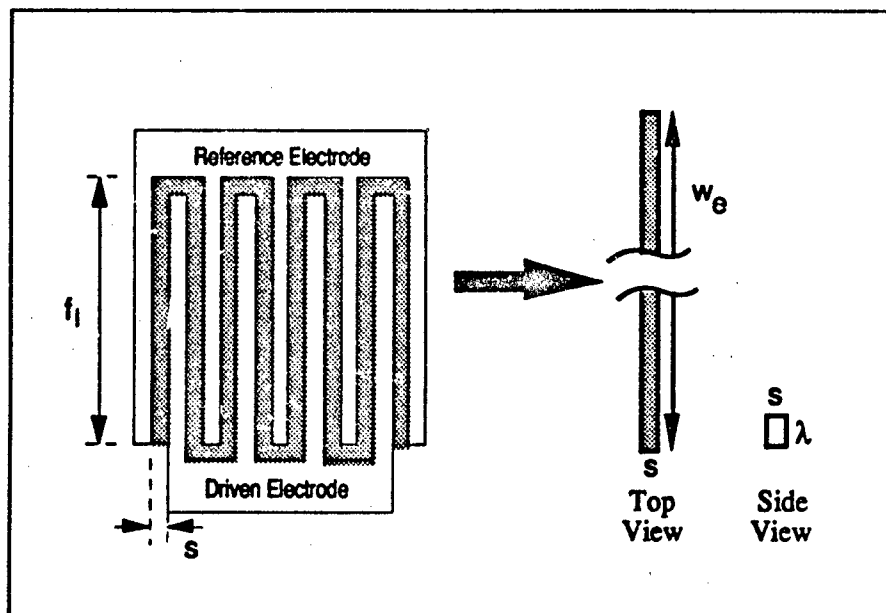


Figure 133. Active (shaded) Area of the Interdigitated Chemiresistor Mapped into a Continuous Chemiresistor of Width,  $w_e$ , and Length,  $s$ . The Edge View Depicts the Volume of Gas Within One Mean Free Path,  $\lambda$ , of the Active Area of the Chemiresistor.

Equation 70,  $\lambda$  is defined by Equation 71, and  $i_{conc}$  is the injected concentration (in the sample loop).

Combining Equations 92 and 94 along with  $\mu_p = 0.2 \text{ cm}^2/(\text{Volt} \cdot \text{sec})$  (129) and an  $i_{conc}$  of 75 ppm, yields a  $\Delta I$  value of approximately 3 pA, which corresponds well with the 1 pA to 3.5 pA values experimentally observed (see Appendix I).

#### Appendix D. *Micromachined Gas Chromatograph Model Program*

The following computer program implements the MMGC model discussed in Chapter 7 using the Turbo Pascal programming language (145). This program is divided into three functional areas. The first functional area consists of variable declarations, the second functional area consists of subroutine declarations, and the third functional area is the main program. Figure 134 depicts the logical flow of the main program. In the `initialize` subroutine, a random starting location is chosen for the simulated molecule. The `move` subroutine takes into account diffusion and longitudinal flow in calculating the current position of the simulated molecule. If the location of the molecule is at the boundary (where the stationary phase is located), the `at boundary` check increments the time variable using the `adsorb` subroutine. Finally, the longitudinal location of the molecule is checked ( $x > L$ ) to determine if it is still in the column. If the molecule is still in the column, the entire process is repeated. Each of the components of the main program are described in greater detail in the following sections.

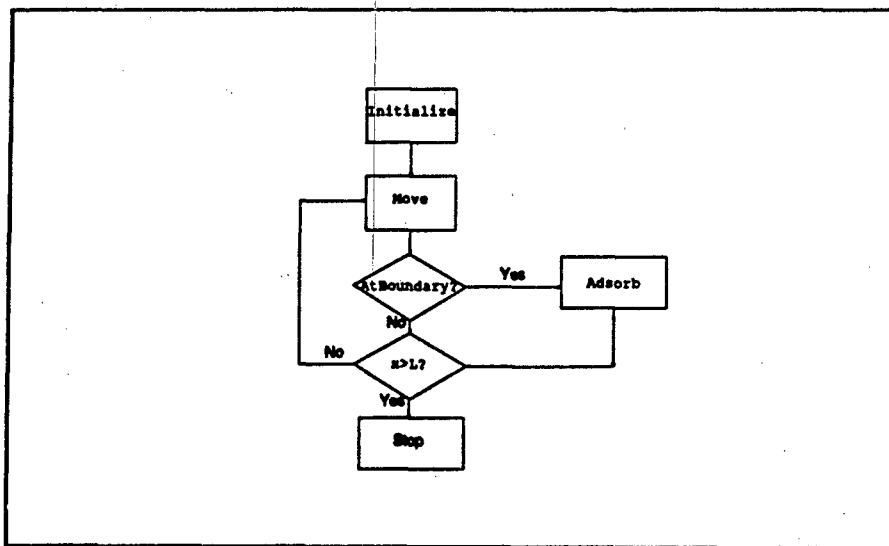


Figure 134. Logical Flow of the Computer Program for the Micromachined Gas Chromatograph Model.

### D.1 Variable Declarations.

The real (floating-point) variables are listed alphabetically with a short description. The actual program code is presented with a distinctive typeface (i.e., program GCMModel) to set it apart from the explanatory remarks.

```
program GCMModel;
uses crt,dos;
var
  coll,      {N02 Collision Frequency}
  d,         {Diffusion Distance per Time Interval}
  dc,        {Diffusion Constant (N02 in Helium)}
  k,         {Boltzmann's Constant}
  L,         {Column Length}
  mfp,       {Mean Free Path (N02 in Helium)}
  mhe,       {Mass of Helium Molecule}
  mno2,      {Mass of N02 Molecule}
  mtbc,      {Mean Time Between Collisions}
  nconc,     {Helium Density}
  no2surf,   {N02 Surface Area}
  nu,        {Experimental Lifetime Constant}
  pav,       {Average Pressure}
  pin,       {Input Pressure}
  po,        {Output Pressure}
  prob,      {Individual Collision Sticking Probability}
  ps,        {Present Time in Seconds (used for run-time)}
  q,         {Column Permeability}
  R,         {Gas Constant}
  she,       {Helium Collisional Diameter}
  sno2,      {N02 Collisional Diameter}
  sqrpipo,   {Pre Calculated Constant--(pin/po)^2}
  stick,     {Total Sticking Probability in One Time Interval}
  t,         {Time Variable}
  temp,      {Temperature}
  ti,        {Time Interval}
  t0,        {Average Adsorbed Lifetime}
  vav,       {Average Velocity of N02 in Helium}
  visc,      {Helium Viscosity}
  vo,        {Output Velocity}
  w,         {Column Width}
  x,         {x-Position Variable for Molecule Location}
  y,         {y-Position Variable for Molecule Location}
  z,         {z-Position Variable for Molecule Location}
  zo         {Column Half-Height}
```

```

: single;
i,j,numits: integer;      {Iteration Variables}
rt: array[0..512] of single; {Retention Time Array}
fname, comments: string;  {Filename and Comments}
ofile: text;              {Output File Variable}
h,m,s,s100: word;         {Used to Access System Time}

```

Although not strictly necessary, the following arrays are augmented with the values indicated when the program is executed to improve the performance of the model (in terms of computational time) by a factor of ten.

```

{The following tables are used to reduce computational time.}
cosarrpi,      {Cosine Lookup Table: 0 to Pi}
sinarrpi,      {Sine Lookup Table: 0 to Pi}
cosarrpi2,     {Cosine Lookup Table: 0 to 2Pi}
sinarrpi2,     {Sine Lookup Table: 0 to 2Pi}
: array[0..255] of single;

```

```

{The following variables are used to implement the
random number generation routines from
"Numerical Recipes in C"}
RanOY: single;
ri: integer;
RanOV: array [1..97] of single;
GasdevIset: integer;
GasdevGset: real;

```

## D.2 Subroutine Declarations.

The first two subroutines (ran0 and gasdev) generate uniform and gaussian random number distributions, respectively. Both subroutines were borrowed from the *Numerical Recipes in Pascal* disk (146). The uniform distribution is used in the random molecular movement calculations, and the gaussian distribution is used to generate an adsorbed lifetime based upon the average adsorbed lifetime.

```

function ran0(var idum: integer): single;
var
  dum: real;
  j: integer;

```

```

begin
  if idum < 0 then begin
    {RandSeed := -idum;}Randomize;
    idum := 1;
    for j := 1 to 97 do
      dum := Random;
    for j := 1 to 97 do
      RanOV[j] := Random;
    RanOY := Random;
  end;
  j := 1+trunc(97.0*RanOY);
  if (j > 97) OR (j < 1) then begin
    repeat j:=1+trunc(97.0*Random); until ((j<98) and (j>0));
  end;
  RanOY := RanOV[j];
  ran0 := RanOY;
  RanOV[j] := Random
end;

function gasdev(var idum: integer): real;
var
  fac,r,v1,v2: real;
begin
  if GasdevIset = 0 then begin
    repeat
      v1 := 2.0*ran0(idum)-1.0;
      v2 := 2.0*ran0(idum)-1.0;
      r := sqr(v1)+sqr(v2);
    until (r < 1.0) and (r > 0.0);
    fac := sqrt(-2.0*ln(r)/r);
    GasdevGset := v1*fac;
    gasdev := v2*fac;
    GasdevIset := 1
  end
  else begin
    GasdevIset := 0;
    gasdev := GasdevGset;
  end
end;
end;

```

The following subroutines were used to perform the basic conversions or calculations as required (see Chapter 2).

(\*\*\*\*\*Unit Conversions\*\*\*\*\*)

```

{Converts PSI to Pascals}
function psi2pa(psi:single):single;
begin
  psi2pa:=psi*6.895E03;
end;

{Converts Atmospheres to Pascals}
function atm2pa(atm:single):single;
begin
  atm2pa:=atm*1.013E05;
end;

(*****Basic Functions*****)

{Permeability of Round Column}
function qround(ro,visc:single):single;
begin
  qround:=8*visc/(ro*ro);
end;

{Permeability of MMGC Column}
function qtsr(zo,visc:single):single;
begin
  qtsr:=3*visc/(zo*zo);
end;

{Column Output Velocity}
{po, pin in pascals, q in poise, L in meters}
function Vout(pin,po,L,q:single):single;
begin
  Vout:=(10*(pin*pin-po*po)/(2*po*q*L));
end;

{Velocity at point x in column}
function Vx(x:single):single;
var xl:single;
begin
  xl:=x/L;
  vx:=vo/sqrt(sqr(pipo*(1-xl)+xl));
end;

```

The subroutines Move, Diffuse, AtBoundary, and Adsorb form the core of the model. Movement of NO<sub>2</sub> molecules is controlled by Move, which takes into account the velocity

of the carrier gas (x-direction) and diffusion (x-, y-, and z-directions). Diffusion is further controlled by Diffuse which selects a random location on a sphere which is one diffusion length (a radius) away from the present location. AtBoundary checks to see if the NO<sub>2</sub> molecule is at one of the column boundaries, and therefore, susceptible to adsorption. Finally, Adsorb increments the time variable for an adsorbed NO<sub>2</sub> molecule.

```

procedure Diffuse(var x,y,z:single);
var
    rth,rph:byte;
    sinrph:single;
begin
    rth:=trunc(ran0(ri)*255);
    rph:=trunc(ran0(ri)*255);
    sinrph:=sinarrpi[rph];
    x:=cosarrpi2[rth]*sinrph*x;
    y:=sinarrpi2[rth]*sinrph*y;
    z:=cosarrpi[rph]+z;
end;

procedure Move(var x,y,z,t:single);
begin
    x:=x+vx(x)*ti;
    Diffuse(x,y,z);
    t:=t+ti;
end;

function AtBoundary(var x,y,z:single):boolean;
begin
    AtBoundary:=false;
    if y>=w then begin y:=w; AtBoundary:=true; exit; end;
    if y<=0 then begin y:=0; AtBoundary:=true; exit; end;
    if z>=2*zo then begin z:=2*zo; AtBoundary:=true; exit; end;
    if z<=0 then begin z:=0; AtBoundary:=true; exit; end;
end;

procedure Adsorb(var t:single);
begin
    if ran0(ri)<stick then t:=t+abs(gasdev(ri)*t0*0.5+t0);
end;

```

The following subroutines perform various initialization and input/output functions. The lookup table is initialized by InitLookup, and InitVariables initializes the various

values used by the model (see the equations in Sections 7.1 and C). The user's input is read with ReadUserData, and the output file is generated with OutputData.

```

procedure InitLookup;
begin
  for i:=0 to 255 do begin
    cosarrpi[i]:=d*cos(i*Pi/255);
    cosarrpi2[i]:=d*cos(i*2*Pi/255);
    sinarrpi[i]:=sin(i*Pi/255);
    sinarrpi2[i]:=d*sin(i*2*Pi/255);
  end;
end;

procedure InitVariables;
begin
  randomize;
  ri:=-1; {init ran # generator}
  gasdeviset:=0;
  she:=21.8E-11; {meters}
  sno2:=90E-11; {meters}
  mhe:=0.004; {kg/mole}
  mno2:=0.047; {kg/mole}
  k:=1.38054E-23; {joule/K}
  R:=8.31433; {joule/(k mole)}
  L:=0.9; {meters}
  pin:=40; {psi}
  po:=1; {atm}
  po:=atm2pa(po);
  pin:=psi2pa(pin)*po;
  sqrpipo:=sqr(pin/po);
  pav:=2/3*(pin*pin*pin-po*po*po)/(pin*pin-po*po);
  visc:=210E-6; {poise}
  zo:=(9.5E-06)/2; {meters, GC1}
  zo:=(11.3E-6)/2; {meters, GC2--comment out if GC1 desired}
  w:=300E-06; {meters}
  vo:=vout(pin,po,L,qtsr(zo,visc));
  vav:=sqr(8*R*temp/(Pi*mno2));
  nconc:=pav/(k*temp); {molecules/meter^3; Adamson,p.55}
  coll:=2*sqr(2)*sqr((she+sno2)/2)*
    sqrt(Pi*R*temp/((mhe*mno2)/(mhe+mno2)))*nconc;
  writeln('Number of Collisions = ',coll,' per second');
  mtbc:=1/coll;
  mfp:=vav/coll; {Adamson,p.62}
  dc:=0.5*mfp*vav; {meters^2/sec}

```

```

nu:=2872; {per sec}
t0:=1/(nu*exp(-36.7e3/(R*temp)));
no2surf:=170E-21; {m-2}
prob:=1-(63E-3/(no2surf)*(sqrt(2*Pi*mno2/6.0225E23*k*373)));
stick:=1-exp(65*ln(prob));
ti:=1E-3;{time increment: sec}
d:=sqrt(2*d0*ti);
end;

procedure ReadUserData;
begin
  write('Temperature (C)? ');
  readln(temp);
  temp:=temp+273;
  write('Number of Molecules? ');
  readln(numits);
  write('File Name? ');
  readln(fname);
  write('Comments? ');
  readln(comments);
end;

procedure OutputData;
begin
  assign(ofile,fname);
  rewrite(ofile);
  writeln(ofile,comments,#9);
  writeln(ofile,temp,#9);
  writeln(ofile,'Average Pressure = ',pav,'Pa',#9);
  writeln(ofile,'Number of Iterations = ',NumIts,#9);
  writeln(ofile,'Average NO2 Velocity = ',vav,' m/sec',#9);
  writeln(ofile,
    'Helium Concentration = ',nconc,' molecules/m3',#9);
  writeln(ofile,'Number of Collisions = ',coll,' per second',#9);
  writeln(ofile,'Mean Free Path = ',mfp,' m',#9);
  writeln(ofile,'Average Adsorbed Lifetime = ',t0,' sec',#9);
  writeln(ofile,'Kappa = ',1-prob,#9);
  writeln(ofile,
    'Sticking Probability in Time Interval ',ti,' = ',stick,#9);
  writeln(ofile,'Column Output Velocity = ',vo,' m/sec',#9);
  for i:=0 to 512 do writeln(ofile,i/4:7:2,#9,rt[i]:8:0);
  close(ofile);
end;

```

### D.3 Main Program.

The main program is relatively straightforward and follows the flow depicted in Figure 134. The `gettime` calls are used to track the computational time, and are not required to implement the model.

```
(*****Main Program*****)
begin
  ReadUserData;
  InitVariables;
  InitLookup;

  gettime(h,m,s,s100);
  ps:=h*3600+m*60+s+s100/100;

  for i:=0 to 512 do rt[i]:=0;
  for i:=1 to NumIts do begin
    x:=0; {begining of column}
    t:=0; {reset clock}
    y:=ran0(ri)*w;
    z:=ran0(ri)*2*zo;
    repeat
      if AtBoundary(x,y,z) then Adsorb(t);
      Move(x,y,z,t);
    until (x>L) or (t>1E4);
    j:=trunc(t/60*4);
    if (j<513) and (j>=0) then rt[j]:=rt[j]+1;
  end;

  (**The following statement integrates the rt array to**)
  (**simulate the action of the chemiresistor      **)
  for i:=511 downto 0 do for j:=i+1 to 512 do rt[j]:=rt[j]+rt[i];

  gettime(h,m,s,s100);
  ps:=h*3600+m*60+s+s100/100-ps;
  writeln('Run-time: ',ps,' Seconds');

  OutputData;

end.
```

## Appendix E. Data Reduction

This appendix describes and includes the non-linear least-squares curve fitting routines used to reduce the experimental data obtained in this research. The main program was essentially the same for all three non-linear least-squares curve fits<sup>1</sup> (only the fitting functional was changed). The program will be discussed first, and then examples of each application (and the corresponding functional) will be presented.

### E.1 Non-Linear Least-Squares Curve Fitting.

The algorithm used to accomplish the non-linear least-squares curve fit is based upon the Levenberg-Marquardt method that is described in *Numerical Recipes in C* (147-149). The logical flow of the main program is shown in Figure 135. During the initialize phase, the variables used by the program are initialized. Next, a variable, *oldchisq*, is set to the value of the current  $\chi^2$ , *chisq*. Then the *mrqmin* subroutine (defined below) is called repeatedly until the value of  $\chi^2$  converges. The computer code was imported and used directly from the corresponding *Numerical Recipes in Pascal* disk (146). A summary of the Levenberg-Marquardt subroutines implemented by Press, et. al., and as used here, follows<sup>2</sup> (147):

The Levenberg-Marquardt algorithm attempts to minimize the value of  $\chi^2$  between a set of points (*x*[1..*ndata*], *y*[1..*ndata*] with standard deviations *sig*[1..*ndata*]), and a nonlinear functional with a total of *ma* parameters. The parameters are stored in the array, *a*[1..*ma*]. The array, *lista*[1..*ma*], provides a means of identifying which of the parameters can be varied by the algorithm, and which are fixed by the user. The first *mfit* elements of the *lista* array correspond to values actually being adjusted. For example, if *ma* is 5, and *mfit* is 3, then the parameters *a*[1] through *a*[3] can be adjusted by the algorithm to obtain the best fit, while the parameters *a*[4] and *a*[5] are held fixed at their initial, user defined values. The program returns the current best-fit values for the *ma* fit parameters, *a*, and  $\chi^2 = \text{chisq}$ .

<sup>1</sup>The chemiresistor evaluation data (Appendix I), the MMGC evaluation data (Appendix J), and the adsorption data (Appendix K) all used these routines.

<sup>2</sup>A more thorough treatment of the Levenberg-Marquardt algorithm can be found in (147:540).

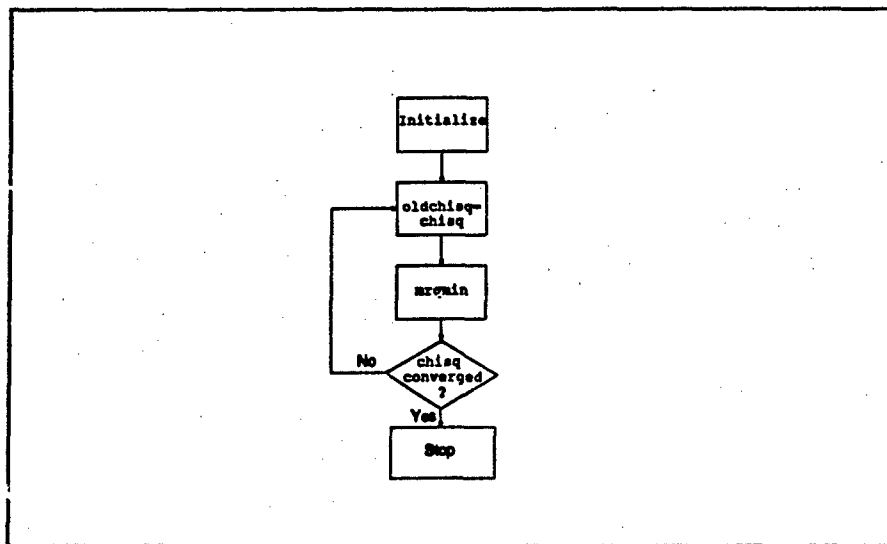


Figure 135. Flowchart for the Non-Linear Least-Squares Curve Fitting Program.

The user supplies a routine called by `funcs(x,a,yfit,dyda,ma)`, that evaluates the fitting function `yfit`, and its derivatives `dyda[1..ma]` with respect to the fitting parameters `a` at `x`. On the first call, the user provides an initial guess for the parameters `a`, and sets `alamda < 0` (for initialization). The algorithm then sets `alamda = .001`. If a step succeeds, `chisq` becomes smaller and `alamda` decreases by a factor of 10. The user calls this routine repeatedly until convergence is achieved (the previous value of  $\chi^2$  differing from the current value by less than 0.001).

```

PROCEDURE mrqmin(VAR x,y,sig: ArrayNDATA;
                 ndata: integer;
                 VAR a: ArrayMA;
                 ma: integer;
                 VAR lista: Integer/ArrayMFIT;
                 mfit: integer;
                 VAR covar,alpha: ArrayMabyMA;
                 VAR chisq,alamda: real);

```

LABEL 99;

VAR

```

  k,kk,j,ihit: integer;
  atry,da: ^ArrayMA;
  oneda: ^ArrayMaby1;

```

```

PROCEDURE mrqcof(VAR x,y,sig: ArrayNDATA;

```

```

        VAR a: ArrayMA;
        VAR lista: IntegerArrayMFIT;
        VAR alpha: ArrayMAbyMA;
        VAR beta: ArrayMA;
        VAR chisq: real);

VAR
    k,j,i: integer;
    ymod,wt,sig2i,dy: real;
    dyda: ^ArrayMA;
BEGIN
    new(dyda);
    FOR j := 1 TO mfit DO BEGIN
        FOR k := 1 TO j DO alpha[j,k] := 0.0;
        beta[j] := 0.0
    END;
    chisq := 0.0;
    FOR i := 1 TO ndata DO BEGIN
        func(x[i],a,ymod,dyda^,ma);
        sig2i := 1.0/(sig[i]*sig[i]);
        dy := y[i]-ymod;
        FOR j := 1 TO mfit DO BEGIN
            wt := dyda^[lista[j]]*sig2i;
            FOR k := 1 TO j DO
                alpha[j,k] := alpha[j,k]+wt*dyda^[lista[k]];
            beta[j] := beta[j]+dy*wt
        END;
        chisq := chisq+dy*dy*sigt2i
    END;
    FOR j := 2 TO mfit DO
        FOR k := 1 TO j-1 DO alpha[k,j] := alpha[j,k];
    dispose(dyda)
END;

BEGIN
    new(da);
    new(onedata);
    new(atry);
    IF alambda < 0.0 THEN BEGIN
        kk := mfit+1;
        FOR j := 1 TO ma DO BEGIN
            ihit := 0;
            FOR k := 1 TO mfit DO
                IF lista[k] = j THEN ihit := ihit+1;
            IF ihit = 0 THEN BEGIN
                lista[kk] := j;

```

```

        kk := kk+1
    END
    ELSE IF ihit > 1 THEN BEGIN
        writeln('pause 1 in routine MRQMIN');
        writeln('Improper permutation in LISTA');
        readln
    END
END;
IF kk <> ma+1 THEN BEGIN
    writeln('pause 2 in routine MRQMIN');
    writeln('Improper permutation in LISTA');
    readln
END;
alamda := 0.001;
mrqcof(x,y,sig,a,lista,alpha,MrqminBeta,chisq);
Mrqmin0chisq := chisq;
FOR j := 1 TO ma DO atry[j] := a[j]
END;
FOR j := 1 TO mfit DO BEGIN
    FOR k := 1 TO mfit DO covar[j,k] := alpha[j,k];
    covar[j,j] := alpha[j,j]*(1.0+alamda);
    oneda[j,1] := MrqminBeta[j]
END;
gaussj(covar,mfit,oneda,1);
FOR j := 1 TO mfit DO
    da[j] := oneda[j,1];
IF alanda = 0.0 THEN BEGIN
    covart(covar,ma,lista,mfit);
    GOTO 99
END;
FOR j := 1 TO mfit DO
    atry[lista[j]] := a[lista[j]]+da[j];
mrqcof(x,y,sig,atry,lista,covar,da,chisq);
IF chisq < Mrqmin0chisq THEN BEGIN
    if alanda > minlamda then alanda := 0.1*alamda;
    Mrqmin0chisq := chisq;
    FOR j := 1 TO mfit DO BEGIN
        FOR k := 1 TO mfit DO alpha[j,k] := covar[j,k];
        MrqminBeta[j] := da[j];
        a[lista[j]] := atry[lista[j]]
    END
END
ELSE BEGIN
    alanda := 10.0*alamda;
    chisq := Mrqmin0chisq

```

```

    END;
99:
    dispose(atry);
    dispose(onedata);
    dispose(da)
END;

```

*E.1.1 Main Program.* The main program follows the instructions provided by Press, et al.: loading the data, initializing the arrays, and making repeated calls to the `mrqmin` routine until convergence is achieved. Once the fit is performed, the fit parameters are saved to an output file for later use.

```

Program CurveFit;
uses Crt,dos;
CONST
    map = 7;
    NdataP = 512;
TYPE
    ArrayNDATA = ARRAY [1..maxpoints] OF real;    {Data Array}
    ArrayMA = ARRAY [1..map] OF real;             {Parameter Array}
    IntegerArrayMFIT = ARRAY [1..map] OF integer;
    ArrayMAbyMA = ARRAY [1..map,1..map] OF real;
    ArrayMAby1 = ARRAY [1..map,1..1] OF real;
VAR
    ifile, ofile:text;                          {Input and Output Files}
    x,y,sig: ArrayNDATA;                        {x,y and sigma arrays}
    NumPoints: integer;                         {Number of points to fit}
    Param: ArrayMA;                             {Parameter array}
    lista: IntegerArrayMFIT;                    {used internally by mrqmin}
    mfit: integer;                              {Number of parameters to fit}
    chisq,oldchisq:real;                        {Current and prior chi-square}
    covar,alpha: ArrayMAbyMA;                   {Covariance and alpha matrices}
    i:integer;                                  {Iteration variable}
    OutFName,InFName:string;                    {I/O File names}

    (*****
    (*** Main Program ***)
    (*****)

begin
    {load data and initialize variables}
    loaddata;
    alambda:=-1.0;

```

```

for i:=1 to map do lista[i]:=i;

{Make initial call to mrqmin to set up
 internal mrqmin variables}
mrqmin(x,y,sig,NumPoints,
      Param,map,lista,mfit,covar,alpha,chisq,alamda);

{Iterate until convergence is achieved}
repeat
  oldchisq:=chisq;
  mrqmin(x,y,sig,NumPoints,
        Param,map,lista,mfit,covar,alpha,chisq,alamda);
until abs(oldchisq-chisq)<1E-3;

{Update Covariance and alpha matrices}
alamda:=0.0;
mrqmin(x,y,sig,NumPoints,
      Param,map,lista,mfit,covar,alpha,chisq,alamda);

{Save Parameters}
SaveParam;
end.

```

## E.2 Chemiresistor Evaluation.

For the chemiresistor's challenge gas exposure response evaluation, the first step involved determining the functional to use in the curve fitting process. It was assumed that any of the gas peaks produced by the sample injector would be gaussian in nature (due to the longitudinal diffusion of the sample as it propagated through the column and the interconnect tubing). Furthermore, the chemiresistor was observed to behave as an integrating detector (its response to injected pulses of the challenge gas would gradually change from its baseline response and plateau, remaining stable for approximately one hour; i.e., sigmoidally-shaped). Thus, the response to the injected samples could potentially be the integral of a gaussian-shaped gas concentration peak.

**E.2.1 Response Function.** If  $a_1$  is the area under a gaussian peak,  $a_2$  the location of the center of the peak, and  $a_3$  the width (standard deviation) of the peak, the gaussian

peak's behavior with respect to time (see Figure 136),  $g(t)$ , can be defined by the following equation (18):

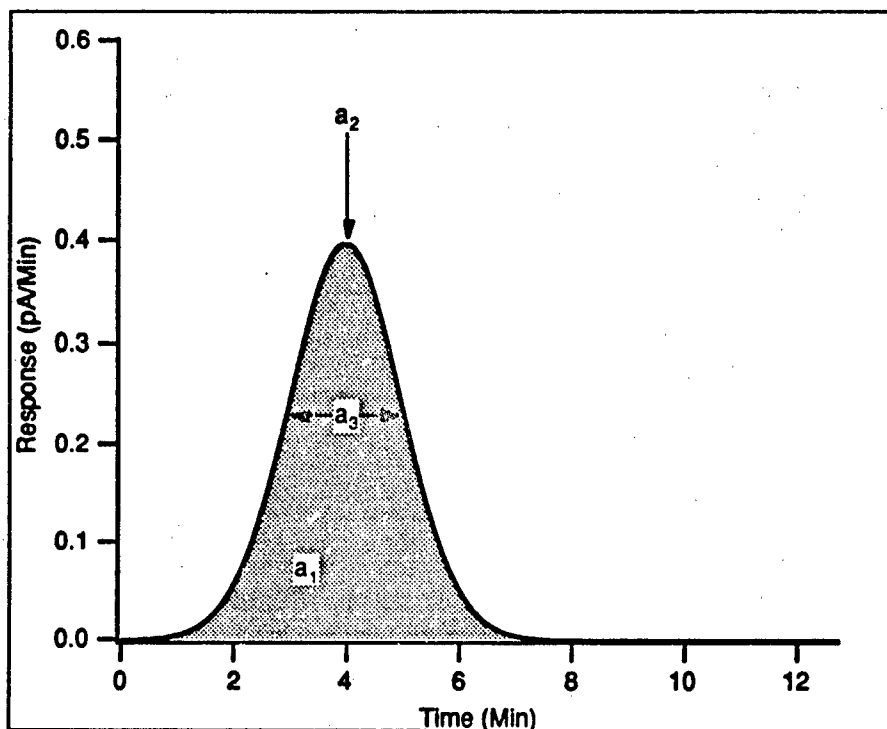


Figure 136. Gaussian Functional with  $a_1 = 1$  pA,  $a_2 = 4$  minutes, and  $a_3 = 2$  minutes.

$$g(t) = \frac{a_1}{\sqrt{2\pi}a_3} \exp \left[ \frac{-(t - a_2)^2}{2a_3^2} \right]. \quad (95)$$

integrating from  $t = 0$  to some arbitrary time,  $\tau$ , yields:

$$\int_0^\tau g(t)dt \approx \frac{a_1}{2} \left[ \operatorname{erf} \left( \frac{\tau - a_2}{\sqrt{2}a_3} \right) + 1 \right]. \quad (96)$$

for  $a_2/a_3 > 0$ . This functional is depicted in Figure 137. Hence, relative to the prior discussion concerning the chemiresistor, the right side of Equation 96 is the basis for the fitting functional for the chemiresistor's data. Since  $\text{NH}_3$  causes a decrease in the electrical conductivity of the chemiresistor,  $a_1$  in Equation 96 becomes negative.

**E.2.2 Computer Program Subroutine.** Equation 96 is implemented in the following computer program subroutine. The derivatives with respect to each parameter are included

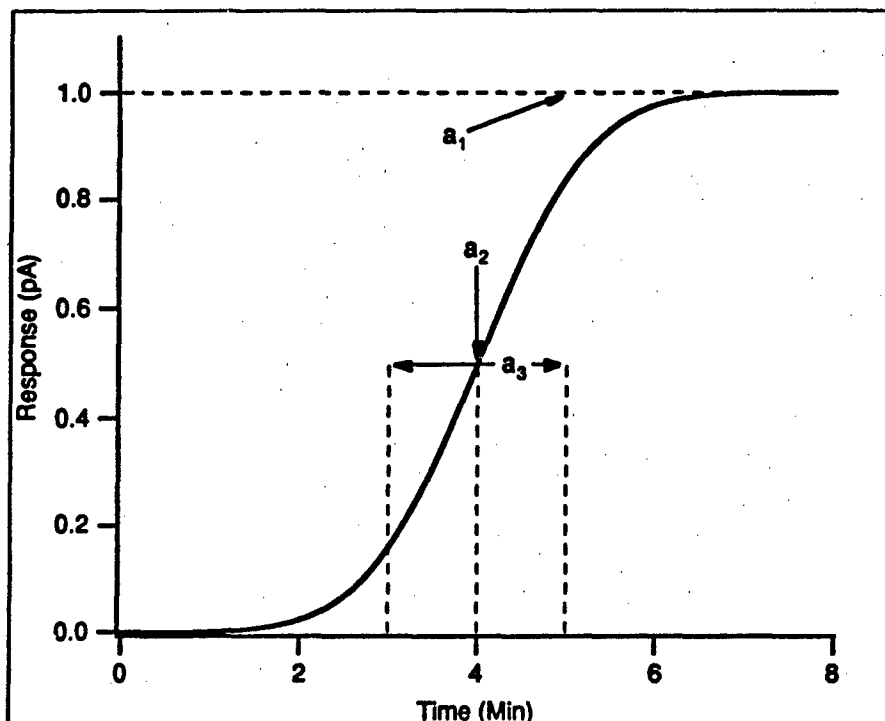


Figure 137. Erf Functional with  $a_1 = 1$  pA,  $a_2 = 4$  minutes, and  $a_3 = 2$  minutes.

as required by the `mrqmin` subroutine, and the parameters are represented as standard Pascal arrays (i.e., parameter  $a_1$  is represented by `a[1]`).

```

PROCEDURE funcs( x: single;           {x-data (time)}
                 VAR a: singleArrayMA; {parameters}
                 VAR y: single;         {y-data (response)}
                 VAR dyda: singleArrayMA; {parameter derivatives}
                 ma: integer);          {parameters to fit}
VAR
    ex1, arg1, erf1, sqrt2, sqrtPi: single; {internal values}

BEGIN
    sqrt2:=sqrt(2);
    sqrtPi:=sqrt(Pi);
    arg1 := ((x)-(a[2]))/((a[3])*sqrt2);
    erf1 := 1+erf(arg1); {For MH3, change to -1-erf(arg1)}
    ex1 := exp(-sqr(arg1));
    y := a[4]+(a[1]*erf1)/2;
    dyda[1] := erf1/2;
    dyda[2] := -a[1]/(sqrt2*sqrtPi*a[3])*ex1;

```

```

dyda[3] := dyda[2]*arg1*sqrt2;
dyda[4] := 1;
END;

```

**E.2.3 Data Reduction Example.** An example of the use of the functional given by Equation 96 to fit a typical set of chemiresistor evaluation experimental data is shown in Figure 138 (the entire set of data is presented in Appendix I). Both the experimental data and the fit to the functional are shown for comparison. For the purposes of quantifying the noise level (to incorporate error bars in the evaluation graphs), the standard deviation between the raw data and fit functional was determined by subtracting the fit functional from the raw data and calculating the standard deviation. The value of this noise level was approximately 0.25 pA in all cases.

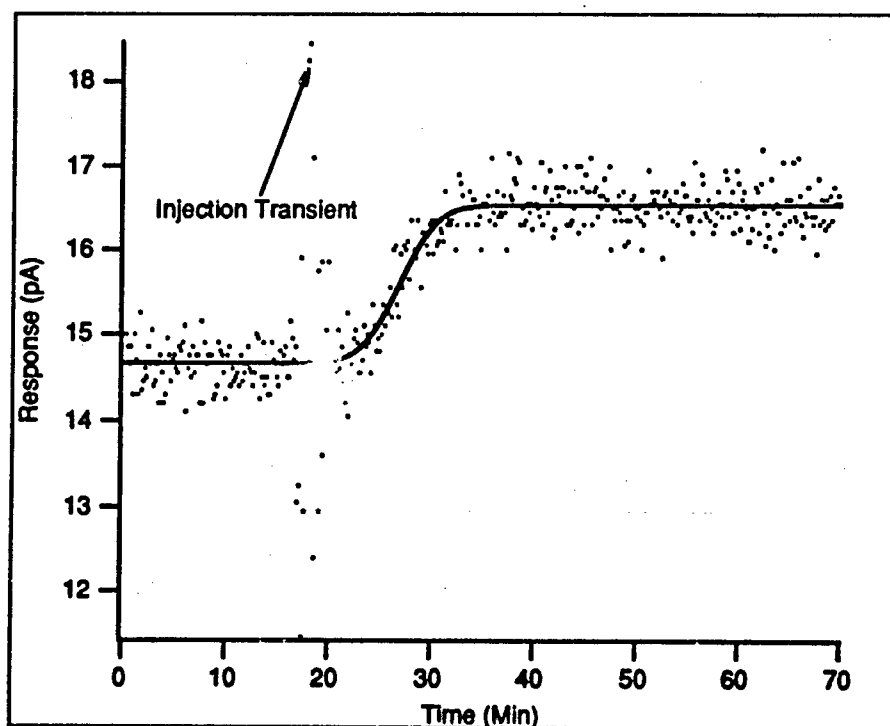


Figure 138. Chemiresistor Evaluation Experimental Data Fit to the Functional Given by Equation 96 (75 ppm NO<sub>2</sub> at 80°C). The Baseline is 14.7 pA, and the Net Response is 1.9 pA.

### E.3 Micromachined Gas Chromatograph Evaluation.

For the MMGC evaluation, the data was composed of both the  $\text{NH}_3$  and  $\text{NO}_2$  responses. By invoking the principle of linear superposition, a trial functional was synthesized which incorporated both responses by using the fundamental form given in Equation 96. However, to maintain a consistent baseline between the two parts of the revised MMGC functional,  $m(t)$ , the  $\text{NH}_3$  functional was multiplied by negative one (to invert the functional) and shifted vertically (by adding two to the expression within the square brackets) to maintain continuity with the  $\text{NO}_2$  functional, yielding:

$$m(t) = \frac{a_1}{2} \left[ 1 - \operatorname{erf} \left( \frac{t - a_2}{\sqrt{2}a_3} \right) \right] + \frac{a_4}{2} \left[ 1 + \operatorname{erf} \left( \frac{t - a_5}{\sqrt{2}a_6} \right) \right] + a_7 \quad (97)$$

where  $a_1$  is the amplitude of the  $\text{NH}_3$  peak,  $a_2$  is the center of the  $\text{NH}_3$  peak,  $a_3$  is the width of the  $\text{NH}_3$  peak,  $a_4$  is the amplitude of the  $\text{NO}_2$  peak,  $a_5$  is the center of the  $\text{NO}_2$  peak,  $a_6$  is the width of the  $\text{NO}_2$  peak, and  $a_7$  is the baseline level. This functional is shown in Figure 139.

*E.3.1 Computer Program Subroutine.* Equation 97, and the corresponding parameter derivatives are implemented in the subroutine that follows:

```
PROCEDURE funcn( x: single;           {x-data (time)}
                 VAR a: singleArrayMA; {parameters}
                 VAR y: single;         {y-data (response)}
                 VAR dyda: singleArrayMA; {parameter derivatives}
                 ma: integer);          {parameters to fit}
VAR
  ex1, ex2, arg1, arg2, erf1, erf2: single; {internal values}

BEGIN
  arg1 := ((x)-(a[2]))/((a[3])*sqrt2);
  arg2 := ((x)-(a[5]))/((a[6])*sqrt2);
  erf1 := 1-erf(arg1); {to insure}
  erf2 := 1+erf(arg2); {compatible baselines}
  ex1 := exp(-sqr(arg1));
  ex2 := exp(-sqr(arg2));
  y := a[7]+(a[1]*erf1+a[4]*erf2)/2;
  dyda[1] := erf1/2;
  dyda[2] := a[1]/(sqrt2*sqrtPi*a[3])*ex1;
```

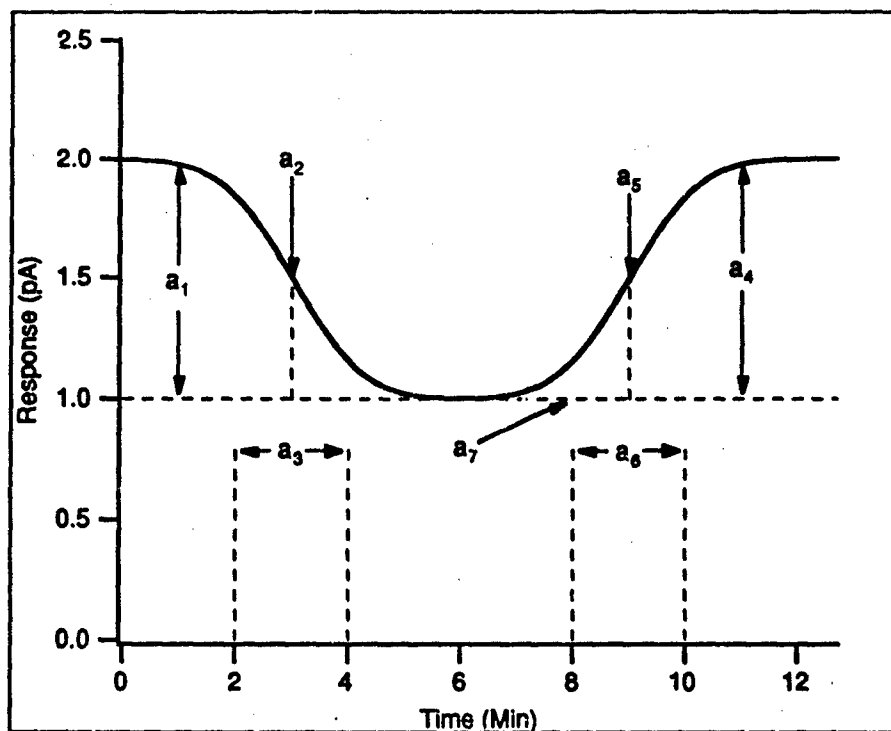


Figure 139. Double Erf Functional with  $a_1 = 1$  pA,  $a_2 = 3$  minutes,  $a_3 = 2$  minutes,  $a_4 = 1$  pA,  $a_5 = 9$  minutes,  $a_6 = 2$  minutes, and  $a_7 = 1$  pA.

```
dyda[3]:=arg1*dyda[2]*sqrt2;
dyda[4] := erf2/2;
dyda[5]:=-a[4]/(sqrt2*sqrtPi*a[6])*ex2;
dyda[6]:=dyda[5]*arg2*sqrt2;
dyda[7] := 1;
```

END;

**E.3.2 MMGC Data Reduction Example.** In order to reduce the effects of noise, six trials at each evaluation point were made and averaged. Figures 140 through 145 depict six typical MMGC evaluation trials before averaging (the entire set of averaged data is presented in Appendix J). Figure 146 shows the use of the functional given in Equation 97 to fit the averaged data from Figures 140 through 145. Both the raw data and the fit to the functional are shown for comparison. For the purposes of quantifying the noise level (to incorporate error bars in the evaluation graphs), the standard deviation between the raw data and fit functional was determined as described in the chemiresistor discussion.

The value of this noise level was approximately 0.09 pA in all cases, and the effect of this noise on the time axis was determined<sup>3</sup> to be approximately 1.3 minutes.

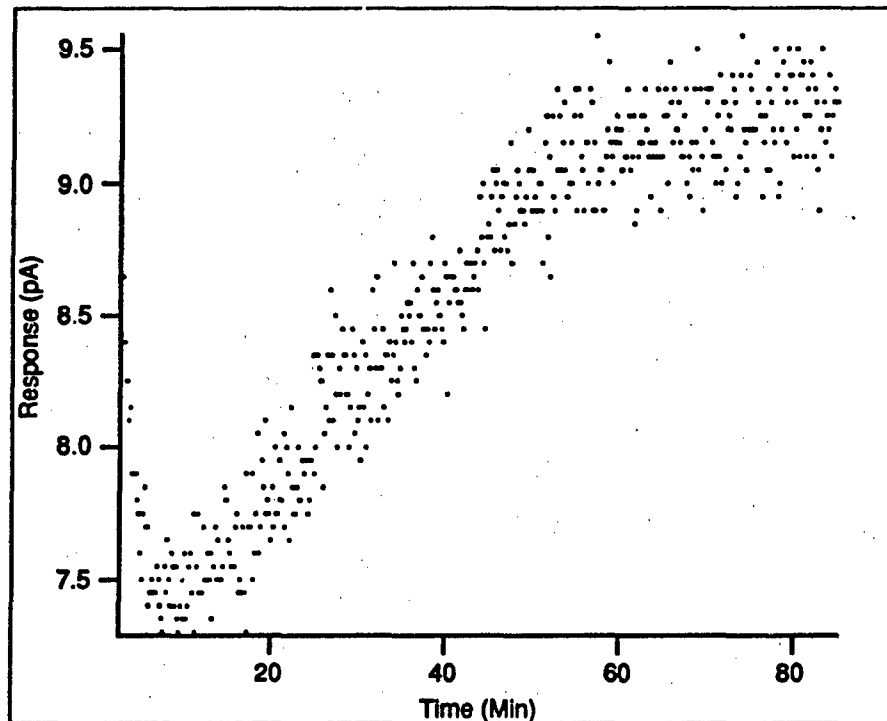


Figure 140. First Trial of a Micromachined Gas Chromatograph Evaluation (75 ppm  $\text{NO}_2$ , 6300 ppm  $\text{NH}_3$ , at  $66^\circ\text{C}$ ).

#### E.4 Adsorption Evaluation.

For the challenge gas adsorption studies described in Appendix C, a third functional was required to determine the parameters  $\alpha$ ,  $\beta$ , and  $a_7$ . This functional was based on Equation 91, where  $R_P$  was replaced by  $a_1$ ,  $R_A$  by  $a_2$ ,  $\alpha$  by  $a_3$ ,  $\beta$  by  $a_4$ ,  $P$  by  $a_5$ ,  $a_7$  by  $a_7$ , and  $a_6$  was introduced to account for an arbitrary pre-exposed initial condition (to account for the lack of complete reversibility due to the extended exposure times; that is, a baseline response offset).

<sup>3</sup>This was accomplished by adding and subtracting the noise level to the fit functional and calculating the width of the resulting band at the functional center on the time axis.

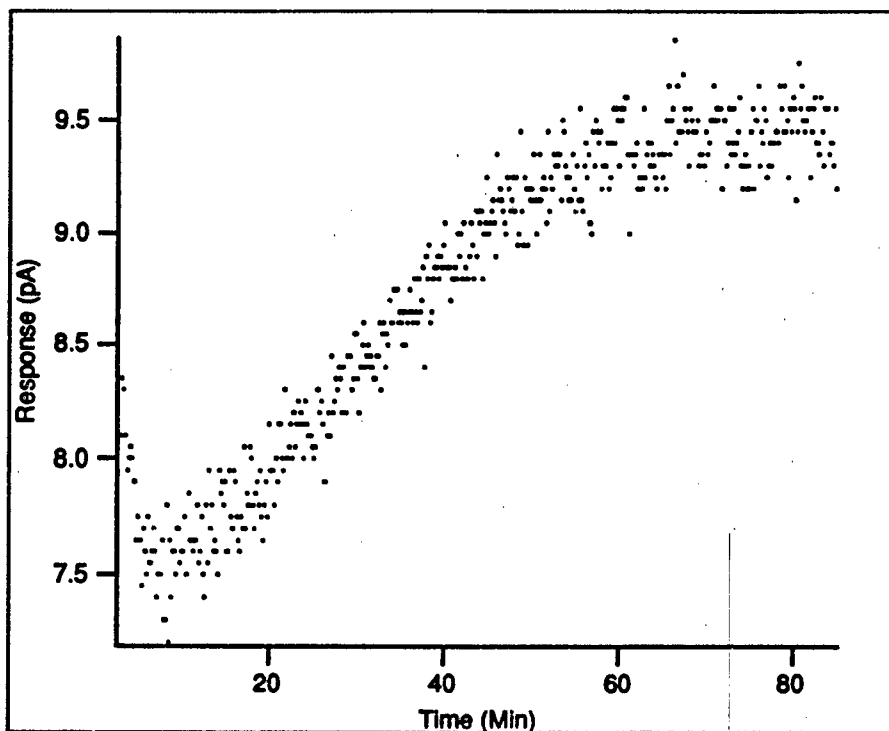


Figure 141. Second Trial of a Micromachined Gas Chromatograph Evaluation (75 ppm  $\text{NO}_2$ , 6300 ppm  $\text{NH}_3$ , at  $66^\circ\text{C}$ ).

*E.4.1 Computer Program Subroutine.* The implementation of this functional, and its parameter derivatives, is shown in the following computer program subroutine:

```

PROCEDURE funcs( x: single;           {x-data (time)}
                 VAR a: singleArrayMA; {parameters}
                 VAR y: single;         {y-data (response)}
                 VAR dyda: singleArrayMA; {parameter derivatives}
                 ma: integer);          {parameters to fit}
VAR
    arg3, is1, is2, arg1, ex1, ex2, ex3, ln1, {internal values}
    iarg1, iarg2, iarg3, iarg4, arg2: double;

BEGIN
    iarg2:=a[7]*(a[3]*a[5]+a[4]);
    iarg1:=-iarg2*(x+a[6]);
    ex1:=1e-50;
    arg1:=(1-ex1);
    arg2:=a[3]*a[5]/(a[7]*(a[3]*a[5]+a[4]));
    arg3:=(a[2]-a[1]);

```

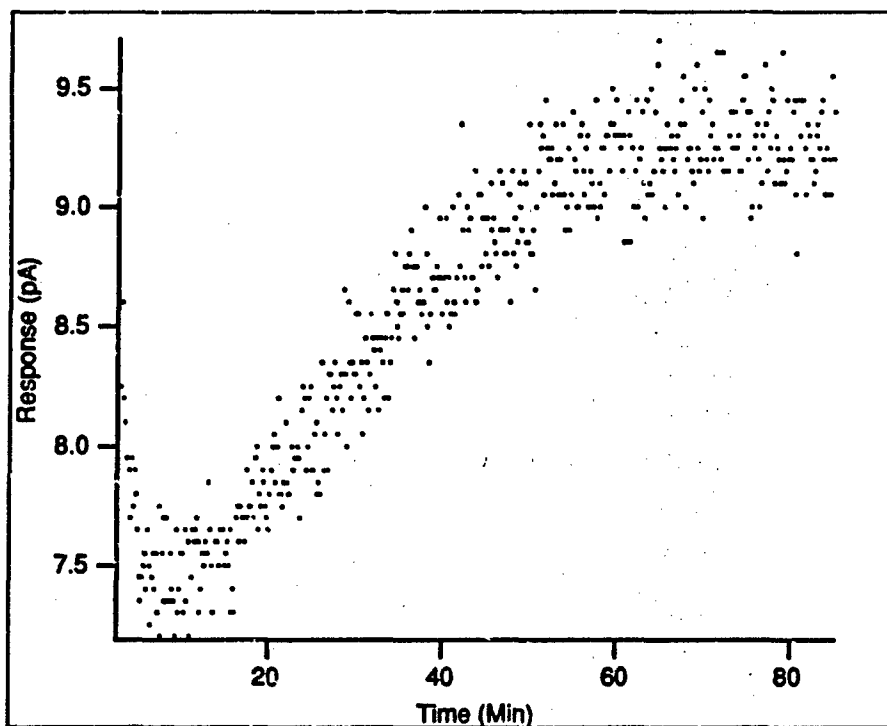


Figure 142. Third Trial of a Micromachined Gas Chromatograph Evaluation (75 ppm NO<sub>2</sub>, 6300 ppm NH<sub>3</sub>, at 66°C).

```

y:=a[1]+arg3*arg2*arg1;
dyda[1]:=1-arg2*arg1;
dyda[2]:=arg2*arg1;
dyda[3]:=arg3*a[5]/iarg2*
(a[4]/iarg2-a[4]*ex1/iarg2+a[3]*a[5]*a[7]*(x+a[6])*ex1);
dyda[4]:=arg3*a[3]*a[5]/iarg2*
(-1/iarg2+ex1/iarg2+(x+a[6])*a[7]*ex1);
dyda[5]:=dyda[3]*a[3]/a[5];
dyda[6]:=arg3*a[3]*a[5]*ex1;
dyda[7]:=arg3*(-a[3]*a[5]/(iarg2*a[7]))*
arg1+ex1*(x+a[6])*a[3]*a[5]/a[7]);
END;

```

*E.4.2 Data Reduction Example.* The entire set of data is presented in Appendix K. Figure 147 depicts the use of the functional to fit the experimental challenge gas adsorption data. The experimental data for a typical set and the fit to the functional are shown for comparison.

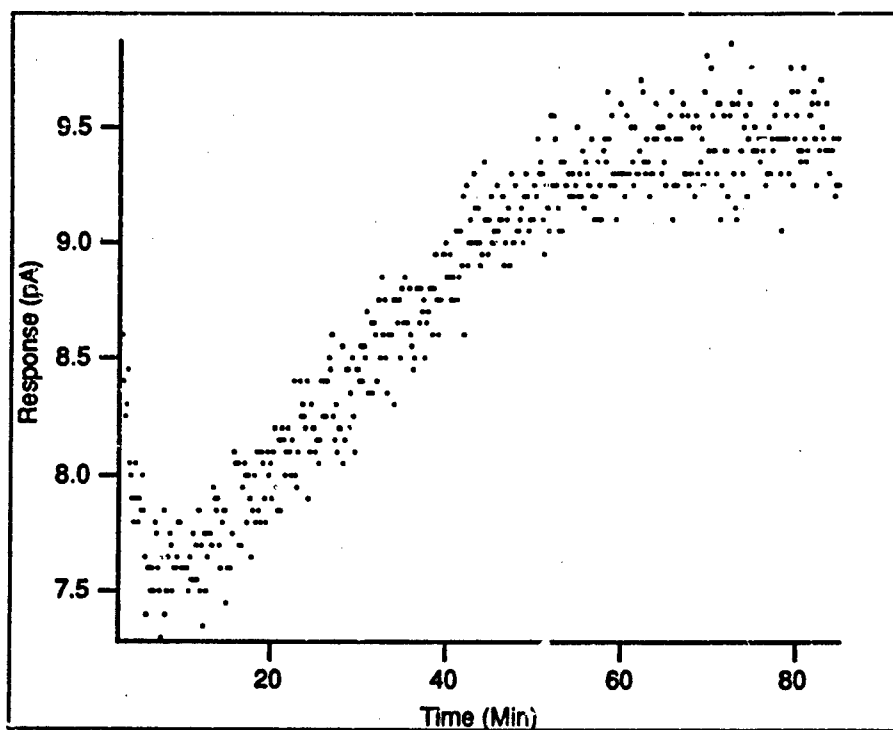


Figure 143. Fourth Trial of a Micromachined Gas Chromatograph Evaluation (75 ppm  $\text{NO}_2$ , 6300 ppm  $\text{NH}_3$ , at  $66^\circ\text{C}$ ).

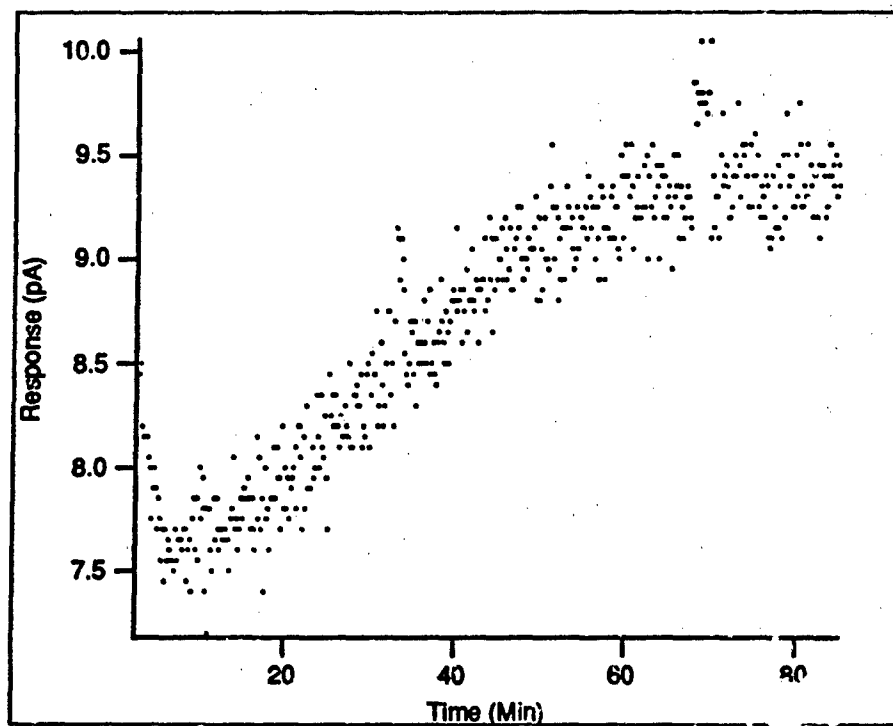


Figure 144. Fifth Trial of a Micromachined Gas Chromatograph Evaluation (75 ppm  $\text{NO}_2$ , 6300 ppm  $\text{NH}_3$ , at  $66^\circ\text{C}$ ).

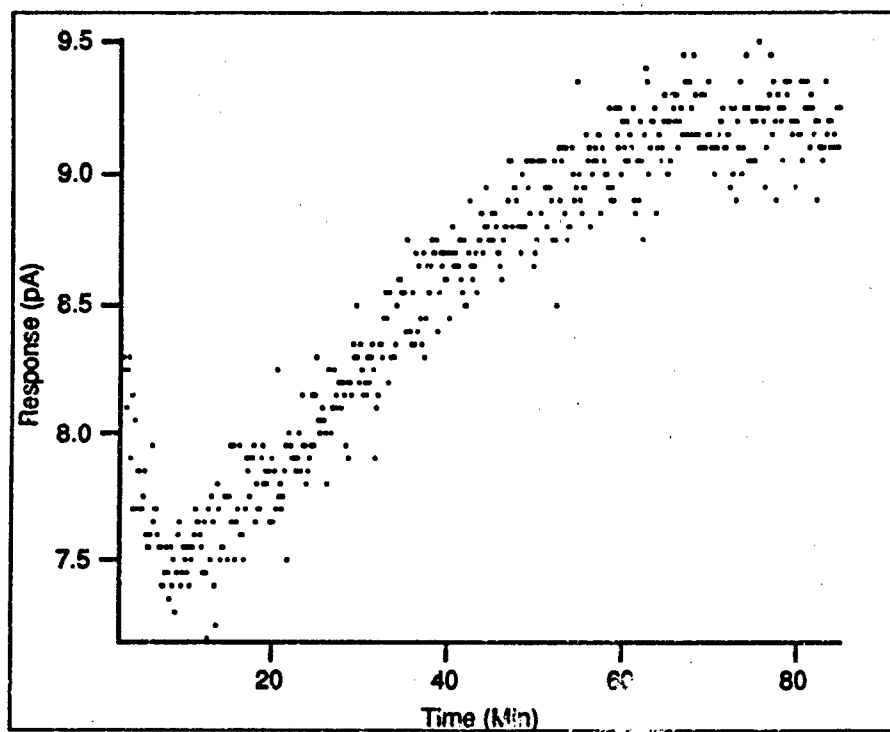
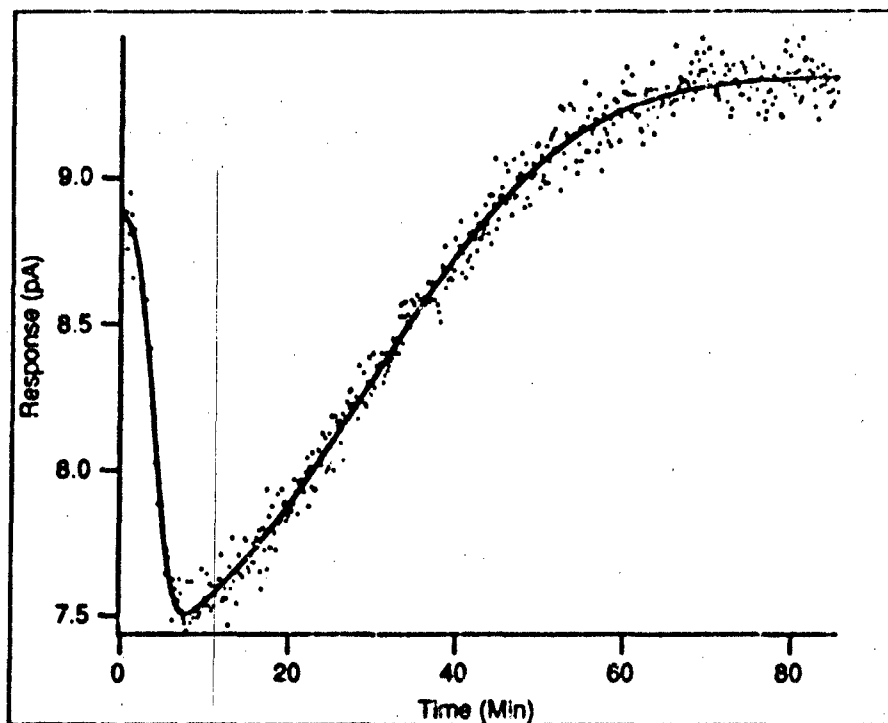


Figure 145. Sixth Trial of a Micromachined Gas Chromatograph Evaluation (75 ppm  $\text{NO}_2$ , 6300 ppm  $\text{NH}_3$ , at  $66^\circ\text{C}$ ).



**Figure 146.** Micromachined Gas Chromatograph Evaluation Experimental Data Fitted to the Functional (75 ppm  $\text{NO}_2$ , 6300 ppm  $\text{NH}_3$ , and  $66^\circ\text{C}$ ). The  $\text{NH}_3$  Response is 1.5 pA, the  $\text{NH}_3$  Peak Center is at 3.8 minutes, the  $\text{NH}_3$  Peak Width is 1.7 minutes, the  $\text{NO}_2$  Response is 2.1 pA, the  $\text{NO}_2$  Peak Center is at 29.4 minutes, and the  $\text{NO}_2$  Peak Width is 18.9 minutes.

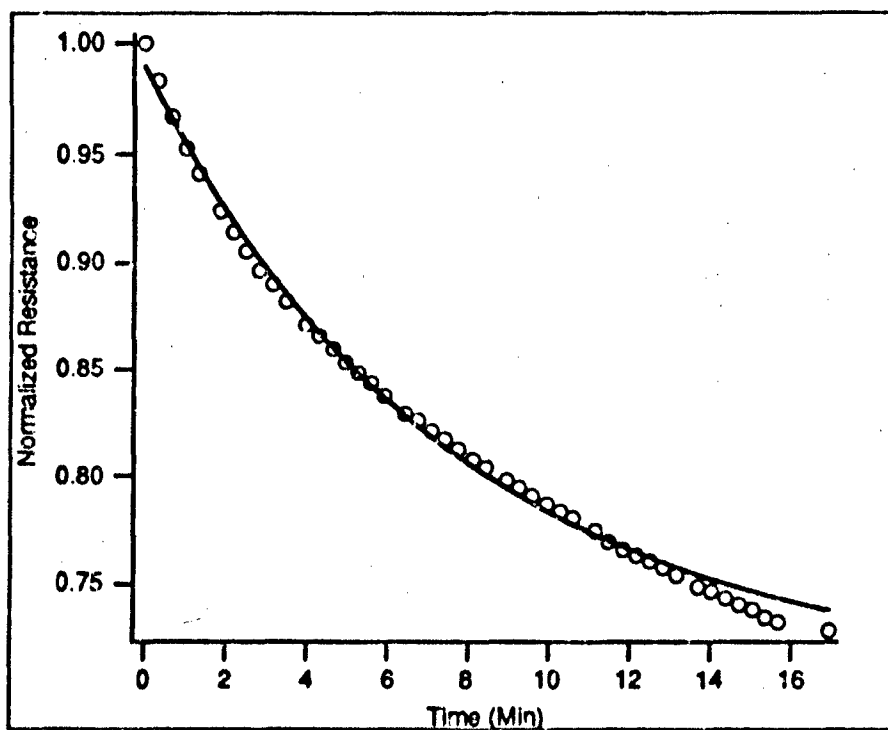


Figure 147. Adsorption Evaluation Data Fit to a Function (100 ppb  $\text{NO}_2$  at  $100^\circ\text{C}$ ).  $\alpha$  is  $4.4 \times 10^{-4} (\text{ppb} \cdot \text{min})^{-1}$ ,  $\beta$  is  $1.2 (\text{min})^{-1}$ , and  $a_r$  is 11 percent.

## Appendix F. Golay's Theory

The following is an excerpt from Marcel Golay's *Theory of Chromatography in Open and Coated Tubular Columns with Round and Rectangular Cross-Sections* (25):

When a gas flows viscously in a tube of either circular or rectangular cross-section (with a large width over thickness ratio for the latter), the average speed of flow has a parabolic profile along any cross-section parallel to the direction of flow, this speed being zero at the walls of the tube. If, on the other hand, one single molecule is followed in its combined drifting and Brownian motion, this molecule will spend an equal time, on average, in every unit area of the tube cross-section and, if the tube walls are uniformly coated with a retentive layer, all molecules having an equal affinity for this coating will spend an equal fraction of time in that fixed phase. Furthermore, there will be statistical fluctuations from the equal values of occupancy of every cross-sectional unit area, and from the average relative occupancies of the moving and fixed phases.

If a gas sample in the form of a small gas packet is injected, at an initial epoch, within the stream of a carrier gas having no affinity for the inner wall coating, these injected molecules will be carried along at an average speed which will be less than that of the carrier gas stream, because of the retentive effect of the fixed phase, and will diffuse about the centre of gravity of the packet.

Two processes will contribute to the overall effect. The first is the static diffusion, which takes place whether the gas is moving or not, and which is a function of elapsed time. The second is the dynamic diffusion, due to the fluctuations in occupancy of the various portions of the tube cross-section and of the fixed phase; some molecules with an extra high occupancy of the tube centre move ahead of the packet, while others with an extra high occupancy of the portions near the wall, or of the fixed phase, lag behind. ... [This] discussion will be devoted essentially to the extension of Taylor's method to the case in which the walls of round or rectangular tubes are coated with a thin retentive layer, within which diffusion is instantaneous.

The diffusion of a gas packet is governed by the vectorial differential equation:

$$D\nabla^2 f = \frac{df}{dt} = \frac{\partial f}{\partial t} + \vec{v} \cdot \nabla f \quad (98)$$

In the absence of flow, and when diffusion in the  $x$  direction only is of interest, (98) may be simplified to:

$$D \frac{\partial^2 f}{\partial x^2} = \frac{\partial f}{\partial t} \quad (99)$$

Let the gas packet of density  $f = f(x, t)$  be normalized to unity:

$$\int_{-\infty}^{+\infty} f dx = 1. \quad (100)$$

Since  $f$  is essentially a positive quantity, it follows from (100) that:

$$f \rightarrow 0, fx \rightarrow 0, \text{ and } \frac{\partial f}{\partial x} x^2 \rightarrow 0 \text{ when } x \rightarrow \pm\infty. \quad (101)$$

Consider the incremental second moment  $du$  of a normalized gas packet:

$$du = d \int_{-\infty}^{+\infty} f x^2 dx. \quad (102)$$

We have, by virtue of (99)

$$du = dt \int_{-\infty}^{+\infty} \frac{\partial f}{\partial t} x^2 dx = D dt \int_{-\infty}^{+\infty} \frac{\partial^2 f}{\partial x^2} x^2 dx. \quad (103)$$

Integrating by parts and taking account of (100) and (101), we obtain:

$$du = D dt \left\{ 2 \int_{-\infty}^{+\infty} f dx - 2[f x]_{-\infty}^{+\infty} + \left[ \frac{\partial f}{\partial x} x^2 \right]_{-\infty}^{+\infty} \right\} = 2D dt. \quad (104)$$

We shall consider now the case of diffusion of sample gas of uniform composition within a viscously flowing inert carrier gas inside a round tube uniformly coated with a retentive layer. Let  $r$ ,  $r_0$ ,  $v_0$  and  $k$  designate, respectively, the distance from the centre, the tube radius, the average carrier gas velocity and the ratio of the sample held in the retentive layer to the sample in vapour form when there is equilibrium between these two phases.

Introducing the well-known expression for Poiseuille flow in (98) we obtain:

$$D \left( \frac{\partial^2}{\partial r^2} + \frac{1}{r} \frac{\partial}{\partial r} + \frac{\partial^2}{\partial x^2} \right) f = \frac{\partial f}{\partial t} + 2v_0 \left( 1 - \frac{r^2}{r_0^2} \right) \frac{\partial f}{\partial x}. \quad (105)$$

The boundary condition at the tube wall is:

$$2 \frac{D}{r_0} \left( \frac{\partial f}{\partial r} \right)_{r=r_0} = -k \left( \frac{\partial f}{\partial t} \right)_{r=r_0}. \quad (106)$$

Because of the retentive property of the tube coating, the average velocity of the sample will be the fraction  $1/(1+k)$  of the average velocity  $v_0$  of the carrier gas, and it will be expedient to effect the change of coordinates:

$$x_1 = x - \frac{v_0}{1+k} t \quad (107)$$

which is equivalent to selecting a new origin of coordinates which moves at the average sample velocity. The former equations (105) and (106) become:

$$D \left( \frac{\partial^2}{\partial r^2} + \frac{1}{r} \frac{\partial}{\partial r} + \frac{\partial^2}{\partial x_1^2} \right) f = \frac{\partial f}{\partial t} + v_0 \left( \frac{1+2k}{1+k} - 2 \frac{r^2}{r_0^2} \right) \frac{\partial f}{\partial x_1} \quad (108)$$

and

$$2 \frac{D}{r_0} \left( \frac{\partial f}{\partial r} \right)_{r=r_0} = -k \left( \frac{\partial f}{\partial t} \right)_{r=r_0} + \frac{k}{1+k} v_0 \left( \frac{\partial f}{\partial x_1} \right)_{r=r_0} \quad (109)$$

Let the new variables  $\bar{f}$  and  $\Delta f$  be defined by:

$$\bar{f} = \frac{2}{r_0^2} \int_0^{r_0} f r dr \quad (110)$$

and

$$f = \bar{f} + \Delta f \quad (111)$$

where  $\Delta f$  obeys the relation:

$$\int_0^{r_0} \Delta f r dr = 0. \quad (112)$$

Let it be stipulated further that only the average diffusion  $\bar{f}$  in the  $x_1$  direction is of physical interest, and only after the diffusive process has operated for a time which is long when compared to that required for equilibrium to occur across the tube. This is equivalent to saying that  $\Delta f$  will be negligibly small when compared to  $f$ , and this may be expressed conveniently with the relation:

$$\Delta f \ll \bar{f} \quad (113)$$

which will constitute the only postulate of this discussion.

If we apply the operator  $\frac{2}{r_0^2} \int_0^{r_0} r dr$  to all members of (108), we obtain, taking (110) to (112) into account:

$$\begin{aligned} 2 \frac{D}{r_0} \left( \frac{\partial \Delta f}{\partial r} \right)_{r=r_0} + D \frac{\partial^2 \bar{f}}{\partial x_1^2} &= \frac{\partial \bar{f}}{\partial t} + \frac{k}{1+k} v_0 \frac{\partial \bar{f}}{\partial x_1} \\ &+ 2 \frac{v_0}{r_0^2} \int_0^{r_0} \left( \frac{1+2k}{1+k} - 2 \frac{r^2}{r_0^2} \right) \frac{\partial \Delta f}{\partial x_1} r dr. \end{aligned} \quad (114)$$

The boundary condition (Equation 109) may be likewise re-written:

$$2 \frac{D}{r_0} \left( \frac{\partial \Delta f}{\partial r} \right)_{r=r_0} = -k \left( \frac{\partial (\bar{f} + \Delta f)}{\partial t} \right)_{r=r_0} + \frac{k}{1+k} v_0 \left( \frac{\partial (\bar{f} + \Delta f)}{\partial x_1} \right)_{r=r_0} \quad (115)$$

Subtracting (115) from (114), member-by-member yields the new relation:

$$D \frac{\partial^2 \bar{f}}{\partial x_1^2} = (1+k) \frac{\partial \bar{f}}{\partial t} + 2 \frac{v_o}{r_o^2} \int_0^{r_o} \left( \frac{1+2k}{1+k} - 2 \frac{r^2}{r_o^2} \right) \frac{\partial \Delta f}{\partial x_1} r dr - \frac{k}{1+k} v_o \left( \frac{\partial \Delta f}{\partial x_1} \right)_{r=r_o} \quad (116)$$

in which the term  $k(\partial \Delta f / \partial t)_{r=r_o}$  has been dropped by virtue of (113), since it is negligible by comparison with  $\partial \bar{f} / \partial t$ .

The terms in  $\partial \Delta f / \partial x_1$ , which would be negligible if compared to terms in  $\partial \bar{f} / \partial x_1$ , in which  $\bar{f}$  is at the same order of differentiation as  $\Delta f$ , are not negligible when compared to  $\partial^2 \bar{f} / \partial x_1^2$ , which is a higher order differential. In order to obtain an expression for the terms containing  $\Delta f$ , an expression is required giving  $\Delta f$  as a function of  $\bar{f}$  differentials, and toward this purpose we begin by substituting for  $f$  in (108) its expression given by (111), and dropping the terms in  $\Delta f$  when there are similar terms in  $f$ :

$$D \left( \frac{\partial^2 \Delta f}{\partial r^2} + \frac{1}{r} \frac{\partial \Delta f}{\partial r} + \frac{\partial^2 \bar{f}}{\partial x_1^2} \right) = \frac{\partial \bar{f}}{\partial t} + v_o \left( \frac{1+2k}{1+k} - 2 \frac{r^2}{r_o^2} \right) \frac{\partial \bar{f}}{\partial x_1} \quad (117)$$

Subtracting (116) from (117), and again dropping the appropriate  $\Delta f$  terms, we obtain:

$$D \left( \frac{\partial^2 \Delta f}{\partial r^2} + \frac{1}{r} \frac{\partial \Delta f}{\partial r} \right) = -k \frac{\partial \bar{f}}{\partial t} + v_o \left( \frac{1+2k}{1+k} - 2 \frac{r^2}{r_o^2} \right) \frac{\partial \bar{f}}{\partial x_1} \quad (118)$$

Solving (118) for  $\Delta f$ , and recalling that  $\Delta f$  must be finite when  $r = 0$ , we obtain:

$$\Delta f = \Delta f_o + \frac{1}{4D} \left[ -k \frac{\partial \bar{f}}{\partial t} r^2 + v_o \left( \frac{1+2k}{1+k} r^2 - \frac{r^4}{2r_o^2} \right) \frac{\partial \bar{f}}{\partial x_1} \right] \quad (119)$$

In principle,  $\Delta f_o$  should be chosen so as to satisfy (112), but when the expression just given for  $\Delta f$  is inserted in (116), the coefficient of  $\Delta f_o$  vanishes, and we obtain, after integrating and re-arranging the terms:

$$\left( D + \frac{1+6k+11k^2}{4(1+k)^2} \frac{v_o^2 r_o^2}{D} \right) \frac{\partial^2 \bar{f}}{\partial x_1^2} = (1+k) \frac{\partial \bar{f}}{\partial t} + \frac{k(1+4k)}{24(1+k)} \frac{v_o r_o^2}{D} \frac{\partial^2 \bar{f}}{\partial x_1 \partial t} \quad (120)$$

This equation shows that the effect of dynamic diffusion is almost as if the diffusion coefficient for the static case (i.e., the case of static diffusion in a coated tube with a coefficient of retentivity  $k$ ) were merely increased by the second term shown in the first parenthesis of (120). The departure from

this simple concept is represented by the term in  $\partial^2 \bar{f} / \partial x_1 \partial t$  which becomes eventually negligible when  $v_0 r_0$  is on the order of  $D$  (which will be seen to be the case in practical cases) and when diffusion has proceeded to the point where  $r_0(\partial \bar{f} / \partial x_1)$  is small when compared to  $\bar{f}$ . However, the rate of increase of the second moment and the overall rate of flow of the component are not affected by the  $\partial^2 \bar{f} / \partial x_1 \partial t$  term, as will be shown immediately.

Re-writing (120):

$$\frac{\partial \bar{f}}{\partial t} = a \frac{\partial^2 \bar{f}}{\partial x_1^2} - b \frac{\partial^2 \bar{f}}{\partial x_1 \partial t} \quad (121)$$

for short, we obtain for the incremental second moment:

$$\begin{aligned} du &= d \int_{-\infty}^{+\infty} \bar{f} x_1^2 dx_1 = dt \int_{-\infty}^{+\infty} \frac{\partial \bar{f}}{\partial t} x_1^2 dx_1 \\ &= dt \int_{-\infty}^{+\infty} \left( a \frac{\partial^2 \bar{f}}{\partial x_1^2} - b \frac{\partial^2 \bar{f}}{\partial x_1 \partial t} \right) x_1^2 dx_1. \end{aligned} \quad (122)$$

The first term of the integral leads to an expression similar to the incremental second moment obtained in (104).

The essential part of the second term in the integral can be written:

$$\int_{-\infty}^{+\infty} \frac{\partial^2 \bar{f}}{\partial x_1 \partial t} x_1^2 dx_1 = \left[ \frac{\partial \bar{f}}{\partial t} x_1^2 \right]_{-\infty}^{+\infty} - 2 \int_{-\infty}^{+\infty} \frac{\partial \bar{f}}{\partial t} x_1 dx_1. \quad (123)$$

The first term of the R.H.S. can be set to zero because of the known behaviour of the solution of (121) at infinity. The second integral can be written:

$$\int_{-\infty}^{+\infty} \frac{\partial \bar{f}}{\partial t} x_1 dx_1 = a \int_{-\infty}^{+\infty} \frac{\partial^2 \bar{f}}{\partial x_1^2} x_1 dx_1 - b \int_{-\infty}^{+\infty} \frac{\partial^2 \bar{f}}{\partial x_1 \partial t} x_1 dx_1. \quad (124)$$

The first integral of the R.H.S. can be written:

$$\int_{-\infty}^{+\infty} \frac{\partial^2 \bar{f}}{\partial x_1^2} x_1 dx_1 = \left[ \frac{\partial \bar{f}}{\partial x_1} x_1 - \bar{f} \right]_{-\infty}^{+\infty} \quad (125)$$

and vanishes by virtue of (101). The second integral can be written:

$$\int_{-\infty}^{+\infty} \frac{\partial^2 \bar{f}}{\partial x_1 \partial t} x_1 dx_1 = \left[ \frac{\partial \bar{f}}{\partial t} x_1 \right]_{-\infty}^{+\infty} - \frac{\partial}{\partial t} \int_{-\infty}^{+\infty} \bar{f} dx_1. \quad (126)$$

The first term of the second member vanishes by virtue of (101) and the second term vanishes because of the conservation of mass. Thus, the rate of increase of the second moment when diffusion is governed by (120) or (121) is the same as if the term in  $\partial^2 \bar{f} / \partial x_1 \partial t$  were absent.

Lastly, it will be observed that the L.H.S. of (124) could be written:

$$\frac{\partial}{\partial t} \int_{-\infty}^{+\infty} \bar{f} x_1 dx_1 \quad (127)$$

and since this term is the speed of the centre of gravity of the sample gas packet in the  $x_1$  coordinate, and vanishes because the last term of (123) vanishes, it is concluded that the overall motion of the mass sample in the  $x_1$  direction is indeed that adopted in (107) for the  $x \rightarrow x_1$  coordinate change, namely  $v_o/(1+k)$ .

The second moment for the case of gas flow studied here can be obtained by treating (120) as (39) was treated to obtain (104), and this gives:

$$du = \frac{2}{1+k} \left( D + \frac{1+6k+11k^2}{48(1+k)^2} \frac{v_o^2 r_o^2}{D} \right) dt. \quad (128)$$

The time required for a component with a given  $k$  to travel an elementary length  $dx_1$  of the tubular column is  $[(1+k)/v_o]dx_1$ , and when this expression is substituted for  $dt$  in (128) we obtain:

$$du = \left( 2 \frac{D}{v_o} + \frac{1+6k+11k^2}{24(1+k)^2} \frac{v_o r_o^2}{D} \right) dx_1. \quad (129)$$

... A formula similar to (129) can be derived for columns with a rectangular cross-section of thickness  $2z_o$ ...

$$du = \left( 2 \frac{D}{v_o} + \frac{4(1+9k+51k^2/2)}{105(1+k)^2} \frac{v_o z_o^2}{D} \right) dx_1. \quad (130)$$

## Appendix G. *Mathematica Code for Figures*

The following segments of Mathematica code were used to create some of the figures in this dissertation (150).

- This is the Mathematica code used to generate Figure 9:

```
v[x1_,p_]:=Sqrt[p^2(1-x1)+x1]^(-1)

Plot[Release[Table[v[x,p],{p,1,10,3}]],{x,0,1}]
```

- This is the Mathematica code used to generate Figure 12:

```
a[n_]:= (2 n-1) Pi/2;

<<Integral.m

vc2[y_,z_,b_,c_]:= -Sum[(Cos[n Pi] ((c n Pi)^2
-2 c^2-c(n Pi)^2)+2 c^2)/((n Pi)^3 Cosh[n Pi
b/(2 c)]) Cosh[n Pi y/c] Sin[n Pi z/c],
{n,1,Infinity}]

vp2[z_,c_]:= .5(z c-z^2)

Plot[vp2[z,1]/vp2[.5,1],{z,0,1}]
```

- This is the Mathematica code used to generate Figure 13:

```
a[n_]:= (2 n-1) Pi/2;

<<Integral.m

vc2[y_,z_,b_,c_]:= -Sum[(Cos[n Pi] ((c n Pi)^2
-2 c^2-c(n Pi)^2)+2 c^2)/((n Pi)^3 Cosh[n Pi
b/(2 c)]) Cosh[n Pi y/c] Sin[n Pi z/c],
{n,1,Infinity}]

vp2[z_,c_]:= .5(z c-z^2)

Plot3D[vp2[z,1]+vc2[y,z,6,1],{z,0,1},{y,-3,3}]

Show[%,{BoxRatios->{1,3,1}}]
```

- This is the Mathematica code used to generate Figure 14:

```
<<Integral.m
```

```
vave[c_,b_]:=4 c^2/b(b/48-4 c Pi^(-5)
  NSum[(n)^(-5) Tanh[n Pi b/(2 c)],
    {n,1,Infinity,2}])
```

```
Plot[100 vave[1,b]/.08333,{b,0,15},{PlotRange->{0,100}}]
```

- This is the Mathematica code used to generate Figure 15:

```
<<Integral.m
```

```
vave[c_,b_]:=4 c^2/b(b/48-4 c Pi^(-5)
  NSum[(n)^(-5) Tanh[n Pi b/(2 c)],
    {n,1,Infinity,2}])
```

```
qrect[c_,b_,mu_]:=mu/vave[c,b]
```

```
qpar[c_,mu_]:=12 mu/c^2
```

```
qr=SI[qrect[30 Micron, 130 Micron, 200 Micro Poise]]//N
```

```
qp=SI[qpar[30 Micron,200 Micro Poise]]//N
```

```
vout[q_,p_]:=-(1 Atmosphere)^2+p^2/
  (2 q (1 Atmosphere) 50 Centi Meter)
```

```
Plot[{N[Convert[vout[qp,p Psi+1 Atmosphere]
  4414 Micron^2,
  Micro Liter/Second] Second/Liter/Micro],
  N[Convert[vout[qr,p Psi+1 Atmosphere]
  4414 Micron^2,
  Micro Liter/Second] Second/Liter/Micro]},
  {p,1,50}]
```

```
grph1=%
```

```
realdata={{5,1},{10,2.5},{15,4},{20,6.5},
  {25,8.3},{30,11},{35,14.4},{40,16.7},
  {45,20},{50,24}};
```

```
ListPlot[realdata]
```

```
grph2=%
```

```
Show[grph1,grph2]
```

- This is the Mathematica code used to generate Figure 17:

```
kr[k_]:= 2 k
kf[k_]:= k
hround[k_,d_,v_,ro_]:=2 d/v + (1+6 k+11 k^2)/
(24 (1+k)^2) v ro^2/d;
hflat[k_,d_,v_,zo_]:=2 d/v + 4(1+9 k+51/2 k^2)/
(105 (1+k)^2) v zo^2/d;
sround[k_]:= (kr[k]/(kr[k]+1))^2 / hround[kr[k],1,1,1]
sflat[k_]:= (kf[k]/(kf[k]+1))^2 / hflat[kf[k],1,1,1]
Limit[sround[k],k->10^90]//N
0.4067796610169491525
Plot[{sround[k]/.40678,sflat[k]/.40678},{k,0,10},
{PlotStyle->{GrayLevel[0],
GrayLevel[.25]},PlotRange->{0,1}}]
```

- This is the Mathematica code used to generate Figure 38:

```
<<Units.m
vo[pi_,zo_,visc_,len_]:=zo^2 (pi^2-(1 Atmosphere)^2)/
(6 visc len 1 Atmosphere)
kf[w_,zo_,y_,k_]:=w(2 zo +y)/(zc y) k
j[pi_,po_]:=0
g[pi_,po_]:=9/8 ((pi/po)^4-1)((pi/po)^2-1)/
((pi/po)^3-1)^2
hflat[k_,d_,zo_,pi_,len_,visc_,partcoef_]:=((
2 d/vo[pi,zo,visc,len] +
4(1+9 k+51/2 k^2)/(105 (1+k)^2)
vo[pi,zo,visc,len] zo^2/d) g[pi,1 Atmosphere]+
j[pi,1 Atmosphere] vo[pi,zo,visc,len] 2 k^3 zo^2/
(3(1+k)^2 partcoef^2
10^-6 (Centi Meter)^2/Second));
sflat[k_,d_,zo_,pi_,len_,visc_,w_,y_]:=SI[len
(kf[w,zo,y,k]/(kf[w,zo,y,k]+1))^2 /
```

```

hflat[kf[w,zo,y,k],d,zo,pi,len,visc,k]]

sfquick[zo_,pi_,k_]:=SI[sflat[k,0.1 (Centi Meter)^2/Second,
zo Micro Meter,
pi Psi+1 Atmosphere,.5 Meter,200 Micro Poise,
0.1 Micro Meter,0.01 Centi Meter]]];

Plot[{sfquick[zo,10,100],sfquick[zo,20,100],
sfquick[zo,30,100],sfquick[zo,60,100]},
{zo,0.1,50},{PlotRange->{0,14000}}]

```

• This is the Mathematica code used to generate Figure 39:

```

<<Units.m

vo[pi_,zo_,visc_,len_]:=zo^2 (pi^2-(1 Atmosphere)^2)/
(6 visc len 1 Atmosphere)

kf[w_,zo_,y_,k_]:=w(2 zo +y)/(zo y) k

j[pi_,po_]:=0

g[pi_,po_]:=9/8 ((pi/po)^4-1)((pi/po)^2-1)/
((pi/po)^3-1)^2

hflat[k_,d_,zo_,pi_,len_,visc_,partcoef_]:=((
2 d/vo[pi,zo,visc,len] +
4(1+9 k+51/2 k^2)/(105 (1+k)^2)
vo[pi,zo,visc,len] zo^2/d) g[pi,1 Atmosphere]+
j[pi,1 Atmosphere] vo[pi,zo,visc,len] 2 k^3 zo^2/
(3(1+k)^2 partcoef^2
10^-6 (Centi Meter)^2/Second));

sflat[k_,d_,zo_,pi_,len_,visc_,w_,y_]:=SI[len
(kf[w,zo,y,k]/(kf[w,zo,y,k]+1))^2 /
hflat[kf[w,zo,y,k],d,zo,pi,len,visc,k]]

sflog[zo_,pi_,k_]:=Log[
SI[sflat[k,0.1 (Centi Meter)^2/Second,
zo Micro Meter,
pi Psi+1 Atmosphere,.5 Meter,200 Micro Poise,
0.1 Micro Meter,0.01 Centi Meter]]];

Plot[{sflog[zo,30,1],sflog[zo,30,10],
sflog[zo,30,100],sflog[zo,30,1000]},
{zo,0.1,50}]

```

Appendix H. *Flowmeter Calibration Table*

Table 17. Flowmeter Calibration Table (Gilmont Instruments, Inc., Model 8555-8654).

Flow Meter Scale	Flow Rate (ml/min)	Flow Meter Scale	Flow Rate (ml/min)
1	1.44	17	17.4
2	1.85	18	19.1
3	2.33	19	21.1
4	2.87	20	23.2
5	3.49	21	25.3
6	4.17	22	27.5
7	4.94	23	29.7
8	5.78	24	31.9
9	6.71	25	34.2
10	7.72	26	36.7
11	8.81	27	39.2
12	10	28	41.7
13	11.3	29	44.3
14	12.7	30	46.9
15	14.1	31	49.6
16	15.7	32	52.3

### Appendix I. Chemiresistor Evaluation Data

This appendix contains the data collected during the chemiresistor evaluation. A summary of the pertinent parameters is provided in Tables 18 and 19, while Figures 148 through 186 depict each evaluation.

Table 18. Chemiresistor Evaluation Summary with NO<sub>2</sub> as the Challenge Gas.

NO <sub>2</sub> Concentration (ppm)	Temperature (°C)	Response (pA)	Baseline (pA)
75	50	7.4	5.2
75	55	5.8	6.4
75	60	5.1	7.0
75	68	3.3	9.4
75	70	3.1	10.2
75	80	1.9	14.7
75	90	1.3	20.2
255	70	6.2	10.1
255	80	3.9	14.3
255	90	2.5	20.0
350	70	7.2	10.1
350	80	4.5	14.5
350	90	3.0	20.2
460	70	8.3	10.0
460	80	5.4	14.0
460	90	3.6	20.0
570	70	9.4	9.8
570	80	5.9	14.2
570	90	3.6	20.3

**Table 19. Chemiresistor Evaluation Summary with NH<sub>3</sub> as the Challenge Gas.**

NH <sub>3</sub> Concentration (ppm)	Temperature (°C)	Response (pA)	Baseline (pA)
6300	55	1.5	6.0
6300	60	1.6	7.2
6300	70	1.5	10.0
6300	75	1.6	12.2
6300	80	1.6	14.4
5000	70	1.5	10.2
5000	80	1.6	14.1
5000	90	1.6	20.2
4000	70	1.5	10.0
4000	80	1.5	14.2
4000	90	1.6	20.2
3000	70	1.6	10.0
3000	80	1.4	14.2
3000	90	1.6	20.0
1500	70	0.8	9.9
1500	80	0.8	14.5
1500	90	0.7	20.0
500	70	0.4	10.2
500	80	0.3	14.4
500	90	0.3	20.1

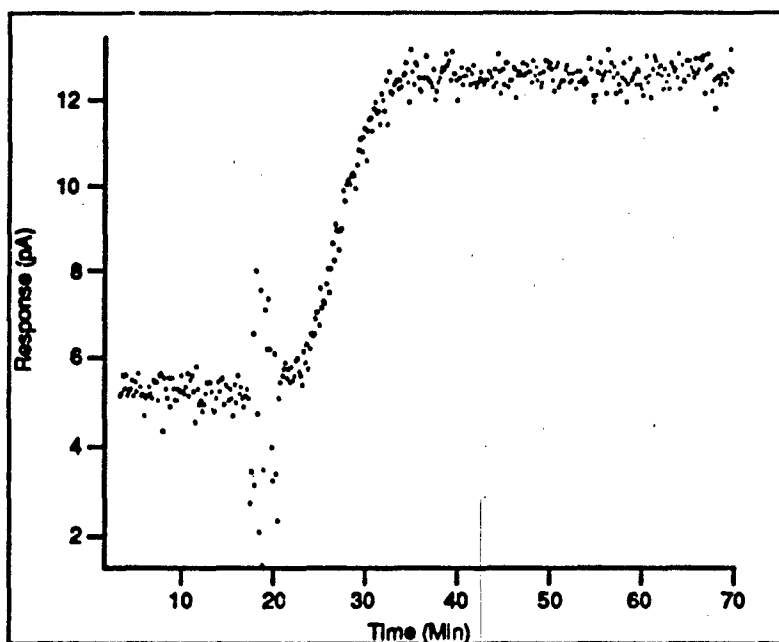


Figure 148. Chemiresistor Evaluation (75 ppm  $\text{NO}_2$  and  $50^\circ\text{C}$ ). The Response is 7.4 pA, and the Baseline is 5.2 pA.

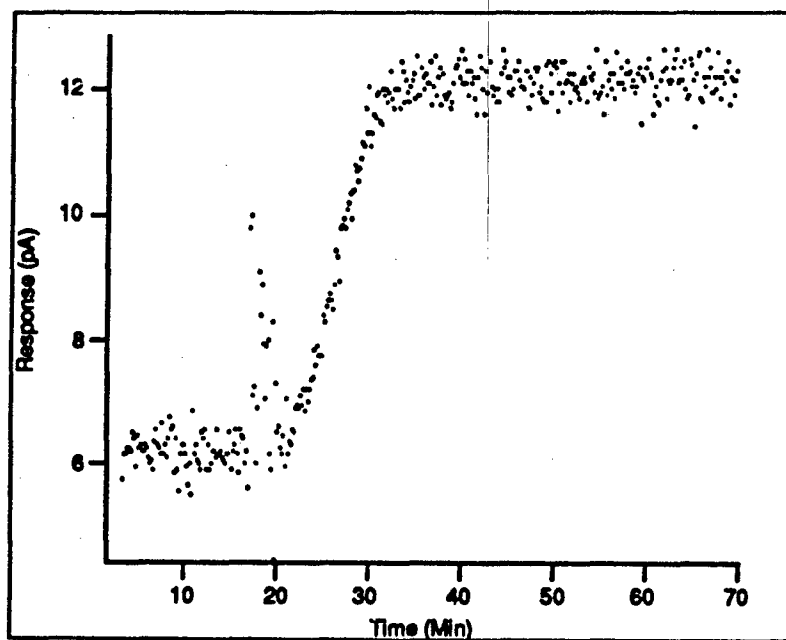


Figure 149. Chemiresistor Evaluation (75 ppm  $\text{NO}_2$  and  $55^\circ\text{C}$ ). The Response is 5.8 pA, and the Baseline is 6.4 pA.

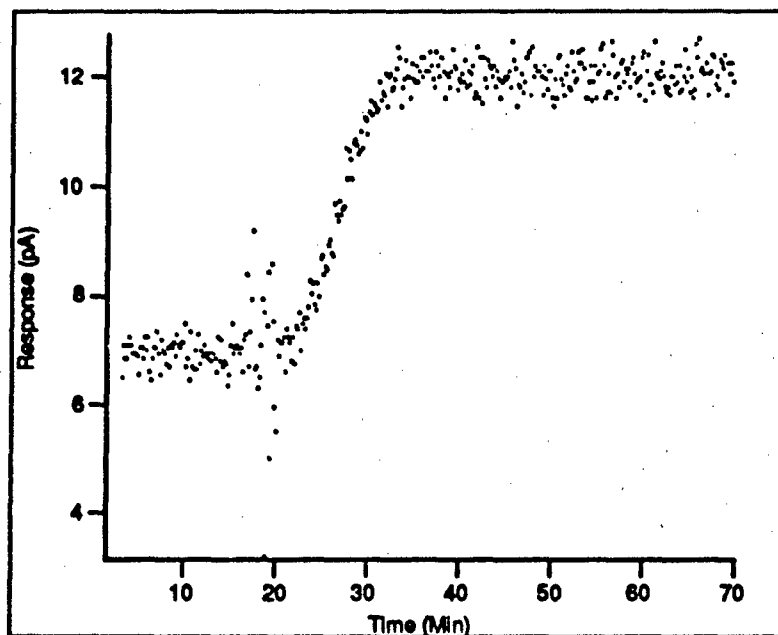


Figure 150. Chemiresistor Evaluation (75 ppm NO<sub>2</sub> and 60°C). The Response is 5.1 pA, and the Baseline is 7 pA.

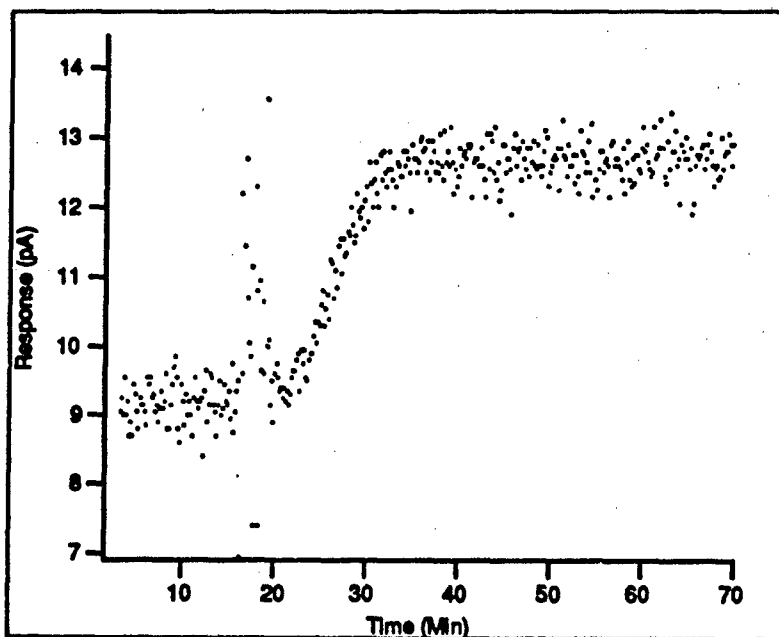


Figure 151. Chemiresistor Evaluation (75 ppm NO<sub>2</sub> and 68°C). The Response is 3.3 pA, and the Baseline is 9.4 pA.

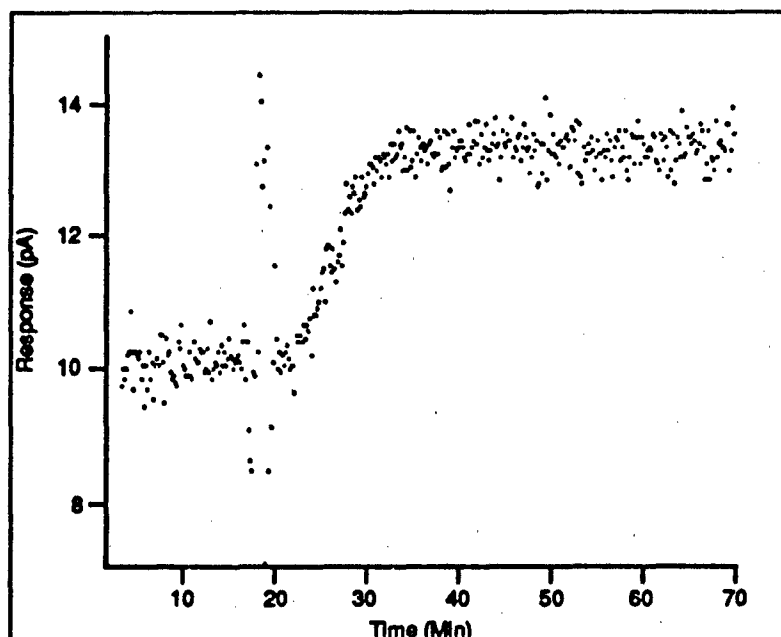


Figure 152. Chemiresistor Evaluation (75 ppm NO<sub>2</sub> and 70°C). The Response is 3.1 pA, and the Baseline is 10.2 pA.

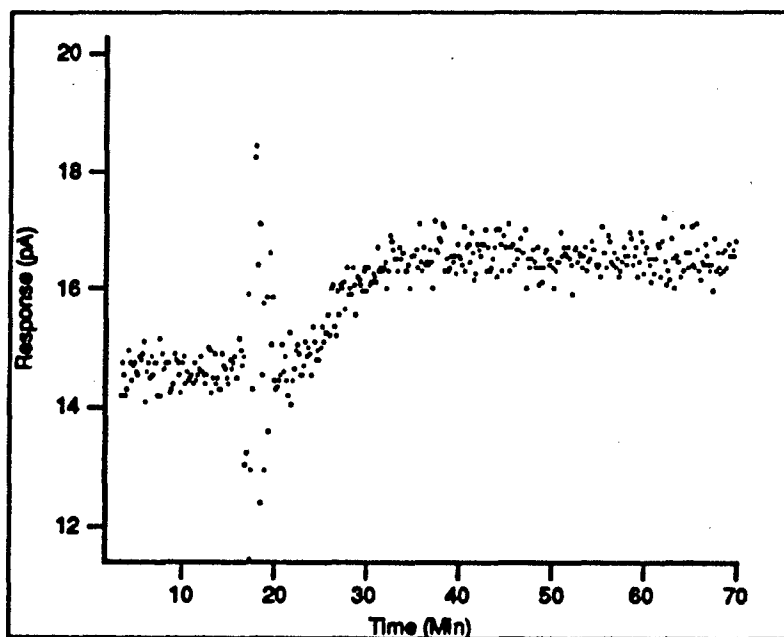


Figure 153. Chemiresistor Evaluation (75 ppm NO<sub>2</sub> and 80°C). The Response is 1.9 pA, and the Baseline is 14.7 pA.

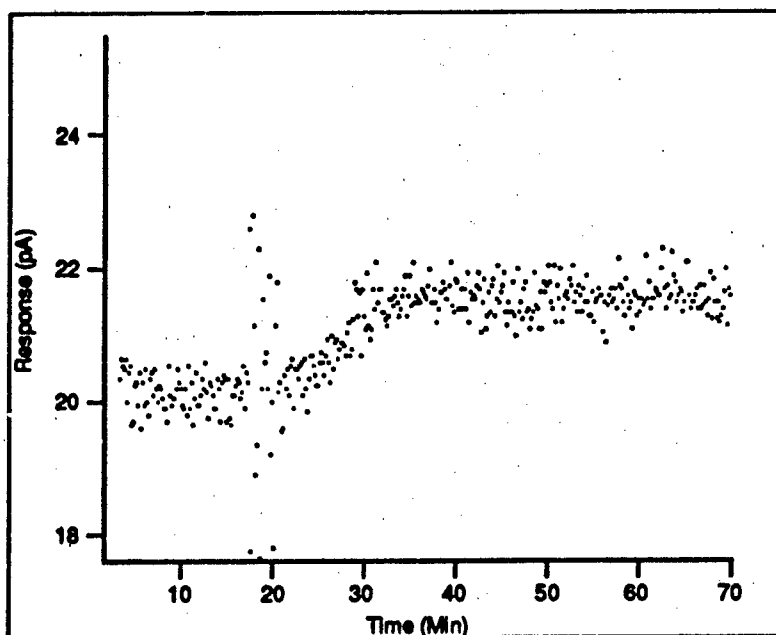


Figure 154. Chemiresistor Evaluation (75 ppm  $\text{NO}_2$  and  $90^\circ\text{C}$ ). The Response is 1.3 pA, and the Baseline is 20.2 pA.

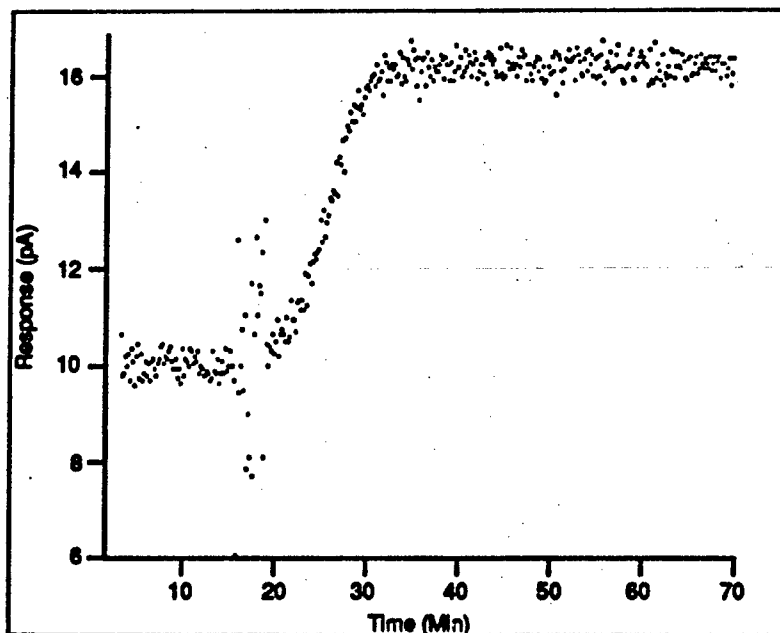


Figure 155. Chemiresistor Evaluation (255 ppm  $\text{NO}_2$  and  $70^\circ\text{C}$ ). The Response is 6.2 pA, and the Baseline is 10.1 pA.

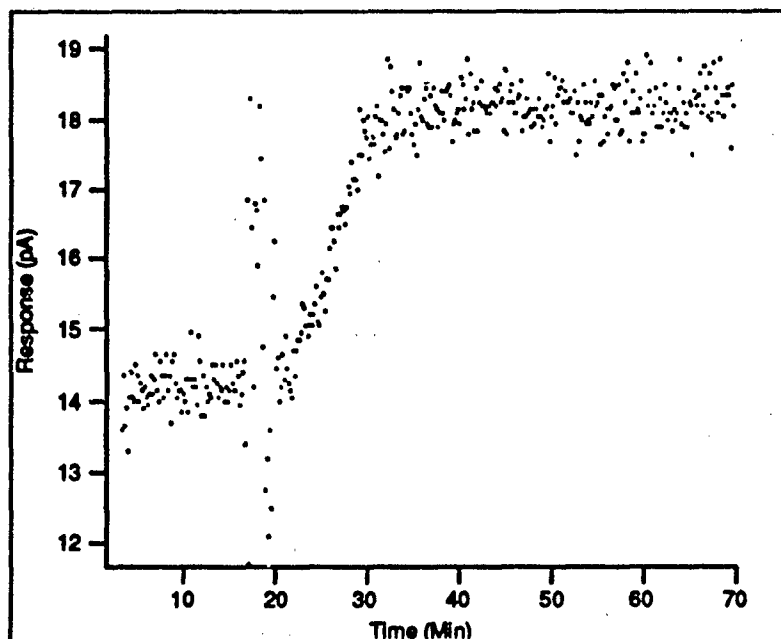


Figure 156. Chemiresistor Evaluation (255 ppm  $\text{NO}_2$  and  $80^\circ\text{C}$ ). The Response is 3.9 pA, and the Baseline is 14.3 pA.

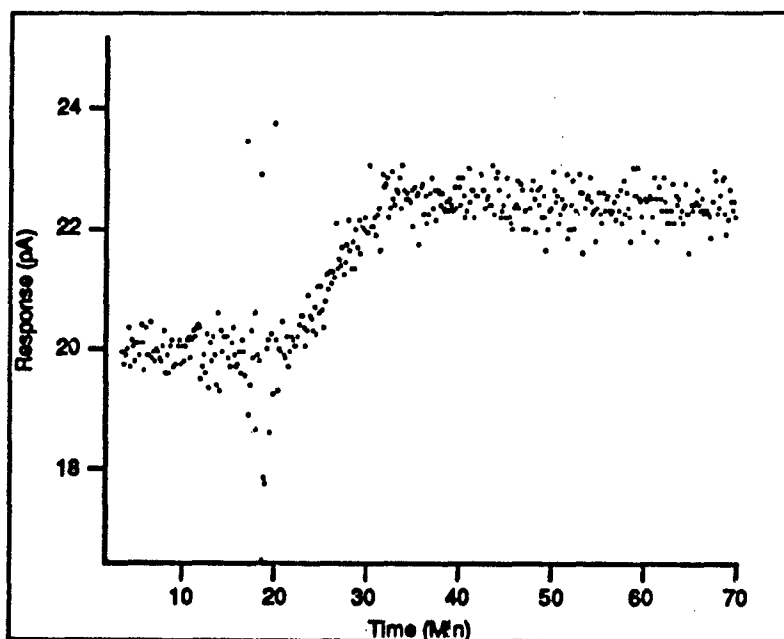


Figure 157. Chemiresistor Evaluation (255 ppm  $\text{NO}_2$  and  $90^\circ\text{C}$ ). The Response is 2.5 pA, and the Baseline is 20 pA.

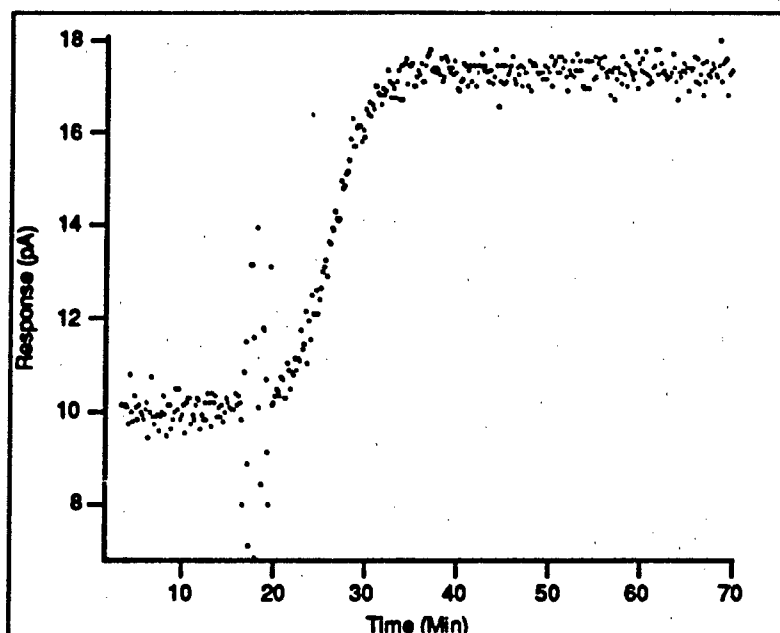


Figure 158. Chemiresistor Evaluation (350 ppm  $\text{NO}_2$  and  $70^\circ\text{C}$ ). The Response is 7.2 pA, and the Baseline is 10.1 pA.

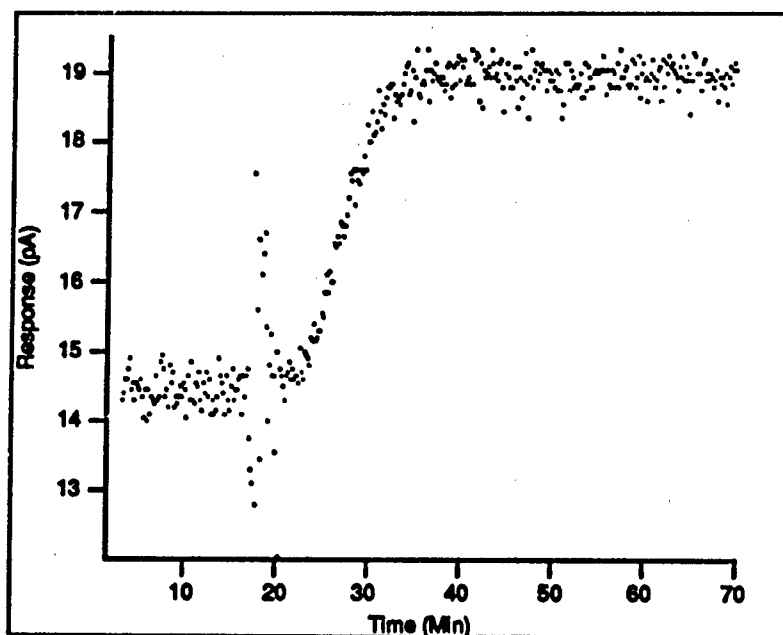


Figure 159. Chemiresistor Evaluation (350 ppm  $\text{NO}_2$  and  $80^\circ\text{C}$ ). The Response is 4.5 pA, and the Baseline is 14.5 pA.

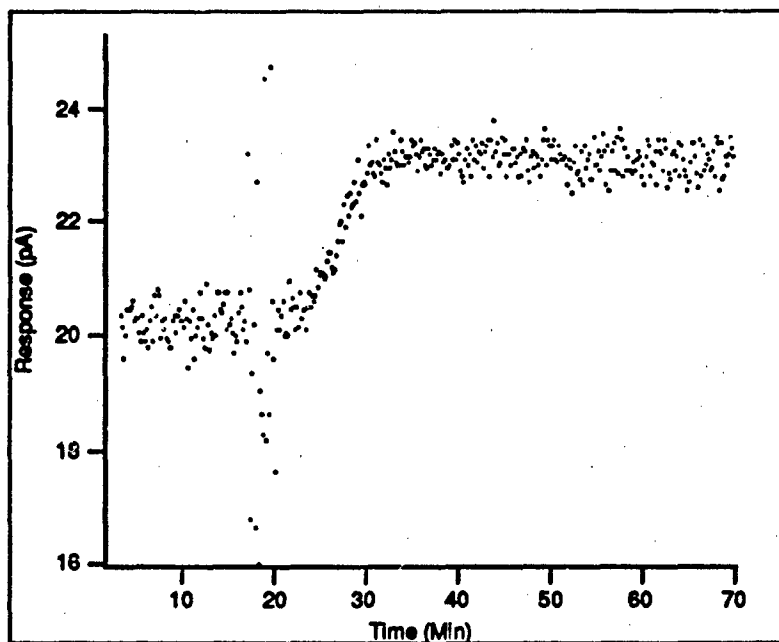


Figure 160. Chemiresistor Evaluation (350 ppm  $\text{NO}_2$  and  $90^\circ\text{C}$ ). The Response is 3 pA, and the Baseline is 20.2 pA.

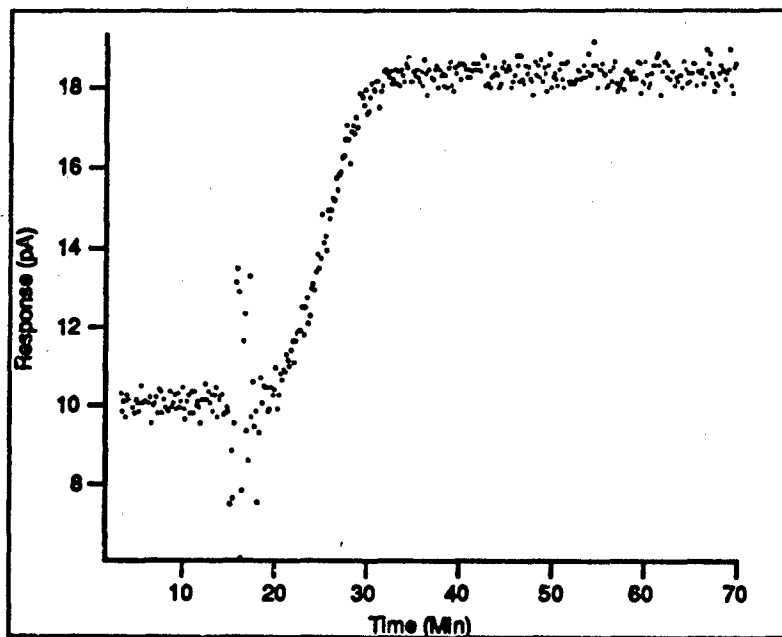


Figure 161. Chemiresistor Evaluation (460 ppm  $\text{NO}_2$  and  $70^\circ\text{C}$ ). The Response is 8.3 pA, and the Baseline is 10 pA.

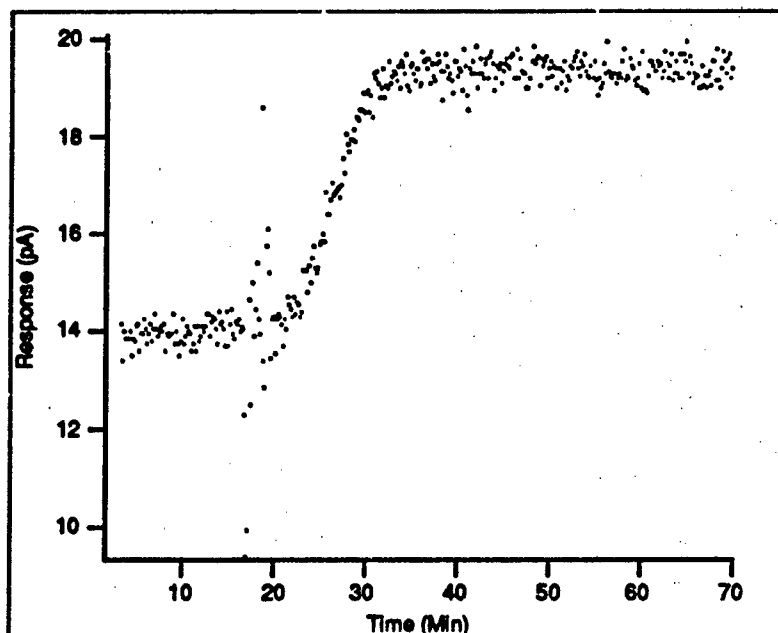


Figure 162. Chemiresistor Evaluation (460 ppm NO<sub>2</sub> and 80°C). The Response is 5.4 pA, and the Baseline is 14 pA.

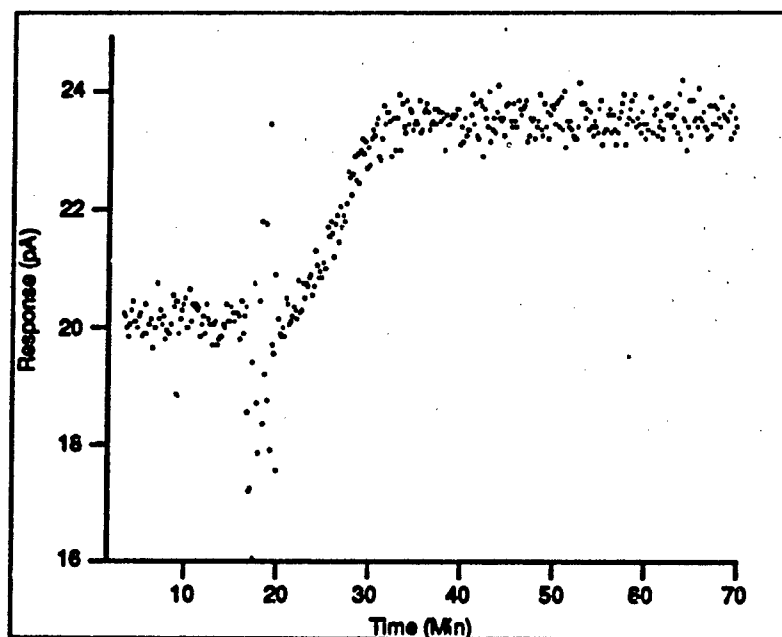


Figure 163. Chemiresistor Evaluation (460 ppm NO<sub>2</sub> and 90°C). The Response is 3.6 pA, and the Baseline is 20 pA.

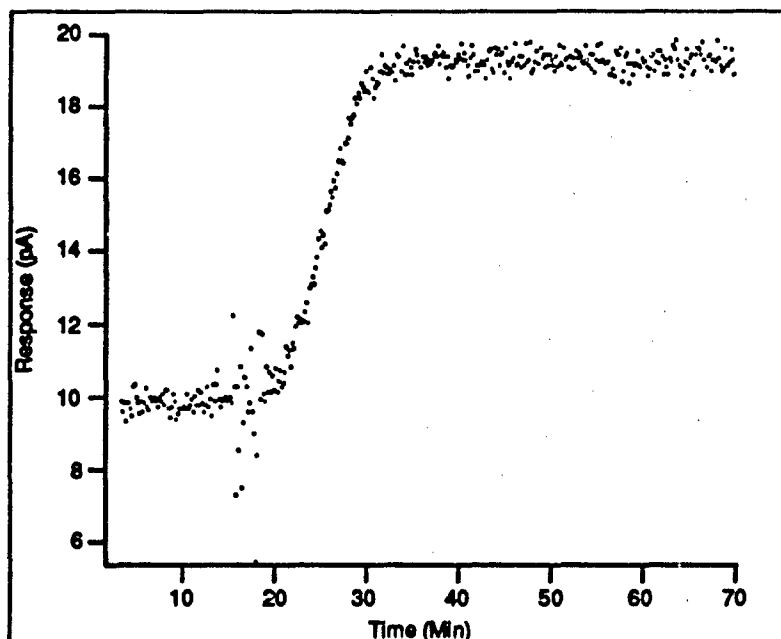


Figure 164. Chemiresistor Evaluation (570 ppm NO<sub>2</sub> and 70°C). The Response is 9.4 pA, and the Baseline is 9.8 pA.

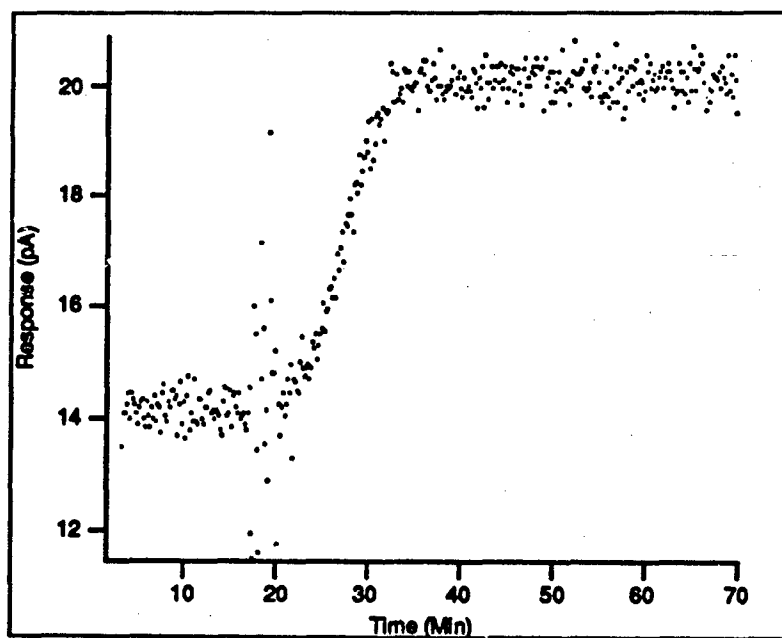


Figure 165. Chemiresistor Evaluation (570 ppm NO<sub>2</sub> and 80°C). The Response is 5.9 pA, and the Baseline is 14.2 pA.

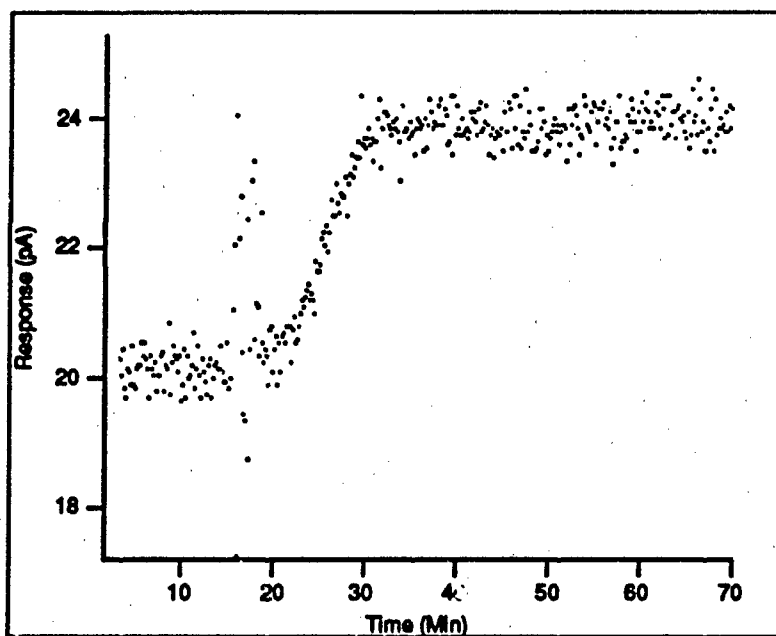


Figure 166. Chemiresistor Evaluation (570 ppm  $\text{NO}_2$  and  $90^\circ\text{C}$ ). The Response is 3.6 pA, the Baseline is 20.3 pA.

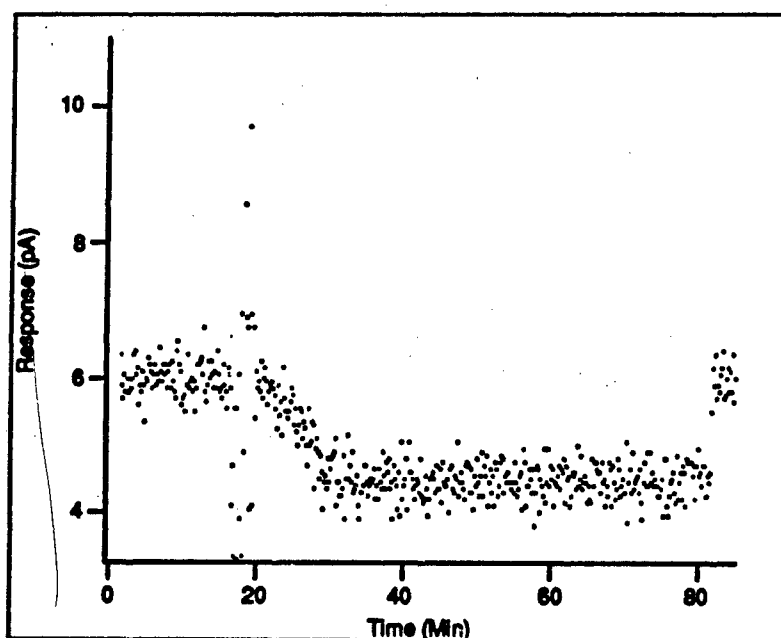


Figure 167. Chemiresistor Evaluation (6300 ppm  $\text{NH}_3$  and  $55^\circ\text{C}$ ). The Response is 1.5 pA, and the Baseline is 6 pA.

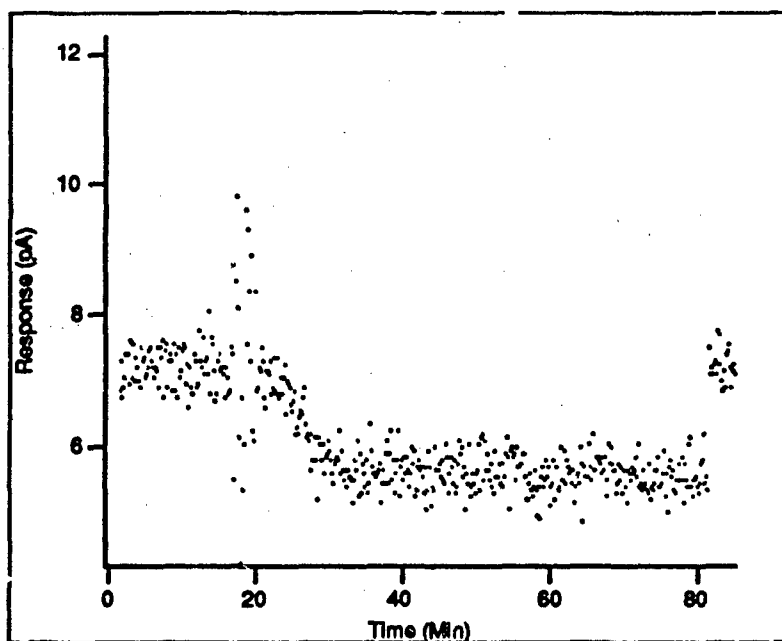


Figure 168. Chemiresistor Evaluation (6300 ppm  $\text{NH}_3$  and  $60^\circ\text{C}$ ). The Response is 1.6 pA, and the Baseline is 7.2 pA.

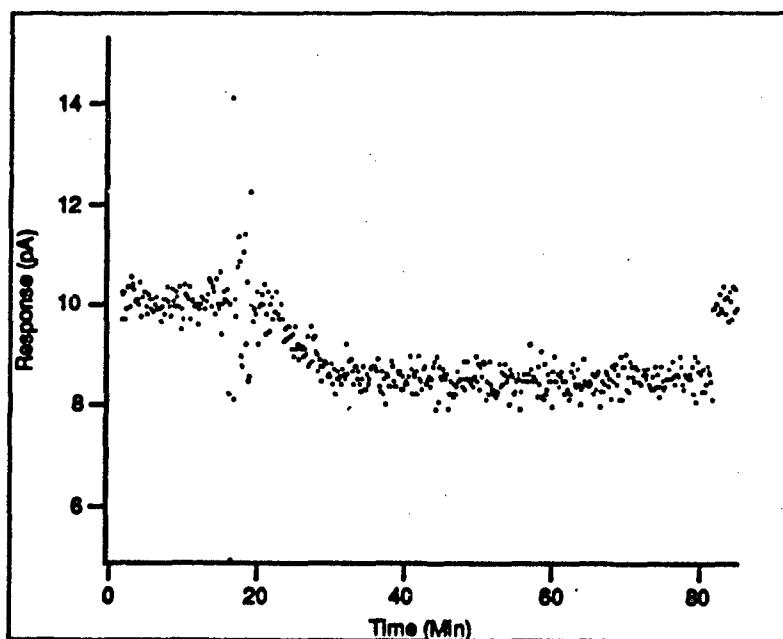


Figure 169. Chemiresistor Evaluation (6300 ppm  $\text{NH}_3$  and  $70^\circ\text{C}$ ). The Response is 1.5 pA, and the Baseline is 10 pA.

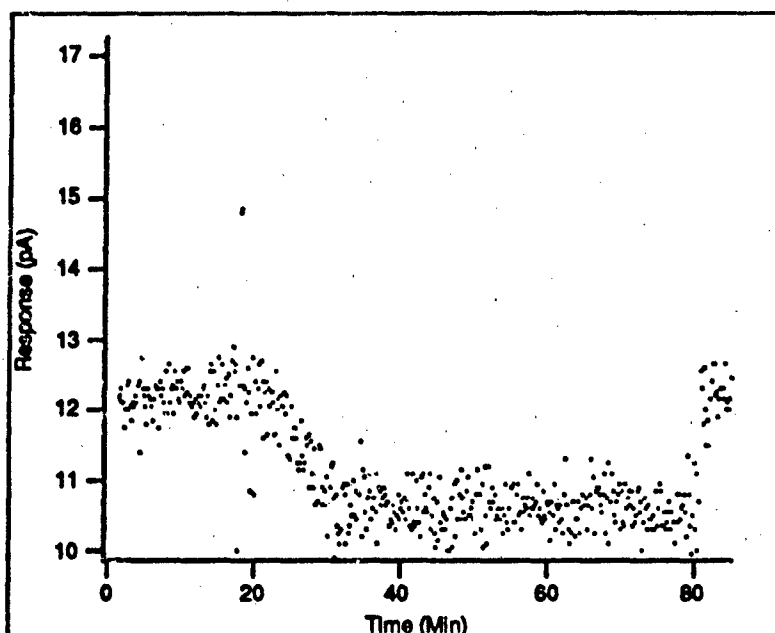


Figure 170. Chemiresistor Evaluation (6300 ppm  $\text{NH}_3$  and  $75^\circ\text{C}$ ). The Response is 1.6 pA, and the Baseline is 12.2 pA.

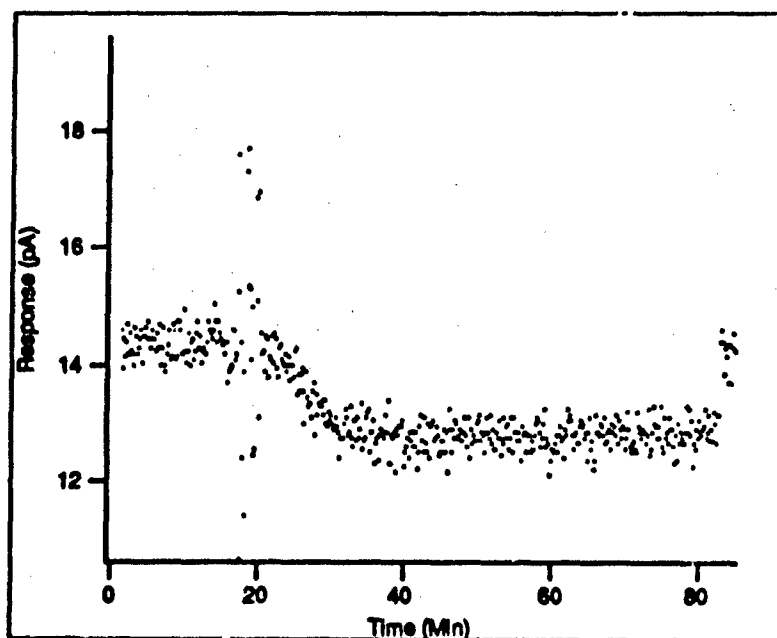


Figure 171. Chemiresistor Evaluation (6300 ppm  $\text{NH}_3$  and  $80^\circ\text{C}$ ). The Response is 1.6 pA, and the Baseline is 14.4 pA.

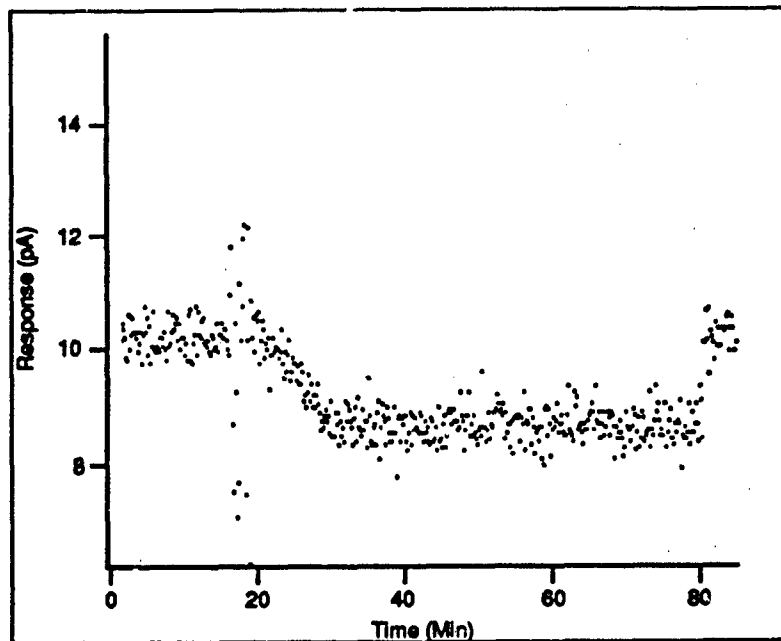


Figure 172. Chemiresistor Evaluation (5000 ppm  $\text{NH}_3$  and  $70^\circ\text{C}$ ). The Response is 1.5 pA, and the Baseline is 10.2 pA.

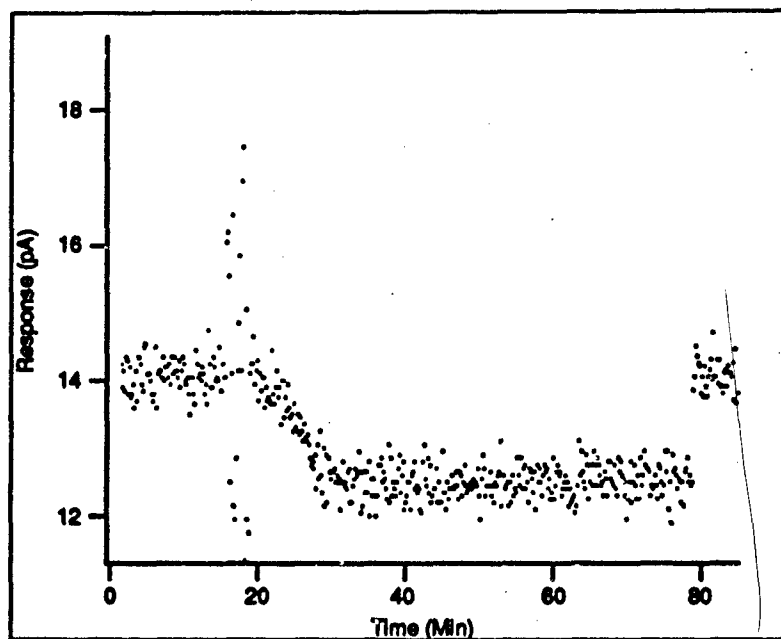


Figure 173. Chemiresistor Evaluation (5000 ppm  $\text{NH}_3$  and  $80^\circ\text{C}$ ). The Response is 1.6 pA, and the Baseline is 14.1 pA.

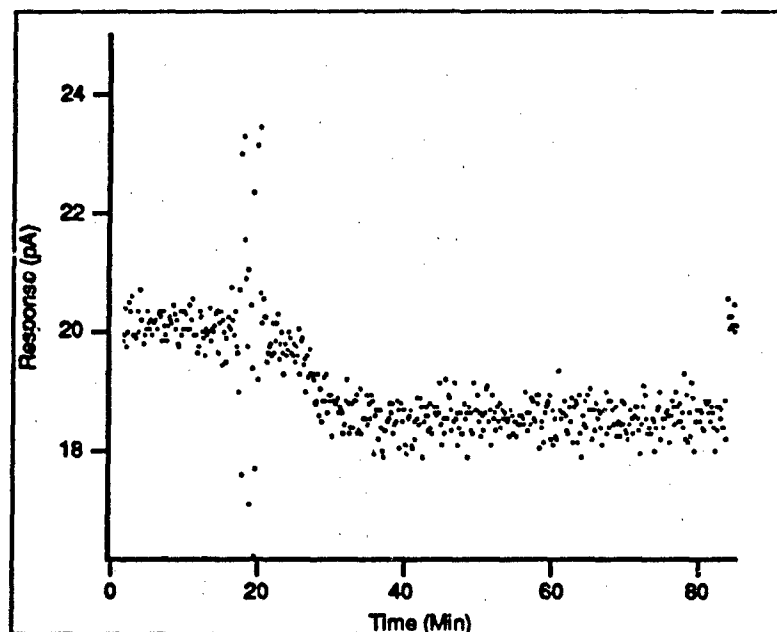


Figure 174. Chemiresistor Evaluation (5000 ppm  $\text{NH}_3$  and  $90^\circ\text{C}$ ). The Response is 1.6 pA, and the Baseline is 20.2 pA.

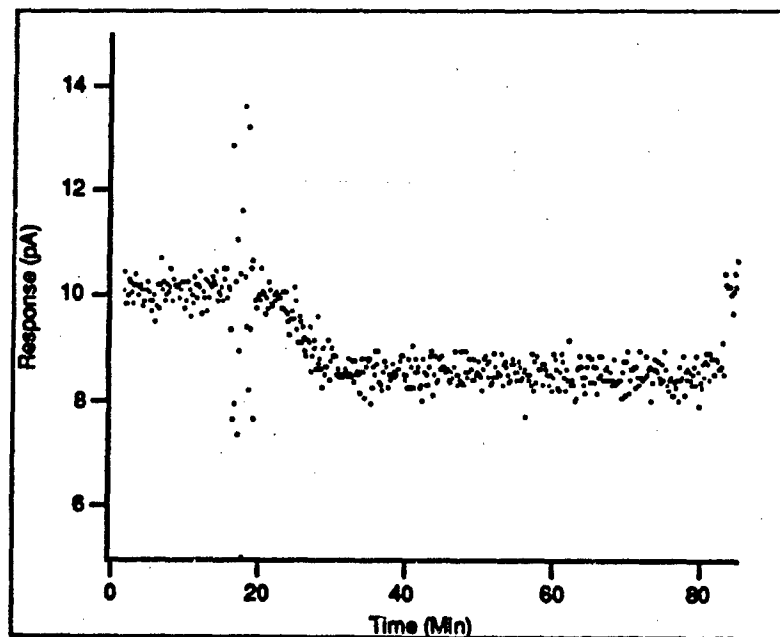


Figure 175. Chemiresistor Evaluation (4000 ppm  $\text{NH}_3$  and  $70^\circ\text{C}$ ). The Response is 1.5 pA, and the Baseline is 10 pA.

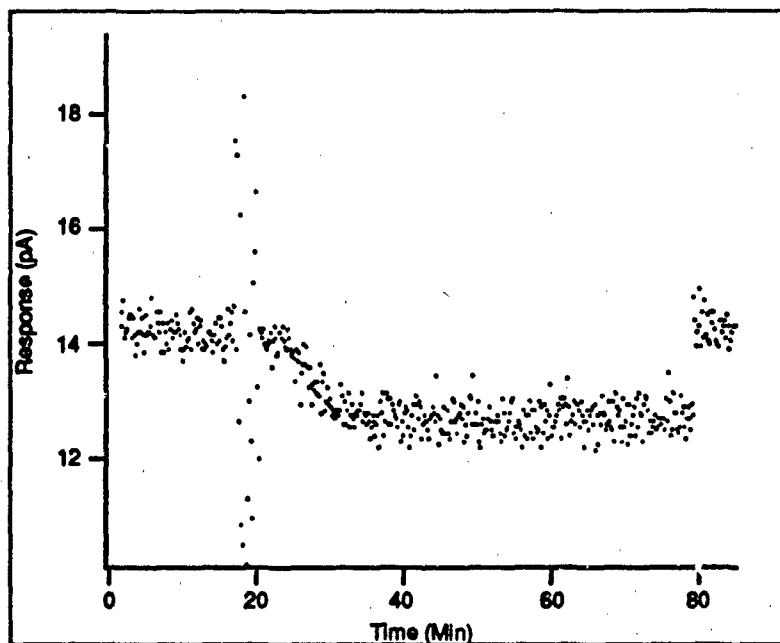


Figure 176. Chemiresistor Evaluation (4000 ppm  $\text{NH}_3$  and  $80^\circ\text{C}$ ). The Response is 1.5 pA, and the Baseline is 14.2 pA.

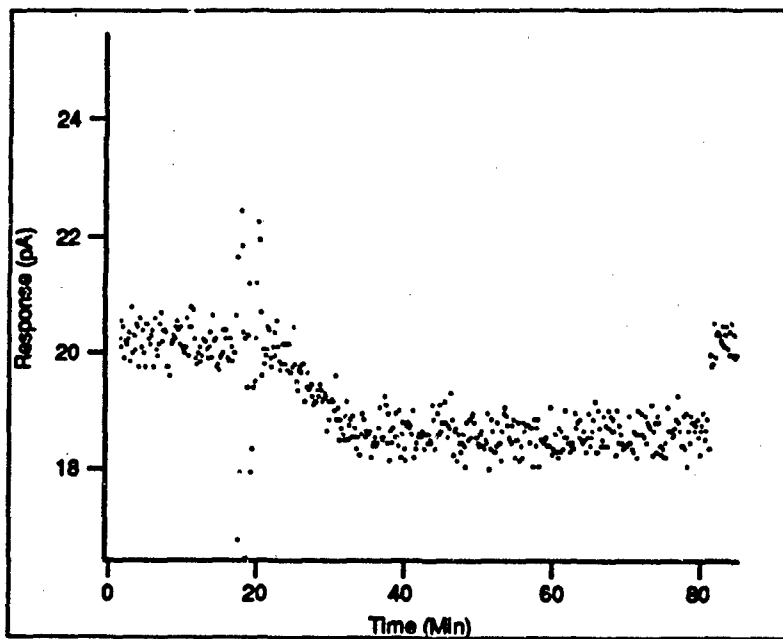


Figure 177. Chemiresistor Evaluation (4000 ppm  $\text{NH}_3$  and  $90^\circ\text{C}$ ). The Response is 1.6 pA, and the Baseline is 20.2 pA.

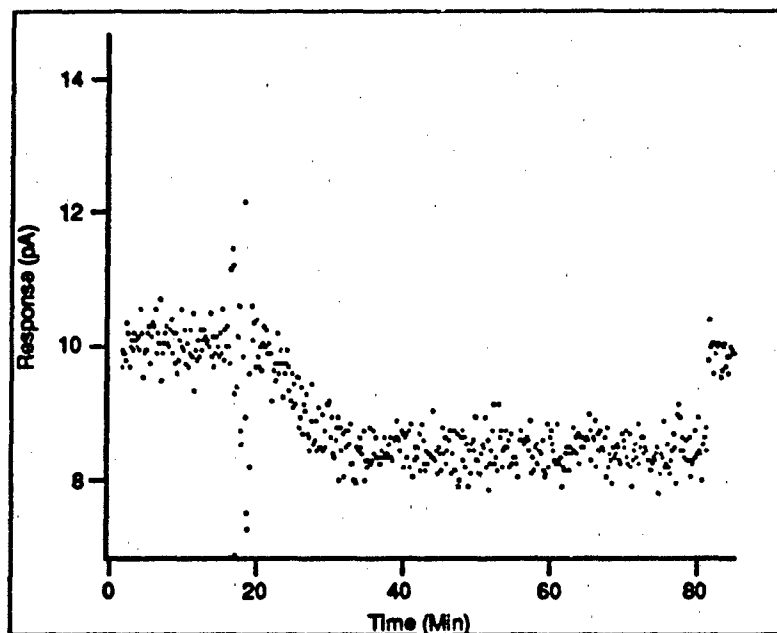


Figure 178. Chemiresistor Evaluation (3000 ppm  $\text{NH}_3$  and  $70^\circ\text{C}$ ). The Response is 1.6 pA, and the Baseline is 10 pA.

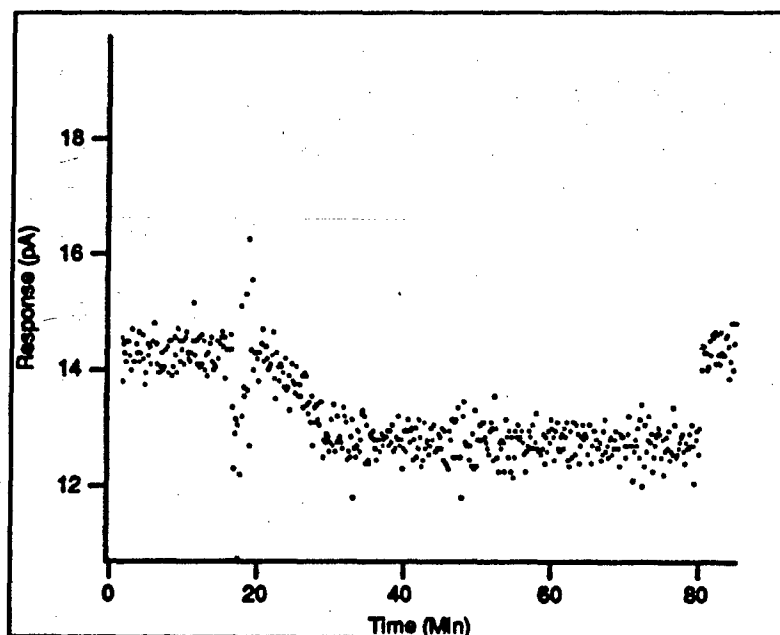


Figure 179. Chemiresistor Evaluation (3000 ppm  $\text{NH}_3$  and  $80^\circ\text{C}$ ). The Response is 1.4 pA, and the Baseline is 14.2 pA.

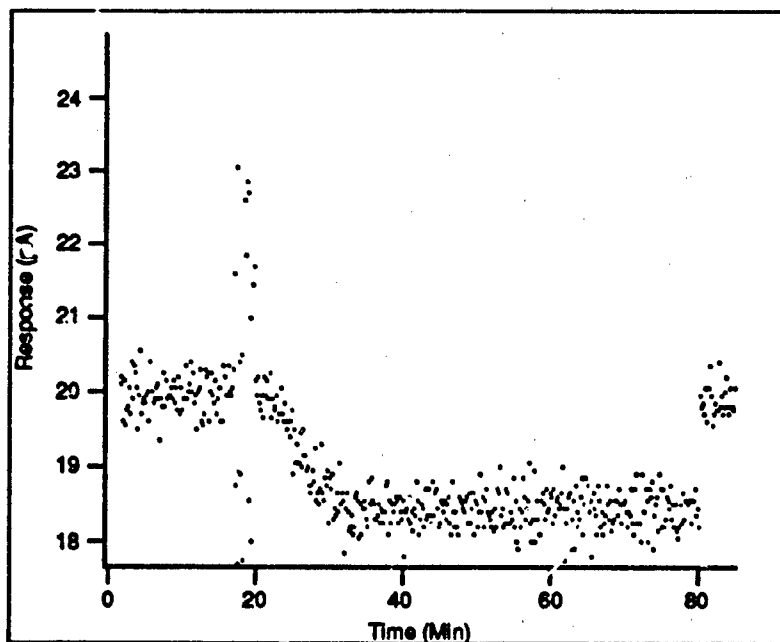


Figure 180. Chemiresistor Evaluation (3000 ppm  $\text{NH}_3$  and  $90^\circ\text{C}$ ). The Response is 1.6 pA, and the Baseline is 20 pA.

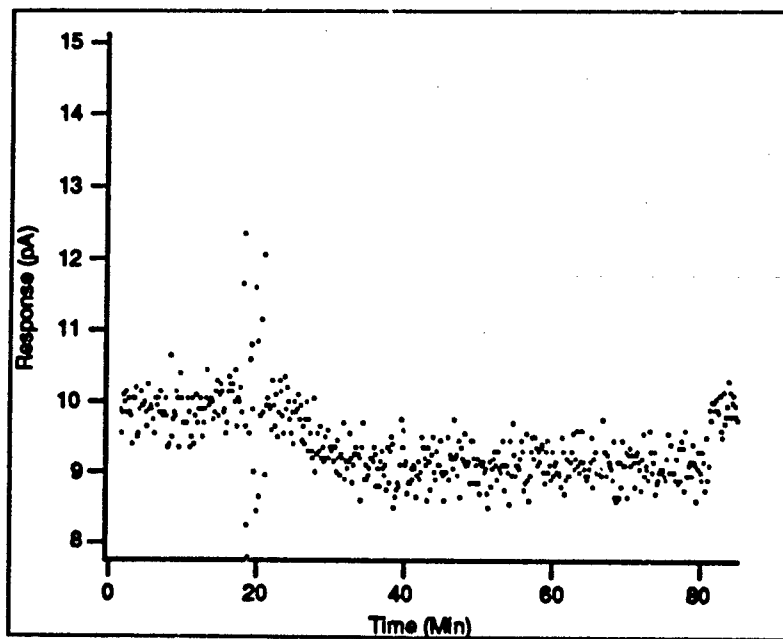


Figure 181. Chemiresistor Evaluation (1500 ppm  $\text{NH}_3$  and  $70^\circ\text{C}$ ). The Response is 0.8 pA, and the Baseline is 9.9 pA.

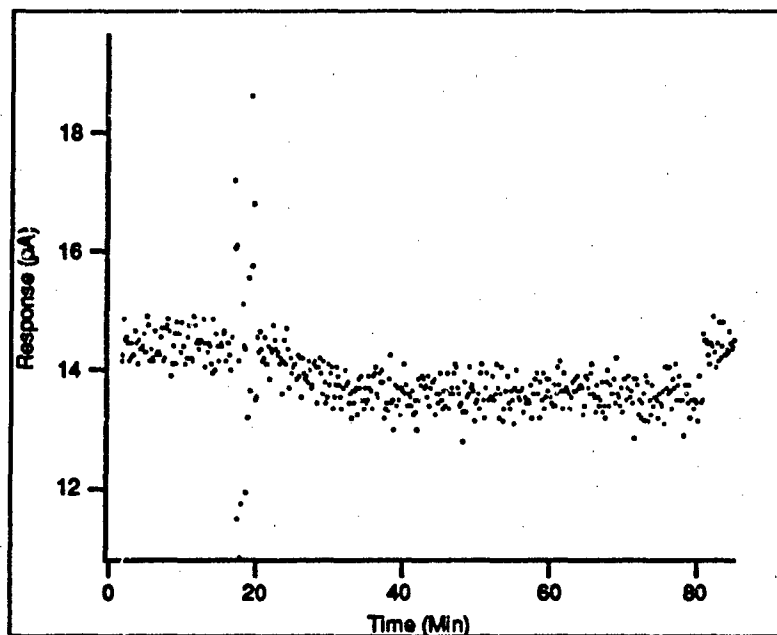


Figure 182. Chemiresistor Evaluation (1500 ppm  $\text{NH}_3$  and  $80^\circ\text{C}$ ). The Response is 0.8 pA, and the Baseline is 14.5 pA.

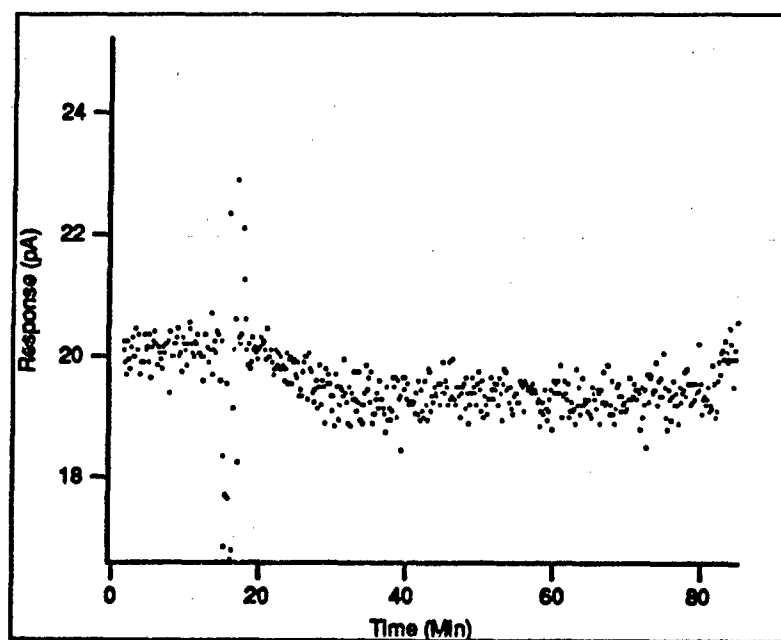


Figure 183. Chemiresistor Evaluation (1500 ppm  $\text{NH}_3$  and  $90^\circ\text{C}$ ). The Response is 0.7 pA, and the Baseline is 20 pA.

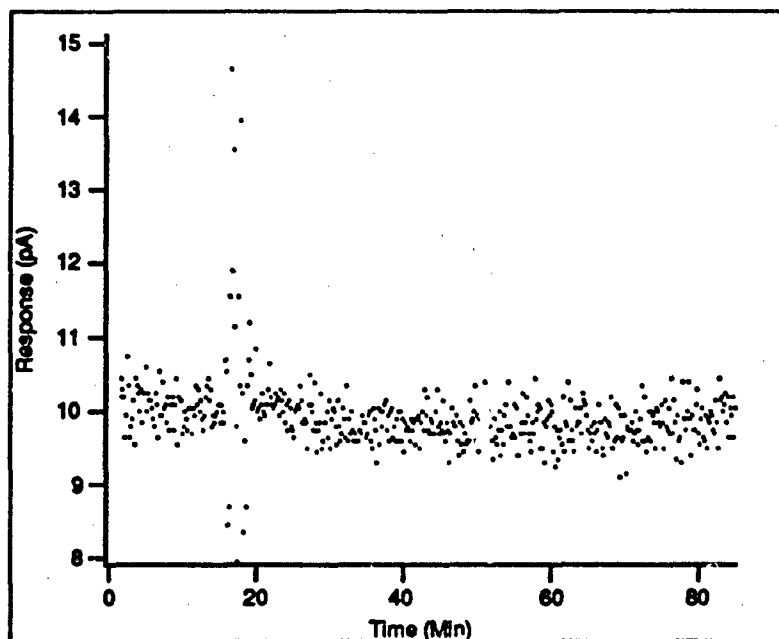


Figure 184. Chemiresistor Evaluation (500 ppm  $\text{NH}_3$  and  $70^\circ\text{C}$ ). The Response is 0.4 pA, and the Baseline is 10.2 pA.

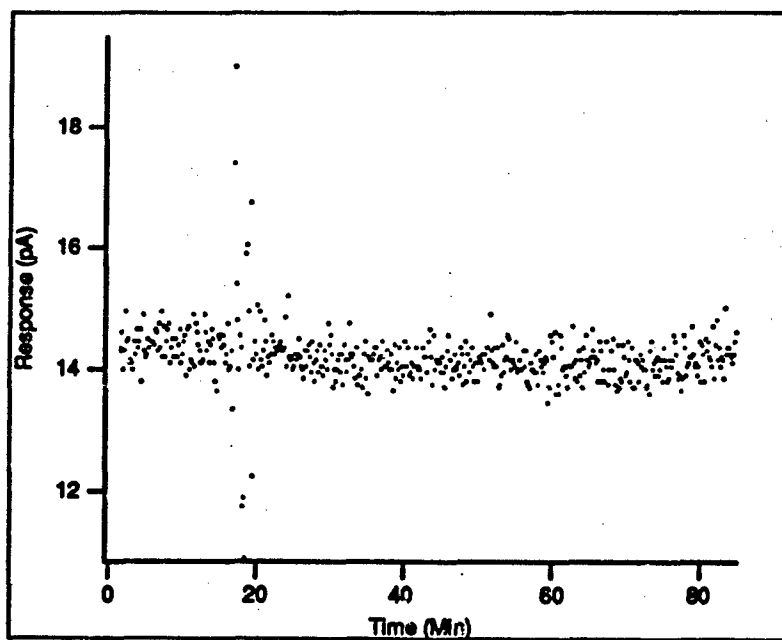
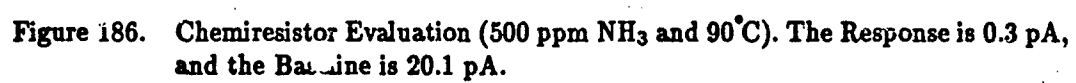


Figure 185. Chemiresistor Evaluation (500 ppm  $\text{NH}_3$  and  $80^\circ\text{C}$ ). The Response is 0.3 pA, and the Baseline is 14.4 pA.



### Appendix J. Micromachined Gas Chromatograph Evaluation Data

This appendix contains the data collected during the micromachined gas chromatograph evaluation. Summaries of the parameters obtained from the non-linear least-squares curve fitting process are provided in Tables 20 through 23, while Figures 187 through 216 depict the average of the six trials for each evaluation.

Table 20. Summary of the NO<sub>2</sub> Parameters Collected from MMGC #1 During the Micromachined Gas Chromatograph Evaluation.

NO <sub>2</sub> Concentration (ppm)	NH <sub>3</sub> Concentration (ppm)	Temperature (°C)	Response (pA)	Center (min)	Width (min)
75	6300	55	3.5	44.8	21.3
75	6300	58	2.9	40.5	22.7
75	6300	66	2.1	29.4	18.9
75	6300	73	1.7	23.3	19.1
75	6300	75	1.4	20.4	20.5
75	6300	80	1.1	19.5	12.8
210	6300	80	1.7	17.4	13.4
270	6300	80	2.0	18.5	15.6
500	6300	80	2.3	17.9	14.5
560	6900	80	2.7	17.5	12.9
500	7300	80	2.3	17.8	14.5
500	4800	80	2.3	19.4	15.3
500	4100	80	2.2	19.1	15.5
500	3500	80	2.4	18.5	12.6
500	2700	80	2.2	19.7	14.7
500	1600	80	2.2	20.7	14.6
300	480	80	2.2	18.5	13.8

Table 21. Summary of the  $\text{NH}_3$  Parameters Collected from MMGC #1 During the Micromachined Gas Chromatograph Evaluation.

$\text{NO}_2$ Concentration (ppm)	$\text{NH}_3$ Concentration (ppm)	Temperature ( $^{\circ}\text{C}$ )	Response (pA)	Center (min)	Width (min)
75	6300	55	1.5	4	1.6
75	6300	58	1.5	3.7	1.6
75	6300	66	1.5	3.8	1.7
75	6300	73	1.4	3.4	1.5
75	6300	75	1.6	4.0	1.6
75	6300	80	1.5	4.0	1.9
210	6300	80	1.4	3.6	1.6
270	6300	80	1.5	3.7	1.7
500	6300	80	1.5	3.7	1.7
560	6900	80	1.5	3.7	1.7
500	7300	80	1.7	3.8	1.9
500	4800	80	1.6	3.1	1.4
500	4100	80	1.6	3.3	1.9
500	3500	80	1.5	3.7	1.9
500	2700	80	1.3	3.9	1.6
500	1600	80	0.8	4.2	1.4
500	480	80	0.3	4.1	1.4

Table 22. Summary of the NO<sub>2</sub> Parameters Collected from MMGC #2 During the Micromachined Gas Chromatograph Evaluation.

NO <sub>2</sub> Concentration (ppm)	NH <sub>3</sub> Concentration (ppm)	Temperature (°C)	Response (pA)	Center (min)	Width (min)
90	5700	61	3.3	23.7	13.7
90	5700	68	2.5	19.9	14.4
90	5700	57	4.2	29.1	17.3
90	5700	75	1.9	14.5	15.1
90	5700	83	1.4	10.7	10.9
140	5700	83	2.0	8.4	13.2
240	5700	83	2.2	8.3	15.1
350	5700	83	2.4	11.6	11.5
500	5700	83	2.6	10.3	11.4
500	4500	83	2.7	11.9	10.8
500	2800	83	2.3	11.3	12.5
500	1800	83	2.6	11.0	10.6
500	500	83	3.3	8.4	14.7

**Table 23. Summary of the NH<sub>3</sub> Parameters Collected from MMGC #2 During the Micromachined Gas Chromatograph Evaluation.**

NO <sub>2</sub> Concentration (ppm)	NH <sub>3</sub> Concentration (ppm)	Temperature (°C)	Response (pA)	Center (min)	Width (min)
90	5700	61	1.6	2.5	1.4
90	5700	68	1.6	2.3	1.1
90	5700	57	1.6	2.3	1.5
90	5700	75	1.4	2.6	1.4
90	5700	83	1.4	2.5	1.2
140	5700	83	1.8	2.6	1.4
240	5700	83	1.6	2.9	1.2
350	5700	83	1.5	2.4	1.2
500	5700	83	1.5	2.4	1.4
500	4500	83	1.8	2.5	1.7
500	2800	83	1.5	2.6	1.4
500	1800	83	0.8	2.3	1.2
500	500	83	0.5	2.8	1.7

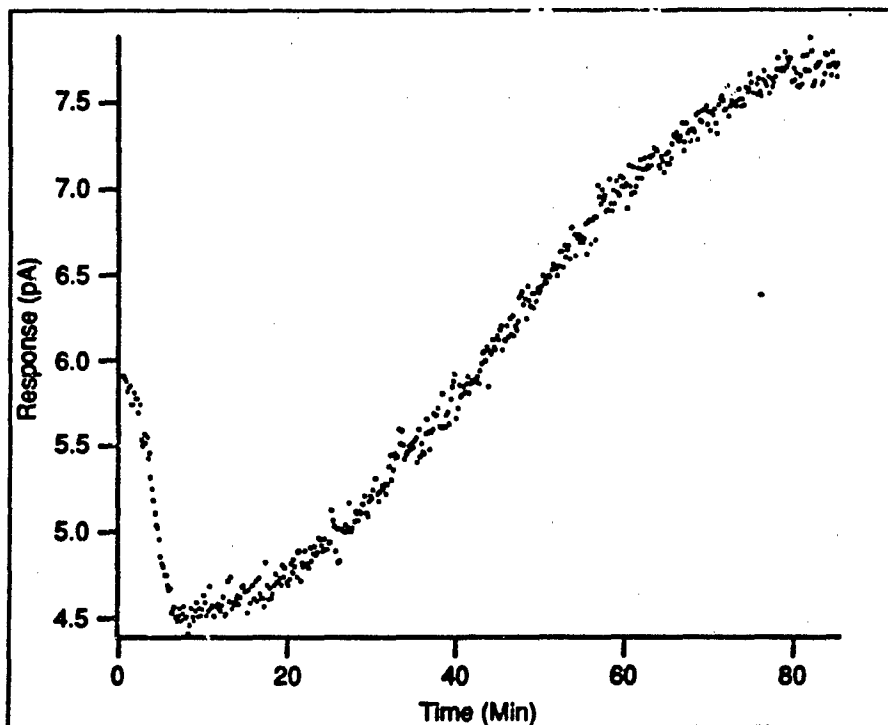


Figure 187. Micromachined Gas Chromatograph #1 Evaluation (75 ppm NO<sub>2</sub>, 6300 ppm NH<sub>3</sub>, and 55°C). The NH<sub>3</sub> Response is 1.5 pA, the NH<sub>3</sub> Peak Center is at 4 minutes, the NH<sub>3</sub> Peak Width is 1.6 minutes, the NO<sub>2</sub> Response is 3.5 pA, the NO<sub>2</sub> Peak Center is at 44.8 minutes, and the NO<sub>2</sub> Peak Width is 21.3 minutes.

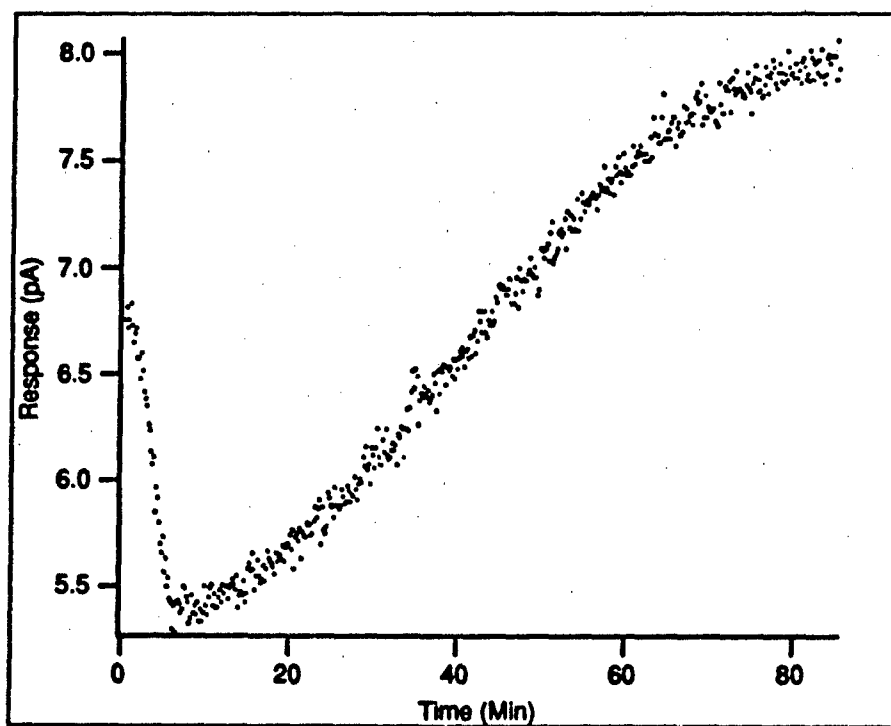


Figure 188. Micromachined Gas Chromatograph #1 Evaluation (75 ppm  $\text{NO}_2$ , 6300 ppm  $\text{NH}_3$ , and  $58^\circ\text{C}$ ). The  $\text{NH}_3$  Response is 1.5 pA, the  $\text{NH}_3$  Peak Center is at 3.7 minutes, the  $\text{NH}_3$  Peak Width is 1.6 minutes, the  $\text{NO}_2$  Response is 2.9 pA, the  $\text{NO}_2$  Peak Center is at 40.5 minutes, and the  $\text{NO}_2$  Peak Width is 22.7 minutes.

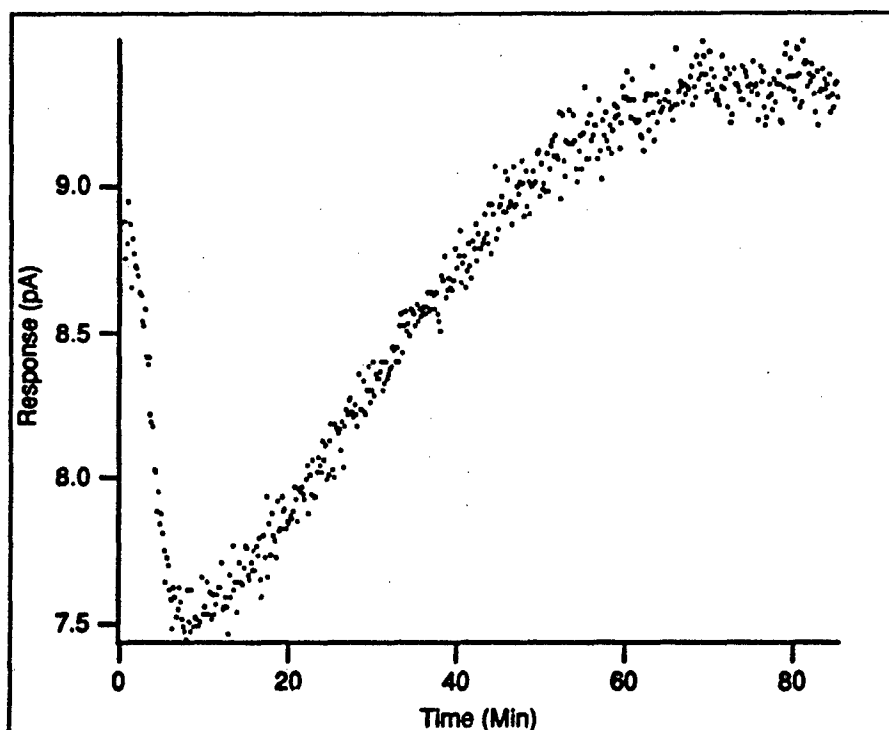


Figure 189. Micromachined Gas Chromatograph #1 Evaluation (75 ppm  $\text{NC}_7$ , 6300 ppm  $\text{NH}_3$ , and  $66^\circ\text{C}$ ). The  $\text{NH}_3$  Response is 1.5 pA, the  $\text{NH}_3$  Peak Center is at 3.8 minutes, the  $\text{NH}_3$  Peak Width is 1.7 minutes, the  $\text{NO}_2$  Response is 2.1 pA, the  $\text{NO}_2$  Peak Center is at 29.4 minutes, and the  $\text{NO}_2$  Peak Width is 18.9 minutes.

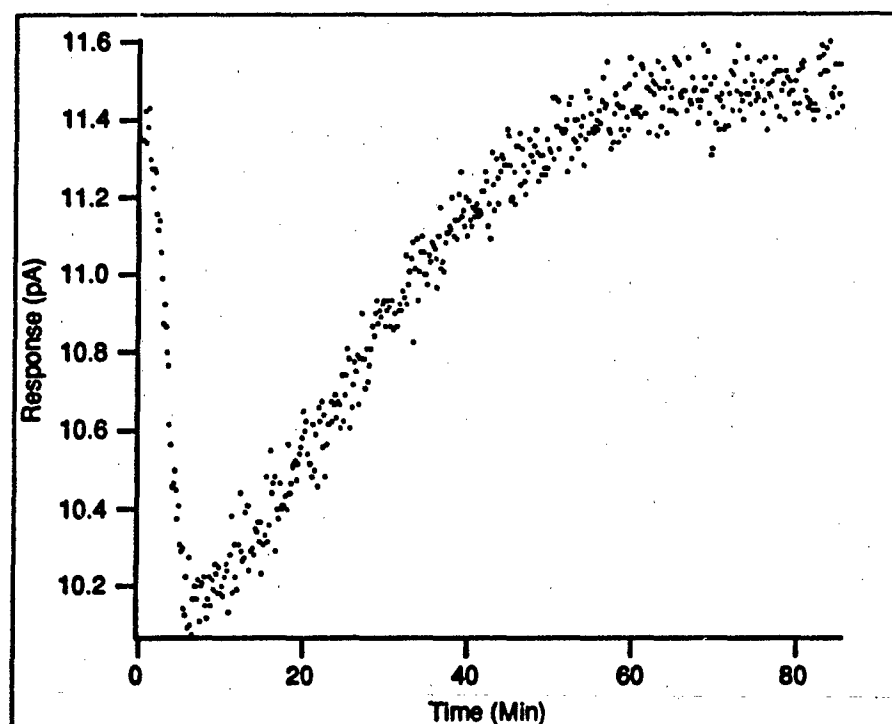


Figure 190. Micromachined Gas Chromatograph #1 Evaluation (75 ppm  $\text{NO}_2$ , 6300 ppm  $\text{NH}_3$ , and  $73^\circ\text{C}$ ). The  $\text{NH}_3$  Response is 1.4 pA, the  $\text{NH}_3$  Peak Center is at 3.4 minutes, the  $\text{NH}_3$  Peak Width is 1.5 minutes, the  $\text{NO}_2$  Response is 1.7 pA, the  $\text{NO}_2$  Peak Center is at 23.3 minutes, and the  $\text{NO}_2$  Peak Width is 19.1 minutes.

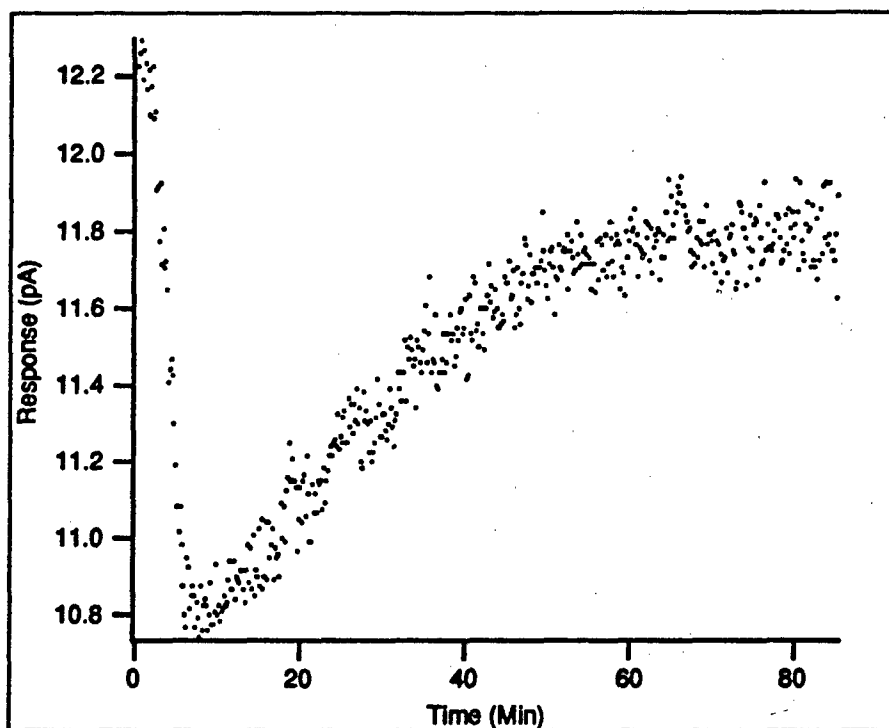


Figure 191. Micromachined Gas Chromatograph #1 Evaluation (75 ppm  $\text{NO}_2$ , 6300 ppm  $\text{NH}_3$ , and  $75^\circ\text{C}$ ). The  $\text{NH}_3$  Response is 1.6 pA, the  $\text{NH}_3$  Peak Center is at 4 minutes, the  $\text{NH}_3$  Peak Width is 1.6 minutes, the  $\text{NO}_2$  Response is 1.4 pA, the  $\text{NO}_2$  Peak Center is at 20.4 minutes, and the  $\text{NO}_2$  Peak Width is 20.5 minutes.

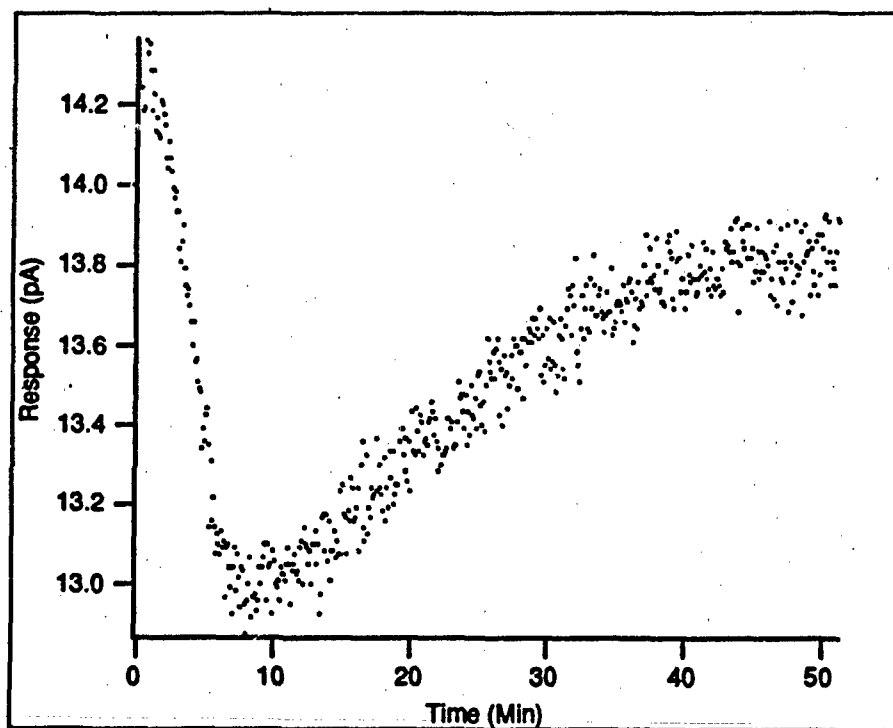
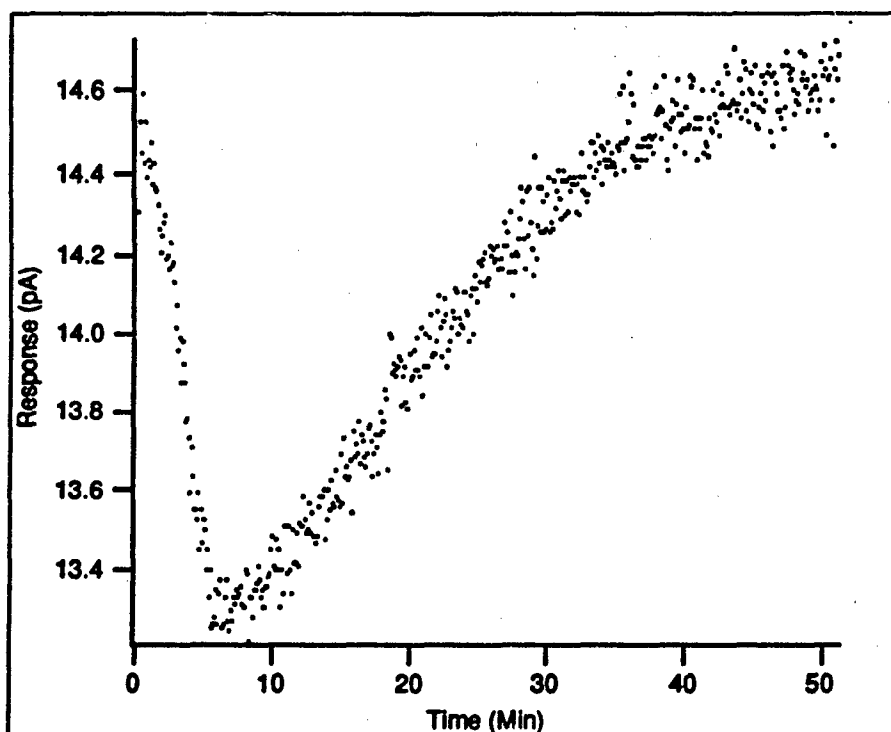


Figure 192. Micromachined Gas Chromatograph #1 Evaluation (75 ppm  $\text{NO}_2$ , 6300 ppm  $\text{NH}_3$ , and  $80^\circ\text{C}$ ). The  $\text{NH}_3$  Response is 1.5 pA, the  $\text{NH}_3$  Peak Center is at 4 minutes, the  $\text{NH}_3$  Peak Width is 1.9 minutes, the  $\text{NO}_2$  Response is 1.1 pA, the  $\text{NO}_2$  Peak Center is at 19.5 minutes, and the  $\text{NO}_2$  Peak Width is 12.8 minutes.



**Figure 193. Micromachined Gas Chromatograph #1 Evaluation (210 ppm NO<sub>2</sub>, 6300 ppm NH<sub>3</sub>, and 80°C). The NH<sub>3</sub> Response is 1.4 pA, the NH<sub>3</sub> Peak Center is at 3.6 minutes, the NH<sub>3</sub> Peak Width is 1.6 minutes, the NO<sub>2</sub> Response is 1.7 pA, the NO<sub>2</sub> Peak Center is at 17.4 minutes, and the NO<sub>2</sub> Peak Width is 13.4 minutes.**

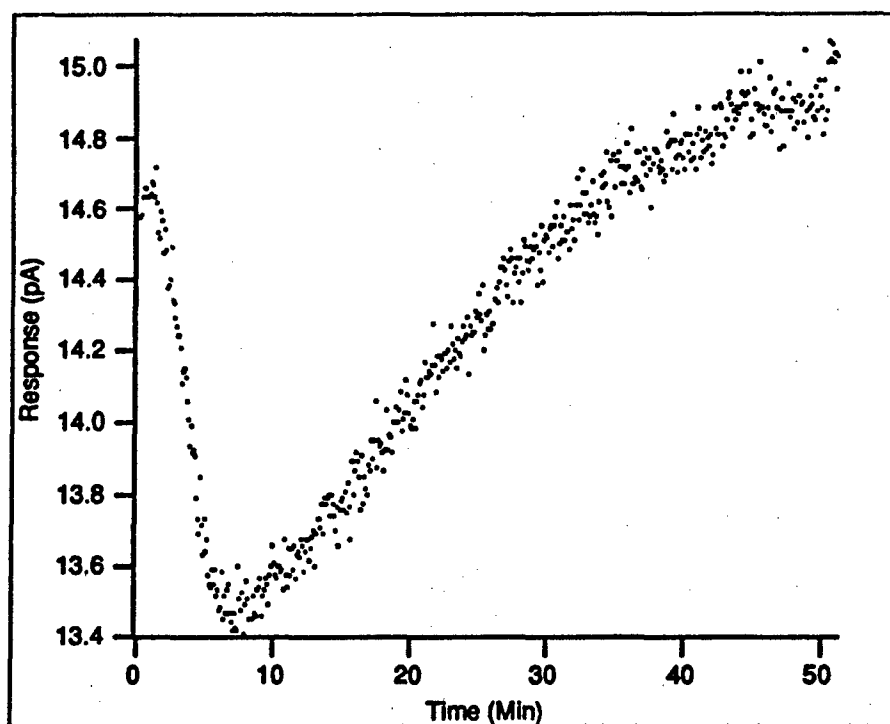


Figure 194. Micromachined Gas Chromatograph #1 Evaluation (270 ppm NO<sub>2</sub>, 6300 ppm NH<sub>3</sub>, and 80°C). The NH<sub>3</sub> Response is 1.5 pA, the NH<sub>3</sub> Peak Center is at 3.7 minutes, the NH<sub>3</sub> Peak Width is 1.7 minutes, the NO<sub>2</sub> Response is 2 pA, the NO<sub>2</sub> Peak Center is at 18.5 minutes, and the NO<sub>2</sub> Peak Width is 15.6 minutes.

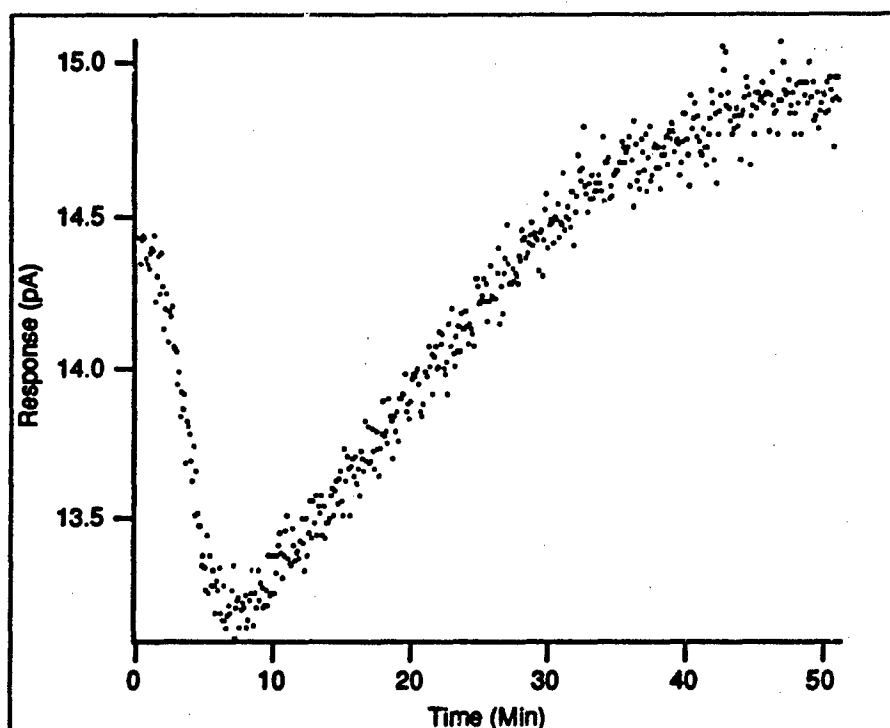


Figure 195. Micromachined Gas Chromatograph #1 Evaluation (500 ppm NO<sub>2</sub>, 6300 ppm NH<sub>3</sub>, and 80°C). The NH<sub>3</sub> Response is 1.5 pA, the NH<sub>3</sub> Peak Center is at 3.7 minutes, the NH<sub>3</sub> Peak Width is 1.7 minutes, the NO<sub>2</sub> Response is 2.3 pA, the NO<sub>2</sub> Peak Center is at 17.9 minutes, and the NO<sub>2</sub> Peak Width is 14.5 minutes.

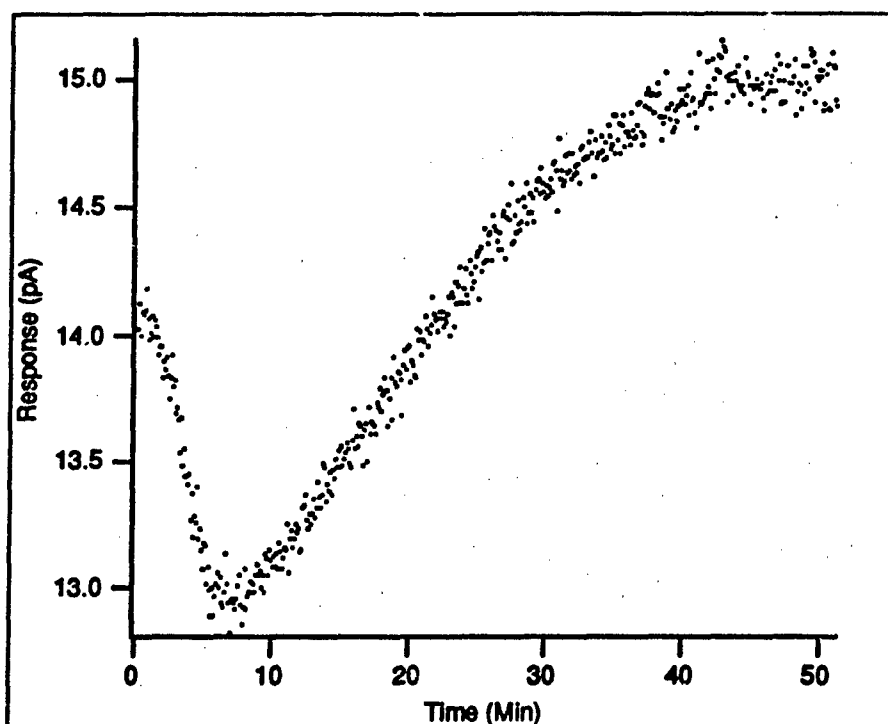


Figure 196. Micromachined Gas Chromatograph #1 Evaluation (560 ppm NO<sub>2</sub>, 6900 ppm NH<sub>3</sub>, and 80°C). The NH<sub>3</sub> Response is 1.5 pA, the NH<sub>3</sub> Peak Center is at 3.7 minutes, the NH<sub>3</sub> Peak Width is 1.7 minutes, the NO<sub>2</sub> Response is 2.7 pA, the NO<sub>2</sub> Peak Center is at 17.5 minutes, and the NO<sub>2</sub> Peak Width is 12.9 minutes.

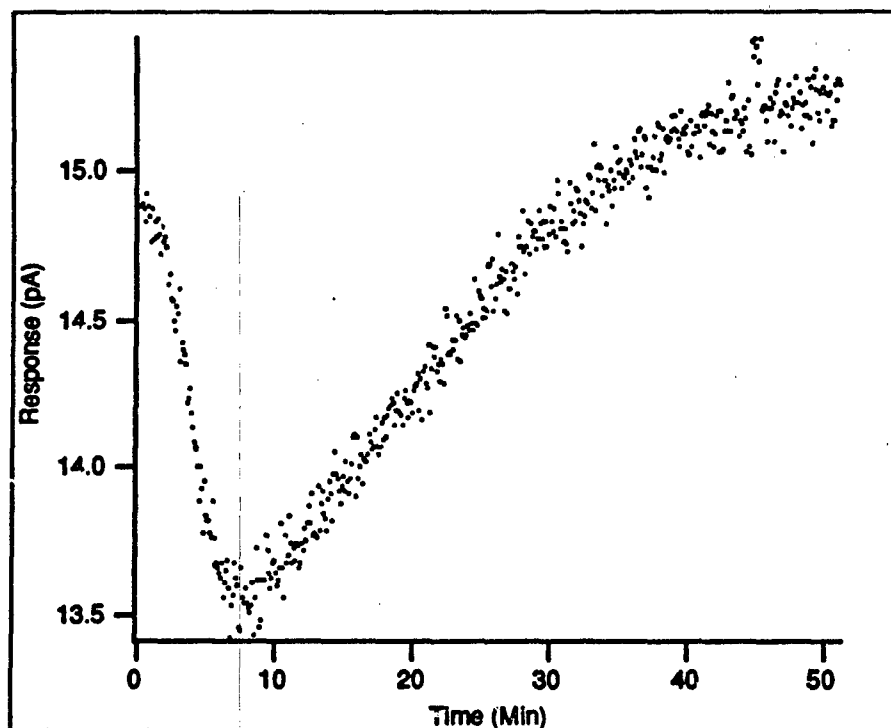


Figure 197. Micromachined Gas Chromatograph #1 Evaluation (500 ppm NO<sub>2</sub>, 7300 ppm NH<sub>3</sub>, and 80°C). The NH<sub>3</sub> Response is 1.7 pA, the NH<sub>3</sub> Peak Center is at 3.8 minutes, the NH<sub>3</sub> Peak Width is 1.9 minutes, the NO<sub>2</sub> Response is 2.3 pA, the NO<sub>2</sub> Peak Center is at 17.8 minutes, and the NO<sub>2</sub> Peak Width is 14.5 minutes.

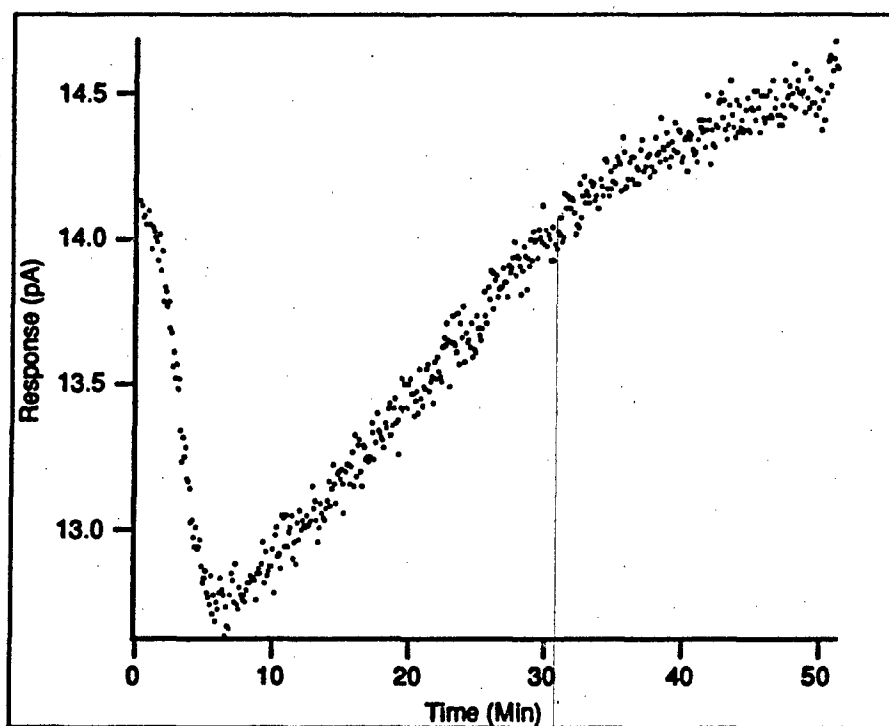


Figure 198. Micromachined Gas Chromatograph #1 Evaluation (500 ppm NO<sub>2</sub>, 4800 ppm NH<sub>3</sub>, and 80°C). The NH<sub>3</sub> Response is 1.6 pA, the NH<sub>3</sub> Peak Center is at 3.1 minutes, the NH<sub>3</sub> Peak Width is 1.4 minutes, the NO<sub>2</sub> Response is 2.3 pA, the NO<sub>2</sub> Peak Center is at 19.4 minutes, and the NO<sub>2</sub> Peak Width is 15.3 minutes.

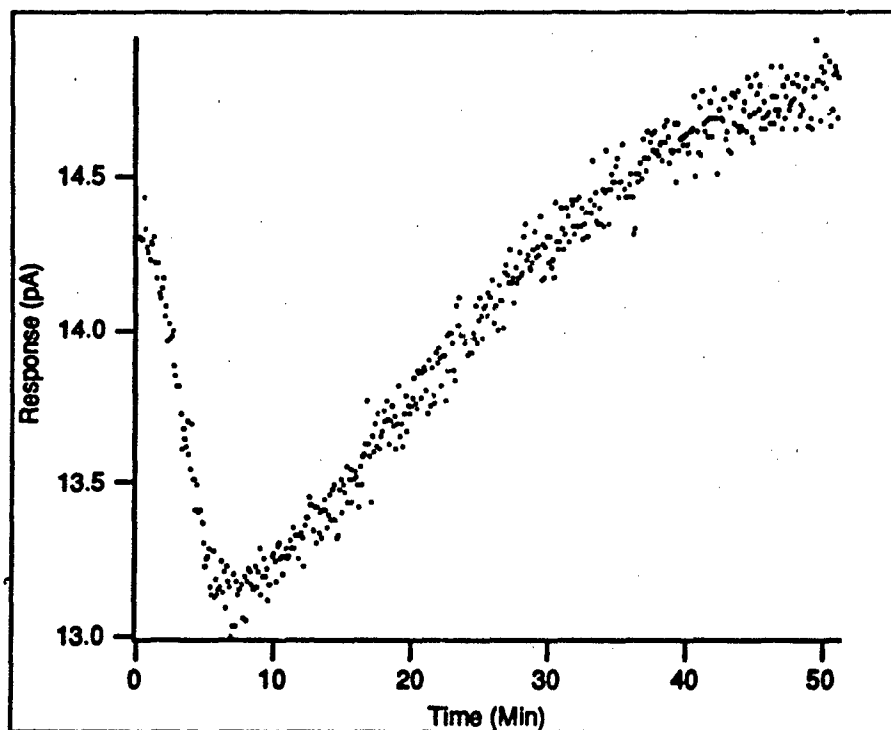
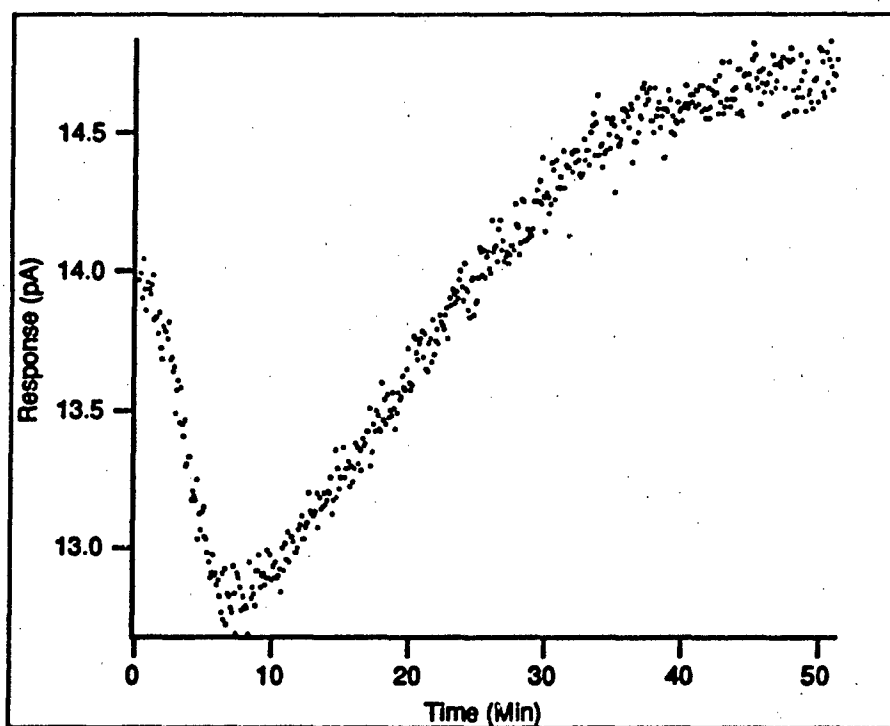
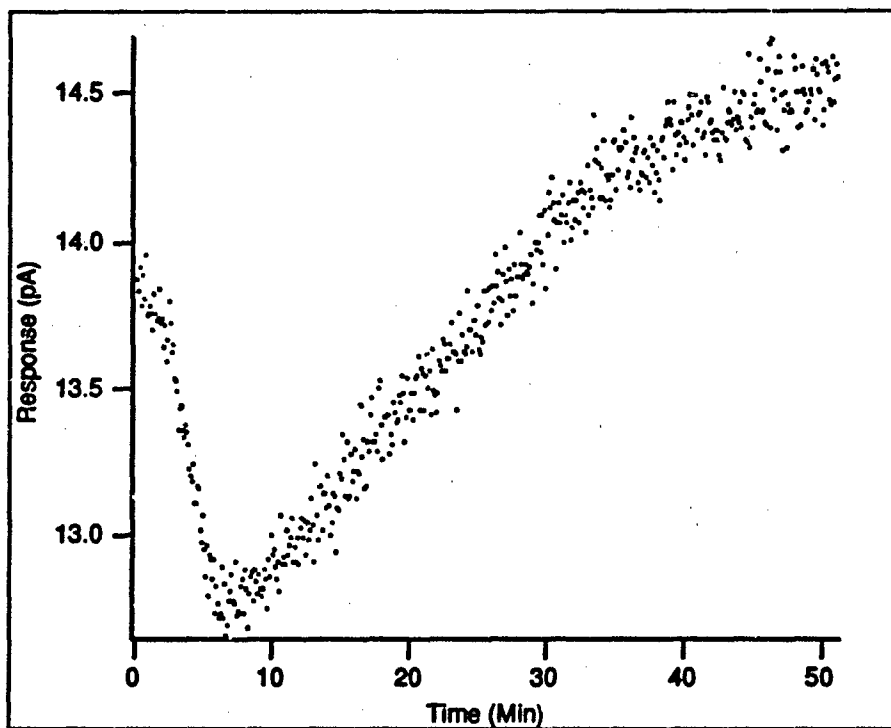


Figure 199. Micromachined Gas Chromatograph #1 Evaluation (500 ppm NO<sub>2</sub>, 4100 ppm NH<sub>3</sub>, and 80°C). The NH<sub>3</sub> Response is 1.6 pA, the NH<sub>3</sub> Peak Center is at 3.3 minutes, the NH<sub>3</sub> Peak Width is 1.9 minutes, the NO<sub>2</sub> Response is 2.2 pA, the NO<sub>2</sub> Peak Center is at 19.1 minutes, and the NO<sub>2</sub> Peak Width is 15.5 minutes.



**Figure 200.** Micromachined Gas Chromatograph #1 Evaluation (500 ppm NO<sub>2</sub>, 3500 ppm NH<sub>3</sub>, and 80°C). The NH<sub>3</sub> Response is 1.5 pA, the NH<sub>3</sub> Peak Center is at 3.7 minutes, the NH<sub>3</sub> Peak Width is 1.9 minutes, the NO<sub>2</sub> Response is 2.4 pA, the NO<sub>2</sub> Peak Center is at 18.5 minutes, and the NO<sub>2</sub> Peak Width is 12.6 minutes.



**Figure 201. Micromachined Gas Chromatograph #1 Evaluation (500 ppm  $\text{NO}_2$ , 2700 ppm  $\text{NH}_3$ , and  $80^\circ\text{C}$ ). The  $\text{NH}_3$  Response is 1.3 pA, the  $\text{NH}_3$  Peak Center is at 3.9 minutes, the  $\text{NH}_3$  Peak Width is 1.6 minutes, the  $\text{NO}_2$  Response is 2.2 pA, the  $\text{NO}_2$  Peak Center is at 19.7 minutes, and the  $\text{NO}_2$  Peak Width is 14.7 minutes.**

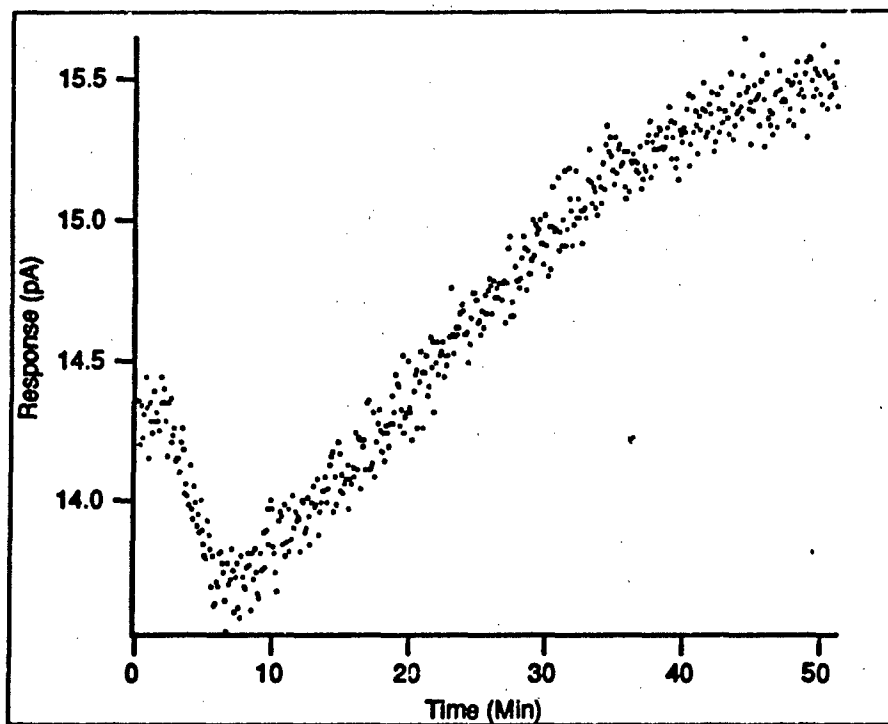
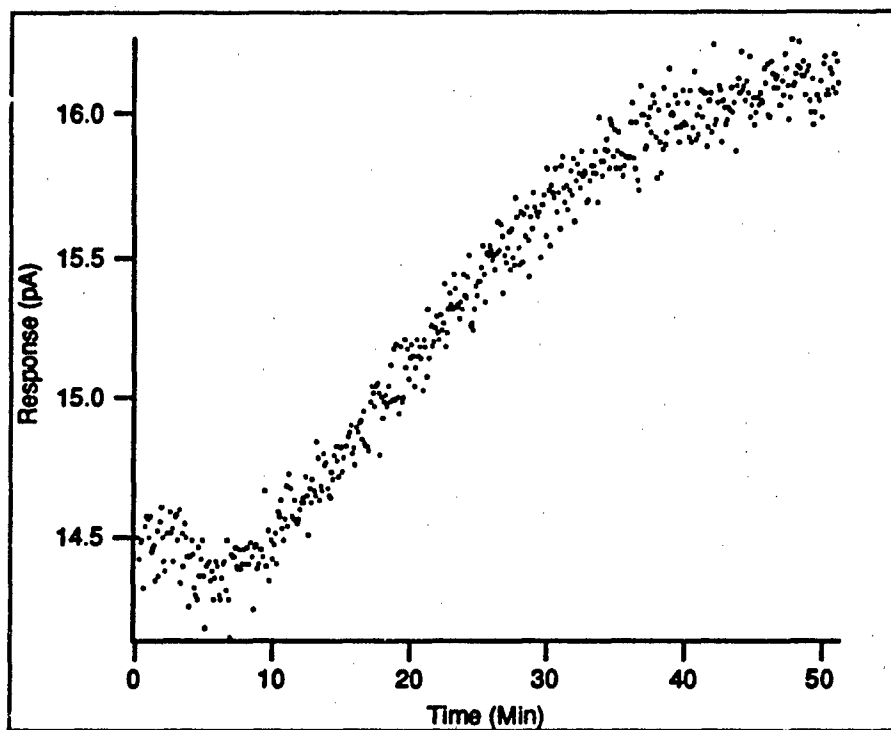
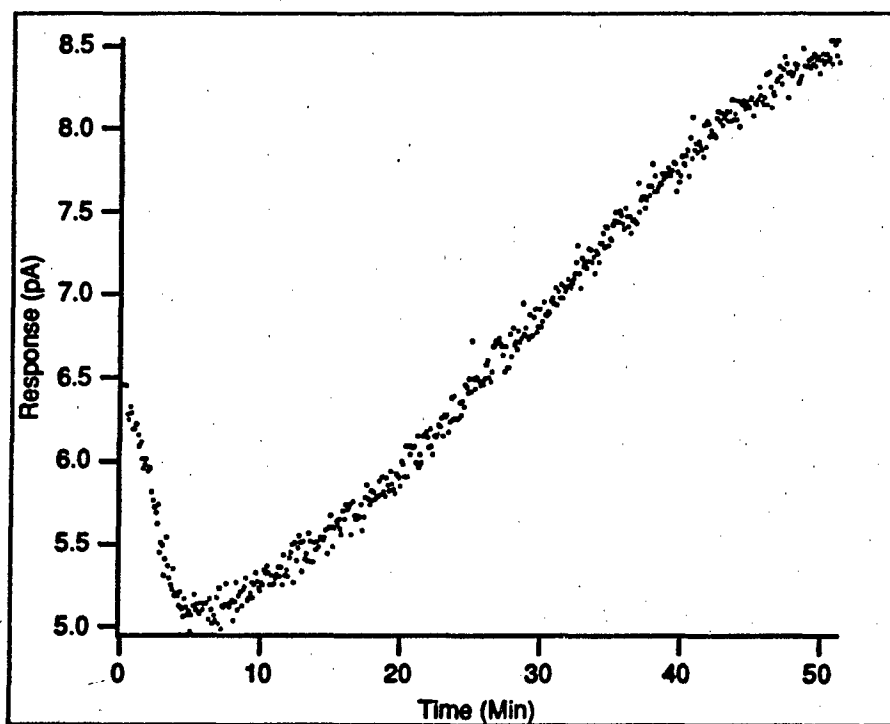


Figure 202. Micromachined Gas Chromatograph #1 Evaluation (500 ppm  $\text{NO}_2$ , 1600 ppm  $\text{NH}_3$ , and  $80^\circ\text{C}$ ). The  $\text{NH}_3$  Response is 0.8 pA, the  $\text{NH}_3$  Peak Center is at 4.2 minutes, the  $\text{NH}_3$  Peak Width is 1.4 minutes, the  $\text{NO}_2$  Response is 2.2 pA, the  $\text{NO}_2$  Peak Center is at 20.7 minutes, and the  $\text{NO}_2$  Peak Width is 14.6 minutes.



**Figure 203.** Micromachined Gas Chromatograph #1 Evaluation (500 ppm NO<sub>2</sub>, 480 ppm NH<sub>3</sub>, and 80°C). The NH<sub>3</sub> Response is 0.3 pA, the NH<sub>3</sub> Peak Center is at 4.1 minutes, the NH<sub>3</sub> Peak Width is 1.4 minutes, the NO<sub>2</sub> Response is 2.2 pA, the NO<sub>2</sub> Peak Center is at 18.5 minutes, and the NO<sub>2</sub> Peak Width is 13.8 minutes.



**Figure 204.** Micromachined Gas Chromatograph #2 Evaluation (90 ppm NO<sub>2</sub>, 5700 ppm NH<sub>3</sub>, and 57°C). The NH<sub>3</sub> Response is 1.6 pA, the NH<sub>3</sub> Peak Center is at 2.3 minutes, the NH<sub>3</sub> Peak Width is 1.5 minutes, the NO<sub>2</sub> Response is 4.2 pA, the NO<sub>2</sub> Peak Center is at 29.1 minutes, and the NO<sub>2</sub> Peak Width is 17.3 minutes.

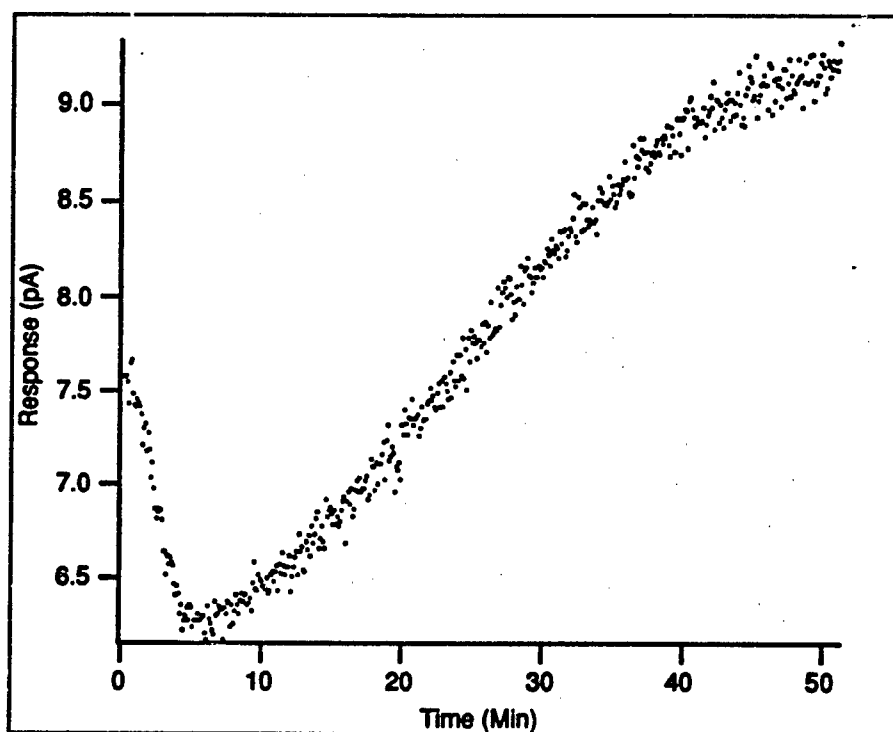
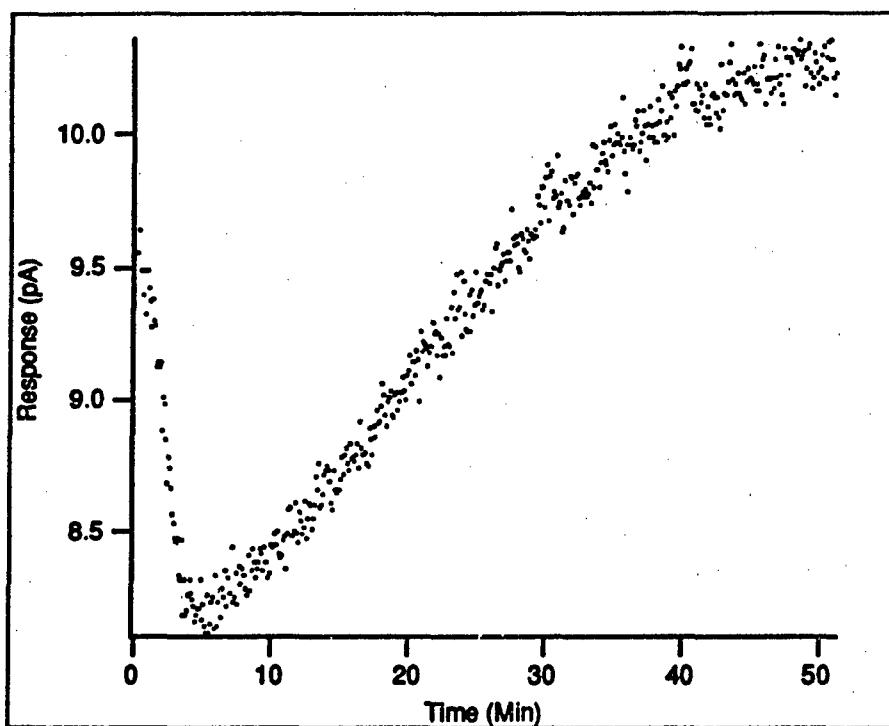


Figure 205. Micromachined Gas Chromatograph #2 Evaluation (90 ppm NO<sub>2</sub>, 5700 ppm NH<sub>3</sub>, and 61°C). The NH<sub>3</sub> Response is 1.6 pA, the NH<sub>3</sub> Peak Center is at 2.5 minutes, the NH<sub>3</sub> Peak Width is 1.4 minutes, the NO<sub>2</sub> Response is 3.3 pA, the NO<sub>2</sub> Peak Center is at 23.7 minutes, and the NO<sub>2</sub> Peak Width is 13.7 minutes.



**Figure 206.** Micromachined Gas Chromatograph #2 Evaluation (90 ppm NO<sub>2</sub>, 5700 ppm NH<sub>3</sub>, and 68°C). The NH<sub>3</sub> Response is 1.6 pA, the NH<sub>3</sub> Peak Center is at 2.3 minutes, the NH<sub>3</sub> Peak Width is 1.1 minutes, the NO<sub>2</sub> Response is 2.5 pA, the NO<sub>2</sub> Peak Center is at 19.9 minutes, and the NO<sub>2</sub> Peak Width is 14.4 minutes.

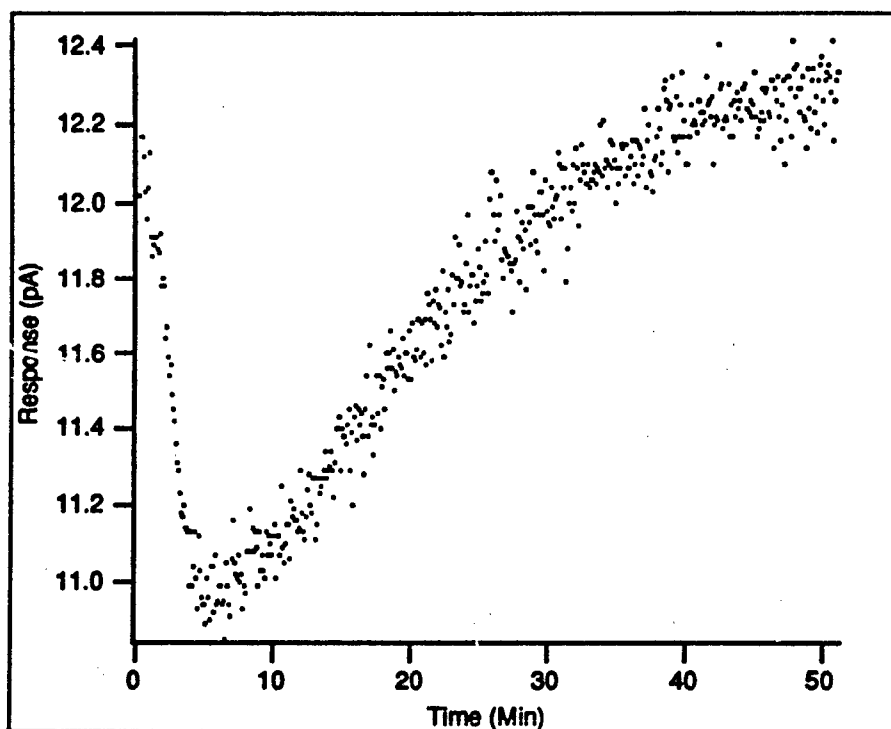


Figure 207. Micromachined Gas Chromatograph #2 Evaluation (90 ppm NO<sub>2</sub>, 5700 ppm NH<sub>3</sub>, and 75°C). The NH<sub>3</sub> Response is 1.4 pA, the NH<sub>3</sub> Peak Center is at 2.6 minutes, the NH<sub>3</sub> Peak Width is 1.4 minutes, the NO<sub>2</sub> Response is 1.9 pA, the NO<sub>2</sub> Peak Center is at 14.5 minutes, and the NO<sub>2</sub> Peak Width is 15.1 minutes.

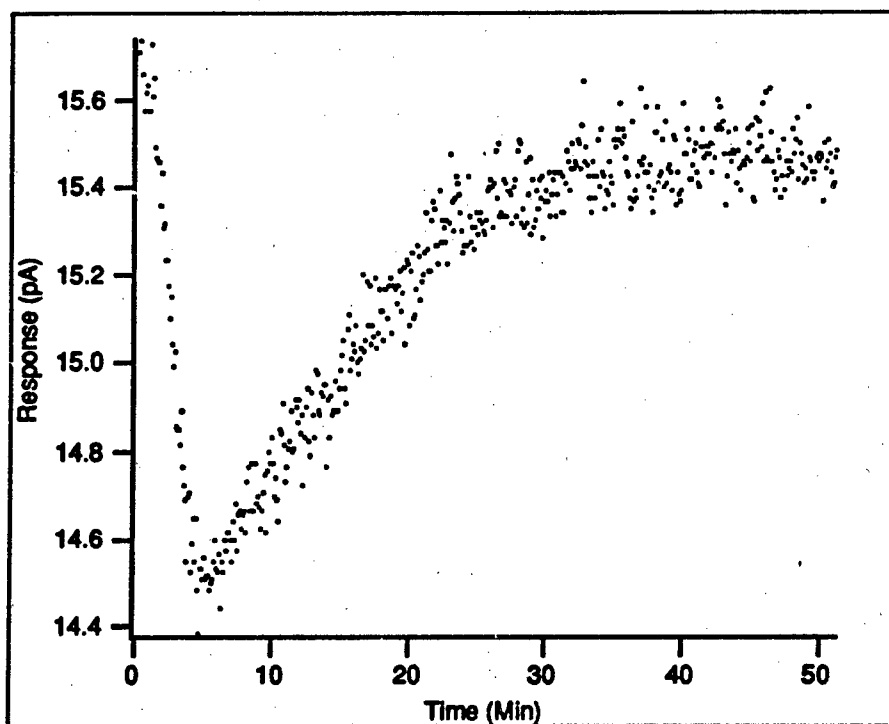


Figure 208. Micromachined Gas Chromatograph #2 Evaluation (90 ppm NO<sub>2</sub>, 5700 ppm NH<sub>3</sub>, and 83°C). The NH<sub>3</sub> Response is 1.4 pA, the NH<sub>3</sub> Peak Center is at 2.6 minutes, the NH<sub>3</sub> Peak Width is 1.2 minutes, the NO<sub>2</sub> Response is 1.4 pA, the NO<sub>2</sub> Peak Center is at 10.7 minutes, and the NO<sub>2</sub> Peak Width is 10.9 minutes.

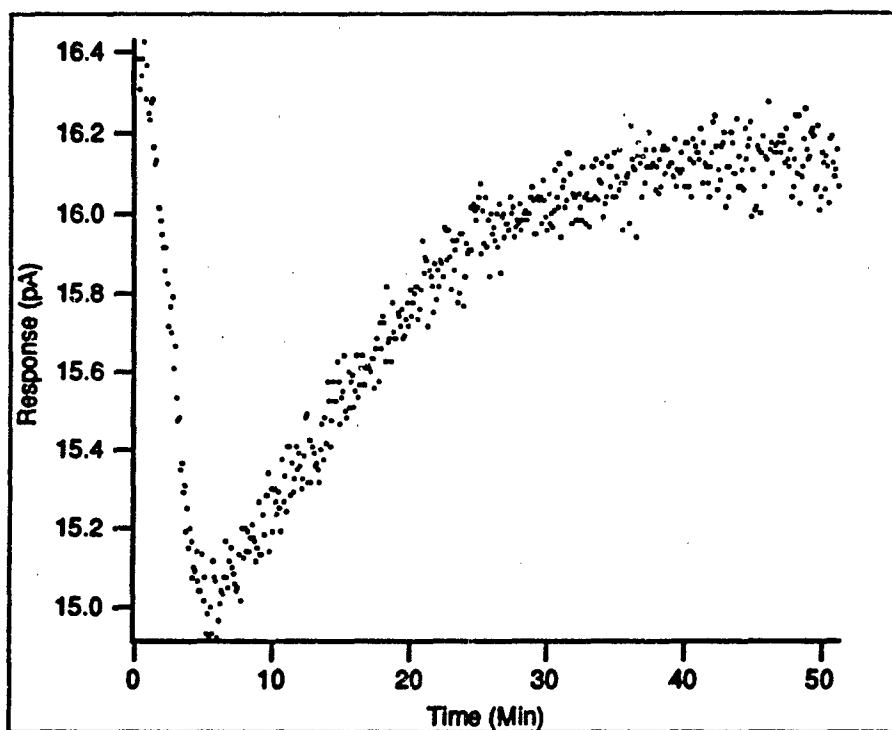


Figure 209. Micromachined Gas Chromatograph #2 Evaluation (140 ppm NO<sub>2</sub>, 5700 ppm NH<sub>3</sub>, and 83°C). The NH<sub>3</sub> Response is 1.8 pA, the NH<sub>3</sub> Peak Center is at 2.6 minutes, the NH<sub>3</sub> Peak Width is 1.4 minutes, the NO<sub>2</sub> Response is 2 pA, the NO<sub>2</sub> Peak Center is at 8.4 minutes, and the NO<sub>2</sub> Peak Width is 13.2 minutes.

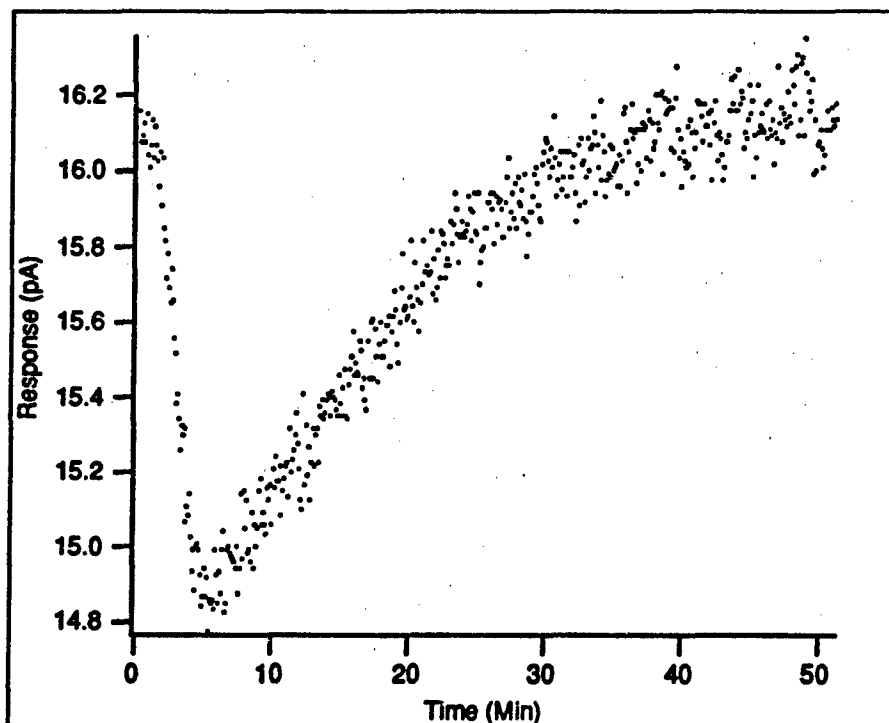


Figure 210. Micromachined Gas Chromatograph #2 Evaluation (240 ppm NO<sub>2</sub>, 5700 ppm NH<sub>3</sub>, and 83°C). The NH<sub>3</sub> Response is 1.6 pA, the NH<sub>3</sub> Peak Center is at 2.9 minutes, the NH<sub>3</sub> Peak Width is 1.2 minutes, the NO<sub>2</sub> Response is 2.2 pA, the NO<sub>2</sub> Peak Center is at 8.3 minutes, and the NO<sub>2</sub> Peak Width is 15.1 minutes.

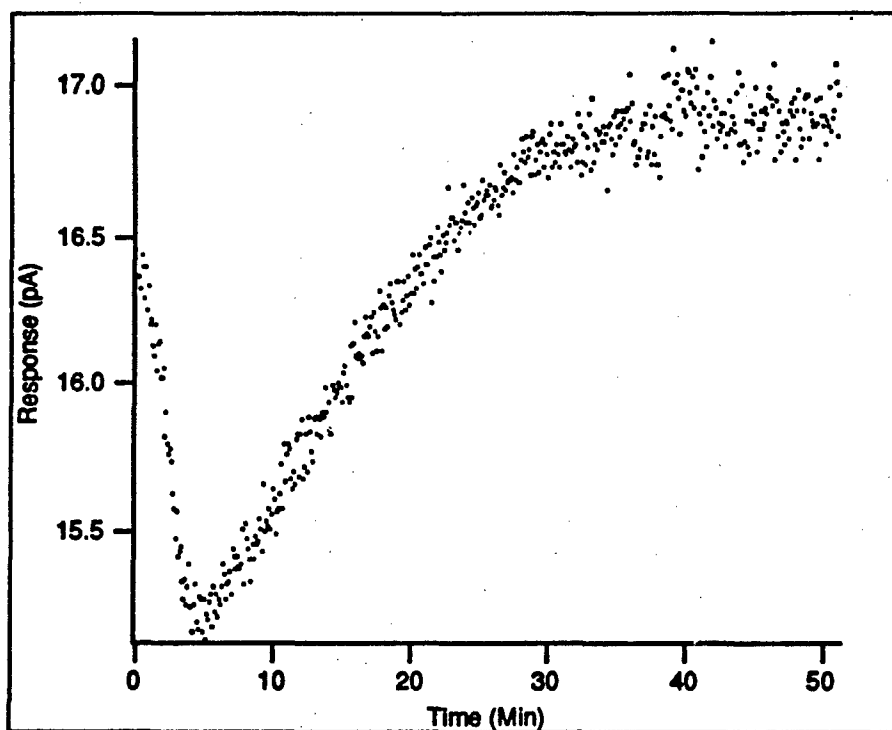
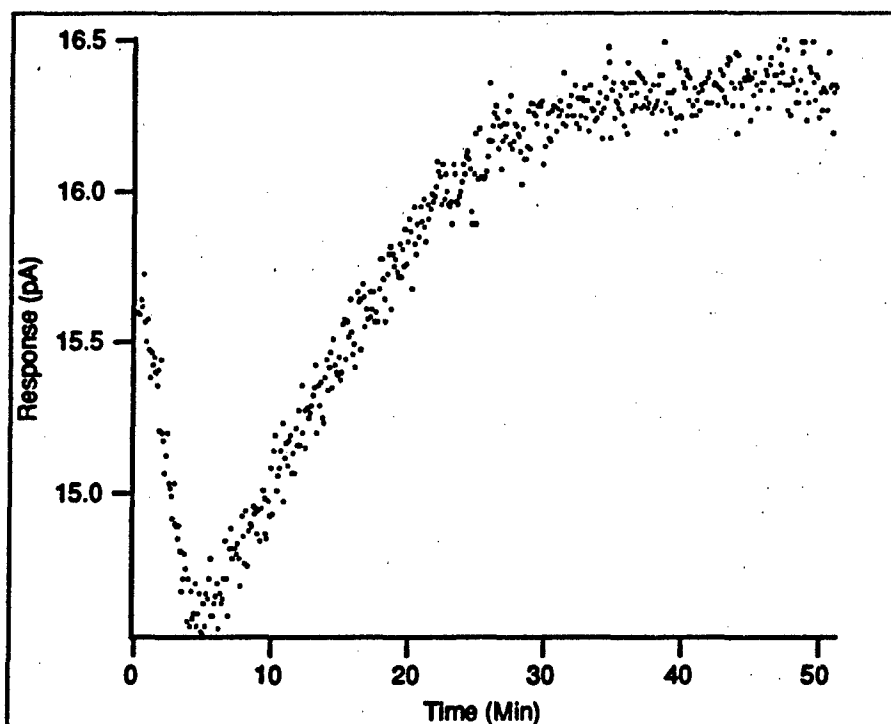


Figure 211. Micromachined Gas Chromatograph #2 Evaluation (350 ppm NO<sub>2</sub>, 5700 ppm NH<sub>3</sub>, and 83°C). The NH<sub>3</sub> Response is 1.5 pA, the NH<sub>3</sub> Peak Center is at 2.4 minutes, the NH<sub>3</sub> Peak Width is 1.2 minutes, the NO<sub>2</sub> Response is 2.4 pA, the NO<sub>2</sub> Peak Center is at 11.6 minutes, and the NO<sub>2</sub> Peak Width is 11.5 minutes.



**Figure 212.** Micromachined Gas Chromatograph #2 Evaluation (500 ppm NO<sub>2</sub>, 5700 ppm NH<sub>3</sub>, and 83°C). The NH<sub>3</sub> Response is 1.5 pA, the NH<sub>3</sub> Peak Center is at 2.4 minutes, the NH<sub>3</sub> Peak Width is 1.4 minutes, the NO<sub>2</sub> Response is 2.6 pA, the NO<sub>2</sub> Peak Center is at 10.3 minutes, and the NO<sub>2</sub> Peak Width is 11.4 minutes.

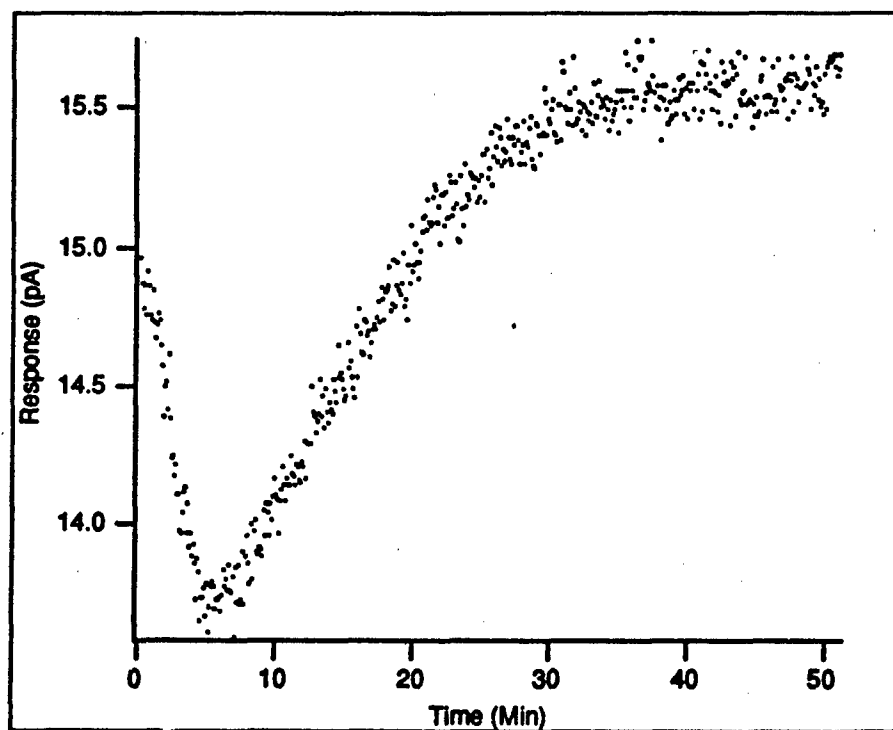


Figure 213. Micromachined Gas Chromatograph #2 Evaluation (500 ppm  $\text{NO}_2$ , 4500 ppm  $\text{NH}_3$ , and  $83^\circ\text{C}$ ). The  $\text{NH}_3$  Response is 1.8 pA, the  $\text{NH}_3$  Peak Center is at 2.5 minutes, the  $\text{NH}_3$  Peak Width is 1.7 minutes, the  $\text{NO}_2$  Response is 2.7 pA, the  $\text{NO}_2$  Peak Center is at 11.9 minutes, and the  $\text{NO}_2$  Peak Width is 10.8 minutes.

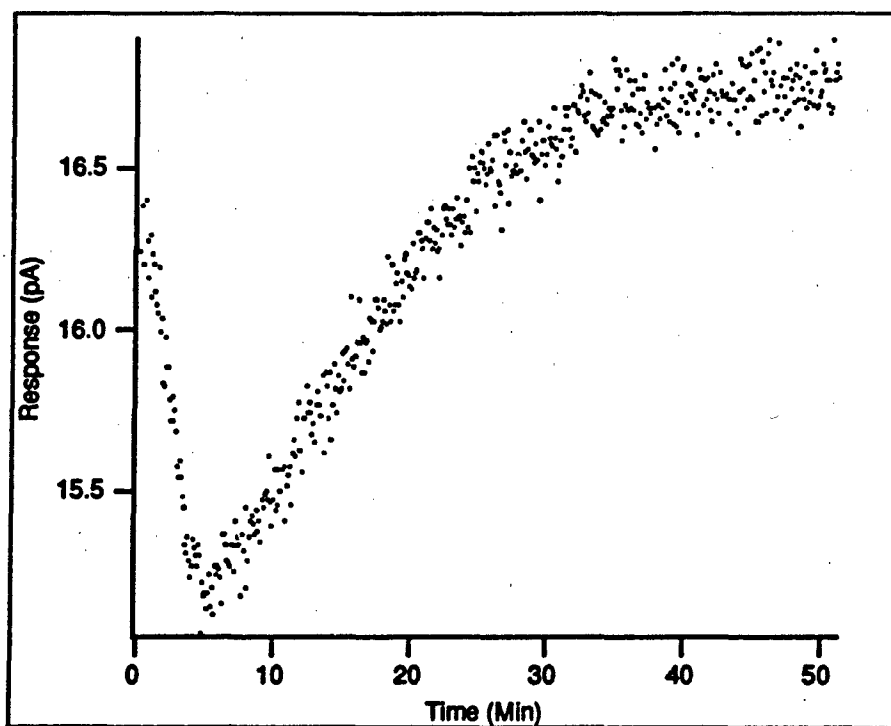


Figure 214. Micromachined Gas Chromatograph #2 Evaluation (500 ppm  $\text{NO}_2$ , 2800 ppm  $\text{NH}_3$ , and  $83^\circ\text{C}$ ). The  $\text{NH}_3$  Response is 1.5 pA, the  $\text{NH}_3$  Peak Center is at 2.6 minutes, the  $\text{NH}_3$  Peak Width is 1.4 minutes, the  $\text{NO}_2$  Response is 2.3 pA, the  $\text{NO}_2$  Peak Center is at 11.3 minutes, and the  $\text{NO}_2$  Peak Width is 12.5 minutes.

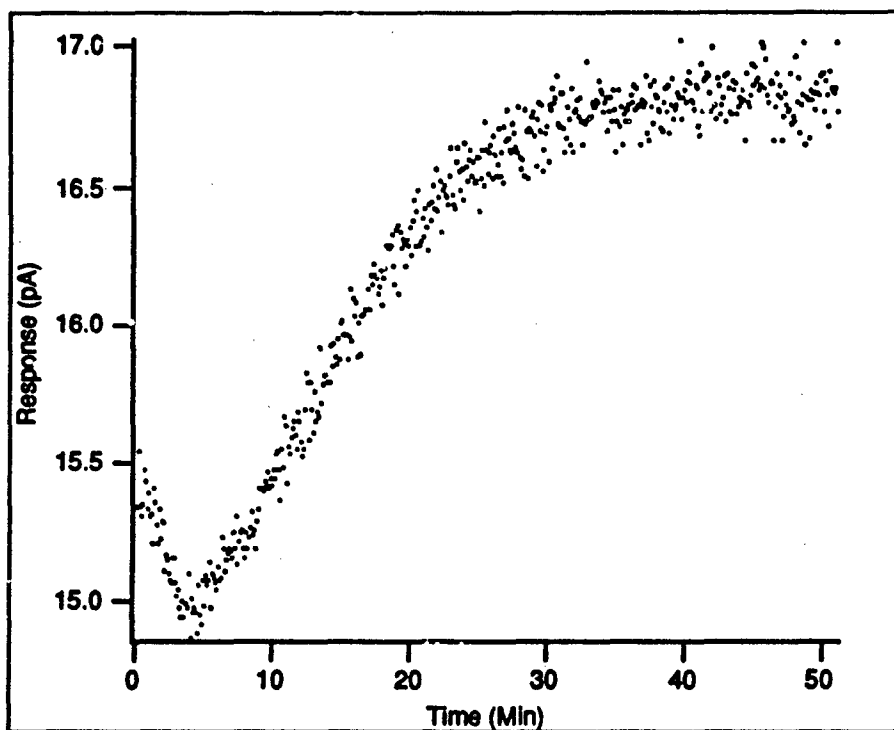
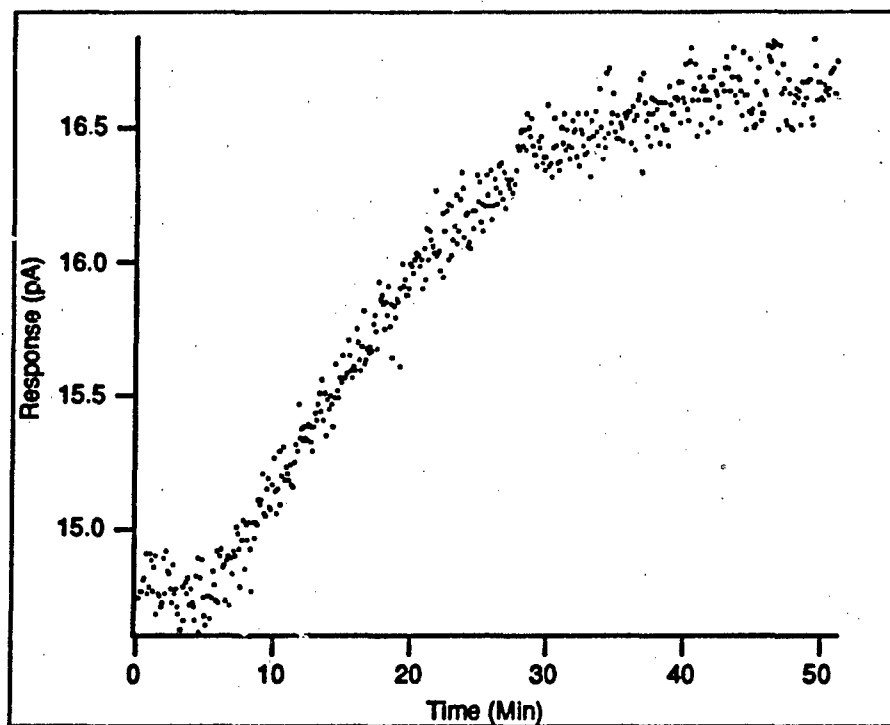


Figure 215. Micromachined Gas Chromatograph #2 Evaluation (500 ppm  $\text{NO}_2$ , 1800 ppm  $\text{NH}_3$ , and  $83^\circ\text{C}$ ). The  $\text{NH}_3$  Response is 0.8 pA, the  $\text{NH}_3$  Peak Center is at 2.3 minutes, the  $\text{NH}_3$  Peak Width is 1.2 minutes, the  $\text{NO}_2$  Response is 2.6 pA, the  $\text{NO}_2$  Peak Center is at 11 minutes, and the  $\text{NO}_2$  Peak Width is 10.6 minutes.



**Figure 216.** Micromachined Gas Chromatograph #2 Evaluation (500 ppm  $\text{NO}_2$ , 500 ppm  $\text{NH}_3$ , and  $83^\circ\text{C}$ ). The  $\text{NH}_3$  Response is 0.5 pA, the  $\text{NH}_3$  Peak Center is at 2.8 minutes, the  $\text{NH}_3$  Peak Width is 1.7 minutes, the  $\text{NO}_2$  Response is 3.3 pA, the  $\text{NO}_2$  Peak Center is at 8.4 minutes, and the  $\text{NO}_2$  Peak Width is 14.7 minutes.

### Appendix K. Adsorption Evaluation Data

This appendix contains the data collected during the adsorption evaluation. A summary of the parameters obtained from the non-linear least-squares curve fitting process is provided in Table 24, while Figures 217 through 225 depict each evaluation.

Table 24. Summary of the Parameters Collected During the Adsorption Evaluation.

NO <sub>2</sub> Concentration (ppb)	$\alpha$ $\times 10^{-4}(\text{ppb} \cdot \text{min})^{-1}$	$\beta$ $(\text{min})^{-1}$	$a_r$ (percent)
100	3.9	1.0	11
100	4.1	1.0	13
100	4.4	1.2	11
200	4.1	1.4	12
200	5.4	1.2	14
200	3.8	1.0	17
400	3.1	1.5	14
400	3.1	1.5	15
400	2.7	1.4	14

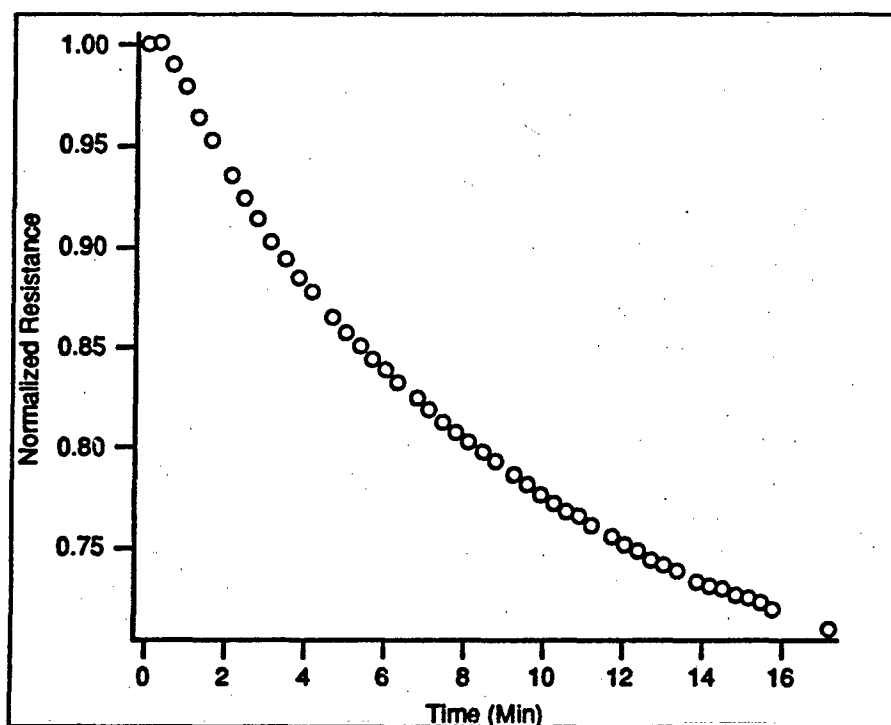


Figure 217. Adsorption Evaluation (100 ppb  $\text{NO}_2$ ).  $\alpha$  is  $3.9 \times 10^{-4} (\text{ppb} \cdot \text{min})^{-1}$ ,  $\beta$  is  $1.0 (\text{min})^{-1}$ , and  $a_r$  is 11 percent.

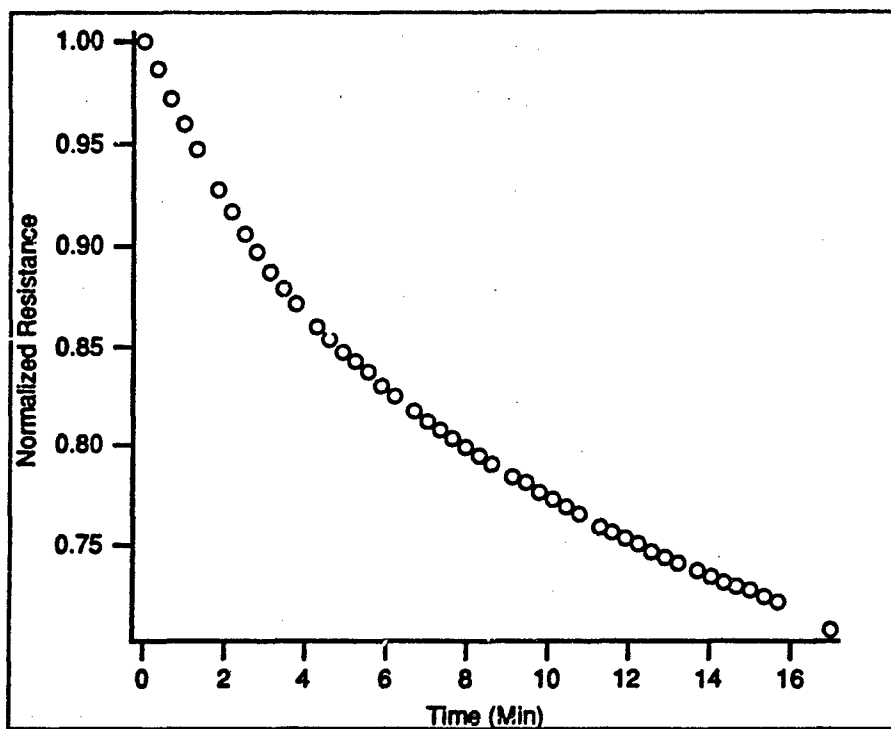


Figure 218. Adsorption Evaluation (100 ppb  $\text{NO}_2$ ).  $\alpha$  is  $4.1 \times 10^{-4} (\text{ppb} \cdot \text{min})^{-1}$ ,  $\beta$  is  $1.0 (\text{min})^{-1}$ , and  $\alpha_r$  is 13 percent.

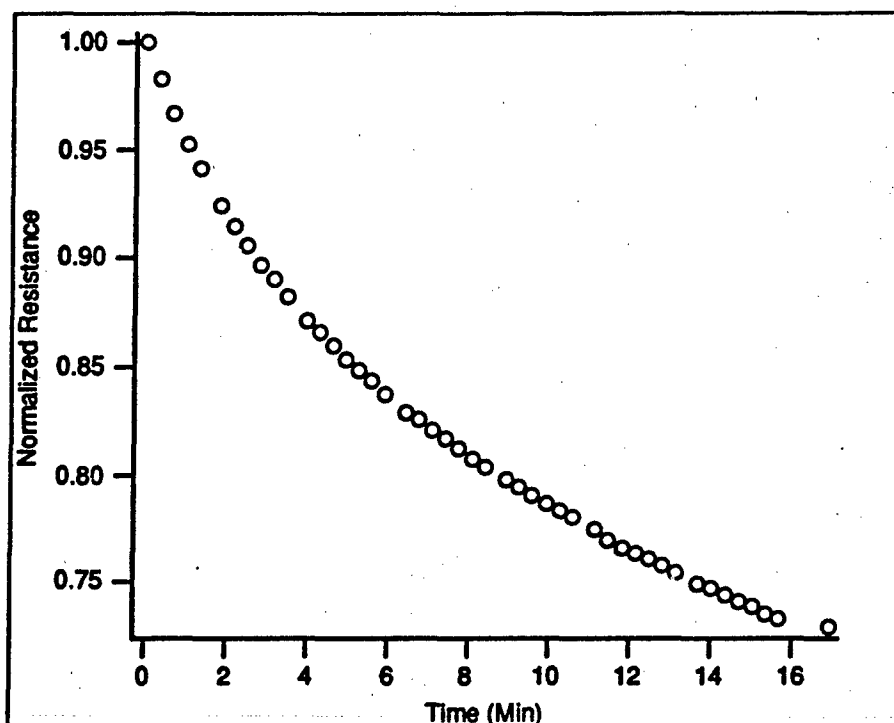


Figure 219. Adsorption Evaluation (100 ppb  $\text{NO}_2$ ).  $\alpha$  is  $4.4 \times 10^{-4} (\text{ppb} \cdot \text{min})^{-1}$ ,  $\beta$  is  $1.2 (\text{min})^{-1}$ , and  $a_r$  is 11 percent.

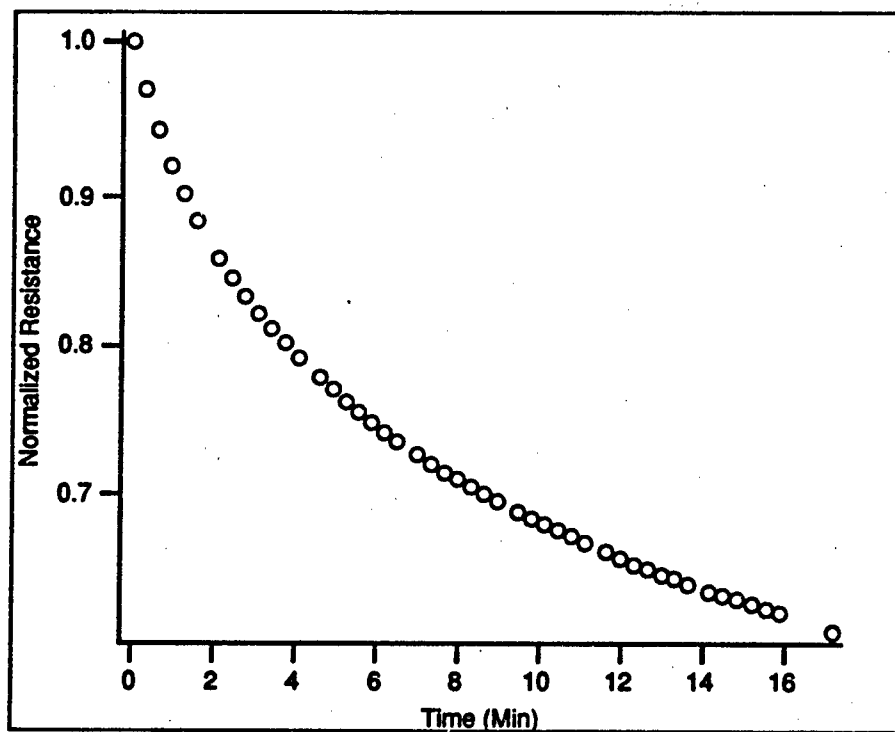


Figure 220. Adsorption Evaluation (200 ppb  $\text{NO}_2$ ).  $\alpha$  is  $4.1 \times 10^{-4} (\text{ppb} \cdot \text{min})^{-1}$ ,  $\beta$  is  $1.4 (\text{min})^{-1}$ , and  $a_r$  is 12 percent.

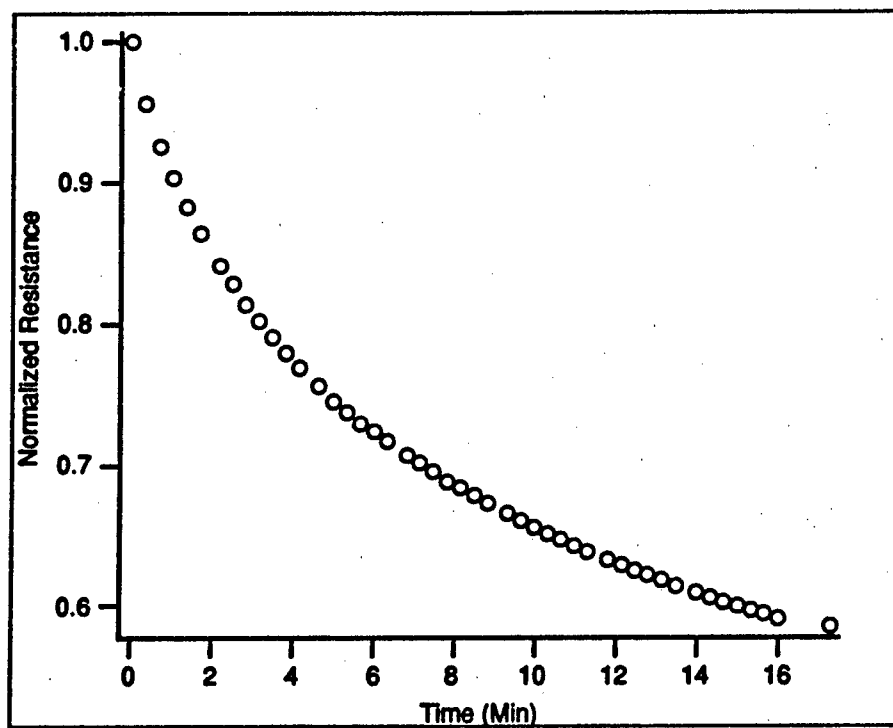


Figure 221. Adsorption Evaluation (200 ppb  $\text{NO}_2$ ).  $\alpha$  is  $5.4 \times 10^{-4} (\text{ppb} \cdot \text{min})^{-1}$ ,  $\beta$  is  $1.2 (\text{min})^{-1}$ , and  $a_r$  is 14 percent.

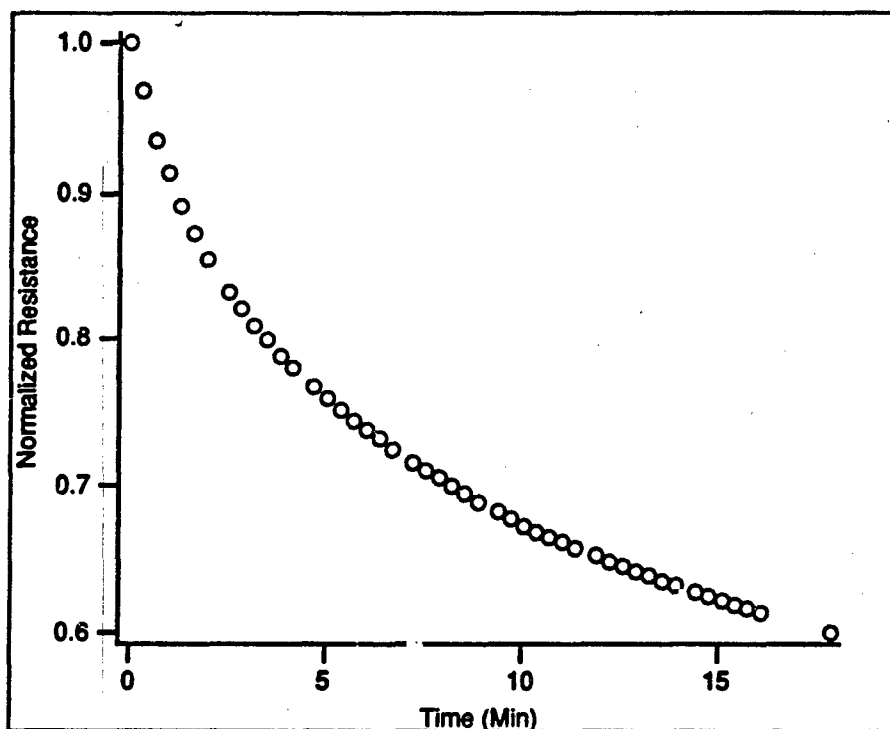


Figure 222. Adsorption Evaluation (200 ppb  $\text{NO}_2$ ).  $\alpha$  is  $3.8 \times 10^{-4} (\text{ppb} \cdot \text{min})^{-1}$ ,  $\beta$  is  $1.0 (\text{min})^{-1}$ , and  $a_r$  is 17 percent.

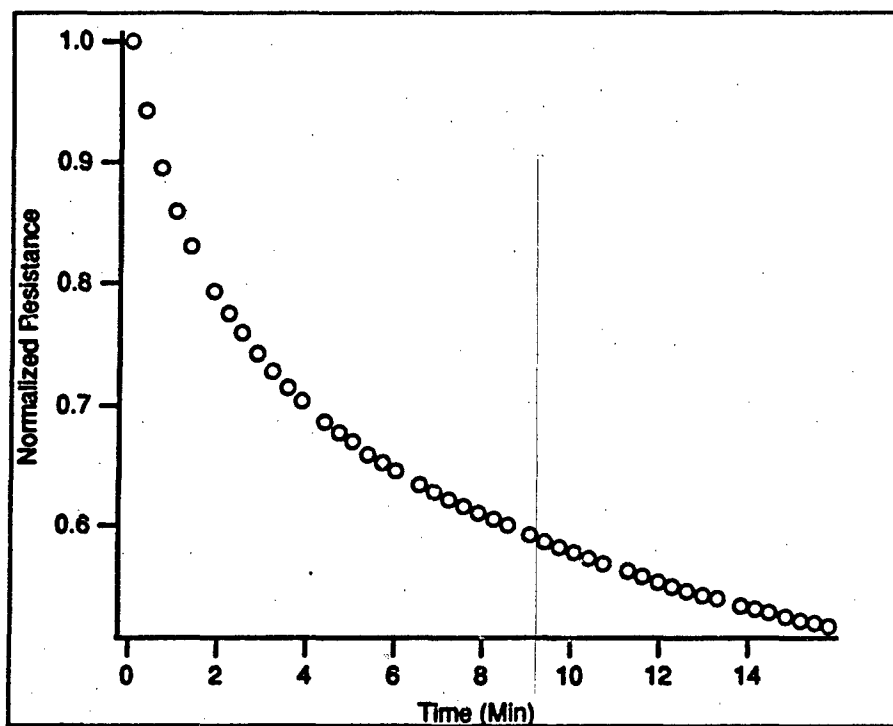


Figure 223. Adsorption Evaluation (400 ppb  $\text{NO}_2$ ).  $\alpha$  is  $3.1 \times 10^{-4} (\text{ppb} \cdot \text{min})^{-1}$ ,  $\beta$  is  $1.5 (\text{min})^{-1}$ , and  $\alpha_r$  is 14 percent.

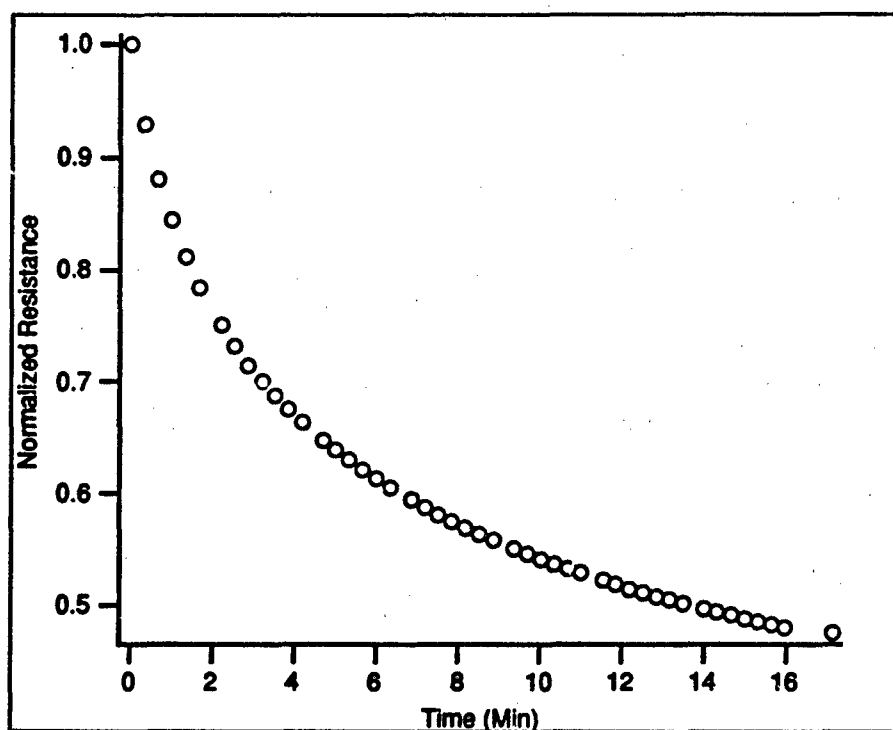


Figure 224. Adsorption Evaluation (400 ppb  $\text{NO}_2$ ).  $\alpha$  is  $3.1 \times 10^{-4} (\text{ppb} \cdot \text{min})^{-1}$ ,  $\beta$  is  $1.5 (\text{min})^{-1}$ , and  $\alpha_r$  is 15 percent.

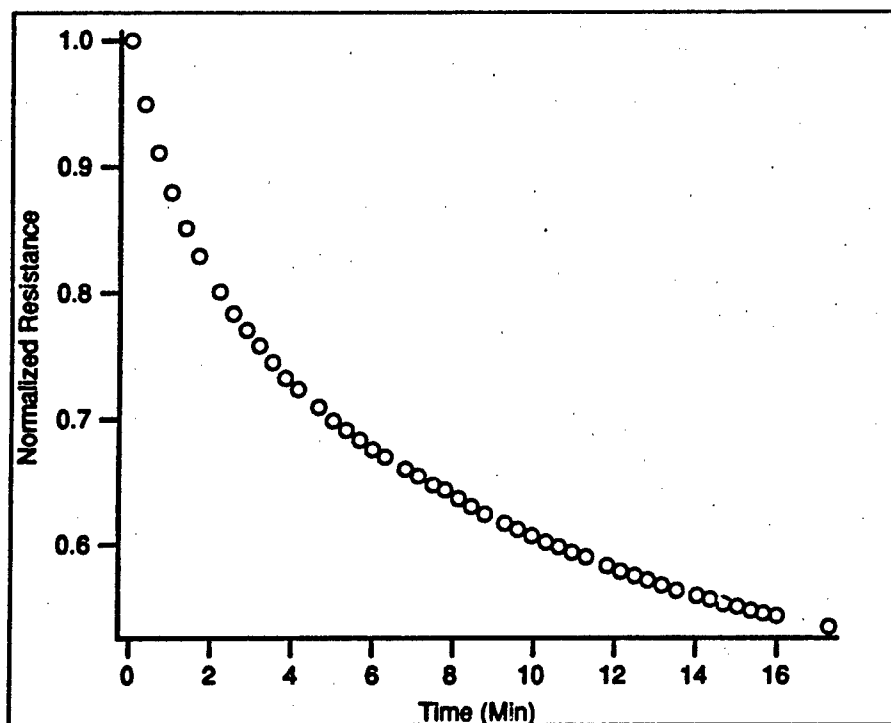


Figure 225. Adsorption Evaluation (400 ppb  $\text{NO}_2$ ).  $\alpha$  is  $2.7 \times 10^{-4} (\text{ppb} \cdot \text{min})^{-1}$ ,  $\beta$  is  $1.4 (\text{min})^{-1}$ , and  $a_r$  is 14 percent.

### *Bibliography*

1. O'Brien, M. J. "Detectors, Part II." *Modern Practice of Gas Chromatography*, edited by R. L. Grob, New York, NY: John Wiley & Sons, 1977.
2. McGonigle, E. J. "Drug Analysis Using Gas Chromatography." *Modern Practice of Gas Chromatography*, edited by R. L. Grob, New York, NY: John Wiley & Sons, 1977.
3. Rothbart, H. L. "Gas Chromatographic Analysis of Food." *Modern Practice of Gas Chromatography*, edited by R. L. Grob, New York, NY: John Wiley & Sons, 1977.
4. Grob, R. L. "Introduction." *Modern Practice of Gas Chromatography*, edited by R. L. Grob, New York, NY: John Wiley & Sons, 1977.
5. Aero Propulsion Laboratory. *Aspects of High-Resolution Gas Chromatography as Applied to the Analysis of Hydrocarbon Fuels and Other Complex Organic Molecules*. Report AFWAL-TR-84-2096 Vol. I. Wright-Patterson AFB, OH: Air Force Wright Aeronautical Laboratories, 1985.
6. Touchstone, J. C. and M. F. Dobbins. "Clinical Applications of Gas Chromatography." *Modern Practice of Gas Chromatography*, edited by R. L. Grob, New York, NY: John Wiley & Sons, 1977.
7. Kolevar, Jr., E. S. and J. M. Wiseman. "Interdigitated Gate Electrode Field Effect Transistor for the Selective Detection of Nitrogen Dioxide and Diisopropyl Methylphosphonate," *Analytical Chemistry*, 61:2355-2361 (November 1989).
8. Prantis, D. M. and M. E. Meyerhoff. "Continuous Monitoring of Ambient Ammonia with a Membrane-Electrode-Based Detector," *Analytical Chemistry*, 59:2345-2350 (October 1987).
9. McConnell, J. C. "Atmospheric Ammonia," *Journal of Geophysical Research*, 78:7812-7821 (November 1973).
10. Sax, N. I. and R. J. Lewis. *Hazardous Chemicals Desk Reference*. New York, NY: Van Nostrand Reinhold, 1987.
11. Terry, S. C. *A Gas Chromatography System Fabricated on a Silicon Wafer Using Integrated Circuit Technology*. PhD Dissertation, Stanford University, Stanford, CA, 1975 (75-25,618).
12. Terry, S. C., et al. "A Gas Chromatographic Air Analyzer Fabricated on a Silicon Wafer," *IEEE Transactions on Electron Devices*, ED-26:1880-1886 (December 1979).
13. Sherma, J. "Principles and Techniques." *CRC Handbook of Chromatography: General Data and Principles, Volume II*, edited by G. Zweig and J. Sherma, Boca Raton, FL: CRC Press, Inc., 1972.
14. Fritz, J. S. and G. H. Schenk. *Quantitative Analytical Chemistry* (Third Edition). Boston, MA: Allyn and Bacon, Inc., 1974.

15. Willett, J. E. *Gas Chromatography*. Chichester, England: John Wiley & Sons, 1987.
16. Grob, R. L. "Theory of Gas Chromatography." *Modern Practice of Gas Chromatography*, edited by R. L. Grob, New York, NY: John Wiley & Sons, 1977.
17. Fox, L. Handout distributed by Hewlett Packard Technical Representative in a briefing given to the Toxicology Branch of the Armstrong Aerospace Medical Research Laboratory, Wright-Patterson AFB, OH.
18. Littlewood, A. B. *Gas Chromatography: Principles, Techniques and Applications* (Second Edition). New York, NY: Academic Press, 1970.
19. Purnell, J. H. "The Correlation of Separating Power and Efficiency of Gas-chromatographic Columns," *Chemical Society Journal*, 1268-1274 (1960).
20. Nogare, S. D. I and R. S. Juvet, Jr. *Gas-Liquid Chromatography: Theory and Practice*. New York, NY: John Wiley & Sons, Inc., 1962.
21. Halász, I. and E. Heine. "Optimum Conditions in Gas Chromatographic Analysis." *Progress in Gas Chromatography 6*, edited by Purnell J. H., New York, NY: John Wiley & Sons, Inc., 1968.
22. Supina, W. R. "Columns and Column Selection in Gas Chromatography." *Modern Practice of Gas Chromatography*, edited by R. L. Grob, New York, NY: John Wiley & Sons, 1977.
23. Giddings, J. C., et al. "Plate Height in Gas Chromatography," *Analytical Chemistry*, 32:867-870 (June 1960).
24. Halliday, D. and R. Resnick. *Fundamentals of Physics* (Second Edition). New York, NY: John Wiley & Sons, Inc., 1981.
25. Golay, M. J. E. "Theory of Chromatography in Open and Coated Tubular Columns with Round and Rectangular Cross-Sections." *Gas Chromatography*, edited by D. H. Desty, New York, NY: Academic Press, Inc., 1958.
26. Yih, C. S. *Fluid Mechanics: A Concise Introduction to the Theory*. New York, NY: McGraw-Hill Book Company, 1969.
27. Kreyszig, E. *Advanced Engineering Mathematics* (Fifth Edition). New York, NY: John Wiley & Sons, 1983.
28. Sullivan, J. J. "Detectors, Part I." *Modern Practice of Gas Chromatography*, edited by R. L. Grob, New York, NY: John Wiley & Sons, 1977.
29. Pattison, J. B. *A Programmed Introduction to Gas-Liquid Chromatography*. London, England: Heyden & Son Ltd., 1969.
30. Jeffery, P. G. and P. J. Kipping. *Gas Analysis by Gas Chromatography*. New York, NY: The Macmillan Company, 1964.
31. Sapoff, M. and R. M. Oppenheim. "Theory and Application of Self-Heated Thermistors," *Proceedings of the IEEE*, 51:1292-1305 (October 1963).
32. Buhl, D. "New Approach to Understanding the Operation of Thermistors in Gas Chromatography," *Analytical Chemistry*, 40:715-726 (April 1968).

33. *Thermometrics Thermistors*. Product Catalog 183. 808 U.S. Highway 1, Edison, NJ, 1988.
34. Sternberg, J. C. "Detection Devices for Gas Chromatography." *Gas Chromatography*, edited by L. Fowler, London, England: Academic Press Inc., 1963.
35. Kelker, H., et al. "Rational Integration Procedures in Gas Chromatography Involving Novel Combinations of Instruments." *Gas Chromatography 1962*, edited by M. van Swaay, Washington, D.C.: Butterworth, Inc., 1962.
36. Sawicki, E., et al. "Flame Ionization Detector." *Methods of Air Sampling and Analysis*, (3rd Edition), edited by J. P. Lodge, Jr., Chelsea, MI: Lewis Publishers, Inc., 1989.
37. Leathard, D. A. and B. C. Shurlock. "Gas Chromatographic Identification." *Progress in Gas Chromatography 6*, edited by J. H. Purnell, New York, NY: John Wiley & Sons, Inc., 1968.
38. *Gas Chromatography Supplies Catalog*. Product Catalog G1. The Perkin-Elmer Corporation, Norwalk, CT, 1990.
39. Clement, R. E., et al. "Gas Chromatography," *Analytical Chemistry*, 60:279-294 (June 1988).
40. Lucklum, R., et al. "Quartz Microbalance Sensors for Gas Detection," *Sensors and Actuators A*, 25-27:705-710 (1991).
41. Ballantine, Jr., D. S. and H. Wohltjen. "Surface Acoustic Wave Devices for Chemical Analysis," *Analytical Chemistry*, 61:704A-715A (June 1989).
42. Grate, J. W., et al. "Determination of Partition Coefficients from Surface Acoustic Wave Vapor Sensor Responses and Correlation with Gas-Liquid Chromatographic Partition Coefficients," *Analytical Chemistry*, 60:869-875 (May 1988).
43. Kraus, J. D. *Electromagnetics*. New York, NY: McGraw-Hill Book Company, 1984.
44. Snow, A. W. and W. R. Barger. "Phthalocyanine Films in Chemical Sensors." *Phthalocyanines: Properties and Applications*, edited by C. C. Leznoff and A. B. P. Lever, New York, NY: VCH Publishers, Inc., 1989.
45. Wright, J. D. "Gas Adsorption on Phthalocyanines and its Effects on Electrical Properties," *Progress in Surface Science*, 31:1-60 (1989).
46. Kothny, E. L., et al. "Determination of Ammonia in the Atmosphere (Indophenol Method)." *Methods of Air Sampling and Analysis*, (3rd Edition), edited by J. P. Lodge, Jr., Chelsea, MI: Lewis Publishers, Inc., 1989.
47. Possanzini, M. and V. Di Palo. "Determination of Atmospheric Ammonia as M-Toluamide by Denuder Sampling and HPLC-UV Detection," *Chromatographia*, 28:27-30 (July 1989).
48. Fox, D. L. "Air Pollution," *Analytical Chemistry*, 63:292R-301R (June 1991).
49. Kim, H. J. "Analysis of Nitrogen Dioxide in Ambient Air by Ion-Exclusion Chromatography with Electrochemical Detection," *Journal of Chromatography*, 509:466-470 (1990).

50. Saltzman, B. E., et al. "Determination of Nitrogen Dioxide Content of the Atmosphere (Griess-Saltzman Reaction)." *Methods of Air Sampling and Analysis*, (3rd Edition), edited by J. P. Lodge, Jr., Chelsea, MI: Lewis Publishers, Inc., 1989.
51. Punkkinen, R. K. "Automatic Colorimetric Detector for Traces of Nitrogen Dioxide in Air," *Review of Scientific Instruments*, 59:163-166 (January 1988).
52. Levaggi, D. A., et al. "Continuous Monitoring of Atmospheric Nitric Oxide and Nitrogen Dioxide by Chemiluminescence." *Methods of Air Sampling and Analysis*, (3rd Edition), edited by J. P. Lodge, Jr., Chelsea, MI: Lewis Publishers, Inc., 1989.
53. Joseph, D. W. and C. W. Spicer. "Chemiluminescence Method for Atmospheric Monitoring of Nitric Acid and Nitrogen Oxides," *Analytical Chemistry*, 50:1400-1403 (August 1978).
54. Levaggi, D. A., et al. "Analysis for Atmospheric Nitrogen Dioxide (24-H Average)." *Methods of Air Sampling and Analysis*, (3rd Edition), edited by J. P. Lodge, Jr., Chelsea, MI: Lewis Publishers, Inc., 1989.
55. Burkhardt, M. R., et al. "Gas Chromatographic Method for Measuring Nitrogen Dioxide and Peroxyacetyl Nitrate in Air without Compressed Gas Cylinders," *Analytical Chemistry*, 60:816-819 (April 1988).
56. Ko, W. H. and J. T. Suminto. "Semiconductor Integrated Circuit Technology and Micromachining." *Sensors: A Comprehensive Survey, Volume 1: Fundamentals and General Aspects*, edited by W. Gopel, et al., New York, NY: VCH Publishers, Inc., 1989.
57. Van de Pol, F. C. M., et al. "A Thermo-Pneumatic Actuation Principle for a Microminiature Pump and Other Micromechanical Devices," *Sensors and Actuators*, 17:139-143 (May 1989).
58. Van de Pol, F. C. M., et al. "A Thermopneumatic Micropump Based on Micro-Engineering Techniques," *Sensors and Actuators*, A21-A23:198-202 (1990).
59. Esashi, M., et al. "Normally Close Microvalve and Micropump Fabricated on a Silicon Wafer." *Micro Electro Mechanical Systems: An Investigation of Micro Structures, Sensors, Actuators, Machines and Robots*. 29-34. Piscataway, NJ: IEEE Press, 1989.
60. Studt, T. "Micromachines: Miniature Devices Come of Age," *R & D Magazine*, 32:36-40 (December 1990).
61. Bryzek, J., et al. "Silicon's Synthesis: Sensors to Systems," *InTech*, 36:40-44 (January 1989).
62. Shoji, S., et al. "Prototype Miniature Blood Gas Analyser Fabricated on a Silicon Wafer," *Sensors and Actuators*, 14:101-107 (June 1988).
63. Mehregany, M., et al. "Micro Gears and Turbines Etched from Silicon," *Sensors and Actuators*, 12:341-348 (November 1987).
64. Mehregany, M., et al. "Integrated Fabrication of Polysilicon Mechanisms," *IEEE Transactions on Electron Devices*, 35:719-723 (June 1988).

65. Fan, L. S., et al. "Integrated Movable Micromechanical Structures for Sensors and Actuators," *IEEE Transactions on Electron Devices*, 35:724-730 (June 1988).
66. Muller, R. S. and R. M. White. "Research on Silicon-Based Microsensors," *The Microelectronics Innovation and Computer Research Opportunities MICRO Program*, 1987-88:87-89 (August 1989).
67. Johnson, R. G. and R. E. Higashi. "A Highly Sensitive Silicon Chip Microtransducer for Air Flow and Differential Pressure Sensing Applications," *Sensors and Actuators*, 11:63-72 (January 1987).
68. Petersen, K. E. and J. Brown. "High-Precision, High-Performance Mass-Flow Sensor with Integrated Laminar Flow Micro-Channels." *Transducers '85: International Conference on Solid-State Sensors and Actuators*. 361-363. Piscataway, NJ: IEEE Press, 1985.
69. Muller, R. S. "Compatible Circuits for Integrated Sensors," *The Microelectronics Innovation and Computer Research Opportunities MICRO Program*, 1987-88:85-86 (August 1989).
70. Bergveld, P. "Sensors and Actuators, Twente," *Sensors and Actuators*, 17:3-26 (May 1989).
71. Petersen, K. E. "Silicon Sensor Technologies." *International Electron Devices Meeting*. 2-7. New York, NY: IEEE Press, 1985.
72. Buser, R. A. and N. F. De Rooij. "Resonant Silicon Structures," *Sensors and Actuators*, 17:145-154 (May 1989).
73. Hök, B. "Micromechanics and Micromachining of Semiconductor Sensors." *Acta Polytechnica Scandinavica, Electrical Engineering Series No. 63, Microelectronics: Progress in Sensor Technology*, edited by Riitta Paananen and Markku Ylilammi, Helsinki: Technical Research Center of Finland, 1988.
74. Riethmuller, W. and W. Benecke. "Thermally Excited Silicon Microactuators," *IEEE Transactions on Electron Devices*, 35:758-763 (June 1988).
75. Fujita, H. and A. Omodaka. "The Fabrication of an Electrostatic Linear Actuator by Silicon Micromachining," *IEEE Transactions on Electron Devices*, 35:731-734 (June 1988).
76. Backlund, Y., et al. "Micromachining of Silicon for Thermal and Position-Sensitive Nuclear Detector Applications," *Nuclear Instruments and Methods in Physics Research*, 279:555-559 (July 1989).
77. Chi-Lung, K., et al. "A Micropipe Fabrication Process." *Micro Electro Mechanical Systems: An Investigation of Micro Structures, Sensors, Actuators, Machines and Robots*. 80-85. New York, NY: IEEE Press, 1991.
78. Parmeswaran, M., et al. "Fabrication of Microbridges in Standard Complementary Metal Oxide Semiconductor Technology," *Canadian Journal of Physics*, 67:184-189 (April 1989).
79. Parmeswaran, M., et al. "A New Approach for the Fabrication of Micromechanical Structures," *Sensors and Actuators*, 19:289-307 (September 1989).

80. Trimmer, W. S. N. "Microrobots and Micromechanical Systems," *Sensors and Actuators*, 19:267-287 (September 1989).
81. Hök, B. "Vibration Analysis of Micromechanical Elements," *Sensors and Actuators*, 8:235-243 (November 1985).
82. Bart, S. F., et al. "Design Considerations for Micromachined Electric Actuators," *Sensors and Actuators*, 14:269-292 (July 1988).
83. Vaganov, V. I. "Construction Problems in Sensors," *Sensors and Actuators A*, 28:161-172 (January 1991).
84. Muller, R. S. "Microdynamics," *Sensors and Actuators A*, 21-23:1-8 (1990).
85. Weihs, T. P., et al. "Mechanical Deflection of Cantilever Microbeams: A New Technique for Testing the Mechanical Properties of Thin Films," *Journal of Materials Research*, 3:931-942 (September 1989).
86. Ghandi, S. K. *VLSI Fabrication Principles*. New York, NY: John Wiley & Sons, 1983.
87. Till, W. C. and J. T. Luxon. *Integrated Circuits: Materials, Devices, and Fabrication*. Englewood Cliffs, NJ: Prentice-Hall, Inc., 1982.
88. Delapierre, G. "Micro-Machining: A Survey of the Most Commonly Used Processes," *Sensors and Actuators*, 17:123-138 (May 1989).
89. Sze, S. M. *Semiconductor Devices: Physics and Technology*. New York, NY: John Wiley & Sons, 1985.
90. Rubye, W. A., Environmental Sciences Group. Personal interview. University of Dayton Research Institute, Dayton, OH, 28 November 1989.
91. Robbins, H. and B. Schwartz. "Chemical Etching of Silicon: II. The System HF, HNO<sub>3</sub>, H<sub>2</sub>O, and HC<sub>2</sub>H<sub>3</sub>O<sub>2</sub>," *Journal of the Electrochemical Society*, 107:108-111 (February 1960).
92. Robbins, H. and B. Schwartz. "Chemical Etching of Silicon: I. The System HF, HNO<sub>3</sub>, and H<sub>2</sub>O," *Journal of the Electrochemical Society*, 106:505-508 (June 1959).
93. Schwartz, B. and H. Robbins. "Chemical Etching of Silicon: III. A Temperature Study in the Acid System," *Journal of the Electrochemical Society*, 108:365-372 (April 1961).
94. Schwartz, B. and H. Robbins. "Chemical Etching of Silicon: IV. Etching Technology," *Journal of the Electrochemical Society*, 123:1903-1909 (December 1976).
95. Lee, D. B. "Anisotropic Etching of Silicon," *Journal of Applied Physics*, 40:4569-4574 (October 1969).
96. Allen, D. M. and I. A. Routledge. "Anisotropic Etching of Silicon: A Model Diffusion-Controlled Reaction," *IEEE Proceedings*, 130:49-56 (April 1983).
97. Shimura, F. *Semiconductor Silicon Crystal Technology*. San Diego, CA: Academic Press, Inc., 1989.

98. Kolesar, Jr., E. S. and M. W. Carver. "Deep Anisotropic Etching of Tapered Channels in (110)-Oriented Silicon," *Chemistry of Materials*, 1:634-639 (November 1989).
99. Kendall, D. L. and G. R. de Guel. "Orientations of the Third Kind: The Coming of Age of (110) Silicon." *Micromachining and Micropackaging of Transducers*, edited by Clifford D. Fung, et al., The Netherlands: Elsevier Science Publishers, 1985.
100. Bean, K. "Anisotropic Etching of Silicon," *IEEE Transactions on Electron Devices*, ED-25:1185-1193 (October 1978).
101. Yam, J. D. I., et al. "An Investigation of the Anisotropic Etching of (100) Silicon Using Cesium Hydroxide," *Sensors and Actuators A*, 29:121-126 (April 1991).
102. Clark, Jr., L. D. and D. J. Edell. "KOH:H<sub>2</sub>O Etching of (110) Si, (111) Si, SiO<sub>2</sub>, and Ta: An Experimental Study." *Micro Robots and Teleoperators Workshop: An Investigation of Micromechanical Structures, Actuators and Sensors*. (Reprint) 1-6. Hyannis, MA: IEEE Press, 1987.
103. Van Zant, P. *Microchip Fabrication: A Practical Guide to Semiconductor Processing*. New York, NY: McGraw-Hill, Inc., 1990.
104. Wallis, G. and D. I. Pomerantz. "Field Assisted Glass-Metal Sealing," *Journal of Applied Physics*, 40:3946-3949 (September 1969).
105. United States Patent Office. *Anodic Bonding*. Patent No. 3,397,278. Washington, D. C.: Government Printing Office, 1968.
106. Kanda, Y., et al. "The Mechanism of Field-assisted Silicon-Glass Bonding," *Sensors and Actuators*, A21-A23:939-943 (1990).
107. Ko, W. H., et al. "Bonding Techniques for Microsensors." *Micromachining and Micropackaging of Transducers*, edited by Clifford D. Fung, et al., The Netherlands: Elsevier Science Publishers, 1985.
108. DeNee, P. B. "Low Energy Metal-Glass Bonding," *Journal of Applied Physics*, 40:5396-5397 (1969).
109. Hanneborg, A. "Silicon Wafer Bonding Techniques for Assembly of Micromechanical Elements." *Micro Electro Mechanical Systems: An Investigation of Micro Structures, Sensors, Actuators, Machines and Robots*. 92-98. Nara, Japan: IEEE Press, 1991.
110. *Tempax Boro-Glass*. Product Information Sheet. Schott America, 3 Odell Plaza, Yonkers, NY.
111. J. McCulloch, Technical Support Representative. Telephone interview. Supelco, Inc., Supelco Park, Bellefonte, PA, 23 April 1990.
112. Vary, E. M. *Investigation of Phthalocyanines Using Gas Chromatography*. PhD Dissertation, University of California, Los Angeles, CA, 1966.
113. Schuetzle, D. and R. Hammerley. *Fundamentals and Applications of Chemical Sensors*, ACS Symposium Series 309. Washington, D.C.: American Chemical Society, 1986.
114. Greene, S. A. and H. Pust. "The Determination of Heats of Adsorption by Gas-Solid Chromatography," *Journal of Physical Chemistry*, 62:55-58 (January 1958).

115. United States Patent Office. *Miniature Gas Chromatograph Apparatus*. Patent No. 4,474,889. Washington, D. C.: Government Printing Office, 1984.
116. Wiseman, Capt J. M. *Investigation of the Impedance Modulation of Thin Films with a Chemically Sensitive Field Effect Transistor*. MS Thesis, AFIT/GE/ENG/88D-61, School of Engineering, Air Force Institute of Technology (AU), Wright-Patterson AFB, OH, December 1988.
117. Jenkins, Capt T. J. *Evaluation of Doped Phthalocyanine and a Chemically Sensitive Field Effect Transistor for Detecting Nitrogen Dioxide*. MS Thesis, AFIT/GE/ENG/89D-18, School of Engineering, Air Force Institute of Technology (AU), Wright-Patterson AFB, OH, December 1989.
118. Weast, R. C. "Viscosity and Diffusivity Tables." *CRC Handbook of Chemistry and Physics*, (56th Edition), edited by R. C. Weast, Cleveland, OH: CRC Press, 1975.
119. Valco Instruments Co. Inc.. Product Catalog Rev. 9/89. P.O. Box 55603, Houston, TX, 1989.
120. Jerman, J. H. and J. W. Knutti. "Silicon Sensors for Gas Flow and Thermal Measurements," *Sensors*, 5-13 (August 1987).
121. Howe, Capt C. P. *Characterizing the Sensitivity, Selectivity, and Reversibility of the Metal-Doped Phthalocyanine Thin-Films used with the Interdigitated Gate Electrode Field-Effect Transistor (IGFET) to Detect Organophosphorus Compounds and Nitrogen Dioxide*. MS Thesis, AFIT/GE/ENG/91D-26, School of Engineering, Air Force Institute of Technology (AU), Wright-Patterson AFB, OH, December 1991.
122. Moser, F. and A. Thomas. *The Phthalocyanines, Vol II: Applications*. Boca Raton, FL: CRC Press, Inc., 1983.
123. Weast, R. C. "Thermal Conductivity of Gases." *CRC Handbook of Chemistry and Physics*, (56th Edition), edited by R. C. Weast, Cleveland, OH: CRC Press, 1975.
124. *Waycoat Negative Photoresist*. Technical Information Pamphlet MI 1311/0675. Olin Hunt Specialty Products, Inc., 5 Garret Mountain Plaza, West Paterson, NJ, Undated.
125. Adamson, A. W. *Physical Chemistry of Surfaces*. New York, NY: John Wiley & Sons, Inc., 1990.
126. Adamson, A. W. *A Textbook of Physical Chemistry*. New York, NY: Academic Press, 1979.
127. Moser, F. and A. Thomas. *Phthalocyanine Compounds*. New York: Reinhold Publishing, Inc., 1963.
128. Lever, A. "The Phthalocyanines." *Advances in Inorganic Chemistry and Radiochemistry*, edited by H. Emeleus and A. Sharp, New York, NY: Academic Press, Inc., 1965.
129. Moser, F. and A. Thomas. *The Phthalocyanines, Vol I: Properties*. Boca Raton, FL: CRC Press, Inc., 1983.

130. Garrett, C. "Organic Semiconductors." *Semiconductors*, edited by N. Hannay, New York, NY: Reinhold Publishing Corp., 1959.
131. Schechtman, B. H. *Photoemission and Optical Studies of Organic Solids: Phthalocyanines and Porphyrins*. PhD Dissertation, Stanford University, Stanford, CA, 1968 (69-14,014).
132. Westgate, C. R. *Transient Current Measurements in Phthalocyanine, an Organic Semiconductor*. PhD Dissertation, Princeton University, Princeton, NJ, 1966 (66-9652).
133. Heilmeyer, G. H. *Semiconduction in Phthalocyanine: A Study in Organic Semiconduction*. PhD Dissertation, Princeton University, Princeton, NJ, 1962 (63-526).
134. Rona, M. *A Measurement of the Hall Effect in Metal Free Phthalocyanine*. PhD Dissertation, Princeton University, Princeton, NJ, 1966 (67-5747).
135. Wright, J. *Molecular Crystals*. Cambridge: Cambridge University Press, 1987.
136. Inokuchi, H. and H. Akamutu. "Electrical Conductivity of Organic Semiconductors." *Solid State Physics: Advances in Research and Applications*, edited by F. Seitz and D. Turnbull, New York, NY: Academic Press, Inc., 1961.
137. Gutmann, F., et al. *Organic Semiconductors Part B*. Malabar, FL: Robert E. Kreiger Publishing Co., 1983.
138. Bolto, B. "Semiconducting Organic Polymers Containing Metal Groups." *Organic Semiconducting Polymers*, edited by J. Katon, New York, NY: Marcel Dekker, Inc., 1968.
139. Gutmann, F. and L. Lyons. *Organic Semiconductors*. New York, NY: John Wiley and Sons, Inc., 1967.
140. Simon, J. and J. Andre. "Photoelectrical Properties and Solar Cells." *Molecular Semiconductors*, edited by J. Lehn and C. Rees, Berlin: Springer-Verlag, 1985.
141. Ruihua, W. and T. A. Jones. "The Characteristics of Gas-Sensitive Multilayer Devices Based on Lead Phthalocyanine," *Sensors and Actuators B*, 12:33-42 (1990).
142. *Sadtler Index of Infrared Spectra*. Technical Report. Sadtler Research Laboratories, Inc., 1967.
143. Ashida, M., et al. "Unit Cell Metastable-form Constants of Various Phthalocyanines," *Bulletin of the Chemical Society of Japan*, 39:2616-2624 (December 1966).
144. Wolkenstein, T. *Electronic Processes on Semiconductor Surfaces during Chemisorption*. New York, NY: Consultants Bureau, 1990.
145. Borland International, Inc. *Turbo Pascal Reference Manual*. Scotts Valley, CA: Borland International, Inc., 1985.
146. Press, W. H., et al. *Numerical Recipes Pascal Diskette V2.0*. Cambridge: Cambridge University Press, 1989.
147. Press, W. H., et al. *Numerical Recipes in C: The Art of Scientific Computing*. Cambridge: Cambridge University Press, 1988.

148. Bevington, P. R. *Data Reduction and Error Analysis for the Physical Sciences*. New York, NY: McGraw-Hill, Inc., 1992.
149. Boukamp, B. A. "A Nonlinear Least Squares Fit Procedure for Analysis of Immitance Data of Electrochemical Systems," *Solid State Ionics*, 20:31-44 (1986).
150. Wolfram, S. *Mathematica: A System for Doing Mathematics by Computer*. Redwood City, CA: Addison-Wesley Publishing Company, Inc., 1988.

### **Vita**

Captain Rocky R. Reston was born on September 8, 1962 in Cheyenne, Wyoming, the son of Beverly E. Reston and Russell T. Reston. He graduated from Air Academy High School in 1980, and immediately entered the United States Air Force Academy where he graduated in 1984 with a Bachelor of Science in Electrical Engineering and a commission as a second lieutenant in the United States Air Force. Upon graduation, he was assigned to the Radar Test Facility of the 4484<sup>th</sup> Test Squadron, Tyndall Air Force Base, Florida as an instrumentation engineer. In June 1987, he entered the School of Engineering, Air Force Institute of Technology, and graduated in December 1988 with a Master of Science in Electrical Engineering. He was then selected for the doctoral program of the School of Engineering, Air Force Institute of Technology in January 1989. Currently, he is assigned to the Solid State Electronics Directorate of Wright Laboratories, Wright-Patterson Air Force Base, Ohio as an electronic device processing engineer.

Permanent address: 5125 Sideburn Rd.  
Fairfax, Virginia 22032

# REPORT DOCUMENTATION PAGE

Form Approved  
OMB No. 0704-0188

Public reporting burden for this collection of information is estimated to average 1 hour per response, including the time for reviewing instructions, searching existing data sources, gathering and maintaining the data needed, and completing and reviewing the collection of information. Send comments regarding this burden estimate or any other aspect of this collection of information, including suggestions for reducing this burden, to Washington Headquarters Services, Directorate for Information Operations and Reports, 1215 Jefferson Davis Highway, Suite 1204, Arlington, VA 22202-4302, and to the Office of Management and Budget, Paperwork Reduction Project (0704-0188), Washington, DC 20503.

1. AGENCY USE ONLY (Leave blank)		2. REPORT DATE March, 1993	3. REPORT TYPE AND DATES COVERED PHD DISSERTATION
4. TITLE AND SUBTITLE Design and Performance Evaluation of a Gas Chromatograph Micromachined in a Single Crystal Silicon Substrate			5. FUNDING NUMBERS
6. AUTHOR(S) Rocky Russell Reston			
7. PERFORMING ORGANIZATION NAME(S) AND ADDRESS(ES) AFIT/ENG Wright-Patterson AFB, OH 45433			8. PERFORMING ORGANIZATION REPORT NUMBER  AFIT/DS/ENG/93M-01
9. SPONSORING/MONITORING AGENCY NAME(S) AND ADDRESS(ES) AL/OEDR Brooks AFB, TX 78235			10. SPONSORING/MONITORING AGENCY REPORT NUMBER
11. SUPPLEMENTARY NOTES			
12a. DISTRIBUTION/AVAILABILITY STATEMENT  Approved for public release; Distribution Unlimited			12b. DISTRIBUTION CODE
13. ABSTRACT (Maximum 200 words)  This investigation designed and developed a miniature gas chromatograph (GC) using silicon micromachining techniques. The GC is composed of a miniature sample injector (10 µl sample loop); a 0.9 m long, rectangular-shaped (300 µm width and 10 µm height) capillary column coated with a 0.2 µm thick copper phthalocyanine (CuPc) stationary phase; and a dual-detector scheme incorporating a CuPc-coated chemiresistor and a 125 µm diameter thermal conductivity detector bead. Micromachining was employed to fabricate the sample injector interface, the GC column, and the dual-detector cavity. A novel processing technique was developed to sublime the CuPc stationary phase coating on the GC column walls. The miniature GC system has been used to separate parts-per-million ammonia and nitrogen dioxide concentrations in less than 30 minutes (10 µl sample injected at 40 psi). A secondary discovery was the heat of adsorption of nitrogen dioxide (0.38 eV) on a polycrystalline CuPc film (0.2 µm thick). This research demonstrated the utilization of a miniature GC to investigate the adsorptive properties of thin films. Also, the time-domain performance model of the miniature GC developed in this investigation will facilitate the optimization of future miniature GC designs.			
14. SUBJECT TERMS GAS CHROMATOGRAPH, MICROMACHINING, CHEMIREISTOR, CUPC, COPPER PHTHALOCYANINE, GC, ANODIC BONDING, SILICON, HEAT OF ADSORPTION, THIN FILM, AMMONIA, NITROGEN DIOXIDE			15. NUMBER OF PAGES 363
			16. PRICE CODE
17. SECURITY CLASSIFICATION OF REPORT UNCLASSIFIED	18. SECURITY CLASSIFICATION OF THIS PAGE UNCLASSIFIED	19. SECURITY CLASSIFICATION OF ABSTRACT UNCLASSIFIED	20. LIMITATION OF ABSTRACT UL